School of Earth and Planetary Sciences

Listening Through Rock Salt: Quantifying Petrofabrics and Seismic Velocity Anisotropy of Evaporites to Improve Seismic Imaging

Johanna Heeb

0000-0003-3310-2583

This thesis is presented for the Collaborative Degree of
Doctor of Philosophy
of
Curtin University
and
University of Aberdeen

September 2021

DECLARATION

The thesis has been composed by me and the work presented is my own. All quotations have been distinguished as quotations and the sources of information specifically acknowledged. If any results were obtained partly in association with others, the nature and extent of this help, if substantial, was especially acknowledged.

To the best of my knowledge and belief this thesis contains no material previously published by any other person except where due acknowledgement has been made.

This thesis contains no material which has been accepted for the award of any other degree or diploma in any university.

This thesis has been written as part of the Collaborative Doctoral Programme undertaken at Curtin University, Perth, Australia, and University of Aberdeen, Scotland, UK.

Signature: _____ Date: 31st of August 2021

Johanna Heeb

ACKNOWLEDGEMENT OF COUNTRY

I acknowledge the Traditional Custodians of this land on which I live, work and study, the Whadjuk people of the Noongar nation. I recognise the contributions of the Whadjuk people of the Noongar nation as the first scientists of this land. I am respectful of their Elder past, present and emerging, and acknowledge they are the keepers of the local traditional Whadjuk culture, stories, sites, and natural environments in this region.

The Covid-19 crisis that broke out in 2019 has had critical impact on this PhD project and my life.

I want to acknowledge and pay my respect to the victims of the pandemic and the people whose lives were or still are in danger or have lost relatives and friends.

ABSTRACT

Evaporitic deposits and rock salt structures are part of many sedimentary basins worldwide and therefore often present on seismic reflection surveys. In seismic imaging, salt deposits are generally treated as homogenous bodies in regards to internal structure and composition (e.g., as halite, which is isotropic). However, in reality evaporitic rock salt formations are polymineralic, commonly incorporating anisotropic minerals such as anhydrite and gypsum, are structurally heterogeneous, and the minerals often display fabrics (crystallographic and shape preferred orientations; CPO and SPO, respectively). Yet, quantitative microstructural characterisation of natural polymineralic evaporites is understudied, and published seismic velocity data on these rock types are scarce. It is also unknown to what extent mineralogical, microstructural, and textural inhomogeneities and anisotropies contribute to P-and S-wave velocity anisotropy in rock salt. Especially the effects of grain boundaries, where grains in a rock have a shape preferred orientation (SPO), are not understood.

A new MATLAB^{TM} toolbox is presented for **G**rain **B**oundary **Pa**ttern **Q**uantification (GBPaQ) for automated quantification of SPO in 2D for any crystalline solid. The functionality of GBPaQ is showcased using a range of natural and simulated (from full-field viscoplasticity models) grain boundary patterns that have been incrementally deformed. Results are visualised as rose diagrams for grain fitted-ellipse axes, grain boundary segment orientations, and grain boundary segment intercept density. These provide a more complete, detailed pattern anisotropy quantification for single- and two-phase materials during progressive coaxial and non-coaxial deformation.

Two suites of natural evaporitic samples - Zechstein anhydrite (cores from the North Sea) and anhydrite + gypsum (outcrop samples from Òdena, South Pyrenean foreland basin, Spain) - are characterised for crystallographic preferred orientation (CPO, via electron backscatter diffraction EBSD) and SPO (via GBPaQ). The results are set into the context of measured ultrasonic wave velocity (V_P and V_S). The findings show a clear difference between the two sample types, with lower V_P and V_S velocities for Òdena samples. The V_P velocities are also slower than polycrystalline evaporite aggregate V_P values found in the literature. The observed and measured CPO, SPO, and gypsum filled veins in Òdena samples are likely influencing seismic wave velocity and thus, may cause seismic anisotropy.

Finally, the impact of stress on the hydration of polycrystalline anhydrite is investigated via triaxial deformation experiments on Òdena evaporites using a triaxial deformation apparatus, with post-experiment microstructural characterisation. Stress-strain data reveal that samples that underwent long steady state differential compaction are weaker. The microstructural analysis of samples shows that there is a strong temporal and spatial connection between the geometry, distribution, and evolution of fractures and hydration. The newly-formed gypsum locally shows a systematic crystallographic preferred orientation, likely due to selective inheritance of crystal orientations from favourably oriented wall-rock anhydrite grains, which minimizes the free energy necessary for nucleation under stress. A sequence is suggested for rapid hydration under stress that requires the development of fractures accompanied by localised hydration. Importantly, hydration of anhydrite to gypsum was achieved under triaxial stress over timescales of hours.

ACKNOWLEDGEMENTS

I am immensely grateful to my supervisors Nick Timms, David Healy, Chris Elders and Enrique Gomez-Rivas for the incredible opportunity to work on this project and for their invaluable support, expertise, and the time they invested to assist in the creation of this work.

I also want to thank the Aberdeen-Curtin Alliance for creating this unique opportunity to study, learn from and do research with experts at Curtin University and University of Aberdeen. The experiences gained from working and living in both places are invaluable to me.

This thesis benefited considerably from help of staff from various facilities around the world. Thanks to Colin W. Taylor from University of Aberdeen, John Still and ACEMAC Nano Scale Electron Microscopy and Analysis Facility from the University of Aberdeen, and Elaine Miller and the John de Laeter Research Centre, Curtin University.

The acquisition of sample material was essential for this project. I thank the following people and organisations who made this project possible by offering their help, information and most importantly by providing sample material: North Sea Core and Henk Kombrink, Roberto Rizzo, J.D. Martín-Martín, F. Ortí, and ICL Boulby and Phil Welsh.

I want to dedicate this thesis to my grandparents Erika Heeb and Günter Zantow. For everything they have been.

And to my parents Walter and Ilona, my sister Christina, and my nephew Aike, for their unconditional love and support.

I am especially thankful to

Karin Meierhöfer, who was and is always there for me.

&

Jolien Linckens, for her invaluable advice and friendship.

To my new friends from Perth and Aberdeen and my old friends from home, who have been an irreplaceable part of the last years: thank you for sharing this experience, your support and most valuable friendship.

Stephanie D. Montalvo Delgado,

Paulina A. Dzianach, Hannah Vogel, Hilary Chen,

Monica Gomez, Jessica Pugsley, Maria Del Pilar Di Martino Perez,

Silvia Volante, Vitor Rodrigues Barrotte, Eleanore Blureau,

Laura Fuchs, Wilken Verleger, Andrea Luft, Julia Krullikovski,

David Fox, Sean Makin, Riley Rohrer,

Isabel Zutterkirch, Taryn Scharf, Cilva Joseph,

Raiza R. Quintero Mendez

STATEMENT OF ATTRIBUTION

Johanna Heeb

Chapter 1: Literature research, planning, and writing.

Chapter 2: Development of the method concept, literature research, development of test scenarios and automation concept. Processing of results. Writing and preparation of the manuscript and development of visual presentation of results. Concept and preparation of Figures 2.3-end.

Chapter 3: Development of test scenarios and literature research. Processing of results. Writing and preparation of the manuscript and development of visual presentation of results. Conceptualisation and preparation of the Figures.

Chapter 4: Organisation, acquisition, preparation, and management of sample material. Sample preparation and analysis. Processing of results. Literature research. Writing and preparation of the manuscript. Conceptualisation and preparation of all Figures, except Figure 4.1.

Chapter 5: Design, planning and execution of laboratory experiments. Literature research. Preparation and management of samples and acquisition of part of the samples. Analysis and processing of the results. Writing and preparation of the manuscript. Conceptualisation and preparation of Figures.

Chapter 6: Conceptualisation planning and writing. Concept and preparation of Figure 6.1.

Nick Timms

Chapter 1: Assistance with structure of the manuscript. Concept and construction of Figure 1.2.

Chapter 2: Assistance in project development and design. Assistance with manuscript preparation and editing.

Chapter 3: Assistance with manuscript preparation and editing.

Chapter 4: Assistance with project development and design. Assistance with manuscript and figure preparation and editing.

Chapter 5: Assistance with manuscript and figure preparation and editing.

Chapter 6: Assistance with manuscript preparation and editing.

Signature: _____

Nick Timms

Dave Healy

Chapter 1: Assistance with editing the manuscript.

Chapter 2: Assistance in project development and design. Programming of the method as automated toolbox. Assistance with editing the manuscript.

Chapter 3: Assistance with editing the manuscript.

Chapter 4: Assistance with project development and design. Assisted with sample analysis and processing of results. Assistance with manuscript editing.

Chapter 5: Assisted with project management and design. Oversaw planning and running of laboratory experiments.

Chapter 6: Assisted with editing the manuscript.

Signature: _____

Dave Healy

Enrique Gomez-Rivas

Chapter 1: Assisted with editing the manuscript.

Chapter 2: Running of numerical simulations. Assistance with editing the manuscript.

Chapter 3: Assistance with project development and design. Running of simulations. Assistance with editing the manuscript.

Chapter 4: Acquisition and preparation of part of the samples. Assistance with editing the manuscript.

Chapter 5: Acquisition and preparation of a part of the samples. Assistance with editing the manuscript.

Chapter 6: Assisted with editing the manuscript.

Signature: _____

Enrique Gomez-Rivas

Chris Elders Assisted with the editing of all chapters and planning of the thesis.

Signature: _____

Chris Elders

TABLE OF CONTENTS

LIST OF FIGURES

CHAPTER 1

CHAPTER 2

CHAPTER 3

CHAPTER 6

LIST OF TABLES

CHAPTER 1

CHAPTER 2

CHAPTER 3

CHAPTER 4

CHAPTER 5

GLOSSARY

BSE	Backscatter electron
CPO	Crystallographic preferred orientation
DTNNM	Delaunay triangulation nearest neighbour method
EBSD	Electron backscatter diffraction
EDS	Energy dispersive spectroscopy
ECD	Equivalent circular diameter
GBM	Grain boundary migration
GBS	Grain boundary sliding
GBSI(s)	Grain boundary segment intercept(s)
MR dir'n	Mean intensity direction with 95% confidence interval
MSO	Mean segment orientation
NNM	Nearest-neighbour method
SEM	Secondary electron microscopy
SGR	Subgrain rotation
SPO	Shape preferred orientation
ssdc	Steady state differential compaction
STD	Standard deviation

CHAPTER 1

THESIS INTRODUCTION

1.1 The significance of evaporitic rocks

Evaporitic deposits and rock salt structures are part of over 120 sedimentary basins worldwide, forming stratigraphic layers and diapirs, among other structures. Halite is by far the most abundant mineral in rock salt and its characteristics and rheology predominantly defines the behaviour of rock salt bodies. There are over eighty different evaporitic minerals recorded in marine evaporite deposits, with twelve being major constituents (Stewart, 1963). Table 1.1 lists the nine most important evaporitic minerals together with their basic properties. The low density of ~ 2.1 g cm^{-3} coupled with the fact that it can be mobilised and flow viscously under upper crustal conditions (< 5 km depth, T = ~ 20 to 200 °C, lithostatic pressure < 120 MPa) makes rock salt unique compared to other surface and near-surface rocks like carbonates and siliciclastic rocks. The modal composition of rock salt depends on the composition of the source liquid, the natural precipitation sequence of evaporite minerals, and the availability of water, brine, or other fluids.

Table 1.1: List of the most common evaporitic minerals of rock salt deposits (carbonates not included). *CS* – crystal system; *MSH* – Mohs scale hardness; ρ_M – mineral density in g cm^{-3}; ρ_{BR} – bulk rock density in g cm^{-3}; *Vp* – average compressional wave velocity in ms^{-1}; *n.d.* – no data available. *Wireline log rock densities after Urai et al. (2008); **after Jones and Davison (2014).

Mineral	*Formula*	*Class*	*CS*	*MSH*	ρ_M	ρ_{BR}*	*Vp***
Halite	NaCl	chloride	cubic	2.5	2.20	2.04	4500
Gypsum	$CaSO_4 \cdot 2H_2O$	sulphate	monoclinic	1.5-2	2.30	2.35	5700
Anhydrite	$CaSO_4$	sulphate	orthorhombic	3.5	2.90	2.98	6500
Sylvite	KCl	chloride	cubic	1.5-2	1.99	1.86	4110
Carnallite	$KMgCl_3 \cdot 6(H_2O)$	chloride	orthorhombic	2.5	1.60	1.57	3900
Kieserite	$MgSO_4 \cdot H_2O$	sulphate	monoclinic	3.5	2.55	2.59	*n.d.*
Bischofite	$MgCl_2 \cdot 6H_2O$	chloride	monoclinic	1-2	1.59	1.56	*n.d.*
Kainite	$KMg(SO_4)Cl \cdot 3H_2O$	chloride	monoclinic	2.5-3	2.10	2.12	*n.d.*
Polyhalite	$K_2SO_4 \cdot MgSO_4 \cdot 2CaSO_4 \cdot 2H_2O$	sulphate	triclinic	2.5-3.5	2.79	2.79	5300

The diverse polymineralic character and the ability to flow are both major reasons why natural rock salt very often develops high-level complexity of mineral compositions, fabrics, and microstructures. Ductile deformation has been studied successfully in laboratory experiments on rock salt (e.g., Carter and Heard, 1970; Poirier, 1985; Urai et al., 1987; Spiers et al., 1990; Franssen, 1994; Ter Heege et al., 2005a,b; Pennock et al., 2002; 2004; 2005; 2006; Armann, 2008; Wenk et al., 2009; Desbois et al., 2010; Linckens et al., 2016).

Rock salt deposits are generally weak compared to their surrounding siliciclastic or carbonate sediments, and this weakness can have a significant influence on the rheology of a basin (e.g., Heard and Rubey, 1966; Hildyard et al., 2011a). Oil and gas are often trapped in reservoirs in or on the flanks of salt diapirs, as rock salt can form both structural traps and seals such as folds and faults (e.g., Hudec and Jackson, 2017). Understanding the deformation of mono- and polymineralic evaporites and how the resulting fabrics determine their petrophysical properties can be key to better imaging of salt bodies and their encasing rocks. There are typically chaotic reflectors and transparent zones in and around salt diapirs, which are a consequence of poorly implemented processing parameters. The resolution of structures adjacent to salt diapirs could be improved with better velocity models for natural salt.

Due to its ability to readily flow in a ductile way and seal cracks and fractures, rock salt is important not only for the oil and gas industry but also for nuclear, carbon dioxide, and hazardous waste, hydrogen, and compressed air storage for geo-energy applications (e.g., Hunsche and Hampel, 1999; Mertineit et al., 2012; Singh et al., 2018). As the strength and rheological behaviour of rock salt differs from most other sediments and rocks, it can be significant for mining salt, potash and other evaporitic minerals, civil engineering as well, for the stability and maintenance of tunnels or building sites (e.g., Sass and Burbaum, 2010; Singh et al., 2018).

A principal aim of this study is the development of methods for the quantification of microstructures to improve the assessment of seismic anisotropy of evaporites. The quantification of microstructures also enables the study of the processes behind the formation and evolution of microstructures during salt rock deformation, as these are not yet fully understood. The quantification of microstructures is of major interest for

a vast field of geological questions to gain an understanding of how rocks (and other materials) deform, recrystallise, evolve, and behave.

Rock salt has the potential to serve as a useful analogue material that is deformable under laboratory conditions for relatable processes of the mantle and deep crustal rocks. Rock salt has been extensively used as an analogue for crustal rock deformation (e.g., silicates). Various quantification approaches for microstructures and fracture networks (e.g., Ramsay, 1976; Fry, 1979; Panozzo, 1984; 1987; Launeau and Robin, 1996; Volland and Kruhl, 2004; Kruhl, 2013; Healy et al., 2017) have been employed to analyse shape preferred orientations and (in)homogeneity at different scales (Fig. 1.1).

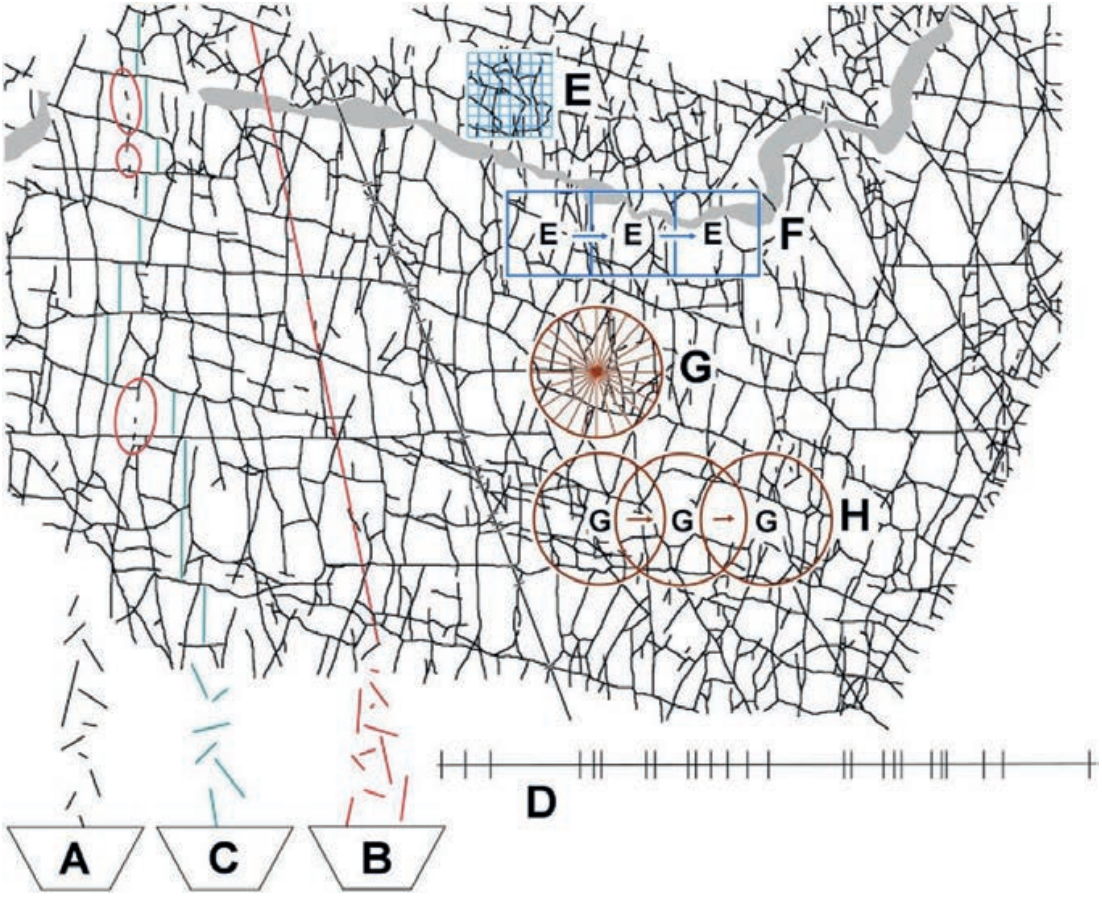

Figure 1.1: Different types of quantification of a fracture pattern based on a field photograph by various methods. After Kruhl (2013). Light grey: areas where the fracture pattern is masked. Ellipses: regions where fractures become arrays of microfractures, invisible on the scale of the photograph. A) Disassembling of the pattern into segments for statistical treatment. B) Analysis of segments or spacing between parts of the pattern along scan lines for statistical treatments. C) Analysis of spacing or widths of planar parts of the pattern for statistical treatment. D) Sequence of intercepts between

the pattern and a scan-line, leading to a Cantor set. E) Application of box-counting, providing information about the arrangement of the pattern relative to each other, i.e., internal structure of the pattern. F) Box-counting applied to small areas that are shifted over the pattern for inhomogeneity analysis of the pattern. G) 1D methods, e.g., Cantor-Dust method. H) Combined quantification of inhomogeneity.

Microstructures control physical or mechanical rock characteristics and behaviour, for example, seismic anisotropy and mechanical strength. Microstructures are an intrinsic material property and as such play an active, central role in the evolution of a rock (Gottstein, 2004).

Imposed environmental factors like stress, pressure, and temperature have an influence on the spatial arrangement (e.g., grain size, grain shape, and phase distribution), crystal structure, and rheological properties of constituent phases (including fluids). In turn, these control rheological properties and the processes that may be active, like mineral phase transformations (e.g., hydration or dehydration reactions), and deformation mechanisms (e.g., dislocation creep, pressure solution, cataclasis) (e.g., Piazolo et al*.,* 2019; Gomez-Rivas et al., 2020). Together, environmental conditions, material characteristics, material reactivity, and dominance of deformation mechanisms/processes control the behaviour of a rock and ultimately the shape of its microstructures (Knipe, 1989).

Rock-forming grains and crystals are commonly non-equidimensional, leading to an aspect ratio of > 1 (here defined as longest axis/shortest axis of a grain). The shape of grains in rocks and crystalline materials is controlled by many factors, including mineral habit and primary grain growth, subsequent deformation, recrystallisation, mineral reactions (e.g., diagenetic, metamorphic reactions), and processes of erosion and transport of detrital grains.

Shape preferred orientation (SPO) is generally defined as a measure of the alignment of non-equidimensional grains in a rock or crystalline material and is a fundamental descriptor of material microstructures and petrofabrics (Panozzo, 1984; Passchier and Trouw, 2005; Launeau et al*.*, 2010). A SPO is a common feature of many natural rocks, ceramics, and metals, and can be formed either during rock formation, e.g., by magmatic flow alignment of crystals, deposition of sediments, for example under the influence of water or airflow, or as a consequence of deformation.

Quantification of SPO can provide useful information on the deformation history of polycrystalline aggregates, their diagenetic and metamorphic evolution, and the bulk strain field (Panozzo, 1987; Launeau and Robin, 1996; Berger et al., 2011). The shape, size, and orientation arrangement of grains control the grain boundary microstructure. Grain boundary pattern anisotropy is dependent on the orientation and linked elongation of particles and grains. Grain boundary networks can have first-order effects on fluid flow, seismic wave attenuation, electrical properties, and strength of a material, among others. ***Therefore, quantitative analysis of geometric characteristics of evolving grain boundary networks can provide powerful insights into our understanding of such processes, including deformation mechanisms.***

In seismic imaging, salt deposits are generally treated as homogeneous bodies in regard to their internal structure and their composition, which is often assumed to be pure halite. Such homogeneous models have a certain validity because halite is the main constituent in natural rock salt bodies with an abundance of ~ 95 % (Raymer and Kendall, 1997). The diverse polymineralic character and ability to flow are both major aspects of why natural rock salt bodies very often develop a range of mineral compositions, fabrics, and microstructures. Rock salt bodies generally show high-level structural complexity, including anisotropic characteristics, and associated large velocity contrasts (Raymer and Kendall, 1997).

Single crystals of all evaporite minerals are anisotropic in their elastic properties (Raymer and Kendall, 1997; Raymer et al., 2000a,b). All minerals are by nature elastically anisotropic, caused by directional variations of atomic bonds in their crystal lattice structure (e.g., Healy et al., 2020). Variations in single-crystal elastic properties result in directional variations in ultrasonic wave velocity and polarization directions, so-called seismic anisotropy, which mimic the crystal symmetry of the mineral (Fig. 1.2; e.g., Vargas-Meleza et al., 2015).

Different types of seismic anisotropy, of P-wave velocity (V_P), both polarized S-waves velocities (Vs_1 (fast), Vs_2 (slow)), and S-wave splitting (ΔV_S) anisotropy, can be derived from elastic constants (Mainprice, 1990; Mainprice and Humbert, 1994; Lloyd and Kendall, 2005). The anisotropy in seismic P-wave velocities of each phase is different, with 5700 m s^{-1} for gypsum (36 % anisotropy) and 6500 m s^{-1} (Jones and Davison, 2014; Table 1.1) for anhydrite (43 % anisotropy) (Table 1.1 and Fig. 1.2).

It is known that evaporitic minerals, and consequently evaporitic deposits, are seismically anisotropic.

However, up to now research has not been extensive enough to allow the quantification of the effect different structural and compositional rock characteristics have on seismic velocity anisotropy.

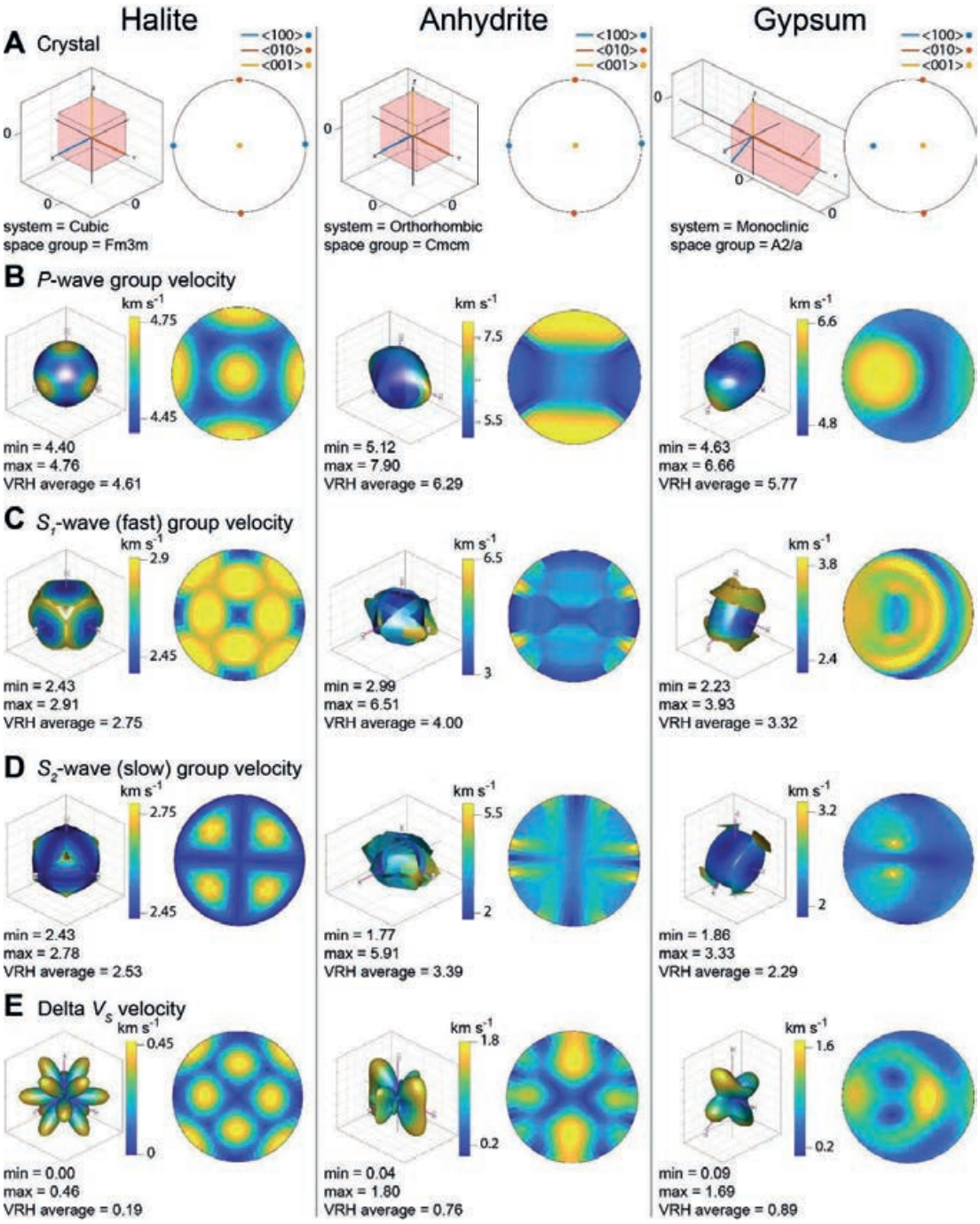

Figure 1.2: Single crystal ultrasonic velocity anisotropy for halite, anhydrite, and gypsum calculated using the AnisoVis MATLAB™ Toolbox (Healy et al., 2020), plotted as 3D surfaces (left) and equal area, lower hemisphere, stereographic projections (right)

relative to the mineral form. A) Unit cell, B) *P*-wave group velocity (V_P), C) fast *S*-wave group velocity (V_{S1}), D) slow S-wave group velocity (V_{S2}), E) shear-wave splitting (ΔV_S). Seismic properties were calculated using single-crystal elastic properties (Bass, 1995). Note that the velocity distribution reflects the symmetry class of each mineral. Minimum (min), maximum (max), and Voigt-Reuss-Hill (VRH) average values are indicated below the projections.

In polycrystalline aggregate es, seismic velocity anisotropy is commonly demonstrated to be dominated by the crystallographic alignment of all mineral constituents, which is equivalent to the dependence on the overall intrinsic crystal structure of the sum of all grains. Structural features like content, orientation, and alignment of grain boundaries (SPO), cracks, or pores can also have a major impact on seismic velocity anisotropy (e.g., Crampin, 1985; Lo et al., 1986; Popp and Kern, 1998; Raymer and Kendall, 1998; Mah and Schmitt, 2003; Healy et al., 2009; Lloyd et al., 2011; Zong et al., 2014).

Other factors that have a strong influence are variations in the spatial distribution of phases, changing phase content proportions (Llorens et al., 2020), layering, grain size, and shape fabrics (e.g., Kern and Wenk, 1985). Published seismic velocity data on non-halite and polymineralic evaporites are extremely rare, numbering just a handful of studies (Levin, 1979; Ross et al., 1987; Raymer and Kendall, 1997; 1998; Raymer et al., 2000a,b; Tripetta et al., 2010; Vargas-Meleza et al., 2015). Furthermore, the extent to which mineralogical and textural variations contribute to seismic velocity anisotropy effects in evaporites remains understudied.

An outstanding issue for investigating the contribution of SPO to velocity anisotropy is the definition of an appropriate quantitative measure of SPO fit for this purpose.

The behaviour of evaporites under stress is important for understanding the strength and rheology of evaporites and, by extension, evaporite-bearing sedimentary basins and fold/thrust belts (e.g., Hildyard et al., 2011a). Stress has a critical impact on grain boundary and fracture interface processes and can therefore influence the transmission of fluids, grain boundary dissolution/precipitation, and crack/seal processes, which are all considered important in evaporite bodies. Yet, the response of evaporites under stress remains understudied.

Hydration is a process that is linked to mechanical strength. Anhydrite and gypsum are, next to halite, two of the most common minerals in evaporitic deposits. Both are part of the $CaSO_4$ H_2O system, where the general mineralogy and structure depend on the first order of the water content (hydration stage). Three main phases represent different degrees of hydration: from most to least hydrated, these are gypsum (dihydrate; $CaSO_4*2H_2O$), bassanite (hemihydrate; $CaSO_4*0.5H_2O$), and anhydrite (anhydrous form; $CaSO_4$). Hydration of anhydrite and dehydration of gypsum in evaporitic deposits are common processes that depend on the availability of water (e.g., Farnsworth, 1925; De Paola et al., 2007; Bedford, 2017).

Therefore, it is important to understand the conditions at which hydration occurs and study the role of stress in the process.

The process of dehydration of gypsum to anhydrite has received considerable attention in experimental studies (Olgaard et al., 1995; Ko et al., 1995; 1997; Wang and Wong 2003; Milsch and Scholz 2005; Milsch et al., 2011; Llana-Fúnez et al., 2012; Leclère et al., 2016). Publications focussing on the hydration of anhydrite to gypsum are limited to either laboratory studies of particles rather than polycrystalline aggregates, or anhydrite polycrystalline aggregates under hydrostatic conditions (e.g., Ramsdell and Partridge, 1929; Conley and Bundy, 1958; Hardie, 1967; Sievert et al., 2005; Fig. 1.3). However, laboratory experiments under hydrostatic conditions have also failed to produce hydration, even over durations of months (Hardie, 1967).

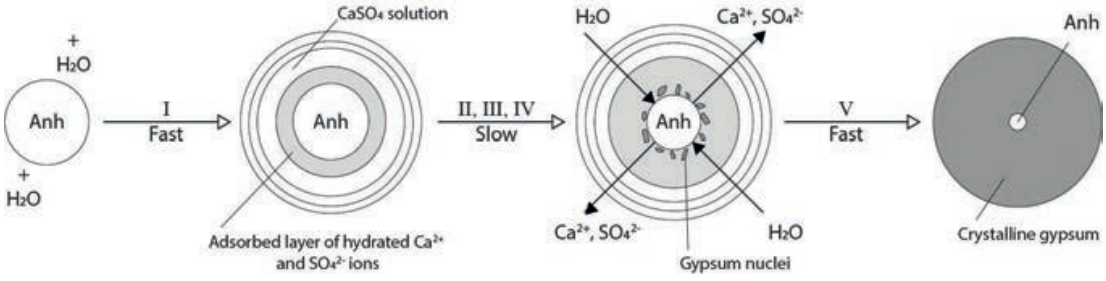

Figure 1.3: The mechanism of hydration of anhydrite particles in water as described by Sievert et al. (2005). a) to b) step I: initial partial dissolution of $CaSO_4$ and adsorption of hydrated Ca^{2+} and SO_4^{2-} ions at the surface of anhydrite, fast process. b) to c) step II: increase of thickness of adsorbed layer; step III: crack formation in the adsorbed layer and counter migration of H_2O and Ca^{2+} and SO_4^{2-} ions; IV: formation of gypsum nuclei at the surface of anhydrite. Steps II to IV describe slow processes. c) to d) step V: rapid hydration of anhydrite to gypsum.

1.2 Aims and objectives

The main aim of this thesis is to study the link between petrofabrics and seismic anisotropy, with a focus on the quantification of grain boundary patterns, evaporite petrofabrics, and experimental hydration of anhydrite to gypsum under stress. This is achieved via the following specific objectives:

1. To investigate and develop a new method to quantify grain boundary networks
2. To evaluate this method against data from controlled numerical experiments
3. To investigate the links between seismic velocity anisotropy and the diversity of microstructures found in naturally deformed evaporites
4. To investigate the role of stress, rather than pressure, in the hydration of anhydrite to gypsum

1.3 Thesis structure

The thesis is written as research chapters that are individual draft manuscripts and include topic specific introductions that outline the published literature and state of art for each field of research. Therefore, this thesis does not contain an independent literature review chapter. The main body of this thesis is comprised of chapters 2 to 5. All chapters are in preparation for submission for publication in international journals. The order of chapters is such that a quantification methodology is developed in chapters 2 and 3. Chapter 4 applies this method to natural samples and relates the results to seismic velocity measurements. Chapter 5 uses samples analysed in chapter 4 for experimental investigation of hydration under stress. Discussion and conclusions of the thesis are presented in chapter 6.

CHAPTER 2

Grain boundary networks and Shape preferred orientation – A fresh angle on pattern quantification

This chapter presents a new, automated MATLAB^{TM} toolbox named GBPaQ that incorporates different methods for grain boundary pattern quantification for applications like seismic wave attenuation estimation. Furthermore, a minimum

intensity of grain boundary intercepts (I_{min}) is introduced as a new parameter for the quantitative analysis of SPO strength.

GBPaQ is tested on two example grain boundary patterns, including a granular texture and a foam texture that have been manually stretched and analysed stepwise to analyse their SPO evolution. The results show that a combination of grain-fitted ellipse, grain boundary segment orientation, and grain boundary segment intercept density rose diagrams provide a complete, detailed quantification of grain boundary pattern anisotropy.

We find that such a combination of complementary methods might unlock the identification and quantification of complex patterns and the study of other microstructural grain boundary characteristics linked to deformation mechanisms, multiple phases with different viscosity, local or directional inhomogeneity, or strain geometry.

The minimum intensity (I_{min}) provides a powerful tool to track the homogeneous deformation history of polycrystalline aggregates if plotted against the average axial ratio of grain-fitted ellipses (r).

CHAPTER 3

Grain boundary (shape) evolution of single and dual-phase aggregates during plane-strain deformation – Combining numerical simulations with grain boundary intercept based SPO quantification

This study focuses on the application of grain boundary segment-based SPO analysis, developed in chapter 2, to simulated, evolving microstructures. Such analysis unlocks a new understanding of SPO pattern development during progressive shear and in single and two-phase materials.

Viscoplastic numerical simulations of single- and two-phase materials are used to generate grain boundary patterns with pre-defined characteristics that are deformed under different boundary conditions. Eight distinct numerical deformation simulations were run to a finite natural strain of up to 2 in 100 time steps. These models used dislocation glide and the strain geometry end-members of simple shear and pure shear

on single- and two-phase foam texture grain boundary networks, with coarse and fine grain sizes.

General trends and patterns observed during deformation include grain elongation and rotation according to the applied strain geometry and increasing preferred orientation distribution. Grain boundary segment orientation and density analysis show that SPO is weaker in two-phase models at the same natural strain. The two-phase models consistently have weaker SPOs compared to single viscosity models. The grains with lower viscosity become elongated several orders of magnitude faster and form sigmoidal clasts.

The resultant microstructures manifest as distinctive shapes of grain boundary intercept density contour plots, with distinct characteristics for different strain geometry end-members and single and dual viscosity models.

CHAPTER 4

Effects of mixed phase content, fractures, and grain boundary anisotropy on acoustic wave velocities in evaporites

The study combines ultrasonic velocity measurements on cuboids and cores of natural evaporites with different mineral compositions and microstructures with the methodology developed in chapters 2 and 3. Velocity data from measurements on natural evaporites with halite, polyhalite, anhydrite, gypsum, and mixed phase rocks from three deposits is presented. Crystallographic preferred orientation (CPO) analysis of two sample sets (pure anhydrite and anhydrite with gypsum content) shows CPO is higher in pure anhydrite compared to mixed anhydrite with gypsum sample material, with microstructures and impact of deformation differing between the two. The V_P and V_S ranges are generally lower than expected from single crystal ranges (that relate to crystallographic orientation), indicating other contributions to velocity variations than simply intrinsic mineralogical anisotropy.

New velocity data for natural evaporites is presented, with velocity anisotropy (AVP) up to 60 % AV_P and 34 % AV_S %. A workflow is introduced that combines CPO analysis with fracture analysis, grain boundary network analysis, and grain boundary intercept-based methods.

CHAPTER 5

Rapid hydration and weakening under stress - Implications for Earth Systems

This chapter uses sample material from chapter 4 to study the effects of triaxial stress on the hydration of samples of polycrystalline anhydrite in laboratory experiments. Steady state differential compaction, dry and 'wet' tests under confining pressure, and axial stress were conducted to investigate the influence of stress on hydration in anhydrite-gypsum aggregates. Characterization of the samples before and, where possible, after triaxial experiments were performed with optical and scanning electron microscopy, including energy dispersive spectroscopy and electron backscatter diffraction mapping.

Stress-strain data reveals that samples that underwent steady state differential compaction are mechanically weaker. The microstructural analysis shows that there is a strong temporal and spatial connection between the geometry, distribution, and evolution of fractures and hydration. Newly-formed vein gypsum locally exhibits a systematic crystallographic preferred orientation, which is not always topotactically linked to the wall-rock anhydrite. Selective inheritance of crystal orientations from favourably oriented wall-rock anhydrite grains is proposed to lead to systematic crystal orientation in the new gypsum veins.

These findings imply that non-hydrostatic stress has a significant influence on hydration rates and subsequent mechanical strength of rocks. This phenomenon is applicable across a wide range of geological environments in Earth's crust and upper mantle.

CHAPTER 2

Grain boundary networks and shape preferred orientation – A fresh angle on pattern quantification

Abstract

A quantitative understanding of grain shape preferred orientation (SPO) and grain boundary networks as fundamental characteristics of rocks and other crystalline solids is of major interest in geology and material science. Grain boundary networks contain useful information on the deformation history of polycrystalline aggregates, and their diagenetic and metamorphic histories. SPO can have major impact on material characteristics such as permeability, acoustic velocity and mechanical strength, and as reaction surfaces.

The objective of this study is to present a semi-automated toolbox of MATLAB™ scripts, named Grain Boundary Pattern Quantification (GBPaQ), that incorporates different methods for grain boundary pattern quantification for application to, for example, seismic wave attenuation estimation. GBPaQ is tested on two example grain boundary patterns, a granular texture and a foam texture with equant grains, which have been digitally stretched (deformed) to analyse their SPO evolution.

The results show that a combination of grain ellipse, grain boundary segment orientation, and grain boundary segment intercept density rose diagrams provide a complete, detailed quantification of grain boundary pattern anisotropy. Grain boundary segment intercepts (GBSI) analysis using GBPaQ yields a new grain boundary pattern parameter – the minimum intensity of grain boundary intercepts (I_{min}) – which follows a power law relationship with the average axial ratio of grain-fitted ellipses (r) during SPO development.

We propose that I_{min} can be used for the quantitative analysis of SPO strength as a useful tool to assess the deformation history of polycrystalline aggregates. Further studies involving a broader range of different patterns and strain histories are necessary to fully investigate the potential of (I_{min}) versus r diagrams.

2.1 Introduction

Rock-forming grains and crystals are commonly non-equidimensional, leading to an aspect ratio > 1 (aspect ratio here defined as longest axis divided by the shortest axis). The shape of grains in rocks and crystalline materials is controlled by many factors, including mineral habit and primary grain growth, deformation, recrystallisation, mineral reactions (e.g., diagenetic, metamorphic), and processes of erosion and transport of detrital grains. The shape preferred orientation (SPO) is generally defined as a measure of the alignment of non-equidimensional grains in a rock or crystalline material and is a fundamental descriptor of material microstructures and petrofabrics (Panozzo, 1984; Passchier and Trouw, 2005; Launeau et al., 2010).

An SPO in a rock can be formed either during rock formation, e.g., by magmatic flow alignment of crystals or vesicles (Herrero-Bervera et al., 2001), alignment of particles during sediment deposition (Mulchrone and Meere, 2015), or as a consequence of deformation, and is a common feature of many natural rocks, ceramics, and metals. As such, quantification of SPO can provide useful information on the deformation history of polycrystalline aggregates, their diagenetic and metamorphic evolution, and the bulk strain field (Panozzo, 1987; Launeau and Robin, 1996; Berger et al., 2011). Furthermore, SPO can have a major impact on material characteristics, especially the anisotropy of mechanical and petrophysical properties, such as permeability, acoustic velocity, and mechanical strength.

The shape, size, and orientation arrangement of grains control the grain boundary microstructure. Given that grain boundaries are inherently weaker than grains, they can be transmissive to fluids, and can be sites of diffusion of vacancies, elements, and reactive transport (Urai et al., 2008). Accordingly, grain boundary networks exert a primary influence on the mechanical strength, permeability, and reactivity of a rock or material. The orientation of grain boundaries may also be used to define an SPO.

Grain boundary pattern quantification requires reliable resolution of grain boundaries via imaging (Launeau et al., 1990; Jähne, 1993; Bartozzi et al., 2000; Lebichot et al., 2005; Pirard and Sardini, 2011). A full description of an SPO should consider three dimensions because grains are 3D objects. However, our view of microstructures is often restricted to 2D surfaces, such as 2D outcrops and thin sections, and therefore SPO quantification techniques are most commonly developed for 2D analyses.

While 3D methods are being developed (e.g., FIB-SEM etc.), and the results are valuable, there is a "legacy database" of thousands of 2D thin sections and images. The take from this "legacy database" ought to be maximised. Manual recording (tracing) of different grain boundary patterns may take up to fifty times as long as digital processing and automated recording (Peternell and Kruhl, 2009; Kruhl, 2013).

The most established approaches to SPO quantification rely on the identification of grains, and other fabric objects such as xenoliths, clasts, or pebbles, as discrete objects (Webber, 2012), followed by the representation of their shapes as ellipses (in 2D) or ellipsoids (in 3D), which can be plotted on a Flinn plot (Flinn, 1962), a R_f/ϕ plot (Dunnet, 1969; Ramsay, 1976; Ramsay and Huber, 1983; Lisle, 1985), or as rose diagrams of grain long axis azimuths (in 2D). Moreover, the analysis of the positions of the ellipse centroids via the centre-to-centre method (Ramsay, 1976), its successor the Delaunay Triangulation Nearest Neighbour Method, and the Fry method (Fry, 1979) allow the finite strain ellipse (or ellipsoid in 3D) to be reconstructed (Sorby, 1849; Harker, 1885 and Becker, 1893).

A hyperbolic vector mean method has been introduced to expand ellipse-based 2D strain analysis to incorporate hyperbolic (non-Euclidean) geometry (e.g., Yamaji, 2008; 2013a,b; Vollmer, 2018). This can be applied to data from, i.e., R_f/ϕ, centre-to-centre, and kinematic vorticity analysis, and equal area and gnomonic projections of the hyperboloid is demonstrably useful for estimating the optimal strain and its error by means of formal statistical methodology (e.g., Yamaji, 2008; 2013a,b; Vollmer, 2018).

Grain-based SPO approaches are recognised for being effective to derive principal strain axes from a population of deformed grains or objects, and are established tools for strain analysis (Webber, 2012; Kruhl, 2013). However, much information about the grain boundary network (pattern) is lost when grains are approximated as ellipses or in grain centroid approaches, highlighting the need for more sophisticated approaches for describing the geometry of grain boundary networks (or patterns) more thoroughly (Kruhl, 2013).

Methods for quantifying grain boundary patterns include those that analyse grain boundary attribute statistics, such as segment lengths and azimuths, and those that quantify grain boundary distribution statistics, such as intercepts along scan lines.

Quantification of grain boundary segment orientation distributions (e.g., as grain boundary tensors) is advantageous because it does not rely on any geometric simplifications. A limitation of statistical analysis of the length and orientation of 'line elements' via cumulated frequency distributions (e.g., Sanderson, 1977; Sanderson and Phillips, 1987) is the loss of relationships of grain boundary segments relative to each other, grain size, and grain ellipticity (Kruhl, 2013).

Grain boundary-based scan line quantification methods, such as the (inverse) SURFOR method of Panozzo (1983, 1984, 1987), intercept method of Launeau and Robin (1996) or the Cantor-dust method (Volland and Kruhl, 2004), include more information about the shape and size of grains and pattern characteristics by analysing the relationship between the pattern and the scan line orientation. Scan lines preserve a detailed evaluation but are limited to the features in the pattern section that they capture (Kruhl, 2013).

The automated version of the SURFOR wheel from Panozzo (1984; 1987) has been implemented by the introduction of the SURFOR code (Heilbronner and Barrett, 2014). This FORTRAN program was created to quantify fabrics defined by linear traces of grain surfaces from section images, and as such is ultimately a 2-D limited tool. The SURFOR method has been used in hundreds of publications and has been applied to solve many geological problems (Herwegh et al., 1999; Molli and Heilbronner, 1999; Stipp et al., 2002; Kilian et al., 2011). These methods are commonly used to analyse SPO and strain in granites (Stein, 2000; Kurz, 2005; Vigneresse, 2015; Thabet et al., 2017), eclogites (Mauler et al., 2001; Pleuger et al., 2003); Kurz et al., 2004), mylonites (Stünitz and Gerald, 1993; Trullenque et al., 2006) and very common in marble and limestones (Schweigl and Neubauer, 1997; Molli et al., 2000; Cantisani et al., 2009). Some studies use the SURFOR approach to study hydration reactions (Marti et al., 2018a; 2018b).

The *intercept method* is one of the oldest methods for quantitative analysis of grain boundary pattern anisotropy (Launeau and Robin, 1996), was first suggested by Saltykov (1958), and later used in stereology by Underwood (1970) and is based on counting intercepted grain boundary segments along parallel sets of scan lines that are rotated systematically. The number of boundaries that are intercepted along a scan line is called the intercept number.

The most successful version of an intercept-based pattern quantification method is that developed by Launeau and Robin (1996), following Launeau et al. (1990) and followed by Launeau and Robin (2005) and Launeau et al. (2010). Launeau and Robin (1996) added the Fourier analysis of intercept count to the intercept method. Fast Fourier Transform is part of autocorrelation and rose of intercept length (Launeau and Robin, 1996). A great advantage of this method is that that direction-dependent pattern characteristics can be quantified, and this is especially important to link microstructures with the physical and mechanical behaviour of rocks in terms of seismic wave attenuation, deformation, or materials engineering.

Scan line-based methods are more selective because they utilize fragmented orientation and sectional results, depending on the position, angle, and length of scan lines. Information is lost by most scan line-based quantification approaches, because of the 10° angle between scan lines or the gaps between parallel scan lines in a grid. In general, scan line-based methods are strong for fast SPO quantification in simple patterns (Panozzo, 1983; 1984; 1987; Srivastava, 1995; Launeau and Robin, 1996).

The scan line and grain boundary-based quantification methods from Panozzo (1984; 1987) and Launeau and Robin (1996) are commonly applied to geological and other patterns for quantification analysis of finite strain and anisotropy, including seismic anisotropy (Lee and Jung, 2015; Jung et al., 2020; Kim and Jung, 2020). They are also applied to studies involving anisotropic magnetic susceptibility (Launeau and Cruden, 1998; Jayangondaperumal and Dubey, 2001).

The Cantor-Dust (or Cantor-Set) method was first proposed as a concept by Velde et al. (1990) and Harris et al. (1991). It is a method that combines boundary intercepts and grain size to describe a pattern. The method uses the distance between intercepts rather than the number of intercepts and is often used to analyse fractures or fracture spacing (Gerik and Kruhl, 2009). Volland and Kruhl (2004) modified the method for fractal pattern quantification and automated as software tool AMOCADO by Gerik and Kruhl (2009). Yet, published automated grain boundary pattern quantification software are limited by inherent simplifications in approach that omit important details of the patterns. The specific aim of this study is to introduce GBPaQ, a new collection, or toolbox, of MATLAB^{TM} programs, developed from FracPaQ (Healy et al., 2017) for the automated quantitative analysis of grain boundary patterns.

To illustrate and compare SPO quantification methods, two initial grain boundary patterns with narrow ranges in initial grain size distributions and low initial grain axial ratios were stretched, and the changes in SPOs tracked. GBPaQ requires vector graphic input. In this contribution we first introduce the GBPaQ approach and method and then demonstrate it using two different examples of grain boundary patterns.

2.2 Material and methods

2.2.1 Case studies

To illustrate grain boundary segment-based SPO quantification, two 2D grain boundary patterns have been selected (Fig. 2.5; Appendix A) as examples: a polycrystalline aggregate microstructure comprising grains with a high degree of roundness ('Granular') derived from an ELLE microdynamic numerical model published in Piazolo et al. (2019), and a polycrystalline foam texture based on an electron backscatter diffraction map of a sintered zirconia ceramic sample ('Foam').

The granular pattern was originally created to simulate trace element diffusion with fractionation during surface-energy driven grain boundary migration (Jessell et al., 2003; Steinbach et al., 2016; Llorens et al., 2019; Piazolo et al., 2019). It provides an example of a pattern with very low initial grain aspect ratios and minor variations in grain size distribution, whereas the grain shapes in 'Foam' are highly polygonal with relatively straight boundaries, minor variations in grain size, and homogeneous distribution (Table 2.1).

Both patterns have very low variance in grain size, low SPO strength, relatively simple grain boundary patterns, and different grain shape symmetries. The patterns are mapped manually via a vector graphics program to create datasets in SVG file format for analysis with linear grain boundary line segments. Equivalent circular diameter (ECD) and axial ratio (r) are calculated from data analysis of these maps with freely available raster graphics software (ImageJ; Schneider et al., 2012).

Table 2.1: Selection criteria of the primary patterns. *s* = number of segments in a pattern; #grains = number of whole grains per sample; *n*ECD = equivalent circular diameter normalized to 1; *n*SD = normalized standard deviation; *r* = grain aspect ratio.

Sample	*s*	#grains	*n*ECD ± *n*SD	*r* ± SD
'Granular'	5293	657	1±0.39	1.38±0.33
'Foam'	5925	953	1±0.50	1.59±0.50

To study evolution of SPO, grain boundary segment azimuths, and scan line intercept density, the two initial texture patterns are incrementally 'stretched' in the horizontal direction (using a vector graphics program) by 5 %, 10 %, and 50 %, whereas the vertical dimension is held constant.

These stretches do not simulate isochoric strain, as the area (and therefore volume in 3D) of the grains, and therefore the grain size, increases with progressive deformation. As such, these strains are analogous to x-y plane views of plane-strain deformation.

2.2.2 Grain boundary segment-based automated analysis with GBPaQ

In this study, grain boundary patterns were analysed using a customised version of the MATLAB™ toolbox FracPaQ, originally designed to quantify fracture patterns (Healy et al., 2017), and renamed GBPaQ (**G**rain **B**oundary **P**attern **Q**uantification).

Grain boundary attribute distributions and spatial variations are quantified based on the length and angle of line segments that comprise a pattern, displayed as segment angle (azimuth) rose diagrams, optionally length-weighted, and grain boundary (or fabric) 2^{nd}, 4^{th} and higher ranked tensors, based on the formulations of Oda (1983) (for applications see also Suzuki et al., 1998; and Brown and Bruhn, 1998).

FracPaQ uses a 2^{nd} rank tensor approximation and calculates the anisotropy of permeability in 2D by default, and GBPaQ uses the same approach. In GBPaQ, fabric tensors are calculated using the density of segments (number per unit area), squared lengths of segments, and the orientation matrix of Woodstock (1977).

In GBPaQ, the analysis of the grain boundary segments by azimuth and the resulting rose diagram shows that the longest axis of the fitted ellipse and the vector that marks the circular mean, or mean segment orientation (MSO), have the same angle. Yet it captures more detailed pattern geometries compared to the grain-fitted ellipse-based approach (Fig. 2.1).

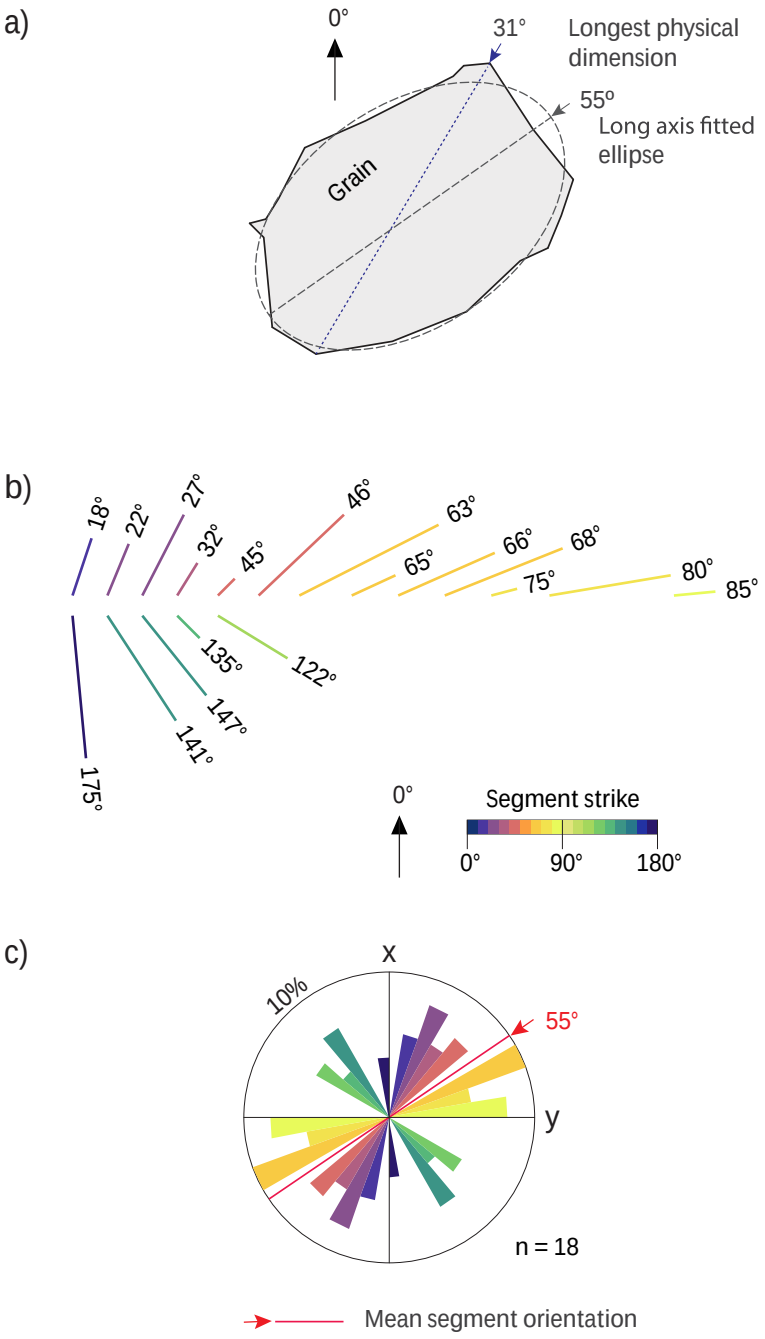

Figure 2.1: Grain boundary segment analysis of a single grain. a) Grain with longest physical dimension and the fitted ellipse with the longest axis. b) All grain boundary segments of the same grain, coloured and sorted by their strike. c) Equal area rose plot of the grain boundary segment orientations.

2.2.3 Scan line and intercept-based analysis of grain boundary segments

The basic concept of SPO analysis using scan lines is that a scan line parallel to the preferred grain elongation orientation of a pattern crosses less grain boundaries than in any other orientation.

The distance between grain boundary segments depends to a first order, on grain size, grain shape, grain boundary symmetry, the pattern geometry (sum of all grain boundary geometries in the pattern), and pattern homogeneity (grain size sorting, foliation domains, etc.).

The presence of multiple phases and their specific differences in grain symmetries, sizes and shapes are also a factor for the characteristics of a grain boundary pattern. Grain size, intercept density and intensity variations are important in terms of the number of crossed segments: the more grains, the bigger the dataset, the more holistic the resulting description of a pattern, assuming it is homogeneous. Therefore, grain boundary pattern analysis should be conducted relative to grain size to analyse a statistically robust number of grains.

For grain boundaries described by a segment, length and angle are the key characteristics that need to be included in any method that attempts to quantify grain boundary-based pattern characteristics. A pattern with a well-defined SPO generally consists of long segments (or more numerous segments of equal lengths) parallel to the direction of SPO, and shorter segments with increasing angular deviation from the SPO orientation. This relationship gets more pronounced with increasing SPO strength.

It is statistically less likely to cross a short segment than a long one, with increasing angular difference (up to 90°) to the scan line. However, the likelihood of intercepting closely spaced grain boundary segments increases normal to the SPO direction, which increases intercept density in these scan line orientations.

For any given analysis or a grain boundary pattern, the position and number of scan lines have a statistical impact and determine if the analysis describes a sample in 1D, 2D, or 3D space (Fig. 2.2). A single scan line provides a 1D description of the grain boundary density. Several parallel scan lines provide a 2D component to pattern quantification, but only describe the intercept density in one direction.

Robust use of scan lines in 2D pattern analysis involves two concepts: a centre approach, where the scan lines rotate around a centre, and a grid approach, where a set of parallel scan lines is simultaneously rotated. The angle between scan lines in a centre approach and the angle increment of grid rotation matter in terms of the precision and scale at which the pattern is analysed.

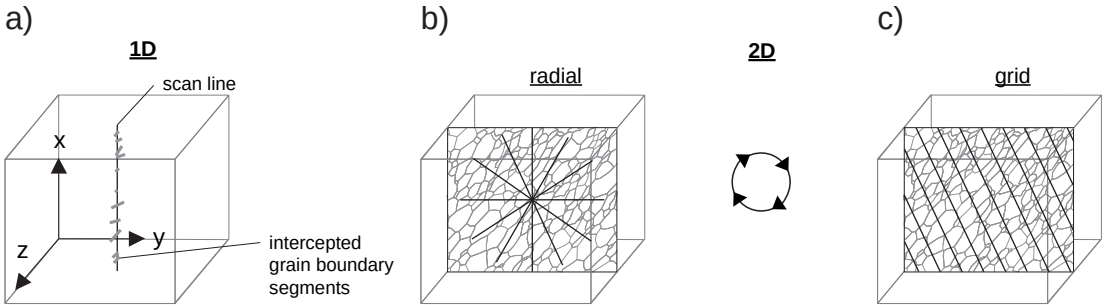

Figure 2.2: Basic considerations for scan line distribution for 1D measurement and optional grid and radial scan line distribution for 2D method application.

2.2.4 Grain boundary pattern analysis

Analysis of the initial grain boundary patterns and each stretch increment was conducted using three different approaches. The first one is based on the fitted ellipse of grains. The length and angle of the fitted ellipse longest grain axis and axial ratio of the longest and shortest axis of the fitted ellipse are calculated with ImageJ.

The mean intensity direction with 95 % confidence interval (MR dir'n) was calculated from the long axis of the fitted ellipse with GEOrient. The mean intensity is the direction of the resultant to the (unit) vectors describing the directions (Fischer, 1993; Mardia and Jupp, 2000). All directions are rounded to integer values and the mean resultant is given to the nearest integer direction.

The 95 % confidence interval of the mean direction is an estimate, based on the percentiles of the wrapped normal distribution using circular standard error after Fischer (1993). The generated angles and rose diagrams are displayed counterclockwise with respect to the horizontal X, which corresponds to 0°. This was adjusted so that X is vertical and a clockwise display of angles is used.

The second approach to display the data is by showing angles and lengths of each segment in the patterns using equal area rose plots generated by GBPaQ, and uses code from FracPaQ (Healy et al., 2017). The mean segment orientation (MSO) or circular mean, is calculated for each pattern but is only truly valid for unimodal distributions.

The third approach uses grain boundary segment intercepts (GBSIs) by scan lines to identify the orientation of the minimum GBSI density α and the maximum GBSI density γ (Table 2.2) via GBPaQ.

Table 2.2: List of symbols and abbreviations used.

Symbol	Description
r	Average axial ratio of grain-fitted ellipses
N	Number of segment intercepts
θ	Scan line angle (between 0 to 180° from an arbitrary reference frame)
$d\beta$	Angular intervals between scan lines
n	Total number of scan lines with the same orientation
l	Total length of all scan lines
α	Orientation of scan line(s) with minimum segment intercept density
γ	Orientation of scan line(s) with maximum segment intercept density
ϕ	Angle between minimum and maximum segment intercept scan lines
$N(\alpha)$	Minimum number of segment intercepts
$N(\gamma)$	Maximum number of segment intercepts
$\bar{x}N$	Average number of segment intercepts (total number of intercepts divided by number of scan lines)
$D_L(\theta)$	Orientation dependent segment intercept density (number of intercepts along one scan line orientation divided by scan line length of scan line(s) with this orientation)
$\bar{x}D_L(\theta)$	Average orientation dependent segment intercept density (grid approach)
$\bar{x}N_L(\theta)$	Average number of orientation dependent segment intercepts (grid approach)
$D_L(\alpha)$	Minimum segment intercept density
$D_L(\gamma)$	Maximum segment intercept density
$Imin$	Minimum intensity

GBPaQ analysis consists of two parts. The first is the approach used for fracture patterns in FracPaQ (Healy et al., 2017) and based on line statistics derived from coordinate geometry. Uploaded patterns are coloured for segment azimuth and a grain boundary tensor can be calculated in the same way as a crack tensor. The output options include grain boundary length histograms, density maps, and orientation rose diagrams (Healy et al., 2017). Further, the patterns are entirely deconstructed, i.e., the grain boundary segments were removed from their spatial context, and the segment length and azimuth are statistically analysed and plotted as segment orientation rose diagrams (Fig. 2.1c). The second part is a grain boundary intercept-based analysis (Fig. 2.2).

GBPaQ in its current form has an automated radial centre setting, so that it runs one rotation centre intercept analysis with 360 orientation steps per semicircle ($d\beta$ = 0.5°, adjustable) (Fig. 2.3). The GBSI density is calculated per pixel and displayed as a GBSI density contour rose (equal area). GBPaQ scan lines in this setting have constant length, defined by the smallest dimension of the input pattern image. A radial line scan is placed in the middle of the uploaded pattern. The interval between scan lines $d\beta$ can be defined.

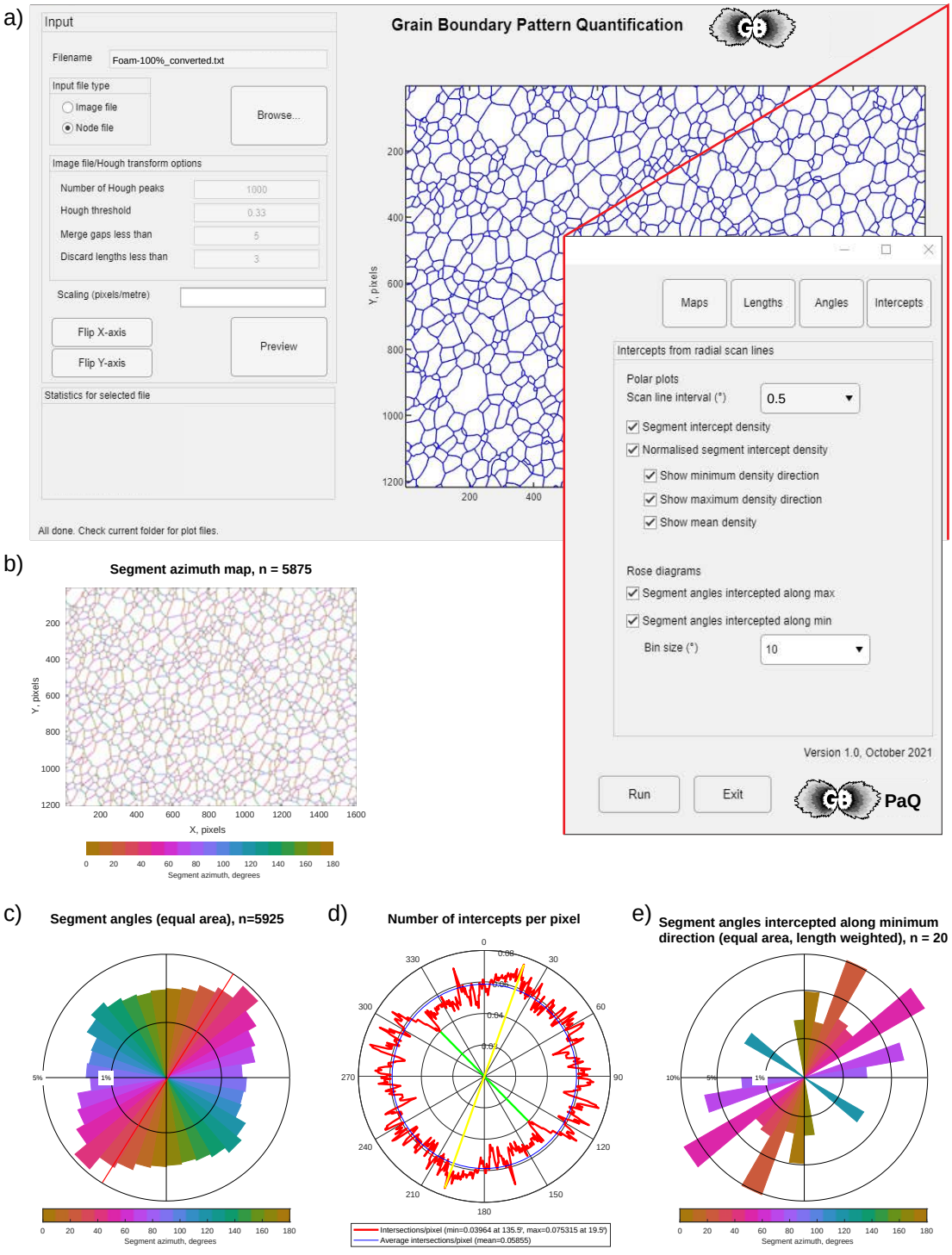

Figure 2.3: Screenshot of GBPaQ software graphical interface and output figures specific to GBPaQ. a) GBPaQ main application window with input of the original (100 % stretch) 'Granular' pattern as SVG file. b) Grain boundary pattern map with segments coloured by azimuth. c) Grain boundary segment orientation rose, not length-weighted, analysis utilizes FracPaQ code. d) GBSI density contour plot from analysis with scan line interval $d\beta = 1°$. e) Grain boundary segment orientation rose of segments intercepted along α and γ, length-weighted.

GBSIs are counted along scan lines and reported as total numbers, intercepts per pixel, and in a GBSI density rose diagram. The GBSI density can be calculated in any chosen unit and scale. The GBSI density contour rose also shows the maximum and minimum segment intercept density orientations α and γ (intensity and azimuth).

The average GBSI density $\bar{x}D_L(\theta)$ is marked by a circular line on rose plots. Values for intensity and azimuth of intercepts for maximum, minimum and average intercept number and density are annotated. Two additional roses show azimuth and intensity of the grain boundary segments intercepted in α and γ.

2.3 Theory / calculation

The SPO equivalent direction of minimum number of grain boundary segment intercepts can be used to calculate a minimum intensity I_{min} (Eq. 1; Table 2.2), which relates the minimum number of grain boundary segment intercepts $N(\alpha)$ to the average number of grain boundary segment intercepts $\bar{x}N$. $\bar{x}N$ is the total number of intercepted grain boundary segments over all profiles (scan lines) divided by the number of profiles:

$$I_{\min} = \frac{N(\alpha)}{\bar{x}N} \quad [1]$$

I_{min} as a rule ranges between 0 and 1, where 1 equals $\bar{x}N$, the average. The closer to 1, the weaker the SPO. With I_{min} decreasing towards 0, the SPO strength increases. This calculation allows I_{min} to be a dimensionless, independent value useful to compare several patterns with different characteristics. I_{min} combines grain orientation distribution and elongation. This form of minimum intensity calculation requires that the length of all scan lines is equal. It can be adapted for multiple radial scan line centres and adjusted for variation of scan line length using GBSI density instead of number of intercepts.

The total number of GBSIs over multiple scan lines with the same orientation (θ) can be defined as $\sum_{i=1}^{n} N(\theta)_j$. The total number of scan lines in orientation θ is defined as n. $N(\theta)$ stands for the total number of GBSIs by one scan line with orientation θ. For the average number of GBSIs, the total number of GBSIs is divided by the total number of scan lines (constant length) used.

For a grid scenario, it is more efficient to use scan lines with different lengths, and therefore use GBSI density as a measure. The total number of GBSIs of all scan lines in one orientation, *N(θ),* is divided by the total length *(l)* of all scan lines ($\sum_{i=1}^{n} l_i$) with that orientation to calculate the total orientation dependent grain boundary segment density $D_L(\theta)$:

$$D_L(\theta) = \frac{\sum_{i=1}^{n} N(\theta)}{\sum_{i=1}^{n} l_i} \quad [2]$$

The average number of orientation dependent GBSIs divided by scan line length of one scan line, under the condition that the scan line length is consistent, gives the average orientation dependent grain boundary segment density $\bar{x}D_L(\theta)$ for that orientation:

$$\bar{x}D_L(\theta) = \frac{\bar{x}N_L(\theta)}{l_{(\theta)}} \quad [3]$$

2.4 Results

The 'Granular' initial pattern does not preserve a SPO by all methods (Fig. 2.4a). The long axis fitted ellipse orientation includes a maximum azimuth magnitude that covers 8.7 % of the data at 38°, with the mean segment orientation (MSO) at 29°. The GBSI density rose is uniformly rounded in shape overall, α is 28.5°, respectively.

The 'Foam' initial pattern (Fig. 2.4b) shows a stronger fitted ellipse long axis preferred orientation with the maximum azimuth magnitude of 12.2 % and a well-defined 'neck' perpendicular to the maximum segment. The segment orientation rose has a distinct symmetry with a rhombic shape. The shape of the GBSI density contour rose is almost hexagonal, with straight flanks and several maxima, and α at 135.5°.

Incremental stretching of both initial patterns resulted in the systematic development of SPO (Fig. 2.4c,d). During the steps, the maximum azimuth magnitude of the long axis orientation rose increases to 43 % and 63.7 % for 'Granular' and 'Foam' patterns, respectively, whereas the 95 % confidence interval decreases. The segment orientation rose of 'Foam' retails a rhombohedral shape until 400 % stretch, with progressive thinning and elongation of the rhombus. The shape of the GBSI density rose for the 'Foam' pattern initially changes towards rhombic (at ~ 110-200 % stretch), and then rapidly develops an hourglass shape with α close to 90°, whereas the 'Granular' pattern forms the hourglass shape after ~ 250 % stretch.

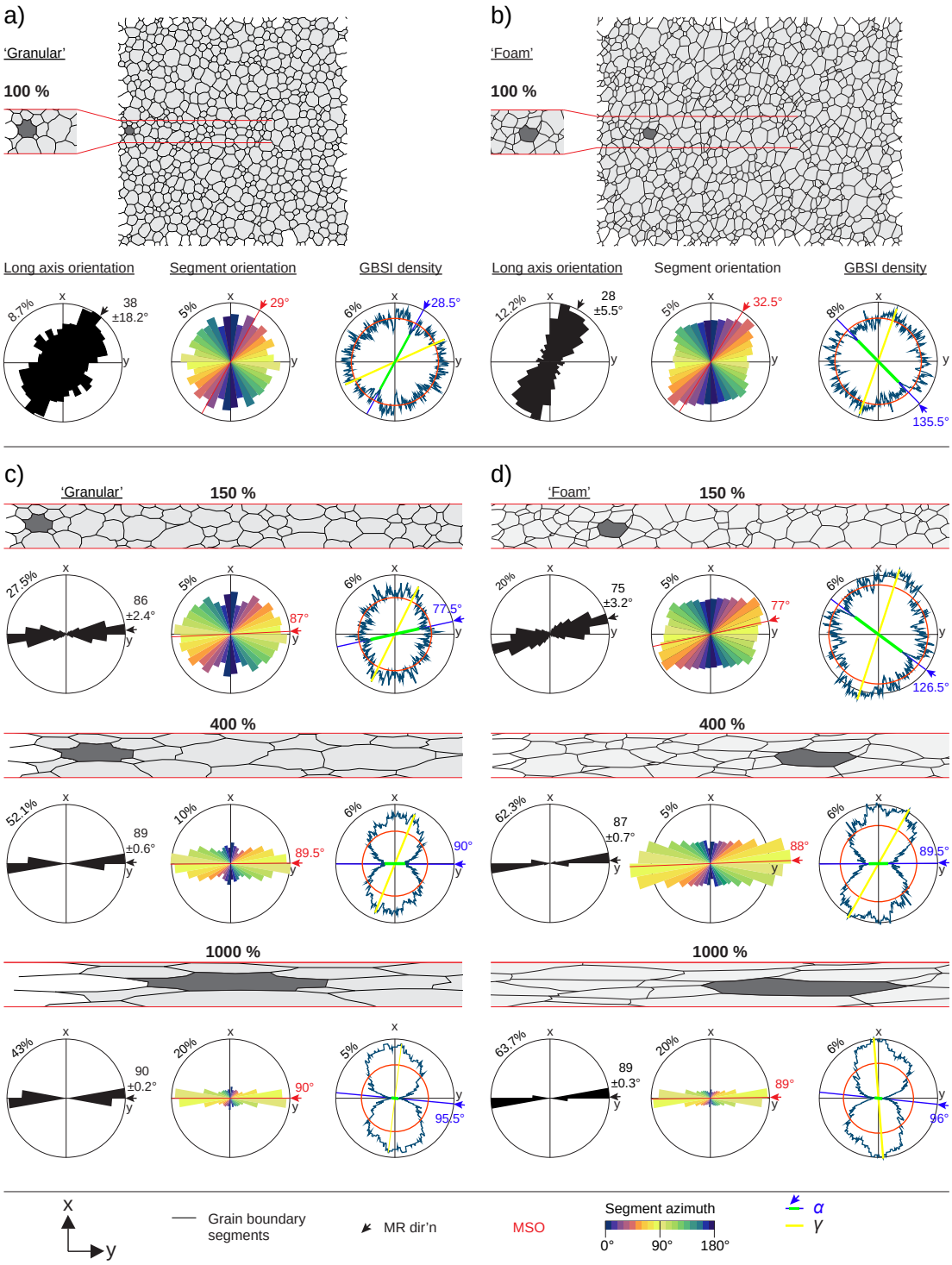

Figure 2.4: Two case studies of 'simple' initial 2D grain microstructures: 'Granular' and 'Foam', analysed via three different analytical methods. a) and b) Analysis of original trace patterns of each microstructure with long axis orientation rose plots, based on the long axis of the fitted (grain) ellipses from ImageJ analysis data. Grains cut by the frame are excluded from analysis, and (grain boundary) segment orientation plotted as equal area, non-length-weighted roses via GBPaQ. Dataset includes segments of rim grains. GBSI density contour rose diagrams from radial scan line distribution analysis are also

presented, where the average GBSI density is shown as red circle and the orientation dependent GBSI density is marked by a blue contour. c) and d) show the evolution of the patterns with stretching steps. A section of the grain boundary pattern with one grain marked throughout the stretching steps is shown for each selected step.

2.5 Discussion

2.5.1 Comparison of different methods and the impact of length-weighting

The long axis orientation (fitted ellipse), segment orientation, and GBSI density and orientation results of the 'Granular' pattern are perfectly consistent with each other (Fig. 2.4a,c). The 'Foam' pattern results show distinct deviations between the different methods (Fig. 2.4b,d). While the long axis orientation and segment orientation roses are consistent at low stretch, GBSI density α is different by ~ 100°. Therefore, α is susceptible to subtle variations in the pattern at low strains (weak SPOs).

Length-weighting makes only a slight difference for the initial 'Granular' pattern with regular radial distribution of increasing and decreasing bin lengths, whereas stretching of the 'Granular' and the 'Foam' patterns both show weakening and intensification over several orientation bins (Fig. 2.5a). The non-length-weighted rose is very evenly rhombohedral, whereas the length-weighted rose shows that the maximum azimuth magnitude is surrounded by several similar intensity peaks (plateau) (Fig. 2.5a). The long axis orientation and the circular mean segment orientation (MSO) are based on the complete pattern, whereas the GBSI analysis without smoothing is selective. Single radial scan results are susceptible to pattern inhomogeneity (i.e., stochastic variation), and are consequently sensitive to the positions of the scan lines. The distinct deviation of density contour shape and angle of α from GBSI density analysis, compared to results from the other methods (Fig. 2.4b,d) are direct measure of inhomogeneity (stochastic fluctuations) in the grain boundary pattern rather than an 'uncertainty' due to imprecise quantification. The location of α depends on a single minimum value, which may be subject to such stochastic fluctuations in the grain boundary pattern.

The application of a smoothing function could significantly reduce the impact of such stochastic fluctuations. However, contrary to conventional more sophisticated strain analysis methods, any smoothing algorithm needs to honour the complex shape of the GBSI density plots rather than smoothing these complex shapes to perfect ellipses. For example, some smoothing algorithms could easily eradicate GBSI minima and

maxima, and therefore features like the rhombohedral GBSI density contour of the 'Foam' pattern would be lost. Therefore, it is necessary to evaluate the degree of necessary smoothing to allow for complex shapes.

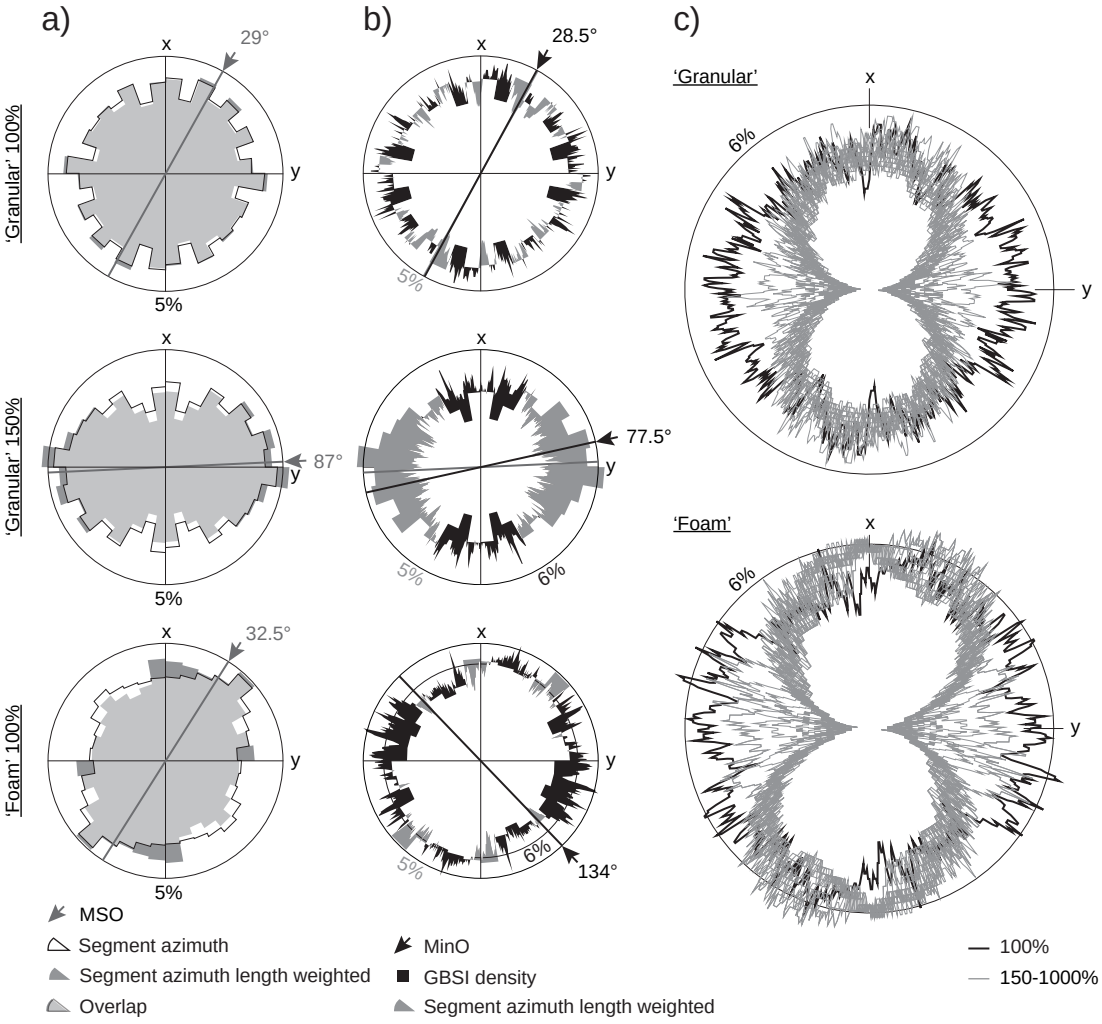

Figure 2.5: Segment azimuth and GBSI density for 'Granular' and 'Foam' grain boundary patterns. a) Comparison of length-weighted and not length-weighted segment orientation roses from GBPaQ analysis. b) Diagrams comprise superimposed length-weighted segment orientation and GBSI density plots. c) GBSI density contour rose diagram of all stretching steps of the 'Granular' pattern and the 'Foam' grain boundary pattern, respectively.

2.5.2 Systematic evolution of I_{min} with increasing SPO strength

Values of $\bar{x}N_L(\theta)$, $N_L(\alpha)$ and $N_L(\gamma)$, as well as I_{min}, have been calculated automatically for each stretching step using GBPaQ. The SPO evolution is analysed by plotting I_{min} against r. The results of the I_{min} development show that I_{min} first decreases rapidly

towards 0 with increasing stretching (Fig. 2.6). Both patterns have I_{min} trends that evolve following a general power law function ($y = x^{-a}$) during stretching.

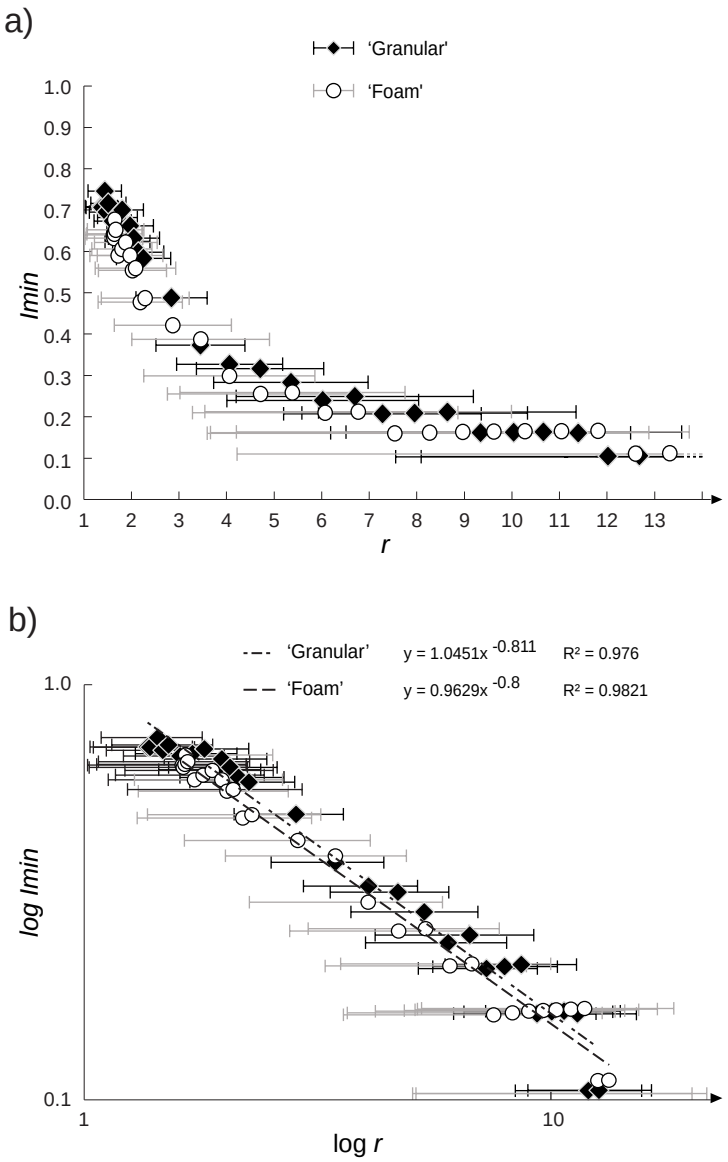

Figure 2.6: Minimum intercept intensity I_{min} of the two patterns and stretching steps, plotted versus axial ratio *r* of the fitted ellipse in a), and as power law trend lines in log-log space in b).

The power law relationship of I_{min} and *r* is consistent with the simple geometrical consideration that the stronger the SPO, the greater the spacing between grain boundary segments in the maximum grain elongation alignment direction. Hence, stretching (strain) results in the rapid decrease of the number of GBSIs in α. This is a power law relationship, visible in the I_{min} versus *r* diagram (Fig. 2.6) and GBSI density contour diagrams (Fig. 2.5c), where the contours at first rapidly (exponentially) close

in parallel with the stretching orientation. The grain boundary segments get re-oriented and increase in length successively with increasing stretch. The degree of this rotation during stretching is strongly dependent on the initial orientation and to a slightly lesser degree, on their length. Segments with closer azimuths to the direction of stretch rotate within the first increments of strain and lengthen more rapidly. The segments intercepted along α are selectively shorter and increasingly sorted for angles perpendicular to the orientation from the scan line with increasing SPO strength.

2.5.3 Potential applications of GBSI-based quantification to geological problems

The power law trend relation is also a combination of two method approaches, as it combines fitted ellipse-based r and GBSI-based I_{min} concept. The calculation of I_{min} provides a powerful tool for quantifying the SPO strength without being limited by scale or unit, and therefore makes it easy to compare a pattern to any other.

The I_{min} versus r diagram with the definition of a reference power law trend makes it possible to plot any r or I_{min} and determine a range of the corresponding value. For the establishment of such a reference diagram, further investigations with different strain geometries and patterns with more complex geometry are inevitable. Further, the variance of I_{min} needs to be investigated. Identification and quantification of deformation mechanisms using a GBSI-based method in combination with quantitative grain boundary irregularity via sphericity parameter determination, as introduced by Fan et al. (2021) may be of great value.

The big advantage of a GBSI approach is that pattern characteristics like the directional density of grain boundaries, directly using grain boundary segments, as well as grain and grain pattern geometry are analysed directionally. Thus, the GBSI rose plot can be used to study the impact of grain boundaries on directional characteristics like acoustic wave velocity anisotropy. Though it is known that seismic velocity is controlled to a high order by crystallographic preferred orientation (CPO) (e.g., Lloyd et al., 2011a; Zhong et al., 2014; Vel et al., 2016), the impact of other petrofabrics like grain boundaries and SPO is not yet fully understood (e.g., Burlini and Kunze, 2000; Valcke et al., 2006; Vargas-Meleza et al., 2015). Three possible main applications that involve GBSI-based quantification analysis via GBPaQ are identified, illustrating different strengths of this approach:

I) More representative pattern quantification combining fitted ellipse, segment geometry, and GBSI methods provides the opportunity of analysing more complex patterns than was possible before.

II) Comparative, quick SPO quantification of different, potentially unrelated patterns by calculating I_{min} values, and with the potential to determine correspondent pattern characteristics using a future, more refined I_{min} versus r diagram with reference power law curve(s).

III) Direction-based grain boundary pattern quantification via GBSI density and orientation analysis provides more representative data on directional characteristics. GBPaQ could develop into a useful tool for studying the impact of grain boundary pattern inhomogeneity and anisotropy on rock characteristics like seismic wave attenuation, physical and mechanical behaviour.

2.6 Conclusions

Given established importance of grain boundary networks, it is critical that we quantify them with objective, robust, repeatable and open source methods. Accordingly, it is of major importance to quantify grain boundaries using state of the art automation (with toolboxes like GBPaQ) to support recent analytical developments (e.g., micro-CT).

The minimum intercept intensity power law trend and GBSI density contour rose diagram are promising tools for further SPO and grain boundary pattern geometry quantification. Testing of the GBSI approach on three different grain boundary network patterns has led to the following findings:

- Length-weighting of segment orientation roses represents pattern geometry that may weaken SPO quantification but gives a more representative depiction of the pattern without simplification.
- GBSI roses capture a more representative depiction of directional characteristics of a grain boundary pattern, yet the orientations of α and ɣ are more likely to have big angular variations compared to non–GBSI-based methods. Higher angular variations in α and γ are anticipated for populations of approximately equant grains.
- Plotting the evolution of I_{min} versus r as data points shows a general trend that can be described by a power law.

CHAPTER 3

Grain boundary (shape) evolution of single and dual-phase aggregates during plane-strain deformation – Combining numerical simulations with grain boundary intercept based SPO quantification

Abstract

Application of a grain boundary segment-based shape preferred orientation (SPO) analysis to simulated, evolving microstructures unlocks a new understanding of SPO pattern development during progressive shear and in single and multi-phase rocks. Viscoplastic numerical simulations were used to generate grain boundary patterns with pre-defined characteristics deformed under different conditions. Variables in initial models included single- and two-phase materials with two grain sizes. Numerical deformation simulations that incorporate dislocation glide were run with end-member simple shear and pure shear strain geometries, resulting in significant grain elongation and rotation. SPO is stronger in single-phase models, independent from strain geometry, and visible in grain boundary segment azimuth and grain boundary segment intercept (GBSI) density analysis. Grain boundary segment azimuth roses show different mean orientation evolution depending on strain geometry. GBSI density-based minimum intensity (I_{min}) shows that pure shear models have slightly stronger SPO. The contour plots of GBSI density evolution have strain geometry specific shapes. The applied GBSI method was capable to quantify different deformation mechanisms and parameters. Future work might focus on further deformation mechanisms like dislocation climb, grain boundary migration, grain boundary sliding, and application to natural rocks.

3.1 Introduction

It has long been established how the orientations of macroscopic "bulk" lineations evolve during progressive deformation in shear zones (e.g., Simpson and De Paor, 1993*;* Fossen and Cavalcante, 2017), but details of the evolution of grain shapes in polycrystalline aggregates at the microstructural scale have received comparatively less attention. A shape preferred orientation (SPO) is defined as a measure of the

alignment of non-equidimensional grains in a rock or crystalline material and is a fundamental descriptor of material microstructures and petrofabrics (Panozzo, 1984; Passchier and Trouw, 2005; Launeau et al., 2010). Furthermore, the effects of second phases are not generally considered for the development of lineations or SPOs in established models of shear zones, even though most natural rocks are comprised of more than one mineral phase that controls their microstructures and rheology (e.g., Jessell et al., 2009; Llorens et al., 2019).

Previous studies of SPO quantification have focussed on the analysis of long axes of grains, whereas the evolution of grain boundary patterns, which are key for the characterisation of the rock microstructure, has been given little attention. Understanding how grain boundary patterns evolve is important because grain interfaces can host and transmit fluids (e.g., Rutter, 1976; Isrealachvili, 1992; 2011; Hickman and Evans, 1995), be preferred sites where diagenetic and metamorphic reactions occur (e.g., Urai et al., 1986a,b Wheeler, 2018), exert a first-order control on the material strength, and attenuate tele seismic waves (e.g., Kern and Wenk, 1985; Valcke et al., 2006; Vargas-Meleza et al., 2015). Therefore, the significance of developing an understanding of the behaviour of grain boundary patterns during progressive deformation of polycrystalline materials broadly applies across metamorphic petrology, tectonics, structural geology, geophysics, mineral and rock physics, and material science.

Microstructures are a coupling link between material properties, boundary conditions and processes that together control the behaviour and evolution of a rock (Piazolo et al., 2019). They describe the state a rock achieves as a result of the interplay between various processes and boundary conditions. A microstructure might be preserved for millions or billions of years, whereas temperature or elastic strain is ephemeral (Piazolo et al., 2019). Therefore, microstructures are one of the prime forensic tools that can be used to unravel the history of a rock, allowing us to deduce the succession of strain rates, stresses, diagenetic and metamorphic conditions as well as rock rheology before, during and after deformation (e.g., Passchier and Trouw, 2005). However, a microstructure plays an active and central role in the evolution of a rock (Gottstein, 2004). Consequently, rigorous analyses and correct interpretations of rock microstructures is crucial in understanding rock deformation and rheology (Piazolo et al., 2019).

The grain boundary pattern has long been used as a tool for strain analysis (Flinn, 1962; Ramsay, 1976; Fry, 1979; Fossen, 2016). The most common way of SPO quantification in 2D polished sections is by using fitted ellipses to roughly elliptic shaped grains and particles (Flinn, 1962; Dunnet, 1969; Elliott, 1970; Ramsay, 1976). Grains (or objects such as ooids, pebbles, lapilli) are typically approximated as fitted ellipses or ellipsoids, and an SPO can be defined by the orientation distribution and axial ratios of their longest and shortest principal axes. For homogeneous strains in 3D, a dataset of multiple grains/objects can then be fitted with a finite strain ellipsoid, which has three mutually orthogonal planes of symmetry that represent the relative orientation and stretch of the principal strain axes (Fossen, 2016).

Another method for 2D strain determination from SPOs in deformed rocks is the regular SURFOR (SURFace ORientation) and inverse SURFOR wheel analysis, developed by Panozzo (1983; 1984; 1987). The inverse SURFOR wheel is based on the concept of change of probability of interception of grain boundaries on a given traverse as a function of its orientation. A set of parallel scan lines that are rotated counter clockwise towards 18 different orientations in 10° steps are used to collect the data. The intercept density is then plotted as a strain ellipse, or as a sinusoidal curve, against the orientation of the scan line. Other parameters like the distance between intercepts (Panozzo, 1987; Launeau et al., 2010) or the tie lines between centre points of neighbouring grains (Ramsay, 1976; Mulchrone, 2003) are also quantified. Grain boundary intercept-based methods have the advantage that they are based on the grain boundary pattern geometry and, thus, provide more information than the fitted ellipse approach that merely summarizes the grain boundaries. Automated intercept-based versions rely on image processing (Launeau et al., 1990; Heilbronner, 2000; Herwegh, 2000) for quick and systematic identification of grain boundaries.

A more detailed analysis of the grain boundary pattern characteristics can be generated from the combination of the well-established and widely-used approach of using segments for fracture analysis (vectors describing a fracture) by using the MATLAB™ toolbox FracPaQ (Healy et al., 2017), with an adjusted version of the grain boundary intercept method.. Tracing microstructural elements manually is a time intensive but common technique, primarily used for microstructure analysis with freely available raster graphics software (e.g., ImageJ; Schneider et al., 2012) and also the basis for the fitted ellipse-based strain analysis. The here introduced minimum intensity (I_{min})

(chapter 2) is a quantifiable parameter, useful to determine the strength of weak SPOs, and complements other approaches, such as fitted ellipse axial ratios.

Our understanding of the evolution of SPO during progressive deformation is mostly limited to simplification of the geometry of the finite strain ellipse in simple and pure shear. However, no studies have documented the evolution of grain boundary patterns in detail yet.

Furthermore, the grain boundary pattern evolution in two-phase systems has not yet been quantitatively investigated. Numerical models of two-phase systems, where there are minerals, objects, or layers with different mechanical behaviours, are generally used to study the evolution of polymineralic aggregates, rigid object rotation, or folding, among others (e.g., Jessell et al., 2009; Griera et al., 2013; Ran et al., 2018).

For example, the interaction of rigid or soft inclusions relative to a matrix can be used to simulate ductile deformation of conglomerates and to predict in what situations porphyroclasts and porphyroblasts rotate (Jessell et al., 2009; Griera et al., 2013; Ran et al., 2018). Clusters of phases are known to change the deformation dynamics such that the deformation of one phase is impeded due to the presence of another phase, and formation of clusters of high viscosity particles cause disturbances of the matrix flow (Ildefonse et al., 1992a,b; Samanta and Bhattacharyya, 2003; Marques et al., 2014). Closely spaced particles are known to form clusters or trains that mechanically act as single particles (Blumenfeld and Bouchez, 1988; Tikoff and Teyssier, 1994; Jessell et al., 2009).

This study presents a workflow for the characterization of grain boundary patterns (ELLE maps and GBPaQ analytical results), for fine- and coarse grained single- and two-phase materials during progressive pure- and simple shear. The evolution of a) the bulk GBSI density by azimuth, b), the minimum and maximum GBSI intercept density orientations (α and γ), c) the grain boundary segment orientations intercepted by the minimum and maximum GBSI density scan lines, and d) the minimum grain boundary intercept intensity (I_{min}) is quantified.

3.2 Methods

Using numerically simulated microstructures are advantageous for testing methods for SPO quantification because they offer the opportunity to (a) control initial parameters

(e.g., number of phases, their rheological properties, strain geometry, phase distribution, and grain size and shape distributions), and (b) investigate the evolution of microstructures with progressive strain. Therefore, a series of simulations with the open-source VPFFT-ELLE approach (http://elle.ws) were run for this study. This couples the viscoplastic Fast Fourier Transform (VPFFT) code (Lebensohn, 2001; Lebensohn et al., 2008; Griera et al., 2013; Llorens et al., 2016; Ran et al., 2018) with ELLE modules.

Eight ELLE model configurations simulated the deformation of 2D single- and two-phase microstructures of initial homogeneous foam texture patterns, with two different initial grain sizes, and in progressive pure shear and simple shear plane-strain end-member boundary conditions. Models were run up to a natural strain of 2 in 100 time steps, with natural strain increments of 0.2. The grain boundary patterns were analysed via automated grain boundary segment orientation analysis (FracPaQ, Healy et al., 2017) and the newly-developed automated grain boundary segment intercept (GBSI) based methods (GBPaQ, chapter 2).

3.2.1 Numerical modelling with VPFFT-ELLE

The initial microstructure in ELLE consists of straight segments connecting boundary nodes (*bnodes*). These segments form polygons (also termed *flynns* or grains). There are two types of boundary nodes: double nodes, which have two neighbour nodes and belong to two polygons, and triple nodes, which have three neighbour nodes and belong to three polygons. This analysis process considers that each segment between two consecutive *bnodes* is an individual grain boundary segment. VPFFT uses a regular mesh of nodes, termed unconnected nodes or *undoes*, which are not related to the boundary nodes, and that store properties such as crystal lattice orientation and dislocation density.

The model boundaries are periodic both in X and Y, so if a grain is cut by the model boundary, the other half of the same grain can be found on the opposite side of the model (e.g., Jessell et al., 2009). The four boundaries of the ELLE bounding are periodic, and thus the pattern can be multiplied due to this periodicity, forming an infinite mosaic. For simple shear simulations, a routine repositions all the nodes and segments into a 1x1 bounding box, to allow visualisation of the microstructure up to high strains. The boundary conditions in simple shear were applied along randomly

positioned horizontal lines at every incremental time step to spread their effect through the whole model. For pure shear simulations, the pattern was multiplied once in Y, meaning that the pure shear pattern is composed of two sets of the exact same pattern used for simple shear.

The software platform ELLE was coupled with the VPFFT code, thus allowing the full-field simulation of various systems with different mineralogy, deformation mechanisms, etc. Lebensohn (2001), Lebensohn et al. (2008; 2009) Griera et al. (2011; 2013) and Llorens et al. (2016).

Dislocation glide was used as the only deformation mechanism for the numerical simulations in this study. The results are therefore relevant to rocks or materials that have been deformed in the dislocation glide-dominated creep regime. Dislocation glide, along with dislocation climb, is an essential part of dislocation creep. Dislocation glide is known as the dominant deformation mechanism throughout metamorphic zones affecting minerals and aggregates at low- and medium-grade metamorphism. Understanding deformation glide, how it operates, and the resulting flow laws are key to ultimately understanding the rheology of rocks under metamorphic conditions. In the case of natural salt deposits, which are of major impact for basin rheology, dislocation creep processes, as well as solution-precipitation creep and water-assisted dynamic recrystallisation, are all of major importance (Urai et al., 1987; Schléder and Urai, 2005; Urai et al., 2008).

Dislocation glide was simulated in a way that each point is a crystallite with a certain lattice orientation. Crystal symmetry and the available slip systems were defined, together with the ratios of critically resolved shear stress (CRSS) required to activate glide of dislocations for each slip system concerning the softer system. In this way, deformation was accommodated according to the lattice orientation and available slip systems. The models used in this study were limited to deformation via dislocation glide in a way that dislocation climb and recrystallisation processes were not simulated. A hexagonal base symmetry was used with three slip systems: basal, pyramidal, and prismatic, similar to Griera et al. (2011; 2013), Ran et al. (2018; 2019), and Llorens et al. (2019). The models are limited to single- and two-phase simulations. In the single-phase models all grains had the same effective viscosity, in which the CRSS ratio for all slip systems is 1. Two-phase simulations included grains of two

isotropic phases, meaning the CRSS ratios for the slip systems of each phase were the same, but in which the CRSS needed to activate dislocation glide for the hard phase (high viscosity phase) was five times higher than that required to activate the soft one (low viscosity phase). The two-phase models initially had 50 % of the grains of each phase (hard and soft).

Several statistical grain boundary pattern characteristics were exported from ELLE per time step (Appendix B; Fig. B.1, and B.3; digital Appendix B). They included the minimum and maximum angles from a reference orientation. The maximum and minimum angles were measured from segments defined by consecutive boundary nodes. The number of grains in the models changed slightly across time steps due to topological modifications that were conducted every time step to be able to reach high strain. There was a minimum and maximum boundary node separation. If the distance between two neighbour grain boundary nodes was too high a new node is added. If the distance got too small, a node was removed. Moreover, when two triple nodes got too close, switches were applied to maintain a grain pattern that could be deformed in the next time step.

There were also situations in which a grain is split into two or two grains are merged. Moreover, a minimum number of crystallites (unconnected nodes) was needed within each grain and ELLE automatically does topology changes to maintain this. Accordingly, this parameter was not meaningful in the models presented here. However, it is useful when there are recrystallisation processes active (e.g., subgrain rotation, grain boundary migration, new grain nucleation), which can increase or reduce the number of grains due to physical processes and not because of topology checks. The relationship between crystallographic preferred orientation and grain boundaries was deliberately excluded, as the scope of the study is limited to quantification of the shape of microstructures. Other exportable parameters related to the grain boundary length, grain boundary elongation, angles were valuable for SPO quantification.

3.2.2 Case studies

All models were based on two different initial foam textures (Fig. 3.1a,b; Fig. 3.3a; Table. 3.1), generated to simulate equant grains with randomly oriented (no/weak SPO) grain boundary patterns and small variance in grain size. The coarse-grained

model, which initially had 250 grains, and a grain boundary pattern built by 3,475 linear grain boundary segments, of which 1,615 were phase boundary segments. The fine-grained model, which initially had 2,626 grains, contained a grain boundary pattern consisting of 26,805 linear grain boundary segments, with 12,730 of them being phase boundary segments.

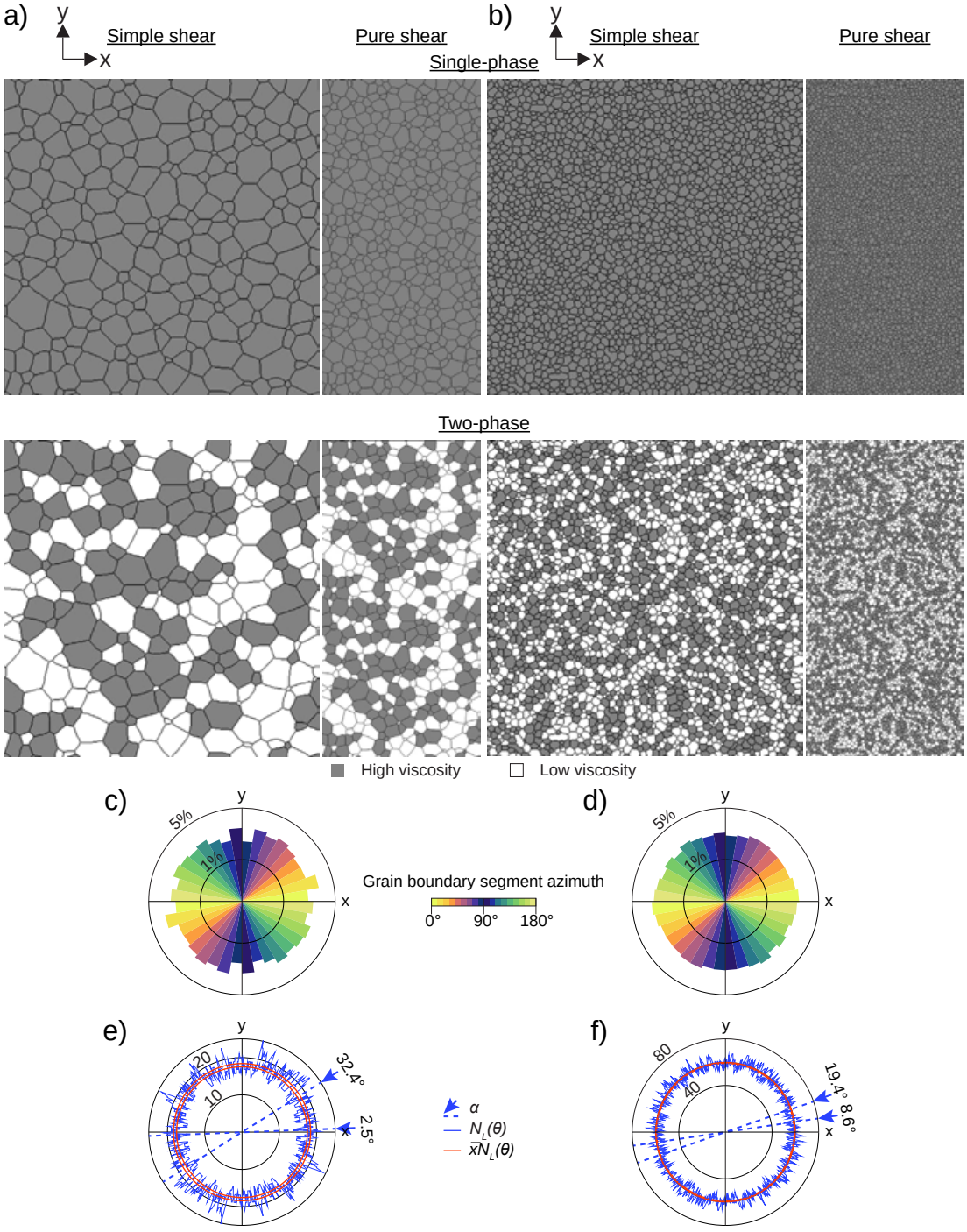

Figure 3.1: Maps and plots of initial (time step = 0) microstructural models used for deformation simulations and quantification of the evolution of SPO. a) The four time

step 0 maps for coarse grained simple shear and pure shear, single-phase and two-phase deformation models. b) The four fine grained time step 0 maps equivalent to a). White grains have lower viscosity; grey grains have five times higher critical resolved shear stress. For pure shear, the basic pattern used for simple shear is vertically repeated. c) Bulk grain boundary segment azimuth rose plot of coarse-grained basic grain boundary patterns, representative for all four models based on the grain boundary pattern. Azimuth is plotted against the frequency (%) in equal area, not length-weighted rose diagrams. d) Bulk grain boundary segment azimuth rose plot representative for all initial fine grained basic grain boundary patterns. e) GBSI density rose plot for coarse grained basic grain boundary patterns. Results from GBPaQ GBSI density analysis, using one central radial scan line centre with 0.5° angles between scan lines. The GBSI density (per pixel) is plotted against scan line orientation as blue contours. The average grain boundary intercept density ($\overline{x}N_L(\theta)$) from all scan lines is plotted as red circles. f) GBSI density rose plot of the fine-grained basic grain boundary patterns. e) and f) each contain two blue lines and two red circles that reveal a difference based on simple shear and pure shear maps. This is due to the different placement of the rotation centre in the double pattern pure shear maps.

Table 3.1: GBPaQ results at initial time step 0 ($\varepsilon_n = 0$) and final time step 100 ($\varepsilon_n = 2$). % = relative to initial value; 1v = single-phase model, 2v = two-phase model; *final step 66 ($\varepsilon_n = 1.32$). Rest of parameter symbols explained in Table 3.2.

		Coarse-grained				Fine-grained			
		Simple shear		Pure shear		Simple shear		Pure shear	
Parameter	ε_n	1v	2v	1v	2v	1v	2v	1v	2v
S	0	3,475	3,475	6,969	6,969	25,805	25,805	51,670	51,670
	2	8,580	7,321	15,772	16,230	55,812	46,213	98,358	87,720
	2 [%]	247	211	226	233	216	179	190	170
$\overline{x}N_L(\theta)$ [ppx]	0	18.2	18.2	17.5	17.5	58.9	58.9	59.7	59.7
	2	45.7	36.2	38.7*	40.0	134.3	107.3	120.2	109.8
	2 [%]	251	199	221	229	229	182	201	184
α [°]	0	2	2	32	32	19.5	19.5	8.5	8.5
	2	14	16	0*	0	15	17	2	7
$N_L(\alpha)$ [ppx]	0	14.8	14.8	13.7	13.7	50.5	50.5	50.5	50.5
	2	6.3	14.7	4.0*	11.9	14.7	33.7	11.9	23.8
ɣ	0	14	14	52	52	331.5	331.5	307.5	307.5
	2	332	346	14*	18	339	355.5	359.5	3
$N_L(\gamma)$ [ppx]	0	23.2	23.2	21.1	21.1	71.6	71.6	68.4	68.4
	2	74.7	60.0	65.9*	59.5	223.2	170.5	214.3	190.5
I_{min}	0	0.80	0.80	0.78	0.78	0.86	0.86	0.85	0.85
	2	0.12	0.35	0.10*	0.19	0.11	0.31	0.10	0.22

The comparison of these two initial models allows evaluating the influence of grain size. The coarse- and fine-grained basic grain boundary patterns were used for running four different models each (Fig. 3.1a, b): i – single-phase in simple shear, ii – single-phase in pure shear, iii - two-phase in simple shear, and iv - two-phase in pure shear. For the models with two-phase grains, approximately 50 % of grains of the pattern were randomly assigned to one of the two viscosities, resulting in a statistically homogeneous distribution of phases. Square 2D models were used for simple shear simulations. For pure shear, they were duplicated to form a 1:2 length to height ratio. The grain boundary patterns were generated to seamlessly fit together, and the set of grain boundary segments was duplicated. Limitation of the models to phase boundary segments reduced the number of segments analysed by more than half. The phase boundary distribution followed the foam pattern and randomly created clusters that included one to several grains of the same viscosity (Fig. 3.2a,b).

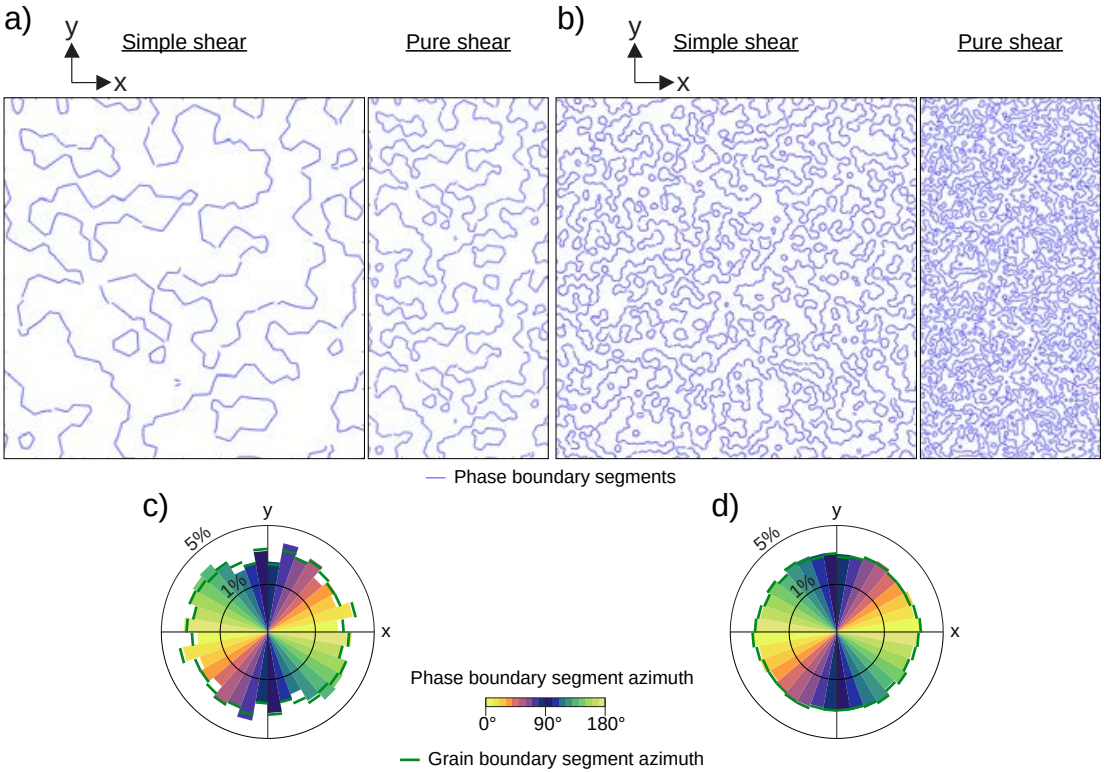

Figure 3.2: Maps and plots of initial (time step = 0) phase boundary models. a) Two time step 0 maps for coarse grained simple shear and pure shear two-phase deformation models. b) Two fine grained time step 0 maps equivalent to a). c) And d) show bulk phase boundary segment azimuth rose plots of coarse grained and fine-grained initial grain boundary patterns. Azimuth is plotted against the frequency (%) in equal area, not length-weighted rose diagrams. See Appendix B, Fig. B.2 for GBSI density rose plots for

all four initial two-phase models. For details on the grain boundary segment azimuth analysis see Fig. 3.2.

3.2.3 Grain boundary segment intercepts and based minimum intensity

The grain boundary segment intercept (GBSI) density method is described and discussed in detail in chapter 2. Intercept-based methods that utilize scan lines are long established in stereology and geoscience (Saltykov, 1958; Underwood, 1970; Daniel et al., 1988). The most utilized versions of intercept-based pattern quantification, including automation, are those of regular SURFOR (Panozzo, 1984) and inverse SURFOR (Panozzo, 1987) methods, and the intercept method version developed by Launeau and Robin (1996), and Launeau et al. (2010). Strain analysis by intercept density is based on the change of orientation of surfaces (i.e., grain boundaries) as a function of strain (Panozzo, 1984).

The main difference is that the GBSI density is calculated for patterns undergoing deformation for this study with the focus on SPO, and not primarily to determine the strain ellipsoid of a specific sample. The method is more dependable in determining the strength of a PO, than in determining its orientation for patterns deformed at low strain (chapter 2). Further, the advantages and disadvantages of minimum intensity (I_{min}) as a tool have not yet been sufficiently studied. The minimum and maximum grain boundary segment density orientations (α and γ) have been shown to differ slightly from the short axis and long axis of the finite strain ellipse (Chapter 2). The GBSI density analysis conducted by GBPaQ is based on radial scan lines emanating from the pattern centre and, therefore, analyses grain boundary segments of part of the pattern and not the whole pattern.

The GBSI density method was applied as follows: GBSI density was calculated along a single set of equal length radial scan lines placed in the centre of the sample patterns, using the MATLAB^{TM} toolbox GBPaQ (chapter 2). Scan line length was determined by the smallest dimension of the pattern (length or height). The angle between scan lines ($d\beta$) was set to 0.5°. The density was calculated as a total measure. A 0.5°-degree distance between scan lines means that the same segment will be counted multiple times by neighbouring scan lines and was chosen because the objective is to find the minimum grain boundary intercept density ($N_L(\alpha)$), rather than the strain ellipsoid through intercepts.

Minimum intensity I_{min} is introduced in chapter 2. It provides a tool that combines preferred grain orientation variation and elongation. Minimum intensity (I_{min}) relates the minimum GBSI density ($N_L(\alpha)$) to the average GBSI density ($\bar{x}N_L(\theta)$).

$$I_{\min} = \frac{N_L(\alpha)}{\bar{x}N_L(\theta)} \quad [1]$$

Alternatively to using densities, it can also be calculated using the minimum number of GBSIs ($N(\alpha)$) divided by the average number of GBSIs intercepted per scan line ($\bar{x}N$), under the condition that the scan line length is constant and the number of scan lines in each orientation is considered.

$$I_{\min} = \frac{N(\alpha)}{\bar{x}N} \quad [2]$$

Minimum intensity is dimensionless and ranges between 0 and 1. SPO weakens towards 1 and increases in strength towards 0. It is a method to calculate a dimensionless strength of SPO for different patterns.

Table 3.2: List of symbols used in relation to GBSI-based quantification

Symbol	Description
S	Number of grain boundary segments
N	Number of grain boundary segment intercepts
θ	Scan line angle (between 0 to 180°, anticlockwise from x)
$d\beta$	Angular intervals between scan lines
α	Orientation of (scan line with) minimum intercept density [°]
γ	Orientation of (scan line with) maximum intercept density [°]
ϕ	Angle between minimum and maximum intercept density orientations (scan lines) [°]
$N(\alpha)$	Minimum number of intercepts
$N(\gamma)$	Maximum number of intercepts
$\bar{x}N$	Average number of intercepts
$\bar{x}N_L(\theta)$	Average orientation dependent segment intercept density
$N_L(\alpha)$	Minimum segment intercept density
$N_L(\gamma)$	Maximum segment intercept density
$I(min)$	Minimum intensity

3.3 Results

3.3.1 Initial grain boundary pattern characteristics

Pattern analysis was conducted using ELLE statistical monitoring data during the deformation for each time step (0-100) and GBPaQ data on the grain boundary segments and GBSI analysis (Fig. 3.1; Table 3.1). The GBSI density rose diagrams (Fig. 3.1e,f) show a slight variation in the GBSI density outline and $\bar{x}N_L(\theta)$ (red circles)

between simple shear and pure shear maps, which is most visible in the data from coarse grained models.

Conversely, α is significantly different between strain models, with a ~ 30° angle (2.5° to 32.4°) between simple and pure shear grain boundary maps for the 250/500 grain pattern and ~ 11° (8.6° to 19.4°) for the 2,626/5,252 grain boundary map (Fig. 3.1e,f, blue arrows). Both grain boundary segment azimuth plots (Fig. 3.1c,d) and GBSI density rose plots (Fig. 3.1e,f) of initial patterns show the absence of a SPO and are effective visualizations of the randomly oriented and distributed grain boundary segments, respectively.

Consistent grain boundary intercept magnitudes with orientation results in an almost isotropic GBSI density of initial patterns. Furthermore, I_{min} for initial patterns was high, ranging between 0.86 and 0.78 (Table 3.1). The outlines of segment azimuth roses of the fine-grained grain boundary pattern (Fig. 1d) is smoother than for the coarse-grained models. The slightly hexagonal shape of segment azimuth roses is explained by foam textures tending to the energetically most ideal state, which is achieved by grain boundary curvature and length reduction, and triple junctions stabilising at 120º.

The phase boundary segment azimuth plot of the initial pattern of the two-phase coarse-grained models (Fig. 3.2c) differs slightly from the grain boundary segment azimuth plot (Fig. 3.1c), with more variation in magnitude between neighbouring orientation. The absence of a SPO is still indicated. The corresponding grain boundary segment and phase boundary segment azimuth plots of the fine-grained models are almost identical (Fig. 3.1d, and 3.2c), despite a significant reduction of segments analysed.

3.3.2 Grain boundary pattern evolution

Single-phase models (both pure, and simple shear) show the development of a pattern that can be described as a single foliation, which intensifies with increasing strain (Fig. 3.3, left side). The two-phase models (both pure, and simple shear) initial formation of an anastomosing pattern, which develops into systematic S-C or shear band fabric with increasing strain (Fig. 3.3, right side). Low viscosity grains tend to align to form shear bands.

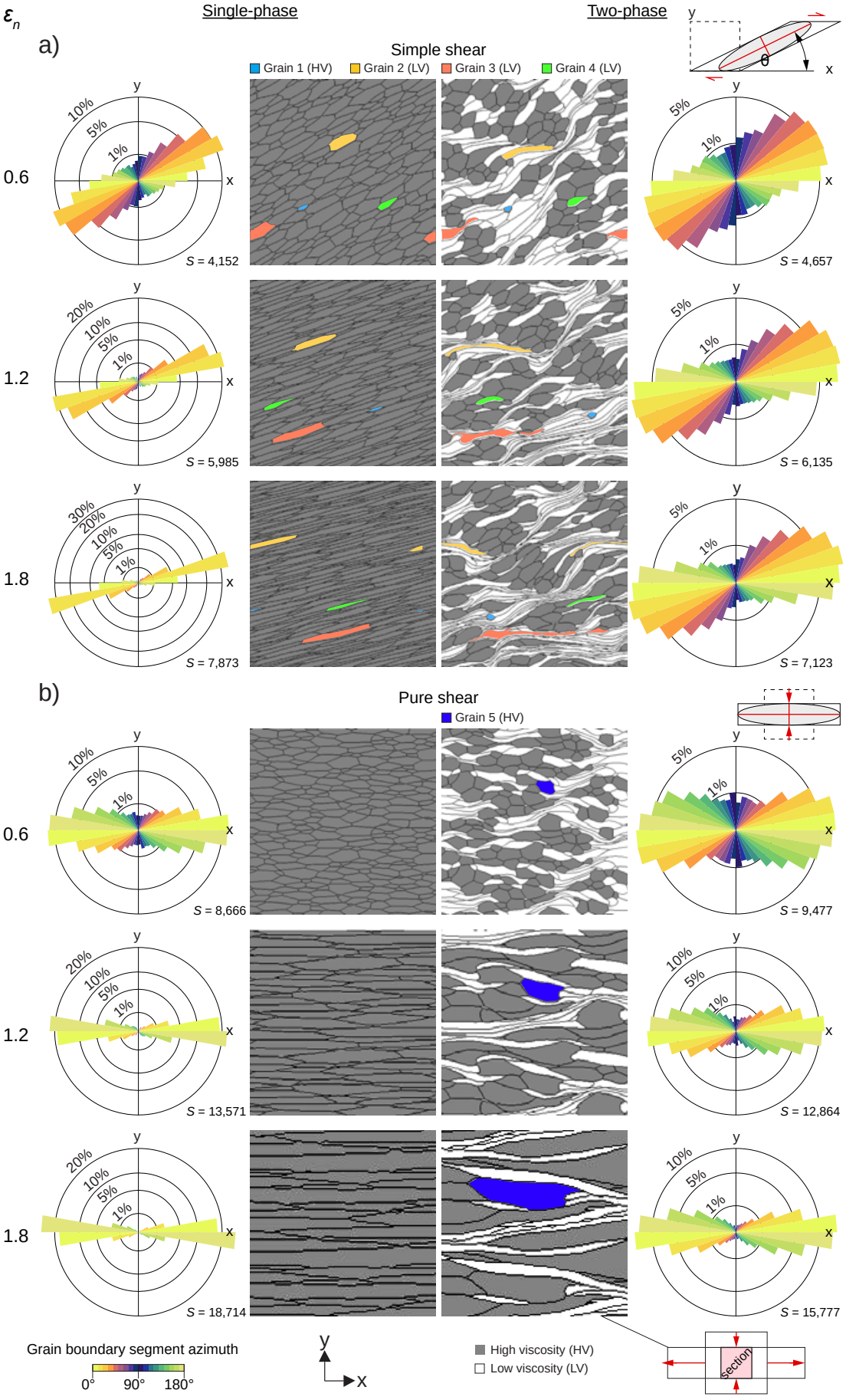
ε_n
Single-phase
Two-phase
a)
Simple shear
Grain 1 (HV)
Grain 2 (LV)
Grain 3 (LV)
Grain 4 (LV)
θ
0.6
1.2
1.8
S = 4,152
S = 4,657
S = 5,985
S = 6,135
S = 7,873
S = 7,123
b)
Pure shear
Grain 5 (HV)
S = 8,666
S = 9,477
S = 13,571
S = 12,864
S = 18,714
S = 15,777
Grain boundary segment azimuth
0°
90°
180°
High viscosity (HV)
Low viscosity (LV)
section

Figure 3.3: Development of the four coarse grain size models represented by the pattern maps and equal area, length-weighted grain boundary segment azimuth rose plots at natural strains (ε_n) of 0.6, 1.2 and 1.8 (time steps 30, 60 and 90) for a) simple shear and b) pure shear. The maps shown for b) pure shear are square sub-areas, enlarged from the centre of each simulation. *S* is the number of segments analysed. Four grains are marked by assorted colours in a) to track the effect of strain geometry and viscosity variance over simulated strain. Grain 1 in the simple shear two-phase model has five times the viscosity of grains two, three and four in the same model. A different grain is marked in b) pure shear, two-phase model to track the evolution of a high viscosity grain. Due to the pure shear strain geometry, the shape of the used grain boundary map (originally 1:2) significantly increases in length, as the map height decreases. The pure strain maps have been magnified accordingly, showing only a square section of the very centre of the elongating map.

The two-phase, simple shear model (Fig. 3.3a, right side) shows that the higher viscosity grains (in grey) develop weaker elongation compared to the lower viscosity grains (in white) and to the grains of the single-phase model (Fig. 3.3, left side). The low viscosity grains become strongly elongated and form shawls (sigmoidal clusters) throughout the pattern (Fig. 3.3).

3.3.2.1 Tracking of viscosity dependent grain evolution

Comparison of grain shape evolution shows how fundamentally different the microstructures develop between the single- and two-phase scenarios. This is illustrated by tracking several grains in the coarse grain boundary pattern (labelled 1 to 5 in Fig. 3.3; Appendix B, Fig. B.4). In the simple shear single-phase model, all grains show similar shape and orientation evolution that is somewhat representative of the SPO defined by the entire microstructure, forming a foliation (Fig. 3.3a, left side). The two-phase models show the formation of sigmoidal grains as part of developing shear bands (Fig. 3.3a, right side). Each tracked grain of the two-phase models displays a fundamentally different strain behaviour.

Grain 1 shows how a grain with high viscosity, surrounded by low viscosity grains rotated synchronously to the surrounding low viscosity grains, but did not undergo significant elongation (Fig. 3.3a, right side).

A low viscosity grain (Grain 2) surrounded an equally proportion of low and high viscosity grains (Fig. 3.3a, right side) elongated quickly as part of a cluster built by the

surrounding low viscosity grains and deformed more compared to its equivalent in the single-phase model (Fig. 3.3a, left side). It also takes on a sigmoidal shape, the same as the cluster that is strongly elongated in the *x* direction (Fig. 3.3a, right side).

Grain 3 is a low viscosity grain surrounded mostly by other low viscosity grains that became less sigmoidal compared to Grain 2 and very elongated parallel to *x* (Fig. 3.3a, right side). In between time step 36 and 45 (natural strain of 0.72 and 0.90), this grain is situated between two high viscosity grains, which causes it to neck and separate into two grains.

A solitary low viscosity grain (Grain 4) surrounded by high viscosity grains evolves in a similar way to its single-phase counterpart, both in rotation and elongation magnitudes (Fig. 3.3a, right side). Grain 5, only marked in the pure shear two-phase map (Fig. 3.3b, right side), is a case study for a high viscosity grain initially surrounded by both, low and high viscosity grains. Rotation towards 0° (*x*) is reached within the first few increments of deformation.

It is evident from the maps in Figure 3.3b that the elongation of the low viscosity grains in the pure shear two-phase models (Fig. 3.3b, right side) is much weaker compared to the grains in the pure shear single-viscosity models (Fig. 3.3b, left side). High viscosity grains and clusters in the pure shear two-phase models are strongly elongated and sigmoidal (Fig. 3.3b, right side).

3.3.2.2 Evolution of grain boundary segment azimuths

Both grain-scale observations and grain boundary segment azimuth rose plots show increasing elongation and strengthening of SPO with increasing natural strain (Fig. 3.3). Trends in all results for coarse- and fine-grained models are similar, with the main difference being that coarse grained models tend to yield results with more ‘statistical noise’ due to fewer grains analysed. The maps and corresponding segment angle orientation rose plots (Fig. 3.3) show increasing strengthening of the segment azimuth based SPO with increasing natural strain. The rotation of the segment azimuth based SPO is also visible in the maps (Fig. 33).

Successive increase in magnitude and rotation of the grain boundary segment peaks towards 0° (*x*-axis) are a result of the strengthening of SPO, as is the successive reduction in the number of segments normal to this orientation. The grain boundary segments parallel to grain elongation are significantly reduced during the first time

steps in the single-phase model, whereas the shapes of the segment azimuth rose diagrams of the two-phase model develops from an ellipse to an hourglass shape to a slightly asymmetric hourglass shape, with successive reduction in magnitude. Another difference between single and two-phase models is the increase of maximum intercept magnitudes. For single-phase models the absolute magnitudes of intercept density increase from > 10 % to > 30 % from natural strain of 0.6 to 1.8 (Fig. 3.3a, left side). There is only a slight increase around 5 % visible for the two-phase model from natural strain of 0.6 to 1.8 (Fig. 3.3a, right side).

The pure shear simulations (Fig. 3.3b) show a rapid re-orientation of the SPO, with all maps and segment azimuth rose plots developing a strong preferred orientation at 0/180° from *x*. A rapid increase in the strength of the SPO (increase in magnitude of maxima and narrowing in segment azimuths present) is visible for single-phase and two-phase alike. Compared to the simple shear models, SPO strength of the single-phase pure shear model increases slower, whereas the strength of the SPO of the two-phase pure shear model increases at a higher rate.

The elongation of low viscosity grains in all two-phase simulations increases at a higher rate than that of high viscosity grains. For example, at a natural strain of 1.34 quantification of the axial ratios of the two grain populations of the coarse grained two-phase simple shear model shows that ~ 75 % of the high viscosity grains fall into the range of axial ratios of 2 to 4, whereas the low viscosity grain fraction covers a much broader range of axial ratios, from 2 to 25, with the maximum bin including ~ 15 % of all low viscosity grains (Fig. 3.4b).

At the beginning of the simulation (time step 0), high and low viscosity grains alike have a relative axial ratio of 1 (Fig. 3.1a,b; Appendix B, Fig. B.3A, ELLE statistics). The grain boundary segment azimuth roses for low and high viscosity grain populations in the coarse grained two-phase simple shear model (Fig. 3.4c) show that there are only minor differences between mean grain boundary segment orientations and maximum bin magnitude of the two grain populations. The shape of the segment azimuth rose of high viscosity grain boundaries shows slightly less pronounced minima and several bins ranging around the maximum with close magnitudes.

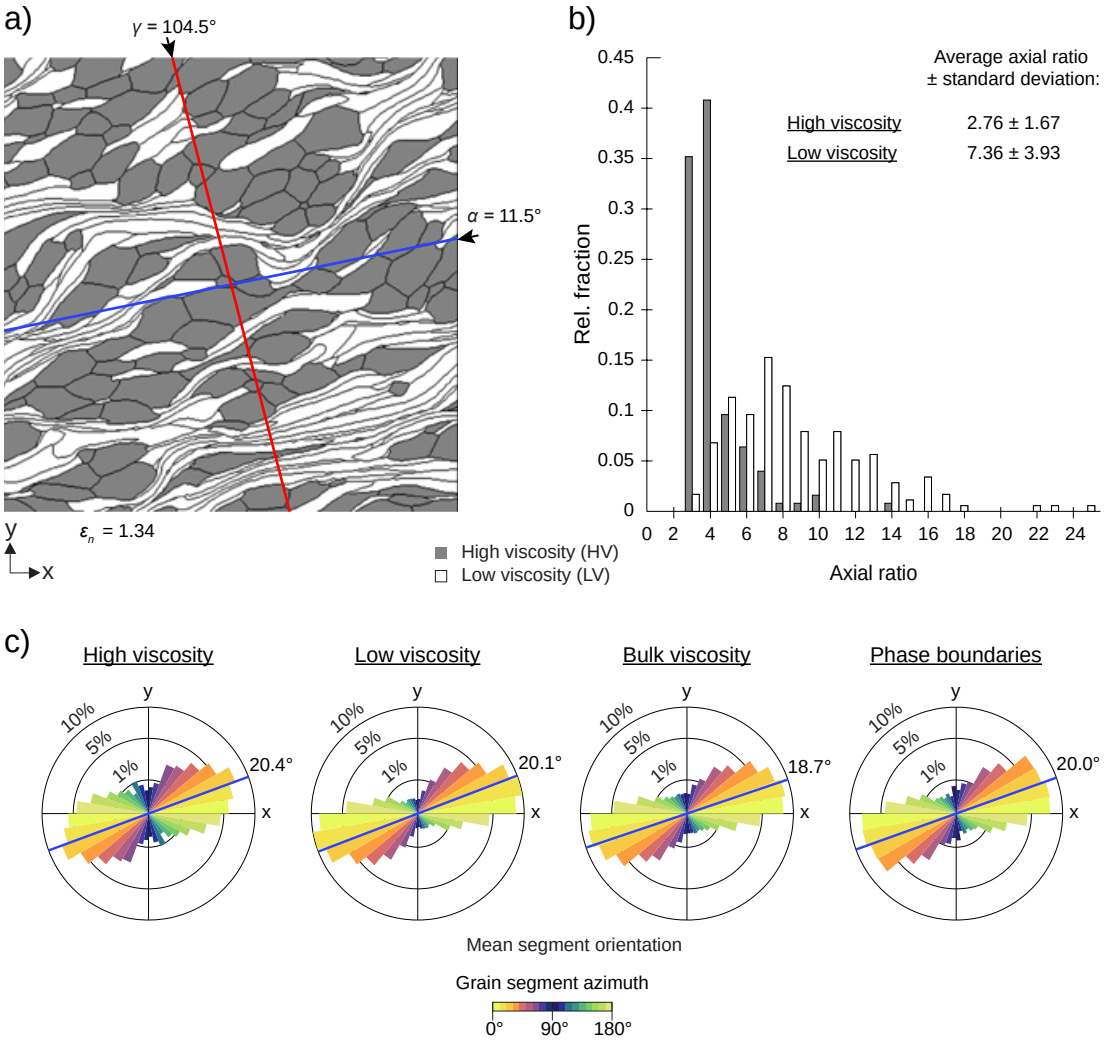

Figure 3.4: Phase specific SPO analysis of coarse grained two-phase simple shear at time step 67. a) Grain boundary pattern with α and γ scan line position marked. b) Axial ratios of the long through the short axis of the fitted grain ellipse (ImageJ analysis) as relative fractions for high and low viscosity grain populations and average (mean) values. c) Grain boundary segment orientation rose plots for grain boundary segments of low and high viscosity grains, all grain boundaries in the pattern (bulk viscosity), and phase boundaries. The bulk viscosity and phase boundary segment orientation rose is based on an original ELLE-VPFFT files, but low and high viscosity grains were remapped manually, resulting in a small divergence of mean segment azimuths. Azimuth is plotted against the frequency (%) in the equal area and length-weighted rose diagrams.

3.3.2.3 Evolution of phase boundary segment azimuths

Results from phase boundary segment azimuth analysis of all four two-phase models show the same trends of cluster and shear band formation as the grain boundary pattern maps (Fig. 3.3a, right side, 3.5c; Appendix B, Fig. B.6c). Rotation of phase boundary segments has been predominantly controlled by simple and pure shear strain geometry

of phase boundary segments, similar to that observed for grain boundary segments during plane-strain deformation (Fig. 3.3, 3.5; Appendix B, Fig.B.6).

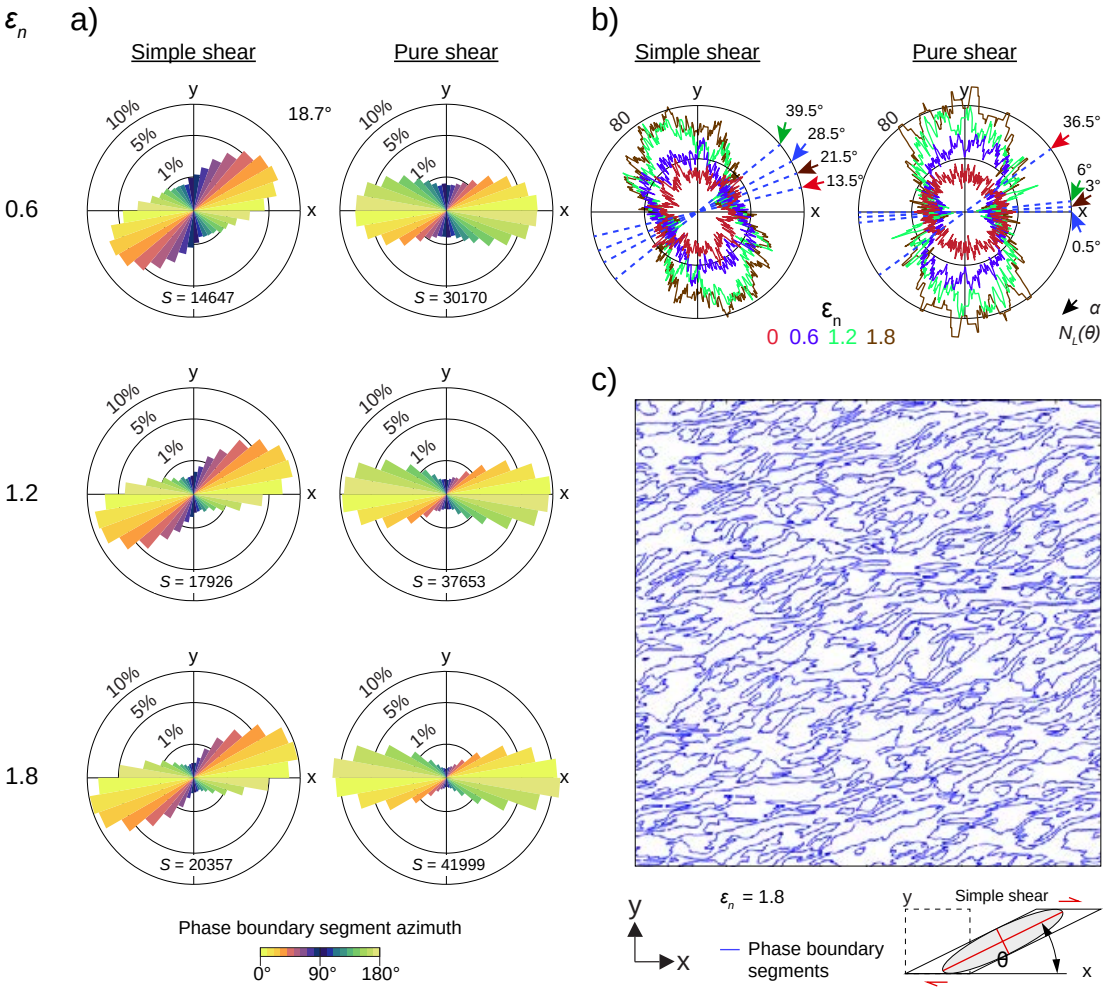

Figure 3.5: Evolution of phase boundary segment azimuths of fine grained two-phase simple shear and pure shear models. a) Equal area, length-weighted phase boundary segment azimuth rose plots at natural strains (ε_n) of 0.6, 1.2 and 1.8 (time steps 30, 60 and 90). *S* is the number of segments analysed. b) Contoured rose plots of phase boundary segment intercept density per pixel plotted against scan line orientation (θ) for the same natural strains in a). Analysis was done using a single rotation centre with 0.5° angles between scan lines, placed in the centre of the analysed map. The location of minimum GBSI density scan line is marked as α. c) Phase boundary pattern of the simple shear fine grained two-phase model at a natural strain of 1.8.

After rapid re-orientation and evolving formation of phase clusters, the pure shear simulations develop a strong preferred orientation or phase boundaries at 0/180° from *x*, as the simple shear simulations successively re-oriented towards 0/180° from *x*. Successive increase in magnitude and rotation of the phase boundary segment azimuth

peaks, and successive reduction in magnitude (Fig. 3.5a; Appendix B, Fig. B.6a) have been generally slower and SPO was weaker compared to any of the corresponding grain boundary segment azimuth peaks of single-phase and two-phase models (Fig. 3.3).

3.3.3 Segment intercept density evolution

Contoured rose plots of the GBSI density evolution (Fig. 3.6) are showing distinct differences between the deformation modes simple shear and pure shear. The differences between single- and two-phase, and the impact of grain size on GBSI density were apparent throughout progressive deformation. All eight contoured GBSI density plots (Fig. 3.6a to h) display the evolution from a circular shape towards an hourglass shape. In general, the single-phase models develop a more pronounced minimum ('neck') in the *x*-axis orientation (0/180°). Simple shear (Fig. 3.6a to d) results in rounded hourglass shapes that are oriented diagonally, with α rotating towards 0/180° and broader ɣ distribution around 70/110°. The contoured GBSI density analysis for the pure shear models results in hourglass shapes, that successively form smaller γ distributions ('tips') with increasing natural strain. This is especially pronounced in the fine grained, single-phase model (Fig. 3.6g).

The general difference between the coarse grained and the fine-grained models is that the GBSI density contours are smoother (Fig. 3.6). The number of grain boundaries intercepted along α in the coarse grained, single-phase, pure shear model (Fig. 3.6e) dropped to zero at time step 67, and thus no further intercept data was available after a natural strain of 1.32 was reached. This was not the case for the two-phase models. The difference in viscosity between the phases resulted in the development of a pattern with a generally lower GBSI density, with less pronounced successive increases in maximum density per strain increment, regardless of orientation, for both simple shear and pure shear models. There is no distinct difference in the 'shape' of the GBSI density plots between simple shear of single-phase and two-phase models.

Pure shear deformation models (Fig. 3.6e to h) show very pronounced differences between viscosity, and grain size variation. The hourglass 'tips' are very pronounced and strongly perpendicular from α for the fine grained, single-phase GBSI density contours (Fig. 3.6g), but the coarse grained, single-phase contours (Fig. 3.6e) develop a shape with a number of local maxima.

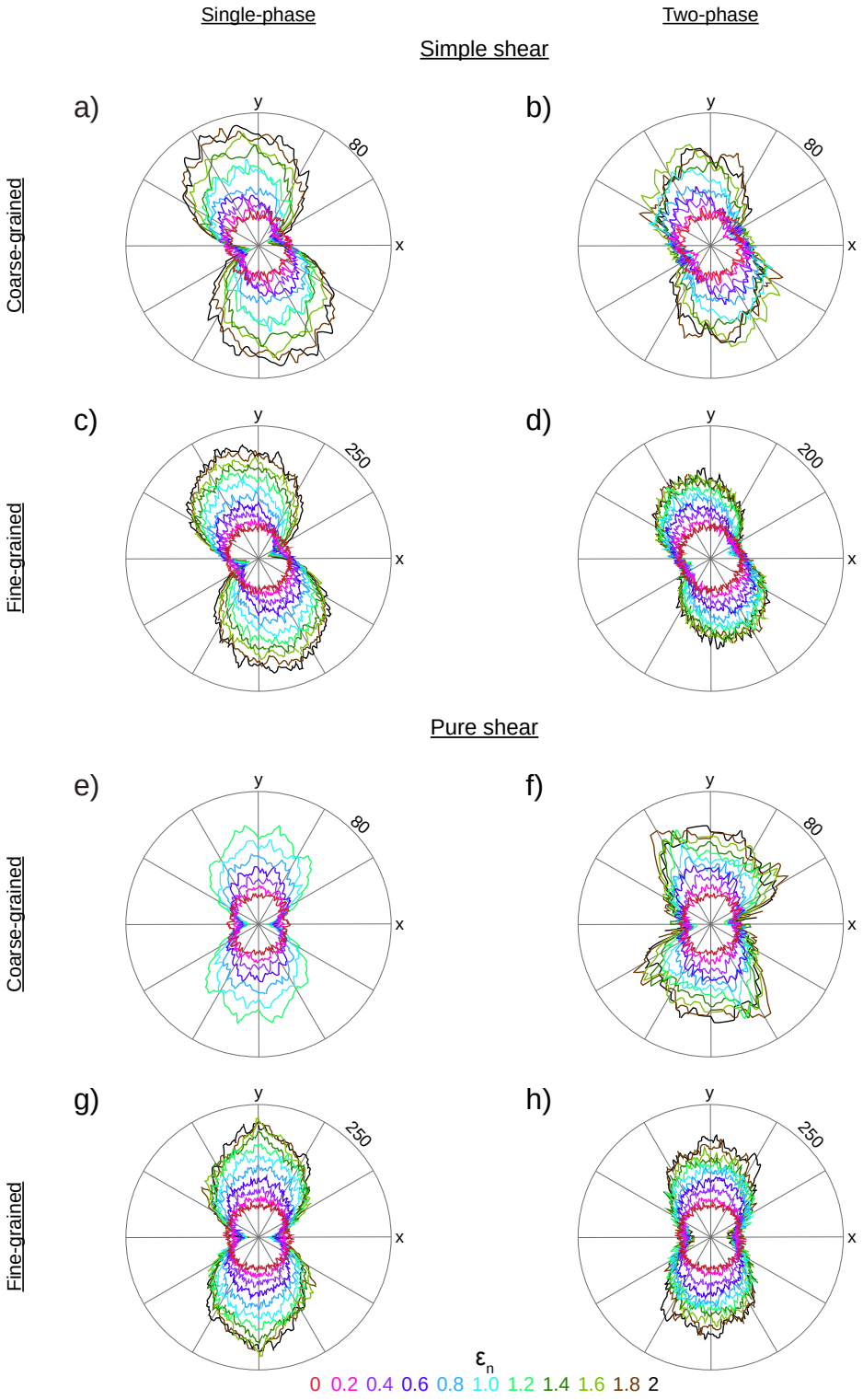

Figure 3.6: Contoured rose plots of grain boundary segment intercept (GBSI) density per pixel plotted against scan line orientation (θ) for all eight simulations. Each plot shows the initial distribution (time step = 0) in red and final natural strain ε_n of 2 in black. Analysis was done using a single rotation centre with 0.5° angles between scan lines, placed in the centre of the analysed map.

The two-phase model data stacks both show a double 'fan' shape, with strong maxima. This means that the SPO is defined by a range of orientations, but weaker compared to single-phase models. The 'fan' for the coarse-grained model (Fig. 3.6f) is distributed over a wider orientation range with an asymmetry (i.e., the 'fan' is more open towards 30°), whereas this feature is less distinct in the fine-grained model contours (Fig. 3.6h). The fine grained GBSI density contours of the pure shear model form an intermediate hourglass shape between with 'tips' and 'fans'. In general, GBSI density contours tend to increase (get denser) towards α with higher degrees of natural strain.

The phase boundary segment intercept density contours (Fig. 3.5b; Appendix B, Fig. B.6b) shows the same trends as the corresponding GBSI density contoured rose plots (Fig. 3.6, two-phase models), but are significantly less smooth.

3.3.4 Evolution of minimum and maximum segment intercept densities

The evolution of α, γ, $N_L(\alpha)$ and $N_L(\gamma)$ for all eight grain boundary segment models shows that $N_L(\gamma)$ increases in intensity over a relative wide range of orientations, whereas $N_L(\alpha)$ decreases with smaller orientation range (Fig. 3.7). γ of the fine-grained models (Fig. 3.7c,d and g,h) has stronger intensities and less angular variation throughout simulated deformation compared to the coarse-grained models. For example, in case of the coarse grained, simple shear, single-phase model (Fig. 3.7a), the γ azimuth progresses from ~ 70° to ~ 140° and back to ~ 90° to finish at ~ 120° at the termination of the model. The total angular range is ~ 70°. The evolution of γ of the fine grained, simple shear, single-phase model (Fig. 3.7c) shows less angular variation, with a total angular range of ~ 20°. In the case of the pure shear, single-phase, fine-grained model (Fig. 3.7g), γ shows a strong trend towards 90°, quickly established after a natural strain of 1.2 and is reached with only a few degrees of variation subsequently.

In general, all two-phase grain boundary segment models show more angular variation and less $N_L(\gamma)$ intensity compared to the single-phase models. One exception is the coarse grained, pure shear model (Fig. 3.7f), where a very distinct trend occurs at a natural strain of 0.4 to 1.6 and γ successively (linearly) changes from ~ 105° towards ~ 115°.

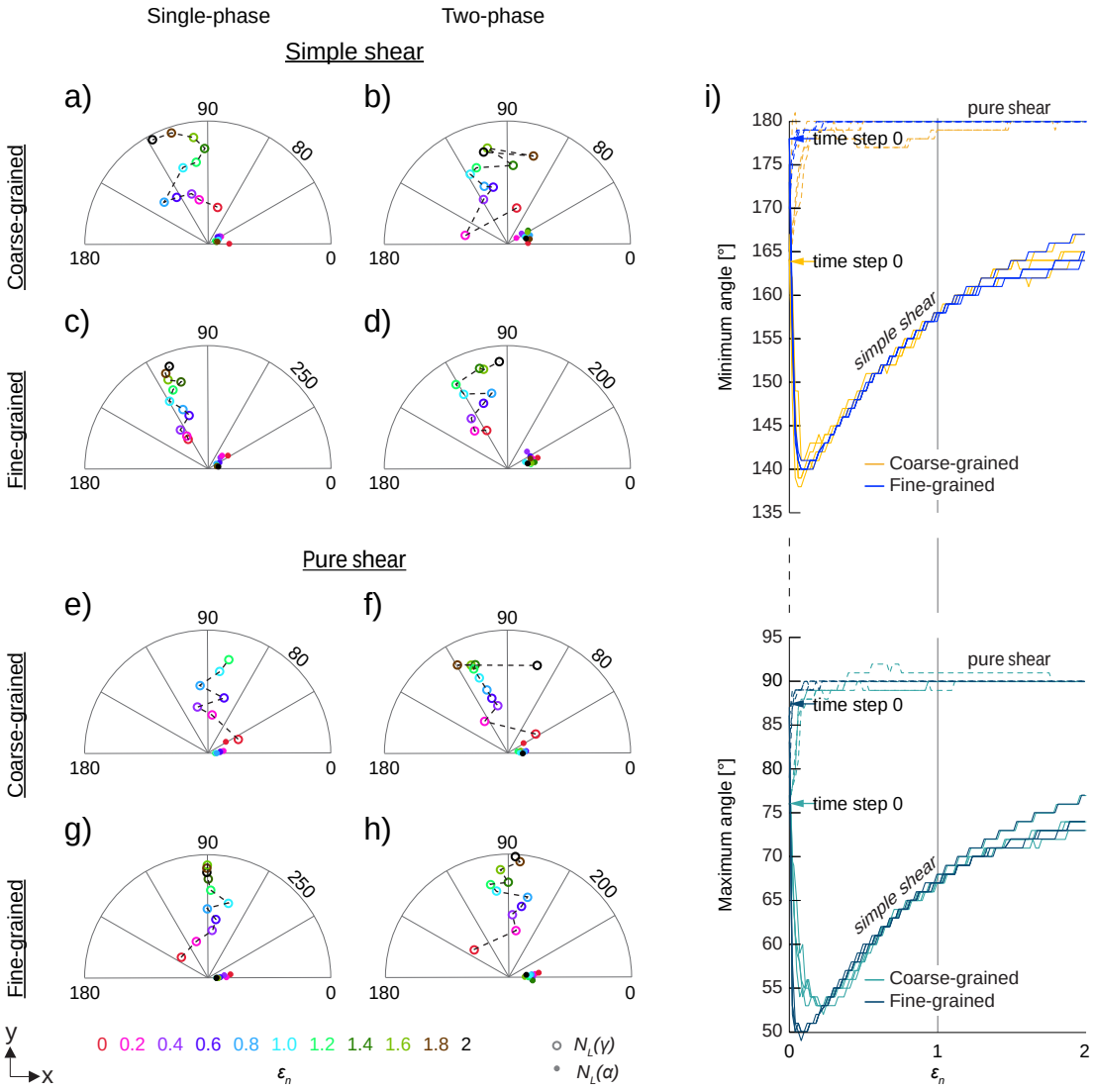

Figure 3.7: Orientation of the minimum and maximum angles *α* and *γ* throughout simulated deformation. a) – h) Semi-circular rose diagrams of values for maximum and minimum GBSI density $N_L(\gamma)$ and $N_L(\alpha)$ (per pixel) and azimuth [°] for all eight simulations. i) Maximum and minimum angle evolution as a function of natural strain for all eight simulations. Angles are measured from segments defined by consecutive boundary nodes. Curves are coloured for coarse grained and fine-grained grain boundary patterns, with two curves each for pure shear single- and two-phase models and three curves each for simple shear single-phase models, two-phase low viscosity, and high viscosity phases. Arrows mark the starting angle at time step 0.

The ELLE statistical minimum and maximum angles (Fig. 3.7i; Table 3.2) are inverse to $N_L(\gamma)$ and $N_L(\alpha)$ density, as expected. Grain boundary segments perpendicular or close to perpendicular relative to the direction of elongation are least common if SPO is present. Hence, minimum angles (Fig. 3.7i top) and γ are equivalent. The evolution of all maximum and minimum curves fits very well to the classic strain model for

simple shear and pure shear, with immediately rotation for pure shear, and successive convergence for simple shear towards 90/270° and 0/180°.

The azimuths of grain boundary segments intercepted along scan directions α and γ (Appendix B, Fig. B.5 and Table B.1) prove the systematics behind the concepts of intercepts (Panozzo, 1984; Panozzo, 1987). In γ, increasingly perpendicular oriented segments are intercepted with an increase of strain and SPO strength (Fig. B.4a), and more and more segments rotate and successively 'grow' in length towards the direction of elongation, α (Fig. B.4b). Hence, grain boundary segments intercepted along α are increasingly closer in angle. The impact of deformation modes and viscosity variation is not distinct enough at this level of analysis.

Selective sampling of corresponding phase boundary segment intercept density and azimuths of α shows similar but overall noisier trends compared to the grain boundary segments-based azimuth of α (Fig. 3.5b; Appendix B, Fig. B.6b).

3.3.5 Evolution of the GBSI minimum intensity (I_{min})

Results from the evolution of minimum GBSI density $N_L(\alpha)$, average orientation dependent GBSI density $\bar{x}N_L(\theta)$ and maximum GBSI density $N_L(\gamma)$ relative to their initial values in the base grain boundary pattern (Fig. 3.8a, c) showed that the $N_L(\alpha)$ curve is mirrored by that of $N_L(\gamma)$, but has stronger pronounced local maxima and minima. The $\bar{x}N_L(\theta)$ curves are smoother.

Curves for two-phase models tend to be closer to the $\bar{x}N_L(\theta)$ curves relative to the single-phase models. In all cases, two-phase model curves are also less smooth compared to their single-phase equivalents, with even smoother shapes defined by the fine-grained models. Logarithmic scale diagrams of minimum intensity I_{min} (Fig. 3.8b, d) for all eight models give a higher magnitude view of the first increment of deformation (especially the first ten time steps up to a natural strain of 0.2), highlighting the variations of the last increment (Fig. 3.8). The data for the fine-grained models defined curves with good fit ($R^2 \geq 0.9$), whereas coarse grained models have more variance of data ($R^2 \geq 0.65$) (Table 3.3). The main difference visible in both datasets is that the single-phase model data has more consistent absolute values and lower I_{min} with increasing natural strain.

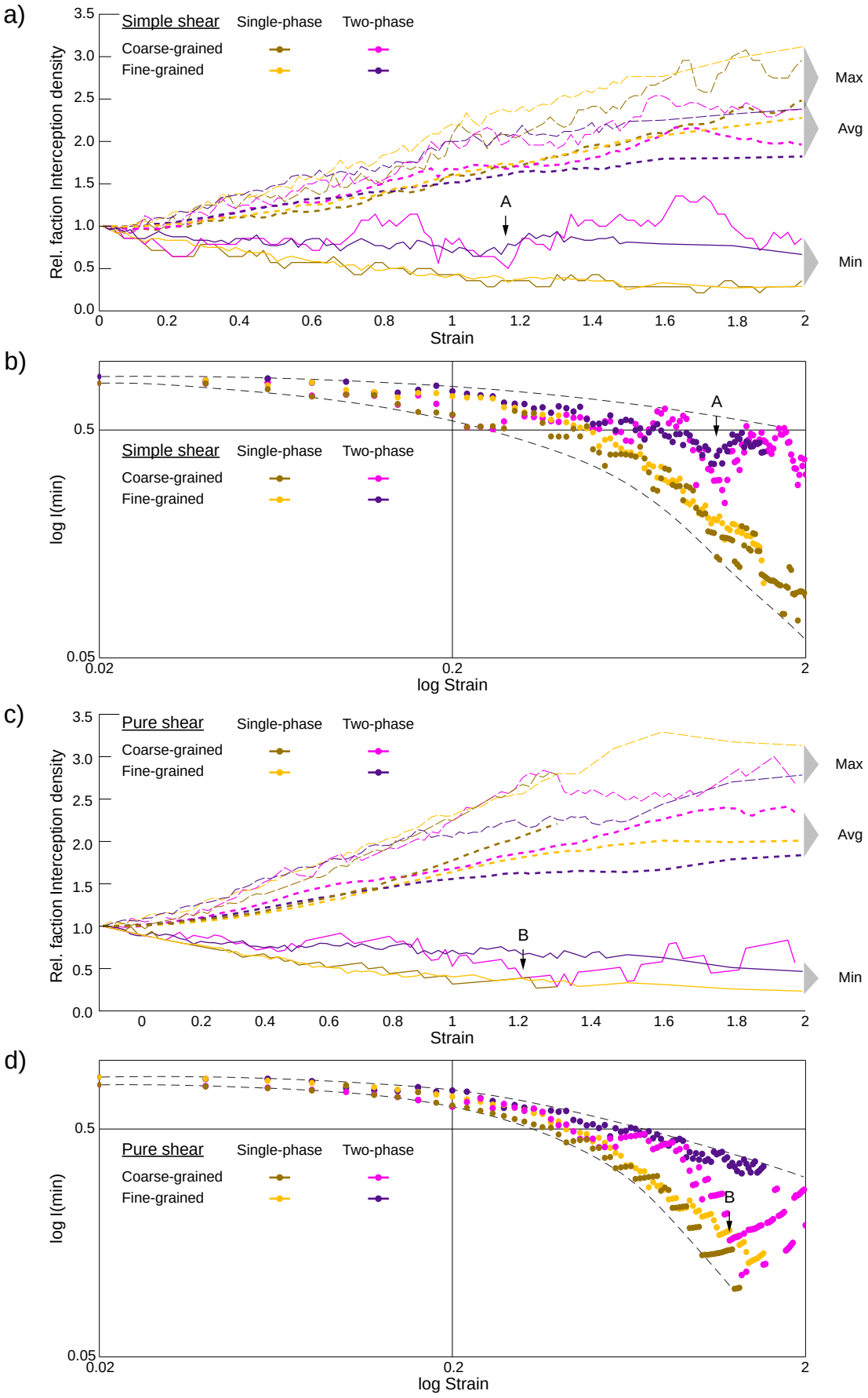
a)
Simple shear
Single-phase
Two-phase
Coarse-grained
Fine-grained
Rel. faction Interception density
Strain
Max
Avg
Min
A
b)
log I(min)
log Strain
c)
Pure shear
B
d)

Figure 3.8: Minimum GBSI density $N_L(\alpha)$, maximum GBSI density $N_L(\gamma)$, average GBSI density $\overline{x}N_L(\theta)$, and minimum intensity I_{min} as a function of natural strain (ε_n). a) Simple shear and c) pure shear curves of the $N_L(\alpha)$, $N_L(\gamma)$ and $\overline{x}N_L(\theta)$ fraction relative to their starting density. Fine grained models after time step 75 (ε_n = 1.5) were analysed at time steps 80, 90 and 100 (ε_n = 1.6; 1.8; and 2). b) Simple shear and d) pure shear logarithmic scale diagrams of I_{min} plotted against natural strain. Time step 0 (ε_n = 0) is not included due to the logarithmic scale. Data of the fine-grained models after time step 75 was not included. Black arrows A and B mark prominent local minima at ε_n = 1.16; and 1.22.

The single-phase model curves drop at a higher rate in I_{min} and are almost linear after a natural strain of ~ 1.4 (Fig. 3.8). The I_{min} curves of the two-phase models tend to have shallower slopes initially, followed by significant fluctuations developing after a natural strain of ~ 0.7 (Fig. 3.8).

The most significant deviation from the fitted curves occurs as local minima (labelled A and B in Fig. 3.8c, d). Both, simple shear two-phase models have local minima of around 1.16-1.18 natural strain. These minima are stronger in the case of the coarse-grained simple shear two-phase model, where it is flanked by two strong maxima (Fig. 3.8b). The pure shear local minimum B is very distinct from the coarse-grained pure shear two-phase in the logarithmic diagram (Fig. 3.8d). The minimum value B is reached at a natural strain of 1.22.

A and B reflect heterogeneity in the grain boundary patterns. All pure shear models, except that of the fine-grained two-phase model, show a characteristic pattern. Repeatedly I_{min} data points align with successive increases towards higher I_{min} until a jump to a lower I_{min} (Fig. 3.8d)

The trends for I_{min} plotted against ε_n (Table. 3.4) best fit an exponential curve for the single-phase models. The coefficient of determination (R^2) for coarse grained single-phase simple shear is at 0.958 and even > 0.98 for the other three single-phase models (Table 3.3). The R^2 values for the two-phase model fit better to a logarithmic curve but with low coefficients of determination of 0.65 for the two-phase simple shear coarse grained model, whereas they are 0.86 and 0.90 for the coarse-grained pure shear and fine-grained simple shear two-phase models (Table 3.3). The two-phase fine grained pure shear model has the best R^2 value with an exponential curve (0.94) (Table 3.3).

Table 3.3: Trend line fitting for I_{min} plotted against ε_n,. Additional to Figure 3.8. Exp. = exponential: $y = a\text{-}^{nx}$; Log. = logarithmic: $y = -aln(x)+b$.

	Single-phase				Two-phase			
	Simple shear		Pure shear		Simple shear		Pure shear	
Trend	y	R^2	y	R^2	y	R^2	y	R^2
Coarse grained								
Exp.	$0.751e^{-0.023x}$	**0.958**	$0.8926e^{-0.032x}$	**0.982**	$0.6271e^{-0.006x}$	0.460	$0.7071e^{-0.016x}$	0.767
Log.	$-0.206ln(x)+1.0436$	0.931	$-0.218ln(x)+1.072$	0.905	$-0.104ln(x)+0.8571$	**0.646**	$-0.186in(x)+1.0376$	**0.858**
Power	$2.5997x^{-0.663}$	0.804	$2.0765x^{-0.59}$	0.766	$0.9604x^{-0.199}$	0.535	$1.8084x^{-0.479}$	0.709
Fine grained								
Exp.	$0.8821e^{-0.025x}$	**0.983**	$0.8636e^{-0.027x}$	**0.983**	$0.7504e^{-0.01x}$	0.814	$0.7648e^{-0.012x}$	**0.940**
Log.	$-0.242ln(x)+1.2075$	0.935	$-0.231ln(x)+1.1474$	0.923	$-0.137ln(x)+0.9963$	**0.900**	$-0.158ln(x)+1.0245$	0.939
Power	$2.6708x^{-0.613}$	0.840	$2.2752x^{-0.592}$	0.830	$1.1472x^{-0.234}$	0.849	$1.2715x^{-0.293}$	0.890

3.4 Discussion

3.4.1 SPO evolution during plane strain and effects of a second phase on SPO development

3.4.1.1 Single- versus two-phase systems

The minimum intensity (I_{min}) data plotted against natural strain ε_n (Fig. 3.8b, d) shows that the viscosity contrast in two-phase models has a major impact on SPO development. By comparison, the strain geometry is of minor influence and visible from the aligned data with a successive increase towards higher I_{min} feature of pure shear data (Fig. 3.8a,b; Appendix B, Fig. B.7). Dual viscosity (two-phase models) results in higher I_{min} values as well as local minima and maxima in the case of simple shear. The absence of dynamic recrystallization and deformation being limited to dislocation glide may explain why less variation between the models is inevitable at low natural strains.

The splitting into two major trends depending on viscosity variation shows that the SPO is developing earlier and stronger in the single-phase models. The cause is that two-phase specific SPOs with different shape elongation and weaker preferred orientation evolve dynamically through the models. Therefore, different viscosity contrasts and variation of phase content should plot as different I_{min} trends. The presence of a viscosity contrast between two-phases changes the elongation and rotation behaviour of all grains in the system, and consequently the evolution of grain boundary segment length, angle, and density evolution of the grain boundary pattern.

The two-phase models portray significantly different evolutions for low and high viscosity grains (Fig. 3.3, 3.4). The low viscosity grains quickly form low I_{min} because their elongation is rapid, which results in most grain boundaries in the pattern being long and parallel to each other, thus SPO is strong and GBSI results are more distinct. The high viscosity grains do not develop a strong SPO in the two-phase models. They elongate only slightly, and their finite rotation is variable, ultimately resulting in higher I_{min} trends for the two-phase models. These higher I_{min} trends of two-phase models exist because there is a dominance of the grain boundary segments of high viscosity grains over the sigmoidal character of the low viscosity grain boundaries through the phase boundaries.

3.4.1.2 Successive increase of I_{min} at high natural strains

The strain versus I_{min} curves of the pure shear models (Fig. 3.8c,d) show an artefact that gets successively stronger with ongoing deformation. The GBSI density reduces significantly within the first time steps ('jumps') and then flattens for several consecutive time steps, with a slight increase of I_{min} only in pure shear models. There is an increase of $N_L(\gamma)$ and $\bar{x}N_L(\theta)$ during that phase of deformation (Fig. 3.8c), which causes a slight increase of I_{min}. As soon as the number of GBSIs along α decreases by losing a single GBSI, there is a jump towards lower I_{min}. The fine grained two-phase pure shear model rarely displays this behaviour due to its fine grain size coupled with the weaker SPO (Fig. 3.8d, purple). The fine grained, single-phase, pure shear model (Fig. 3.8c,d, yellow) has smaller I_{min} decrease, and more frequent offsets (jumps) between shorter aligned I_{min} sections compared to the coarse-grained models (Fig. 3.8c,d, beige and pink).

A correction for a curve fit (exponential or other) is to exclude all but the lowest I_{min} value from such an upwards trending alignment of data points and recalculate the trend line. Exclusion of all I_{min} values that are higher than the ones before results in exponential trend line R^2 values rising to 0.99 for pure shear coarse grained and fine grained single-phase.

3.4.1.3 Grain boundary pattern evolution

The average viscosity in the two-phase models is lower than that of the single-phase models because of the addition of a low-viscosity phase, whereas the 'strong' phase

remains identical across both models. So, one might anticipate strong fabrics to develop in the two-phase models.

Observations of the microstructural evolution (Fig. 3.3) confirm that viscosity contrast strongly influences the deformation behaviour and that clusters of grains with the same viscosity are formed that change the deformation dynamics. However, elongation and rotation of the low viscosity phase are highly impacted by the presence of the high viscosity phase. Elongation and rotation are slowed down and in parts stopped, depending on the neighbouring grain characteristics (viscosity, shape) and behaviour (viscosity, formation of clusters). Clusters are formed by grains that deform in a similar manner to one another. All these findings are in agreement with those made in studies involving simulations of conglomerates (Samanta and Bhattacharyya, 2003; Jessell et al., 2009; Ran et al., 2018).

The results from grain boundary segment azimuth analysis match the observations from the grain deformation from the maps (Fig. 3.3). The presence of two phases results in the formation of two different SPOs in the case of simple shear (Fig. 3.4), where elongation and rotation are different for each phase. The rotation of grains due to simulated deformation is not as homogeneous as in the single-phase models, even at higher natural strain and stronger SPO.

The formation of shear bands in a two-phase aggregate results in wider orientation variations in the grain boundary segment azimuth rose. For pure shear (Fig. 3.3b), two-phase models, the rotation and the SPO seem to be equally strong for both viscosities through deformation, whereas elongation is an order of magnitudes apart.

The individual SPOs of the two viscosities in the two-phase models is weaker compared to the SPOs of the single-phase pure shear models. This results in the almost symmetric grain boundary segment roses. It can be concluded that two-phase, no matter what strain geometry was active, results in weaker SPOs compared to single-phase for a given strain.

3.4.1.4 Local maxima and minima I_{min} evolution in two-phase models

Both two-phase, simple shear grain boundary models (Fig. 3.8b) show a local minimum I_{min} labelled A around a natural strain of 1.16 and 1.14. The fine grained two-phase pure shear model (Fig. 3.9d) does not show any such distinct local variation.

The coarse grained two-phase pure shear model conversely has a strong local minimum, B (Fig. 3.8c and d).

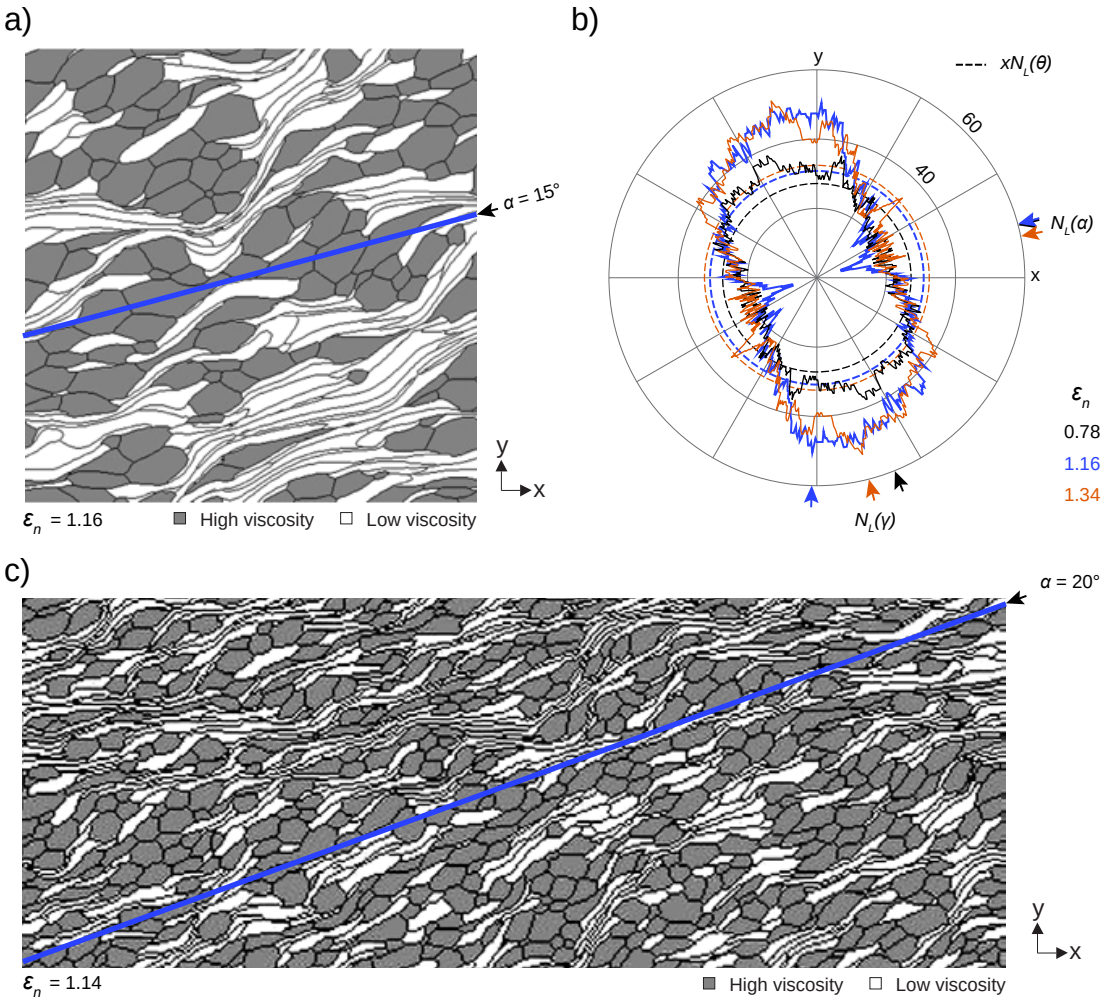

Figure 3.9: Grain boundary pattern characteristics as a reason for local I_{min} minima and maxima and the role of two phases. a) Grain boundary pattern of coarse grained two-phase simple shear model at local minimum A (Fig. 3.8a,b; time step 58, ε_n = 1.16) with orientation α and location of minimum GBSI density scan line marked (blue line). b) Contoured GBSI density rose plots for local minimum A and the neighbouring local maxima (maximum 1 at time step 39, ε_n = 0.78; grey contour and arrows; and maximum 2 at time step 67, ε_n = 1.34; orange contour and arrows). The GBSI density (per pixel) is plotted against scan line orientation. Analysis was done using a single rotation centre with 0.5° angles between scan lines, placed in the centre of the analysed map. c) Part of the grain boundary pattern of the fine grained two-phase simple shear model at the time step of local minimum A (Fig. 3.8a,b; time step 57) with orientation and location of minimum GBSI density scan line marked.

The explanation for local maxima and minima is heterogeneity in the grain distribution in the pattern, amplified by the difference in elongation between the two viscosity grain populations. It is also an effect that is minimized by finer grain size. For coarse grained two-phase simple shear models, grain boundary map, and contoured GBSI density rose plots of the local minimum A (Fig. 3.9a, b) show that almost exclusively grain boundaries of high viscosity grains with lower elongation are intercepted along α, which results in a distinctive low minimum density. All three contours have a rectangular shape, except for a very narrow waist at the natural strain of the local minimum A.

The rectangular shape of the plots means that there is a range of high GBSI density orientations. The elongation of the low viscosity grains is orders of magnitudes higher (Fig. 3.4), these grains are mostly of sigmoidal shape, and often come as parallel grain clusters. Thus, $N_L(\alpha)$ can decrease if mostly low viscosity grain boundaries are intercepted. In the case of the fine-grained minimum A, the grain boundary map (Fig. 3.9c) shows that more high viscosity grains are intercepted, but they also are strongly aligned.

Local grain boundary pattern anomalies of a very good alignment of low viscosity grains or mostly high viscosity grain boundary intercepts are the cause for local deviation of I_{min} trends. Due to the strain geometry pure shear, the number of GBSIs drops significantly with increasing strain and in a coarser grained two-phase setting (Fig. 3.8d), which adds to heterogeneous pattern characteristics, phenomena like minimum B, as well as the following variation of data points are to be expected. Overall, local trend variation seems to increase with increasing strain.

3.4.1.5 GBSI density evolution

Contoured rose plots of GBSI density (Fig. 3.6) show essential differences between simple shear and pure shear in form of round hourglass shapes (Fig. 3.6a to d) and the 'tipped' hourglass shapes (Fig. 3.6e to h). There is an additional difference between single- and two-phase for pure shear, though the formation of a 'fan' shape with lateral (local) $N_L(\gamma)$, highlighting the individual SPOs of the two viscosities in the two-phase models.

The microstructural effects of dual viscosity (two-phase models) are visible in terms of overall higher GBSI density increase (and inversely proportional decrease). The

effect of a second phase, with less distinct bulk preferred orientation compared to single-phase models (e.g., Fig. 3.3) can be connected to this GBSI density difference.

3.4.2 Phase boundary evolution

The phase distribution of the two-phase models was statistically homogeneous at the initial time step (0), therefore the variation in distribution and size of clusters in coarse grained and fine-grained models is also supposed to be homogeneous. However, due to the size of multi-grain clusters, a certain sampling volume is required to negate local inhomogeneity. The coarse-grained phase boundary maps, and the comparison of the corresponding phase and grain boundary segment azimuth rose plots (Fig. 3.2a,c) show inhomogeneity, indicating the GBSI density analysis of the two-phase coarse grained phase boundary segment models had higher 'statistical noise' than the fine grained two-phase model (Appendix B, Fig. B.6b). Analysis of phase boundary evolution in is subjected to higher statistical noise than corresponding grain boundary segment analysis, and the number of potential intercepts for any scan line orientation is lower.

Despite higher statistical noise, analysis of phase boundary segment azimuths, and intercept density reflect results from the corresponding grain boundary segment analysis, with strong influence of SPO, strain geometry, and connected formation of shear bands (Fig. 3.4, 3.5, and 3.10; Appendix B, Fig. B.6).

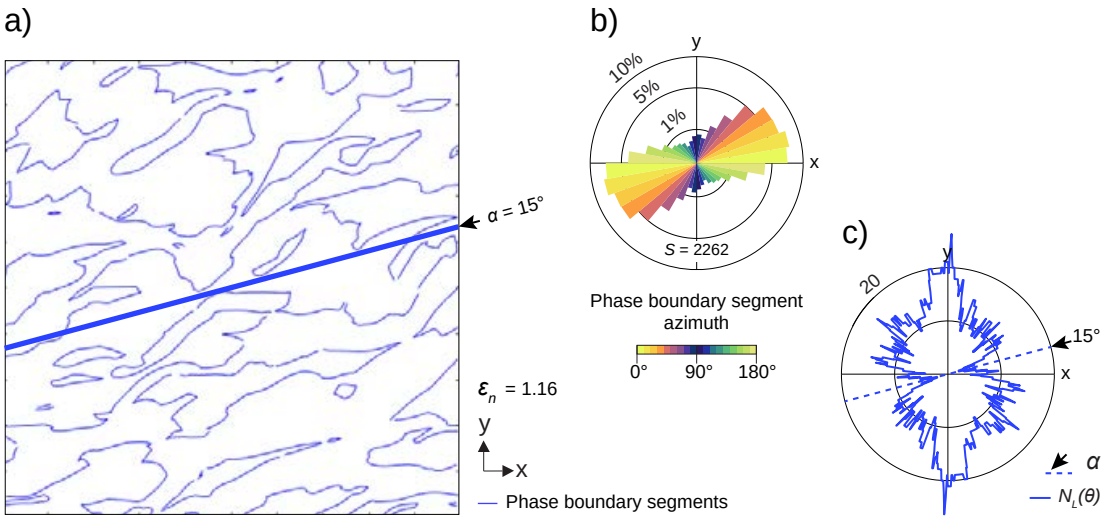

Figure 3.10: Phase boundary pattern characteristics as a reason for local I_{min} minima and maxima. a) Phase boundary pattern of coarse grained two-phase simple shear model at local minimum A (Fig. 3.9a,b; time step 58, ε_n = 1.16) with orientation α and location of minimum GBSI density scan line marked (blue line). b) Equal area, length-weighted

phase boundary segment orientation rose plot at local minimum A, with mean segment orientation marked. c) GBSI density rose plot at local minimum A, using one central radial scan line centre with 0.5° angles between scan lines for analysis. The GBSI density (per pixel) is plotted against scan line orientation as blue contour.

Phase boundary analysis of the coarse grained two-phase simple shear model at natural strain ε_n = 1.16 (time step 58) where local I_{min} minimum A was detected (Fig. 3.8a,b, and 3.9a,b) shows that only two phase boundaries are intercepted along α detected by GBSI density analysis. Boundary segment intercept density analysis of the phase and grain boundary segment pattern show that the minimum density azimuth is 15° at local minimum A (Fig. 3.9b, and 3.10a,c). This is in support of local I_{min} maxima and minima due to phase cluster distribution heterogeneity in the pattern.

3.4.3 Appraisal of the GBSI method

3.4.3.1 The use of one radial scan line centre for GBSI density analysis

The difference of $\bar{x}N_L(\theta)$ for the initial grain boundary patterns (Fig. 3.1e; Table 3.1) is due to the placement of the radial scan lines. The closer a pattern is to isotropy, the more susceptible α values are to angular variations given the stochastic effects. The grain size histograms and grain boundary segment azimuth roses are similar for simple shear and pure shear (Fig. 3.1c, d) because the same dataset is simply multiplied. The radial scan line centre for GBSI analysis is always placed in the centre of a map and thus, the analysed data is different.

For the 1:2 base map of pure shear, a different section of the same base grain boundary pattern is analysed. As the patterns are stipulated to have homogeneous initial grain size and grain size distribution, the difference between simple shear and pure shear is only slight in terms of the density contours and $\bar{x}N_L(\theta)$.

Multiple radial scans or a scan line grid-based analysis would give a more profound result with standard deviations. It can be argued that the minimal difference means that the analysis with one scan line centre is sufficient to quantify pattern anisotropy and therefore SPO. Also, pattern characteristics that change progressive or sectional could be analysed with the placement of multiple rotation centres along a profile. The same spatial resolution concept is applicable to scan line grids. In summary, multiple scan line centres, as well as scan line grids, can either provide a result with standard

deviation, or give a gradual change of GBSI pattern density and thus, quantify strain variations across an area of analysis.

3.4.3.2 Evolution of minimum and maximum GBSI density angles α and γ

The comparison between α, γ and the connection to the strain field (i.e., the orientation of minimum and maximum angle from the ELLE statistics) shows angular inconsistency of the GBSI-based orientations (Fig. 3.7). The fine-grained models (Fig. 3.7c, d, g, h; Table 3.3) have a better fit to the ELLE trends (Fig. 3.7i). Therefore, grain size plays a major role for α and γ. α generally shows less variation in comparison to the ELLE minimum angle trends but is still off by a few degrees.

The variation of α is a source of error for I_{min}, but not of major importance for SPO strength quantification if $d\beta$ is small and thus, the detected $N_L(\alpha)$ is close to the GBSI density in grain elongation direction. Longest (maximum) and shortest (minimum) axis of the strain ellipsoid are necessarily perpendicular to each other (e.g., Ramsay, 1976; Fossen, 2016), which is indicated by the ELLE statistics minimum and maximum angle relationship (Fig. 3.7i). α and γ show this relation only approximately (Fig. 3.7a to h; Appendix B, Fig. B.5; Tables B.1, B.2).

Due to this angular 'imprecision' of the detected orientations not mirroring the strain ellipse long and short axis and not being perpendicular to each other, strain analysis should not be conducted using GBSI density method alone. The diversion from a perpendicular relationship between minima and maxima is known from intercept methods and has been criticized before (Trayner, 1986; Webber, 2012). However, it can still be argued that α and γ are direct measurements, showing that especially at low strain, there is a discrepancy between grain shape/grain boundary pattern and strain ellipse. Multiple scan line centres, smaller $d\beta$ (> 0.5°), even finer grain size or a scan line grid approach might provide more information about the precision for angle determination.

The coarse grained, two-phase, pure shear model diverts from the perpendicular relation, especially for its detected γ. This is visible in the contoured rose plot of GBSI density (Fig. 3.6f) and from the way α and γ plot in the semi-circular rose diagrams (Fig. 3.7f). Data smoothing approaches have been explored before to resolve the equivalents of angles of α and γ for strain analysis using SURFOR, inverse SURFOR

(Panozzo, 1983; 1984; 1987) and intercept method (Launeau and Robin, 1996; Launeau et al., 2010).

A cause for the consecutive formation of 'alternative' ɣ over several time steps is due to pattern inhomogeneity combined with sampling issues. With only one rotation scan line, limited in scan line length by the shortest dimension of the map that significantly shrinks due to the deformation mode of pure shear, the amount of data analysed is successively shrinking and thus, it is easy to create different γ. Pattern heterogeneity in form of clusters of strongly elongated, low viscosity grains can also explain these results. In comparison, neither the single-phase pure shear models, nor the fine grained two-phase pure shear model shows such strong alternative γ trends.

3.4.4 Geological implications

The results of this study are most relevant for rocks or materials that have undergone deformation in the dislocation glide field, as our results may be transferable to such microstructure evolutions in nature. Dislocation glide is mostly active in low- to medium-grade metamorphic rocks. Additionally, it is possible to use GBSI methods on rocks that have more than one phase and thus, complex grain boundary patterns for SPO quantification. This qualifies GBSI methods once again for quantification of directional grain boundary pattern anisotropy, with implications for the impact of grain boundaries on seismic velocity anisotropy in rocks.

Two future objectives for the use of minimum intensity should be considered:

1 - There is a potential to reconstruct unknown parameters for deformation. If I_{min} of a sample is known, normal or log-log diagrams can be used to determine a range of natural strain for the sample and the other way around, reconstruction of a range of I_{min} (SPO strength) from natural strain is possible. The same principle should work with parameters like fitted ellipse axial ratio or the ratio calculated from ELLE statistics.

2 – If a sample I_{min} and either the natural strain ε_n, or the fitted ellipse axial ratio are known, which is a portrait of the strain conditions and SPO, a trend line (exponential if strain is used or power if elongation is available) can be calculated using the theoretical initial perfect pattern, where all grains are isometric (Panozzo, 1984; Srivastava, 1995), that is plotting at $I_{min} = 1$ and $\varepsilon_n = 0$. The calculation of such trend lines bears the possibility to reconstruct the past and future of SPO and pattern

evolution throughout the deformation of a sample, if strain conditions and deformation mechanism do not change. Testing with further model variations, dynamic recrystallization, grain size variation, different viscosity settings and more is necessary to refine this method and make it applicable for real samples.

3.4.5 Future directions

This study provides important tests of the capabilities of a grain boundary-based pattern characterisation. Beneficial future research prospects are:

i) Refinement of the GBSI method, i.e., scan line density, frequency, and distribution.

ii) Study the capabilities of the method to quantify different deformation mechanisms and parameters, i.e., dislocation climb, grain boundary migration/sliding via tracing the evolution of simulated pattern deformation.

iii) Development towards 3D models for GBSI density, to study the impact of grain boundaries on acoustic wave velocity anisotropy of aggregates.

iv) Applications of the GBSI density method to real rocks, including a workflow that incorporates grain boundary segment azimuth and fitted ellipse-based and other established SPO quantification methods to further assess/exploit the comparative strengths and weaknesses of the GBSI method approach.

3.5 Conclusions

This study is the first attempt of tracking grain boundary segment characteristics systematically during the ongoing (simulated) deformation and by using a GBSI method in combination with other quantification methods for grains and grain boundaries. The main response to simulated deformation is the formation of SPO, which increases over the duration of deformation. A single foliation develops in the single-phase models, whereas shear bands form in the two-phase models. Additionally, the GBSI method was used to analyse the phase boundary pattern evolution during deformation of the two-phase models. The size of grain boundary datasets (grain size) has a visible influence, which is mostly statistical, and results are scalable.

- Grain size affects the sampling statistics such that the finer the grain size, the clearer the results. There is less variation in the intensity of intercepts in fine grained models compared to the coarse-grained models. All major trends are

visible in coarse grained and fine-grained model results. But phenomena like the 'false' maximum density orientation or the minimum intercept local minimum A and B are stronger and more common compared to the fine-grained examples.

The comparison of single- and two-phase simulations shows that phase composition has a strong influence on the grain boundary development, which is recorded by the GBSI method.

- Dual viscosity (two-phase models) results in the development of shear bands with weaker SPO of each phase, individually and combined, compared to single-phase models. Each of the two grain phase populations changes in shape and shape orientation, which proves to be interdependent of each other's distribution (cluster formation) and neighbouring grain contacts.
- SPO is stronger in single-phase models compared to two-phase models at any given natural strain > 0.04, and independent from the end-member strain model.
- The grain boundary segment azimuth analysis shows the weaker SPO in the two-phase models by a broader range of weaker peaks.
- This weaker SPO is visible in the GBSI density contour plots by weaker minima and maxima of two-phase patterns, with higher minimum intensity compared to single-phase models.
- GBSI density based minimum intensity (I_{min}) analysis shows that differences are minimal at low strains and become more pronounced after > 0.2 natural strain, with two-phase models having weaker GBSI density minima and maxima.

Grain boundary-based analysis can differentiate between strain geometries. SPO develops after ~ 0.1 natural strain in both, simple and pure shear models. , A preferred orientation quickly stabilises in pure shear, and evolves in orientation in simple shear. This is in agreement with literature and models of shear zones.

- Grain boundary segment azimuth roses show different mean orientation evolution depending on strain geometry.
- The pure shear models have a slightly stronger SPO compared to simple shear models. GBSI density based I_{min} for the simple shear models is always slightly higher.

- The difference between simple shear and pure shear is very clear from the shape of the GBSI density contour evolution, whereas minima and maxima are roughly the same strength.

Results from GBSI analysis limited to phase boundaries show similar but weaker trends compared to grain boundary pattern analysis that disregards grain mineralogy. Using the same set of methods, phase boundary analysis of the two-phase models is more impacted by fabric heterogeneity due to the size of the dataset and nature of the phase distribution in the models. Signals from SPO and strain geometry are noisier, showing that application of this method to analyse phase boundary segments needs to be selective and results should be treated with caution.

A combination of several methods for SPO quantification is preferable for a detailed analysis. GBSI-based contour and I_{min} analysis have great value for comparing grain boundary patterns with each other in greater detail than a method that is summarising data or depends on a uniform dataset of i.e., ooids. Samples from different areas of a shear zone can be easily compared to each other using minimum intensity I_{min}. Further, combined with grain elongation or strain, GBSI I_{min} is useful to compare different geological settings with each other.

CHAPTER 4

Effects of mixed phase content, fractures, and grain boundary anisotropy on acoustic wave velocities in evaporites

Abstract

It has been recognized that acoustic wave velocity anisotropy in evaporite rocks is not only controlled by crystallographic (preferred) orientation but that other factors like grain boundary alignment, fractures, fluid inclusions, and mixtures of evaporitic minerals contribute too. However, how each of them contributes specifically and their combined impact on acoustic wave velocity anisotropy is not yet fully understood.

This study analyses crystallographic orientation, grain boundary pattern characteristics, fracture distribution, and the presence of veins of second mineral phases with the aim of constraining their likely impact on acoustic wave velocity anisotropy of evaporites. Ultrasonic wave velocity data for bulk aggregates of various pure and mixed phase evaporite samples are measured from cuboid and core samples. The microstructure of the core samples was then analysed for crystallographic orientation (using electron backscatter diffraction), grain boundary pattern geometry (using the modified grain boundary intercept method and grain fitted ellipse approach), phase content (via greyscale threshold analysis of backscattered electron images), and fracture and vein distribution and geometry (using the FracPaQ toolbox).

The presented velocity measurements for natural evaporites with halite, polyhalite, anhydrite, gypsum, and mixed phase rocks from three deposits (North Sea, Òdena, Boulby) show significant velocity anisotropy. Maximum seismic velocity anisotropy for P wave, (AV_P) is 60 % and maximum seismic velocity anisotropy for S wave (AV_S) is 34 % for a sample from Boulby mine. Also, the V_P and V_S ranges are generally lower than expected according to single crystal ranges. Microstructural analysis of North Sea anhydrite showed mean anhydrite grain sizes between 26.50 ± 31.61 µm and 89.71 ± 57.32 µm, with maximum grain sizes of 430 µm to 493 µm. Systematic preferred orientation of grain boundaries is caused by a dual shape preferred orientation of orthogonally oriented elongate blocky anhydrite grains. Òdena anhydrite with gypsum has common spherulitic features comprising radial bladed anhydrite

grains with minor gypsum distributed along grain boundaries. Crystallographic preferred orientation in anhydrite form both point clusters and weak girdle distributions of {100} and {001} poles, with an absence of mechanical twins and few low-angle (< 10°) boundaries, interpreted to represent dynamic recrystallisation by grain boundary migration and potentially subgrain rotation (associated with Regime 1). Gypsum veins are also preferred systematically oriented.

The grain boundary microstructure and systematic gypsum vein network are potentially the cause for the slow and anisotropic nature of the measured ultrasonic velocities in these rocks. This study adds to the limited dataset on velocity anisotropy in evaporitic rocks and presents a workflow to build on in future studies to quantify the impact of petrofabrics on acoustic wave velocity anisotropy more rigorously.

4.1 Introduction

Evaporite deposits are part of many sedimentary basins worldwide, and commonly form stratigraphic detachment horizons (e.g., Jura fold belt), and/or intrusive salt diapirs (e.g., North German plain). Oil and gas are often trapped in reservoirs in or next to such salt structures. In seismic imaging, salt deposits have generally been treated as homogeneous bodies in terms of their internal structure and composition, which is often assumed to be pure halite and is close to isotropic in its petrophysical properties.

Yet, evaporitic rock salt structures and formations are commonly polymineralic, incorporating anisotropic minerals such as gypsum, anhydrite, polyhalite, and carnallite. Furthermore, the low strength of the minerals that comprise rock salt enables ductile flow under upper crustal conditions, and this deformation is associated with the formation of strong petrofabrics, which also result in the development of anisotropy. However, it is unknown to what extent mineralogical and textural variations contribute to P- and S- wave velocity anisotropy (AV_P and AV_S, respectively): published acoustic velocity data on polymineralic evaporites are rare; and studies of evaporites tend to concentrate on deformation mechanisms and microstructures in monomineralic aggregates of the three main evaporitic minerals: halite, anhydrite, and gypsum. Nevertheless, errors in interpretation of seismic reflection data can be expensive if, for example, discovered at the drilling stage in oil exploration.

The acoustic impedance of rock salt results in transparent zones and zones of chaotic reflectors. Travel-time effects due to anisotropy often lead to false localisation of subsalt oil traps (Raymer et al. 2000b). Rock salt bodies generally show high-level structural complexity and associated large velocity contrasts (Raymer and Kendall, 1997). There is a need to improve seismic images and seismic velocity models, which is the overall objective of this study. Furthermore, new data will be of great significance to the mining industry (e.g., potash, table salt), agencies considering the storage of waste and geo-energy (e.g., hydrogen and compressed air in salt caverns) in salt structures, and the understanding of rheology and dynamics in sedimentary basins and mountain belts.

The aims of this study are to: (a) increase the database of ultrasonic velocity measurements from natural evaporites; (b) characterise petrofabrics of natural evaporites that comprise anisotropic minerals anhydrite and gypsum by quantifying their crystallographic preferred orientation (CPO) and shape preferred orientation (SPO); and (c) to investigate the effects of mineralogy, microstructures, and crystallography on ultrasonic wave velocity anisotropy in natural evaporites.

Directional ultrasonic velocity measurements were collected from five cuboid samples with different natural evaporitic mineral compositions, including halite, halite with clay, potash, polyhalite, and anhydrite, and twelve cores from two different natural sample suites: pure anhydrite; and anhydrite plus gypsum. Quantification of CPO, grain size, shape, and SPO were analysed via electron backscatter diffraction (EBSD) mapping, backscattered electron (BSE) image analysis, and grain boundary and fracture pattern analysis (FracPaQ; Healy et al., 2017; GBPaQ, see chapter 2 of this thesis) of oriented thin sections.

4.1.1 Deformation and petrofabric development in evaporites

The significant mineralogical and physical differences between some of the over 80 evaporitic minerals (Steward, 1963) can ultimately result in strong petrofabrics in rock salt bodies, and these fabrics control the ultrasonic velocity anisotropy. Natural evaporitic rock salt can be complex in terms of its polymineralic character, its strong fabrics, and other microstructures. All these factors can have an impact on the velocity characteristics (including velocity anisotropy), but their effects remain to be fully explored and understood.

Deformation mechanisms (e.g., dislocation creep, pressure-solution creep) and deformation processes (e.g., intracrystalline recovery) control the formation and evolution of rock deformation microstructures. These result in flow laws, which control the deformation of the rocks at a larger scale. Lithology and microstructure determine the dominant deformation processes (and vice versa) through mineralogical composition, spatial distribution of phases, inter-granular fluids, porosity, permeability, grain size, and crystallographic preferred orientation. All those factors are known to, or have been considered to, influence acoustic velocity anisotropy (Fig. 4.1).

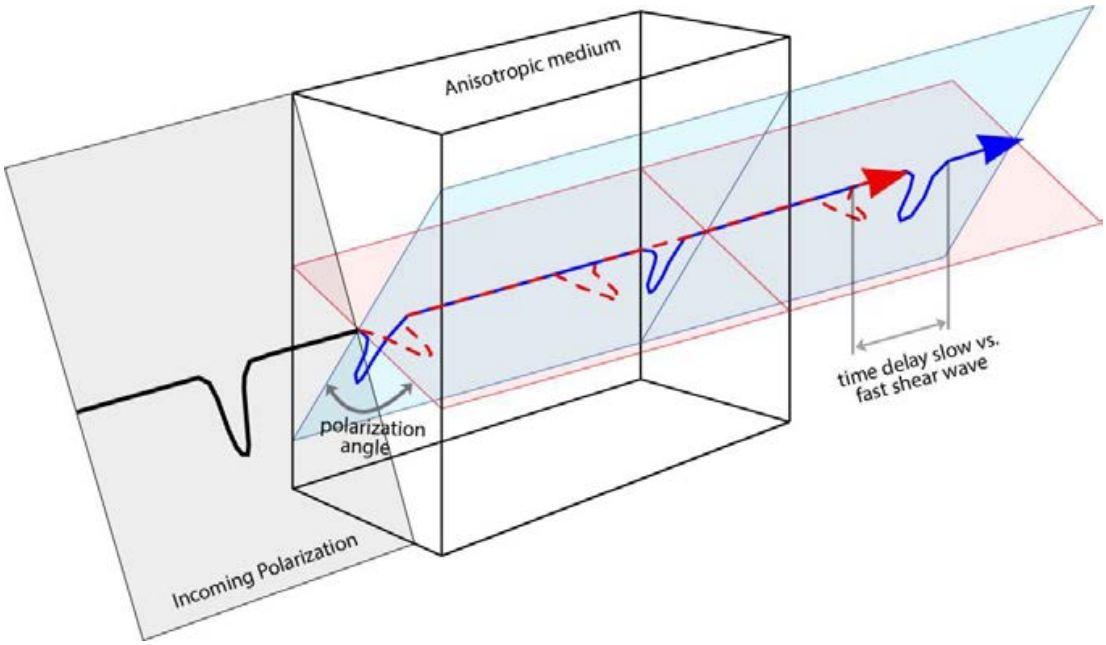

Figure 4.1: Shear wave splitting, resulting from the propagation of a wave through an anisotropic medium. After Garnero, E. J. (http://garnero.asu.edu/research_images/index.html).

Crystallographic preferred orientation (CPO) is assumed to have the strongest control on *intrinsic* anisotropy (e.g., Vargas-Meleza et al., 2015). CPO is commonly caused by dislocation creep, and therefore depends on the operative slip systems for dislocation glide in constituent minerals. Dislocation creep and intracrystalline recovery are significantly enhanced by the presence of grain boundary fluid inclusions (Urai et al. 1986a,b). Dynamic recrystallisation by grain boundary migration (GBM) or pure recrystallisation (static grain growth) may create a GBM-induced CPO by favouring certain crystallographic orientations or remove grains with unfavourable orientations for dislocation glide. The characteristics of a CPO pattern depend on: a)

the type of operating slip systems and their relative activity; b) the strain rate and bulk strain field (i.e., flattening, constriction) that determines towards which direction crystals tend to rotate and thereby the shape of the fabric; c) the finite strain; and d) the kinematic vorticity (Passchier and Trouw, 2005).

In halite-dominated rocks, two main deformation mechanisms have been identified from microstructural analysis: dislocation creep and pressure solution in combination with grain boundary sliding (GBS; Boullier and Gueguen, 1975; Poirier, 1985). In nature, rock salt deforms in the transition between these two mechanisms (e.g., Urai 1987; Spiers et al., 1990; Desbois et al., 2010). Within the dislocation creep regime, two sub-cases occur; dry halite (and halite at low temperatures), where subgrain rotation (SGR) dominates, and wet halite (and halite at high temperatures), where grain boundary migration (GBM) is active (Urai et al., 2008). The primary, most easily activated orthogonal slip systems in halite (which is cubic) are {110}<110>, followed by {100}<110> and {111}<110> (e.g., Franssen, 1993; 1994; Skrotzki et al., 1996; Linckens et al., 2016). The type of slip system that is active in a crystal depends on the orientation and magnitude of the stress field with respect to the crystallographic orientation of the grain and on the critical resolved shear stress (CRSS) for the specific slip system (Passchier and Trouw, 2005). The CRSS contrast between these three slip systems is 1, 2, and 3, respectively, but the stress exponent is normally assumed to be high (n = 7) for the halite slip systems.

Anhydrite has been studied with a focus on texture development and CPO evolution (e.g., Ross et al., 1987; Heidelbach et al., 2001). High-temperature deformation experiments showed that anhydrite deforms either through twinning and dislocation creep with SGR, as well as grain and twin boundary migration (Regime 1), or through diffusion creep combined with GBS, which is grain size sensitive (Regime 2) (Dell'Angelo and Olgaard, 1995). Both flow regimes result in a CPO. The transition between the two flow regimes can be regarded as a third regime, where recrystallisation via SGR, diffusion creep, dislocation creep, and possible grain boundary sliding occur (Dell'Angelo and Olgaard, 1995). Three slip systems and one twin mode have been identified in anhydrite (e.g., Heidelbach et al., 2001; Hildyard et al., 2009; 2011a). Glide systems are (100)[001], (100)[010], and (001)[100] in the Cmcm space group (orthorhombic) reference frame (Hildyard et al., 2009; 2011a). Deformation twinning in anhydrite mostly occurs along {110} and can be described

by crystallographic rotation relative to the host crystal (misorientation) around an axis parallel to [100] by 83.5° (e.g., Klassen-Neklyudova, 1964; Hildyard et al., 2009). Naturally, deformed anhydrite can preserve fibre textures with strong point maxima in poles to {001}, and weaker point clusters and girdles in poles to {100} and {010} (Hildyard et al., 2011a; Vargas-Meleza et al., 2015). An accompanying SPO can have a strong relationship with CPO such that grain long axes (elongation directions) at high angles to <001> (short dimension of the grains) (Hildyard et al., 2011a).

Deformation experiments on wet, granular gypsum (De Meer and Spiers, 1997) show grain boundary diffusion and pressure solution, with precipitation of new gypsum being the controlling factor. Gypsum has monoclinic symmetry, with space group C2/c. Natural gypsum-dominated deposits can form CPOs with girdle-like clusters of poles to {100} parallel to the foliation and poles to {010} clustered perpendicular to the foliation (Vargas-Meleza et al., 2015). Carnallite deforms plastically through intra-crystalline slip and mechanical twinning, whereas recrystallization operates via SGR as well as GBM and solution transfer under natural conditions (Urai and Boland, 1985; Urai et al., 1986a,b; 1987). There are no published studies on the deformation mechanisms of polyhalite.

4.1.2 Controls on ultrasonic wave velocity anisotropy

Ultrasonic waves are high frequency, short wavelength acoustic waves that migrate through solid media and are readily measured to high degrees of accuracy for rock samples using acoustic emission equipment (e.g., Lo et al., 1986; Mah and Schmitt, 2003; Vargas-Meleza et al., 2015). The velocity essentially depends on the material density and elastic properties. Velocity anisotropy describes an orientation dependent variation of wave velocity. Velocity measured on dry and homogeneous material is independent of wave frequency, with minimal change of the shape of the signal during the propagation through the material (Popp and Kern, 1998). The transmitted wave can be significantly distorted due to the energy scattering produced by the heterogeneities in heterogeneous rocks (Vargas-Meleza et al., 2015).

Velocity anisotropy of polycrystalline aggregates reflects the bulk mineral alignment, which is equivalent to the dependence on the overall intrinsic crystal structure of the sum of all grains. Structural features like density, orientation, and alignment of grain boundaries, cracks, or pores also have a major impact on seismic velocity anisotropy

(e.g., Crampin, 1985; Lo et al., 1986; Popp and Kern, 1998; Raymer and Kendall, 1998; Mah and Schmitt, 2003; Lloyd et al., 2011; Zong et al., 2014). Other factors that have a strong impact are variations in the spatial distribution of phases, changing phase content proportions, layering, grain size and shape fabrics, as well as gradual variations in grain boundary properties (e.g., Kern and Wenk, 1985).

Shape preferred orientation (SPO) is another factor that has been recognised as an important contributor to total anisotropy measured with laboratory ultrasonic velocity tests (e.g., Burlini and Kunze, 2000). The alignment of grain boundaries is dependent on the strength of the SPO, which describes a pattern of elongated grains with a similar orientation of their long and short axes. The stronger the SPO and the more elongated the grains, the more grain boundaries align in an aggregate and the stronger is the predicted contribution to an ultrasonic velocity anisotropy. The formation of SPO depends mainly on strain parameters. The relationship between CPO and SPO and effects on seismic velocity anisotropy in evaporites and sedimentary rocks, in general, are poorly understood (e.g., Valcke et al., 2006), and the effects of SPO are not yet determined for evaporites.

There are many studies on materials and rocks other than rock salt which investigate the relationship between acoustic velocity properties, fabric orientation, and finite strain to understand seismic anisotropy and improve seismic imaging, to gain a better understanding of those parameters. A focus lies on monomineralic and polymineralic aggregates (crustal-scale shear zone, Almqvist et al., 2013; Carrara marble mylonites, Burlini and Kunze, 2000; lower continental crust, Lloyd et al., 2011; mylonitic quartz, Lloyd and Kendall, 2005; sandstone, shale and granite, Lo et al., 1986).

An established workflow is based on using a ‘rock recipe’ approach with data that are derived from measured CPOs of each individual mineral, respectively on subsets of individual rock fabric CPO, combined with their modal proportions (Lloyd et al., 2011). This rock recipe approach uses the data from the measured polycrystalline aggregates, including the measured CPO, with different modal compositions to create a model for changing composition. The fabric recipe approach conversely uses subsets of individual rock fabric CPO instead of modal composition and thus, allows the effect of different fabrics, meaning foliations, to be studied from the seismic response (e.g.,

Lloyd et al., 2011). Alternative approaches for the estimation of velocity anisotropy from CPOs are those of Zhong et al. (2014) and Vel et al. (2016).

Recently, researchers have started to identify new ways to create more precise seismic velocity models (e.g., Oliveira et al., 2015; Jones and Davison, 2014). The approach involves the identification and quantification of the differences between velocity models and natural rock salt deposits. The developed method uses amplitude response to differentiate and identify rock velocities and consequently lithological heterogeneities (e.g., Oliveira et al., 2015; González et al., 2016). It has only been applied on velocity models from the Brazilian basins and is still in the developing stage (e.g., Meneguim et al., 2015; Jardim et al., 2015; Barros et al., 2017).

Deviation of models from nature is also caused by the omission of seismic velocity anisotropy as an effect of intrinsic crystal structure, respectively CPO. The assumptions that evaporitic bodies are homogeneous and isotropic for seismic velocity models are valid in cases where halite is the main constituent in natural rock salt bodies, typically with an abundance of ~ 95 % (Raymer and Kendall, 1997). However, an assumption of isotropy can cause false reflector depths for anisotropic bodies (e.g., Raymer and Kendall, 1997; Jones and Davison, 2014). Jones and Davison (2014) list anisotropy representation and parameterization as one of the major pitfalls when rock salt bodies are involved in seismic imaging. The need to include anisotropy in seismological studies of the crust, nonetheless, is increasingly recognised (Mah and Schmitt, 2003; Prasse et al., 2020).

Research on mixed evaporite phases and the corresponding effect on microstructures and ultrasonic velocity properties, specifically anisotropy, is extremely rare in the literature. Ross et al. (1987) performed simple shear experiments on anhydrite-halite mylonites and state that the effect of phase mixing on the strength of CPO is not significant in comparison to single phase experiments. Raymer and Kendall (1997) looked at rock salt with anhydrite as secondary phases and concluded that there is a potential large effect of anhydrite alignment (CPO) on bulk elastic anisotropy, contributing to the high anisotropy of anhydrite. Trippetta et al. (2010) measured P-wave velocity using an alternating sequence of anhydrite and gypsum. They conclude that the resulting seismic anisotropy is generally low and that the average P-wave velocity (V_P) increases with increasing confining pressure. They also inferred from

their results that cracks influence V_P only in dry conditions and for low confining pressure (Trippetta et al., 2010). Basic gypsum seismic velocity anisotropy data was obtained by Levin (1979), who measured seismic velocity in weathered gypsum-rich rocks.

Vargas-Meleza et al. (2015) investigated the influence of relative mineral contribution of halite, anhydrite, and gypsum to seismic velocity anisotropy by modelling bulk elastic properties to calculate seismic velocities for polymineralic evaporites using a rock recipe approach. Predictions from the rock recipe approach include that an increasing modal anhydrite grain proportion contributes to a significantly higher seismic anisotropy in halite-dominated mixed rock salt, and to a lesser extent in gypsum-dominated aggregates. In the latter case, the seismic anisotropy decreases until a specific threshold proportion is reached, where anisotropy increases again. CPO was assumed to be the most important factor for bulk seismic properties. However, a difference between rock recipe-based anisotropy due to CPO and ultrasonic wave velocity measurements was attributed to SPO and grain boundary effects (Vargas-Meleza et al., 2015).

4.2 Approach and methods

4.2.1 Sample material

Natural evaporite samples from three different sites are used: i) hand samples from Boulby mine, Loftus, Saltburn-by-the-Sea, North Yorkshire, England, UK, ii) core samples from offshore sites in the North Sea and iii) outcrop samples from the Òdena quarry, Catalan Potash Basin (South Pyrenean foreland basin, Spain). These samples contain most of the common rock salt minerals, including halite, anhydrite, and anhydrite with gypsum content.

i) Four samples of Permian Zechstein rock salt from Boulby mine were selected to represent the variety of evaporitic minerals in rock salt deposits, a lack of discernible macroscopic scale anisotropic features such as lineations, SPO, or systematic phase distributions (e.g., banding). These samples comprise: pure halite from a 15 cm wide halite vein within polyhalite (BH2-2); halite with minor silt (BH5-1); pure polyhalite (PB1-2); and potash (Ba7-2; Fig. 4.2).

The vein halite in BH2-2 is colourless to white with blocky crystals and a grain size on centimetre scale. The same sample was cut parallel to the vein margin, and the polyhalite vein rims were trimmed off. No SPO is visible from a macroscopic scale. The halite in BH5-1 is transparent to white, with a slight champagne (yellowish) tint, and silt is mid-grey. There is no indication of the orientation of this sample relative to any fabric. The grain size of the halite is smaller than in BH2-2, on a millimetre to centimetre scale.

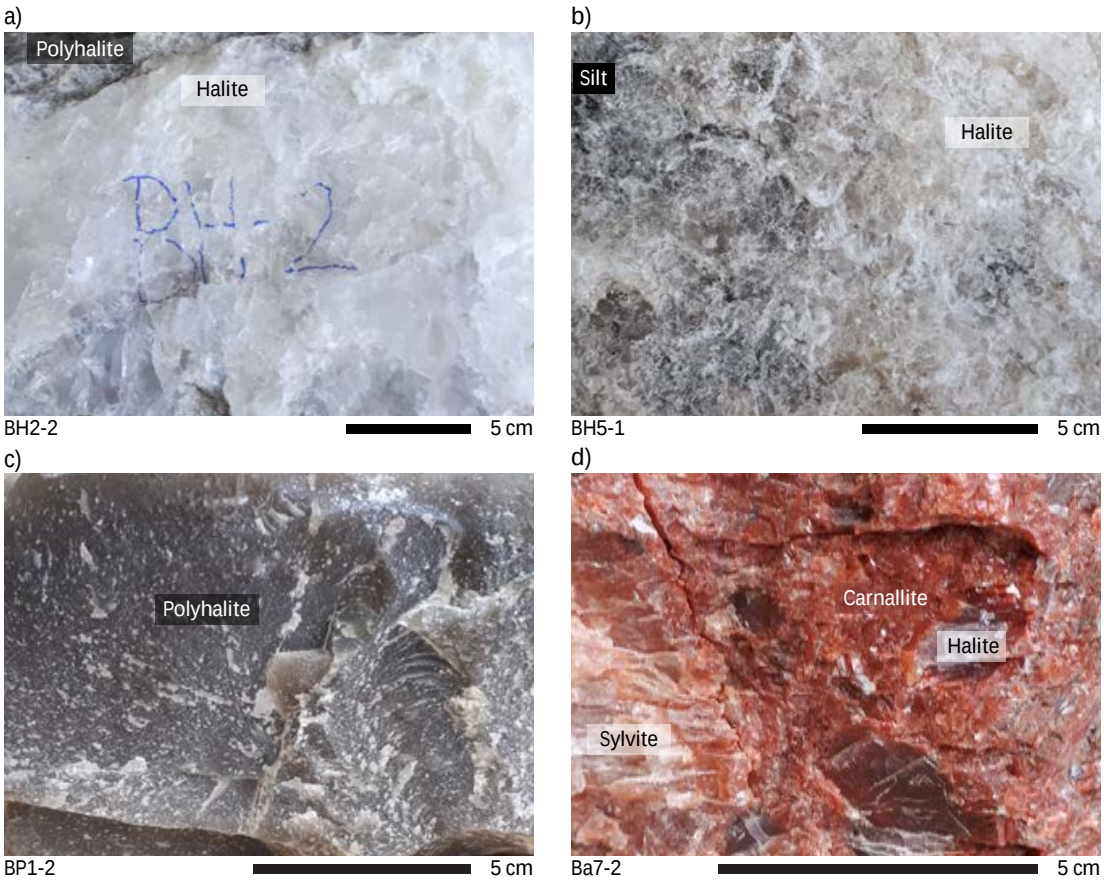

Figure 4.2: Cleavage of the material blocks from Boulby mine, UK, later cut into cuboids. a) Pure halite vein in polyhalite, b) Halite mixed with silt, c) pure polyhalite with conchoidal fracturing, and d) potash with carnallite (red), sylvite (white), and halite (transparent).

Polyhalite in BP1-2 is mid-grey and massive, with conchoidal fracturing, the block was picked without indication of any orientation relative to a fabric. Individual crystals are not discernible on a macroscale.

Potash in (Ba7-2) is typical of that in Boulby mine, predominantly comprised of halite and sylvite with a minor silt/clay content and some minor carnallite. There was no

indication for orientation relative to a fabric. However, the sample is enriched in carnallite, and the KCl content is likely to be approximately 30 to 35 %, according to Boulby Mine specialists (Welsh, pers. comm., 24th of February 2020).

ii) Nine samples from three different sections of a drill core of late Permian Zechstein Formation anhydrite from the margin of the West Central Graben in North Sea are used (Fig. 4.3; Appendix C, Fig. C.1).

The material was taken from well 21/16-4 (surface latitude: 57° 25’ 05.76’’ N; TD latitude: 57° 25’ 05.49’’ N; surface longitude: 00° 07’ 41.69’’ E; TD longitude: 00° 07’ 41.28’’ E; completed January 1996; Amerada Hess Limited) at true vertical depths below sea level between 7241 and 7355 ft. (2207 to 2242 m). Samples were selected for high degrees of mineralogical purity and textural homogeneity.

Three sample intervals include the upper, middle, and lower units of the Zechstein Formation represented in the drill core, and include a range of macroscale fabrics such as: bands of white and pink massive anhydrite, several cm to dm thick; and white or light grey irregular nodules with centimetre scale diameter in a diffuse to distinct mid grey to brown thin clay membrane/film network, commonly called ‘chicken-wire’ texture (Warren, 2016; Fig. 4.3; Appendix C, Fig. C.1 to C.4).

iii) Six samples (AA-3, BA-4, 5, 6, 7, 9) were collected from an anhydrite-dominated outcrop of the Òdena Gypsum Formation (Upper Eocene), located at the margin of the Catalan Potash Basin in the South Pyrenean foreland basin, around the village of Òdena in Catalonia, Spain (Fig. 4.4; Appendix C, Fig. C.5).

All samples are beige, with light brown clay or mud inclusions. Clusters of microscopic fibro-radiate crystals of anhydrite define spherulitic features in the millimetre range in diameter, which comprises between 25 and 40 % of the rock.

Backscattered electron image analysis shows that a minor amount of gypsum is located between anhydrite blades of the spherulites in veins and along grain boundaries (Appendix C, Fig. C.6 and C.7).

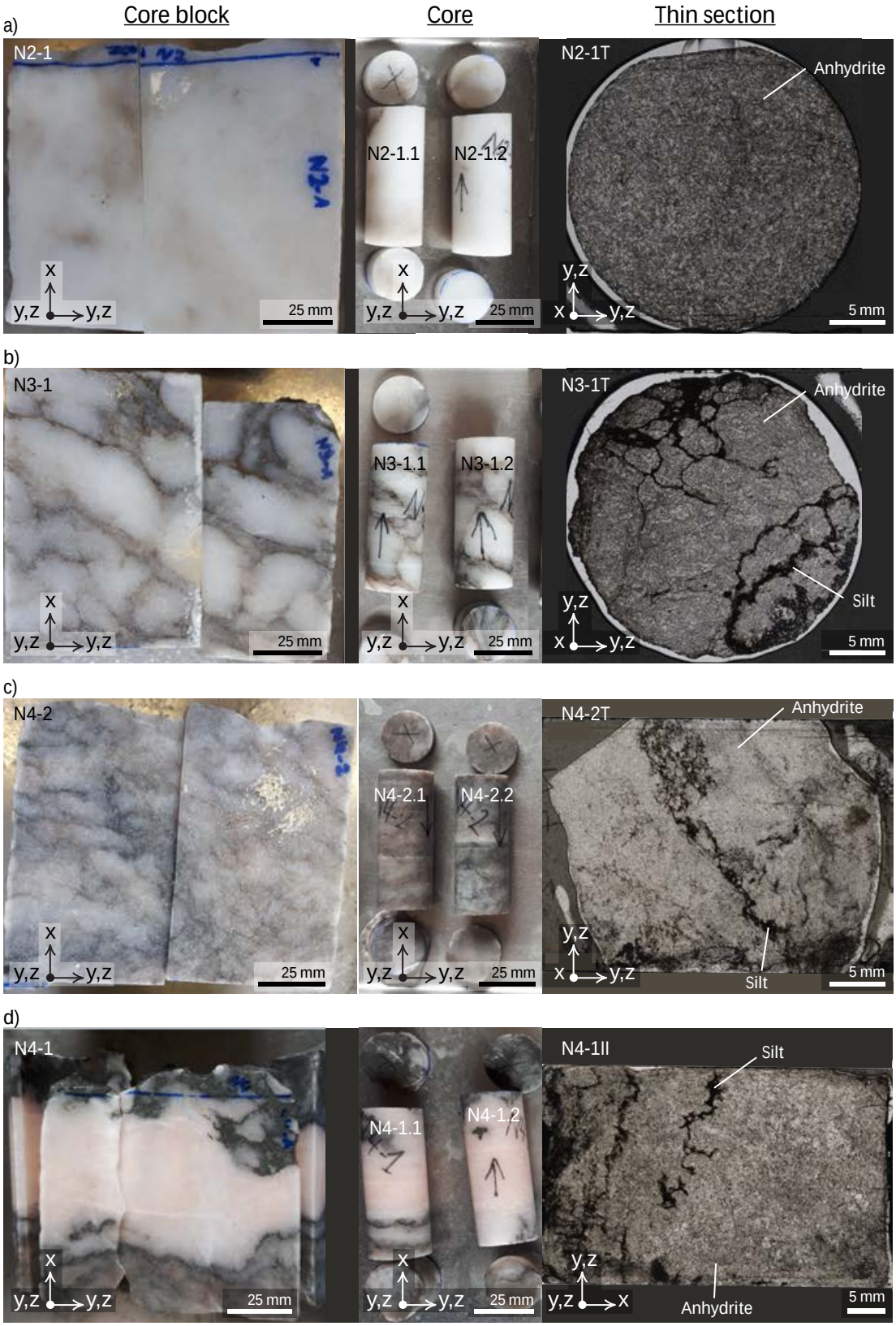

Figure 4.3: Overview of North Sea anhydrite samples, including cuts from the original drill core, twin sample cores drilled parallel to each other from the cuts of the original core cuts, and plane polarized light images (Zeiss Axio optical microscope) of thin sections from one of the cores in the central column.

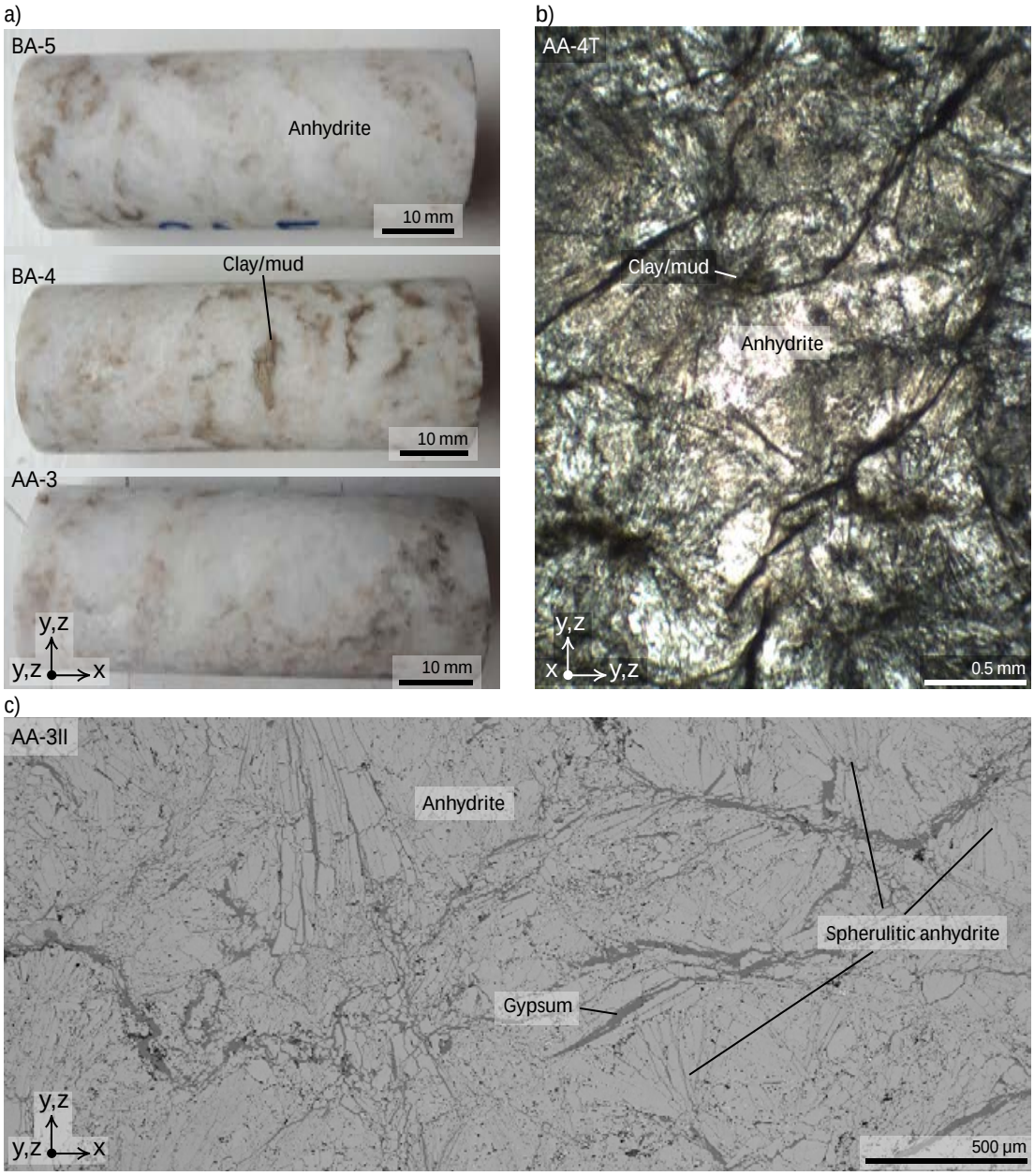

Figure 4.4: Òdena anhydrite with gypsum samples. a) Three cores cut randomly from outcrop blocks, b) plane polarized light image of the sample material (clay inclusions darken areas with gypsum veins) and c) backscattered electron image.

4.2.2 Sample preparation

All four samples from Boulby mine and one from North Sea (N2-1) were cut with a rock saw into cuboids with face dimensions ranging from 27 to 82 mm. The size of the cuboids differs due to grain size and dimensions of the available sample. Cutting and grinding were done dry, due to the high solubility of the constituent minerals in water. The material from North Sea and Òdena quarry is less reactive with water and was cut using a rock saw with water as coolant/lubricant and then immediately put in a drying

oven for 2 hours at ~ 65 °C. The cuboid facets were then mechanically polished to yield planar surfaces to facilitate ultrasonic wave velocity measurements.

For each sample, the dimensions were measured (mean of ten calliper readings), and weight was measured with a standard micro scale, yielding volume and density for each sample (Table 4.1). The error of the volume was calculated as the difference between the volume calculated with mean lengths (X, Y and Z, directions assigned arbitrarily) and the volume calculated with the sum of mean lengths plus the standard deviation of the respective ten measurements of X, Y and Z lengths. The sum of volume and error of volume is used to calculate the error of the density.

Table 4.1: Sample characteristics, including mean dimensions (lx,y,z) of the cuboids and the diameter d of the cores, calculated volume (V), mass (M), and density (ρ). hal = halite; potash* = halite, sylvite, carnallite, and silt; anh = anhydrite; gyp = gypsum.

	Sample	Content	l_X [mm]	l_y [mm]	l_z [mm]	d [mm]	V [cm^3]	M [g]	ρ [gcm^{-3}]
i)	BH2-2	hal	81.56 ± 0.23	60.70 ± 0.14	58.70 ± 0.41	-	290.58 ± 3.54	617.12	2.124 ± 0.026
	BH5-1	hal, silt	44.61 ± 0.26	61.98 ± 0.14	60.77 ± 0.20	-	168.01 ± 1.91	353.08	2.102 ± 0.024
	BP1-2	polyhal	53.13 ± 0.21	48.18 ± 0.21	48.21 ± 0.20	-	123.40 ± 1.56	339.02	2.747 ± 0.034
	Ba7-2	potash*	59.15 ± 0.15	27.72 ± 0.03	32.96 ± 0.11	-	54.04 ± 0.38	111.24	2.058 ± 0.014
ii)	N2-1	anh	37.89 ± 0.30	64.18 ± 0.07	49.80 ± 0.15	-	121.12 ± 1.43	353.68	2.920 ± 0.034
	N2-1.1	anh	61.81 ± 0.03	-	-	25.41 ± 0.05	31.34 ± 0.15	92.24	2.943 ± 0.014
	N2-1.2	anh	62.00 ± 0.03	-	-	25.35 ± 0.03	31.30 ± 0.08	92.10	2.942 ± 0.007
	N2-2.2	anh	61.99 ± 0.05	-	-	25.41 ± 0.04	31.44 ± 0.12	92.51	2.943 ± 0.011
	N4-1.2	anh	62.03 ± 0.05	-	-	25.41 ± 0.03	31.45 ± 0.10	91.94	2.924 ± 0.009
	N4-3.1	anh	61.87 ± 0.09	-	-	25.33 ± 0.10	31.17 ± 0.30	91.47	2.935 ± 0.027
	N5-1.1	anh	61.90 ± 0.04	-	-	25.41 ± 0.04	31.38 ± 0.11	92.32	2.942 ± 0.010
	N5-1.2	anh	62.02 ± 0.08	-	-	25.45 ± 0.01	31.55 ± 0.07	93.05	2.950 ± 0.066
	N5-4.2	anh	62.04 ± 0.04	-	-	25.42 ± 0.04	31.47 ± 0.11	92.61	2.943 ± 0.011
	N5-5.1	anh	62.04 ± 0.02	-	-	25.43 ± 0.04	31.51 ± 0.11	92.62	2.939 ± 0.010
iii)	BA-6	anh, gyp	61.80 ± 0.26	-	-	25.44 ± 0.01	31.41 ± 0.15	88.14	2.806 ± 0.013
	BA-7	anh, gyp	62.07 ± 0.08	-	-	25.43 ± 0.02	31.53 ± 0.09	87.00	2.760 ± 0.008
	BA-9	anh, gyp	61.85 ± 0.09	-	-	25.38 ± 0.08	31.28 ± 0.24	87.65	2.802 ± 0.021

Core plugs with a length (X axis) of 60 mm and a diameter of 25 mm (Y, Z dimension) were drilled out of sample blocks (Òdena quarry samples) and core material (North Sea samples). Given that the spherulitic Òdena quarry anhydrite does not display any kind of preferred orientation fabric and is derived from an outcrop, cores were drilled in arbitrary orientations, approximately perpendicular to bedding.

Multiple adjacent cores of the coarse crystalline Zechstein anhydrite were drilled normal to the bedding, and thus bedding is perpendicular to X and parallel to Y, Z.

Core plugs were drilled in the presence of water and were air-dried for 24 hours immediately afterward to mitigate any potential alteration effects. The Òdena quarry cores were cut at the University of Barcelona and North Sea sample at the University of Aberdeen.

4.2.3 Ultrasonic wave velocity measurements

Ultrasonic wave velocity measurements were performed using the same methods and equipment described in Vargas-Meleza et al. (2015) for cuboid and core samples described previously. In the case of the cuboids, wave velocity was measured along the three principal orthogonal X-Y-Z directions to assess the grain scale effects contributing to the total anisotropy (Fig. 4.5a).

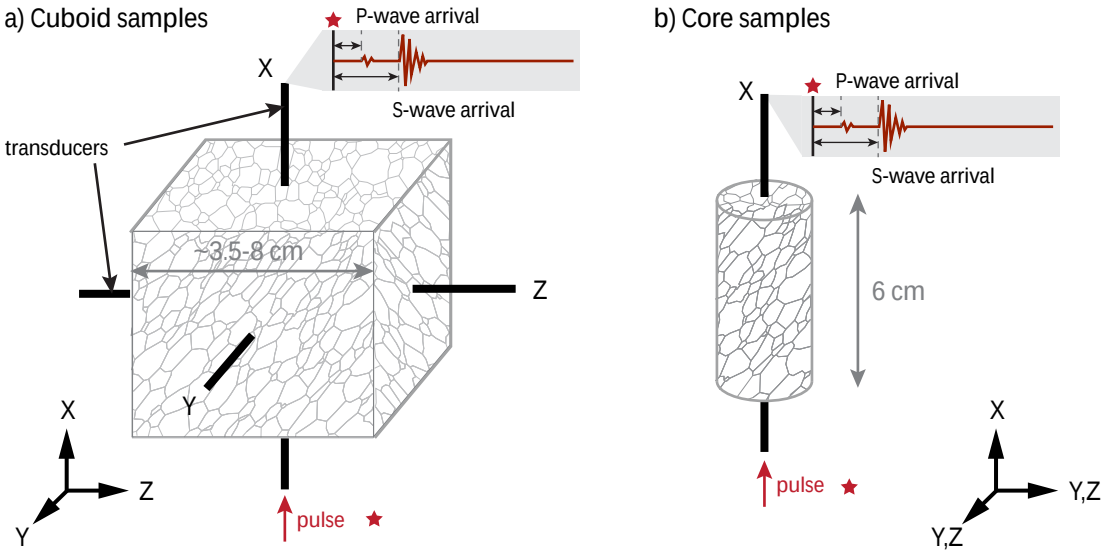

Figure 4.5: Ultrasonic velocity measurement directions and setup for cuboids and cores.

For core samples, the ultrasonic velocity was measured along the long axis (X; Fig. 4.5b), and in alternating directions (core was rotated about 180° and remeasured).

The instrumental setup is comprised of a pulse generator-receiver unit, four piezoelectric transducers (two pairs of one emitter and one receiver each). The transducers have a 2.54 cm diameter and cover up to 1 MHz oscillation frequency. The final instrument is a digital oscilloscope.

For the Panametrics V103 type compressional-wave device, the polarisation is in the direction of the emitted signal, i.e., normal to the face. For the Panametrics V153 shear-wave device, the polarisation is parallel to the transducer face and aligned with the junction of the cable meeting the housing.

Bench-top velocity measurements were taken under ambient laboratory conditions (atmospheric pressure (*atm*) and room temperature (*RT*). Two sets of measurements were made: one dry and one with silicone lubricant gel applied to increase contact signal strength. For the cuboids, a 350 g weight was added (top of top transducer) to stabilize the contact between transducers and cuboid. The cores were fastened in a steel holder, where the transducers were mounted in previously.

The wave velocity-based procedure applied to rocks is based on the ultrasonic pulse transmission method of Birch (1960). Birch's (1960) method uses the first-arrival travel time of an acoustic signal after propagation through a medium. The procedure used for this study includes placing a rock sample between two transducers (one emitter and one receiver). A pulse generator initiates an electrical signal, which is sent through the sample to the emitter (oscillated at 1 kHz frequency). The velocity of propagation for different types of waves (P-waves and S-waves) is calculated by linear regression of the relation $v = l/t$ (Vargas-Meleza et al., 2015). The transit time of the transmitted signal t and the distance it travelled through, i.e., the length l of the sample are measured (Vargas-Meleza et al., 2015).

A cuboid of pure aluminium (solid) with a standard V_P of 6.35 km s^{-1} and V_S of 3.12 km s^{-1} was used for calibration of the ultrasonic velocity measurements (Song et al., 2004). Samples were measured after a standard deviation of 0.1 % after five consecutive measurements of the aluminium block complete the calibration.

The P-wave velocities of the cuboids are measured by first measuring along one direction from one side and then rotating the cuboid 180° and sending the wave through from the other side. This is repeated three times, resulting in a total of 6 transit time measurements along each principal (orthogonal) direction. Thus, the results of V_P measurement for a single cuboid include 18 single transit time measurements. The average of each set of six transit times was calculated. The standard deviation is in the range of 0.0274 to 0.4215 µs. The number of measurements was reduced from six to four for V_P measurements on the cores and lubricating gel was used for the core

measurements. *Vs* is also measured only four times (two from each side of the cuboid/core). Different from the V_P measurements, the transducers were rotated 90° on the surface of the sample. XY means the wave propagated in X direction through the sample and a linear marker on the transducer is oriented perpendicular to Y (and parallel to Z). Then the transducer was rotated 90° and the measurement is conducted in X and perpendicular to Z (XZ).

Quantification of velocity variations, the coefficient of anisotropy, is the fractional difference between the maximum and the minimum velocities in different directions in percent (Sheriff, 2002) and commonly calculated using the following two equations:

$$AV_P = 200\ ((V_{P,}max - V_{P,}min)/(\ V_{P,}max + V_{P,}min)) \quad [1]$$

$$AV_S = 200\ ((V_{S1,}max - V_{S2,}min)/(V_{S1,}max + V_{S2,}min)) \quad [2]$$

The coefficient of anisotropy is a measure of the ultrasonic velocity anisotropy for P-wave (AV_P) and S-wave (AV_S) anisotropy, respectively. The calculation of directional ultrasonic wave anisotropy for this study is limited to the three principal orthogonal directions (X, Y, and Z). After Lloyd and Kendall (2005), the full determination of azimuthal anisotropy requires velocity measurement in a minimum of five directions, which limits the results of this study.

4.2.4 Microstructural characterisation (EBSD)

4.2.4.1 Sample preparation

Thin sections were made for North Sea samples and Òdena quarry samples only. For the North sea samples, surplus material sourced from directly adjacent to the core plugs was used to prepare polished thin sections in the core plug reference frame parallel to the long axis of the cores (i.e., the X-(Y, Z) plane) or perpendicular to it (i.e., the Y-Z plane) to characterise the samples. Thin sections with the same specifications of the Òdena quarry samples were prepared using additional cores (i.e., BA-4), as no other material was available. All thin sections were prepared for scanning electron microscopy (SEM) with alumina in glycol, followed by a final polish with 0.6 µm colloidal silica in glycol using a Buehler Vibromet II polisher for 2 to 4 hours. An evaporative carbon coating was applied to mitigate charging during SEM.

4.2.4.2 Imaging

Optical microscopy images of full thin sections were collected in reflected and transmitted light, with a plane and crossed polarizers using a Zeiss Axio Imager microscope with an automated stage at Curtin University. Scanning electron microscopy was done using the facilities at the John de Laeter Centre at Curtin University and the University of Aberdeen.

Backscattered electron (BSE) imaging and point energy dispersive X-ray (EDX) analysis was conducted at University of Aberdeen with a Zeiss Gemini MA10 scanning electron microscope (SEM) fitted with an Oxford Instruments INCA X-ray microanalysis system. At Curtin University, a Tescan MIRA3 field emission scanning electron microscope (FE-SEM) with an Oxford instruments AZtec combined EDX and electron backscatter diffraction (EBSD) acquisition system, including a Symmetry EBSD detector and XMax 20 mm SDD EDX detector, to quantify phases and crystallographic microstructures. Secondary electron (SE) and BSE images were acquired, and EBSD maps with step sizes ranging from 2 to 20 µm were collected. Data acquisition and processing settings as well as processing procedures (Table 4.2) followed those of Vargas-Meleza et al. (2015) and Timms et al. (2017; 2019).

Table 4.2: Scanning electron microscopy settings and electron backscatter diffraction acquisition and processing parameters.

SEM					
	Make/model			Tescan MIRA3 FE-SEM	
	EBSD acquisition system			Oxford Instruments AZtec/Symmetry EBSD Detector	
	EDX acquisition system			Oxford Instruments AZtec/XMax 20 mm SDD	
	EBSD processing software			Oxford Instruments Channel 5.12.72.0	
	Acceleration voltage (kV)			20	
	Working distance (mm)			18.5	
	Tilt			70°	
EBSD match units					
	Phase	Space group	β (°)		
	Anhydrite	Cmcm		Hawthorne and Ferguson, 1975	
	Gypsum	C2/c	114.3	Schonfield et al., 1996; Boeyens and Ichhram, 2002; Hildyard et al., 2009	
EBSP acquisition, indexing and processing					
	EBSP acquisition speed (Hz)		40	Band detection (min/max)	6/8
	EBSP Background (frames)		64	Mean angular deviation (all phases)	< 1°
	EBSP Binning		4 x 4	Wild spike correction	yes
	EBSP Grain		high	Nearest neighbour zero solution extrapolation	6
	Hough resolution		60		

Match units for indexing EBSD patterns of anhydrite and gypsum were developed from crystallographic data of Boeyens and Ichhram (2002) and Hawthorne and Ferguson (1975), after Hildyard et al. (2009) and Vargas-Meleza et al. (2015) (Table 4.2).

Oxford instruments Channel 5.12.72.0 (release date 26/9/2017) Tango software was used for processing and displaying EBSD data as thematic EBSD maps and pole figures, as well as data on grain shape, size, and orientation, respectively. Beforehand, isolated, erroneous EBSD data points were removed using a 'wildspike' correction, and a zero solution extrapolation to 6 nearest neighbours was applied routinely. The grain detection algorithm in Tango used a 10° neighbour misorientation threshold. Some large area maps contain minor artefacts from stitching together multiple panels with subtle angular mismatches at the edges.

Anhydrite was processed to eliminate systematic misindexing, which was present in some anhydrite grains and manifest as two or more randomly distributed indexed orientations, giving the grains a speckled appearance. Misindexing occurred as distinctive and consistent misorientation angle/axis relationships, commonly with multiple symmetric equivalent misorientations (Appendix C, Table C.1).

Maps were corrected for a total of 67 misorientation angle/axis relationships present in misindexed grains (for a full list see Appendix C), which did not include the known twin relationship in anhydrite. Low-angle (2 to 10°), high-angle (> 10°), and twin (83.5° / {100}) boundaries were visualised in anhydrite EBSD maps.

Grains were fitted with ellipses using the algorithm in Tango, which were used to generate maps and graphs of grain size (using the length of the long axis of the fitted ellipse grain size parameter) and grain aspect ratios. Angular stitching artefacts in large area maps do not significantly affect grain statistics and were ignored. A combination of BSE images and EBSD mapping were used to manually trace the networks of grain boundaries, fractures, and pores network using Adobe Illustrator, resulting in vector graphics maps of the phase distribution of anhydrite, gypsum, dolomite, and pores where appropriate. Additionally, grains were fitted with ellipses using ImageJ, and grain size distributions were calculated.

4.2.4.3 Crystallographic preferred orientation (CPO) quantification

CPOs were visualised as pole figures of low-index planes for each indexed phase present in the samples using EBSD map data using the Mambo software in Channel 5.12 and displayed as lower hemisphere plots in the maps X-Y-Z reference frame. All data for each phase were used to generate contoured plots using Mambo. The statistical description of the intensity of the fabric based on clustering of poles on pole figures, known as the 'multiple of uniform density' (m.u.d.).

As an additional quantitative measure of fabric strength the M-index (Skemer et al., 2005) was used as a measure of phase specific CPO strength. The *M*-index is based on the distribution of uncorrelated misorientation angles, and scaled from $M = 0$, representing a random fabric, and $M = 1$, representing a single crystal. *M*-index is known to correlate well with seismic anisotropy (e.g., Skemer et al., 2005; Jung et al., 2010; Michibayashi et al., 2012).

4.3.4.4 Shape preferred orientation (SPO) quantification

EBSD data is analysed for SPO quantification and the results are compared to additional SPO quantification from BSE and EBSD map-based manual grain boundary trace maps. Vector graphic maps were created via manual tracing of combined BSE and EBSD maps include interpretation of the grain boundary pattern, phase distribution of anhydrite, gypsum, dolomite, fractures, and pores, appropriate to the sample characteristics. SPO quantification of four North Sea samples was accomplished using the following four methods/techniques:

A. Maps and rose diagrams using the long axis of the fitted ellipse of grains detected via Tango in Channel software. Maps are of grain orientations using the orientation of the long axis of the fitted ellipse.

B. Rose diagrams plot the orientation of the long axis of fitted ellipses of all grains detected using data from ImageJ analysis of manually traced grain boundary maps.

C. Grain boundary segment orientation rose diagrams were generated from grain boundary traces via GBPaQ, which is automated for such plots. This means that all linear segments (vectors) that describe the grain boundary pattern are statistically analysed and the magnitude is plotted against the orientation of the grain boundary segment (length-weighted).

D. Grain boundary segment intercept (GBSI)-based analysis via GBPaQ. One central radial scan line centre is superimposed on top of the grain boundary pattern. The angle between scan lines is 0.5°. GBSI density per pixel for all scan line orientations is calculated and the minimum orientation and density, maximum orientation and density, and average GBSI density are determined. Minimum intensity (I_{min}) is determined for each sample, calculated by dividing the minimum GBSI density by the average GBSI density.

The Òdena quarry anhydrite with gypsum samples has an inhomogeneous structure, including spherulites and sections with blocky anhydrite crystals. An exemplary spherulitic structure is interpreted via manual tracing and processed analytically using the following two methods:

A. Greyscale threshold-based phase content analysis (ImageJ) of BSE images, where the area of defined individual greyscale phase thresholds is used to calculate the percentage relative to the total area of the map.

B. Fracture geometry quantification performed with the MATLAB^{TM} toolbox FracPaQ (Healy et al., 2017) for gypsum-filled veins and intra-grain fractures on manually traced linear segments from BSE images and EBSD maps.

Further grain boundary segment-based analysis and GBSI analysis are not done because the spherulitic section only represents a partial pattern characteristic that makes up ~ 40 % of the complete sample (Fig. 4.5b). Phase distribution and fracture distribution are more representative, concluding from backscatter images of the Òdena quarry samples (Fig. 4.5c).

4.3 Results

4.3.1 Ultrasonic wave velocity measurements

P-wave velocities (V_P) of the cuboids show that the three samples BH2-2, BP1-2, Ba7-2 with the least difference of V_P between principal directions (V_P X, V_P Y, and V_P Z) plot in a very close range of literature velocities from Jones and Davison (2014) (Table 4.3). Calculation of the P-wave anisotropy AV_P shows that BH2-2 (pure halite), BP1-2 (pure polyhalite), and Ba7-2 (potash with halite) have very little ultrasonic anisotropy under 5 % (Fig. 4.6a; Table 4.3).

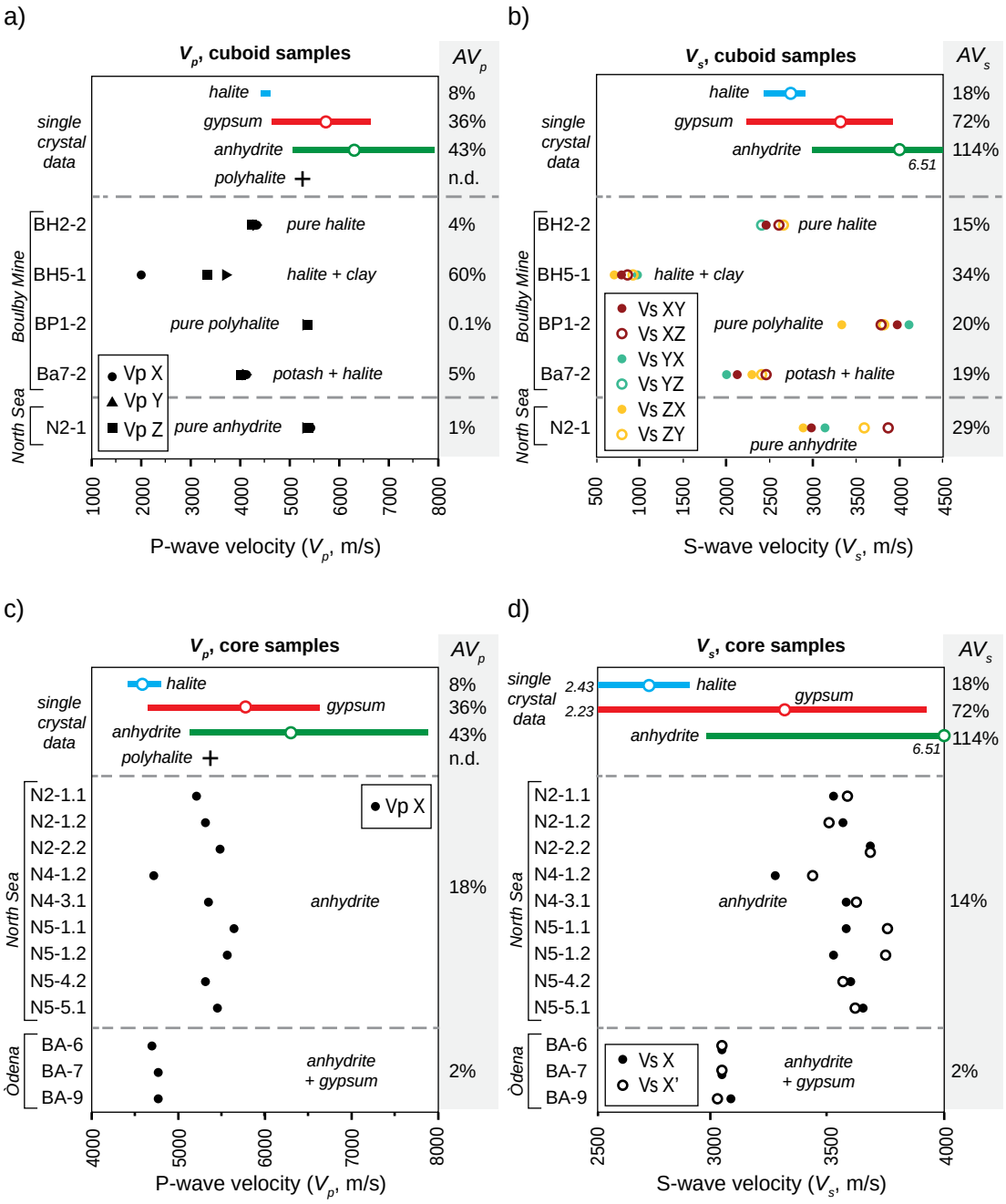

Figure 4.6: Results of ultrasonic velocity measurements for V_P and V_S from all samples in this study. Ranges in V_P and V_S for single crystals, shown as coloured bars, are calculated from single crystal ultrasonic velocity anisotropy for halite, anhydrite, and gypsum via AnisoVis MATLAB™ Toolbox (Healy et al., 2020) (chapter 1, Fig. 1.1). V_P ranges were also published by Vargas-Meleza et al. (2015). For c), and d) the measurements of one material (North Sea or Òdena quarry) are combined to calculate AV_P and AV_S. d) The difference between V_S X and V_S X' is that the emitter is rotated 90° on the surface for measurement of shear wave splitting.

Of the two remaining samples, BH5-1 (halite mixed with clay) has the highest AV_P with 60 %. The cuboid of the North Sea anhydrite, N2-1, shows the most difference from the literature P-wave velocity (Jones and Davison, 2014) but has one of the smallest AV_P with 1 %. In comparison to single crystal AV_P ranges of halite, gypsum, and anhydrite from Vargas-Meleza et al. (2015), the cuboids have generally slower velocities. Only BH2-2 and N2-1 are within the slower end of the ranges of single crystal P-wave velocities.

Table 4.3: Literature data and results of this study on density [g cm^{-3}] and compressional wave velocity V_P [m s^{-1}] in directions X, Y and Z; ΔV_P - range of V_P, and anisotropy AV_P [%], calculated by equation 1. [1] Official mineral density (e.g., Mineralogy Database - webmineral.com); [2] wireline log rock densities after Urai et al. (2008); [3] after Jones and Davison (2014). *calculation excluding N4-1.2, without this the V_P X range is 5,229 to 5,663 m s^{-1} and range is 434 m s^{-1}.

		Samples		Values literature			Vp results this study				
	Name	Rock density	Mineral content	Mineral density [1]	Rock density [2]	V_P [3]	V_P X	V_P Y	V_P Z	ΔV_P	AV_P
i)	**BH2-2**	2.124	halite	2.170	2.040	4500	4394	4374	4215	179	4.15
	BH5-1	2.102	halite	2.170	2.040	4500	2034	3731	3337	1697	58.9
	BP1-2	2.747	polyhalite	2.77-2.78	2.790	5300	5356	5355	5348	8	0.1
	Ba7-2	1.058	potash	1.281			4021	4157	4206	185	4.5
			halite	2.170	2.040	4500					
			carnallite	1.600	1.570	3900					
			sylvite	1.990	1.860	4110					
ii)	**N2-1**	2920	anhydrite	2.970	2.980	6500	5423	5362	5389	61	1.13
	N	2.940	anhydrite	2.970	2.980	6500	4742 -5663			921	17.7; 7.96*
iii)	**BA**	2.789	anhydrite	2.970	2.980	6500	4714 -4798			84	1.77
			gypsum	2.300	2.350	5700					

The results from analysing S-wave velocities of the cuboids confirm that BH2-2 and BH5-1 have very different ultrasonic characteristics (Fig. 4.6b; Table 4.4). The halite and clay mixture (BH5-1) has slower P- and S-wave velocities compared to the pure halite (BH2-2) sample. The shear wave anisotropy is doubled for BH5-1 (34 %) compared to BH2-2 (15 %), but overall lower than the respective AV_P.

All samples except BH5-1 have higher AV_S than AV_P. Especially pure polyhalite (BP1-2) and pure anhydrite (N2-1), which had the lowest AV_S under 1 % have relatively strong AV_P with 20 % and 29 %.

Table 4.4: S-wave velocities V_S [m s^{-1}] for all samples. *no silicone lubricant gel used. ΔV_S is the shear wave splitting, the difference between fastest and slowest shear wave velocity from the mean values presented in this table. AV_S is the velocity anisotropy of the S-waves [%], calculated from the mean values presented in this table using equation 2.

	Sample	V_S XY	V_S XZ	V_S YX	V_S YZ	V_S ZX	V_S ZY	ΔV_S	AV_S
i)	**BH2-2***	2271.8	2409.3	2503.6	2648.4	2467.0	2618.4	376.6	15.31
	BH5-1*	708.048	982.533	916.849	823.094	699.287	870.602	283.2	33.68
	BP1-2	4110.7	4094.9	3816.1	3973.4	3347.7	3795.8	763.0	20.46
	Ba7-2	2292.7	2008.5	2400.2	2122.7	2405.6	2441.2	432.7	19.45
		Vs X	***Vs X'***						
ii)	**N2-1**	2888.2	3139.4	3605.7	2992.1	2921.1	3883.4	995.2	29.39
	N2-1.1	3536.0	3585.2					49.2	1.38
	N2-1.2	3573.5	3512.8					6.1	1.71
	N2-2.2	3686.7	3690.0					3.3	0.09
	N4-1.2	3273.2	3441.2					168.0	5.00
	N4-3.1	3581.5	3623.4					42.0	1.16
	N5-1.1	3584.0	3763.8					179.8	4.89
	N5-1.2	3530.7	3755.1					224.5	6.16
	N5-4.2	3596.3	3570.5					25.9	0.72
	N5-5.1	3643.9	3617.4					26.6	0.73
iii)	**BA-6**	3041.2	3041.2					0	0
	BA-7	3050.9	3043.4					17.9	0.25
	BA-9	3081.5	3025.0					56.5	1.85

In contrast to the cuboid samples, core samples allow ultrasonic wave velocity only in one principal direction (X), due to sample shape and the size of the transducers. Also, various samples of the same rock type, either pure anhydrite (N samples; North Sea) or a mixture of anhydrite with gypsum (BA samples; Òdena quarry) are measured and V_P and V_S values combined to get material dependent anisotropy (AV_P and AV_S).

P-wave velocities of North Sea anhydrite samples are very slow for anhydrite (Fig. 4.6c); Table 4.3). They are way below the velocities of Jones and Davison (2014) and at the lower boundary of single crystal AV_P (values from Vargas-Meleza et al., 2015).

One sample, N4-1.2, has distinctively slow V_P. With the N4-1.2 minimum P-wave velocity values, AV_P is at 18 %. Without the N4-1.2 values, AV_P is considerately lower with 8 % (Table 4.3). V_P velocities of the three Òdena quarry samples are within 2 % AV_P and also distinctively slower than the literature anhydrite and gypsum velocities (Jones and Davison, 2014).

Compared to single crystal P-wave anisotropy (Vargas-Meleza et al., 2015), the Òdena quarry samples, that contain anhydrite and gypsum, plot at the very slow end of the anisotropy range for gypsum.

The S-wave velocities of the pure anhydrite core samples (North Sea) are generally faster than those of the anhydrite and gypsum mixed samples (Òdena; Fig. 4.6d; Table 4.4). Shear wave splitting (ΔV_S; the difference between V_S X and V_S X') is < 50 m s^{-1} for six (N2-1.1, N2-1.2, N2-2.2, N4-3.1, N5-4.2, N5-5.1) out of nine North Sea anhydrite samples and therefore in the same range as the shear wave splitting of the Òdena quarry samples that is < 60 m s^{-1}. N4-1.2, N5-1.1, and N5-1.2 have stronger shear wave splitting in the range of 168 to 225 m s^{-1}.

AV_S measured for the cores has not changed much from AV_P for both sample materials. It is constant at 2 % for the Òdena quarry samples and slightly lower with 14 % for the North Sea samples.

4.3.2 Microstructural characterisation

The study of microstructures for assessment of systematic features that might cause or influence ultrasonic anisotropy is limited to North Sea samples and Òdena quarry samples.

4.3.2.1 North Sea anhydrite samples

Four examples of EBSD analytical datasets of sample material from four different core sections of North Sea anhydrite were analysed, three from thin sections with orientation perpendicular to the long axis of the core (X; N2-1T, N3-1T, and N4-2T) and one from a thin section cut parallel to the core long axis (N4-1II).

Crystallographic orientation maps of these four samples generally show spatial clusters of grains with different preferred crystallographic orientations (blue, green clusters, and pink and violet clusters, Fig. 4.7a and 4.8a; Appendix C, Fig. C.8a and C.13a).

Low-angle boundaries (2-10° misorientation) are more common in grains with smaller grain size compared to large grains, which can be free of such low angle boundaries. No twin boundaries ([100] by 83.5°) were detected. The grain size (Fig. 4.7b and 4.8b) is dominated by medium to small grain sizes, often as clusters of grains with similar grain sizes.

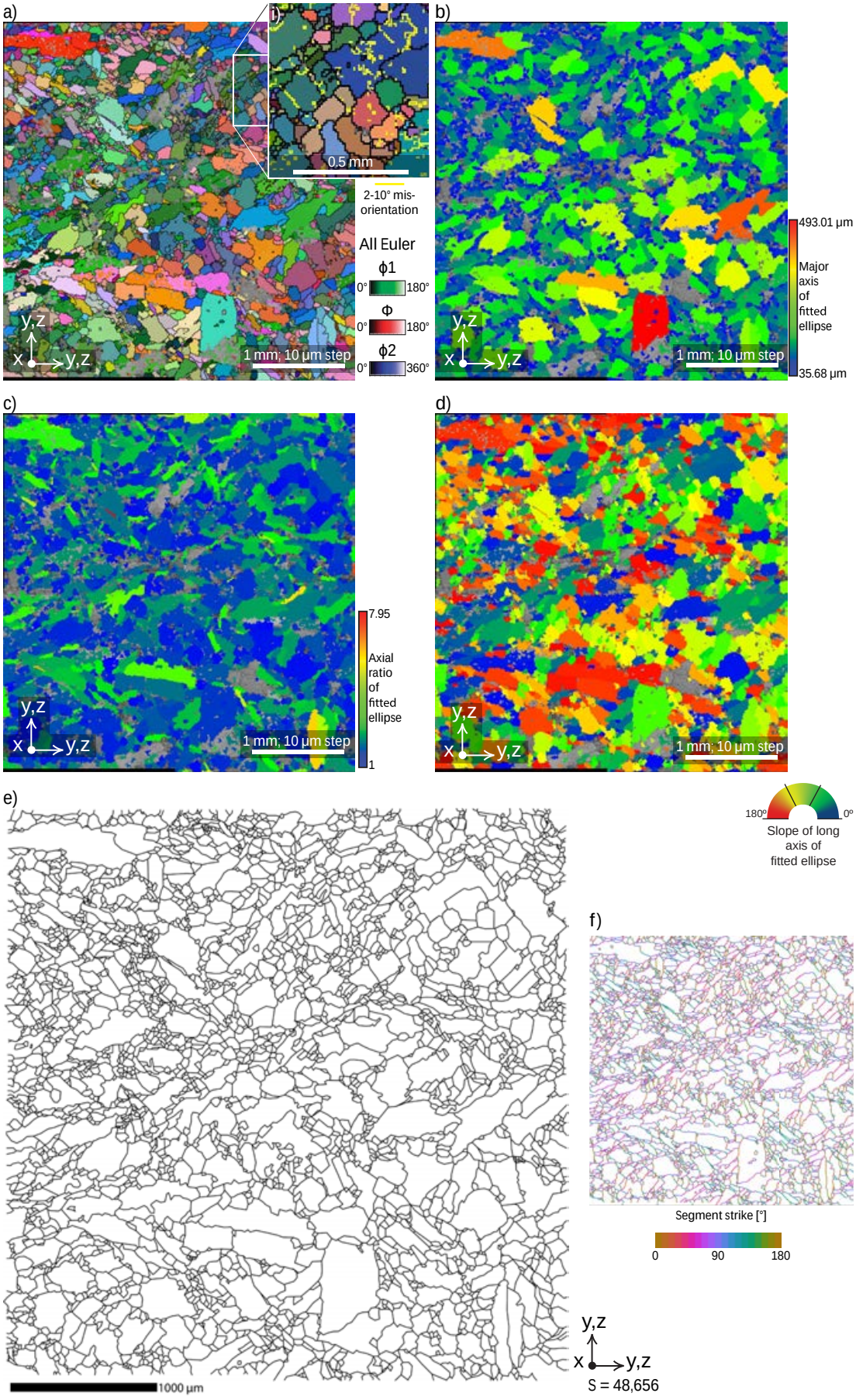
a)
i)
0.5 mm
2-10° mis-orientation
All Euler
ϕ1
0°
180°
Φ
0°
180°
ϕ2
0°
360°
y,z
x
y,z
1 mm; 10 µm step
b)
493.01 µm
Major axis of fitted ellipse
35.68 µm
c)
7.95
Axial ratio of fitted ellipse
1
d)
e)
1000 µm
180°
0°
Slope of long axis of fitted ellipse
f)
Segment strike [°]
0
90
180
S = 48,656

Figure 4.7: Microstructural analysis of sample N3-1T, on a thin section with perpendicular orientation to X direction (long core axis). a) Crystallographic orientation map (Euler), with i) including low angle boundaries > 2° in yellow and grain boundaries (> 10°) in black (full map and additional data in Appendix C, Fig. C.11, C.12), b) grain size map, c) grain shape map, d) grain shape preferred orientation map. Slope means orientation of the long axis of the fitted ellipse of grains. a) to d) are based on EBSD analysis. e) Grain boundary trace map, based on manual tracing of BSE and crystallographic orientation map of the same area. *S* is the number of grain boundary trace segments of the data set. f) Grain boundary segment orientation map, based on e) and analysed via GBPaQ.

The grain shape maps contain few grains with a medium axial ratio. There seems to be a relation between the axial ratio and azimuth of the grains. Elongated grains are often subparallel or perpendicular to each other.

SPO maps categorise grains by the angle of the longest axis of a fitted ellipse, showing domains that are dominated by certain angles (Fig. 4.7d, 4.8d, Appendix C, Fig. C.8d, C.13d). For example, the lower part of the SPO map of sample N2-1T (Appendix C, and C.8d) is dominated by angles around 45° and 135°, with a successive increase of grains with 0/180° orientation towards the top of the map.

The grain boundary trace map (Fig. 4.7e) includes data that has not been indexed via EBSD. The interpretation from combined EBSD and BSE image analysis includes a great number of grains with a considerable smaller grain size.

Large, lath shaped anhydrite grains have slightly lobate grain boundaries, and are predominantly oriented subparallel or perpendicular to one another (Fig. 4.7e,f and Fig. 4.8e,f; Appendix C, Fig. C.8e,f, and C.13e,f). Grain boundary segment orientation maps (Fig. 4.7f, and 4.8f, Appendix C, Fig. C.8f, and C.13f) show a dominance of segment orientations around 45° and 135° (pink and green colour).

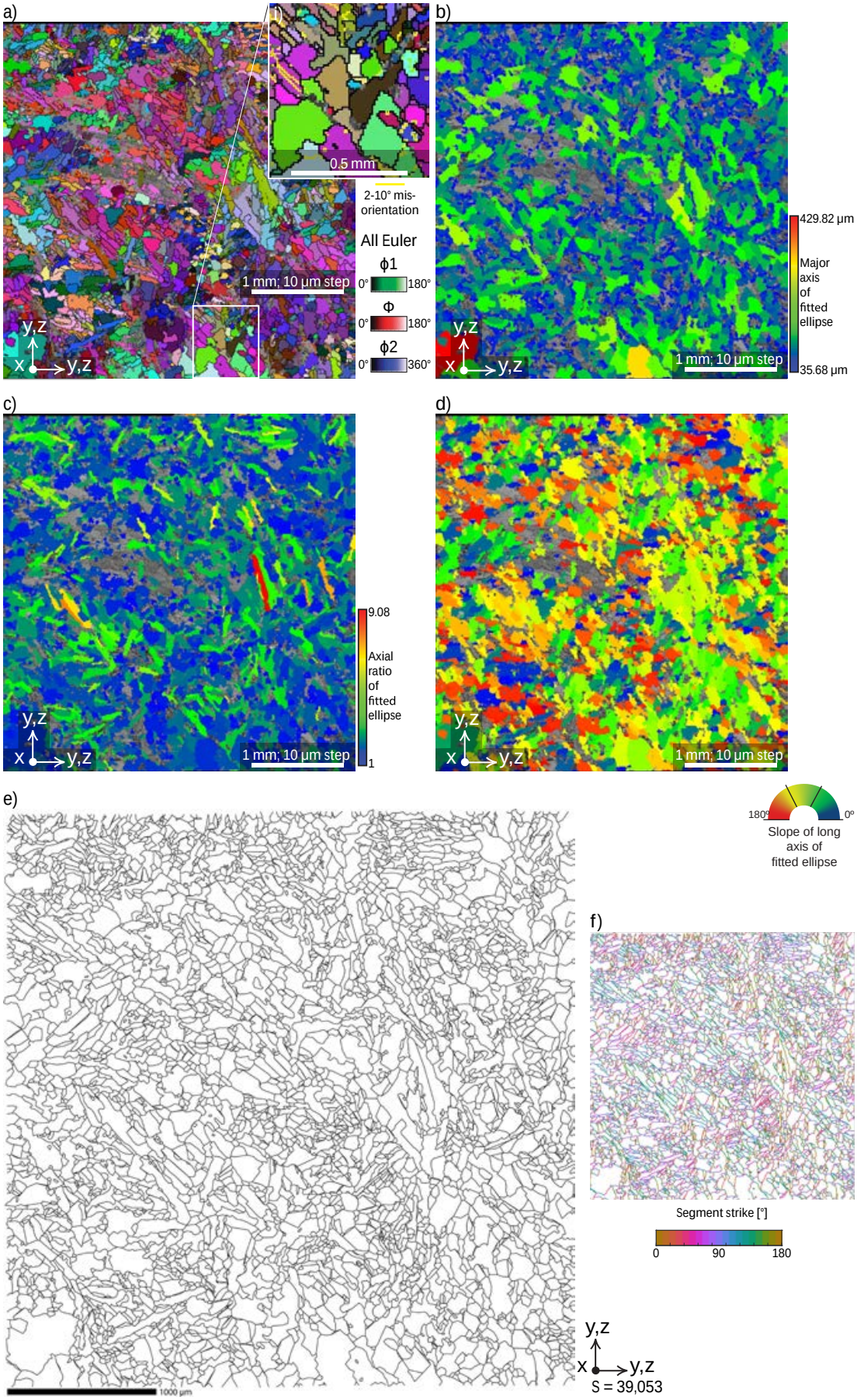
a)
0.5 mm
2-10° mis-orientation
All Euler
ϕ1
0°
180°
Φ
0°
180°
ϕ2
0°
360°
1 mm; 10 µm step
y,z
x
y,z
b)
429.82 µm
Major axis of fitted ellipse
35.68 µm
1 mm; 10 µm step
c)
9.08
Axial ratio of fitted ellipse
1
1 mm; 10 µm step
d)
1 mm; 10 µm step
e)
180°
0°
Slope of long axis of fitted ellipse
1000 µm
f)
Segment strike [°]
0
90
180
S = 39,053

Figure 4.8: Microstructural analysis of sample N4-2T, on a thin section with perpendicular orientation to X direction (long core axis). a) Crystallographic orientation map, with i) including low angle boundaries > 2° in yellow and grain boundaries (> 10°) in black (full map in Appendix C, Fig. C.16), b) grain size map, c) grain shape map, d) shape preferred orientation map. a) to d) are based on EBSD analysis. e) Grain boundary trace map, based on manual tracing of BSE and crystallographic orientation map. *S* is the number of trace segments of the map. f) Grain boundary segment orientation map, based on e) and analysed via GBPaQ.

Crystallographic orientation pole figures (Fig. 4.9a, 4.10a; Appendix C, Fig. C.9a, C.14a) of the indexed anhydrite of the EBSD datasets presented show clustering of poles with maximum m.u.d. ranging from 5.50 (N3-1T, Fig. 4.9a) to 4.15 (N4-2II, Fig. 4.10a).

Results of fitted ellipse long axis orientation rose plots of EBSD data and trace maps (Fig. 4.9bii and cii, Fig. 4.10bii and cii; Appendix C., Fig. C.9bii and cii, C.4bii and cii) are consistent with orientations, and with only slight differences in magnitudes for all four datasets. For example, the mean orientation of sample N3-1T are consistent with orientations of 88° and 89°, while the maximum magnitude differs by 1% (8.1 % and 7.1 %; Fig. 4.9bii and cii). However, the trace map-based roses of all datasets (i.e., Fig. 4.9cii) show that there are various strong secondary orientations, ranging within ~ 90° from another. (Fig. 4.9cii; Appendix C, Fig. C.9cii and C.14cii).

The segment orientation rose plots (Fig. 4.9d, 4.10d, Appendix C, Fig. C.9d, C.14d) have a distinctive rectangular shape, confirming previous results of a bimodal SPO. The primary and secondary maximum bins are of very similar magnitude and oriented perpendicular to each other.

The shapes of the GBSI density roses (Fig. 4.9e, 4.10e; Appendix C, Fig. C.9e, C.14e) range from almost round (N3-1T, Fig. 4.9e), to showing square (N4-2II, Fig. 4.10e, and N4-1T, Appendix C, Fig. C.14e) or rhombic geometry (N2-1T, Appendix C, Fig. C.9e). While a circular shape strongly indicates weak to no SPO, square and rhombic shapes display bimodal SPO, which is in agreement with results of segment orientation rose plots.

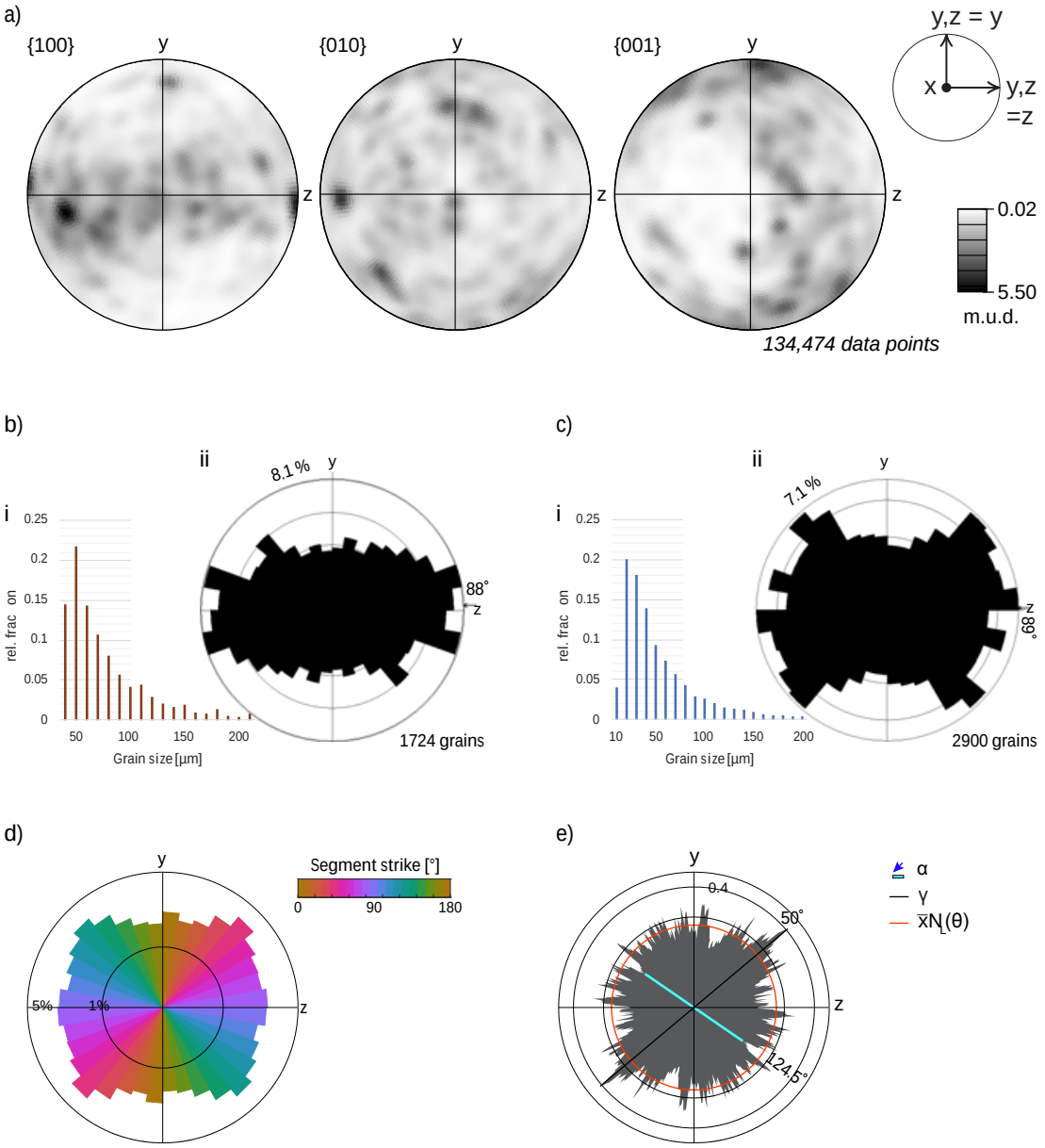

Figure 4.9: Crystallographic and shape preferred orientation analysis of sample N3-1T, based on the maps shown in Figure 4.7. a) Crystallographic orientation pole figures for anhydrite based on EBSD data. b) Fitted ellipse analysis of EBSD data, i) grain size histogram and ii) rose diagram of the long axes angles of fitted ellipses. c) Fitted ellipse analysis of trace map data (48,656 segments), i) grain size histogram and ii) rose diagram of the long axes angles of fitted ellipses. d) Equal area, length-weighted grain boundary segment orientation rose of the trace map, resulting from GBPaQ analysis. e) GBSI density rose plot from GBPaQ analysis. The angle between scan lines = 0.5°. *α* is the minimum GBSI density (scan line) angle. *γ* is the maximum GBSI density (scan line) angle. $\bar{x}N(\theta)$ is the average GBSI density, in GBSI per pixel.

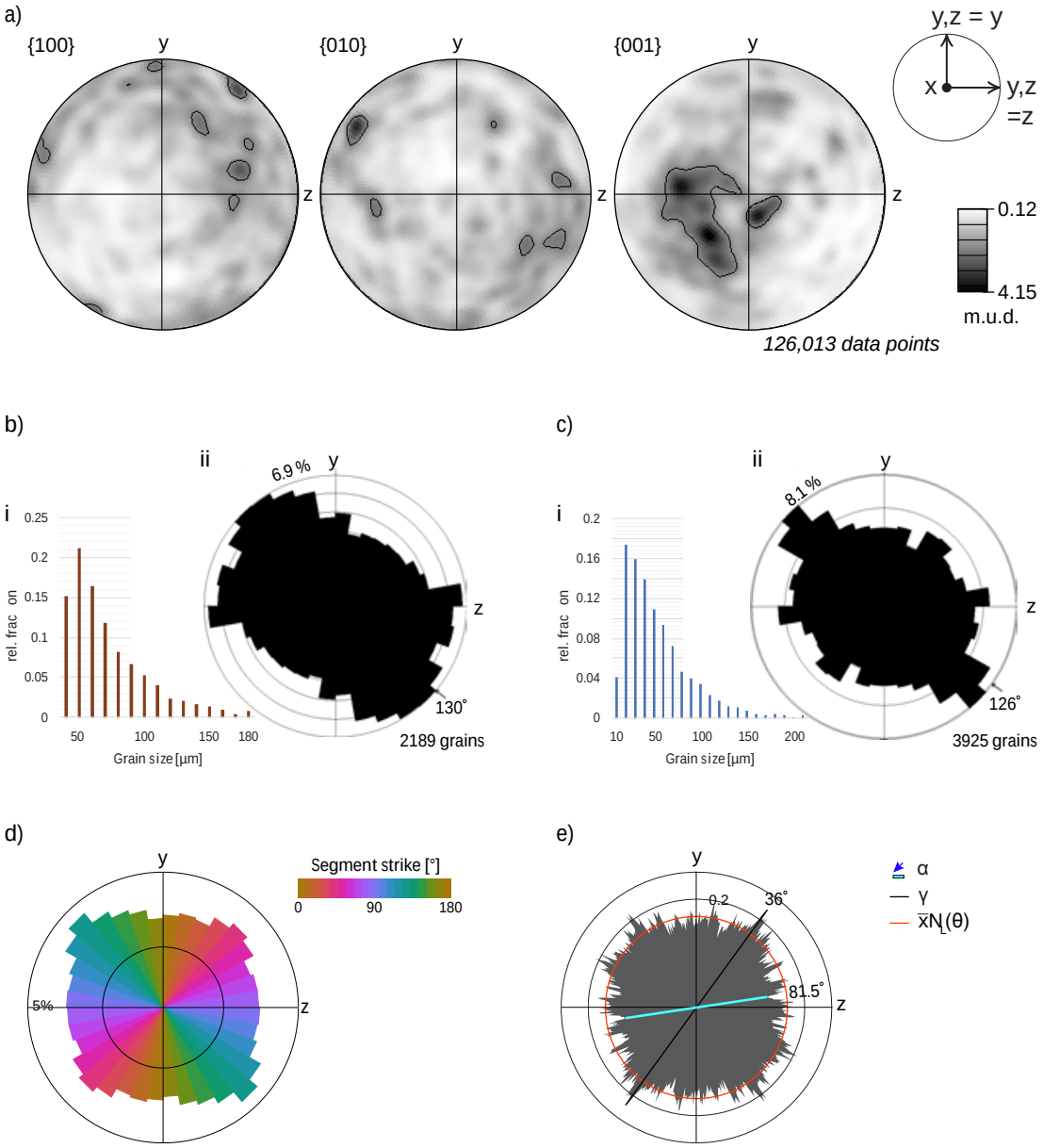

Figure 4.10: Crystallographic and shape preferred orientation analysis of sample N4-2T, based on the maps shown in Figure 4.8. a) Crystallographic orientation pole figures for anhydrite based on EBSD data. b) Fitted ellipse analysis of EBSD data, i) grain size histogram and ii) rose diagram of the long axes angles of fitted ellipses. c) Fitted ellipse analysis of trace map data (39,053 segments), i) grain size histogram and ii) rose diagram of the long axes angles of fitted ellipses. d) Equal area, length-weighted grain boundary segment orientation rose of the trace map, resulting from GBPaQ analysis. e) GBSI density rose plot from GBPaQ analysis. The angle between scan lines is 0.5°. *α* is the minimum GBSI density (scan line) angle. *γ* is the maximum GBSI density (scan line) angle. $\bar{x}N(\theta)$ is the average GBSI density, in GBSI per pixel.

The results from EBSD data and grain boundary tracing of microstructural analysis of the North Sea anhydrite samples are summarised in table 4.5. In general, the number of grains analysed rises significantly due to grain boundary tracing, whereas the grain size is generally smaller and the axial ratio is slightly higher. Mean resultant directions and approximate 95 % confidence intervals, both measures of SPO strength and orientation, are very similar between the analytical methods.

Table 4.5: Microstructural analysis from EBSD data and grain boundary tracing. # = number of grains; ECD = mean equivalent circular diameter ± standard deviation; *r* = mean axial ratio of longest axis/ shortest axis of fitted grain ellipses ± standard deviation; MRD = mean resultant direction ± approx. 95 % confidence interval.

	EBSD data grain statistics				Grain boundary trace maps grain statistics			
Sample	#	ECD [µm]	*r*	MRD [°]	#	ECD [µm]	*r*	MRD [°]
N2-1T	4620	39.26 ± 36.67	2.01 ± 0.82	170 ± 7.5	6777	26.50± 31.63	2.35± 1.29	171± 7.7
N3-1T	1724	77.41 ± 52.34	1.70 ± 0.69	88 ± 12.9	2900	52.32 ± 48.98	2.08 ± 0.94	89 ± 11.2
N4-1II	1204	89.71 ± 57.32	2.05 ± 0.85	58 ± 30.2	1464	79.62± 59.30	2.22 ± 1.04	58 ± 33.0
N4-2T	2189	69.41 ± 35.32	2.17 ± 0.94	130 ± 14.1	3925	49.01 ± 37.08	2.29 ± 1.07	126 ± 13.3

The mean grain size equivalent circular diameter (ECD) analysed parallel to the long axis of the cores (N4-1II) is 89.71 ± 57.32 µm (EBSD statistics)/ 79.62 ± 59.30 µm (trace map statistics), and therefore bigger than the mean grain sizes measured perpendicular to that axis (N4-2T), with 69.41 ± 35.32 µm (EBSD statistics)/ 49.01 ± 37.08 µm (trace map statistics).

The maximum grain size determined via EBSD grain size statistics (i.e., Fig. 4.7b) is between 430 µm and 493 µm. The mean ECD resulting from the analysis of N2-1T is about half as big as that of every other map, with a visibly larger population of small grains (i.e., Fig. 4.7e; Appendix C, Fig. C.8;). The mean axial ratio *r* is lowest for N3-1T with 1.71.70 ± 0.69 (EBSD statistics)/ 2.08 ± 0.94 (trace map statistics) but very consistent over the other data sets, where it ranges between 2.01 ± 0.82 (N2-1T, EBSD statistics) and 2.35 ± 1.29 (N2-1T, trace map statistics).

GBSI density analysis results are used to calculate the minimum intensity (Table 4.6), a value that quantifies the strength of the SPO. The minimum intensity is highest for N4-2T and lowest for N2-1T. SPO is generally weaker in the N4-2T grain boundary map, and N2-1T has the strongest SPO out of the analysed North Sea samples.

CPO is strongest in N2-1 with M = 0.15 (m.u.d. of 5.36), followed by N3-1T with M = 0.14 (m.u.d. of 5.5) and N4-1II with M = 0.13 (m.u.d. of 4.89). N4-2T has the weakest CPO of the North Sea samples, with M = 0.12 (m.u.d. of 4.15).

Table 4.6: Grain boundary intercept based results and CPO strength based on *M*-index. α = minimum GBSI density (scan line) angle; γ = maximum GBSI density (scan line) angle; $NL(\alpha)$ = minimum GBSI density; $NL(\gamma)$ = maximum GBSI density; $\bar{x}NL(\theta)$ = average GBSI density; I_{min} = minimum intensity. I/ppx = GBSIs per scan line. Additional data for M-index can be found in Appendix C, Fig. C.19 and Table C.5.

Sample	α [°]	γ [°]	$N_L(\alpha)$ [I/ppx]	$N_L(\gamma)$ [I/ppx]	$\bar{x}N_L(\theta)$ [I/ppx]	I_{min}	*M*-index
N2-1T	177	95.5	0.50062	1.1991	0.84687	0.5911	0.15
N3-1T	124.5	50	0.19734	0.40702	0.27400	0.7047	0.14
N4-1II	164	109.5	0.08275	0.19309	0.13365	0.6192	0.13
N4-2T	81.5	36	0.13263	0.22316	0.16816	0.7887	0.12

The minimum intensity can be plotted against the mean axial ratio r of EBSD and grain boundary tracing analysis. Figure 4.11 shows that all axial ratios are around r = 2, with variation of minimum intensity between ~ 0.79 and ~0.59, possibly relating to initial elongate anhydrite grains.

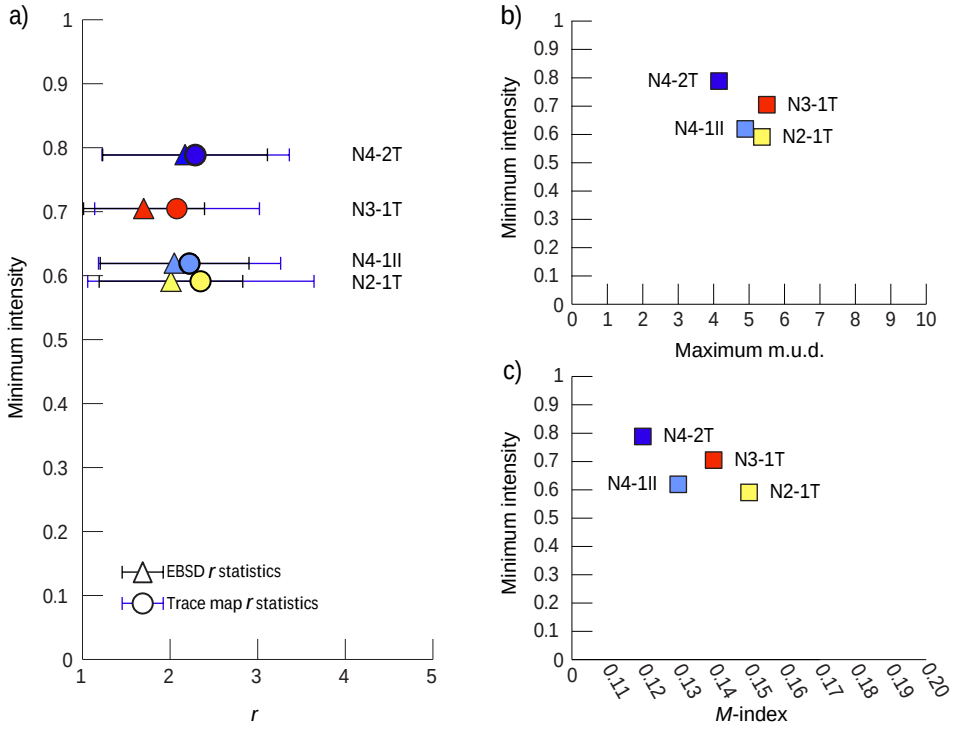

Figure 4.11: North Sea anhydrite minimum intensities (I_{min}) plotted a) against axial ratio r, calculated from EBSD and trace maps fitted ellipse statistics, b) against multiple of uniform density (m.u.d.), and c) against CPO strength in form of *M*-index.

4.3.2.2 Òdena quarry anhydrite with gypsum

Overall, indexing of the Òdena quarry samples via EBSD has been difficult due to polishing that resulted in gypsum loss and generation of surface topography. Over 30 % of the EBSD map of AA-4T was misindexed, and these data were disregarded. Nevertheless, observations from the correctly indexed points of the crystallographic orientation EBSD map (Fig. 4.12a) show that the spherulitic features comprise radial anhydrite 'blades' that have a systematic change of orientation over several crystals, i.e., with low-angle misorientations. Furthermore, there are clusters of grains with similar crystallographic orientations and clusters with more random orientations.

Low-angle misorientation boundaries (2° to 10°) are common in spherulitic and non-spherulitic anhydrite (Fig. 4.12ai). The low-angle boundaries in spherulitic anhydrite blades are mostly radial, following the radial distribution of the crystals. Twin boundaries (83.5° / [100]) were not detected.

The pole figures show a clustering of poles with a low maximum m.u.d. of 2.84. The map covers a large area that includes several spherulitic structures and more blocky areas. Despite the high rate of misindexing, the data collected should be representative for analysing CPO strength of the material. The *M*-index calculated from the anhydrite data set is M = 0.12, indicating low CPO, similar to N4-2II (Table 4.6; Appendix C, Fig. C.19, Table C.5).

Further analysis of the EBSD data for AA-4T shows that larger grains are also strongly elongated, high axial ratio grains and most often forming spherulites (Fig. 4.17a,b). The shape preferred orientation map (Fig. 4.17c) shows that SPO is very inhomogeneous. There are areas where grains have similar grain shape orientation, next to areas with different orientations being dominant. Overall, there seems to be no uniform SPO in the sample. This is consistent with the macroscopic observations.

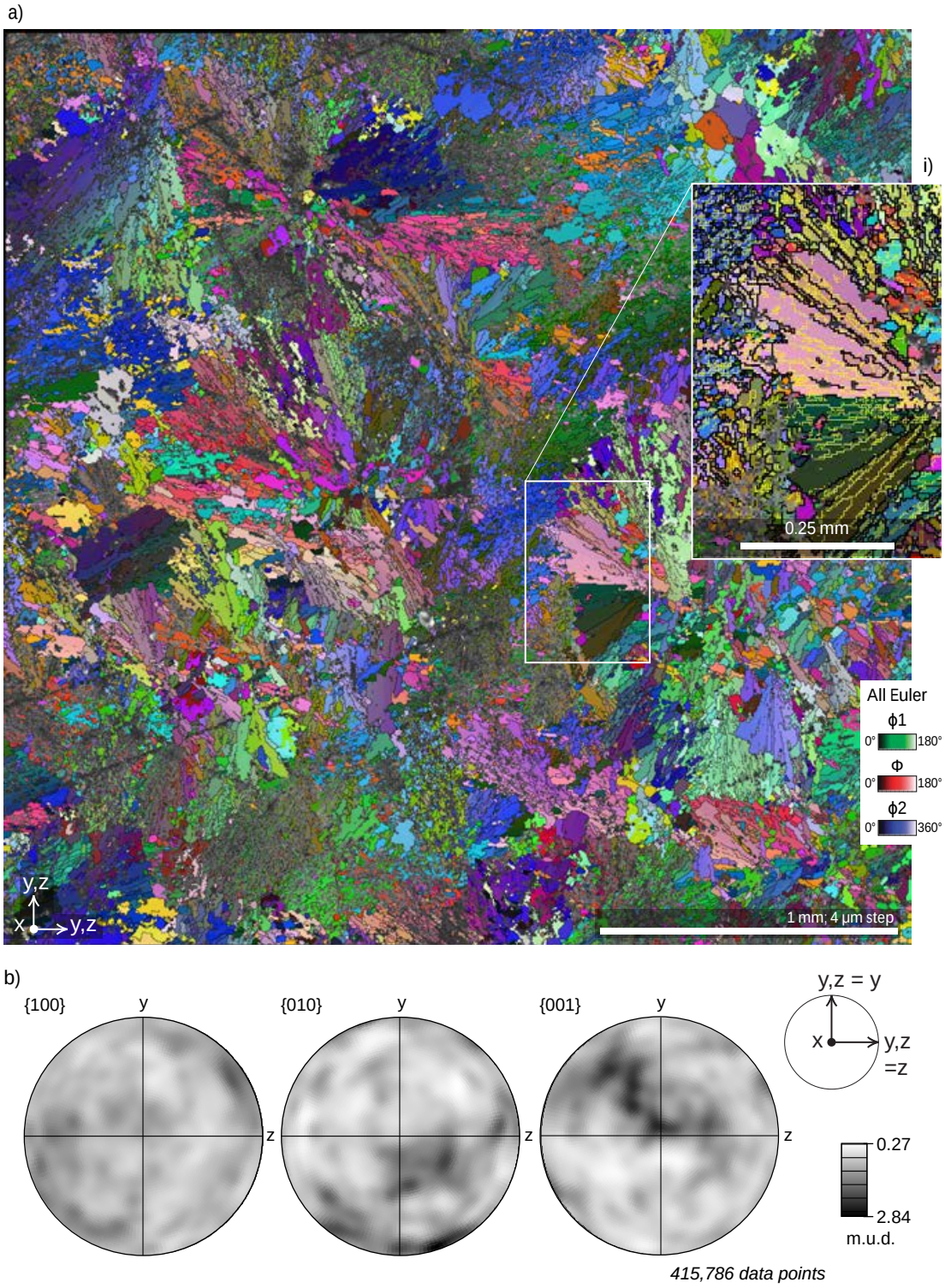

Figure 4.12: Microstructural analysis of sample AA-4, on a thin section with perpendicular orientation to X direction (long core axis). a) Crystallographic orientation map, with i) including low angle boundaries > 2° in yellow and grain boundaries (> 10°) in black (full map in Appendix C, Fig. C.17), b) crystallographic orientation pole figures for anhydrite based on EBSD data.

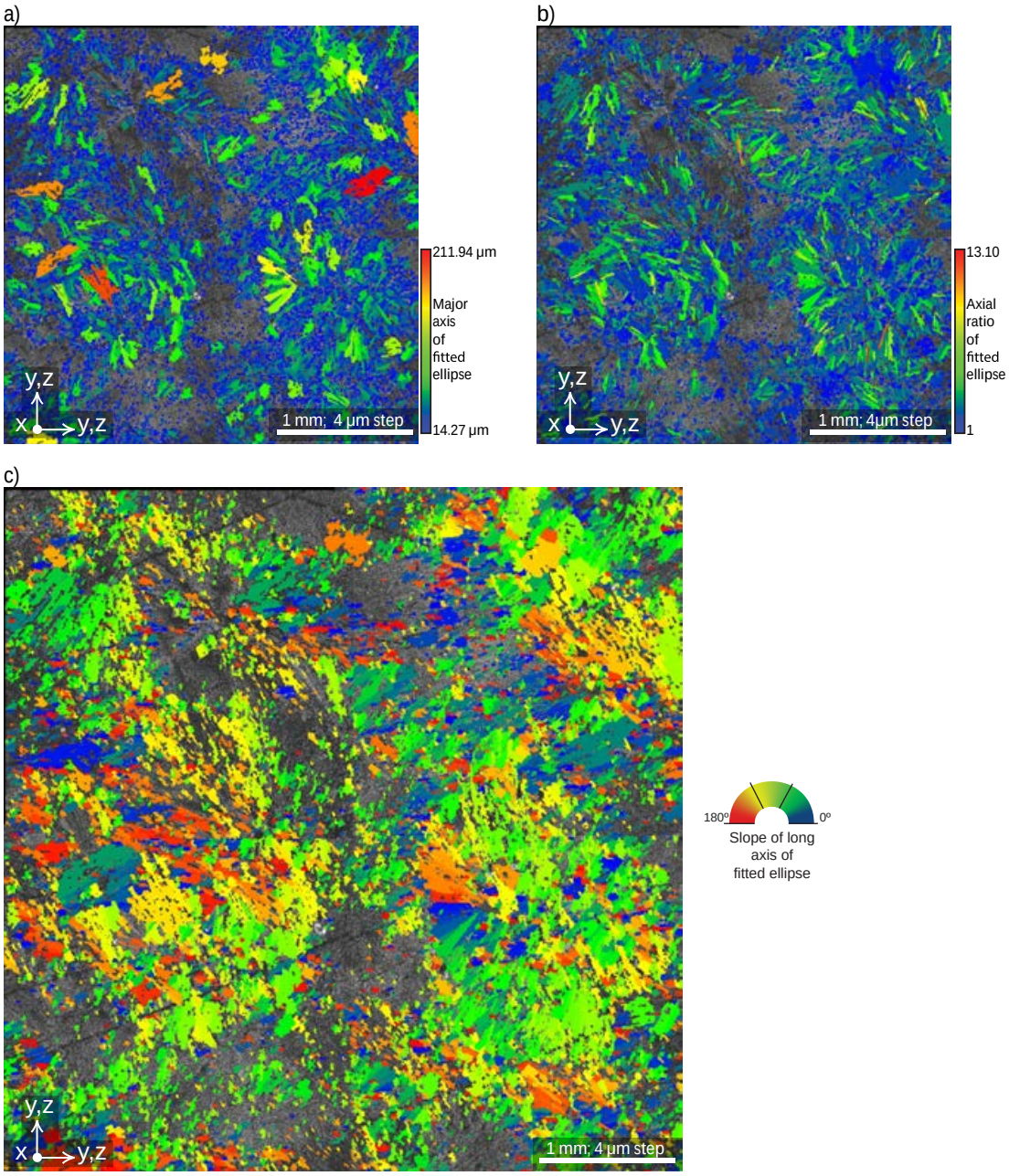

Figure 4.13: Microstructural analysis of sample AA-4, same map as Figure 4.12; a) grain size map, b) grain shape map and c) shape preferred orientation map. All based on EBSD data.

Trace map analysis of Òdena quarry sample material that is representative for the sample characteristics is very time consuming due to the inhomogeneity of structures. Therefore, a single spherulitic structure is analysed (Fig. 4.14), as a representative for phase content and distribution of those features. The trace map of anhydrite grain boundaries (Fig. 4.14b) includes 3,217 single anhydrite grains (grains truncated by the image boundaries were not included) with a mean equivalent circular diameter (ECD) of 8.07 µm and a standard deviation of ± 7.91 µm.

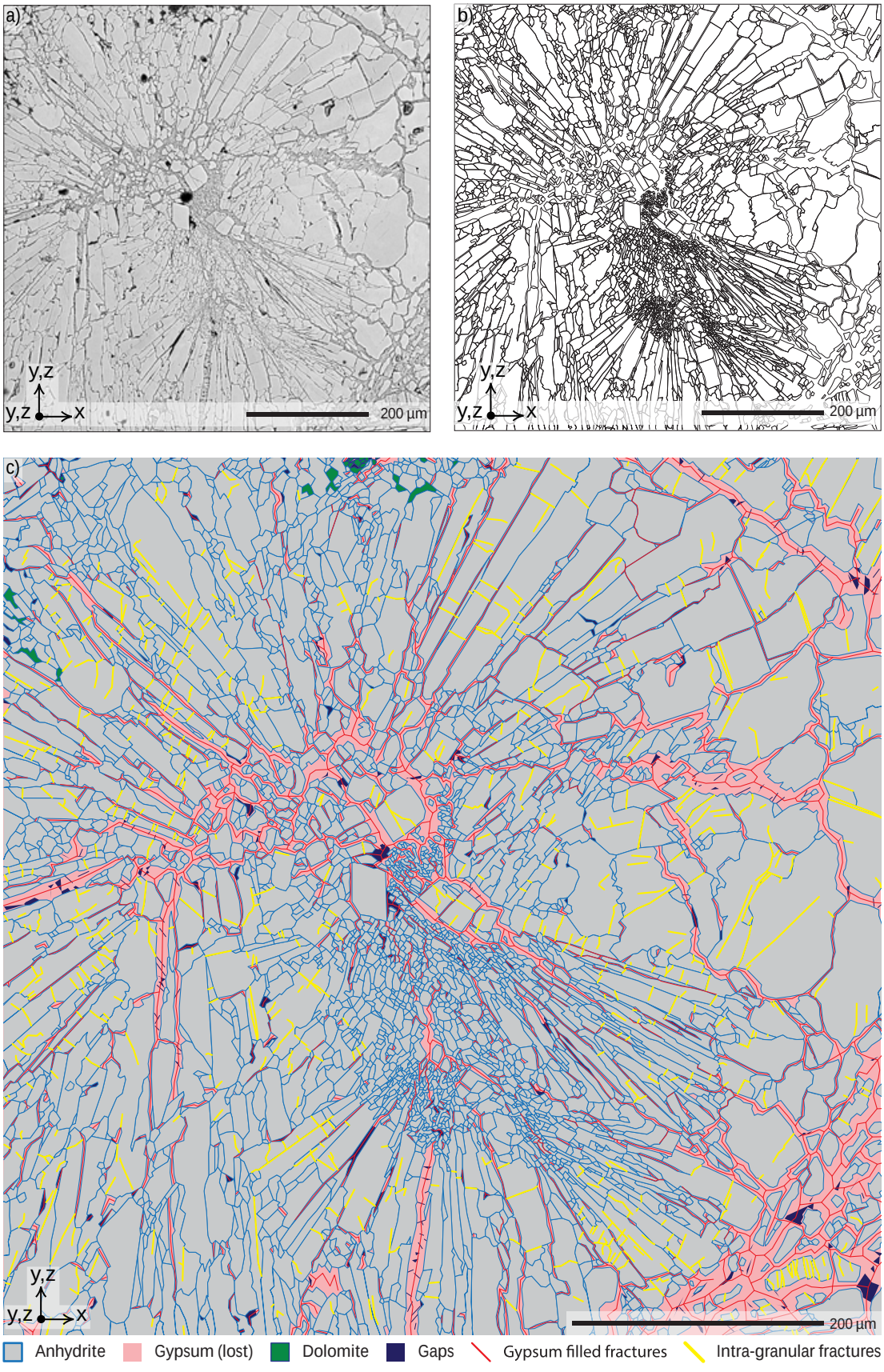

Figure 4.14: Analysis of a section in Òdena quarry anhydrite and gypsum sample BA-4II with a spherulitic feature and in an orientation parallel to X. a) BSE image with anhydrite in light grey. Gypsum was lost due to polishing but the former gypsum veins

are visible from topography in between anhydrite laths. b) Grain boundary trace map based on the BSE image in a). c) Interpretation of the BSE image includes phase, gypsum vein, and fracture distribution analysis.

The mean axial ratio *r* of the fitted ellipses is 2.80 ± 2.20. The trace map shows how anhydrite blades are radially distributed around central domains that contain blocky anhydrite grains and gypsum as a matrix. The radial blades are segmented into several 'fans'. Elongated grains with an orientation parallel to X are very rare. There seem to be three main orientations of elongated grains: 140°, 30° to 60°, and, less dominant, 0° (perpendicular to X).

The grain boundary-fracture-vein map (Fig. 4.14c), which was generated by tracing microstructures of the BSE image at up to 1800 times magnification (Fig. 4.14a), shows that gypsum is present along both fractures and grain boundaries. However, it is not clear from the map alone whether there is any preferential orientation for gypsum-filled microstructures.

A greyscale threshold analysis was performed on a BSE image of a spherulite in order to quantify 2D phase distribution (Fig. 4.14, and 4.15). The results of three different threshold modifications show that the anhydrite content is between 84 % and 86 %. Gypsum content analysis shows between 10 % and 18 % gypsum and dolomite ranges between 2 and 3 %. Greyscale threshold-based analysis of the spherulitic trace map (Fig. 4.15a) from sample AA-4T results in 75 % anhydrite and 12 % gypsum content, with 11 % of the area taken up by grain boundary traces. Assuming that half of these traces are anhydrite and half gypsum, the phase content of anhydrite is at 80 % and that of gypsum at 17 %, which is well within the range of phase content found for the large BSE image greyscale threshold phase analysis (Fig. 4.4c; Appendix D, Fig. D.25 to D.28, and Table D.1).

Analysis of gypsum-filled veins and grain boundaries (Fig. 4.15c,d,e) from the trace map (Fig. 4.14c) via fracture segment angle and length analysis (FracPaQ) shows that there are two preferred orientations of gypsum filled veins and grain boundaries around 30° to 60° and 120° to 150° to the core Y-direction (Fig. 4.14d).

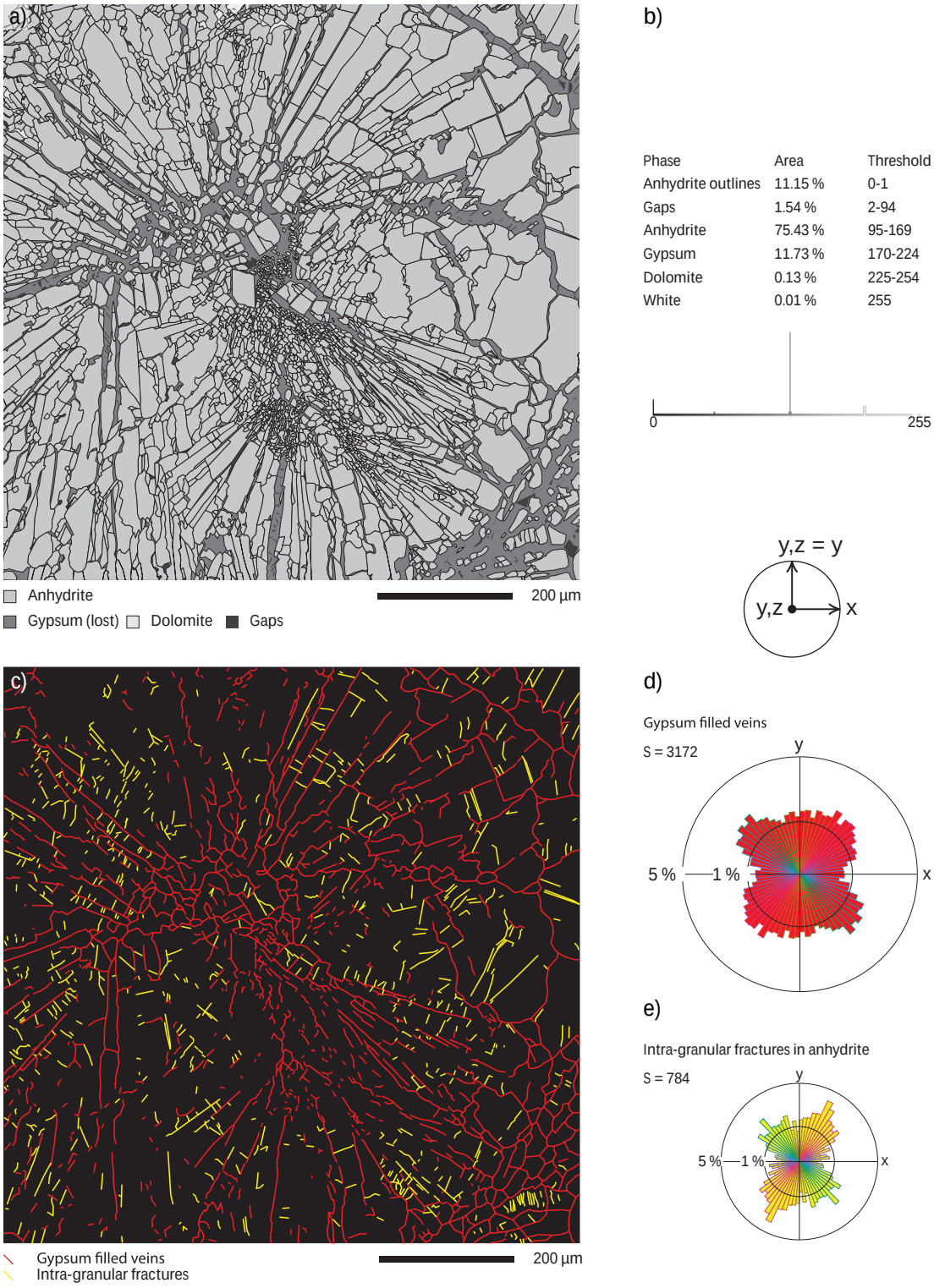

Figure 4.15: Quantification of phase content and gypsum vein and fracture distribution, based on the trace map interpretation of BA-4II, shown in Figure 4.14. a) Phase distribution for anhydrite, gypsum, dolomite, and pores (gaps). b) Results of phase content analysis via greyscale threshold using ImageJ toolbox. c) Distribution of gypsum filled veins and intra-granular fractures. d) Fracture segment orientation analysis for gypsum filled veins via length-weighted rose of fracture segment orientation using the

FracPaQ toolbox. Bin size is 5°. e) Length-weighted fracture orientation analysis of intra-granular fractures in anhydrite grains with no gypsum infill, using the FracPaQ toolbox. Bin size is 5°. *S* is the number of linear fracture segments (vectors) analysed.

4.4 Discussion

4.4.1 Anisotropy and other variations in ultrasonic velocity

The ultrasonic velocity measurements on the five cuboid samples show velocity anisotropy for P- and S-waves. Exceptions are BP1-2 and N2-1 P-wave velocity anisotropy of only 0.1 % and 1 %. Pure halite (BH2-2), halite dominated (BH5-1), and pure anhydrite (N2-1) cuboids have lower P-wave velocities than expected from single crystal anisotropy data (Vargas-Meleza et al., 2015) and established literature (Jones and Davison, 2014) for V_P of pure halite and anhydrite minerals. The P-wave anisotropy is low for nearly all samples (0.1 % to 5 %), except the halite with clay sample (BH5-1; 60 %). Because potash is a mixture but still has an AV_P of only 5 %, it is unlikely that the P-wave velocity anisotropy of BH5-1 of 60 % can be explained solely by mixed phase content. For the samples with V_P measured lower than that expected from single crystal velocities (BH2-2, BH5-1), other factors are required to contribute to low velocities, such as second phase content and distribution, grain size, CPO, fractures, and grain (boundary) shape preferred orientation.

In four out of five cases, the AV_S is higher than the AV_P. S-wave velocity is in all cases slower than P- wave velocity. The relation between the different samples is consistent for P- and S-wave velocities, the order from slowest to fastest is BH5-1, Ba7-2, BH2-2, N2-1, and BP1-2. AV_P of single crystal data is also always higher than that of this study, with exception of BH5-1.

The ultrasonic velocity of North Sea anhydrite is measured in three principal directions on one cuboid and along the long axis of nine core plugs oriented parallel to the main drill core, all within 28 m of one another. However, there is no obvious connection between ultrasonic velocity characteristics and sample depth (order: N2, N3; 15 m deeper N5; 6.5 m deeper N4). The measured V_P of the cuboid (N2-1) is at the high end of that measured on cores and has a very low AV_P (1 %). V_P of the cuboid N2-1 is in the range of V_P measured from the cores. AV_P calculated using maximum and minimum V_P of all North Sea anhydrite cores is at 18 % and thus, 18 times higher.

This means that the samples must have varying characteristics, causing such inhomogeneity. For seismic averaging, this implies that the length scales of this heterogeneity are of importance. Especially as evaporites often form cyclical deposits. The AV_S of the cores in X direction (sub vertical true direction) is smaller (14 %), compared to that of the cuboid (29 %) calculated with X, Y and Z velocities, as should be expected. For V_P and V_S core measurements, N4-1.2 has by far the slowest V_P and V_S, and highest velocity anisotropy. Compared to the AV_P single crystal anhydrite, the measured AV_P for N4-1.2 falls out of this range. The other eight North Sea cores and the cuboid plot inside that very range but are still significantly below the general V_P recorded for anhydrite (Fig. 4.6a,c; Table 4.3; Jones and Davison, 2014).

The Òdena quarry anhydrite with gypsum core V_S and V_P velocities are below that of the North Sea pure anhydrite samples, with the exception of P-wave velocity of N4-1.2. All three Òdena quarry samples (BA-6,7,9) are significantly slower than the literature V_P for gypsum and at the very end of the single crystal AV_P range (Fig. 4.6c). Both AV_P and V_S are at ~ 2 %, with indications of the cores being very similar to each other in their characteristics. The velocity and anisotropy analysis show differences among the North Sea samples, and between North Sea and Òdena quarry samples that are significant, which could indicate that CPO, grain boundary pattern geometry, SPO, and mineral content could all play significant roles.

4.4.2 Crystallographic preferred orientation and ultrasonic velocity

4.4.2.1 Formation of crystallographic preferred orientation

Analysis of crystallographic orientation data from North Sea and Òdena quarry sample material shows no twinning (laths along {110} with 83.5° misorientations around [100]) in any of the samples, indicating that the microstructures were not generated under conditions favourable for mechanical twinning. Mechanical twins need stress to form, therefore the lack of twinning may indicate either low stress conditions, or another factor such as grain size has limited twin development. Yet, distinct clustering of poles and weak CPOs are present in all analysed sample areas. However, low-angle boundaries point towards deformation by dislocation creep (Regime 1). Diffusion creep by grain boundary sliding (Regime 2) or alignment due to primary growth are possible causes for CPO formation.

The anhydrite in the North Sea samples is lath-shaped and has orthorhombic cleavage. It is known that new anhydrite laths may successively break (mechanically) and rotate earlier formed laths (Warren, 2016). Deformation in the diffusion creep regime for synthetic anhydrite was described by Dell'Angelo and Olgaard (1995), who reported equant, polygonal grains with very low dislocation densities, no subgrain boundaries, no undulatory extinction, and smooth to gently curved grain boundaries after 42 % strain. They also stated that this microstructure was very similar to that in the undeformed anhydrite samples.

The North Sea samples have few low-angle boundaries in larger lath shaped crystals but also grains with higher low-angle boundary content (2° to 10° misorientation). Some of the larger grains also have subgrain areas. For example, in N3-1T it seems that grains that contain low-angle boundaries (i.e., with higher dislocation density) are consumed by low dislocation density grains (Fig. 4.7ai), which is grain boundary migration (GBM). GBM is also known to cause smooth grain boundaries, which can be found in all North Sea samples. It follows that dynamic recrystallisation by GBM and potentially SGR (Regime 1) might have occurred.

The Òdena quarry sample shows a more even distribution of low-angle boundaries throughout, with low-angle boundaries between and along high axial ratio spherulite blades (Fig. 4.12ai). The interpretation of the microstructure of the Òdena quarry sample is that primary gypsum was replaced by anhydrite through a three-dimensional network. Afterwards, secondary gypsum formed through the same network. The presence of blade structures and bands could indicate that these features comprised primary gypsum which, as well as the spherulites, are a typical form of gypsum crystallization, and were pseudomorphed by anhydritization. A secondary, incomplete gypsification stage is evident because gypsum seems to have filled cracks between the anhydrite blades. Preservation of the bladed anhydrite forming spherulites, absence of twin boundaries, and the seemingly random distribution of low-angle misorientation boundaries can all be interpreted as signs of little to no influence of crystal-plastic deformation on the sample.

4.4.2.2 Contribution of crystallographic preferred orientation to ultrasonic velocity

Minimum intensity from four North Sea anhydrite data sets plotted against m.u.d. and *M*-index (Fig. 4.11) shows an inverse correlation of decreasing minimum intensity

with increasing maximum m.u.d. and *M*-index. CPO is strongest in N2-1 with M = 0.15, and the weakest in N4-2T with M = 0.12. The N4 section also produced the slowest S- and P-wave velocities of all samples with N4-1.2 (Fig. 4.6). Limited data on the Òdena quarry anhydrite-gypsum samples suggest a weak CPO for anhydrite with an *M*-index of M = 0.12 and an m.u.d. of 2.84. The absence of twinning in the Òdena sample and preservation of spherulitic features point to the weak CPO being formed by primary growth.

Based on the presented data set, it is unlikely that the differences in CPO alone cause the differences between the measured ultrasonic velocities for both V_P and V_S for the samples. Nevertheless, the AV_P and AV_S are higher for the North Sea samples, where the CPO is generally stronger for the presented data set.

Nearly all North Sea and all Òdena quarry samples have very low ultrasonic velocities, but within the ranges expected for single crystal end member V_P. This indicates that both rock types possibly have either: a strong CPO in a slow V_P crystal orientation, which means the CPO over all samples is very similar; or the sample suite contains other characteristics that result in lower-than-expected velocities. Therefore, quantifying the microstructural differences between the North Sea samples and combining the results with those of the three Òdena quarry samples, with emphasis on variation of mineral content, is necessary to evaluate if other factors impact the velocity and velocity anisotropy other than CPO.

The ‘shape’ of CPOs of the North Sea samples are similar to previously reported CPOs in anhydrite, with a point cluster for {100} in the sample X direction (Hildyard et al., 2011a; Vargas-Meleza et al., 2015). This type of CPO means that the direction of measurement (sample X) is parallel to the fast p-wave velocity direction, i.e., the fast direction is normal to bedding in real space. The point orientation data from sample N3-1T for {100} also suggests fast velocities, but closer to the Y-Z plane. The {100} poles of N4-1II suggest medium velocities in the Y-Z plane, as does N4-2T. The poles to {010}, which has intermediate V_P and V_S, are almost randomly oriented for all North Sea sample data sets. The CPO for the Òdena quarry sample are weaker than North Sea samples, especially in {100}. In {010}, the clusters of poles are horizontal, which indicates slower velocity directions are in the Y-Z plane for these samples. As S-waves

oscillate perpendicular to the direction of wave propagation, the characteristics of the Y-Z plane is also of importance.

4.4.3 Formation of shape preferred orientation and potential influence on ultrasonic velocity

The most obvious feature in all North Sea samples is the dual SPO, with two sets of lath-shaped grains that are aligned approximately perpendicular to each other. One reason might be that an orthogonal arrangement maximises the packing density of cuboids/laths. The orientation of these SPOs in relation to the axes of the core samples is random in Y-Z and only X is a defined direction, where the long axes of the sample cores match the long axis of the original core (vertical relative to Earth's surface, and approximately normal to layering). The formation of dual SPO is interpreted as an effect of growth, displacement, and breakage of anhydrite laths, rather than a change in the stress field during deformation. There are no signs of pseudomorphism due to the replacement of gypsum.

The maximum magnitude of the fitted ellipse roses ranges between 6.9 % and 8.1 %. Analysis of trace map based fitted ellipse long axis orientation, grain boundary segment orientation statistics, and GBSI density roses all show that there are two preferred orientations of grains, which are most significant in N3-1T and N4-1II (Fig. 4.9 and Appendix C, Fig. C.14). The secondary SPO is weak to negligible in N2-1T (Fig. 4.8) and N4-2T (Appendix C, Fig. C.9 and Fig. 4.10). The SPO strength analysis via GBSI-based minimum intensity analysis plots the North Sea samples over a range of minimum intensities between 0.8 and 0.6. Minimum intensity of 0.8 or above in natural samples can be considered an extremely weak SPO (same as starting patterns for chapters 2 and 3). The minimum intensity analysis shows that N4-2T has the weakest SPO, and N2-1T the strongest SPO of the samples in this study. N2-1T has a relatively high population of small grains that surround few significantly larger grains. The pattern is more inhomogeneous compared to the other maps and the influence of such a grain size distribution on the GBSI method is not understood in detail yet. Weak SPO of N4-2T is visible overall analytical methods, including EBSD fitted ellipse long axis angle rose, grain boundary segment orientation rose and GBSI density rose.

4.4.4 Importance of grain boundaries and fractures for second phase distribution

Grain boundaries and fractures are important sites for reactions (see chapter 5). Therefore, such features must be quantified in terms of their geometric and microstructural characteristics. Further, Vargas-Meleza et al. (2015) have shown that gypsum samples with larger content of anhydrite have lower anisotropies than gypsum samples with less or no anhydrite content. They reported AV_P results between 1.37 and 3.48 % and AV_S results between 0.82 and 13.8 %. Vargas-Meleza et al. (2015) explained such low anisotropies with a strong control of abundance and distribution of porosity and open fractures at ambient laboratory conditions (1 atm and ~ 25ºC). Low porosity and connected higher aggregate density due to increasing anhydrite content is assumed to be directly linked to low anisotropy (Vargas-Meleza et al., 2015).

The density of the Òdena quarry samples is 2.76 g cm^{-3} (BA-7) and 2.80 gcm^{-3} (BA-6,9), which is higher than the literature density value for gypsum of 2.31-2.33 g cm^{-3} and closer to the literature density for anhydrite of 2.97 g cm^{-3} shows that they are an anhydrite-dominated mixture. Greyscale threshold analysis of the Òdena quarry anhydrite with gypsum content on various BSE and trace maps results in an anhydrite content of 80 % to 86 % and a gypsum content between 10 % to 18 %. The North Sea anhydrite density ranges between 2.92 g cm^{-3} (N2-1 cuboid) and 2.95 g cm^{-3} (N5-1.2), very close to the published value for pure anhydrite.

In summary, the anhydrite samples with gypsum content have slower P- and S-wave velocities, and low AV_P and AV_S anisotropies (2 %) parallel to the long axis of the cores (X), and lower densities compared to the pure anhydrite samples. Compared to literature values, the anhydrite gypsum samples have slower P-wave velocities than the end-member single crystal anisotropy of anhydrite, and slower P-wave velocities than expected for bulk aggregates of anhydrite and gypsum (Fig. 4.6c). Their AV_P is at the low end of that expected for gypsum single crystals.

Presumably, rocks with little or no SPO have slower P-wave velocities and lower AV_P compared to bulk anhydrite and gypsum, and are at the very low end of the AV_P range of single crystal gypsum anisotropy (Vargas-Meleza et al., 2015).

However, data presented here suggests that gypsum veins have systematic orientations and spatial distributions because they exploit grain boundaries and fractures of particular orientations. The analysed spherulitic feature (Fig. 4.14, and 4.15) shows

that the smallest number of gypsum veins are oriented parallel to the X direction (long axis of the core and also the direction of ultrasonic velocity measurement). Most gypsum veins and grain boundaries are oblique relative to X. This means that the density of gypsum veins and grain boundaries is relatively high in the X direction. The ultrasonic waves have to pass through more phase transition 'surfaces' (i.e., reflectors, attenuators) along X. The distribution of vein gypsum along systematic grain boundaries creates abundant phase transition surfaces.

4.4.5 Wider applicability of the study

The analysed North Sea anhydrite comes from one of Earth's the largest known salt formations, the Permian Zechstein Supergroup (ZSG). Seismic reflection data and very sparse borehole data from the north-western margin of the North Permian Basin demonstrate that the ZSG can be several hundreds or even kilometres thick (e.g., Jackson et al., 2018) and is characterised by a thick sequence of halite and anhydrite in the basin centre (Clark et al., 1998). In the North Sea, the ZSG is also strongly associated with oil and gas exploration and production and been of interest for these industries for a while. But sampling of the salt structures in the ZSG itself is rare, as it is actively avoided during drilling and as a consequence, only limited data is available. Therefore the data presented by this study provides insights that are not solvable with normal exploration tools. The North Sea anhydrite samples used for this study show weak CPO (*M*-index between 0.12 and 0.15) and weak bimodal shape preferred orientation of anhydrite laths. P-wave velocities are very slow for anhydrite (Fig. 4.6c; Table 4.3) and with exception of one sample, AV_P is ~ 8 %, whereas AV_S is considerable at 14 %.

All samples in this study show velocity anisotropies, some are very high, up to 60 % AV_P and 34 % AV_S. These early results certainly have indications, as assumption of isotropy can cause false reflector depths for any anisotropic bodies (e.g., Raymer and Kendall, 1997; Jones and Davison, 2014), not only the ZSG.

The results presented for Òdena gypsum show velocities distinctively slower than the literature anhydrite and gypsum velocities (Fig. 4.6) and AV_P and AV_s are both 2 %. The inhomogeneous fabric and gypsum veins represent systematic phase boundaries and demonstrate how processes like hydration are of major importance, as they impact

phase content, and create systematic phase distribution, are relevant for seismic velocity measurements in evaporates and other rocks.

4.5 Conclusions

This study contributed to various key issues that have been identified in the past by e.g., Vargas-Meleza et al. (2015), including that velocity anisotropy of evaporites is impacted by more than CPO. The new results support these statements, even though the direct link between the measured ultrasonic velocities and the microstructural anisotropy of the rock salt cuboids could not be determined. There are three main themes this study contributes to:

1) New velocity data is presented

New velocity measurements for natural evaporites with halite, polyhalite, anhydrite, gypsum, and mixed phase rocks from three deposits (North Sea, Òdena, Boulby) were analysed. All samples show velocity anisotropies, some are very high, up to 60 % AV_P and 34 % AV_S. The V_P and V_S ranges are generally lower than expected from single crystal ranges (that relate to crystallographic orientation), indicating other contributions to velocity variations than simply intrinsic mineralogical anisotropy. Nearly all North Sea and all Òdena quarry samples have V_P in the lower end of the ranges for single phase materials. Therefore, both types of rocks possibly have either: a strong CPO in a slow V_P crystal orientation, which means the CPO over all samples is very similar; or, the sample suite contains other characteristics that lower the velocities. The former idea could be tested by a rock recipe approach. Future work is necessary to quantify the impact of CPO. What was shown is that the grain boundary patterns of both microstructurally analysed sample suites had different characteristics. A systematic study of the influence of anhydrite textures, i.e., textures inherited from primary gypsum compared to porphyroblastic anhydrite textures can provide more insight on the influence of SPO on ultrasonic velocity anisotropy of evaporites.

2) Formation of evaporite microstructures

Crystallographic preferred orientation (CPO) is present in both analysed sample sets. Using multiples of uniform distribution (m.u.d.) and *M*-index as a measure of CPO strength, the maximum strength in North Sea anhydrite is M = 0.15 (N2-1T) and the maximum m.u.d. is 5.50 (N3-1T) and a little lower in Òdena quarry samples with *M* =

0.12 and m.u.d. of 2.84. Low-angle subgrain boundaries (2° to 10° misorientation) are common, whereas twinning with misorientations of 83.5° around an axis parallel to [100] is not recorded for either of the sample sets.

The two sample suites tested show very different microstructures. The North Sea anhydrite samples had a systematic orientation of grain boundaries, caused by a dual SPO of lath-shaped grains, with a perpendicular relationship. The mean grain size ranges between 26.50 ± 31.61 µm and 89.71 ± 57.32 µm, the mean axial ratio between 1.70 ± 0.69 and 2.35 ± 1.29, and the minimum intensity, introduced for quantification of SPO strength, ranges between 0.8 and 0.6.

SPO was not quantified for the Òdena quarry samples, and based on the spherulitic and cleaved texture, it is assumed that there is none. Although, the spherulitic texture might also have an impact on variations of V_S and V_P velocities, as it is a common geometrical feature of the microstructure of these samples. Further, the gypsum veins in the Òdena quarry samples were also systematically oriented and distributed.

The North Sea samples show grain boundary migration features and therefore, dynamic recrystallisation by GBM and potentially SGR (Regime 1) might have occurred. Preservation of the blades, absence of twin boundaries, and the rather random distribution of low-angle misorientation boundaries of Òdena quarry samples can all be interpreted as signs for low to no impact of deformation on the sample. The main formation mechanisms are dehydration and hydration.

3) Introduction of a workflow

A more complete microstructural characterisation of evaporites was presented, which includes CPO and automated grain boundary-based SPO quantification that could be used in predictive models of velocity anisotropy. The workflow combines EBSD crystallographic orientation analysis, established fitted ellipse based SPO quantification, basic grain boundary segment orientation statistical analysis, high resolution grain boundary segment intercept density orientation and minimum intensity analysis, and fracture (vein) distribution and orientation analysis. This workflow is a step to build on in future studies to quantify the impact of petrofabrics on acoustic wave velocity anisotropy.

CHAPTER 5

Rapid hydration and weakening under stress - Implications for Earth Systems

Abstract

Hydration is an important geological process that influences the rheology and geochemistry of rocks, and the fluid budget of the Earth's crust and mantle. Steady state differential compaction (ssdc), dry and 'wet' tests under confining pressure, and axial stress were conducted to investigate the influence of triaxial stress on hydration in anhydrite-gypsum aggregates for the first time. Characterization of the samples before and after triaxial experiments were performed with optical and scanning electron microscopy, including energy dispersive spectroscopy and electron backscatter diffraction mapping.

Stress-strain data reveals that samples that underwent steady state differential compaction in the presence of fluids are ~ 14 to ~ 41 % weaker. The microstructural analysis of samples shows that there is a strong temporal and spatial connection between the geometry, distribution, and evolution of fractures and hydration products. The increasing reaction surface area in combination with pre-existing gypsum in a gypsum-bearing anhydrite rock lead to rapid gypsification.

The crystallographic orientations of newly-formed vein-gypsum have a systematic preferred orientation for long distances along veins, beyond the grain boundaries of wall-rock anhydrite. Gypsum crystallographic orientations in {100} and {010} are systematically and preferentially aligned parallel to the direction of maximum shear stress (45° to σ_1). Gypsum is also not always topotactically linked to the wall-rock anhydrite in the immediate vicinity. This study proposes the selective inheritance of crystal orientations from favourably oriented wall-rock anhydrite grains for the minimization of free energy for nucleation under stress led to the systematic preferred orientation of large new gypsum grains.

A sequence is suggested for hydration under stress that requires the development of fractures accompanied by localised hydration. Hydration along fractures with a range of apertures up to 120 µm occurred in under 6 hours. Once formed, gypsum-filled

veins represent weak surfaces and are the locations of further shear fracturing, brecciation, and eventual brittle failure.

These findings imply that non-hydrostatic stress has a significant influence on hydration rates and subsequent mechanical strength of rocks. This phenomenon is applicable across a wide range of geological environments in Earth's crust and upper mantle.

5.1 Introduction

Hydration of minerals and rocks plays an important role in the Earth's crust and upper mantle, where it is a common process that influences the dynamic evolution of rocks in terms of their fabrics, geochemistry, and rheology (e.g., Olgaard et al., 1995; De Paola et al., 2009; Llana-Fúnez et al., 2012; Leclère et al., 2018). However, hydration of rocks under non-hydrostatic stress conditions has not been fully explored. Given the ubiquitous presence of non-hydrostatic conditions in the Earth, this represents a significant knowledge gap of an important geological process.

This study focuses on the influence of stress on hydration in the $CaSO_4 \cdot H_2O$ system (Fig. 5.1a), specifically the hydration of anhydrite ($CaSO_4$, orthorhombic) to gypsum ($CaSO_4 \cdot 2H_2O$, monoclinic), as an analogue for hydration systems in Earth's crust and upper mantle. This is a simple geochemical system, and hydration should be achievable under moderate laboratory conditions.

Hydration of anhydrite under experimental differential stress conditions using natural polycrystalline rocks has been studied only recently (Li et al., 2019; Xu et al., 2019; Wang et al., 2020), with focus on the mechanical properties of anhydrite (Yin and Xie 2019), and the expansion or swelling associated with hydration (Serafeimidis and Anagnostou, 2013; Xu et al., 2019; Li et al., 2019).

Additionally, long term (several months long) hydration experiments, mainly on powders of sieved natural and synthetic anhydrite under hydrostatic conditions (water) have failed to produce hydration products or show relatively slow hydration rates (e.g., Ramsdell and Patridge, 1929; Leininger et al., 1957; Hardie, 1967;).

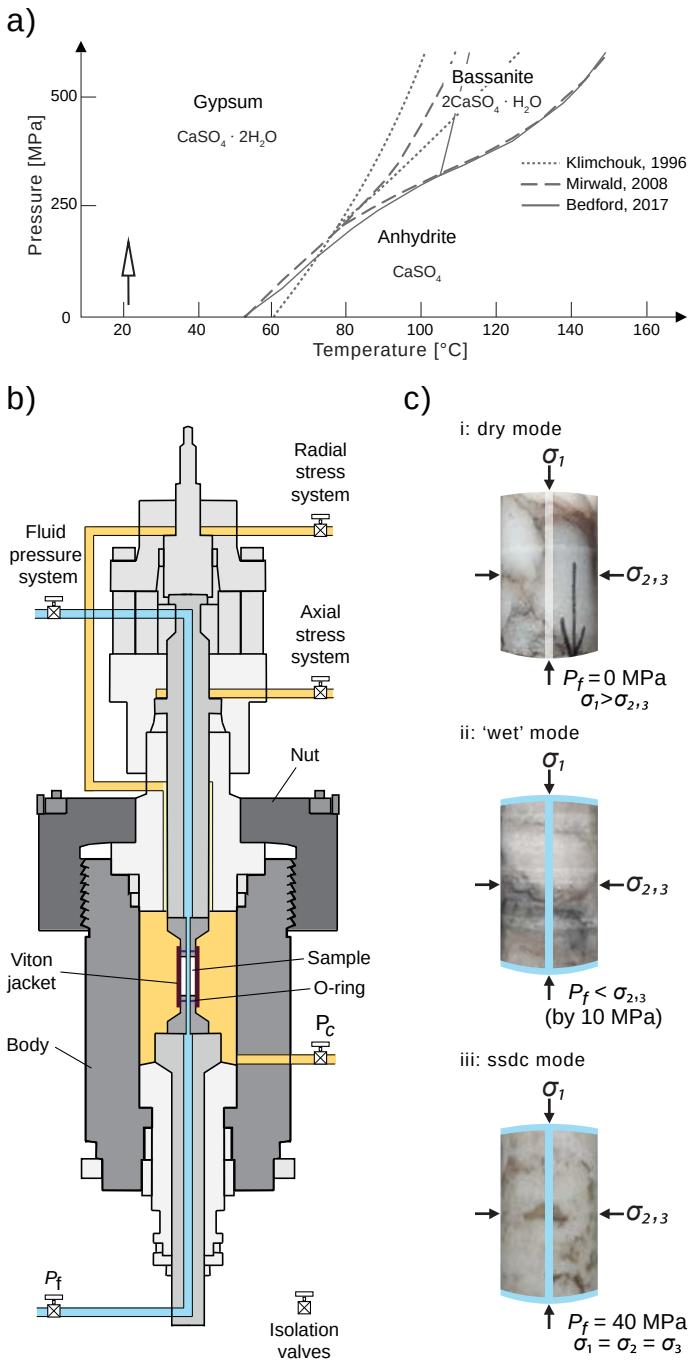

Figure 5.1: Preparation and set up for triaxial experiments. a) Phase diagram of the $CaSO_4 \cdot H_2O$ system, including data from Klimchouk (1996), Mirwald (2008), and Bedford (2017). An arrow marks approximately the pressure–temperature space location of the experiments. b) Schematic diagram of the configuration of the triaxial rock deformation apparatus (Sanchez TRI-X 250MPa/200°C). c) Experimental setup for i: dry, ii: 'wet', and iii: steady state differential compaction (ssdc) mode tests.

Hydration of anhydrite to gypsum, also called gypsification, is of interest in several economic fields, including mining, oil and gas, and storage of hydrocarbons,

hazardous, and nuclear waste (e.g., Mertineit et al., 2012; Singh et al., 2018; Wang et al., 2020). It is also highly relevant in construction, as gypsum is a major cement and plaster ingredient (e.g., Farnsworth, 1925; Leininger et al., 1957; Sievert et al., 2005).

Moreover, predicting anhydrite hydration is key in civil engineering, because of the potential rock volume change related to the reaction (e.g., Sass and Burbaum, 2010; Singh et al., 2018). Due to its relevance in those fields and because gypsification is also very common in nature (e.g., Farnsworth, 1925; De Paola et al., 2007; Bedford, 2017) under surface conditions, the $CaSO_4 \cdot H_2O$ system has been studied scientifically for over 90 years.

Furthermore, anhydrite-bearing evaporite sequences are often the weakest horizons in sedimentary basins and form detachment horizons in foreland fold and thrust belts (e.g., Heard and Rubey, 1966; Hildyard et al., 2011). Therefore, processes that can potentially affect the mechanics of anhydrite-bearing evaporites, such as hydration, are significant because they potentially have control over the rheology and deformation behaviour of sedimentary basins and fold and thrust belts.

Laboratory experiments of hydration of anhydrite under an applied non-hydrostatic stress field have not yet been attempted. Consequently, the effects of stress on hydration remain to be assessed. This study utilises triaxial deformation apparatus to investigate the rheological and microstructural response of natural anhydrite under wet and dry non-hydrostatic conditions and different strain rates.

In more detail, the effects of non-hydrostatic stress and strain rate on the hydration of anhydrite to gypsum via triaxial deformation experiments on natural rock samples with known initial compositions and microstructures were studied. The ability to control parameters governing and influencing the reaction activity (reaction time) of hydration of anhydrite to gypsum is essential to test the magnitude of their effects on the reactions. The following parameters were controlled: i) material-specific characteristics (petrography) such as grain size, mineral content, and fabric; ii) experimentally controllable physical and mechanical parameters, including temperature, fluid, effective, and confining pressure, applied stress field and strain rate; and iii) geochemical parameters like fluid composition.

5.1.1 The influence of stress on chemical reactions

There are two different stress–material interactions to consider for understanding the impact of stress on chemical reactions (Wheeler, 2018). Normal stress (anisotropy) along grain interfaces and between interfaces with different orientations has the main impact on chemical reactions in the Earth, and thus, plays the key role in quantifying stress-related chemical processes (Wheeler, 2014; 2018). Chemical potential depends on a "weighted" mean stress, which means that the magnitude and orientation of stress have a relatively minor impact (Wheeler, 2018).

Experiments show that narrow aqueous or other films along (grain) boundaries may persist, even if normal stress is greater than fluid pressure (Hickman and Evans, 1995, Israelachvili, 2010). They are regarded as stressed solids rather than fluids (e.g., Israelachvili, 1992; Wheeler, 2018), which provide fast diffusion pathways (Rutter, 1976).

Integral parameters for models are the grain boundary structure, assumptions about the mobility of specific components, and reaction activity (Wheeler, 2018). These include grain boundary film properties like the connection between surface and interface energies and film structure (Hickman and Evans, 1995), and the relationship of fluid film thickness to normal stress (Israelachvili, 2010). The basic concept is that grain boundaries, representing a small-scale volume, are locally buffered by (i.e., are in local equilibrium with) the adjacent solids (Wheeler, 2018).

Wheeler (2018) states that diffusion is the main mechanism of stress-related chemical processes and is active along long-range chemical reaction pathways that are provided by interconnected interfaces under crustal conditions. It is established that diffusion rates along interfaces such as grain boundaries are several orders of magnitude faster compared to intracrystalline diffusion (Dohmen and Milke, 2010).

Further, segregation of (incompatible) elements and their enrichment in grain interfaces is considered to have a significant impact on the physical and chemical properties of mantle rocks (Hiraga et al., 2007). Interfacial segregation linked with grain boundary character distribution (GBCD) may lead to grain boundary energy minimization (Tacchetto et al., 2021). It follows that interfacial segregation potentially influences if and where diffusion is active or accelerated in natural samples during hydration.

5.1.2 Review of research in the $CaSO_4 \cdot H_2O$ system

The research on interaction and evolution of stress, permeability, strength, and reaction kinetics has concentrated on the dehydration reaction of gypsum (Olgaard et al., 1995; Ko et al., 1995; 1997; Wang and Wong 2003; Milsch and Scholz 2005; Milsch et al., 2011; Llana-Fúnez et al., 2012; Leclère et al., 2016).

Hydration of anhydrite to gypsum has been studied mainly on powders of sieved natural and synthetic anhydrite under hydrostatic conditions (e.g., Leininger et al., 1957; Hardie, 1967; Sievert et al., 2005). Hardie (1967) studied the influence of temperature on pure anhydrite powders with different grain sizes in experiments lasting about 8 months at different temperatures between 25 - 60°C, without recording hydration. Only the addition of gypsum 'seeds' at similar conditions induced relatively rapid hydration. A 1:1 mixture of polycrystalline anhydrite and gypsum produced 3 % more gypsum after 83 days (Hardie, 1967).

Evolution of strength, stress versus strain behaviour, permeability, and the role of grain size and fabric without any hydration or dehydration reaction in gypsum and anhydrite has been studied by Bell (1994), and De Paola et al. (2009). Bell (1994) found that anhydrite has a 'strong' unconfined compressive strength (102.9 MPa and 97.5 MPa for two types of anhydrites), whereas gypsum is ranked as 'medium' (average ranges between 24.1 MPa and 34.8 MPa, depending on sample depth). Based on the stress versus strain behaviour, the author found that the onset of plastic deformation is at an earlier stage during axial loading for gypsum.

Effective pressure has a significant effect on the permeability evolution under confined stress conditions and controls the brittle to ductile transition of polycrystalline, pure anhydrite during deformation (De Paola et al., 2009). During brittle failure, the permeability increased dynamically to about 2 – 3 orders of magnitude. The dynamic permeability and porosity evolution during the triaxial loading tests can be summarised in three stages: i) permeability and volume reduction through compaction is in progress, ii) permeability increase due to the onset of intra-granular micro-cracking, and iii) volume increase (dilation) and brittle failure (De Paola et al., 2009). The strength of dry anhydrite cap rock during triaxial tests increased with increasing confining pressure and slightly weakened with increasing temperature, while fluid

contact prior to failure changes the effective pressure and lowers the strength, but not the volumetric (permeability) behaviour (Hangx et al., 2010; 2011).

5.1.3 Mechanisms of anhydrite hydration

Petrographic observations from natural rocks and experimental studies indicate that the mechanisms behind hydration (and dehydration) are solution-precipitation, and direct replacement with additional water available (Hardie, 1967; Sievert et al., 2005; Jaworska and Nowak, 2013; Bedford, 2017). Secondary gypsum is produced initially in the most fractured areas of anhydrite rocks, and forms along cracks and grain boundaries (Jaworska, 2012; Warren, 2016).

Activators speed up the time for the appearance of maximum specific surface area and the rate of formation of maximum gypsum. Leininger et al. (1957) studied the effect of acids, bases, and salts, particularly alkali sulphates, and showed that cations serve as activators and accelerate the hydration of gypsum, whereas anions decelerate the reaction.

Sievert et al. (2005) developed a concept for solution-precipitation that is now widely accepted (Pina, 2009; Jaworska and Nowak, 2013; Lebedev and Avilina, 2019). Hydration experiments of natural anhydrite in a ball mill with water and (activator-) solutions, such as H_2SO_4 (pH 1), 5 % $MgSO_4.7H_2O$ and solution of calcium hydroxide, as a function of time and temperature show that the maximum specific surface area develops quickly and does not coincide with the formation rate of the maximum amount of gypsum, which takes rather longer to achieve. There is a time lag between adsorption of ions on the surface of anhydrite, which increases the specific surface area, and the formation of gypsum.

Sievert et al. (2005) proposed a five step mechanism of hydration via solution-precipitation: i) rapid initial partial dissolution of $CaSO_4$ and adsorption of hydrated Ca^{2+} and SO_4^{2-} ions at the surface of anhydrite; ii) slow increase of thickness of adsorbed layer; iii) crack formation in the adsorbed layer and counter migration of H_2O (in) and Ca^{2+}, SO_4^{2-} ions (out); iv) formation of gypsum nuclei at the surface of anhydrite and v) formation of nuclei is followed by rapid gypsum crystallization.

5.2 Material and methods

All samples have been analysed before and, where possible, after triaxial loading tests under confining pressure via scanning electron microscopy using backscattered electron imaging (BSE), energy-dispersive X-ray spectroscopy (EDS), and electron backscatter diffraction (EBSD). Grain and fracture characteristics and mineral content were analysed via a range of software, including FracPaQ (Healy et al., 2017), ImageJ (Schneider et al., 2012), and Oxford Instruments Channel5 for EBSD data processing.

5.2.1 Sample description and preparation

A total of eight natural anhydrite cores were used in triaxial experiments. Six samples were run with water present, and two without the presence of water. The core plugs

were extracted from two anhydrite-dominated surface outcrop field samples (ID prefix 'Ò') of the Òdena Gypsum Formation, which is the lower gypsum term of the Catalonia Saline Formation (upper Eocene) in the Pyrenean basin, Spain (Ortí Cabo et al., 1985).

Macroscopically, the Òdena samples are of a pale beige colour with discrete centimetre-scale domains that contain light brown clay or mud inclusions (Fig. 5.2a). The anhydrite rocks have a minor natural gypsum content. All samples show fibro-radiate crystals of anhydrite (Fig. 5.2b,c). These spherulites appear either isolated or arranged in centimetre long bands.

Microscopically, gypsum is located in between the anhydrite blades of the spherulites in veins (up to 10 µm in aperture), in the spherulite centres, as well as in between spherulites in broader fractures (up to 50 µm in aperture) and in the centre of the band structures.

EBSD analysis shows that the crystal orientation in the spherulite 'blades' changes successively with radial rotation, with lattice orientation being mirrored from the centre (Fig. 5.2d; Appendix D, Fig D.4). The statistical description of the intensity of the fabric based on clustering of poles on pole figures, known as the 'multiple of uniform density' (m.u.d.) was calculated. A preferred fabric, or CPO, exists where m.u.d. > 1.

One additional core of pure gypsum was taken from an outcrop from Volterra, Italy, to compare the stress-strain behaviour and strength of anhydrite-dominated versus gypsum-dominated rocks. Volterra gypsum is a well-studied polycrystalline material (Heard and Rubey, 1966; Ko et al., 1997; Llana-Fúnez et al., 2012), and has been used in many experiments (e.g., Olgaard et al., 1995; Hildyard et al., 2011; Brantut et al., 2012).

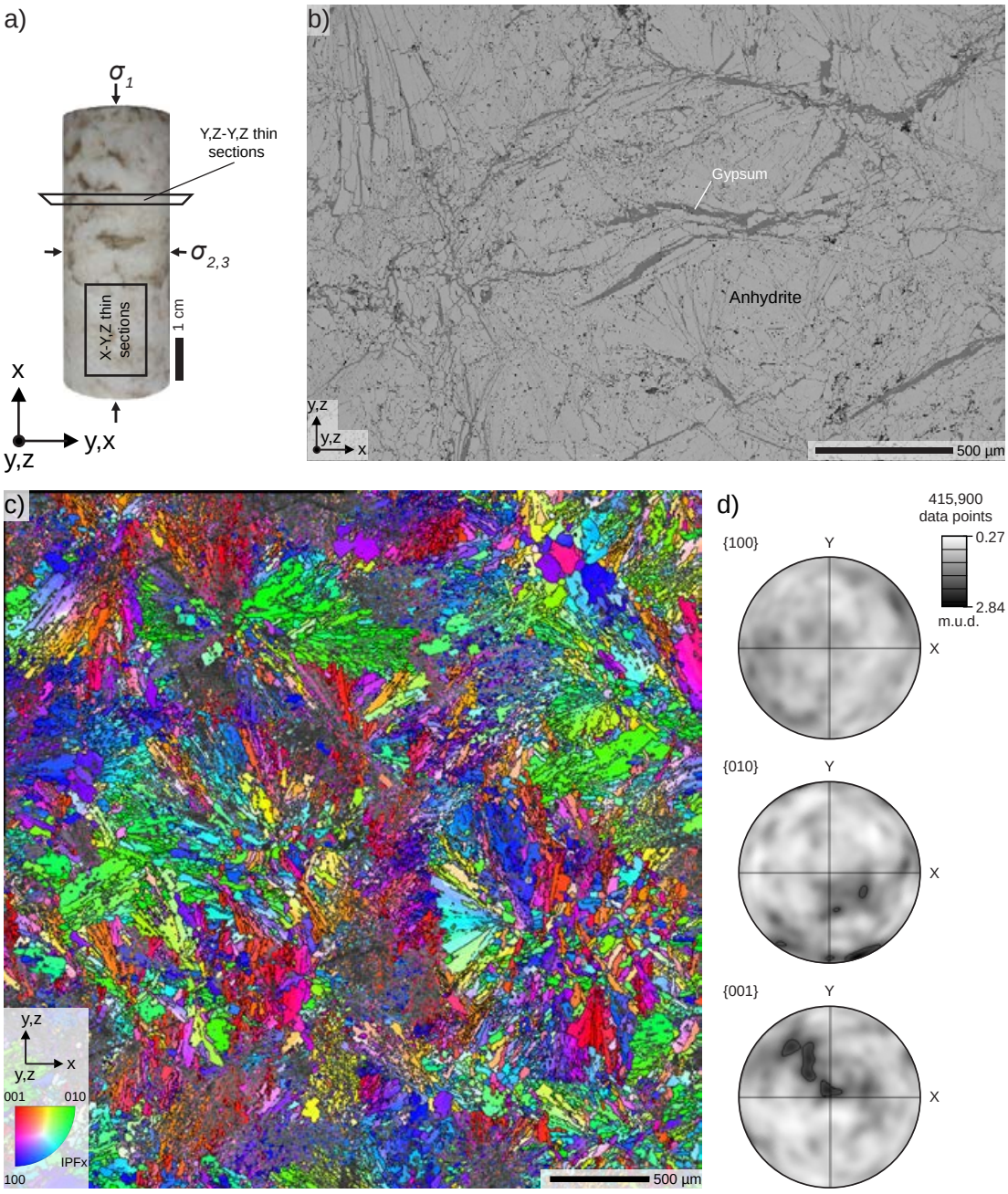

Figure 5.2: Macro- and microscopic sample material characterization. a) Axial orientation of cylindrical samples, whereas the long axis is defined as X and perpendicular directions are YZ (sample Ò2, pre-experiment), b) backscatter electron

image, (sample Ò8, post experiment), c) IPFx EBSD map (sample block, initial material, 4 µm step size), d) equal area, lower hemisphere pole figures of c). See Appendix D, Fig. D.4,5 for further characterization.

As required for the triaxial apparatus, cores with a length (X axis) of 60 mm and a diameter of 25 mm (Y,Z dimension) were drilled out of sample blocks. Given that the sample material does not display any preferred orientation fabric on macroscale and was collected from an outcrop, cores were drilled perpendicular to bedding. The Volterra gypsum is homogeneous with no foliation, thus the orientation of the core from this material is arbitrary.

Core plugs were drilled in the presence of water and were air-dried for 24 hours immediately afterward to mitigate any potential alteration effects. It was presumed that the exposure time to water at ambient laboratory conditions did not permit hydration of the anhydrite before deformation experiments. Pre- and post-experiment analysis of thin sections validates this assumption.

A hole was then drilled (dry) into the centre of the anhydrite cores along X using a drill head with a diameter of 1.5 mm through the axis of each core to increase the fluid flow and sample surface to facilitate faster and more intense hydration. All core plugs intended to be used in the experiment with fluid pressure were immersed in water and left to soak 10 minutes before starting experimental runs.

Core plugs were prepared for triaxial experiments by encapsulation in black viton jackets to ensure a seal is formed during the experiments that shield the sample from the oil used to generate confining pressure in the cell.

5.2.2 Microstructural characterisation

Surplus material sourced from directly adjacent to the core plugs was used to prepare polished thin sections in core plug reference frame X-Y,Z and X=Y,Z-Y,Z direction before starting any experiment. Thin sections of the samples resulting from the experiments were mostly cut parallel to the X axis (σ_1).

Thin sections were prepared for scanning electron microscopy (SEM) via polishing with alumina, followed by a final polish with 0.6 µm colloidal silica in NaOH using a Buehler Vibromet II polisher for 2 to 4 hours. An evaporative carbon coating was applied to prevent charging during SEM. Backscattered electron (BSE) imaging was

conducted with a Zeiss EVO MA10 SEM fitted with an Oxford Instruments INCA X-ray microanalysis system.

A Tescan MIRA3 field emission scanning electron microscope (FE-SEM) with an Oxford instruments electron backscatter diffraction (EBSD) acquisition system, including a Symmetry EBSD detector in John de Laeter Centre at Curtin University, was used to quantify crystallographic microstructures.

Secondary electron (SE) and BSE images were acquired, and EBSD maps with step sizes ranging from 1.7 to 50 μm were collected (Appendix D). Data acquisition and processing settings as well as processing procedures (Table 5.1) followed those of Vargas-Meleza et al. (2015) and Timms et al. (2017; 2019).

Table 5.1: Scanning electron microscopy settings and electron backscatter diffraction acquisition and processing parameters.

SEM					
	Make/model			Tescan MIRA3 FE-SEM	
	EBSD acquisition system			Oxford Instruments AZtec, version 4.3/Symmetry EBSD Detector	
	EDX acquisition system			Oxford Instruments AZtec, version 4.3/XMax 20 mm SDD	
	EBSD processing software			Oxford Instruments Channel 5.12.72.0	
	Acceleration voltage (kV)			20	
	Working distance (mm)			18.5	
	Tilt			70°	
EBSD match units					
	Phase	Space group	β(°)		
	Anhydrite	Cmcm		Hawthorne and Ferguson (1975)	
	Gypsum	C2/c	114.3	Schonfield et al. (1996); Boeyens and Ichhram (2002); Hildyard et al. (2009)	
EBSP acquisition, indexing and processing					
	EBSP acquisition speed (Hz)	40		Band detection (min/max)	6/8
	EBSP Background (frames)	64		Mean angular deviation (all phases)	< 1°
	EBSP Binning	4 x 4		Wild spike correction	yes
	EBSP Grain	high		Nearest neighbour zero solution extrapolation	6
	Hough resolution	60			

Isolated, erroneous EBSD data points were removed using a ‘wild spike’ correction in Channel 5, and a zero-solution extrapolation to 6 nearest neighbours was applied routinely. Misindexing of anhydrite with a range of systematic crystallographic orientation relationships was identified and data were corrected using the function in

the Tango module of Channel 5 (see chapter 4 for further explanation and Table C.1 for a list of corrected relationships)

For phase quantification, BSE images were combined with EDX phase identification data and analysed with ImageJ software (Schneider et al., 2012), using a greyscale threshold to determine phase abundance. Minor uncertainties of this approach include greyscale variation at phase boundaries and/or due to topography of the polished surface. Additionally, fracture patterns in post-experiment sample material were quantified by manual digital tracing of gypsum-filled fractures and veins in BSE images followed by FracPaQ analysis of orientation and length of the mapped linear fracture trace segments (Healy et al., 2017).

5.2.3 Triaxial deformation and hydration experimental methods

All testing was conducted with the high-pressure, high-temperature (HP/HT) triaxial rock deformation apparatus (TRI-X 250 MPa/200°C) from Sanchez Technologies (Fig. 5.1b). The parameters chosen for testing are listed in Table 5.2. The experiments followed three different testing modes: (i) dry; (ii) 'wet'; and (iii) steady state differential compaction (ssdc) under fluid pressure (Fig. 5.1c).

Table 5.2: Triaxial test parameters: $\dot{\varepsilon}$ – strain rate, P_c – confining pressure, P_f – fluid pressure, P_e – effective pressure, $t_{f.e.}$ - fluid exposure time, t_{ssdc} – steady state differential compaction time, failure - stress strain curve / post-experiment core habitus, σ_p – peak differential stress. *Catastrophic failure after 1 hr 11 min during steady state differential compaction. ** peak stress reached during steady state differential compaction.

Mode	Label	$\dot{\varepsilon}$ [s^{-1}]	P_c [MPa]	P_f [MPa]	P_e [MPa]	$t_{f.e.}$ [h:m]	σ_p [MPa]	t_{ssdc} [h:m]
ssdc	Ò1	$9.7 \cdot 10^{-5}$	50	40	10	15:00*	~ 100**	15:00*
	Ò2	$9.7 \cdot 10^{-5}$	50	40	10	06:00	148	06:00
'wet'	Ò3	$4.4 \cdot 10^{-5}$	50	40	10	00:20	123	-
	Ò4	$9.7 \cdot 10^{-7}$	100	90	10	02:50	119	-
	Ò5	$9.7 \cdot 10^{-5}$	50	40	10	01:00	171	-
	Ò6	$9.7 \cdot 10^{-5}$	50	40	10	00:10	169	-
dry	Ò7	$9.7 \cdot 10^{-7}$	100	-	100	-	-	-
	Ò8	$9.7 \cdot 10^{-5}$	50	-	50	-	215	-
	V	$1.0 \cdot 10^{-4}$	50	-	50	-	99	-

The (stress field) principal stress configuration was $\sigma_1 > \sigma_2 = \sigma_3$ throughout runs in (i) and (ii) mode and achieved through the application of a strain rate ('active' deformation). The modes (i) dry and (ii) 'wet' were created to evaluate material

strength and stress versus strain behaviour for the sample material in different strain rate and pressure settings. During 'wet' mode tests, fluid pressure was applied before initiating the strain rate.

In case of (iii) ssdc under fluid pressure, the strain rate was put on hold after achieving ~ 100 MPa differential stress (75 % yield stress of the 'wet' experiments Ò5,6), to achieve micro-cracking and before coalescing shear fractures are supposed to have formed. Only then was water flooded into the sample chamber and fluid pressure applied. The principal stress configuration was isotropic, i.e., $\sigma_1 = \sigma_2 = \sigma_3$.

If failure was not achieved within 15 hours of ssdc, the strain rate was reapplied, which reinstated the respective stress field. At the end of each experiment of modes (ii) and (iii) the vitrion jackets were opened and the samples were placed in an oven at 50°C for ~ 30 minutes to arrest any further hydration from proceeding.

5.3 Results

5.3.1 Triaxial tests – mechanical data

5.3.1.1 Macroscopic sample characteristics

Brittle fractures are readily visible in the post-test cores, with different characteristics depending on the deformation mode (Fig. 5.3a, Appendix D Fig. D.6,7).

All samples deformed in dry mode show bulging around the middle of the long x-axis. The bulging zone is showing intense fracturing via two sets of shear fractures, both with an approximate angle of 30° to σ_1. Most of the samples experienced localized failure.

Samples after 'wet' testing mode show intense fracturing. The fractures follow the same pattern described for the dry samples, with shear fractures.

The main shear faults after ssdc are an area of intense fracturing, filled with brecciated material. The resulting lateral bulges are either not faulted or extremely faulted, compared to the dry and 'wet' test samples. Altogether, the pieces resulting from fracturing seem smaller in size and are coated by a pale grey, soft, viscous layer.

5.3.1.2 Mechanical data

The different modes result in distinctly different deformation behaviour, shown in differential stress versus axial strain curves (Fig. 5.3b). All samples show an initial phase of rapid hardening up until approximately 10 to 20 MPa differential stress. After this, total strain either stabilises or shows a minimal increase, with increasing stress. The next stage is a phase of linear elastic deformation until yield stress is reached, after which the differential stress decreases. Loading after yield stress results in different behaviour, depending on the test mode (see Appendix D, Fig. D.6,7,8,9,10 for details and additional data).

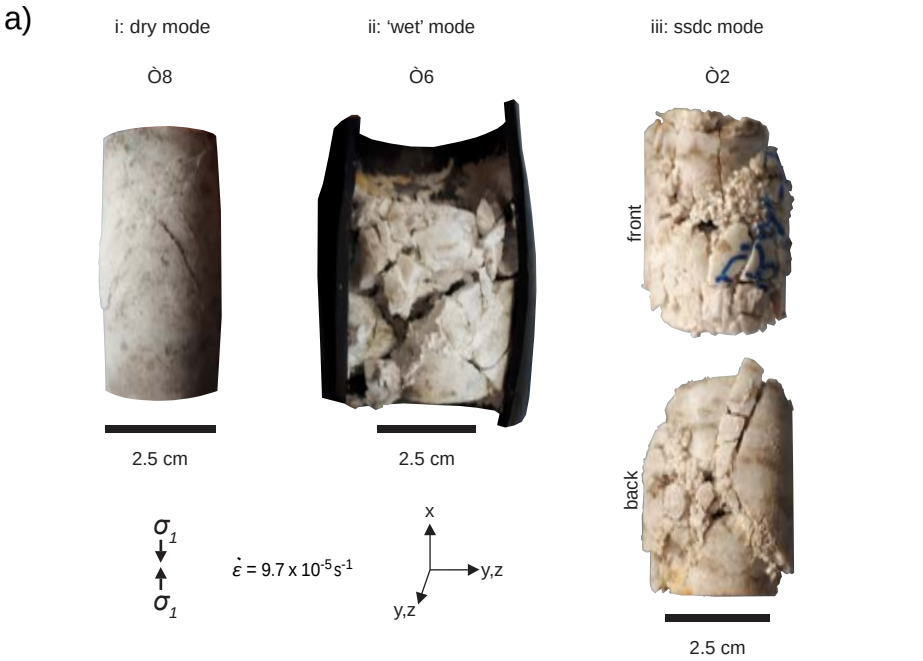

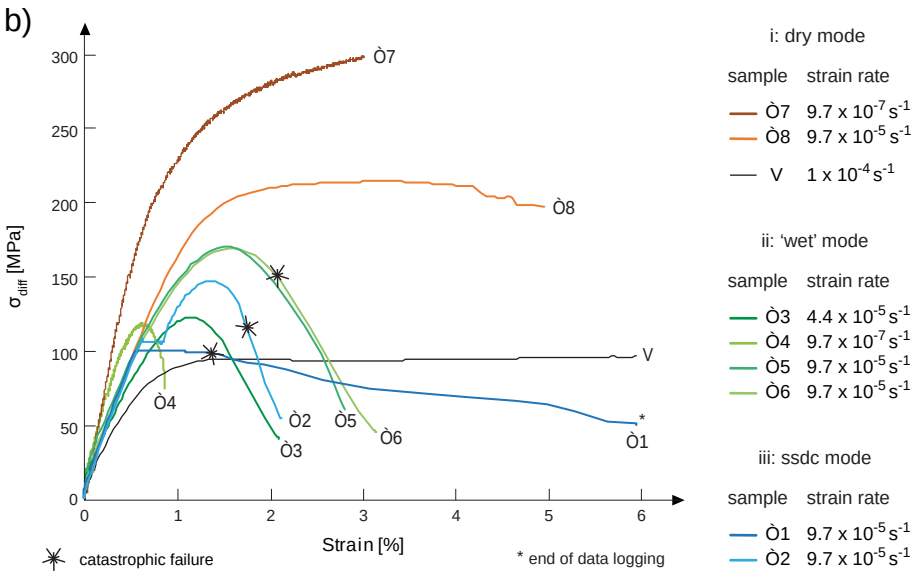

Figure 5.3: Post-experimental mechanical results. a) Photographs of post-experiment cores after undergoing all three test modes. b) Stress versus strain curves, strain (%) in the shortening direction x (σ_1) on the x-axis is plotted against differential stress (σ_{diff}, axial stress/radial pressure) on the y-axis. Catastrophic failure marked for Ò1 at the point of a rapid increase of stable strain during steady state differential compaction (ssdc) phase (no strain rate applied, stable confining and fluid pressure). See Appendix D, Fig. D.6,7,8,9,10, and digital Appendix D for additional information.

Dry tests show either strain hardening (Ò7), or a phase of constant differential stress with increasing strain, and with increasing tendency to slight weakening (Ò8). The Volterra gypsum is considerably weaker compared to all anhydrite tests. The linear elastic response is limited to stresses and strains below 40 MPa and 0.25 %, respectively. The stress-strain relationship of the dry tests shows neither strain hardening nor softening and is without any sign of failure during the ongoing test.

The 'wet' tests show considerably weaker behaviour compared to the dry tests. Strain weakening or softening is displayed after reaching peak differential strength (Table 5.2). The 'wet' experiments are stopped when steep catastrophic strain weakening happens.

The ssdc experiments behave similarly to 'wet' and dry experiments during the first stages until strain rate is set to 0 (constant) before yield point is reached (~ 100 – 110 MPa) and fluid pressure is applied (20 – 90 MPa, Table 5.2) in under one minute. Sample Ò1 was stable with increasing strain for about 1 hour, before catastrophic failure at 1.35 % strain and 99 MPa differential stress.

Catastrophic failure occurred at higher differential stress and lower strain conditions than when 'wet' same condition tests and Ò2 showed steep catastrophic strain weakening. During the ssdc phase, strain increases, and the stress conditions are stable for sample Ò2. Compared with samples Ò5 and Ò6, which were run with the same strain rate, Ò2 is weaker and differential strain decreases in a steeper trend.

5.3.2 Microstructures

5.3.2.1 Fracture and gypsum-filled vein pattern analysis

A fracture pattern was analysed for gypsum-filled veins from BSE images of a thin section from 'wet' mode Ò3 sample. This sample failed via one main shear fracture

(Fig. 5.4, Appendix D, Fig. D.6), which left enough solid material for detailed analysis of a 'wet' mode sample. Mapping of gypsum-filled veins in a part of the sample that features a significant vein system yielded a representative dataset for orientation analysis of all gypsum veins in view with apertures > 25 µm and of a sufficient dataset of identifiable < 25 µm wide narrow gypsum-filled veins.

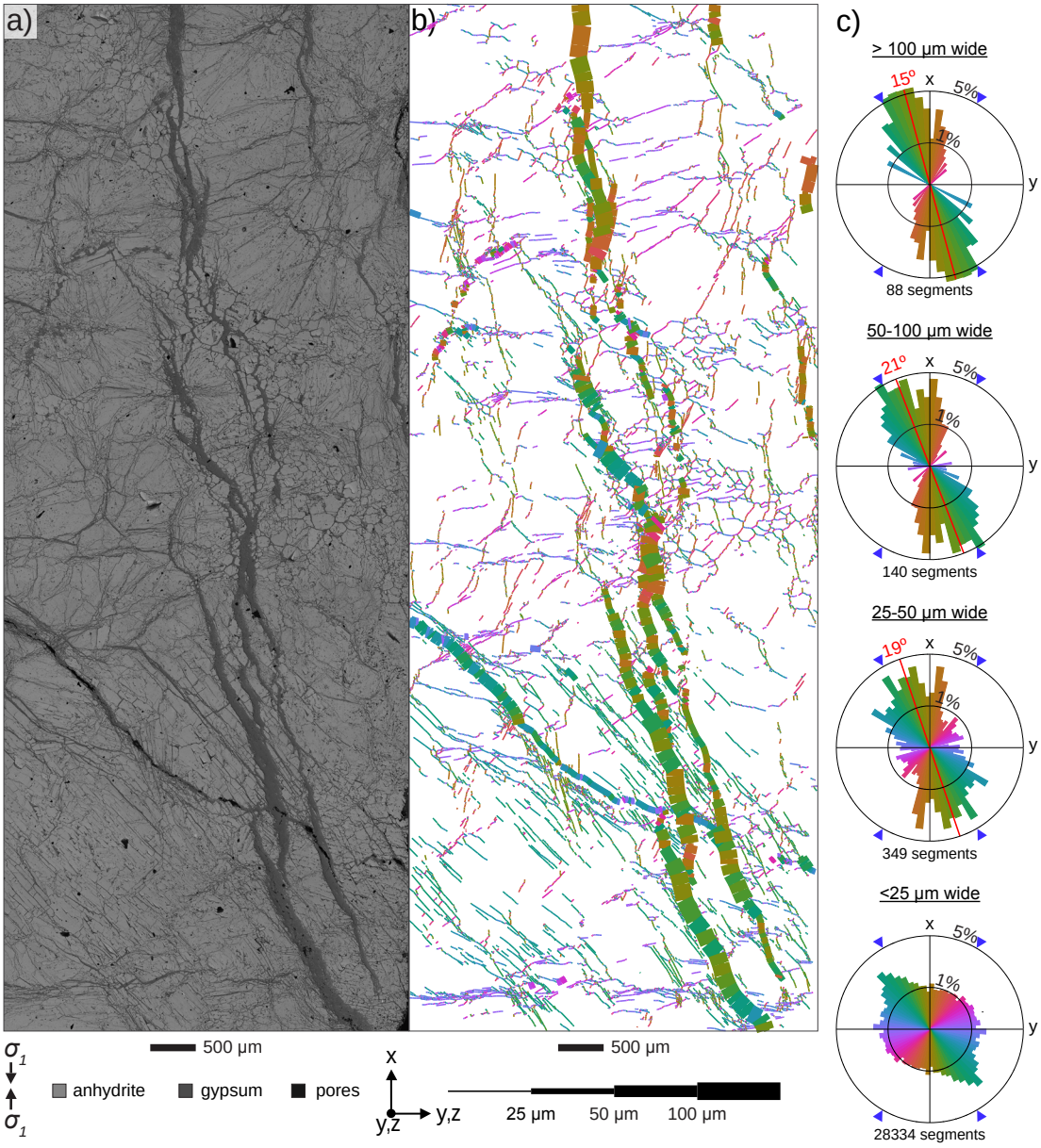

Figure 5.4: Distribution of gypsum veins in sample ÒÌ3 after 'wet' experimental run. a) BSE image showing the distribution of phases. b) Map of gypsum-filled veins, with segments coloured for orientation and line width representing vein widths. Not all fractures smaller 25 µm are traced due to their high abundance. c) Length-weighted segment orientation rose diagrams corresponding to the dataset shown in b), with 5° bin size and consistent colour legend (0 – 180°). Marked in red is the circular mean angle,

calculated by FracPaQ (Healy et al., 2017). Marked in blue is the predicted shear fracture angle of 30° from x (σ_1) in an Andersonian system.

Orientation analysis of all gypsum-filled fracture segments in 2D shows a preferred orientation with a prominent peak close to 30° from the core axis (and therefore to σ_1) of all aperture classes (Fig. 5.4c). The wider, less abundant cracks and gypsum-filled veins show stronger preferred orientations than narrower cracks/veins or those observed in the pre-experiment Òdena anhydrite.

The preferred orientation of > 25 µm gypsum-filled veins is like shear and extensional fracture orientations predicted by the orientation of the applied stress field during the experiment: macroscopic fractures visible in this thin section that were created by the triaxial test should have azimuths of either 30°/210° or 150°/330° relative to X, the equivalent direction of the principal stress σ_1 (Fig. 5.4). However, gypsum infill implies an extensional component to the kinematics of these structures.

In detail, there are two different preferred orientations dominant in fracture populations of different widths. Veins narrower than 25 µm are almost evenly distributed around 1 % for all directions with exception of a distinct peak around 45° counter-clockwise from x (Fig. 5.4c). This peak coincides with the trend of cleavage in a large anhydrite grain that dominates the lower part of the map.

Analysis of gypsum-filled vein segments with widths in the ranges of 25 – 50 µm, 50 – 100 µm, and > 100 µm show that the preferred orientation gets stronger with increasing width of the veins (standard deviation of circular mean decreases, whereas resultant increases with increasing width) (Fig. 5.4c). Furthermore, segment traces are longer (average segment length in pixels: 6.41 – 9.87 – 13.54) with increasing vein width.

5.3.2.2 Crystallographic orientation analysis of newly-formed gypsum

Crystallographic orientation mapping was done for anhydrite and gypsum of the same area of 'wet' mode Ò3 sample from Figure 5.4 (Fig. 5.5, additional data in Appendix D, Fig. D.11,12,13,14,15). The dominant form of anhydrite in the upper part of the map are spherulites comprising radially oriented anhydrite blades that progressively change their crystallographic orientation (Fig. 5.5a). The spherulites have an approximate diameter of ~ 700 to 1250 µm.

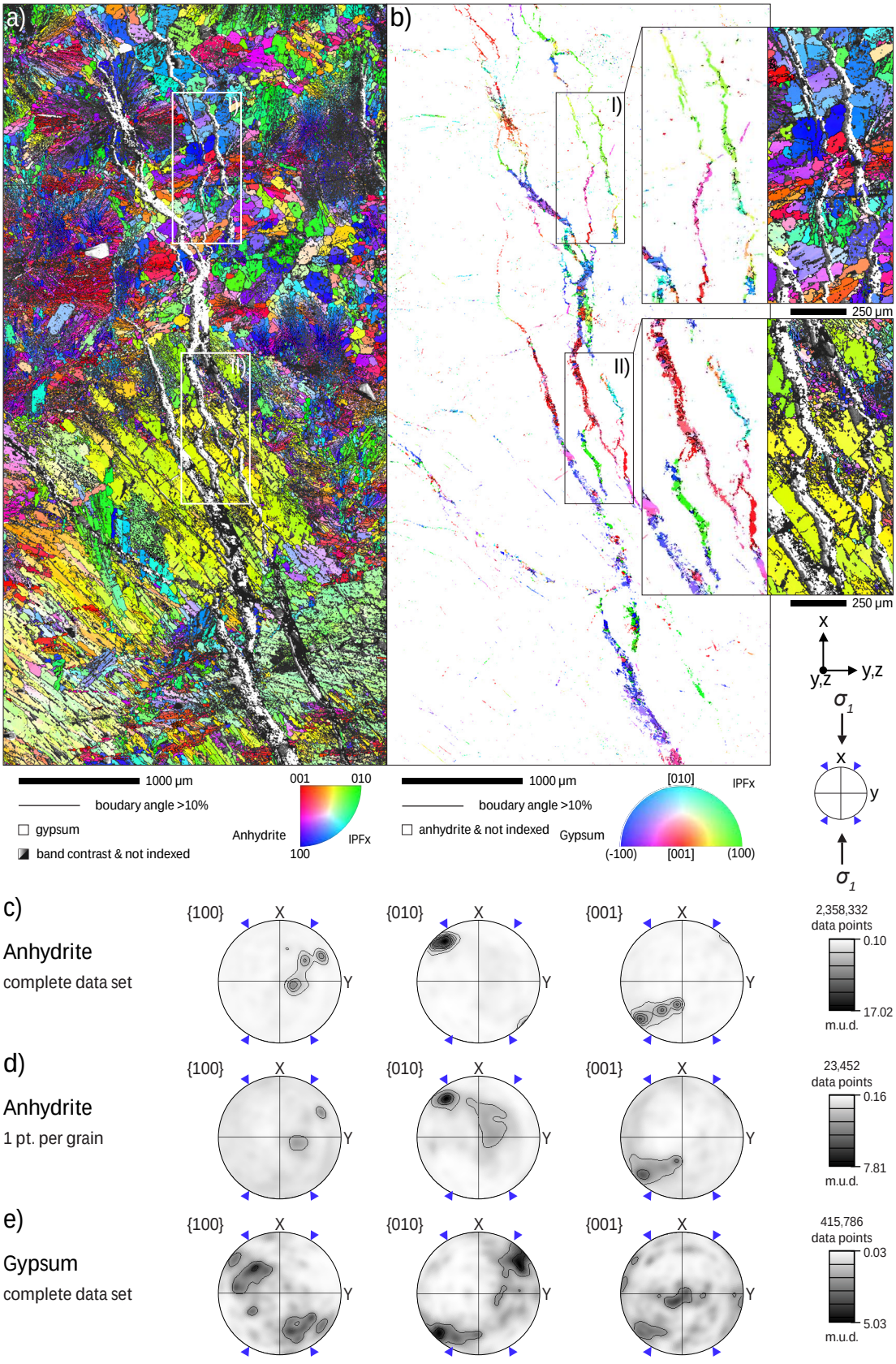

Figure 5.5: Electron backscatter diffraction analysis of the same area shown in Fig. 5.4 from sample Ò3, deformed in 'wet' testing mode. a) EBSD IPFx map of detected anhydrite with underlying backscatter image. b) Complementary IPFx map of detected

gypsum. Magnification of I) and II) to compare IPFx of host anhydrite with vein-hosted gypsum. c), d), and e) Respective equal area, lower hemispheres pole figures of anhydrite and gypsum. Marked in blue is the predicted shear fracture angle of 30° from x (σ_1) in an Andersonian system. See Appendix D, Fig. 12,13,14,15 for additional data.

Scattered between the spherulites are clusters of blocky crystals with approximate diameters in the range of 70 to 350 μm (Fig. 5.5a). The third fabric component is made up of large, strained crystals (1000 μm long) with cleavage, dominating the lower part of the map and visible in green colours in the IPFx map (Fig. 5.5a).

Anhydrite in the mapped area shows a strong CPO with the pole to {010} orientated ~ 40° counter-clockwise from x (Fig. 5.5c). This fabric is dominated by aligned (cleaved) components of the large crystals, whereas the crystallographic orientations of the blocky grains are randomly oriented (Fig. 5.5a). The majority of the gypsum present in the mapped area is concentrated in the main vein structure (Fig. 5.5b). Only a small proportion of the gypsum is distributed in 'traces' inside the anhydrite fabrics.

Orientation mapping shows that the gypsum filling the main veins forms domains (grains) up to ~ 1000 μm long sections have a similar crystallographic orientation (Fig. 5.5bI,II). Only a small fraction of crystals shows different crystallographic orientations. However, the EBSD map shows that, locally, the sizes and spatial positions of gypsum grains in the veins do not have any relationship with neighbouring anhydrite in the wall rock (Fig. 5.5bI,II).

Nevertheless, pole figures show that poles to {010} of anhydrite and poles to {100} of gypsum show broad alignment (Fig. 5.5c,d,e). Similarly, poles to {001} of anhydrite and poles to {010} of gypsum tend to align in some parts of the veins (Fig. 5.5c,d,e; Appendix D, Fig. D.16,17,18,19).

Overall, there is no clear link between crystallographic orientation of vein gypsum and the orientation of principal stress σ_1, or predicted shear fracture planes. However, there is a clustering of poles to {100} and {010} in gypsum at approximately 45° to σ_1, which is parallel to the direction of maximum shear stress (Fig. 5.5c,d,e).

5.3.2.3 Characterisation of fractures after steady state differential compaction

The fabric elements and phase abundance related to ssdc followed by failure are analysed from a BSE image of one of the main shear planes of Ò2 (Fig. 5.6; see Appendix D, Fig. D.20,21,22,23,24 for further data). The thin section of this sample

provides the opportunity to study gypsification related to shear fractures after ssdc. Five domains (A to E) are defined mostly after the phase abundance contrast.

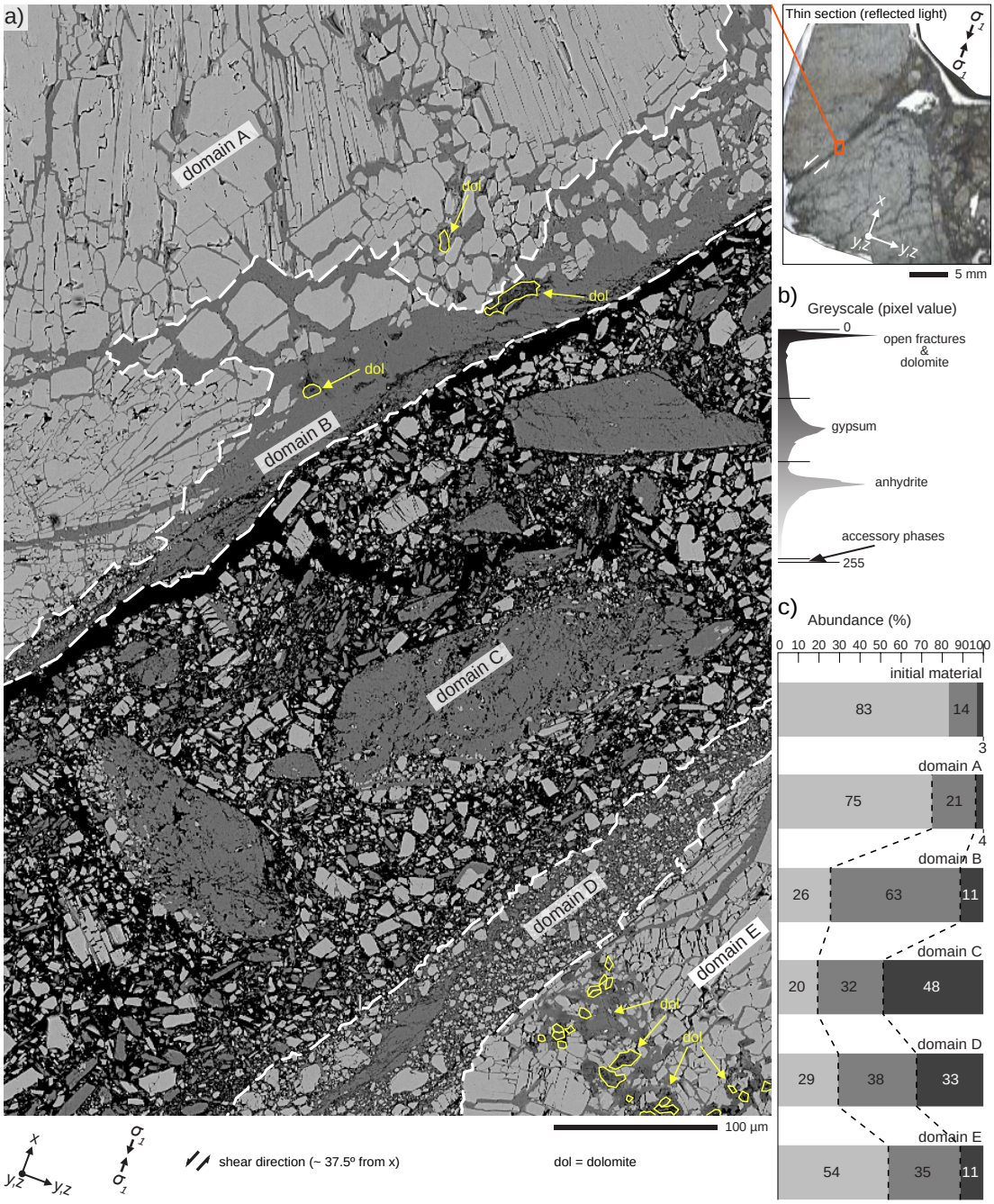

Figure 5.6: Analysis of a shear fracture in sample Ò2 after steady state differential compaction and failure. The area in the image shows the main shear fracture that divides the lower, intact end piece of the sample core from an intact side slab. a) Backscatter electron image with domains (A – D) defined by texture and composition. Dolomite is identified based on habitus and experience from EDX results of other areas in the thin section. b) Greyscale threshold settings defined to quantify % area of phases from the backscatter image analysis via ImageJ. c) Bar chart to show % area of phases in domains

and mean values of the pre-test Òdena anhydrite (same thresholds applied, see Appendix D, Fig. D.25,26,27,28, and Table D.1). Open fractures and dolomite overlap in greyscale.

In detail, defining the A - B boundary is made by compromising between abundance and fabric characteristics. The B – C boundary is easily placed by tracing a fault plane. The C – D boundary is defined mainly by the compaction contrast between domains. The D – E boundary results from a combination of fault horizon and material abundance.

Domain A has mostly blades of anhydrite with sharp edges, the spherulitic structures are still visible and gypsum is located interstitially between these blades. Towards the domain boundary, the anhydrite is blocky, with edges that range from sharp but most commonly are rounded. There is no evidence of rotation of grains in these domains due to the kinematics of the experiment.

Domain B is dominated by gypsum with a mosaic of isolated anhydrite grains (inclusions). Anhydrite is mostly rounded, some with evidence of rotation with respect to one another. The abundance of gypsum increases towards domain C, forming a layer of pure gypsum.

Domain C mainly consists of clasts that contain anhydrite, gypsum, or both, and with no significant matrix. The size (long axis) of the gypsum clasts ranges from < 1 μm to > 100 μm. The big gypsum clasts can be highly fractured, with sporadic smaller anhydrite grains at the rims or as ~ 1 μm small inclusions. Almost half of the domain is porous, and gypsum content is higher than anhydrite content.

In domain D, the anhydrite grains are rotated, and embedded into a gypsum matrix. The edges are round to semi-round in shape and the particle size is up to 25 μm (length of long axis). The domain is highly brecciated with contact between particles. The boundary to domain D is defined by a series of fractures.

The initial fabric is preserved in domain E but highly affected, showing abundant intra- and inter-granular fracturing. Inter-granular fractures are mostly filled with gypsum, whereas intra-granular fractures are predominantly empty. The shape of the edges of the anhydrite grains ranges from sharp to slightly rounded. Abundance analysis results are that more than half of the domain consists of anhydrite.

5.4 Discussion

5.4.1 Evidence for formation of new gypsum

The strongest evidence for successful hydration and formation of gypsum is represented by the breccia vein shown in Figure 5.6. The main vein orientation has an orientation of 37.5° to x (σ_1), which is consistent with a shear fracture caused by the ssdc mode experiment. Optical assessment and greyscale threshold analysis shows that the gypsum content in and around the shear fracture is significantly higher compared to the initial sample material (Fig. 5.2 b, Appendix D Fig. D25,26,27,28, Table D.1). The higher abundance of gypsum and rounded, rotated anhydrite grains in the margins (domain B, D) of the breccia vein are evidence for active (syn-experiment) gypsification.

The centre of the breccia vein (Fig. 5.6, domain C) contains > 100 µm gypsum clasts, which is orders of magnitude larger than any observed pre-experiment gypsum, located in centres of anhydrite spherulites and short narrow (< 50 µm) veins (Fig. 5.2b; Appendix D Fig. D.1,2,3). These clasts can contain small anhydrite inclusions and are derived from newly-formed gypsum (Fig. 5.6 a). Based on the distribution of the anhydrite inclusions at the margins of the gypsum clasts, the gypsum was part of a shear interface with active gypsification before brecciation occurred.

The formation of the gypsum vein system from sample Ò3, documented after a 'wet' mode experiment (Fig. 5.4a,b) is consistent with syn-experiment gypsification and deformation. The wide vein apertures (>> 50 µm) in combination with the systematic orientation and length of the gypsum-filled vein system of > 2.5 cm (Appendix D, Fig. D.1,2,3) was not present in the primary sample material. These are strong indicators for experimentally induced extension and formation of new gypsum. The wide gypsum-filled vein system formed by linked extensional fractures with a minor shear component that progressively coalesced to result in a stepped shear fracture. (Fig. 5.4).

Additionally, the crystallographic orientation of the vein gypsum is such that poles to {010} generally coincide with the direction of maximum shear stress during the experiments. This geometric link between gypsum growth and stress during an experiment and independent of the surrounding anhydrite has not been described before and requires further discussion.

5.4.2 Evolution and mechanisms of hydration

5.4.2.1 Rapid hydration of anhydrite under stress

A significant outcome of this study is that hydration of anhydrite to gypsum was achieved under non-hydrostatic stress conditions over a few hours. The ssdc experiment Ò2 lasted for six hours and produced gypsum in the fracture-related pore space created during the experiment. Sample Ò3 shows a significant amount of new gypsum in veins even after a twenty minute long 'wet' mode experiment.

These results contrast starkly to previous attempts to hydrate anhydrite, which failed to produce gypsum over many months under hydrostatic conditions (e.g., Ramsdell and Patridge, 1929, Leininger et al., 1957; Hardie, 1967). This suggests that there is an intrinsic link (or links) between application of a non-hydrostatic stress field and the rate of the hydration reaction.

5.4.2.2 Spatial distribution and timing relationships between hydration products and fractures

Microstructural observations (Fig. 5.4, 5.5 and 5.6) show a paragenesis that links to the stress-strain evolution. A model to establish the spatial distribution and timing relationships of hydration products and fracture pattern development results from experimental observations was developed (Fig. 5.7).

During elastic stress-strain behaviour, the onset of intra-granular fracturing concentrated in the centre of the core and the orientation of shear planes (30° angle to σ_1) significantly increased sample permeability and provides three-dimensional fracture networks as pathways for fluids (Fig. 5.7a i).

Application of fluid pressure during ssdc and 'wet' mode experiments ensured the fast distribution of H_2O through these networks (Fig. 5.7a ii). At fracture interfaces, the presence of anhydrite, gypsum and H_2O resulted in in situ hydration and gypsum vein formation. Ò2 hat six hours of contact with H_2O in total. Five hours and fifty-six minutes under isotropic principal stress conditions (i.e., $\sigma_1 = \sigma_2 = \sigma_3$), and less than two minutes from re-application of strain rate to maximum differential stress (σ_{max}).

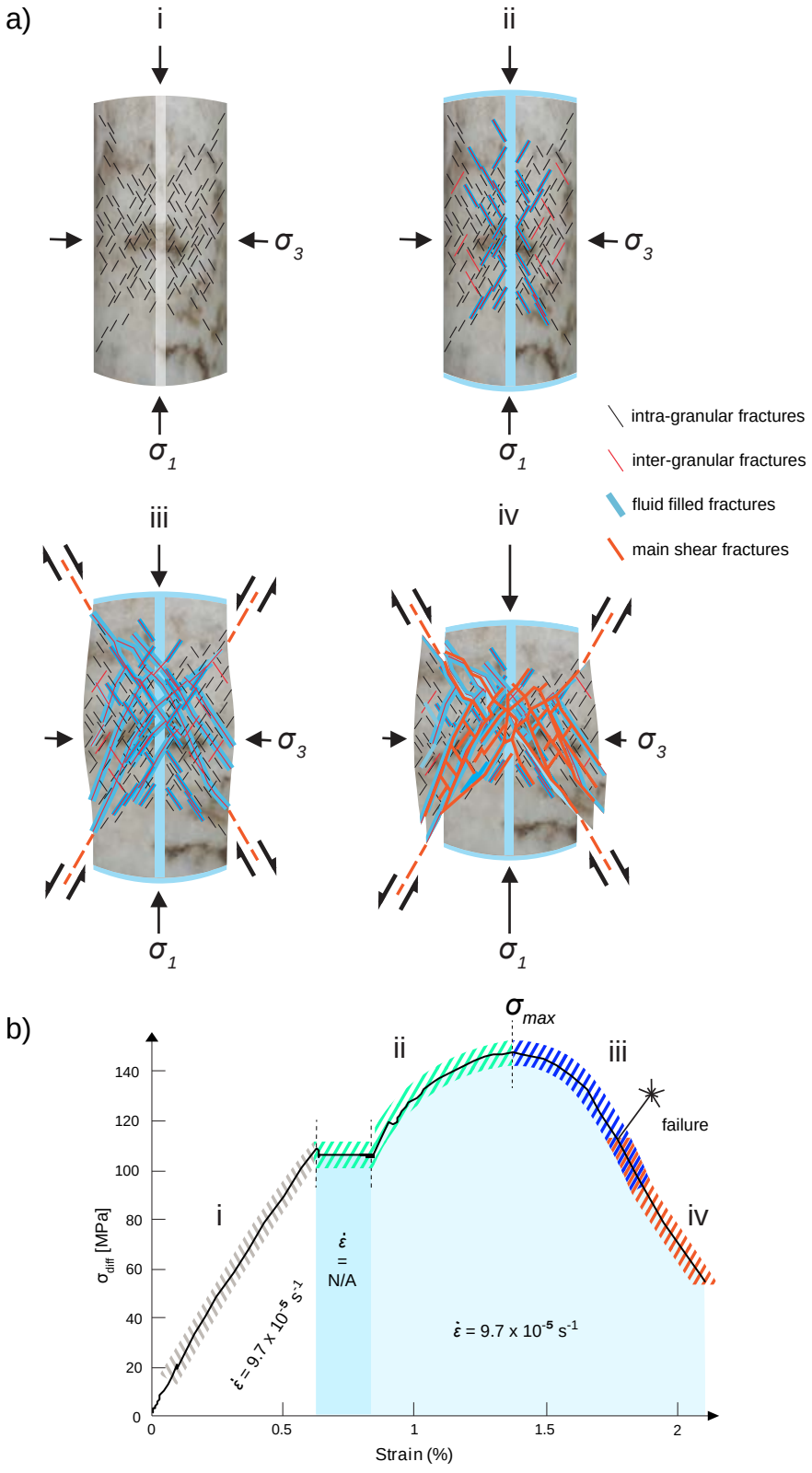

Figure 5.7: Interpretation of fracture formation and fluid distribution in the sample cores throughout triaxial testes. a) Schematic fracture formation. Not all stages apply to all tests, depending on the experimental mode. b) Relation of a) to steady state differential compaction stress-strain curve of sample Ò2.

The gypsum margins and large gypsum clasts contained in the brecciated zone of the shear fractures after ssdc in sample Ò2 exceeded the gypsum formation documented after 'wet' mode experiment in sample Ò3. Combined with the timeline, this larger gypsum content strongly indicates early inter-granular fracturing combined with formation of new gypsum before reaching maximum differential stress.

After maximum differential stress and prior to dynamic hydration brecciation (Fig. 5.7 iii), bulging and (faster) shortening of the sample in the x direction through the activation of shear plane fractures and local extensional operation of a three-dimensional fluid pathway network occurred within two minutes.

Shear along main shear fractures results in rapid shortening in x direction during the last stage (Fig. 5.7a iv) and is characterized by a rapid drop of stress (minus ~ 10 MPa every three seconds) with ongoing strain. The onset of such catastrophic failure thirty seconds after maximum differential stress was reached, led to the formation of cataclastic zones and brecciated veins (Fig. 5.6)

5.4.2.3 Crystallographic orientation of newly-formed gypsum

The crystallographic orientations of newly-formed gypsum in the veins have a systematic preferred orientation for long distances along veins, beyond the grain boundaries of wall-rock anhydrite (Fig. 5.5a,b). Gypsum is not always topotactically linked to the wall-rock anhydrite in the immediate vicinity, indicating that inheritance of crystal orientation from anhydrite did not lead to the strong clustering of poles.

There is also no evidence of alignment of crystals with respect to the vein walls, or evidence of gypsum crystals that grew from the vein margin to its centre, and so alignment by competitive crystal growth of gypsum into the vein is unlikely.

Instead, gypsum crystallographic orientations are systematically and preferentially aligned parallel to the direction of maximum shear stress (Fig. 5.5c). This study proposes that inheritance of crystal orientations from wall-rock anhydrite grains combined with crystal orientations favourable for nucleation and growth under the applied stress field (i.e., stress-related minimisation of the energy barrier for nucleation) led to selective crystallographic orientations of large new gypsum grains.

5.4.3 Mechanical-chemical coupling

The spatial link between newly-formed gypsum and fractures shows that hydration predominantly progressed through the fracture network rather than a front that progressed through the sample, similar to that reported for anhydritization (Wang and Wong, 2003; Llana-Fúnez et al., 2012). A concept for the hydration mechanism of anhydrite particles developed by Sievert et al. (2005) involves dissolution and precipitation, which was adapted here to explain hydration of Òdena anhydrite under stress (Fig. 5.8).

The 'wet' mode experiments make H_2O groups available to new mineral interfaces during the initial intra-granular fracturing. Upon the contact of anhydrite surfaces with water, $CaSO_4$ solution and the surface absorption layer of hydrated Ca^{2+} and SO_4^{2-} ions formed (Fig. 5.8) (Sievert et al., 2005). The increase of thickness of the absorbed layer is reportedly a slow process and needs to be followed by the crack formation in the absorbed layer and counter migration of H_2O and Ca^{2+} as well as SO_4^{2-} ions (Sievert et al., 2005).

Pre-existing gypsum in the samples acted as a natural seeding material, which has been demonstrated elsewhere to enable (or speed up) the hydration reaction process because the kinetically challenging process of forming nuclei (e.g., Hardie, 1967; Wheeler, 1991; Sievert et al., 2005) is skipped. Therefore, hydration was possible as soon as the samples had water contact and more likely in ssdc experiments due to the amount of time of contact with H_2O. However, the importance of this process is difficult to reconcile with the distinct microstructural location of new gypsum (in newly-formed veins), or the lack of gypsum in hydrostatic experiments. Rounded anhydrite inclusions in gypsum margins of shear fractures and as clasts in brecciated veins (Fig. 5.6a) are specific indicators for dissolution of anhydrite.

The role of fractures is threefold: Firstly, they provide new surface area available for reaction. Secondly, they facilitate fluid flow to enable a readily available medium (H_2O) for solution transfer of Ca^{2+} and SO_4^{2-} ions. Thirdly, locally variable stresses associated with fracture propagation give rise to spatial variations in chemical potential and as a consequence, chemical disequilibrium (Llana-Fúnez et al., 2012; Wheeler, 2018).

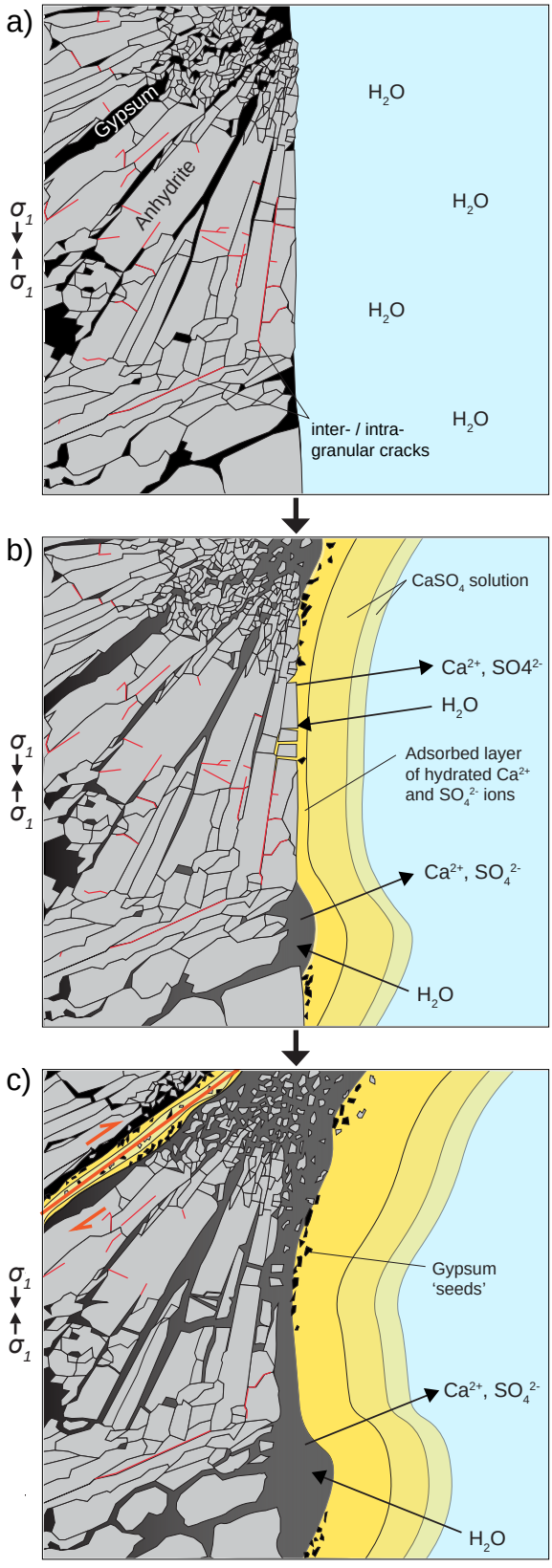

Figure 5.8: Model for solution – precipitation hydration in Òdena anhydrite based on the hydration mechanism suggested by Sievert et al. (2005). The model includes a spherulite structure, cleavage, and blocky anhydrite areas in contact with water. Initial gypsum is located in veins along grain boundaries and the centre of the spherulite.

Solid-fluid contacts will be at the pressure of the fluids (P_f), whilst solid-solid contacts will have a higher average normal stress, depending on the bulk effective pressure and contact area (Llana-Fúnez et al., 2012). That provides different pathways of Ca^{2+} and SO_4^{2-} ions during the reaction. Therefore, anhydrite solution was preferentially formed in the stressed anhydrite at fracture tips, grain boundaries, and at gypsum-anhydrite contacts. Once gypsum nuclei were established, growth was likely to be rapid, following the findings of Sievert et al. (2005).

The transformation of anhydrite to gypsum requires a significant change in volume of solid material (i. e. swelling). Upon contact with water gypsum is no longer solid but partly dissolved and starts to moderately swell (Fig. 8b). Simultaneously, anhydrite dissolution occurs and transfer of Ca^{2+} and SO_4^{2-} ions and H_2O molecules permeate through the gypsum (Fig. 5.8b,c). The consumption of water acts to lower fluid pressure, whereas replacement of anhydrite by gypsum causes swelling, counteracting decrease in fluid pressure. However, the tests are conducted at constant fluid pressure (held at 10 MPa lower than confining pressure) without any induced fluid flow. Nevertheless, fresh supply of H_2O was facilitated by the opening of a connective network of new intergranular fractures (Fig. 5.7a iii). Fracturing combined with the availability of water for the formation of gypsum facilitate dilatancy, which is seen as bulging of the jacketed sample charges (Fig. 5.7a iii).

Swelling (volume increase) and water loss through H_2O groups being bound into the gypsum impact activity of hydration in places. Swelling can seal up cracks and trap or supersede free water. This potentially stops the hydration reaction in places, while the water migrates into other, harder to reach environments, like grain boundaries, and facilitating hydration there with fewer H_2O groups available.

Cataclastic flow and the full development of major shear fractures (Fig. 5.7a,b, iv) occurred after the peak stress was reached. The ‘wet’ tests show that these major shear fractures with thin interconnected parallel fractures and areas of wide fractures are all filled with gypsum. These form planar zones of weakness for catastrophic shear failure.

For the phase after peak stress is achieved, De Paola et al. (2009) recorded a rapid increase in permeability that becomes ‘chaotic’ in the final stage of failure. This is

likely to be coupled with a rapid increase in the area of available reaction surfaces. The macroscopic observations show that the sample cores after experiments with applied fluid pressure, if not failed catastrophically, comprise fragmented debris centimetre to millimetre size, covered with a white slurry. This indicates that rapid gypsum formation may occur during the last, only seconds long stage and upon the failure.

The lower peak stress of Ò2 after re-initiation of a strain rate of $9.7 \cdot 10^{-5} s^{-1}$ can be explained by the development of weakening zones due to the hydration of gypsum and filling of cracks. Only sample Ò1 failed during ssdc. This could be due to a favourable orientation of pre-existing zones of weakness. There is gypsum in the initial sample, in short (< 1 cm) veins with an aperture of < 50 μm. The formation of new gypsum is linked to sample failure.

5.4.3.1 Mechanical strength

A consequence of hydration under stress is the weakening of the mechanical strength during deformation. Samples Ò1,2 that experienced ssdc, have considerably lower peak strength compared to 'wet' and dry runs with the same strain rate of $9.7 \cdot 10^{-5}$ s^{-1}. Slower strain rates (Ò3,4,7) generate weaker peak strengths.

Besides strain rate, the testing mode has the most significant influence on peak differential stress. Ò8 showed the highest peak differential stress (215 MPa), and 'wet' experiments Ò5,6 was intermediate (~ 170 MPa). Sample Ò1 fails catastrophically at the beginning of the ssdc phase, the maximum differential stress before failure was ~ 100 MPa, and therefore about 41 % less compared to 'wet' experiments. Ò2 reaches a peak strength (147 MPa) after reapplication of the strain rate. The peak strength of Ò2 is 14 % lower than that of the 'wet' experiments.

The microstructural analysis shows that the new gypsum is located along fractures in extensional and shear orientations, creating planes of weakness, and lowering the mechanical strength. A stronger connected shear fracture network developed until the onset of isotropic principal stress conditions (i.e., $\sigma_1 = \sigma_2 = \sigma_3$) likely caused the more rapidly developed connective fracture network in Ò1 and Ò2. The coalescence of fractures accompanied by hydration in Ò1 occurred within 71 minutes under isotropic confining stress conditions once fluids were introduced.

5.4.4 Wider applicability of the study

Main implication of this study of the crystalline $CaSO_4 \cdot H_2O$ system is that mechanical-chemical coupling of deformation and hydration is central to permit hydration and causes significant mechanical weakening.

The stability of natural evaporites is of major interest in various settings, especially in context of underground structures with a variety of purposes. Examples are tunnel construction and monitoring, mining of evaporites, and where evaporitic caverns are temporarily used as storage facilities. In general, rock salt deposits are anything but homogeneous or monomineralic (Stewart, 1963), with gypsum and anhydrite being two of the nine most important and common evaporitic minerals and continuous activity of hydration and dehydration reactions.

Germany and the United States of America are already storing (disposing) repositories with low- and intermediate level nuclear waste in rock salt deposits. The basic assumptions are that rock salt functions as a seal, with halokinesis 'healing' potential leaks. The need for more studies to determine the safety and efficiency of salt deposits, also with the future perspective of permanent disposal of all kinds of materials is widely recognised.

The findings of this study, mechanical-chemical weakening through rapid hydration of anhydrite along fractures, show how rapidly mechanical weaknesses may form and threaten the stability of caverns in natural evaporite deposits. This needs to be included into stability models. Anhydrite-bearing evaporite sequences are often the weakest horizons in sedimentary basins and form detachment horizons in foreland fold and thrust belts (e.g., Heard and Rubey, 1966; Hildyard et al., 2011). Hydration of the anhydrite must further weaken the mechanical strength of such sequences and make the formation of detachment horizons easier.

Findings of this study have implications for hydration in a wide variety geological settings. The $CaSO_4 \cdot H_2O$ system could be seen as an analogue for other rock systems that are controlled by hydration, dehydration, and stress, and therefore potentially impacted the mechanical strength of a geologic setting. Common fluid pathways in the Earth include faults, shear zones, and stratigraphic aquifers. This study suggests that hydration along such pathways can be rapid and generate planes of significant weakness in a stressed environment.

Deep crustal earth quakes are often associated with locally weakening of the generally dry, mechanically strong deep crust, through fluid-driven metamorphic reactions (Jamtveit et al., 2019). Studies from the Bergen Arcs is western Norway show that fluid mitigation through shear zones facilitates highly localized eclogitization of anhydrous (granulite) crust along shear zones (e.g., Austrheim and Griffin, 1985; Austrheim, 1987; Jamtveit et al., 1990, Jamtveit et al., 2019) and result in transient mechanical weakening, brittle deformation and earth quakes (e.g., Jamtveit et al., 2019; Bras et al., 2021). At an early stage, eclogite facies mineralogy is even known to be found as veins in extension fractures (Jamtveit et al., 1990).

Subduction of oceanic and continental crusts and active faults (Pérez-Gussinyé and Reston, 2001; Ranero et al., 2003; Bayrakci et al., 2016) transport water even to the deep mantle and create local water rich horizons. Hydration regions surround the three major sites of deep dehydration, the base of the upper mantle, top and bottom of the lower mantle, and slabs in the shallow upper mantle (Ohtani, 2021). Many hydrous minerals such as serpentine, chlorite, and amphibole exist in the crust and slabs descending in the upper mantle. These minerals dehydrate during the descend and release fluids into the overlying mantle (e.g., Mysen 2018, 2019). High-pressure hydrous phases, such as dense hydrous magnesium silicates (DHMS) are stable in the upper mantle and mantle transition zone (Ringwood and Major, 1967).

5.5 Conclusions

This is the first study that looks at the mechanical behaviour and evolution of microstructures linked to hydration in natural samples. Experimental hydration under non-hydrostatic stress conditions was successfully achieved over several hours and evidence for newly-formed gypsum in post experimental ‘wet’ mode and steady-state differential compaction (ssdc) mode samples was found. Syn-experiment gypsum-filled veins and breccia veins with large gypsum clasts formed in extensional and shear orientations. Significant mechanical weakening of the natural Òdena anhydrite accompanied rapid hydration under non-static stress conditions during ssdc mode experiments. The ssdc results in decreased (~ 14 to ~ 41 %) peak strength and lower differential stress and strain during failure compared to the ‘wet’ and dry mode tests. The mechanical-chemical link resulted in failure along gypsum veins after 71 minutes for one sample under ssdc conditions, whereas the other lasted ~ 6 hours in ssdc mode. EBSD analysis shows a selective topotactical link of large gypsum grains to the vein

hosting anhydrite. The crystallographic orientations of the gypsum grains in new veins are also selective, systematic, and preferentially aligned parallel to the direction of maximum shear stress during the experiments. A model for the evolution of fracture formation and hydration involving mechanical-chemical coupling is proposed. The insights into rapid hydration under stress provided by this study has wide implications for geological and engineering settings.

CHAPTER 6

THESIS SYNTHESIS

6.1 Summary of thesis results

Each of the four research chapters presented as part of this thesis is investigating one out of four specific objectives that have been formulated in the thesis introduction chapter (see 1.2 Aims and objectives). They serve the main purpose of this thesis, which is to study the link between petrofabrics and seismic anisotropy, and include the quantification of grain boundary patterns, study of evaporite petrofabrics, and experimental hydration of evaporites under stress.

6.1.1 Segment-based grain boundary pattern quantification

Chapter 2 introduces the new MATLAB^{TM} toolbox GBPaQ (Grain Boundary Pattern Quantification), which incorporates the semi-automation of a new take on a grain boundary segment intercept (GBSI) based quantification method for grain boundary pattern geometries. GBPaQ also has the option of using grain boundary segment azimuths to quantify for example the preferred orientation of the segments.

The GBSI quantification method was designed with the objective to assess and quantify the influence of grain boundary alignment on acoustic velocity anisotropy in samples with simple and complex patterns with i.e., non-homogeneous and mixed grain shapes. The intention was to create a tool with the capability of fast and simple pattern segment and intercept analysis, with the objective to avoid data simplification, loss, or transformation by, for example, the application of high-level smoothing or fitting ellipses used for strain analysis. The presented methodology also has a broad spectrum of potential applications, as grain boundary pattern quantification is, i.e., important for permeability, deformation mechanisms, and reaction interfaces. The study presents results from semi-automated GBPaQ analysis of two grain boundary patterns.

- A new workflow for grain boundary pattern quantification

More complete pattern quantification by combining fitted ellipse, grain boundary segment geometry, and GBSI methods provides the opportunity of analysing more complex patterns than was possible before. The methods complement each other, as each one captures different details of the pattern. The grain boundary segment

geometry statistically analysis the complete grain boundary pattern, via length-weighted azimuths of each grain boundary segment in a pattern. Spatial relationships (i.e., grain specific grain boundary segments) are lost when plotted as rose diagrams or graph, but this analysis is particularly sensitive to SPOs and other geometrically expressed characteristics. The GBSI method analyses a pattern along scan lines, and therefore provides directional data on grain boundary densities.

- SPO 'shapes' as GBSI density contour plots

GBSI density contour roses capture the directional characteristics of a grain boundary pattern and a higher degree of complexity is incorporated. However, the orientations of GBSI density minimum directions (α) and maximum directions (γ) are susceptible to heterogeneities in the grain boundary pattern and scan line positions. GBSI density contour rose plots can display the evolution of a grain boundary pattern throughout progressive deformation. Directional changes of GBSI density dependent on strain geometry and potentially other controlling factors like deformation mechanisms, grain size and grain shape translate well to GBSI density evolution. GBSI density contour rose plots can be integrated in the analysis of acoustic wave velocity anisotropies, as they provide the directional grain boundary density and geometric anisotropy of the grain boundary patterns.

- GBSI density-based minimum intensity (I_{min}) curves

Analysis of GBSI data for progressively deformed patterns reveals a new SPO quantification concept for rapid comparison of different, potentially unrelated patterns. The minimum GBSI density divided by the average GBSI density of one grain boundary pattern can be described as minimum intensity, I_{min}, and is a useful parameter to quantify SPO strength. The I_{min} values of GBSI density change systematically with increasing strain. Plotting the evolution of I_{min} versus the axial ratio (long/short axis of the fitted ellipse) as data points shows a general trend that can be best described by a power law relationship. I_{min} has the potential to be refined to develop generalised I_{min} versus r diagrams with reference power curve(s) that allows not only to compare samples but also to track sample evolution with ongoing strain, and reconstruct and predict grain shapes, SPOs, and related geometric grain boundary pattern characteristics.

6.1.2 Grain boundary (shape) evolution during deformation

The main objective for chapter 3 was the systematic evaluation of GBPaQ and the GBSI methodology by analysing numerical models with pre-defined characteristics and over simulated deformation. Eight models of foam texture grain patterns generated by viscoplastic numerical simulations and with pre-defined characteristics such as variation of grain size (coarse and fine grained), phase content (single- and two-phase, simple, and complex fabrics), and simple and pure shear strain geometry were run up to a natural strain of 2. This evolution was captured in 100 incremental steps, which were analysed via the introduced grain boundary segment- and GBSI-based workflow using GBPaQ. The study shows sensitivity and value of the GBSI method introduced in chapter 2 for the quantification of the pre-defined characteristics:

The evolution of grain boundary patterns is of interest because grain interfaces host and transmit fluids, are preferred sites where genetic and metamorphic reactions occur, exert first-order control on material strength, and attenuate acoustic seismic waves. Therefore, this study has a broad application across metamorphic petrology, tectonics, structural geology, geophysics, mineral and rock physics and material sciences.

- Grain size

Grain size affects the sampling statistics of the GBSI analysis such that the finer the grain size, the clearer the results, therefore results are scalable. All major trends are visible in coarse grained and fine-grained model results.

- Viscosity contrast

The comparison of single- and two-phase simulations shows that phase composition has a strong influence on the grain boundary development, which is recorded by the GBSI method. Dual viscosity (two-phase models) results in the development of shear bands with weaker SPO of each phase, individually and combined, compared to single-phase models that develop a single foliation. Each of the two grain phase populations changes in shape and shape orientation, which proves to be interdependent of each other's distribution (cluster formation) and neighbouring grain contacts.

- Shape preferred orientation

The shape preferred orientation (SPO) is stronger in single-phase models compared to two-phase models at any given natural strain > 0.04, and independent from the end-member strain model. The weaker SPO of two-phase patterns is visible in the GBSI

density contour plots by weaker minima and maxima, with higher minimum intensity (I_{min}) compared to single-phase models.

- GBSI density-based minimum intensity (I_{min})

Differences in the I_{min} evolution of all eight models are minimal at low strains and become more pronounced after > 0.2 natural strain, with two-phase models having weaker GBSI density minima and maxima. The pure shear models have a slightly stronger SPO compared to simple shear. GBSI density based I_{min} for the simple shear models is always slightly higher.

- Strain geometry

Grain boundary segment-based analysis can differentiate between strain geometries. SPO develops quickly in both, simple and pure shear, after ~ 0.1 natural strain, and evolves in orientation in simple shear, whereas a preferred orientation quickly stabilises in pure shear. This agrees with literature and models of shear zones. Grain boundary segment azimuth roses show different mean orientation evolution depending on the strain geometry. The difference between simple shear and pure shear also effects the shape of the GBSI density contour evolution (orientation and round vs. tipped hourglass).

6.1.3 Acoustic wave velocities in evaporites

It has been recognized that acoustic wave velocity anisotropy in evaporite rocks is not only controlled by crystallographic (preferred) orientation but that other factors like grain boundary alignment, fractures, and mixtures of evaporitic minerals contribute too (e.g., Crampin, 1985; Lo et al., 1986; Popp and Kern, 1998; Raymer and Kendall, 1998; Mah and Schmitt, 2003; Lloyd et al., 2011; Zong et al., 2014).

The fourth chapter of this thesis presents new data that will help in the future to understand how each factor contributes specifically, and their combined influence on seismic wave velocity anisotropy, which is still unknown. The improvement of seismic imaging of evaporites is important for various fields, including oil and gas industry, storage of hydrocarbons, toxic and nuclear waste in rock salt bodies, and engineering and maintenance of buildings and tunnels.

Acoustic wave velocity and microstructural analysis of natural evaporites with halite, polyhalite, anhydrite, gypsum, and mixed phase rocks from three deposits (North Sea, Òdena, and Boulby) demonstrate that natural single and mixed phase evaporites can

have significant anisotropic P-wave and S-wave velocity characteristics. These rocks preserve CPOs and SPOs with different strengths and patterns, as well as fractures and veins, which contribute to the measured velocity anisotropy.

- Acoustic velocity data for mono- and polymineralic evaporites

New velocity data from natural evaporites with halite, polyhalite, anhydrite, gypsum, and mixed phase rocks from three deposits attests that all samples show velocity anisotropies of up to 60 % AV_P and 34 % AV_S. The V_P and V_S ranges are generally lower than expected from single crystal ranges (that relate to crystallographic orientation), indicating other contributions to velocity variations than simply intrinsic mineralogical anisotropy. Nearly all North Sea and all Òdena quarry samples have very low but in range single crystal end member V_P.

- Crystallographic preferred orientation

Crystallographic preferred orientation (CPO) is present in both analysed sample sets of North Sea anhydrite and Òdena quarry samples containing anhydrite and gypsum. Using multiples of uniform distribution (m.u.d.) and *M*-index as a measure of CPO strength, the maximum strength is a little lower in Òdena quarry samples. The CPO of North Sea anhydrite with point clusters for {100} in the sample X direction means that the direction of measurement (sample X) is parallel to the fast p-wave velocity direction, i.e., the fast direction is normal to bedding in real space. The point orientation data from sample N3-1T for {100} also suggests fast velocities, but closer to the Y-Z plane. The {100} poles of N4-1II suggest medium velocities in the Y-Z plane, as does N4-2T. The Òdena quarry samples have weaker CPOs than the North Sea samples, especially in {100}. In {010}, the clusters of poles are horizontal, which indicates slower velocity directions are in the Y-Z plane for these samples. As S-waves oscillate perpendicular to the direction of wave propagation, the characteristics of the Y-Z plane is also of importance.

- Microstructures and grain boundary pattern characteristics

The two sample suites tested show very different microstructures. The North Sea anhydrite samples had a systematic orientation of grain boundaries, caused by a bimodal SPO of lath-shaped grains, with a perpendicular grain shape relationship. The mean grain size ranges between 26.50 ± 31.61 µm and 89.71 ± 57.32 µm, the mean axial ratio between 1.70 ± 0.69 and 2.35 ± 1.29, and the minimum intensity,

introduced for quantification of SPO strength, ranges between 0.8 and 0.6. SPO was not quantified for the Òdena quarry samples. Spherulites are a common geometrical feature of the microstructure in the Òdena quarry samples and typically have a successive change of crystallographic orientation over multiple blades. The spherulitic texture is likely to impact variations of V_S and V_P velocities. The gypsum veins in the Òdena quarry samples have two preferred orientations around 30 to 60° and 120 to 150° to the core Y-direction. As both, V_P and V_S velocities are slower for gypsum compared to anhydrite, gypsum veins with crystallographic or spatial preferred orientations potentially cause velocity anisotropy.

- Introduction of a workflow

A more complete microstructural characterisation of evaporites was presented, which includes CPO and automated grain boundary-based SPO quantification that could be used in predictive models of velocity anisotropy. The workflow combines EBSD crystallographic orientation analysis, established fitted ellipse based SPO quantification, basic grain boundary segment orientation statistical analysis, high resolution grain boundary segment intercept density orientation and minimum intensity analysis, and fracture (vein) distribution and orientation analysis. This workflow is a first step to build on in future studies to quantify the impact of petrofabrics on acoustic wave velocity anisotropy.

6.1.4 Rapid hydration and weakening under stress

Chapter 5 studies the effects of non-hydrostatic stress and strain rate on the hydration of polycrystalline anhydrite samples via laboratory triaxial deformation experiments. There is an ongoing discussion about the importance of stress for chemical reactions (e.g., Wheeler, 2018). Chemical reactions and especially hydration reactions are common for rocks under crustal and mantle conditions, where non-hydrostatic stress states are prevalent. Most studies in the $CaSO_4*H_2O$ system have their focus on the dehydration reaction. There is no other study, where natural anhydrite polycrystalline aggregates were successfully hydrated experimentally, and with focus on microstructure, deformation behaviour, and hydration reaction under stress.

Natural anhydrite samples with gypsum in veins (Òdena quarry samples, see chapter 4) were used for the experiments. Three deformation modes (dry, ‘wet’, and steady state differential compaction) were chosen, with the strain rate ranging between

$1.0 * 10^{-3}$ s^{-1} and $9.7 * 10^{-7}$ s^{-1}, confining pressures of 30, 50, or 100 MPa, and fluid pressures of 20, 40, or 90 MPa. Post-experimental microstructural analysis and the mechanical behaviour during the testing showed that new gypsum formed in extensional and shear veins within mere hours and that samples are mechanically weaker.

- Evidence for new gypsum and rapid hydration

Post-experiment samples after 'wet' and steady state differential compaction (ssdc) mode tests show increased gypsum content in veins with extensional and shear sections and brecciated veins, consistently oriented in shear fracture orientation. Gypsum clasts in the brecciated veins are orders of magnitude lager than any observed pre-experiment gypsum. Microstructures formed during a 6-hour long experiment with ssdc conditions also show that the gypsum was part of a shear interface with active gypsification before brecciation occurred. Aperture, length, and orientation of gypsum filled veins are strong indicators for experimentally induced extension and formation of new gypsum in under 20 minutes in a sample that underwent a 'wet' mode experiment. Previous studies failed to produce gypsum over months under hydrostatic condition, which suggests an intrinsic relationship between application of a non-hydrostatic stress field and the rate of hydration reaction.

- The link of gypsum growth to the stress geometry

The study proposes that inheritance of crystal orientations from wall-rock anhydrite grains combined with crystal orientations favourable for nucleation and growth under the applied stress field led to selective crystallographic orientations of the newly-formed vein gypsum. The crystallographic orientations of newly-formed vein gypsum are systematic, and gypsum is not always topotactically linked to the wall-rock anhydrite. The crystallographic orientation of the vein gypsum is such that poles to {010} coincide with the direction of maximum shear stress during the experiments. This geometric link between gypsum growth and stress during an experiment and independent of the surrounding anhydrite has not been described before.

- Mechanical-chemical coupling

The spatial links between newly-formed gypsum and fractures show that hydration predominantly progressed through the fracture network that was created by the experiments. Pre-existing gypsum in the samples acted as a natural seeding material.

Therefore, hydration was possible as soon as the samples had water contact and more likely in ssdc experiments due to the amount of time of contact with H_2O.

Solid-fluid contacts will be at the pressure of the fluids (P_f), whilst solid-solid contacts will have a higher average normal stress, depending on the bulk effective pressure and contact area (Llana-Fúnez et al., 2012). That provides different pathways of Ca^{2+} and SO_4^{2-} ions during the reaction. Therefore, anhydrite solution was preferentially formed in the stressed anhydrite at fracture tips, grain boundaries, and at gypsum-anhydrite contacts. Once gypsum nuclei were established, growth was likely to be rapid, following the findings of Sievert et al. (2005).

Cataclastic flow and the full development of major shear fractures (Fig. 5.7a,b, iv) occurred after peak stress was reached during the experiments. The 'wet' tests show that these major shear fractures are all filled with gypsum. These form planar zones of weakness for catastrophic shear failure.

- Mechanical strength

A consequence of hydration under stress is the weakening of the mechanical strength during deformation. Samples that experienced ssdc have lower peak strength compared to 'wet' and dry runs with the same strain rate. One sample failed catastrophically at the beginning of the ssdc phase, with a maximum differential stress that was 41 % less compared to 'wet' experiments. The other ssdc test reached a peak strength that was 14 % lower than that of the 'wet' experiments. The microstructural analysis shows that the new gypsum is located along fractures in extensional and shear orientations, creating planes of weakness, and lowering the mechanical strength.

6.2 Outlook

There three main future directions this thesis leads to. First, there are the advances for the quantification of boundary-based microstructures with implications for studying the links between deformation mechanisms or chemical reactions and other aspects to grain boundary patterns. Secondly, the development towards a basic understanding, including factor-by-factor quantification, of the impacts of petrofabrics on seismic velocity anisotropy and subsequently the improvement of seismic imaging of evaporites. And finally, insights of the role and processes connected to chemical reactions in stressed environments, which are also of major importance for

understanding the seismic characteristics of evaporitic bodies, where hydration and dehydration reactions are key for mineral composition, mechanical behaviour, and structural characteristics.

There are several future directions that the introduction of GBPaQ (chapter 2) leads to: further development of GBPaQ as an accessible and useful toolbox, application of the GBSI-based method including I_{min} and I_{min} curves, implementation of smoothing functions, study of the potential of GBSI density-based analysis to trace deformation evolution and mechanisms (chapter 3), the link to quantification of the impact of grain boundary patterns on acoustic velocity anisotropy (and ultimately seismic velocity anisotropy), and the application to natural sample sets (chapter 4).

Future studies based on the findings of chapter 3 should include numerical simulations with different parameter space to further evaluate the abilities, strengths and weaknesses of the workflow, a variety of natural samples with corresponding parameter space to undertake the transition from models to natural samples and upscaling of GBSI density to 3D models of SPOs.

The study presented in chapter 4 adds to the currently small database on acoustic velocity measurements of textural and mineralogical complex evaporites. However, a direct quantification of the impact of petrofabrics on acoustic wave velocity requires a systematic study of evaporitic samples of a wide variety, and the means to quantify and compare their characteristics with a customized, highly developed workflow. The presented results are part of the basis for such research.

The following twelve specific directions for future research are a natural continuation of the research presented in this thesis.

6.2.1 Development of GBPaQ

The toolbox GBPaQ needs to be further developed in regards of the addition of flexibility for pattern analysis, such as variation of scan line positioning from radial analysis to grid analysis. Currently, only one central scan line rotation centre is projected on the pattern. Supplementary functions that might be of value are a) adjustable grid points for positioning multiple scan line centres, and b) scan line grids with adjustable distance and number of parallel lines with selected angles. Analysis should be either accumulative, summarising GBSI density from all scan lines with one

direction, or spatial, showing the GBSI density evolution throughout the pattern from scan line to scan line.

6.2.2 Quantification of the deformation evolution of grain boundary patterns

Analysis of a variation of patterns with different characteristics and throughout deformation is necessary to fully understand the potential of this method. Chapter 3 of this thesis includes such a study.

6.2.3 Implementation of GBSI data in seismic velocity studies

Next to CPO in a polycrystalline medium, grain boundary density, and thus SPO, is considered as another impedance factor on velocity anisotropy. Ultrasonic wave velocity is measured via sending an acoustic signal (wave) from a pulse generator to a receiver through a sample body. For anisotropy measurements on cuboids, the wave velocity is measured along the three principal orthogonal X-Y-Z directions to assess the grain scale affects that contribute to the total anisotropy. A 3D volume representing the GBSI density is potentially comparable to ultrasonic velocity anisotropy plotted as 3D surfaces (AnisoVis results). Future objective is to generate a GBSI density toroid from orthogonal data of a natural sample with SPO to study a) the feasibility, b) compare results with the concept model, and b) attempt to combine it with results from acoustic velocity anisotropy measurements and CPO data.

6.2.4 Expansion of parameter space of numerical simulations

Testing the response of the GBSI method to quantify different deformation mechanisms and parameters, i.e., dislocation climb, grain boundary migration, etc. via tracing the evolution of simulated pattern deformation might lead to an innovative workflow that is capable to quantify those mechanisms and parameters in real samples. For example, recrystallisation dominated by subgrain rotation or grain boundary migration has major impact on the grain size, and grain boundary geometry evolution. As such, a refined grain boundary segment intercept density method, including GBSI density I_{min} analysis, and GBSI density contour rose evolution has the potential to impact a broader community that is interested in grain boundary pattern quantification.

6.2.5 Analysis of natural samples with GBPaQ

Samples from simple shear and pure shear zones, with multiple phases (i.e., gneiss) or a single phase (i.e., deformed rock salt) can be analysed via GBPaQ and a workflow that includes the determination of a mean grain axial ratio with standard deviation.

Plotted on an axial ratio versus I_{min} diagram with standardised curves it can transition to reconstruction of the shear zone and to determination of strain. Results of a first attempt with natural samples are presented in chapter 4.

6.2.6 Microstructural link to acoustic velocity anisotropy in cuboid samples

Microstructural analysis of the five studied cuboid samples is necessary to quantify their microstructures and CPO. The study shows that one sample of halite mixed with clay has a P-wave velocity anisotropy as high as 60 % AV_P, whereas another pure halite sample ranges to 4 % AV_P. The presented analysis is not sufficient to understand these differences and further characterisation should provide valuable data. Nearly all North Sea and all Òdena quarry samples have very low but in range single crystal end member V_P means that both types of rocks possibly have either: a strong CPO in a slow V_P crystal orientation, which means the CPO over all samples is very similar; or the sample suite contains other characteristics that lower the velocities. The former idea could be tested by a 'rock recipe' approach (Lloyd et al., 2011), or alternative approaches for the estimation of velocity anisotropy from CPOs (Zhong et al., 2014; Vel et al., 2016).

6.2.7 Sample material for future research

A variety of evaporite samples with a range of different petrofabrics is necessary to systematically study how each extrinsic and intrinsic parameters ultimately influence seismic velocity anisotropy. Key is to detect and control CPO, as it is assumed to be the main contributor. A future objective is to use pure constriction deformation experiments to create strong CPO and SPO. For example, 'dry' halite cuboids at relatively low temperatures (~175 °C), strain rates of $2 * 10^{-7}$ s^{-1} and finite strain of > 40 % should deform via subgrain rotation recrystallisation and result in strong CPO (e.g., Trimby et al., 2000). Relatively higher temperatures (~350 °C), a strain rate of $2 * 10^{-7}$ s^{-1}, and a final strain of 25 %, should deform halite samples via dislocation creep of edge dislocation and fluid assisted grain boundary migration. Such conditions allow the formation and development of strong SPO. Next to experimental control, the preparation of synthetic samples with distinct grain size, phase content and distribution (i.e., foliation) is another option to quantify the impact of such characteristics on acoustic wave velocity anisotropy.

6.2.8 Complete evaluation of V_P and V_S anisotropy

The workflow for grain boundary pattern quantification developed in chapters 2 and 3 that incorporates GBSI density analysis has the potential to lead to 3D GBSI density models (Fig. 6.1). Such models should be comparable to stereographic projections of compressional velocity (V_P), shear-wave splitting (AV_S) and polarisation of the fast shear wave velocity (V_{S1}), calculated using EBSD-derived CPO and stiffness matrix coefficients and densities of single crystals (after Mainprice, 1990).

Naturally, the next step is the quantification of grain boundary SPO from three orthogonal faces from natural evaporite samples to develop 3D grain boundary distribution models that could be used for acoustic wave attenuation calculations. A rigorous combination of 3D grain boundary distribution with CPO information and crack tensors from natural samples provides the workflow for a complete evaluation of V_P and V_S anisotropy.

6.2.9 Upscaling to 3D GBSI density SPO

Most studies of real rocks and other aggregates use three orthogonal sections to model 3D sample characteristics, with only few being able to measure directly in 3D (i.e., Micro-CT). GBSI density-based analysis in 3D has not yet been attempted.

Nevertheless, it can be predicted that 3D GBSI density analysis of grain boundary patterns with simple foliation hypothetically leads to the shape of quasi-toroidal (horn torus), orthorhombic symmetry 3D GBSI density plots (Fig. 6.1). No SPO or very weak SPOs should result in a shape that is close to a sphere. Grains (particles) that form a SPO possibly are equidimensional in two orthogonal directions (uniform flattening or extension).

Uniform flattening (X=Y>>Z) results in a 3D shape of a sphere with a ‘neck’. In case of uniform extension (X>>Y=Z), the sphere develops a symmetric funnel in the centre (horn torus). When the grains (particles) are not equidimensional (plane strain, X>Y>Z), the sphere not only forms funnels but also becomes increasingly elliptical with increasing strain (SPO), with the longest dimension representing the maximum GBSI density orientation (γ) (Fig. 6.1c,d).

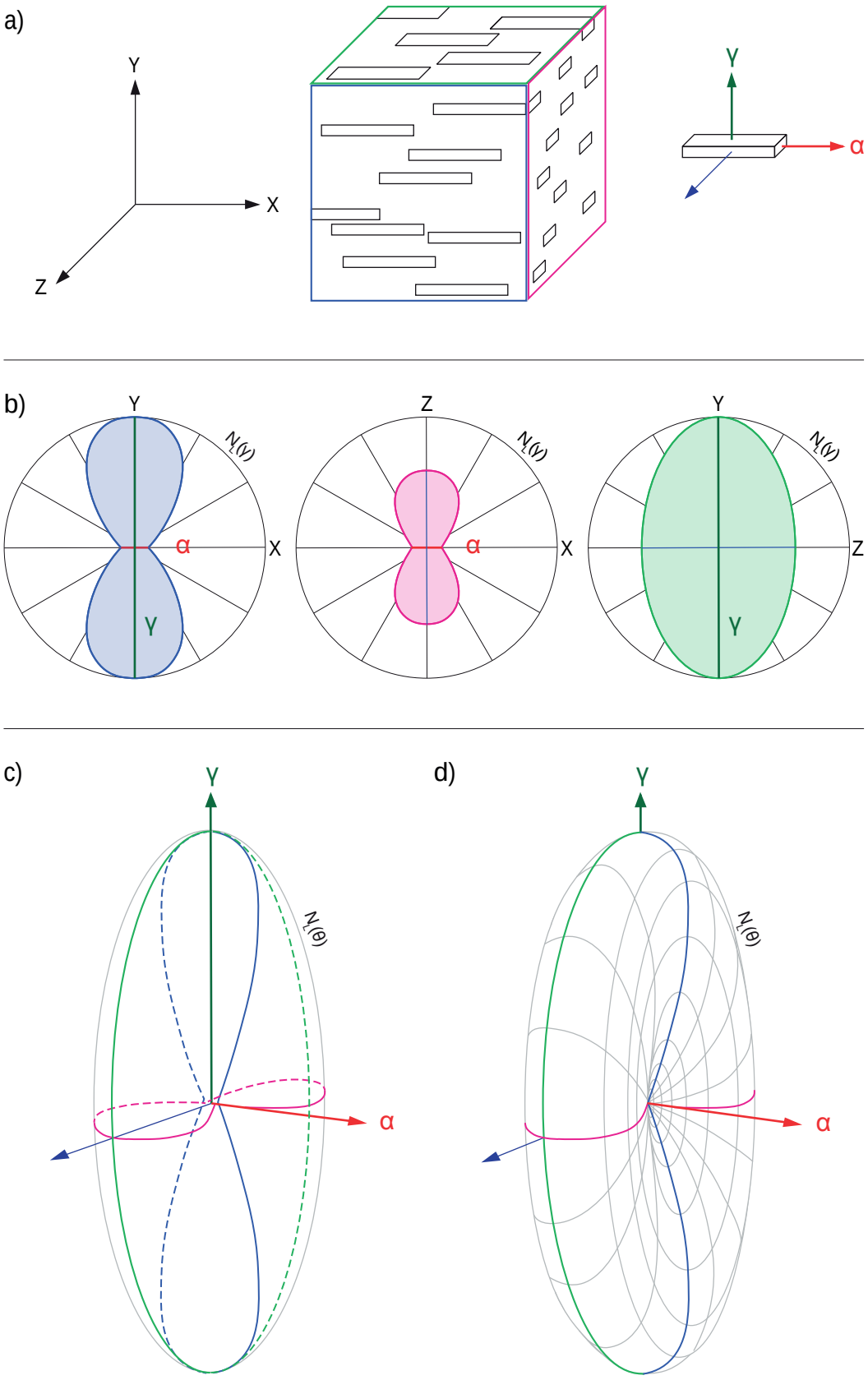

Figure 6.1: Concept model of how GBSI density of what a single foliation SPO is likely to look in 3D, based on a set of three hypothetical, orthogonal GBSI density contours. a) Sketch of three orthogonal surfaces of a sample with simplified SPO, and orientation of a single representative 'particle'. Surfaces and 'particle' are both placed relative to

principal orientations X,Y,Z. α is the minimum, and γ the maximum GBSI density orientation. b) Model GBSI density contour roses of the three orthogonal planes (XY, XZ, and ZY). c) GBSI density contours merged relative to their orientation to each other in 3D. d) Full shape of the horn torus representing the 3D SPO GBSI density.

6.2.10 Analysis of post-experimental microstructures in Zechstein anhydrite

The absence of thin section material and therefore missing microstructural analysis led to chapter 4 including data from only one out of two sample sets. This strongly suggests to continue by analysing the missing Zechstein anhydrite sample set and comparing the outcomes to the presented data.

The mechanical behaviour and observations from the post-experiment pure Zechstein anhydrite samples already show local loss of cohesion in one steady state differential compaction (ssdc) mode test. Intense shear fracturing and expulsion of an off-white slurry were also observed after a 'wet' mode test on Zechstein anhydrite. Clarification of the presence or absence of newly-formed gypsum in the Zechstein anhydrite samples after triaxial tests with water present has not been obtained yet.

6.2.11 Anhydrite hydration and acoustic velocity

The influence of fracturing and hydration in anhydrite on acoustic wave velocity could potentially be measured in situ with special equipment for the high-pressure, high-temperature (HP/HT) triaxial rock deformation apparatus (TRI-X 250 MPa/200 °C) from Sanchez Technologies. Further, such results could then be compared with those on acoustic wave velocity and velocity anisotropy of natural evaporites presented in chapter 4 of this thesis. This also leads to testing whether slower-than expected V_P and V_S in anhydrite is impacted by the presence of hydrated phases along grain and fracture interfaces. Therefore, quantifying the microstructural differences between the North Sea samples and combining the results with those of the three Òdena quarry samples, with emphasis on variation of mineral content, is crucial to evaluate if and how other factors like SPO, mineral content and fractures impact the velocity and velocity anisotropy.

6.2.12 Experiments on anhydrite hydration at different deformation conditions

Further experimental data about the impact of stress on hydration rate in the $CaSO_4 \cdot H_2O$ system will provide more details about the conditions (i.e., temperature, pressure, strain rate, deformation regime) hydration is active under, the hydration

mechanisms, the role of fractures, mineral content, and mechanical strength. Triaxial deformation experiments under conditions in favour of ductile anhydrite deformation including a 'wet' mode and a ssdc mode could be tested. De Paola et al. (2009) found that ductile deformation of anhydrite was achieved in experiments at room temperature, a strain rate of $9 * 10^{-8}$ s^{-1}, 100 MPa confining pressure, and fluid pressure of 40 MPa (effective pressures < 20 MPa) at grain sizes of 10 μm to 1 mm. Evidence for hydration of anhydrite was not found. A form of gypsum seeding, or the use of reaction enhancing cation activators ($K^+ \geq Na^+ \geq NH_4^+ > Mg^{++} > Fe^{++} > H^+ > Al^{+++} > Ca^{++}$; Leininger et al., 1957) in the hydrating fluid and long fluid exposure time could potentially activate and accelerate the hydration reaction.

6.3 Conclusions

Evaporites and their unique characteristics play a key role in several fields of geoscientific research and are strongly connected to engineering challenges, the emerging energy crisis caused by the Russian invasion of Ukraine, and the developments in the oil and gas industry. The improvement of seismic imaging is strongly connected to understanding evaporitic bodies in terms of their inhomogeneous structure, composition, and complex dynamic evolution.

The main objective of this thesis was to study the link between petrofabrics and seismic anisotropy, with focus on the quantification of grain boundary pattern geometry, evaporite petrofabrics and experimental hydration of anhydrite to gypsum under stress. This thesis consists of four scientific chapters, that each focus on specific aspects of the overall objective. These chapters are written as independent manuscripts and are in preparation for publication. The achievements of this thesis include:

A) The presentation of a new, semi-automated toolbox of MATLAB™ scripts, named Grain Boundary Pattern Quantification (GBPaQ). GBPaQ incorporates a grain boundary geometry quantification method based on segment intercepts (GBSI method; chapter 2) for more detailed pattern quantification and directional characterisation of grain boundary networks.

B) Testing of this semi-automated approach for grain boundary pattern evolution assessment on numerical models of single- and two-phase materials that underwent

simulated deformation via dislocation glide in simple and pure shear (chapter 3) with the results that show significant differences for each of the tested models.

C) The presentation of new data for the investigation of the links between petrofabrics and velocity anisotropy in natural evaporitic samples with variations of mineral content, and texture (chapter 4). Effective combination of ultrasonic velocity measurements, crystallographic preferred orientation analysis and the proposed quantification approach for grain boundary pattern geometry.

D) Reports of the first successful hydration of natural anhydrite rocks to gypsum under non-hydrostatic stress conditions, achieved over several hours, and using triaxial deformation experiments (chapter 5). Complex links among mechanical-chemical coupling, microstructure, and the spatial distribution and timing are revealed.

The studies presented in this PhD thesis lay the ground works for future research in several scientific directions. The potential of the application of the semi-automated GBSI quantification methodology to grain boundary pattern quantification for rocks and crystalline materials is promising, and will benefit from future improvements. Studying a broader variety of evolving numerical models with GBPaQ and including grain boundary segment intercept-based quantification methods will further develop how we look at grain boundary networks and deformation mechanisms. The impact of petrofabrics on seismic velocity in evaporites is still not fully understood, and studying a larger, more diverse dataset of evaporitic rocks is required to cover the full range of naturally occurring petrofabrics in rock salt. The role of stress on chemical reactions like hydration is a greatly discussed field of research, yet little experimental data is published and there is much potential for further projects.

THESIS BIBLIOGRAPHY

Agterberg, F. P., Fabbri, A. G. (1978): Spatial correlation of stratigraphic units quantified from geological maps. Computers & Geosciences 4 (3), p. 285–294. DOI: 10.1016/0098-3004(78)90063-8.

Almqvist, B. S. G., Hirt, A. M., Herwegh, M., Ebert, A., Walter, J. M., Leiss, B., Burlini, L. (2013): Seismic anisotropy in the Morcles nappe shear zone. Implications for seismic imaging of crustal scale shear zones. Tectonophysics 603, p. 162–178. DOI: 10.1016/j.tecto.2013.05.025.

Armann, M. (2008): Microstructural and textural development in synthetic rocksalt deformed in torsion. Doctoral Thesis, ETH-Zürich, Switzerland. 127 p. DOI: 10.3929/ethz-a-00566684.

Austrheim, H. (1987): Eclogitization of lower crustal granulites by fluid migration through shear zones. Earth and Planetary Science Letters 81 (2-3), p. 221-232. DOI: 10.1016/0012-821X(87)90158-0.

Austrheim, H., Griffin, W. L. (1985): Shear deformation and eclogite formation within granulite-facies anorthosites of the Bergen Arcs, western Norway. Chemical Geology 50 (1-3), p. 267-281. DOI: 10.1016/0009-2541(85)90124-X.

Bachmann, F., Hielscher, R., Jupp, P. E., Pantleon, W., Schaeben, H., Wegert, E. (2010): Interential statistics of electron backscatter diffraction data from within individual crystalline grains. Journal of Applied Crystallography 43, p. 1338-1355. DOI: 10.1107/S002188981003027X.

Barrett, S. D. (2002): Software for Scanning Microscopy. Proceedings Royal Microscopical Society 37 (3), p. 167–174.

Barrett, S. D., Bickmore, B. R., Rufe, E., Hochella, M. F., Torzo, G., Cerolini, D. (1998): The Use of Macros in Atomic Force Microscopy Image Analysis and Image Processing. Journal of Computer-Assisted Microscopy 10 (2), p. 77–82. DOI: 10.1023/A:1023364405573.

Barros, P., Amaral, P. J., Girardi, T., Martini, A., Maul, A., González, M. (2017): Salt-Focused Inversion in the Santos Basin. 15th International Congress of the Brazilian Geophysical Society & EXPOGEF, Rio de Janeiro, Brazil. Conference Proceedings, p. 1147–1151. DOI: 10.1190/sbgf2017-223.

Bartozzi, M., Boyle, A. P., Prior, D. J. (2000): Automated grain boundary detection and classification in orientation contrast images. Journal of Structural Geology 22 (11-12), p. 1569–1579. DOI: 10.1016/S0191-8141(00)00084-5.

Bass, J. D. (1995): Elasticity of Minerals, Glasses and Melts. Mineral Physics and Crystallography - A handbook of physical constants, Volume 2. American Geophysical Union. p. 45–63. DOI: 10.1029/RF002p0045.

Bayrakci, G., Minshull, T. A., Sawyer, D. S., Reston, T. J., Klaeschen, D., Papenberg, C., Ranero, C., Bull, J. M., Davy, R. G., Shillington, D. J., Perez-Gussinye, M., Morgan, J. K.: Corrigendum (2016): Fault-controlled hydration of the upper mantle during continental rifting. Nature Science 9, p. 384-388. DOI: 10.1038/NGEO2671.

Becker, G. F. (1893): Finite homogeneous strain, flow and rupture of rocks. Geological Society of America Bulletin 4 (1), p. 13–90. DOI: 10.1130/GSAB-4-13.

Bedford, J. (2017): The kinetics and mechanics of a dehydrating system and the deformation of porous rock. Doctoral thesis. University of Liverpool (United Kingdom) ProQuest Dissertation Publishing, 172 p. 2017. 28209468.

Beggan, C., Hamilton, C. W. (2010): New image processing software for analyzing object size-frequency distributions, geometry, orientation, and spatial distribution. Computers & Geosciences 36 (4), p. 539–549. DOI: 10.1016/j.cageo.2009.09.003.

Bell, F. G. (1994): A survey of the engineering properties of some anhydrite and gypsum from the north and midlands of England. Engineering Geology 38 (1-2), p. 1–23. DOI: 10.1016/0013-7952(94)90021-3.

Berger, A., Herwegh, M., Schwarz, J.-O., Putlitz, B. (2011): Quantitative analysis of crystal/grain sizes and their distributions in 2D and 3D. Journal of Structural Geology 33 (12), p. 1751–1763. DOI: 10.1016/j.jsg.2011.07.002.

Bickmore, B. R., Rufe, E., Barrett, S. D., Hochella, M. F. (1999): Measuring Discrete Feature Dimensions in AFM Images with Image SXM. Geological Materials Research 1 (5), p. 1–19.

Birch, F. (1960): The velocity of compressional waves in rocks to 10 kilobars. 1. Journal of Geophysical Research 65 (4), p. 1083–1102. DOI: 10.1029/JZ065i004p01083.

Blumenfeld, P., Bouchez, J.-L. (1988): Shear criteria in granite and migmatite deformed in the magmatic and solid states. Journal of Structural Geology 10 (4), p. 361–372. DOI: 10.1016/0191-8141(88)90014-4.

Boeyens, J. C. A., Ichhram, V. V. H. (2002): Redetermination of the crystal structure of calcium sulphate dihydrate, $CaSO_4*2H_2O$. Zeitschrift fuer Kristallographie 217 (1), p. 9–10. DOI: 10.1524/ncrs.2002.217.1.9.

Boullier, A. M., Gueguen, Y. (1975): SP-Mylonites. Origin of some mylonites by superplastic flow. Contributions to Mineralogy and Petrology 50 (2), p. 93–104. DOI: 10.1007/BF00373329.

Bourke, P. D. (1987): A contouring subroutine. Byte 12 (6), p. 143–150.

Brantut, N., Schubnel, A., David, E. C., Héripré, E., Guéguen, Y., Dimanov, A. (2012): Dehydration-induced damage and deformation in gypsum and implications for subduction zone processes. Journal of Geophysical Research 117 (B3), 17 p. DOI: 10.1029/2011JB008730.

Bras, E., Baïsset, M., Yamato, P., Labrousse, L. (2012): Transient weakening during the granulite to eclogite transformation within hydrous shear zones (Holsnøy, Norway). Tectonophysics 819 (229026), 17 p. DOI: 10.1016/j.tecto.2021.229026.

Brown, S. R., Bruhn, R. L. (1998): Fluid permeability of deformable fracture networks. Journal of Geophysical Research 103 (B2), p. 2489-2500. DOI: 10.1029/97JB03113.

Burlini, L., Kunze, K. (2000): Fabric and seismic properties of Carrara marble mylonite. Physics and Chemistry of the Earth, Part A: Solid Earth and Geodesy 25 (2), p. 133–139. DOI: 10.1016/S1464-1895(00)00022-3.

Cantisani, E., Pecchioni, E., Fratini, F., Garzonio, C. A., Malesani, P., Molli, G. (2009): Thermal stress in the Apuan marbles: Relationship between microstructure and petrophysical characteristics. International Journal of Rock Mechanics and Mining Sciences 46 (1), p. 128–137. DOI: 10.1016/j.ijrmms.2008.06.005.

Capaccioni, B., Nappi, G., Valentini, L. (2001): Directional fabric measurements: an investigative approach to transport and depositional mechanisms in pyroclastic flows. Journal of Volcanology and Geothermal Research 107 (4), p. 275–292. DOI: 10.1016/S0377-0273(00)00316-4.

Capaccioni, B., Sarocchi, D. (1996): Computer-assisted image analysis on clast shape fabric from the Orvieto-Bagnoregio ignimbrite (Vulsini District, central Italy): implications on the emplacement mechanisms. Journal of Volcanology and Geothermal Research 70 (1-2), p. 75–90. DOI: 10.1016/0377-0273(95)00049-6.

Capaccioni, B., Valentini, L., Rocchi, M. B. L., Nappi, G., Sarocchi, D. (1997): Image analysis and circular statistics for shape-fabric analysis: applications to lithified ignimbrites: Bulletin of Volcanology, v. 58, no. 7, p. 501–514. DOI: 10.1007/s004450050158.

Carter, N. L., Heard, H. C. (1970): Temperature and rate dependent deformation of halite. American Journal of Science 269 (3), p. 193–249. DOI: 10.2475/ajs.269.3.193.

Clark, J. A., Stewart, S. A., Cartwright, J. A. (1998: Evolution of the NW margin of the North Permian Basin, UK North Sea. Journal of the Geological Society 155 (4), p. 663-676. DOI: 10.1144/gsjgs.155.4.0663.

Conley, R. F, Bundy, W. M. (1958): Mechanism of gypsification. Geochimica et Cosmochimica Acta 15 (1-2), p. 57–72. DOI: 10.1016/0016-7037(58)90010-3.

Crampin, S. (1985): Evaluation of anisotropy by shear-wave splitting. Geophysics 50 (1), p. 142–152. DOI: 10.1190/1.1441824.

Daniel, T., Gapais, D., Lecorre, C. (1988): Application du traitement de l'image à l'analyse de la déformation des granites. Deformation analysis of granites using image processing. Sciences Géologiques. Bulletin 41 (2), p. 143–161. DOI: 10.3406/sgeol.1988.1788.

De Meer, S., Spiers, C. J. (1997): Uniaxial compaction creep of wet gypsum aggregates. Journal of Geophysical Research, 102, B1, p. 875-891. DOI: 10.1029/96JB02481.

De Paola, N., Collettini, C., Trippetta, F., Barchi, M. R., Minelli, G. (2007): A mechanical model for complex fault patterns induced by evaporite dehydration and cyclic changes in fluid pressure. Journal of Structural Geology 29 (10), p. 1573–1584. DOI: 10.1016/j.jsg.2007.07.015.

De Paola, N., Faulkner, D. R., Collettini, C. (2009): Brittle versus ductile deformation as the main control on the transport properties of low-porosity anhydrite rocks. Journal of Geophysical Research, 114, B06211, 17 p. DOI: 10.1029/2008JB005967.

Dell'Angelo, L. N., Olgaard, D. L. (1995): Experimental deformation of fine-grained anhydrite. Evidence for dislocation and diffusion creep. Journal of Geophysical Research 100 (B8), p. 15425–15440. DOI: 10.1029/95JB00956.

Desbois, G., Zavada, P., Schléder, Z., Urai, J. L. (2010): Deformation and recrystallization mechanisms in naturally deformed salt fountain: microstructural evidence for a switch in deformation mechanisms with increased availability of meteoric water and decreased grain size (Qum Kuh, central Iran). Journal of Structural Geology 32 (4), p. 580–594. DOI: 10.1016/j.jsg.2010.03.005.

Dohmen, R., Milke, R. (2010): Diffusion in polycrystalline materials: grain boundaries, mathematical models, and experimental data. Reviews in Mineralogy and Geochemistry 72, p. 921–970. DOI: 10. 2138/ rmg.2010. 72. 21.

Dunnet, D. (1969): A technique of finite strain analysis using elliptical particles. Tectonophysics 7 (2), p. 117–136. DOI: 10.1016/0040-1951(69)90002-X.

Elliott, D. (1970): Determination of Finite Strain and Initial Shape from Deformed Elliptical Objects. Geological Society of America. Bulletin 81 (8), p. 2221-2236. DOI: 10.1130/0016-7606(1970)81[2221:DOFSAI]2.0.CO;2.

Fan, S., Prior, D. J., Cross, A. J., Goldsby, D. L., Hager, T. F., Negrini, M., Qi, C. (2021): Using grain boundary irregularity to quantify dynamic recrystallization in ice. Acta Materialia 209 (116810), p. 1-22. DOI: 10.1016/j.actamat.2021.116810.

Farnsworth, M. (1925): The Hydration of Anhydrite. Industrial and Engineering Chemistry 17 (9), p. 967-970. DOI: 10.1021/ie50189a037.

Fischer, N. I. (1993): Statistical Analysis of circular Data. Cambridge: Cambridge University Press, UK. 277 p. DOI: 10.1016/0012-8252(89)90031-7.

Flinn, D. (1962): On folding during three-dimensional progressive deformation. Quarterly Journal of the Geological Society 118 (1-4), p. 385–428. DOI: 10.1144/gsjgs.118.1.0385.

Fossen, H. (2016): Structural Geology. Cambridge University Press, 2nd Edition, USA. ISBN: 978-1-107-05764-7.

Fossen, H., Cavalcante, G. C. G. (2017): Shear zones - A review. Earth-Science Reviews 171, p. 434-455. DOI: 10.1016/j.earscirev.2017.05.002.

Franssen, R. C. M. W. (1993): Rheology of synthetic rocksalt with emphasis on the influence of deformation history and geometry on the flow behaviour. PhD Theses No. 113, Rijksuniversiteit Utrecht, 221 p. ISBN: 90-71577-67-8.

Franssen, R. C. M. W. (1994): The rheology of synthetic rock salt in uniaxial compression. Tectonophysics 233 (1-2), p. 1–40. DOI: 10.1016/0040-1951(94)90218-6.

Fry, N. (1979): Random point distribution and strain measurements in rocks. Tectonophysics 60 (1-2), p. 89–105. DOI: 10.1016/0040-1951(79)90135-5

Gerik, A., Kruhl, J. H. (2009): Towards automated pattern quantification: Time-efficient assessment of anisotropy of 2D patterns with AMOCADO. Computers & Geosciences 35 (6), p. 1087–1097. DOI: 10.1016/j.cageo.2008.01.015.

Gomez-Rivas, E., Butler, R. W. H., Healy, D., Alsop, I. (2020): From hot to cold - The temperature dependence on rock deformation processes: An introduction. Journal of Structural Geology 132 (6), p. 1-9. DOI: 10.1016/j.jsg.2020.103977.

González, M., Gobatto, F., Maul, A., Falcão, L., González, G., Oliveira, L. C. (2016): Proposed Workflow to Incorporate Stratification within Salt Section Using Velocity and Seismic Attributes. European Association of Geoscientists & Engineers, 3rd EAGE/SBGf Workshop 2016, Rio de Janeiro, Brazil. Conference Proceedings, 5 p. DOI: 10.3997/2214-4609.201600050.

Gottstein, G. (2004): Integral materials modelling. Modelling and Simulations in Material Science and Engineering 12 (1), 1 pp. DOI: 10.1088/0965-0393/12/1/E01.

Griera, A., Bons, P.D., Jessell, M.W., Lebensohn, R.A., Evans, L., Gomez-Rivas, E. (2011): Strain localization and porphyroclast rotation. Geology 39 (3), p. 275–278. DOI: 10.1130/G31549.1.

Griera, A., Llorens, M.-G., Gomez-Rivas, E., Bons, P.D., Jessell, M.W., Evans, L.A., Lebensohn, R. (2013): Numerical modelling of porphyroclast and porphyroblast rotation in anisotropic rocks. Tectonophysics 587, p. 4–29. DOI: 10.1016/j.tecto.2012.10.008.

Hangx, S. J. T., Spiers, C. J., Peach, C. J. (2010): Mechanical behaviour of anhydrite cap rock and implications for CO 2 sealing capacity. Journal of Geophysical Research 115 (B7), 22 p. DOI: 10.1029/2009JB006954.

Hangx, S.J.T., Spiers, C. J., Peach, C. J. (2011): The mechanical behaviour of anhydrite and the effect of deformation on permeability development–Implications for cap rock integrity during geological storage of CO_2. Energy Procedia 4, p. 5358–5363. DOI: 10.1016/j.egypro.2011.02.518.

Hardie, L. A. (1967): The gypsum-anhydrite equilibrium at one atmosphere pressure. American Mineralogist 52 (1-2), p. 171–200.

Harker, A. (1885): On slaty cleavage and allied rock structures with special reference to the mechanical theories of their origin. Apottiswoode & Company, Printers.

Harris, C., Franssen, R., Loosveld, R. (1991): Fractal analysis of fractures in rocks: the Cantor's Dust method-comment. Tectonophysics 198 (1), p. 107–111. DOI: 10.1016/0040-1951(91)90135-F.

Hawthorne, F. C., Ferguson, R. B. (1975): Anhydrous sulphates. II. Refinement of the crystal structure of anhydrite. The Canadian Mineralogist 13 (3), p. 289-292. ISSN: 0008-4476.

Healy, D., Reddy, S. M., Timms, N. E., Gray, E. M., Brovarone, A. V. (2009): Trench-parallel fast axes of seismic anisotropy due to fluid-filled cracks in subducting slabs. Earth and Planetary Science Letters 283 (1-4), p. 75-86. DOI: 10.1016/j.epsl.2009.03.037.

Healy, D., Rizzo, R.E., Cornwell, D.G., Farrell, N.J.C., Watkins, H., Timms, N.E., Gomez-Rivas, E., Smith, M. (2017): FracPaQ: A MATLAB™ toolbox for the quantification of fracture patterns. Journal of Structural Geology 95 (3), p. 1–16. DOI: 10.1016/j.jsg.2016.12.003.

Healy, D., Timms, N. E., Pearce, M. A. (2020): The variation and visualisation of elastic anisotropy in rock-forming minerals. Solid Earth 11 (2), p. 259-286. DOI: 10.5194/se-11-259-2020.

Heard, H. C., Rubey, W. W. (1966): Tectonic Implications of Gypsum Dehydration. Geological Society of America bulletin 77 (7), p. 741–760. DOI: 10.1130/0016-7606(1966)77[741:TIOGD]2.0.CO.

Heidelbach, F., Stretton, I. C., Kunze, K. (2001): Texture development of polycrystalline anhydrite experimentally deformed in torsion. International Journal of Earth Sciences 90 (1), p. 118–126. DOI: 10.1007/s005310000162.

Heilbronner, R. (2000): Automatic grain boundary detection and grain size analysis using polarized micrographs or orientation images. Journal of Structural Geology 22 (7), p. 969–981. DOI: 10.1016/S0191-8141(00)00014-6.

Heilbronner, R., Barrett, S. (2014): Image Analysis in Earth Sciences: Microstructures and Textures of Earth Materials. Band 129 von Lecture notes in earth system sciences. Springer Science & Business Media, p. 283–303. DOI: 10.1007/978-3-642-10343-8.

Herrero-Bervera, E., Walker, G. P. L., Cañon-Tapia, E., Garcia, M. O. (2001): Magnetic fabric and inferred flow direction of dikes, conesheets and sill swarms, Isle of Skye, Scotland. Journal of Volcanology and Geothermal Research 106 (3-4), p. 195–210. DOI: 10.1016/S0377-0273(00)00293-6.

Herwegh, M. (2000): A new technique to automatically quantify microstructures of fine grained carbonate mylonites: two-step etching combined with SEM imaging and image analysis. Journal of Structural Geology 22 (4), p. 391–400. DOI: 10.1016/S0191-8141(99)00165-0.

Herwegh, M., Handy, M. R., Heilbronner, R. (1999): Evolution of mylonitic microfabrics (EMM), a computer application for educational purposes. Tectonophysics 303 (1-4), p. 141–146. DOI: 10.1016/S0040-1951(98)00252-2.

Hickman, S. H., Evans, B. (1995): Kinetics of pressure solution at halite-silica interfaces and intergranular clay films. Journal of Geophysical Research 100 (B7), p. 13,113-13,132. DOI: 10.1029/95JB00911.

Hildyard, R. C., Llana-Funez, S., Wheeler, J., Faulkner, D. R., Prior, D. J. (2011b): Electron Backscatter Diffraction (EBSD) Analysis of Bassanite Transformation Textures and Crystal Structure Produced from Experimentally Deformed and Dehydrated Gypsum. Journal of Petrology 52 (5), p. 839–856. DOI: 10.1093/petrology/egr004.

Hildyard, R. C., Prior, D. J., Faulkner, D. R., Mariani, E. (2009): Microstructural analysis of anhydrite rocks from the Triassic Evaporites, Umbria-Marche Apennines, Central Italy: An insight into deformation mechanisms and possible slip systems. Journal of Structural Geology 31 (1), p. 92–103. DOI: 10.1016/j.jsg.2008.10.009.

Hildyard, R. C., Prior, D. J., Mariani, E., Faulkner, D. R. (2011a): Characterization of microstructures and interpretation of flow mechanisms in naturally deformed, fine grained anhydrite by means of EBSD analysis. Geological Society, London, Special Publications, 360 (1), p. 237-255. DOI: 10.1144/SP360.14.

Hiraga T., Hirschmann M. M., Kohlstedt, D. L. (2007): Equilibrium interface segregation in the diopside–forsterite system II: applications of interface enrichment to mantle geochemistry. Geochimica et Cosmochimica Acta 71, p. 1281–1289. DOI: 10. 1016/j. gca.2006. 11. 020.

Hudec, M. R., Jackson, M. P. A. (2007): Terra infirma: Understanding salt tectonics. Earth-Science Reviews 82 (1-2), p. 1-28. DOI: 10.1016/j.earscirev.2007.01.001.

Hunsche, U., Hampel, A. (1999): Rock salt – the mechanical properties of the host rock material for a radioactive waste repository. Engineering Geology 52 (3-4), p. 271-291. DOI: 10.1016/S0013-7952(99)00011-3.

Ildefonse, B., Launeau, P., and Bouchez, J.-L. (1992a): Effect of mechanical interactions on the development of shape preferred orientations: a two-dimensional experimental approach. Journal of Structural Geology 14 (1), p. 73–83. DOI: 10.1016/0191-8141(92)90146-N.

Ildefonse, B., Sokoutis, D., and Mancktelow, N.S. (1992b): Mechanical interactions between rigid particles in a deforming ductile matrix. Analogue experiments in simple shear flow. Journal of Structural Geology 14 (10), p. 1253–1266. DOI: 10.1016/0191-8141(92)90074-7.

Israelachvili, J. N. (1992): Adhesion forces between surfaces in liquids and condensable vapors. Surface Science Reports 14 (3), p. 109–159. DOI: 10.1016/0167-5729(92)90015-4.

Israelachvili, J. N. (2010): Intermolecular and Surface Forces. 3rd Edition. Saint Louis: Elsevier Science & Technology, 704 p. DOI: 10.1016/C2009-0-21560-1.

Jackson, C. A.-L., Elliott, G. M., Royce-Rogers, E., Gawthorpe, R. L., Aas, T. E. (2018): Salt thickness and composition influence rift structural style, northern North Sea, offshore Norway. Basin Research 31 (3), p. 514-538. DOI: 10.1111/bre.12332.

Jähne, B. (1993): Digital Image Processing: Concepts, Algorithms, and Scientific Applications. Springer Berlin, Heidelberg. 402 p. DOI: 10.1007/978-3-662-21817-4.

Jamtveit, B., Bucher-Nurminen, K., Austrheim, H. (1990): Fluid controlled eclogitization of granulites in deep crustal shear zones, Bergen arcs, Western Norway. Contributions to Mineralogy and Petrology 140, p. 184-193. DOI: 10.1007/BF00306442.

Jamtveit, B., Petley-Ragan, A., Incel, S., Dunkel, K. G., Aupart, C., Austrheim, H., Corfu, F., Menegon, L., Renard, F. (2019): The Effects of Earthquakes and Fluids on the Metamorphism of the Lower Continental Crust. Journal of Geophysical Research: Solid Earth 124 (8), p. 7725-7755. DOI: 10.1029/2018JB016461.

Jardim, F., Maul, A., Falcao, L., González, G. (2015): Estimating amplitude uncertainties through illumination studies for a pre-salt reservoir. 14th International Congress of the Brazilian Geophysical Society & EXPOGEF, Rio de Janeiro, Brazil. Conference Proceedings, p. 817-821. DOI: 10.1190/sbgf2015-160.

Jaworska, J. (2012): Crystallization, Alternation and Recrystallization of Sulphates. Advances in Crystallization Processes, p. 465–490. DOI: 10.5772/2672.

Jaworska, J., Nowak, M. (2013): Anhydrites from gypsum cap-rock of Zechstein salt diapirs. Geology, Geophysics and Environment 39 (3), p. 233–250. DOI: 10.7494/geol.2013.39.3.233.

Jayangondaperumal, R., Dubey, A. K. (2001): Superposed folding of a blind thrust and formation of klippen: results of anisotropic magnetic susceptibility studies from the Lesser Himalaya. Journal of Asian Earth Sciences 19 (6), p. 713–725. DOI: 10.1016/S1367-9120(00)00066-3.

Jessell, M. W., Kostenko, O., Jamtveit, B. (2003): The preservation potential of microstructures during static grain growth. Journal of Metamorphic Geology 21 (5), p. 481–491. DOI: 10.1046/j.1525-1314.2003.00455.x.

Jessell, M.W., Bons, P.D., Griera, A., Evans, L.A., and Wilson, C.J.L. (2009): A tale of two viscosities. Journal of Structural Geology 31 (7), p. 719–736. DOI: 10.1016/j.jsg.2009.04.010.

Jones, I. F., Davison, I. (2014): Seismic imaging in and around salt bodies. Society of Exploration Geophysicists and American Association of Petroleum Geologists. Interpretation 2 (4), p. 1-20. DOI: 10.1190/INT-2014-0033.1.

Jung, H., Park, M., Jung, S., Lee, J. (2010): Lattice Preferred Orientation, Water Content, and Seismic Anisotropy of Orthopyroxene. Journal of Earth Science 21 (5), p. 55-568. DOI: 10.1007/s12583-010-0118-9.

Jung, S., Jung, H., Austrheim, H. (2020): Microstructural Evolution of Amphibole Peridotites in Åheim, Norway, and the Implications for Seismic Anisotropy in the Mantle Wedge. Minerals 10 (4, 345), p. 1-22. DOI: 10.3390/min10040345.

Kern, H., Wenk, H.-R. (1985): Anisotropy in rocks and the geological significance. Wenk, H-R. (Ed.) Preferred orientation in deformed metals and rocks: an introduction to modern texture analysis, Academic Press, Orlando, p. 537–555. ISBN: 0-12-744020-8.

Kilian, R., Heilbronner, R., Stünitz, H. (2011): Quartz microstructures and crystallographic preferred orientation: Which shear sense do they indicate?. Journal of Structural Geology 33 (10), p. 1446–1466. DOI: 10.1016/j.jsg.2011.08.005.

Kim, J., Jung, H. (2020): Lattice Preferred Orientation (LPO) and Seismic Anisotropy of Amphibole in Gapyeong Amphibolites. Korean Journal of Mineralogy and Petrology 33 (3), p. 259–272. DOI: 10.22807/KJMP.2020.33.3.259.

Klassen-Neklyudova, M. V. (1964) Mechanical Twinning of Crystals. Springer US, 214 p. DOI: 10.1007/978-1-4684-1539-1.

Klimchouk, A. (1996): The dissolution and conversion of gypsum and anhydrite. International Journal of Speleology 25, p. 21–36. DOI: 10.5038/1827-806X.25.3.2.

Knipe, R. J. (1989): Deformation mechanisms – recognition from natural tectonites. Journal of Structural Geology 11 (1-2), p. 127-146. DOI: 10.1016/0191-8141(89)90039-4.

Ko, Suz-chung, Olgaard, D. L., Wong, Teng-fong (1997): Generation and maintenance of pore pressure excess in a dehydrating system 1. Experimental and microstructural observations. Journal of Geophysical Research 102 (B1), p. 825–839. DOI: 10.1029/96JB02485.

Ko, Suz-chung, Olgaard, David L., Briegel, Ueli (1995): The transition from weakening to strengthening in dehydrating gypsum: Evolution of excess pore pressures. Geophysical Research Letters 22 (9), p. 1009–1012. DOI: 10.1029/95GL00886.

Kruhl, J. H. (2013): Fractal-geometry techniques in the quantification of complex rock structures: A special view on scaling regimes, inhomogeneity and anisotropy. Journal of Structural Geology 46 (5347), p. 2–21. DOI: 10.1016/j.jsg.2012.10.002.

Kurz, W. (2005): Constriction during exhumation: Evidence from eclogite microstructures. Tectonophysics 33 (1), p. 37-40. DOI: 10.1130/G20887.1.

Kurz, W., Jansen, E., Hundenborn, R., Pleuger, J., Schäfer, W., Unzog, W. (2004): Microstructures and crystallographic preferred orientations of omphacite in Alpine eclogites: implications for the exhumation of (ultra-) high-pressure units. Journal of Geodynamics 37 (1), p. 1–55. DOI: 10.1016/j.jog.2003.10.001.

Launeau, P., and Robin, P.-Y.F. (1996): Fabric analysis using the intercept method. Tectonophysics 267 (1-4), p. 91–119. DOI: 10.1016/S0040-1951(96)00091-1.

Launeau, P., Archanjo, C.J., Picard, D., Arbaret, L., Robin, P.-Y. (2010): Two- and three-dimensional shape fabric analysis by the intercept method in grey levels. Tectonophysics 492 (1-4), p. 230–239. DOI: 10.1016/j.tecto.2010.06.005.

Launeau, P., Bouchez, J.-L., and Benn, K. (1990): Shape preferred orientation of object populations: automatic analysis of digitized images. Tectonophysics 180 (2-4), p. 201–211. DOI: 10.1016/0040-1951(90)90308-U.

Launeau, P., Cruden, A.R. (1998): Magmatic fabric acquisition mechanisms in a syenite: Results of a combined anisotropy of magnetic susceptibility and image analysis study. Journal of Geophysical Research: Solid Earth 103 (B3), p. 5067–5089. DOI: 10.1029/97JB02670.

Launeau, P., Robin, P.-Y. F. (2005): Determination of fabric and strain ellipsoids from measured sectional ellipses—implementation and applications. Journal of Structural Geology 27 (12), p. 2223–2233. DOI: 10.1016/j.jsg.2005.08.003.

Launeau, P., Robin, Y. F. (2003): SPO 2003-Shape Preferred Orientation 2003.

Lebedev, A. L., Avilina, I. V. (2019): The Kinetics of Gypso Anhydrites Dissolution in Water: Experimental Studies. Moscow University Geology Bulletin 74 (4), p. 429–432. DOI: 10.3103/S0145875219040094.

Lebensohn, R.A. (2001): N-site modeling of a 3D viscoplastic polycrystal using fast Fourier transform. Acta Materialia 49 (14), p. 2723–2737. DOI: 10.1016/S1359-6454(01)00172-0.

Lebensohn, R.A., Brenner, R., Castelnau, O., and Rollett, A.D. (2008): Orientation image-based micromechanical modelling of subgrain texture evolution in polycrystalline copper. Acta Materialia 56 (15), p. 3914–3926. DOI: 10.1016/j.actamat.2008.04.016.

Lebensohn, R.A., Montagnat, M., Mansuy, P., Duval, P., Meysonnier, J., Philip, A. (2009): Modelling viscoplastic behaviour and heterogeneous intracrystalline deformation of columnar ice polycrystals. Acta Materialia 57 (5), p. 1405–1415. DOI: 10.1016/j.actamat.2008.10.057.

Lebichot, S., Dislaire, G., Pirard, E., Launeau, P. (2005): Grey level intercepts distributions and grain size estimation. Proceedings. 8th International Congress on Stereology and Image Analysis, Zakopane, Poland, p. 102–110.

Leclère, H., Faulkner, D., Llana-Fúnez, S., Bedford, J., Wheeler, J. (2018): Reaction fronts, permeability and fluid pressure development during dehydration reactions. Earth and Planetary Science Letters 496, p. 227–237. DOI: 10.1016/j.epsl.2018.05.005.

Leclère, H., Faulkner, D., Wheeler, J., Mariani, E. (2016): Permeability control on transient slip weakening during gypsum dehydration: Implications for earthquakes in subduction zones. Earth and Planetary Science Letters 442, p. 1–12. DOI: 10.1016/j.epsl.2016.02.015.

Lee, J., Jung, H. (2015): Lattice-preferred orientation of olivine found in diamond-bearing garnet peridotites in Finsch, South Africa and implications for seismic anisotropy. Journal of Structural Geology 70, p. 12–22. DOI: 10.1016/j.jsg.2014.10.015.

Leininger, R. K., Conley, Robert F., Bundy, Wayne M. (1957): Rapid Conversion of Anhydrite to Gypsum. Industrial and Engineering Chemistry Research 49 (5), p. 818–821. DOI: 10.1021/ie50569a023.

Levin, F. K. (1979): Seismic velocities in transversely isotropic media. Geophysics 44 (5), p. 918–936. DOI: 10.1190/1.1440985.

Li, Lei, He, Liang, Wang, Yao (2019): Test Study on the Expansion Mechanical Properties of Regenerated Anhydrite Rock. IOP Conference Series: Earth and Environmental Science 358, p. 52029. DOI: 10.1088/1755-1315/358/5/052029.

Linckens, J., Zulauf, G., Hammer, J. (2016): Experimental deformation of coarse-grained rock salt to high strain. Journal of Geophysical Research: Solid Earth 121 (8), p. 6150–6171. DOI: 10.1002/2016JB012890.

Lindqvist, J., Åkesson, U. (2001): Image analysis applied to engineering geology, a literature review. Bulletin of Engineering Geology and the Environment 60 (2), p. 117–122. DOI: 10.1007/s100640100106.

Lisle, R.J. (1985): Geological Strain Analysis: A Manual for the Rf/ϕ Technique. Oxford, New York, Toronto, Sydney, Frankfurt: Pergamon Press. 99 p. DOI: 10.1017/S0016756800034920.

Llana-Fúnez, S., Wheeler, J., Faulkner, D. R. (2012): Metamorphic reaction rate controlled by fluid pressure not confining pressure: implications of dehydration experiments with gypsum. Contributions to Mineralogy and Petrology 164 (1), p. 69–79. DOI: 10.1007/s00410-012-0726-8.

Llorens, M.-G., Gomez-Rivas, E., Ganzhorn, A.-C., Griera, A., Steinbach, F., Roessiger, J., Labrousse, L., Walte, N.P., Weikusat, I., Bons, P.D. (2019): The effect of dynamic recrystallisation on the rheology and microstructures of partially molten rocks. Journal of Structural Geology 118 (170), p. 224–235. DOI: 10.1016/j.jsg.2018.10.013.

Llorens, M.-G., Griera, A., Bons, P. D., Gomez-Rivas, E., Weikusat, I., Prior, D., Kerch, J., Lebensohn, R. A. (2020): Seismic anisotropy of temperate ice in polar ice sheets. Journal of Geophysical Research: Earth Surface 125 (11), e2020JF005714. DOI: 10.1029/2020JF005714.

Llorens, M.-G., Griera, A., Bons, P.D., Roessiger, J., Lebensohn, R., Evans, L., and Weikusat, I. (2016): Dynamic recrystallisation of ice aggregates during co-axial viscoplastic deformation: a numerical approach. Journal of Glaciology 62 (232), p. 359–377. DOI: 10.1017/jog.2016.28.

Lloyd, G. E., Butler, R. W. H., Casey, M., Tatham, D. J., Mainprice, D. (2011): Constraints on the seismic properties of the middle and lower continental crust. Geological Society London Special Publications 360 (1), p. 7–32. DOI: 10.1144/SP360.2.

Lloyd, G., Kendall, J.-M. (2005): Petrofabric-derived seismic properties of a mylonitic quartz simple shear zone - implications for seismic reflection profiling. Geological Society of London Special Publications 240 (1), p. 75-94. DOI: 10.1144/GSL.SP.2005.240.01.07.

Lo, T.-W., Coyner, K. B., Toksöz, M. N. (1986): Experimental determination of elastic anisotropy of Berea sandstone, Chicopee shale, and Chelmsford granite. Geophysics (1), p. 164–171. DOI: 10.1190/1.1442029.

MacDonald, G. J. F. (1953): Anhydrite-gypsum equilibrium relations. American Journal of Science 251 (12), p. 884–898. DOI: 10.2475/ajs.251.12.884.

Mah, M., Schmitt, D. R. (2003): Determination of the complete elastic stiffnesses from ultrasonic phase velocity measurements. Journal of Geophysical Research 108 (B1), p. ECV 6-1-ECV 6-11. DOI: 10.1029/2001JB001586.

Mainprice, D. (1990): A FORTRAN program to calculate seismic anisotropy from the lattice preferred orientation of minerals. Computers & Geosciences 16 (3), p. 385–393. DOI: 10.1016/0098-3004(90)90072-2.

Mainprice, D., Humbert, M. (1994): Methods of calculating petrophysical properties from lattice preferred orientation data. Surveys in Geophysics 15 (5), p. 575-592. DOI: 10.1007/BF00690175.

Mardia, K.V., Jupp, P. E. (2000): Directional Statistics. John Wiley and Sons, London. 464 p. ISBN: 978-0-471-95333-3.

Marques, F.O., Mandal, N., Taborda, R., Antunes, J.V., Bose, S. (2014): The behaviour of deformable and non-deformable inclusions in viscous flow. Earth-Science Reviews 134, p. 16–69. DOI: 10.1016/j.earscirev.2014.03.007.

Marti, S., Stünitz, H., Heilbronner, R., Plümper, O., Kilian, R. (2018a): Syn-kinematic hydration reactions, dissolution-precipitation creep and grain boundary sliding in experimentally deformed plagioclase-pyroxene mixtures. Solid Earth Discussions 1 (1), p. 1-40. DOI: 10.5194/se-2018-39.

Marti, S., Stünitz, H., Heilbronner, R., Plümper, O., Kilian, R. (2018b): Syn-kinematic hydration reactions, grain size reduction, and dissolution–precipitation creep in experimentally deformed plagioclase–pyroxene mixtures. Solid Earth 9 (4), p. 985–1009. DOI: 10.5194/se-9-985-2018.

Mauler, A., Godard, G., Kunze, K. (2001): Crystallographic fabrics of omphacite, rutile and quartz in Vendée eclogites (Armorican Massif, France). Consequences for deformation mechanisms and regimes. Tectonophysics 342 (1-2), p. 81–112. DOI: 10.1016/S0040-1951(01)00157-3.

McNaught, M. (1994): Modifying the normalized fry method for aggregates of non-elliptical grains. Journal of Structural Geology 16 (4), p. 493–503. DOI: 10.1016/0191-8141(94)90093-0.

Meneguim, T. B., Mendes, S. C., Maul, A. R., Fernandes, L. F., Farias, M. G., González, G. (2015): Combining seismic facies analysis and well Information to guide new interval velocity models for a Pre-Salt study, Santos Basin, Brazil. 14th International Congress of the Brazilian Geophysical Society & EXPOGEF, Rio de Janeiro, Brazil. Conference Proceedings, p. 1365–1368. DOI: 10.1190/sbgf2015-271.

Mertineit, M.: Behlau, J., Hammer, J., Schramm, M., Zulauf, G. (2012): Mechanical behaviour of anhydrite rocks: Results of field investigations, mineralogical-geochemical studies and thermomechanical experiments. In Bérest, P., Ghoreychi,

M., Hadj-Hassen, F., Tijani, M. (Eds.), Mechanical Behaviour of Salt VII. Taylor & Francis Group, London, p. 123–129. ISBN: 9780429216923.

Michibayashi, K., Kusafuka, Y., Satsukawa, T., Nasir, S. J. (2012): Seismic properties of peridotite xenoliths as a clue to imaging the lithospheric mantle beneath NE Tasmania, Australia. Tectonophysics 522-523, p. 218-223. DOI: 10.1016/j.tecto.2011.12.002.

Milsch, H. H., Scholz, C. H. (2005): Dehydration-induced weakening and fault slip in gypsum: Implications for the faulting process at intermediate depth in subduction zones. Journal of Geophysical Research 110 (B4), 574 p. DOI: 10.1029/2004JB003324.

Milsch, H., Priegnitz, M., Blöcher, G. (2011): Permeability of gypsum samples dehydrated in air. Geophysical Research Letters 38 (18), L18304. DOI: 10.1029/2011GL048797.

Mirwald, P. W. (2008): Experimental study of the dehydration reactions gypsum-bassanite and bassanite-anhydrite at high pressure: indication of anomalous behaviour of H_2O at high pressure in the temperature range of 50-300 degrees C. The Journal of Chemical Physics 128 (7), 7 p. DOI: 10.1063/1.2826321.

Molli, G., Conti, P., Giorgetti, G., Meccheri, M., Oesterling, N. (2000): Microfabric study on the deformational and thermal history of the Alpi Apuane marbles (Carrara marbles), Italy. Journal of Structural Geology 22 (11-12), p. 1809–1825. DOI: 10.1016/S0191-8141(00)00086-9.

Molli, G., Heilbronner, R. (1999): Microstructures associated with static and dynamic recrystallization of Carrara marble (Alpi Aquane, NW Tuscany, Italy). Geologie en Mijnbouw 78 (1), p. 119–126. DOI: 10.1023/A:1003826904858.

Moore, G. A. (1968): Automatic scanning and computer processes for the quantitative analysis of micrographs and equivalent subjects. Pictorial Pattern Recognition, p. 275-362.

Moreno Chávez, G., Castillo Rivera, F., Sarocchi, D., Borselli, L., Rodríguez-Sedano, L. A. (2018): FabricS: A user-friendly, complete and robust software for particle shape-fabric analysis. Computers & Geosciences 115 (10), p. 20–30. DOI: 10.1016/j.cageo.2018.02.005.

Mulchrone, K. (2003): Dtnnm: A windows program for strain analysis using the delaunay triangulation nearest neighbour method. Computers & Geosciences 31 (8), p. 978–988. DOI: 10.1016/j.cageo.2005.02.004.

Mulchrone, K. F. (2002): Application of Delaunay triangulation to the nearest neighbour method of strain analysis. Journal of Structural Geology 25 (5), p. 689–702. DOI: 10.1016/S0191-8141(02)00067-6.

Mulchrone, K. F., Choudhury, K. R. (2004): Fitting an ellipse to an arbitrary shape: implications for strain analysis. Journal of Structural Geology 26 (1), p. 143–153. DOI: 10.1016/S0191-8141(03)00093-2.

Mulchrone, K. F., McCarthy, D. J., Meere, P. A. (2013): Mathematica code for image analysis, semi-automatic parameter extraction and strain analysis. Computers & Geosciences 61, p. 64–70. DOI: 10.1016/j.cageo.2013.08.001.

Mulchrone, K. F., Meere, P. A. (2015): Shape fabric development in rigid clast populations under pure shear: The influence of no-slip versus slip boundary conditions. Tectonophysics 659 (5), p. 63–69. DOI: 10.1016/j.tecto.2015.08.003.

Mulchrone, K. F., Meere, P. A., Choudhury, K. R. (2005): SAPE: a program for semi-automatic parameter extraction for strain analysis. Journal of Structural Geology 27 (11), p. 2084–2098. DOI: 10.1016/j.jsg.2005.05.019.

Mysen B. (2018): Redox-controlled mechanisms of C and H isotope fractionation between silicate melt and COH fluid in the Earth's interior. Progress in Earth and Planetary Science 5 (46), 17 p. DOI: 10.1186/s40645-018-0203-8.

Mysen B. (2019): Nitrogen in the Earth: abundance and transport. Progress in Earth and Planetary Science 6 (38). DOI: 10.1186/s40645-019-0286-x.

Niessen, F., Nyyssönen, T., Gazder, A. A., Hielscher, R. (2021): Parent grain reconstruction from partially or fully transformed microstructures in MTEX. Journal of Applied Crystallography 55, p. 180-194. DOI: 10.1107/S1600576721011560.

Oda, M. (1983): A method for evaluating the effect of crack geometry on the mechanical behaviour of cracked rock masses. Mechanics of Materials 2 (2), p. 163–171. DOI: 10.1016/0167-6636(83)90035-2.

Ohtani, E. (2021): Hydration and Dehydration in Earth's Interior. Annual Review of Earth and Planetary Sciences 49 (1), p. 253-278. DOI: 10.1146/annurev-earth-080320-062509.

Olgaard, D. L., Ko, Suz-Chung, Wong, Teng-Fong (1995): Deformation and pore pressure in dehydrating gypsum under transiently drained conditions. Tectonophysics 245 (3-4), p. 237–248. DOI: 10.1016/0040-1951(94)00237-4.

Oliveira, L. C., Fernandes, L. F., Maul, A. R., Rosseto, J. A., Farias, M. G., Sanchez, G. G. (2015): Geological Velocity Approach in Order to Obtain a Detailed Velocity Model for the Evaporitic Section - Santos Basin. 14th International Congress of

the Brazilian Geophysical Society & EXPOGEF, Rio de Janeiro, Brazil. SEG Global Meeting Abstracts SB G12015, p. 1374-1377. DOI: 10.1190/sgbf2015-273.

Ortí Cabo, F., Pueyo Mur J. J., Rosell Ortiz, L. (1985): La halite du bassin potassique sud-pyreneen (Eocene superieur, Espagne). Bulletin de la Société Géologique de France I (6), p. 863–872. DOI: 10.2113/gssgfbull.I.6.863.

Owens, W. H. (1984): The calculation of a best-fit ellipsoid from elliptical sections on arbitrarily orientated planes. Journal of Structural Geology 6 (5), p. 571–578. DOI: 10.1016/0191-8141(84)90066-X.

Panozzo Heilbronner, R. (1992): The autocorrelation function: an image processing tool for fabric analysis. Tectonophysics 212 (3-4), p. 351–370. DOI: 10.1016/0040-1951(92)90300-U.

Panozzo, R. (1983): Two-dimensional analysis of shape-fabric using projections of digitized lines in a plane. Tectonophysics 95 (3-4), p. 279–294. DOI: 10.1016/0040-1951(83)90073-2.

Panozzo, R. (1984): Two-dimensional strain from the orientation of lines in a plane. Journal of Structural Geology 6 (1-2), p. 215–221. DOI: 10.1016/0191-8141(84)90098-1.

Panozzo, R. (1987): Two-dimensional strain determination by the inverse SURFOR wheel. Journal of Structural Geology 9 (1), p. 115–119. DOI: 10.1016/0191-8141(87)90049-6.

Passchier, C. W., Trouw, R. A. J. (2005): Microtectonics. 2nd, Revised and Enlarged Edition. Berlin, Heidelberg, Springer-Verlag Berlin Heidelberg, p. 102-109. DOI: 10.1007/3-540-29359-0.

Peach, C. J., Spiers, C. J. (1996): Influence of crystal plastic deformation on dilatancy and permeability development in synthetic salt rock. Tectonophysics 256 (1-4), p. 101-128. DOI: 10.1016/0040-1951(95)00170-0.

Pennock, G. M., Drury, M. R., Peach, C. J., Spiers, C. J. (2006): The influence of water on deformation microstructures and textures in synthetic NaCl measured using EBSD. Journal of Structural Geology 28 (4), p. 588-601. DOI: 10.1016/j.jsg.2006.01.014.

Pennock, G. M., Drury, M. R., Spiers, C. J. (2004): Investigation of subgrain rotation recrystallization in dry polycrystalline NaCl. Materials Science Forum 467-470, p. 597-602. DOI: 10.4028/www.scientific.net/MSF.467-470.597.

Pennock, G. M., Drury, M. R., Spiers, C. J. (2005): The development of subgrain misorientations with strain in dry synthetic NaCl measured using EBSD. Journal of Structural Geology 27 (12), p. 2159-2170. DOI: 10.1016/j.jsg.2005.06.013.

Pennock, G. M., Drury, M. R., Trimby, P. W., Spiers, C. J. (2002): Misorientation distributions in hot deformed NaCl using electron backscattered diffraction. Journal of Microscopy 205 (3), p. 285-294. DOI: 10.1046/j.1365-2818.2002.00993.x.

Pérez-Gussinyé, M., Reston, T. J. (2001): Rheological evolution during extension at nonvolcanic rifted margins: onset of serpentinization and development of detachments leading to continental breakup. Journal of Geophysical Research 106, p. 3961–3975. DOI: 10.1029/2000JB900325.

Peternell, M., Kruhl, J. H. (2009): Automation of pattern recognition and fractal-geometry-based pattern quantification, exemplified by mineral-phase distribution patterns in igneous rocks. Computers & Geosciences 35 (7), p. 1415–1426. DOI: 10.1016/j.cageo.2008.11.001.

Petri, B., Almqvist, B. S. G., Pistone, M. (2020): 3D rock fabric analysis using micro-tomography: An introduction to the open-source TomoFab MATLAB code. Computers & Geosciences 138, 41 p. DOI: 10.1016/j.cageo.2020.104444.

Pfleiderer, S., Ball, D. G. A., Bailey, R. C. (1993): AUTO: A computer program for the determination of the two-dimensional autocorrelation function of digital images. Computers & Geosciences 19 (6), p. 825–829. DOI: 10.1016/0098-3004(93)90053-8.

Piazolo, S., Bons, P.D., Griera, A., Llorens, M.-G., Gomez-Rivas, E., Koehn, D., Wheeler, J., Gardner, R., Godinho, J.R.A., Evans, L., Lebensohn, R.A., Jessell, M.W. (2019): A review of numerical modelling of the dynamics of microstructural development in rocks and ice: Past, present and future. Journal of Structural Geology 125, p. 111–123, DOI: 10.1016/j.jsg.2018.05.025.

Pina, C. M. (2009): Nanoscale dissolution and growth on anhydrite cleavage faces. Geochimica et Cosmochimica Acta 73 (23), p. 7034–7044. DOI: 10.1016/j.gca.2009.08.032.

Pirard, E., Lebichot, S., Krier, W. (2007): Particle texture analysis using polarized light imaging and grey level intercepts. International Journal of Mineral Processing 84 (1-4), p. 299–309. DOI: 10.1016/j.minpro.2007.03.004.

Pirard, E., Sardini, P. (2011): Image analysis for advanced characterization of industrial minerals and geomaterials. European Mineralogical Union Notes in Mineralogy 9 (1), p. 287–340. DOI: 10.1180/EMU-notes.9.3.

Pleuger, J., Hundenborn, R., Kremer, K., Babinka, S., Kurz, W., Jansen, E., Froitzheim, N. (2003): Structural evolution of the Adula nappe, Misox zone, and Tambo nappe in the San Bernardino area: constraints for the exhumation of the Adula eclogites. Mitteilungen der Österreichischen Geologischen Gesellschaft 94, p. 99–122 [in German].

Poirier, J.-P. (1985): Creep of crystals. High-temperature deformation processes in metals, ceramics and minerals. Cambridge Earth Science Series, Cambridge university press, re-issued 2005, p. 38-73. ISBN-10 0-521-26177-5.

Popp, T., Kern, H. (1998): Ultrasonic wave velocities, gas permeability and porosity in natural and granular rock salt. Physics and Chemistry of the Earth 23 (3), p. 373–378. DOI: 10.1016/S0079-1946(98)00040-8.

Prasse, P., Wookey, J., Kendall, J.-M., Roberts, D., Dutko, M. (2020): Seismic anisotropy in deforming halite: evidence from the Mahogany salt body. Geophysical Journal International 223 (3), p. 1672-1687. DOI: 10.1093/gji/ggaa402.

Ragan, D. M. (1985): Structural Geology - An Introduction to Geomaterical Techniques. 4th Edition, Cambridge, 632 p. ISBN: 9780521745833.

Ramsay, J. G., Huber, M.I. (1983): The Techniques of Modern Structural Geology. Volume 1. Strain Analysis: London: Academic Press, 307 pp. ISBN: 978-0125769211

Ramsay, J.G. (1976): Folding and Fracturing of Rocks. McGaw-Hill, New York. International Series in the Earth and Planetary Sciences, 568 p. DOI: 10.1126/science.160.3826.410.

Ramsdell, L. S., Partridge, E. P. (1929): The crystal forms of calcium sulphate. American Mineralogist 14 (2), p. 59–74. ISSN: 0003-004X.

Ran, H., Bons, P. D., Wang, G., Steinbach, F., Finch, M. A., Griera, A., Gomez-Rivas, E., Llorens, M.-G., Ran, S., Liang, X., Zhou, J. (2018): High-strain deformation of conglomerates: Numerical modelling, strain analysis, and an example from the Wutai Mountains, North China Craton. Journal of Structural Geology 114, p. 222–234. DOI: 10.1016/j.jsg.2018.06.018.

Ran, H., Riese, T. de, Llorens, M.-G., Finch, M. A., Evans, L. A., Gomez-Rivas, E., Griera, A., Jessell, M. W., Lebensohn, R. A., Piazolo, S., Bons, P. D. (2019): Time for anisotropy: The significance of mechanical anisotropy for the development of deformation structures. Journal of Structural Geology 125, p. 41–47. DOI: 10.1016/j.jsg.2018.04.019.

Ranero, C. R., Moran, J. P., McIntosh, K., Reichert, C. (2003): Bending-related faulting and mantle serpentinization at the Middle America trench. Nature 425, p. 367–373. DOI: 10.1038/nature01961.

Raymer, D. G., Kendall, J. M. (1998): Seismic Anisotropy in Salt Structures Due to Preferred Crystal Orientation. Revue de l'Institut Francais du Pétrole 53 (5), p. 585–594. DOI: 10.2516/ogst:1998053.

Raymer, D. G., Kendall, J.-M. (1997): Potential pitfalls in imaging salt structures due to preferred crystal orientation and seismic anisotropy. SEG Technical Program Expanded Abstracts 1997, p. 1254–1257. DOI: 10.1190/1.1885627.

Raymer, D. G., Kendall, J-M., Pedlar, D., Kendall, R. R., Mueller, M. C., Beaudoin, G. J. (2000a): The significance of salt anisotropy in seismic imaging. 2000 SEG Annual Meeting, Calgary, Alberta. Conference Proceedings, p. 562–565. DOI: 10.1190/1.1816123.

Raymer, D. G., Tommasi, A., Kendall, J.-M. (2000b): Predicting the seismic implications of salt anisotropy using numerical simulations of halite deformation. Geophysics 65 (4), p.1272-1280. DOI: 10.1190/1.1444818.

Ringwood A. E., Major, A. (1967): High-pressure reconnaissance investigations in the system Mg_2SiO_4-$MgOH_2O$. Earth and Planetary Science Letters 2, p. 130–133. DOI: 10.1016/0012-821x(67)90114-8.

Robin, P.-Y. F. (2002): Determination of fabric and strain ellipsoids from measured sectional ellipses — theory. Journal of Structural Geology 24 (3), p. 531–544. DOI: 10.1016/S0191-8141(01)00081-5.

Ross, J. V., Bauer, S. J., Hansen, F. D. (1987): Textural evolution of synthetic anhydrite-halite mylonites. Tectonophysics 140 (2-4), p. 307–326. DOI: 10.1016/0040-1951(87)90237-X.

Rutter, E. H. (1976): A Discussion on natural strain and geological structures - The kinetics of rock deformation by pressure solution. Philosophical Transactions of The Royal Society London Series A, Mathematical and Physical Sciences 283, p. 203-219. DOI: 10.1098/rsta.1976.0079.

Saltykov, S. A. (1958): Stereometric Metallography, 2nd Edition. State Publishing House for Metals Sciences, Metallurgizdat, Moscow, 446 p.

Samanta, S. K., and Bhattacharyya, G. (2003): Modes of detachment at the inclusion–matrix interface. Journal of Structural Geology 25 (7), p. 1107–1120. DOI: 10.1016/S0191-8141(02)00157-8.

Sanderson, D. J. (1977): The analysis of finite strain using lines with an initial random orientation. Tectonophysics 43 (3-4), p. 199–211. DOI: 10.1016/0040-1951(77)90117-2.

Sanderson, D. J., Phillips, S. J. L. (1987): Strain analysis using length-weighting of deformed random line elements. Journal of Structural Geology 9 (4), p. 511–514. DOI: 10.1016/0191-8141(87)90129-5.

Sass, I., Burbaum, U. (2010): Damage to the historic town of Staufen (Germany) caused by geothermal drillings through anhydrite-bearing formations. Acta Carsologica 39, p. 233–245. DOI: 10.3986/ac.v39i2.96.

Schäfer, A., Teyssen, T. (1987): Size, shape and orientation of grains in sands and sandstones—image analysis applied to rock thin-sections. Sedimentary Geology 52 (3-4), p. 251–271. DOI: 10.1016/0037-0738(87)90064-9.

Schléder, Z., and Urai, J. L. (2005): Microstructural evolution of deformation-modified primary halite from the Middle Triassic Röt Formation at Hengelo, The Netherland. International Journal of Earth Sciences 94 (5-6), p. 941–955. DOI: 10.1007/s00531-005-0503-2.

Schneider, C. A., Rasband, W. S., Eliceiri, K. W. (2012): NIH Image to ImageJ: 25 years of image analysis. Nature methods 9 (7), p. 671–675. DOI: 10.1038/nmeth.2089.

Schofield, P. F., Knight, K. S., Stretton, I. C. (1996): Thermal expansion of gypsum investigated by neutron powder diffraction. American Mineralogist 81 (7-8), p. 847-851. DOI: 10.2138/am-1996-7-807.

Schweigl, J., Neubauer, F. (1997): Semiductile deformation in pelagic limestones at diagenetic conditions. Geologica Carpathica 48 (6), p. 361–370.

Serafeimidis, K., Anagnostou, G. (2013): On the Time-Development of Sulphate Hydration in Anhydritic Swelling Rocks. Rock Mechanics and Rock Engineering 46 (3), p. 619–634. DOI: 10.1007/s00603-013-0376-9.

Serra, J. (1982): Image Analysis and Mathematical Morphology. Academic Press, London. 610 p. DOI: 10.1002/cyto.990040213.

Sheriff, R., 2002. Encyclopedic Dictionary of Exploration Geophysics. Geophysical References Series, Society of Exploration Geophysicists. 429 p. DOI: 10.1190/1.9781560802969.

Sievert, T., Wolter, A., Singh, N. B. (2005): Hydration of anhydrite of gypsum (CaSO4.II) in a ball mill. Cement and Concrete Research 35 (4), p. 623–630. DOI: 10.1016/j.cemconres.2004.02.010.

Simigian, S., Starkey, J. (1986): Automated grain shape analysis. Journal of Structural Geology 8 (5), p. 589–592. DOI: 10.1016/0191-8141(86)90009-X.

Simpson, C. (1985): Deformation of granitic rocks across the brittle-ductile transition. Journal of Structural Geology 7 (5), p. 503–511. DOI: 10.1016/0191-8141(85)90023-9.

Simpson, C., De Paor, C. G. (1993): Strain and kinematic analysis in general shear zones. Journal of Structural Geology 15 (1), p. 1-20. DOI: 10.1016/0191-8141(93)90075L.

Singh, A., Kumar, C., Kannan, L. G., Rao, K. S., Ayothiraman, R. (2018): Engineering properties of rock salt and simplified closed-form deformation solution for circular opening in rock salt under the true triaxial stress state. Engineering Geology 234, p. 218-230. DOI: 10.1016/j.enggeo.2018.07.008.

Skemer, P., Katayama, I., Jiang, Z. T., Karato, S. (2005): The Misorientation Index: Development of a New Method for Calculating the Strength of Lattice-Preferred Orientation. Tectonophysics 411 (1-4), p. 157-167. DOI: 10.1016/j.tecto.2005.08.023.

Skrotzki, W., Dornbusch, H. J., Helming, K., Tamm, R., Bockmeier, H. G. (1996): Development of microstructure and texture in pure shear deformed salt. Proceedings of the 4th Conference on the mechanical behaviour of salt by M. Aubertin, H. R. Hardy, p. 101-114. ISBN: 0-87849-103-1.

Song, I., Suh, M., Woo, Y.-K., Tianyao, H. (2004): Determination of the elastic modulus set of foliated rocks from ultrasonic velocity measurements. Engineering Geology 72 (3-4), p. 293-308. DOI: 10.1016/j.enggeo.2003.10.003.

Sorby, H. C., 1849): On the Origin of Slaty Cleavage. Proceedings of the Yorkshire Geological Society 3, p. 300–312. DOI: 10.1144/pygs.3.300.

Spiers, C. J., Schutjens, P. M. T. M., Brzesowsky, R. H., Peach, C. J., Liezenberg, J. L., Zwart, H. J. (1990): Experimental determination of constitutive parameters governing creep of rocksalt by pressure solution. Knipe, R. J., Rutter, E. H. (Eds.): Deformation Mechanisms, Rheology and Tectonics. Geological Society of London Special Publication 54, p. 215–227. DOI: 10.1144/GSL.SP.1990.054.01.21.

Srivastava, H. B. (1995): Two-dimensional strain estimation from weakly deformed rocks. Annales Tectonicae 9 (1-2), p. 3–6.

Starkey, J., Simigian, S. (1987): IMAGE: a FORTRAN V program for image analysis of particles. Computers & Geosciences 13 (1), p. 37–59. DOI: 10.1016/0098-3004(87)90023-9.

Stein, E. (2000): Zur Platznahme von Granitoiden: Vergleichende Fallstudien zu Gefügen und Platznahmemechanismen aus den White-Inyo Mountains, California, USA, und dem Bergsträßer Odenwald [On the emplacement of granitoids case studies comparing fabrics and emplacement mechanisms of the White-Inyo Mountains, California, USA, and the Bergsträsser Odenwald, Germany]. Stuttgart, E. Schweizerbart'sche Verlagsbuchhandlung, Geotektonische Forschungen 93, 344 pp. [in German]. ISBN: 978-3-510-50059-8.

Steinbach, F., Bons, P. D., Griera, A., Jansen, D., Llorens, M.-G., Roessiger, J., Weikusat, I. (2016): Strain localization and dynamic recrystallization in the ice–air aggregate: a numerical study. The Cryosphere 10 (6), p. 3071–3089. DOI: 10.5194/tc-10-3071-2016.

Stewart, F. H. (1963): Marine Evaporites. Data of Geochemistry. 6th Edition: U.S. Government Printing Office. p. Y1-Y53. DOI: 10.3133/pp440Y.

Stipp, M., Stünitz, H., Heilbronner, R., Schmid, S.M. (2002): The eastern Tonale fault zone: a 'natural laboratory' for crystal plastic deformation of quartz over a temperature range from 250 to 700°C. Journal of Structural Geology 24 (12), p. 1861–1884. DOI: 10.1016/S0191-8141(02)00035-4.

Stünitz, H., Gerald, J. D. F. (1993): Deformation of granitoids at low metamorphic grade. II: Granular flow in albite-rich mylonites. Tectonophysics 221 (3-4), p. 299–324. DOI: 10.1016/0040-1951(93)90164-F.

Suzuki, K., Oda, M., Yamazaki, M., Kuwahara, T. (1998): Permeability changes in granite with crack growth during immersion in hot water. International Journal of Rock Mechanics and Mining Sciences 35 (7), p. 907–921. DOI: 10.1016/S0148-9062(98)00016-3.

Tacchetto, T., Reddy, S. M., Saxey, D. W., Fougerouse, D., Rickard, W. D. A., Clark, C. (2021): Disorientation control on trace element segregation in fluid-affected low-angle boundaries in olivine. Contributions to Mineralogy and Petrology 176 (59), p. 1-16. DOI: 10.1007/s00410-021-01815-3.

Ter Heege, J. H., De Bresser, J. H. P., Spiers, C. J. (2005a): Dynamic recrystallization of wet synthetic polycrystalline halite: Dependence of grain size distribution of flow stress, temperature and strain. Tectonophysics 396 (1-2), p. 35-57. DOI: 10.1016/j.tecto.2004.10.002.

Ter Heege, J. H., De Bresser, J. H. P., Spiers, C. J. (2005b): Rheological behaviour of synthetic rocksalt: the interplay between water, dynamic recrystallization and deformation mechanisms. Journal of Structural Geology 27 (6), 948–963. DOI: 10.1016/j.jsg.2005.04.008.

Thabet, I., Kilias, A., Kamh, S. (2017): Microstructural finite strain analysis of the Hafafit granitoids domes South Central Eastern desert of Egypt. Bulletin of the Geological Society of Greece 47 (2), 667 pp. DOI: 10.12681/bgsg.11100.

Tikoff, B., Teyssier, C. (1994): Strain and fabric analysis based on porphyroclast interaction. Journal of Structural Geology 16 (4), p. 477–491. DOI: 10.1016/0191-8141(94)90092-2.

Timms, N. E., Erickson, T. M., Pearce, M. A., Cavosie, A. J., Schmieder, M., Tohver, E. et al. (2017): A pressure-temperature phase diagram for zircon at extreme conditions. Earth-Science Reviews 165, p. 185–202. DOI: 10.1016/j.earscirev.2016.12.008.

Timms, N. E., Pearce, M. A., Erickson, T. M., Cavosie, A. J., Rae, A. S. P., Wheeler, J. et al. (2019): New shock microstructures in titanite ($CaTiSiO_5$) from the peak ring of the Chicxulub impact structure, Mexico. Contributions to Mineralogy and Petrology 174 (5), p. 245. DOI: 10.1007/s00410-019-1565-7.

Trayner, P.M. (1986): A comparison of Sanderson's and Panozzo's strain measurement methods using calcite grain boundaries from the Variscan fold and thrust belt in Ireland. Journal of Structural Geology 8 (2), p. 205–207. DOI: 10.1016/0191-8141(86)90111-2.

Trimby, P. W., Drury, M. R., Spiers, C. J. (2000): recognising the crystallographic signature Recognising the crystallographic signature of recrystallisation processes in deformed rocks: a study of experimentally deformed rocksalt. Journal of Structural Geology 22 (11-12), p. 1609-1620. DOI: 10.1016/S0191-8141(00)00059-6.

Trippetta, F., Collettini, C., Vinciguerra, S., Meredith, P. G. (2010): Laboratory measurements of the physical properties of Triassic Evaporites from Central Italy and correlation with geophysical data. Tectonophysics 492 (1-4), p. 121–132. DOI: 10.1016/j.tecto.2010.06.001.

Trullenque, G., Kunze, K., Heilbronner, R., Stünitz, H., Schmid, S. M. (2006): Microfabrics of calcite ultramylonites as records of coaxial and non-coaxial deformation kinematics: Examples from the Rocher de l'Yret shear zone (Western Alps). Tectonophysics 424 (1-2), p. 69–97. DOI: 10.1016/j.tecto.2006.06.004.

Underwood, E.E. (1970): Quantitative Stereology. Addison-Wesley series in Metallurgy and Materials, Addison-Wesley Publication Company, University of California, 274 p. ISBN: 0201076500, 9780201076509.

Urai, J. L., Boland, J. N. (1985): Development of microstructures and the origin of hematite in naturally deformed carnallite. Neues Jahrbuch für Mineralogy - Monatshefte 1985 (2), p. 58–72. DOI: 10.1127/0028-3649/2002/2002-0145.

Urai, J. L., Schléder, Z., Spiers, C. J., Kulka, P. A. (2008): Flow and Transport Properties of Salt Rocks. Dynamics of Complex Intracontinental Basins: The Central European Basin System. p. 277–290. DOI: 10.1007/978-3-540-85085-4.

Urai, J. L., Spiers, C. J., Peach, C. J., Franssen, R. C. M. W., Liezenberg, J. L. (1987): Deformation mechanisms operating in naturally deformed halite rocks as deduced from microstructural investigations. Geologie en Mijnbouw 66 (2), p. 165–176. ISSN: 0016-7746.

Urai, J. L., Spiers, C. J., Zwart, H. J., Lister, G. S. (1986a): Weakening of rock salt by water during long-term creep. Nature 324 (6097), p. 554–557. DOI: 10.1038/324554a0.

Urai, J.L., Means, W.D., Lister, G.S. (1986b): Dynamic recrystallization of minerals. Hoobs, B. (Ed.), Mineral and Rock Deformation. Laboratory Studies: The Paterson Volume, p. 161–199. DOI: 10.1029/GM036p0161.

Valcke, S., Casey, M., Lloyd, G., Kendall, J.-M., Fisher, Q. (2006): Lattice preferred orientation and seismic anisotropy in sedimentary rocks. Geophysical Journal International 166 (2), p. 652-666. DOI: 10.1111/j.1365-246X.2006.02987.x.

Valcke, S., Casey, M., Lloyd, G., Kendall, J.-M., Fisher, Q. (2006): Lattice preferred orientation and seismic anisotropy in sedimentary rocks. Geophysical Journal International 166 (2), p. 652-666. DOI: 10.1111/j.1365-246X.2006.02987.x.

Valentini, L., Capaccioni, B., Rossi, P. L., Scandone, R., Sarocchi, D. (2008): Vent area and depositional mechanisms of the Upper Member of the Neapolitan Yellow Tuff (Campi Flegrei, Italy): new insights from directional fabric through image analysis. Bulletin of Volcanology 70 (9), p. 1087–1101. DOI: 10.1007/s00445-007-0191-9.

Vargas-Meleza, L., Healy, D., Alsop, G. I., Timms, N. E. (2015): Exploring the relative contribution of mineralogy and CPO to the seismic velocity anisotropy of evaporites. Journal of Structural Geology 70, p. 39–55. DOI: 10.1016/j.jsg.2014.11.001.

Vel, S. S., Cook, A. C., Johnson, S. E., Gerbi, C. (2016): Computational homogenization and micromechanical analysis of textured polycrystalline materials. Computer Methods in Applied Mechanics and Engineering 310, p. 749-779. DOI: 10.1016/j.cma.2016.07.037.

Velde, B., Dubois, J., Touchard, G., Badri, A. (1990): Fractal analysis of fractures in rocks: the Cantor's Dust method. Tectonophysics 179 (3-4), p. 345–352. DOI: 10.1016/0040-1951(90)90300-W.

Vigneresse, J.-L. (2015): Textures and melt-crystal-gas interactions in granites. Geoscience Frontiers 6 (5), p. 635–663. DOI: 10.1016/j.gsf.2014.12.004.

Volland, S., Kruhl, J. H. (2004): Anisotropy quantification: the application of fractal geometry methods on tectonic fracture patterns of a Hercynian fault zone in NW Sardinia. Journal of Structural Geology 26 (8), p. 1499–1510. DOI: 10.1016/j.jsg.2003.10.005.

Vollmer, F. W. (2018): Automatic contouring of geological fabric and finite strain data on the unit hyperboloid. Computers & Geosciences 115, p. 134-142. DOI: 10.1016/j.cageo.2018.03.006.

Waldron, J. W. F., Wallace, K. D. (2007): Objective fitting of ellipses in the centre-to-centre (Fry) method of strain analysis. Journal of Structural Geology 29 (9), p. 1430–1444. DOI: 10.1016/j.jsg.2007.06.005.

Wallbrecher, E. (1986): Tektonische und gefügeanalytische Arbeitsweisen: graphische, rechnerische und statistische Verfahren. Enke, 244 p.

Wang, H., Zhang, B., Wang, L., Yu, X., Shi, L., Fu, D. (2020): Experimental investigation on the long-term interactions of anhydrite rock, crude oil, and water in a mine-out space for crude-oil storage. Engineering Geology 265, p. 105414. DOI: 10.1016/j.enggeo.2019.105414.

Wang, W.-H., Wong, T.-F. (2003): Effects of reaction kinetics and fluid drainage on the development of pore pressure excess in a dehydrating system. Tectonophysics 370 (1-4), p. 227–239. DOI: 10.1016/S0040-1951(03)00188-4.

Warren, J. K. (2016): Evaporites. A Geological Compendium. 2nd Edition. Springer Cham. 1813 p. DOI: 10.1007/978-3-319-13512-0.

Webber, J. R. (2012): Advances in Rock Fabric Quantification and the Reconstruction of Progressive Dike Replacement in the Coastal Batholith of Central Chile. The University of Vermont, Graduate College Dissertations and Theses 238. https://scholarworks.uvm.edu/graddis/238.

Weger, M. (1991): ELLIROT—A program to view and analyze spatial distributions of ellipses. Computers & Geosciences 17 (2), p. 291–300. DOI: 10.1016/0098-3004(91)90017-8.

Wenk, H.-R., Armann, M., Burlini, L., Kunze, K., Bortolotti, M. (2009): Large strain shearing of halite: Experimental and theoretical evidence for dynamic texture changes. Earth and Planetary Science Letters 280 (1-4), p. 205-210. DOI: 10.1016/j.epsl.2009.01.036.

Wheeler, J. (1991): A view of texture dynamics. Terra Nova 3 (2), p. 123–136. DOI: 10.1111/j.1365-3121.1991.tb00864.x.

Wheeler, J. (2014): Dramatic effects of stress on metamorphic reactions. Geology 42 (8), p. 647–650. DOI: 10.1130/G35718.1.

Wheeler, J. (2018): The effects of stress on reactions in the Earth: Sometimes rather mean, usually normal, always important. Journal of Metamorphic Geology 36 (4), p. 439–461. DOI: 10.1111/jmg.12299.

Woodcock, N. H. (1977): Specification of fabric shapes using an eigenvalue method. Geological Society of America Bulletin 88 (9), p. 1231–1236. DOI: 10.1130/0016-7606(1977)88%3C1231:SOFSUA%3E2.0.CO;2.

Xu, Chongbang, Zhang, Yajun, Yan, Junjie (2019): Test Study on the Expansional Properties of Regenerated Anhydrite Rock. IOP Conference Series: Earth and Environmental Science 330, 6 p. DOI: 10.1088/1755-1315/330/4/042004.

Yamaji, A. (2008): Theories of strain analysis from shape fabrics: A perspective using hyperbolic geometry. Journal of Structural Geology 30 (12), p. 1451-1465. DOI: 10.1016/j.jsg.2008.07.011.

Yamaji, A. (2013a): Comparison of methods of algebraic strain estimation from Rf/ϕ data: A unified theory of 2D strain analysis. Journal of Structural Geology 49, p. 4-12. DOI: 10.1016/j.jsg.2013.01.011.

Yamaji, A. (2013b): Two-dimensional finite deformations evaluated from pre- and post-deformation markers: Application to balanced cross sections. Journal of Structural Geology 51, p. 144-155. DOI: 10.1016/j.jsg.2013.02.002.

Yin, Shuai, Xie, Runcheng (2019): Experimental analysis of dynamic and static mechanical properties of deep thick anhydrite cap rocks under high-stress conditions. Carbonates Evaporites 34 (3), p. 807–823. DOI: 10.1007/s13146-018-0450-1.

Zhong, X., Frehner, M., Kunze, K., Zappone, A. (2014): A novel EBSD-based finite-element wave propagation model for investigating seismic anisotropy: Application to Finero Peridotite, Ivrea-Verbano Zone, Northern Italy. Geophysical Research Letters 41 (20), p. 7105-7114. DOI: 10.1002/2014GL060490.

Zong, J., Steward, R., Dyaur, N. (2014): Salt anisotropy. Ultrasonic lab experiments and travel time ramifications. Society of Exploration Geophysicists, SEG Technical Program Expanded Abstracts, p. 383–388. DOI: 10.1190/segam2014-0938.1.

APPENDIX A

Supplementary material to chapter 2

A.1 Figures

Je

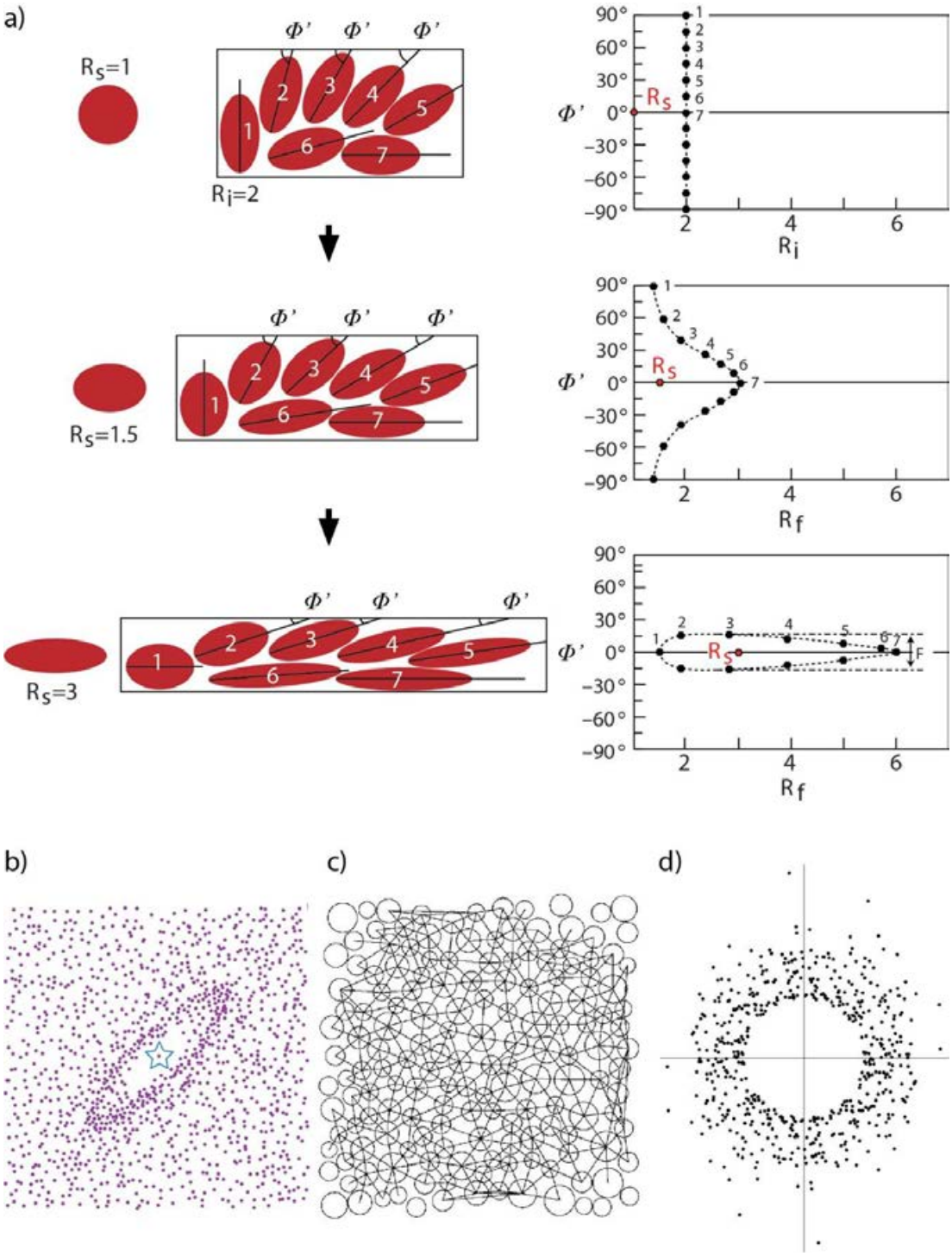

Figure A.1: Graphical summary of grain-based quantification methods after Fossen (2016), who modified from Ramsay and Huber (1983). a) R_f/ϕ method. The ellipses have the same ellipticity (R_i) before deformation starts. The R_f/ϕ diagram to the right indicates that $R_i = 2$. A pure shear is then added with $R_s = 1.5$, followed by a pure shear strain of $R_s = 3$. b) Result of a manually performed Fry analysis, showing the strain ellipsoid defined by a void between data points. Figure after Fossen (2016), who modified from Ramsay and Huber (1983). c) Centre-to-centre distance analysis for DTNNM, after Delaunay triangulation and lines connected to points on the convex hull are omitted. After Mulchrone (2003) and d) Plot of data from modified Delaunay triangulation (Fig. 2.1c) after normalisation. After Mulchrone (2003).

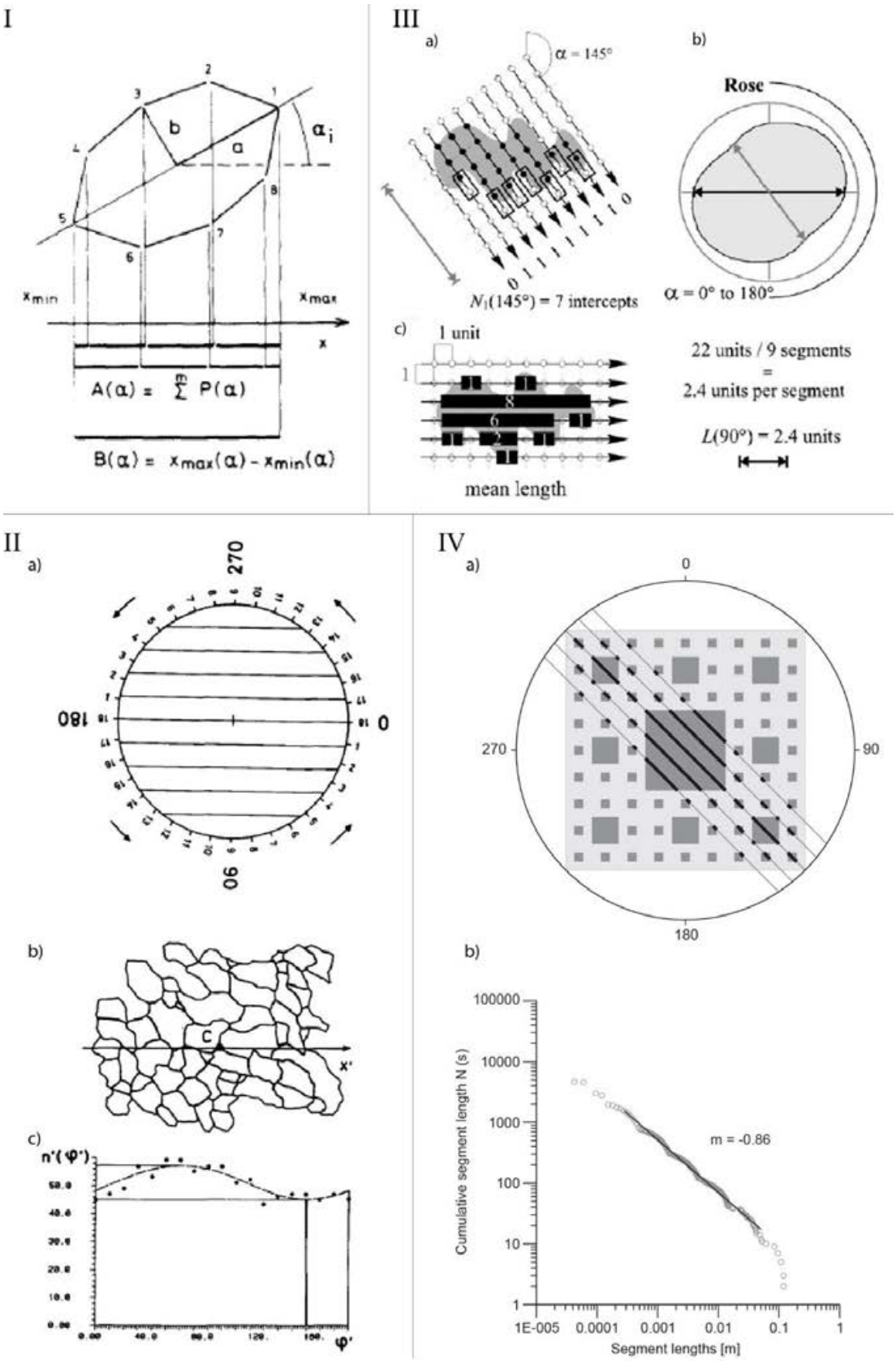

Figure A.2: Graphic summary of grain boundary-based quantification methods. I Projection method (Panozzo, 1983). Projection of an ellipse that is approximated by eight straight-line segments: $\alpha_i = 30°$; $\alpha = 0°$, total projection, A(α), and simple projection. B(α)

are shown schematically. a and b = axes of ellipse: 1 ... 8 = digitized points; x min and x max = minimum and maximum x-coordinates of ellipse. After Panozzo (1984). II Inverse SURFOR techniques by Panozzo (1987). a) Inverse SURFOR wheel and b) outlines of grain boundaries in a quartzite (after Fig. 7.16, p. 118 of Ramsay and Huber, 1983); x' = reference direction = centre and c) analysis of the grain boundaries shown in (b); plot of number of intercepts, n' versus orientation, ϕ'; dashed line = curve fitted through points. After Panozzo (1987). III Intercept method from Launeau and Robin (1996). Counting grid at a) α = 145° on a grey shaded object of a phase X. Analysis points are represented by open when they fall outside the object, and filled dots when they fall in. The number of intercepts N_1 on a line *j*, $N_1(j,\alpha)$, is the number of times, in boxes, a cursor migrating along that line moves out of phase X. For several equally spaced lines parallel to a direction α, the total number of intercepts is $N_1(\alpha)$. b) Rose of intercept counts, $N_1(\alpha)$, plot from 0 and 360°. c) The number of analysis points falling into a phase X divided by the number of intercepts along a line *j*, $N_1(j,\alpha)$, gives the mean intercept length $L(j,\alpha)$. After Launeau et al. (2010). V Cantor-dust method (Volland and Kruhl, 2004) applied to the holes of a Sierpinski carpet. a) In 1° rotation steps a set of parallel scan lines superimposed on the pattern. Inside a circular region of interest segments of each scan line that cover the structure are emphasized. b) Number of segments with lengths is plotted cumulatively against segment length s on a log-log diagram. The black line indicates the corresponding linear regression line with slope m. Dataset from 27 scan lines at 133°. After Gerik and Kruhl (2009).

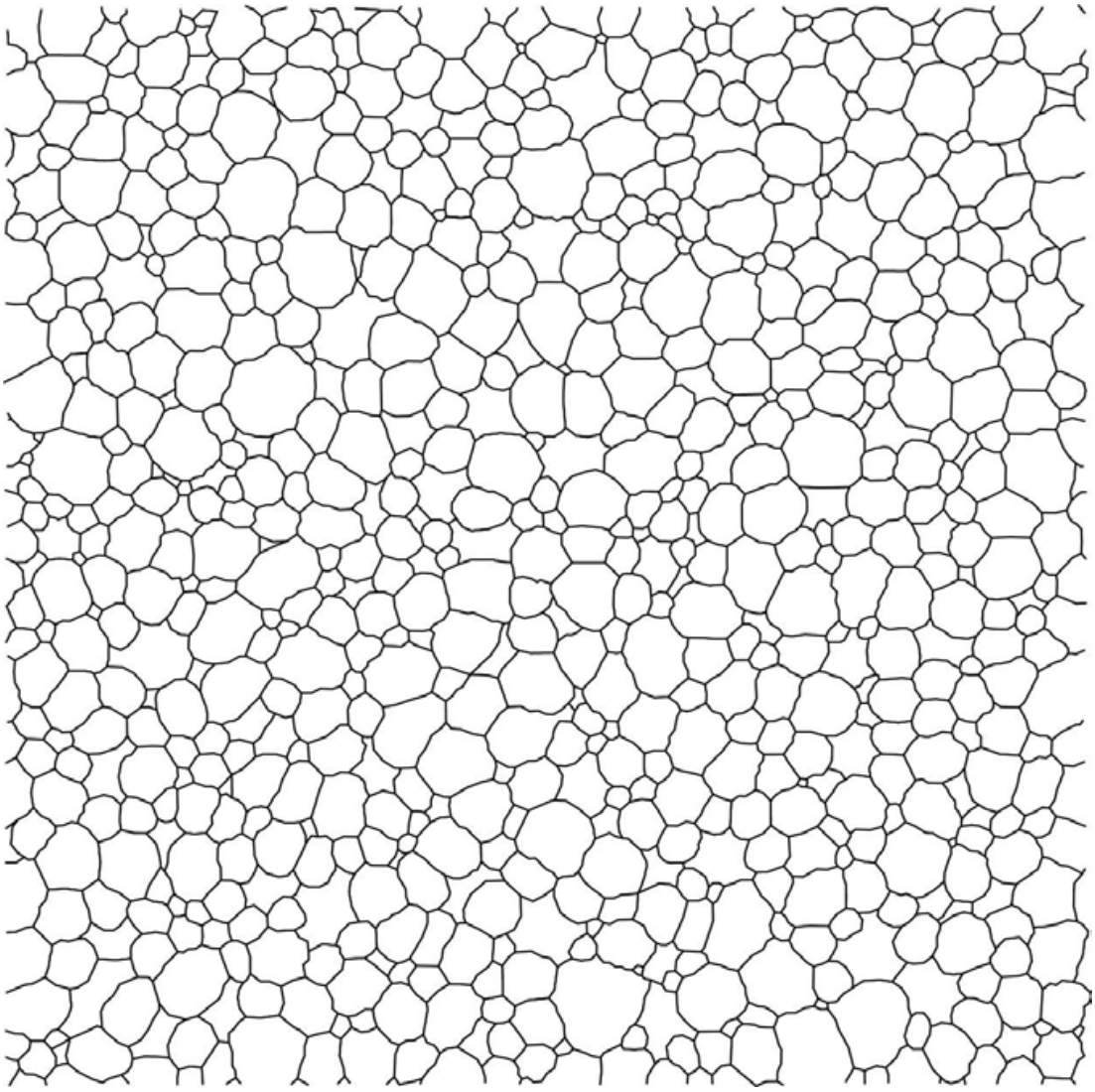

Figure A.3: Initial grain boundary pattern for the analysis of a microstructure with round grains, called 'Granular' during the case studies.

A

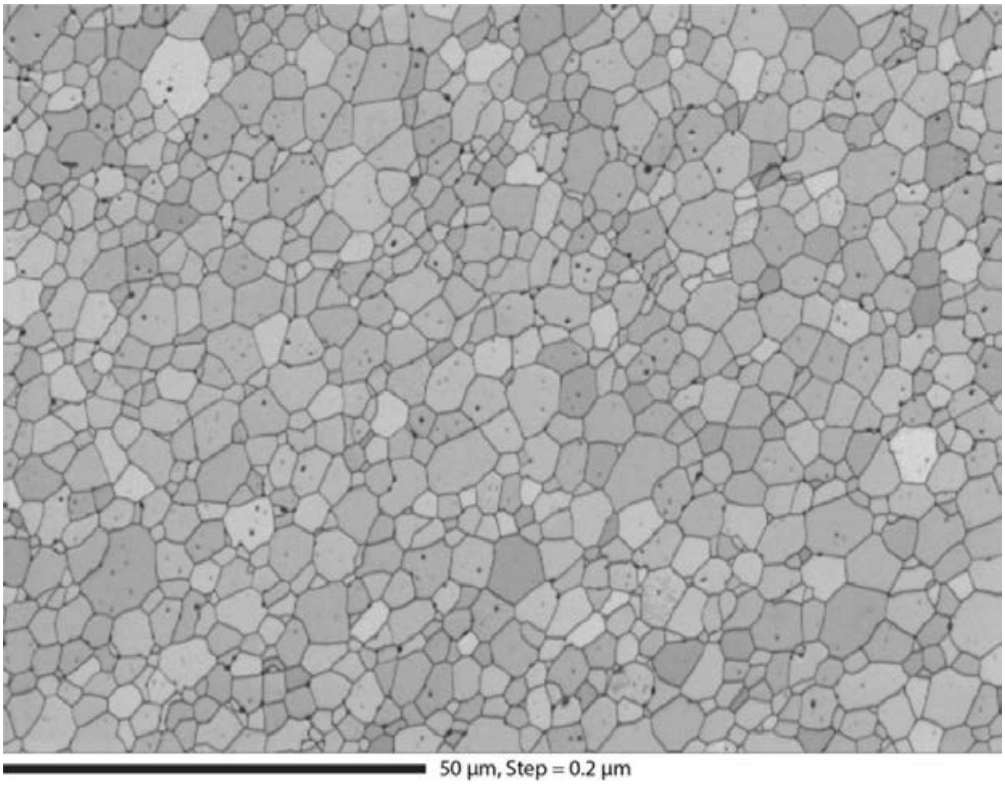

B

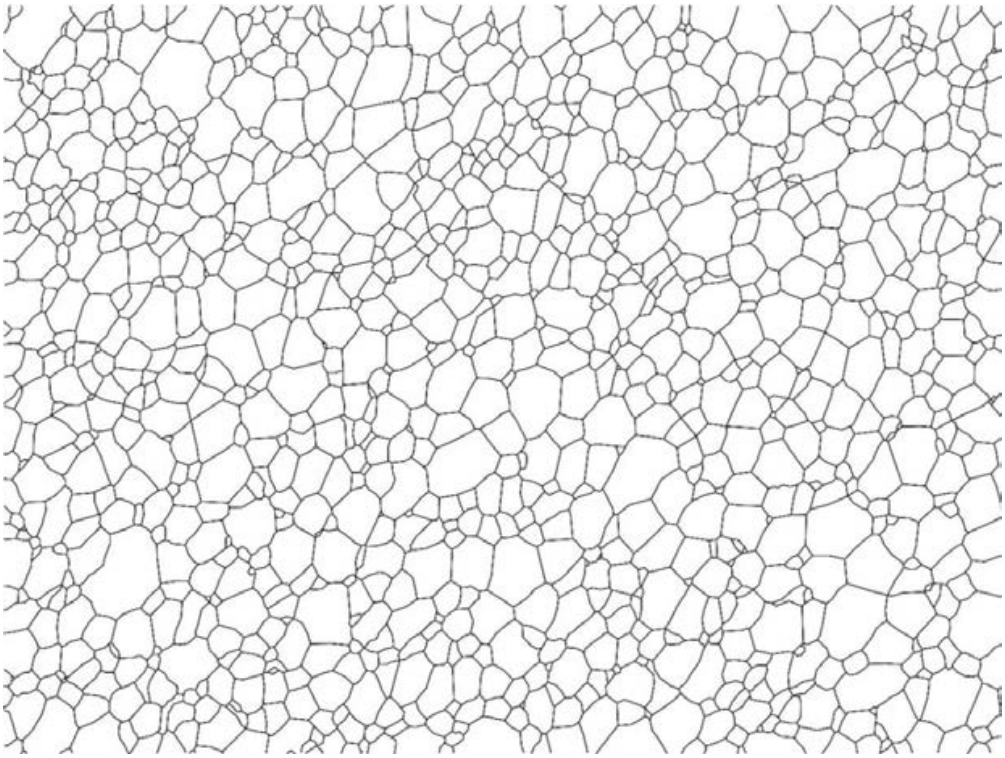

Figure A.4: Backscatter electron image of the polycrystalline foam texture of a zirconia ceramic sample, providing the initial grain boundary pattern for the 'Foam' pattern case study is shown in A. Manual grain boundary tracing with a vector graphics program of the backscatter electron image provided the grain boundary map B.

A.2 Tables

Table A.1: Software tools that quantify preferred orientation (anisotropy) of particles and grain boundary networks. A full overview is exceeding the frame of this literature review. Therefore, the most topic relevant and popular tools are included in the table.

Software tool	Software publication	Applied method(s)	Method development
PAROR (FORTRAN)	Panozzo (1983)	Quantification of particle fabric, i.e., aspect of fabric made up by shape, size and orientation of particles in space; area based.	Panozzo (1983)
SURFOR (FORTRAN)	Panozzo (1984)	Line projection method	Panozzo (1984)
IMAGE (FORTRAN)	Starkey and Simigian (1987)	Automated grain shape analysis: Average ellipses, rectangles fitted which summarize size, aspect ratio and orientation of long axes of particles	Simigian and Starkey (1986) Moore (1968) Serra (1982)
ELLIROT (TurboPascal)	Weger (1991)	3D distribution of elliptical objects, calculation of fitted ellipses, final strain ellipsoid	Weger (1991) Used algorithms: Wallbrecher (1986) Ragan (1985)
AUTO (DOS)	Pfleiderer et al. (1993)	Autocorrelation function; SPO, degree of alignment, distribution anisotropy	Agterberg and Fabbri (1978) Bourke (1987) Jähne (1993) Panozzo Heilbronner (1992)
ImageSXM (Pascal / FORTRAN)	Barrett (2002)	Direct image analysis, analysis of segments, analysis of best-fit ellipses	e.g., Barrett et al. (1998) Bickmore et al. (1999) Barrett (2002)
INTERCEPTS	Launeau and Robin (1996)	Intercept method	Launeau et al. (1990) Launeau and Robin (1996)
SPO2003	Launeau and Robin (2003)	Intercept method	Launeau et al. (1990) Launeau and Robin (1996)
Ellipsoid2003	Launeau and Robin (2005)	Fitting ellipsoid from three or more sectional ellipses of arbitrary orientations.	Robin (2002) Owens (1984)
FryJ and FryJFit (ImageJ toolboxes)	Waldron and Wallace (2007)	Normalized and modified Fry method	Fry (1979) Erslev and Ge (1990) McNaught (1994)
AMOCADO	Gerik and Kruhl (2009)	Modified Cantor-dust method	Volland and Kruhl (2004)
FRY3D (R script)	Webber (2012)	Fry method, written to alleviate the impediments of teaching traditional 3D strain analysis	Fry (1979)
Software written on top of	Mulchrone et al. (2013)	R_f/ϕ method	Ramsay (1976), Dunnet (1969), Ramsay and Huber 1983, Lisle (1985)

Mathematica platform		Fry method	Fry (1979)
		Delaunay Triangulation Nearest Neighbour method	Mulchrone (2002; 2003)
FabricS (MATLAB)	Moreno Chávez et al. (2018)	'Particle by particle' method; circular statistics	Schäfer and Teyssen (1987) Capaccioni and Sarocchi (1996) Capaccioni et al. (1997; 2001) Lindqvist and Åkesson (2001) Valentini et al. (2008) Beggan and Hamilton (2010)
TomoFab (MATLAB)	Petri et al. (2020)	Best fitted ellipsoid based fabric tensor and second-rank symmetric tensor for 3D data from micro-tomography	Petri et al. (2020)
MTEX (MATLAB)	Fan et al. (2021)	Grain analysis by sphericity Geometric properties grain boundaries	e.g., Bachmann et al. (2010); Niessen et al. (2021); Fan et al. (2021)

Table A.2: List of main publications that focus on reviewing pattern quantification methods.

Publication	Title	Methods discussed	Method development
Trayner (1986)	A comparison of Sanderson's and Panozzo's strain measurement methods using calcite grain boundaries from the Variscan fold and thrust belt in Ireland	Sanderson line orientation SURFOR projection	Sanderson (1977) Panozzo (1984)
Mulchrone and Choudhury (2004)	Fitting an ellipse to an arbitrary shape: implications for strain analysis	Overview on fitted ellipse-based methods	Various
Webber (2012)	Advances in Rock Fabric Quantification and the Reconstruction of Progressive Dike Replacement in the Coastal Batholith of Central Chile	R_f/ϕ method	Ramsay (1976), Dunnet (1969), Ramsay and Huber (1983), Lisle (1985)
		Fry method	Fry (1979)
		Sanderson and Panozzo projection methods	Sanderson (1977), Sanderson and Phillips (1987), Panozzo (1984; 1987)
		Delaunay Triangulation Nearest Neighbour method	Mulchrone (2003), Mulchrone et al. (2005)
		Intercept method	Launeau and Robin (1996)
Kruhl (2013)	Fractal-geometry techniques in the quantification of complex rock structures: A special view on scaling regimes, inhomogeneity, and anisotropy	Fractal-geometry methods, intercept method	Various Launeau and Robin (1996)
		Fry method	Fry (1979)
Heilbronner and Barret (2014)	Image Analysis in Earth Sciences. Microstructures and Textures of Earth Materials	Best-fit ellipse SURFOR projection methods	Various Panozzo (1984; 1987)

A.3 Computer Code availability

Name of code: GBPaQ

Developer: David Healy, Johanna Heeb, Nicholas E. Timms, Enrique Gómez-Rivas

E-Mail: d.healy@abdn.ac.uk

Year first available: 2021

Software required: MATLAB 2020

Program language: MATLAB

Program size: 767 MB

Source code: https://github.com/DaveHealy-github/GBPaQ

A.4 Supplementary Data

Supplementary data to this chapter can be also found online at:

https://studentcurtinedu-my.sharepoint.com/:f:/g/personal/19246301_student_curtin_edu_au/EkOz1fYdIF9Dgsa2S0bK7kEBupiKJQ8P5rgQU7Y7mWCJLw?e=dnIS3h

APPENDIX B

Supplementary material to chapter 3

B.1 Figures

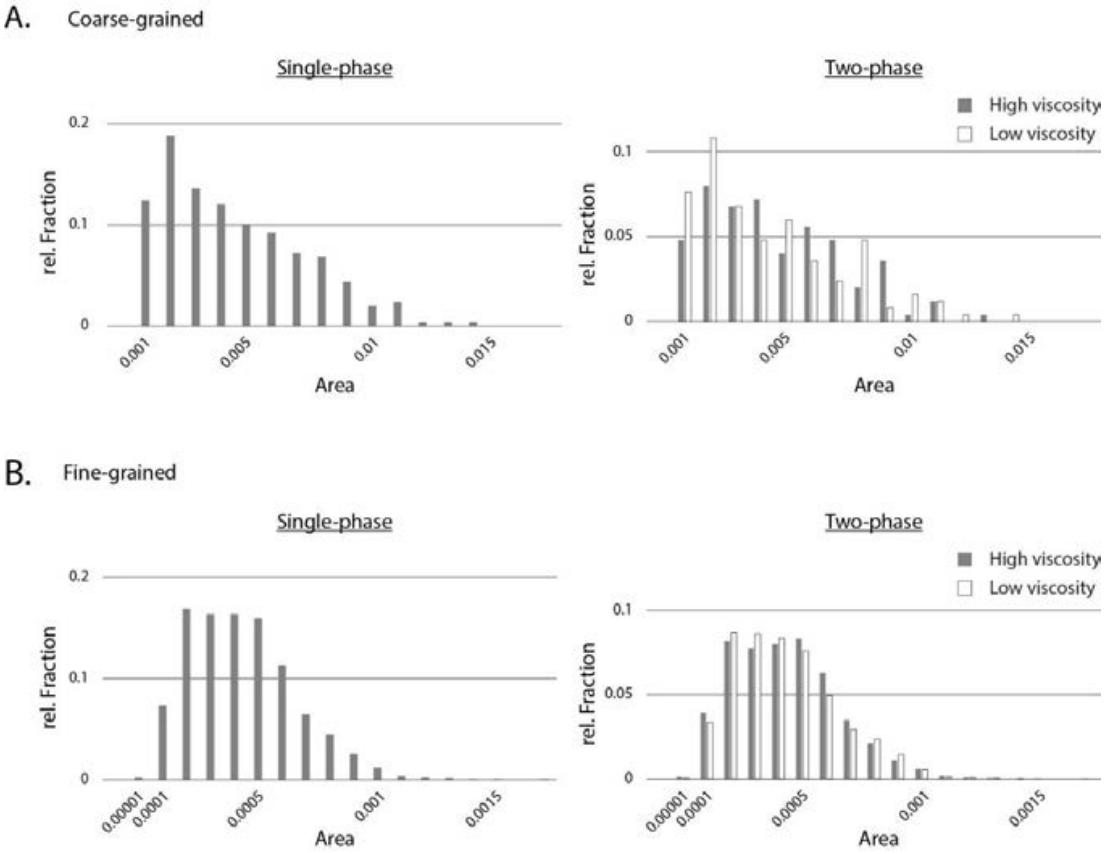

Figure B.1: Grain area histograms for A. coarse-grained, and B. fine-grained single- and two-phase viscosity simple shear models (1:1) at time step 0, based on grain boundary pattern characteristics exported from ELLE.

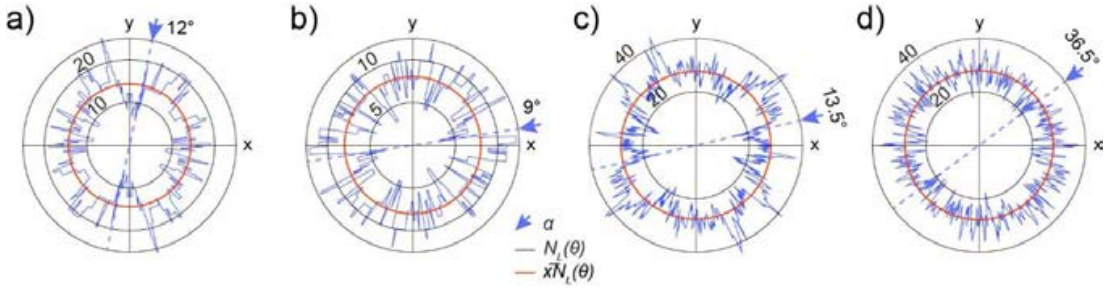

Figure B.2: Phase boundary GBPaQ GBSI density analysis for all basic two-phase models. a) Shows the results for coarse-grained simple shear, b) the results for the coarse-grained pure shear, c) the results for fine-grained simple shear, and d) the results for the fine-grained pure shear initial phase boundary pattern. One central radial scan line centre, with 0.5° angles between scan lines was used for analysis. The GBSI density (per pixel) is plotted against scan line orientation as blue contours. The average grain boundary intercept density ($\bar{x}N_L(\theta)$) from all scan lines is plotted as red circles. The location of minimum GBSI density scan line is marked as α.

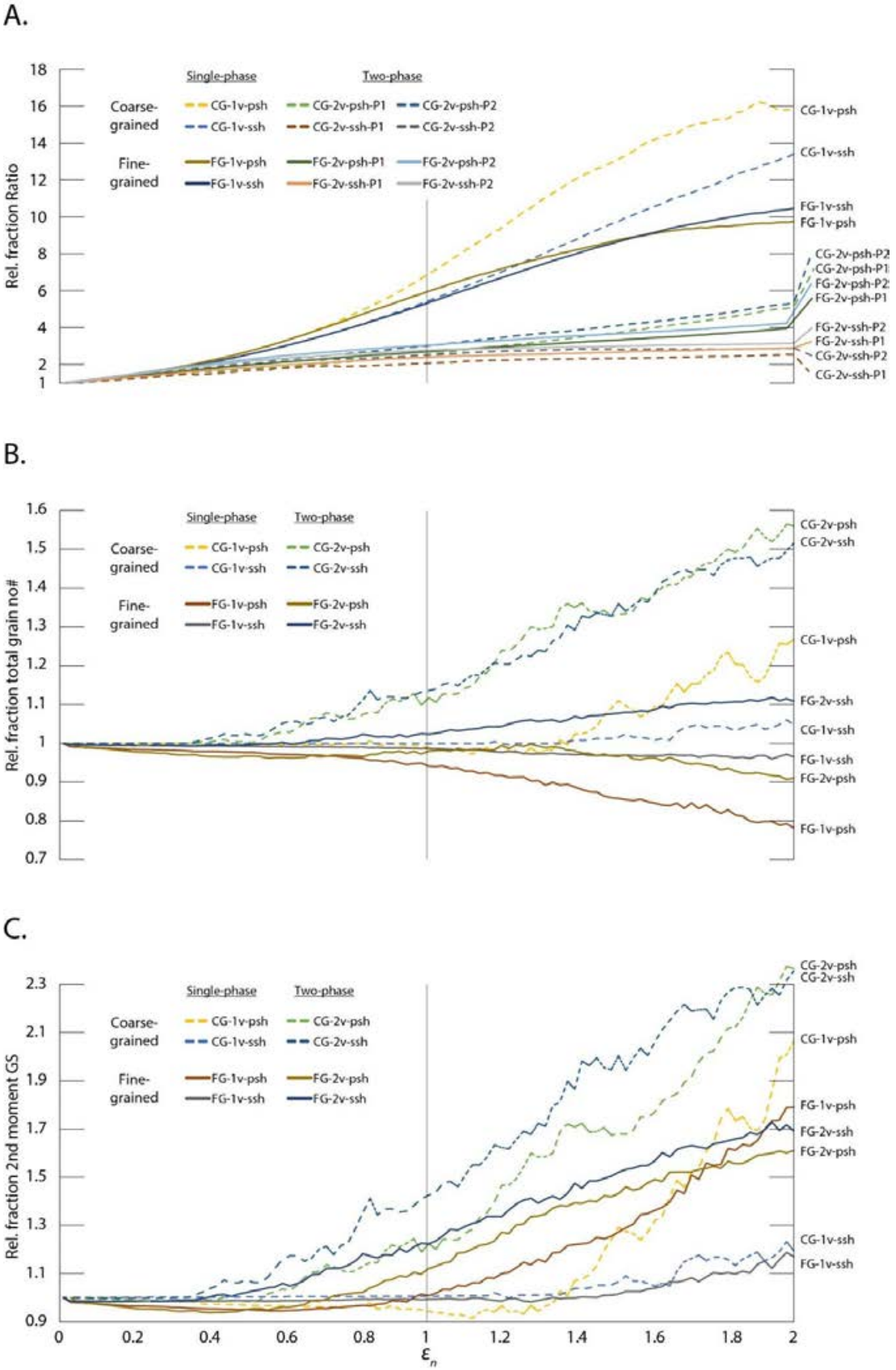

Figure B.3: Pattern statistics for all models, based on ELLE output and calculated as relative fraction of time step 0 and plotted against natural strain ε_n. A. is the axial ratio, B. is the total grain number and C. is the second moment grain size.

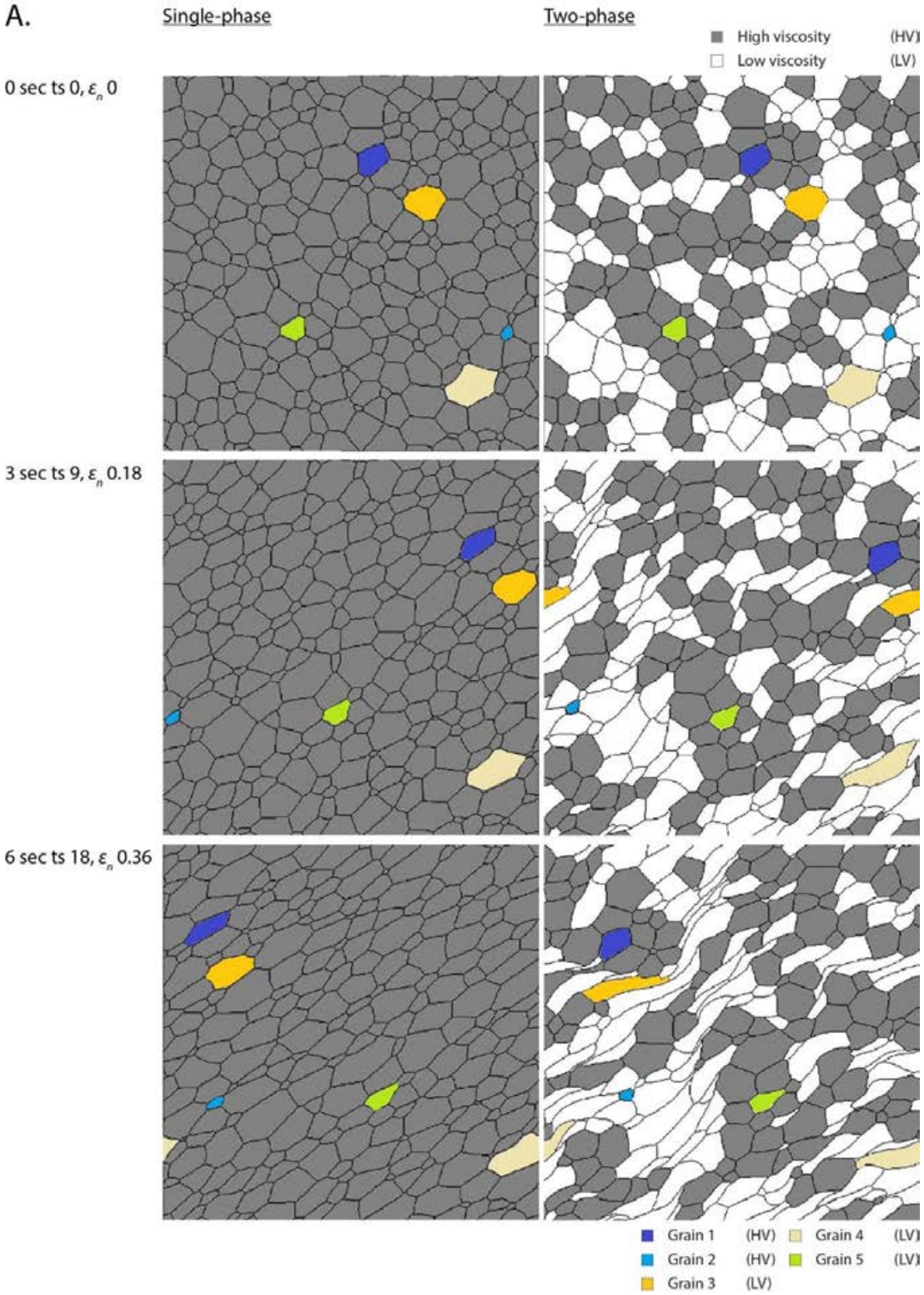
A.
Single-phase
Two-phase
High viscosity (HV)
Low viscosity (LV)
0 sec ts 0, ε_n 0
3 sec ts 9, ε_n 0.18
6 sec ts 18, ε_n 0.36
Grain 1 (HV)
Grain 2 (HV)
Grain 3 (LV)
Grain 4 (LV)
Grain 5 (LV)

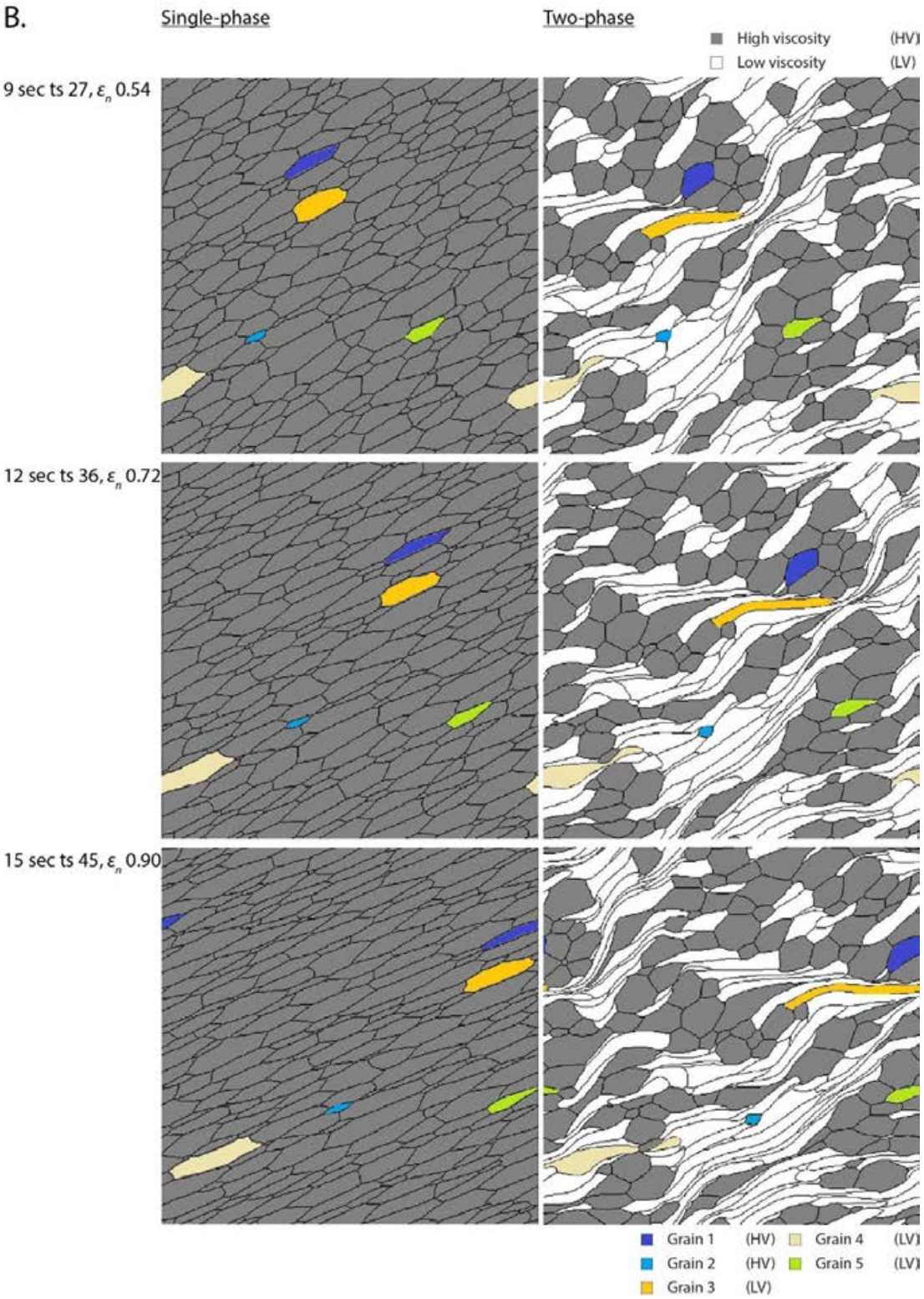
B.
Single-phase
Two-phase
High viscosity (HV)
Low viscosity (LV)
9 sec ts 27, ε_n 0.54
12 sec ts 36, ε_n 0.72
15 sec ts 45, ε_n 0.90
Grain 1 (HV)
Grain 2 (HV)
Grain 3 (LV)
Grain 4 (LV)
Grain 5 (LV)

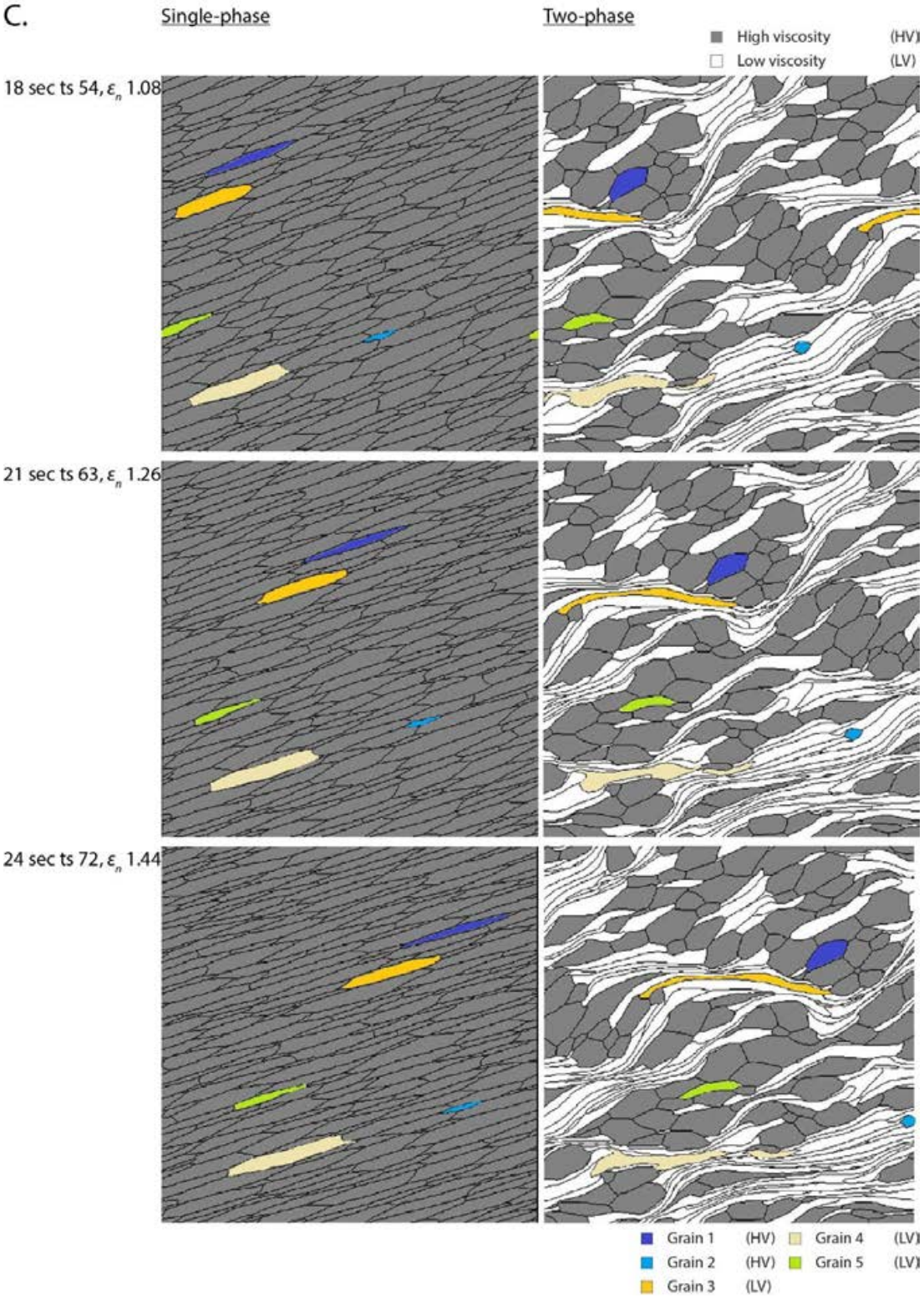
C.
Single-phase
Two-phase
High viscosity (HV)
Low viscosity (LV)
18 sec ts 54, ε_n 1.08
21 sec ts 63, ε_n 1.26
24 sec ts 72, ε_n 1.44
Grain 1 (HV)
Grain 2 (HV)
Grain 3 (LV)
Grain 4 (LV)
Grain 5 (LV)

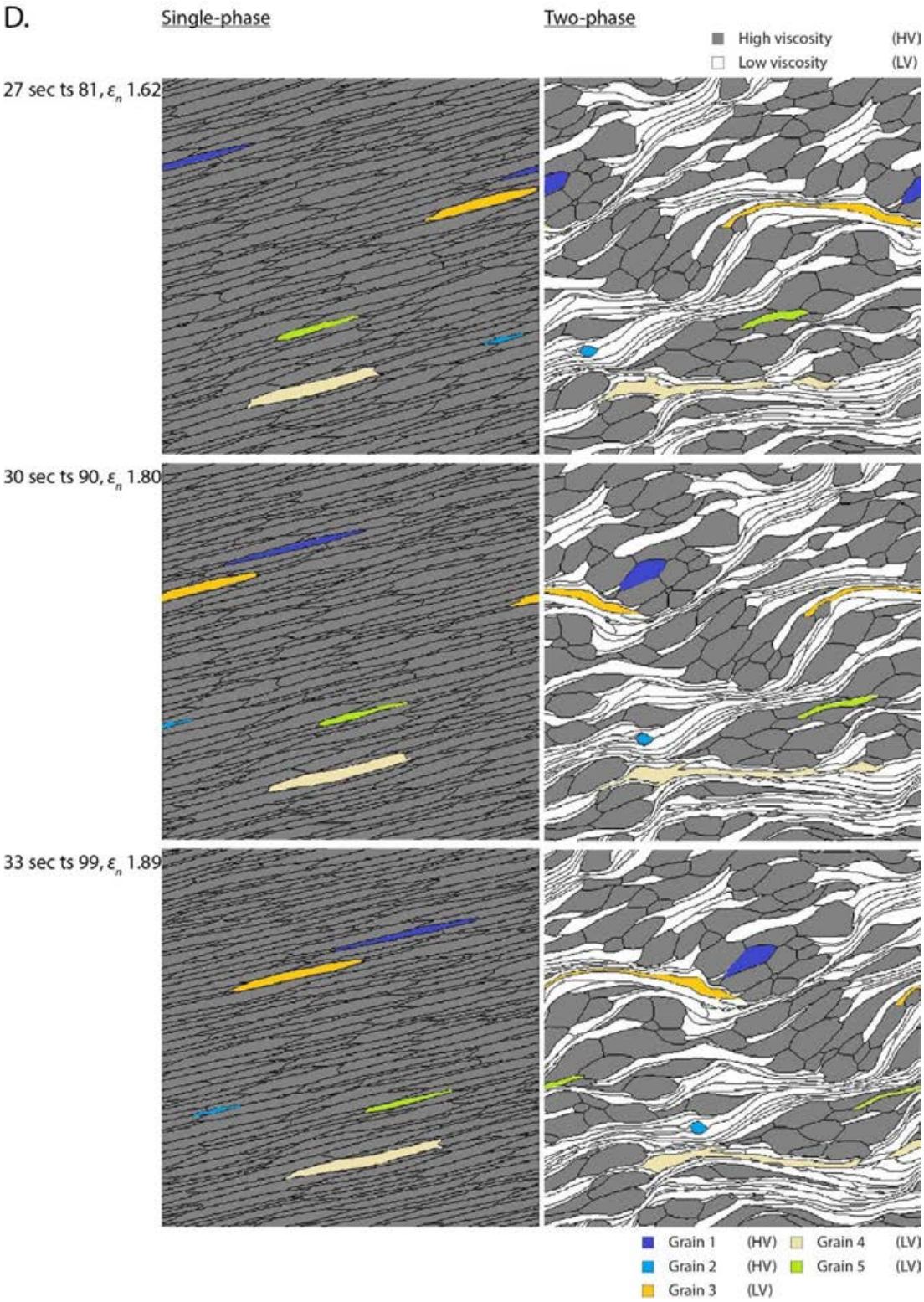

Figure B.4: Evolution of the coarse-grained, simple shear single- and two-phase grain boundary models. The maps show the sample patterns every nine time steps, equivalent to an increase of natural strain of 0.18 % for each step. White are the low viscosity grains and grey are the high viscosity grains in the dual viscosity model. The same 5 grains are tracked throughout the two models. For all models the *x*-axis is oriented horizontal, while the *y*-axis is vertical.

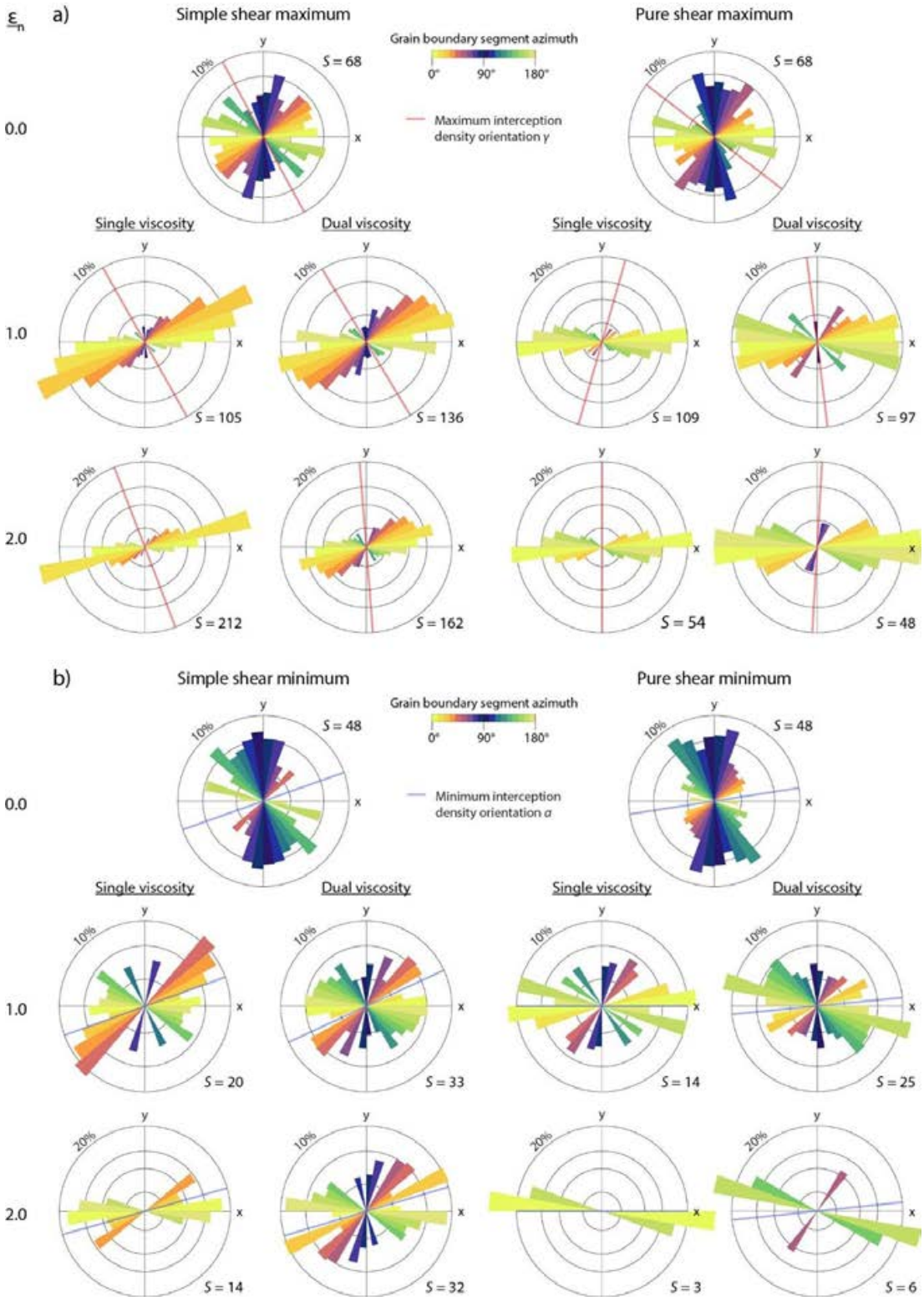

Figure B.5: Grain boundary segment angle orientation rose plots (equal area, length-weighted) of segments intercepted along a) maximum (*y*) and b) minimum (*α*) GBSI density scan lines at natural strains (ε_n) of 0, 1 and 2 (time steps 0, 50 and 100) of the fine-grained strain models. Each plot contains the orientation of the scan line that intercepted the plotted data. Angle values are listed in table 3.3 (Chapter 3). *S* is the number of grain boundary segments analysed.

The analysis of the grain boundary segment characteristics intercepted along α and γ of the fine-grained models by single scan lines (Fig. B.5) shows differences between α and γ, as well as between simple shear and pure shear models. For γ (Fig. B.5a), the intercepted segments at the initial time step are mostly randomly oriented, with gaps around γ, where segments are almost parallel and thus, intercepts unlikely or not possible.

Most segments intercepted along α (Fig. B.5b) at the initial time step are accumulated over a range of 30° to 40°, with a 30° gap around α. In general, the intercepted grain boundary segments along γ are more random in terms of their orientation and intensity, which is inversed rapidly towards medium natural strains, where strongly preferred segment orientations develop.

At a natural strain of 1, the angles and lengths of grain boundary segments intercepted along γ form strong perpendicular high intensity bin clusters relative to γ. The same trend of grain boundary segment re-orientation can be observed for α, with the difference that the bins range around α but are still distributed over a wider range with more bins with medium and high intensities.

At the finite natural strain of 2, the intercepted grain boundary segments generally have less variety in orientation, with main peaks perpendicular to γ and parallel to α. In most cases of two-phase models, the intercepted grain boundary segments are oriented slightly more randomly, covering a greater range of segment angles.

Table B.1 shows that the angle between γ and α (ϕ) is never exactly 90°. Only the fine-grained pure shear single-phase comes close with ϕ = 91.5°. Most other models are off by ~ 10°, except for the pure shear model at the initial stage (ϕ = 46°) and the pure shear single-phase at a natural strain of 1 (ϕ = 73.5°).

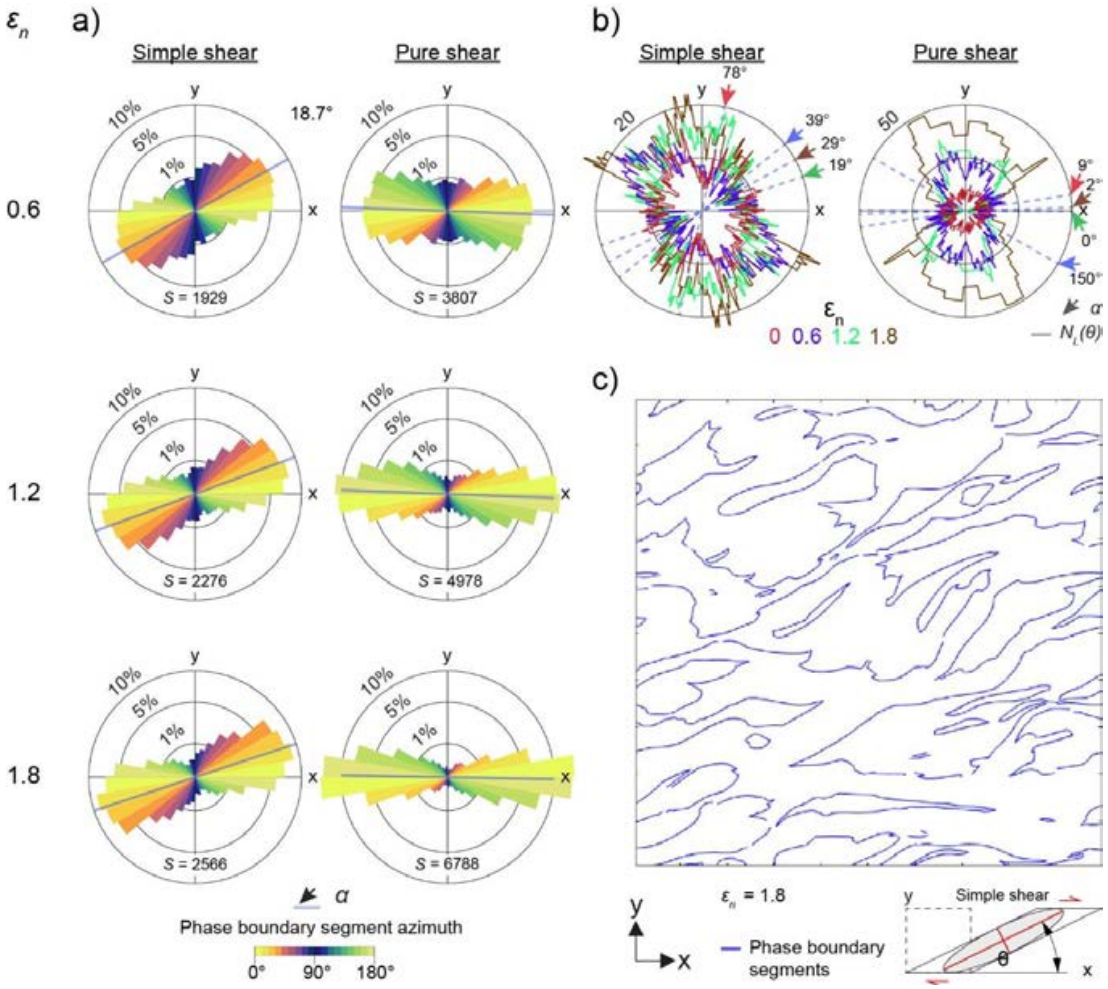

Figure B.6: Evolution of phase boundary segment azimuths of coarse-grained two-phase simple shear and pure shear models. a) Equal area, length-weighted phase boundary segment azimuth rose plots at natural strains (ε_n) of 0.6, 1.2 and 1.8 (time steps 30, 60 and 90). *S* is the number of segments analysed. b) Contoured rose plots of phase boundary segment intercept density per pixel plotted against scan line orientation (θ) for the same natural strains in a). One central radial scan line centre, with 0.5° angles between scan lines was used for analysis. The location of minimum GBSI density scan line is marked as α. c) Phase boundary pattern of the simple shear fine-grained two-phase model at a natural strain of 1.8.

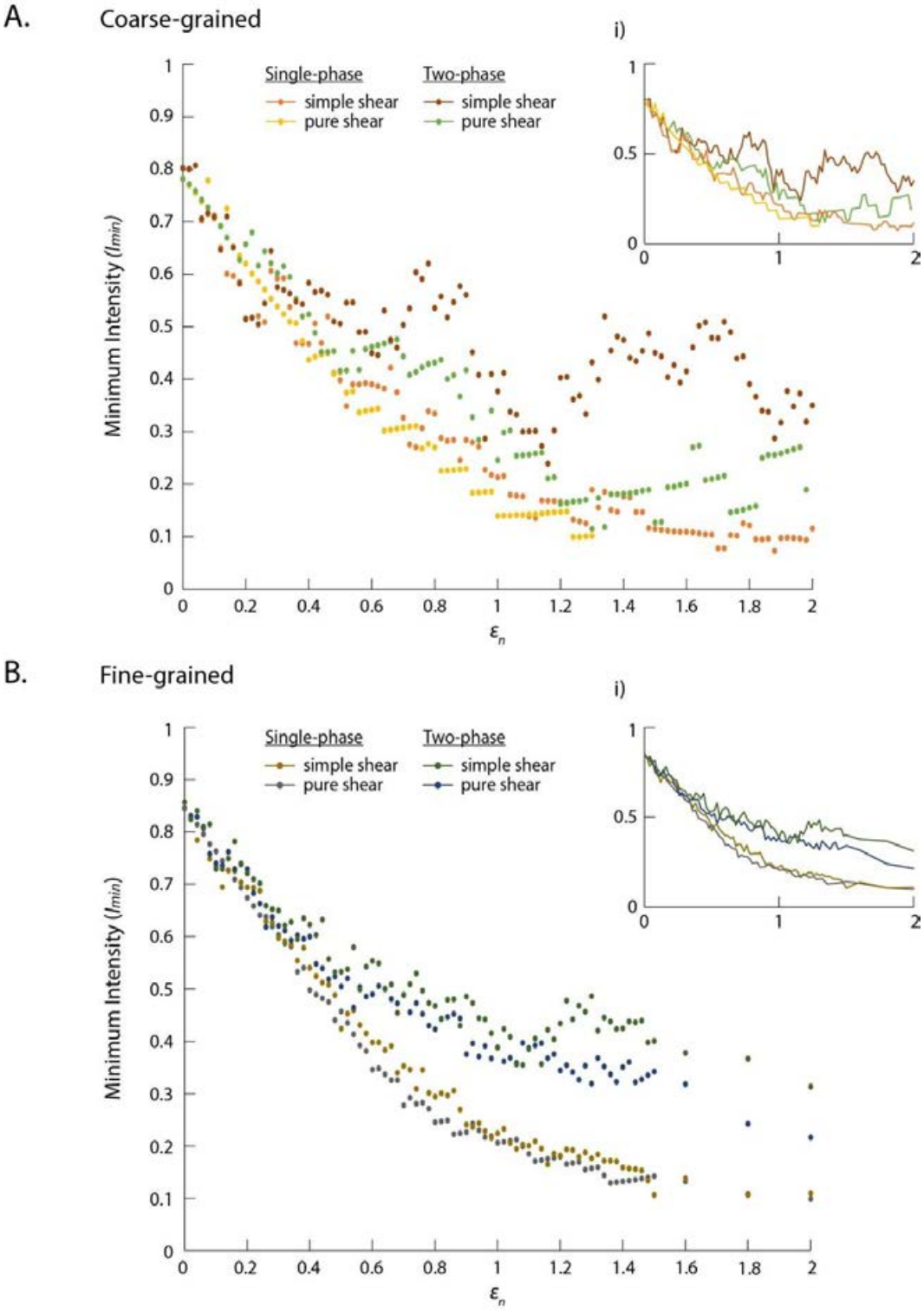

Figure B.7: GBSI density minimum intensity I_{min} versus natural strain ε_n diagrams. The four coarse-grained, simple shear and pure shear, single- and two-phased datasets presented as points in A. and as curves in A.i). The four fine-grained, simple and pure shear, single- and two-phase datasets presented as points in B. and as curves in B.i). Corresponding values are listed in Tables B.1 to B.8.

B.2 Tables

Table B.1: Segment orientation angle [°] of γ, α and ϕ for three time steps of the fine-grained models. Addition to Figure 3.5 and 3.6.

	γ				α				ϕ			
	Simple shear		Pure shear		Simple shear		Pure shear		Simple shear		Pure shear	
ε_n	1v	2v	1v	2v	1v	2v	1v	2v	1v	2v	1v	2v
0	118.5		142.5		19.5		8.5		9		44	
1	119.5	121	74	97	20	24.5	0.5	6	9.5	6.5	16.5	1
2	111	94.5	90.5	87	15	17	2	7	6	167.5	178.5	10

Table B.2: GBPaQ analysis results ($d\beta$ = 0.5° = angular intervals between scan lines). *Step* is the time step; $N_L(\alpha)$ is the minimum GBSI density per pixel; α is the angle of the scan line with the minimum number of grain boundary segment intercepts (α); $N_L(\gamma)$ is the maximum GBSI density per pixel; γ is the angle of the scan line with the maximum number of grain boundary segment intercepts (γ); $\bar{x}N_L(\theta)$ is the mean number of grain boundary segment intercepts per scan line. I_{min} is the minimum intensity.

I) Coarse-grained, pure shear, single-phase model

Step	$N_L(\alpha)$ [px]	α [°]	$N_L(\gamma)$ [px]	γ [°]	$\bar{x}N_L(\theta)$ [px]	I_{min}
0	13.689	32	23.166	38.5	17.5169	0.781474
1	13.422	31.5	22.7146	37.5	17.4534	0.769019
2	13.1585	9.5	24.2926	37.5	17.4305	0.754912
3	12.9129	9.5	23.8391	37.5	17.4964	0.738032
4	13.6408	8.5	23.3842	89	17.5246	0.77838
5	12.4168	8.5	23.8785	96.5	17.59	0.705901
6	12.1688	8	22.4655	33	17.597	0.691527
7	12.8383	7.5	23.8426	62	17.7096	0.724934
8	11.6918	7.5	24.283	61	17.9275	0.652171
9	11.4666	7	24.6972	97.5	18.0593	0.634942
10	11.2424	7	25.0791	83	18.1164	0.620565
11	11.0209	6.5	25.4329	32.5	18.341	0.600889
12	10.8041	6.5	26.5946	32	18.4313	0.586182
13	10.5915	6	26.0715	32	18.5569	0.570758
14	10.3829	6	27.1553	31.5	18.763	0.553371
15	10.1781	5.5	26.6197	78	18.8827	0.539017
16	9.9772	5.5	28.3966	77.5	19.0485	0.523779
17	9.7797	5	28.5868	77	19.1932	0.50954
18	9.8432	5	29.5295	102	19.4259	0.506705
19	9.2715	5.5	29.3596	76	19.5963	0.473125
20	8.6726	5	29.9599	75.5	19.8373	0.437187
21	8.8492	4.5	31.3744	75	19.9813	0.442874
22	9.0297	4.5	32.0145	74.5	20.1988	0.447041
23	9.215	4	31.8335	73.5	20.4958	0.449604
24	8.5472	177	32.4794	73	20.8358	0.410217
25	8.7217	5.5	33.1426	72.5	21.1112	0.413131
26	8.0102	177	33.8207	71.5	21.4197	0.373964
27	8.1732	177	34.5092	71	21.7046	0.376565
28	7.4135	179	35.2142	75.5	22	0.336778
29	7.5649	0	35.9334	72	22.2935	0.339332
30	7.7192	0	36.666	72.5	22.6034	0.341506
31	7.8765	0	36.4289	68	22.9222	0.343619
32	7.0327	178.5	37.1728	67	23.3067	0.301746
33	7.1763	178.5	38.9569	72.5	23.6034	0.304037
34	7.3229	0	39.7528	72	23.9478	0.305786
35	7.4721	0	39.4951	92.5	24.2431	0.308216
36	7.6246	0	41.3906	93	24.6262	0.309613
37	7.7802	0	42.2351	93	25.0177	0.310988
38	6.8047	0	43.0965	93	25.3816	0.268096
39	6.9436	0	43.9759	93	25.0864	0.276787
40	7.0853	0	43.6924	93	26.225	0.270173
41	6.0249	176	44.5841	93	26.73	0.225398

42	6.1481	5.5	46.7255	93.5	27.2119	0.225934
43	6.2734	5	46.4228	93	27.6097	0.227217
44	6.4014	0	47.3705	94	28.026	0.228409
45	6.5322	0	48.337	94	28.5181	0.229055
46	5.3322	1.5	49.3231	94	28.9963	0.183892
47	5.4411	0	50.3298	94.5	29.4957	0.184471
48	5.5521	0	51.3566	94.5	29.9242	0.185539
49	5.6654	0	52.4052	94.5	30.433	0.18616
50	4.3358	178.5	52.0291	82	31.0218	0.139766
51	4.4243	178.5	53.0913	81.5	32	0.140346
52	4.5146	0	54.1754	81	32.1492	0.140427
53	4.6068	0	55.2821	81	32.6355	0.141159
54	4.7007	0	56.4084	96.5	33.2396	0.141419
55	4.7967	0	57.56	100.5	33.6609	0.142501
56	4.8946	0	58.7347	100.5	34.1986	0.143123
57	4.9944	0	58.2683	79.5	34.67	0.144055
58	5.0964	0	59.4578	79	35.0385	0.145451
59	5.2003	0	60.6702	78.5	35.4597	0.146654
60	5.3065	0	62	97.5	35.9875	0.147454
61	5.4148	0	61.3673	97.5	36.5565	0.148121
62	3.6835	0	64.4614	98	36.9986	0.099558
63	3.7587	0	63.8983	99	37.6029	0.099958
64	3.8354	0	65.2014	99.5	38.1144	0.100629
65	3.9137	0	64.5757	75.5	38.5885	0.101421

II) Coarse-grained, simple shear, single-phase model.

Step	$N_L(\alpha)$ [px]	α [°]	$N_L(\gamma)$ [px]	γ [°]	$\bar{x}N_L(\theta)$ [px]	I_{min}
0	14.7547	2	25.2938	77	18.3827	0.802641
1	14.757	3.5	24.2437	44	18.4412	0.800219
2	13.7052	25	24.2477	47	18.1503	0.755095
3	12.6512	46.5	23.1939	111.5	18.0146	0.702275
4	12.6506	28	23.1928	143.5	17.6907	0.715099
5	12.6501	26	26.3544	93.5	17.7718	0.711807
6	11.5955	32.5	27.4076	151.5	17.8238	0.650563
7	10.5398	35	25.2955	138	17.5507	0.600534
8	10.5404	33	24.2429	139.5	17.654	0.597054
9	10.5335	30	25.2804	166.5	18.0077	0.584944
10	9.4806	30.5	28.4418	99	18.3987	0.515286
11	9.4799	33.5	25.2797	100	18.3155	0.517589
12	9.4789	35	26.3303	105	18.2231	0.520158
13	9.4819	37.5	30.5528	118	18.6336	0.50886
14	11.5867	35.5	31.6	114.5	19.0988	0.606672
15	11.582	14.5	31.5873	120	19.5599	0.59213
16	11.5812	16.5	31.585	115	19.5351	0.592841
17	10.5339	13	32.6551	116	19.5922	0.537658
18	9.479	32.5	34.7565	105.5	20.2261	0.468652
19	9.4798	31.5	30.5461	104	20.257	0.467977
20	9.4842	33	32.6678	108	20.2926	0.467372
21	10.5352	25.5	34.7662	125.5	20.8016	0.506461
22	9.487	24	33.7314	121.5	20.2239	0.469098
23	10.5335	18.5	34.7605	109	20.2751	0.519529
24	8.425	30.5	33.6998	111.5	20.4577	0.411825
25	8.4241	28.5	34.7495	110.5	21.1592	0.398129
26	7.371	27.5	32.6428	119.5	21.1592	0.348359
27	8.4258	31.5	33.7033	90.5	21.5904	0.390257
28	8.4374	26.5	34.8044	130.5	21.6143	0.390362
29	8.4265	23	36.866	129	21.471	0.39246
30	8.426	36	35.8104	112.5	21.5938	0.390205
31	8.423	24.5	34.7451	122	21.7703	0.386903
32	8.4231	26.5	35.7981	115.5	22.0449	0.382088
33	9.4771	11.5	41.0672	114	22.4432	0.42227
34	8.4248	32	36.8584	115	22.4408	0.375423
35	7.374	31	36.8701	122	22.5867	0.326475
36	6.3186	32.5	38.9647	129	22.9432	0.275402
37	6.3176	33	41.0641	116.5	23.3177	0.270936
38	7.3704	26.5	38.958	126	24.0083	0.306994
39	8.4247	22	38.9644	126	24.8448	0.339093
40	8.426	17	37.917	98.5	25.1684	0.334785
41	7.3748	18.5	41.0882	126	25.643	0.287595
42	7.3706	18.5	43.1707	112	26.0943	0.28246
43	7.37	20.5	43.1672	110.5	25.936	0.284161
44	6.3217	25.5	42.145	117	25.7166	0.245822
45	7.3741	21	43.191	119.5	25.9663	0.283987
46	7.379	23	42.166	122	26.3537	0.279999
47	7.3721	21.5	47.3922	120	27.1266	0.271766
48	6.3169	23.5	45.2715	96.5	27.7589	0.227563
49	6.3197	20.5	46.3444	122	29.0858	0.217278

50	6.321	20.5	52.6752	98	29.6238	0.213376
51	6.3213	22.5	55.8385	101.5	29.3549	0.215341
52	5.2657	21	53.7098	99.5	29.311	0.179649
53	5.2672	18	52.6718	105	29.5868	0.178025
54	5.2667	17	52.6675	100.5	29.7787	0.176861
55	4.2115	18	48.4328	102.5	30.3599	0.138719
56	4.2109	19	515,834	115.5	31.132	0.13526
57	5.2666	14.5	52.6662	111	31.1658	0.168987
58	5.2637	18.5	52.6371	104.5	31.2567	0.168402
59	5.266	16.5	51.6067	101	31.3899	0.167761
60	5.2644	17	52.644	107	32	0.166267
61	5.2651	15	53.7043	107.5	32.102	0.164012
62	4.2124	15.5	54.7616	112	31.7524	0.132664
63	4.2128	17	55.8202	112.5	32.7036	0.128818
64	4.2129	18	57.9272	114	33.6184	0.125315
65	6.3236	15	55.8589	104	33.4337	0.189139
66	5.2657	18.5	54.7635	114.5	33.7809	0.155878
67	6.32	16.5	55.8268	87.5	34.0998	0.185338
68	5.2641	17	60.0112	83	34.8762	0.150937
69	5.2641	17.5	60.0111	86	35.5756	0.147969
70	6.317	15.5	61.0641	92	35.8064	0.176421
71	6.3185	12	61.0791	88	36.1059	0.174999
72	5.2643	12	58.9606	96	35.7304	0.147334
73	5.2666	12.5	61.0921	92.5	35.7556	0.147294
74	4.2123	16	60.0248	93.5	36.1782	0.116432
75	4.2118	15	63.1772	120.5	36.6884	0.114799
76	4.2116	14.5	64.2267	121.5	37.2457	0.113076
77	4.2111	14	64.2198	95.5	37.8053	0.111389
78	4.2109	17.5	67.3744	97.5	38.3128	0.109908
79	4.2127	18.5	67.4025	100.5	38.6136	0.109099
80	4.2119	17	68.444	98	38.5413	0.109283
81	4.2118	15.5	69.4947	98	38.9256	0.108201
82	4.2125	13.5	70.5586	107	39.6999	0.106109
83	4.2124	15.5	74.7706	109	40.2386	0.104686
84	4.2125	17	74.772	106.5	40.4687	0.104093
85	3.1592	16.5	66.3425	100.5	40.4879	0.078028
86	3.1592	16	65.2897	89.5	40.5333	0.077941
87	4.2133	13.5	65.306	101.5	40.8604	0.103115
88	4.2126	12.5	70.5619	117	41.4181	0.101709
89	5.2653	12	71.6076	113	42.0637	0.125174
90	5.264	10.5	75.8023	108.5	43.247	0.121719
91	4.2117	12.5	76.863	103.5	44.021	0.095675
92	4.2117	12.5	77.9164	100.5	44.3557	0.094953
93	4.2121	14.5	74.7654	93.5	43.6812	0.096428
94	3.1583	13.5	74.7475	104	43.2225	0.073071
95	4.2116	12.5	70.5444	105	43.0506	0.097829
96	4.2116	12	69.4907	112	42.8998	0.098173
97	4.2124	12.5	69.5051	107	43.1453	0.097633
98	4.2122	11.5	69.5011	126	43.6613	0.096474
99	4.2115	11.5	72.6489	108	44.9673	0.093657
100	5.264	12.5	74.7489	118	45.6618	0.115282

III) Coarse-grained, pure shear, two-phase model.

Step	$N_L(\alpha)$ [px]	α [°]	$N_L(\gamma)$ [px]	γ [°]	$\bar{x}N_L(\theta)$ [px]	I_{min}
0	13.689	32	23.166	38.5	17.5169	0.781474
1	13.689	32	23.166	38.5	17.5169	0.781474
2	13.4373	11.5	22.7401	40	17.4156	0.771567
3	13.1705	10	23.3017	37	17.3537	0.758945
4	12.8995	-235	22.8221	96	17.3943	0.741594
5	12.6505	9	25.3011	96	17.4095	0.726643
6	12.3993	8	24.7987	96	17.4845	0.70916
7	12.1586	8	24.3172	53	17.577	0.691734
8	11.9179	8	24.7526	61.5	17.7873	0.670023
9	12.4683	0.5	219.4419	90.5	117.8764	
10	11.4562	7.5	25.556	123	18.269	0.627084
11	12.0988	5.5	25.0618	63	18.4167	0.656947
12	12.7143	5.5	25.4285	87.5	18.697	0.680018
13	11.6252	15.5	26.572	97	18.8567	0.616502
14	12.2058	7.5	26.0391	86.5	18.9526	0.644017
15	11.9739	14	27.9391	88	19.2911	0.620696
16	11.7399	13.5	27.3932	80	19.5199	0.601432
17	12.2722	2	28.3795	99.5	19.9359	0.615583
18	12.0382	1	29.3432	101.5	20.2446	0.594638
19	11.3625	11	30.3	104	20.5701	0.552379
20	10.8174	1.5	30.9068	77	20.8117	0.519775
21	11.0386	2	33.1158	105.5	21.0875	0.523467
22	10.4606	10.5	32.991	106	21.4289	0.488154

23	9.8522	10.5	33.6617	102	21.811	0.451708
24	10.0538	10	35.1883	109.5	22.2515	0.451826
25	10.2571	8	35.8999	111.5	22.6268	0.453316
26	9.594	8.5	37.5037	111.5	23.0541	0.416152
27	9.7909	8.5	39.1637	112.5	23.4977	0.416675
28	10.899	7	38.1466	113	24.0001	0.454123
29	10.1937	7	37.0681	113	24.4066	0.417662
30	11.3472	6	36.8785	106	24.8204	0.457172
31	11.5795	5.5	36.6684	82.5	25.0822	0.461662
32	11.8148	7	39.3826	106.5	25.4103	0.464961
33	12.058	177	41.1983	107	25.7745	0.467827
34	12.3034	176.5	42.0368	107	26.1029	0.471342
35	12.5563	6.5	42.9007	107.5	26.3723	0.476117
36	11.7429	9	40.5664	107	26.4737	0.443569
37	10.8943	6.5	42.4878	109	26.6948	0.408106
38	11.1161	6	41.1295	109	26.8266	0.414369
39	11.3426	7	41.9678	108	26.8401	0.422599
40	11.5763	5.5	42.8323	107.5	26.9916	0.428885
41	11.8089	8.5	43.6929	107.5	27.3505	0.431762
42	12.0523	9	44.5934	107.5	27.5731	0.437104
43	11.0671	7	44.2682	107.5	27.6497	0.400261
44	11.2936	6.5	45.1743	107.5	27.7057	0.407627
45	10.2425	168.5	46.0914	107.5	27.9024	0.367083
46	11.7585	2.5	47.0339	108	28.1794	0.417273
47	9.3325	5	46.6625	70.5	28.4542	0.327983
48	8.1632	5	48.979	108	28.7277	0.284158
49	8.3299	5	48.5911	108	29.0526	0.286718
50	9.916	3	50.9967	108	29.1724	0.33991
51	7.227	6.5	52.0344	110	29.3931	0.245874
52	8.8498	3.5	53.099	110	29.6488	0.298488
53	9.0301	2.5	55.6855	110	29.8894	0.302117
54	7.6791	4	55.2895	110	30.2264	0.254053
55	7.8353	0	56.4138	110	30.6955	0.255259
56	7.9959	0	57.5706	110	31.1563	0.256638
57	8.1586	0	58.7418	110	31.582	0.258331
58	8.3244	0	59.9354	111	32.0113	0.260046
59	6.7953	0	59.4588	111	32.1716	0.21122
60	6.9338	0	60.6709	110	32.5005	0.213344
61	5.3065	0	63.6784	110.5	32.6463	0.162545
62	5.4153	0	64.9839	110.5	32.885	0.164674
63	5.5255	0	64.4639	111	33.0583	0.167144
64	5.6382	0.5	65.7785	111	33.5475	0.168066
65	5.7531	0.5	65.2017	111.5	33.8376	0.170021
66	3.9141	8.5	64.5829	112	34.1983	0.114453
67	5.9904	1.5	59.9042	113	34.4165	0.174056
68	4.0752	8.5	59.0897	112.5	34.4749	0.118208
69	6.276	2	60.2966	114	34.7234	0.180743
70	6.3647	2	59.4043	111.5	35.1694	0.180973
71	6.4951	2.5	60.6211	112	35.7006	0.181933
72	6.6277	2.5	59.6494	116	36.2425	0.182871
73	6.7627	6.5	58.61	116	36.5023	0.185268
74	6.9005	6	59.8041	116.5	36.7547	0.187745
75	7.0418	6	58.682	116.5	37.2537	0.189023
76	4.7899	7	57.4786	40	37.6713	0.12715
77	4.8877	6	58.653	124.5	38.1834	0.128006
78	7.4815	4	57.358	399.5	38.5661	0.193992
79	7.6341	4.5	58.5283	112	39.1165	0.195163
80	7.7904	4.5	59.7262	117	39.2976	0.198241
81	7.9488	5	58.2914	112	39.5163	0.201152
82	10.8146	11.5	59.4802	118	39.9772	0.270519
83	11.0362	8.5	57.9398	113.5	40.3409	0.273573
84	8.4451	13.5	59.1158	114	40.5857	0.208081
85	8.618	7.5	60.3257	114.5	41.0658	0.209858
86	8.7946	7.5	58.6308	117	41.3587	0.212642
87	8.9733	2.5	59.8217	117	41.535	0.216042
88	6.1044	9	61.0444	117.5	41.6474	0.146573
89	6.2289	9	62.2891	117.5	41.8572	0.148813
90	6.356	8.5	63.5599	118	42.0192	0.151264
91	6.4861	9	64.8606	118.5	41.8535	0.154972
92	6.6182	8.5	66.1822	119	41.7976	0.158339
93	10.1302	3.5	64.1581	119.5	40.5256	0.24997
94	10.336	3.5	65.4613	119.5	40.393	0.255886
95	10.5471	6	66.7986	120.5	41.2133	0.255915
96	10.7622	5.5	68.1603	121.5	41.6057	0.258671
97	10.9824	4.5	69.555	123	41.8274	0.262565
98	11.2064	0	67.2383	122.5	42.0123	0.266741

99	11.436	0	64.8041	124	42.2493	0.270679
100	7.7787	1.5	62.2295	105.5	41.0889	0.189314

IV) Coarse-grained, simple shear, two-phase model.

Step	$N_L(\alpha)$ [px]	α [°]	$N_L(\gamma)$ [px]	γ [°]	$\bar{x}N_L(\theta)$ [px]	I_{min}
0	14.7547	2	25.2938	77	18.3827	0.802641
1	14.7468	3	25.2803	154.5	18.4153	0.800791
2	14.7461	1.5	23.1724	47	18.2711	0.807072
3	12.6406	28	24.2278	156	17.8987	0.70623
4	12.6378	26	23.1693	7	17.6465	0.716165
5	12.6413	27	24.2292	9	17.8296	0.709006
6	11.5822	28.5	28.429	147.5	17.9246	0.646162
7	12.6406	47.5	27.3879	145	17.8052	0.709939
8	11.5881	30	24.2297	141	17.7891	0.651416
9	10.5372	25.5	26.343	137.5	18.0945	0.582343
10	9.4764	33.5	26.3233	100.5	18.4226	0.51439
11	9.4795	33	26.3319	130	18.3425	0.516805
12	9.4839	34	28.4516	135	18.788	0.504785
13	10.5329	27	29.492	113.5	19.3317	0.544851
14	12.6402	40	29.4939	127.5	19.6251	0.644083
15	11.583	37.5	28.4311	116.5	20.1458	0.574959
16	11.5996	49.5	30.5807	111	20.334	0.570453
17	11.589	45	33.7133	145.5	20.5784	0.563163
18	11.5831	45	31.5904	112	21.1523	0.547605
19	11.5864	46	30.5459	134	21.3393	0.542961
20	12.6338	34.5	31.5846	116.5	21.6492	0.583569
21	12.6452	43	31.6129	115	22.3366	0.56612
22	12.6459	30	33.7224	118	22.2458	0.568462
23	12.6379	30	32.6478	105	22.5209	0.561163
24	11.5868	27	31.6003	89.5	22.7207	0.509967
25	11.5836	25	33.6978	106.5	22.8941	0.505964
26	12.6427	35.5	33.7138	89.5	23.1578	0.545937
27	12.6375	32	35.8063	125.5	23.1352	0.546246
28	11.5863	34	35.8122	133	23.6488	0.489932
29	11.5812	39.5	37.902	132.5	23.6135	0.490448
30	10.5294	39	37.906	105	23.4101	0.44978
31	10.5377	33	38.9894	121.5	23.6111	0.446303
32	12.6409	25	38.9761	114	23.8178	0.530733
33	11.594	26.5	36.8901	109.5	24.3839	0.475478
34	11.5856	24.5	37.9165	115	25.1842	0.460034
35	12.6372	21	41.0709	116	25.1021	0.503432
36	13.6882	57.5	37.9057	109	25.5742	0.535235
37	15.802	11.5	38.9782	110	26.1642	0.603955
38	15.792	12.5	40.0065	111.5	26.7114	0.591208
39	16.8465	14.5	37.9047	112	27.1697	0.620047
40	14.7432	17	38.9643	112	27.5161	0.535803
41	15.8045	15.5	40.0381	131.5	28.3517	0.557445
42	14.746	23	41.078	95	28.4795	0.517776
43	15.8001	22	44.2404	120	28.8917	0.546873
44	16.8504	20.5	44.2322	115	29.2091	0.576889
45	16.8471	12	44.2237	101	30.0564	0.560516
46	13.6882	13.5	46.3294	116.5	30.3264	0.451363
47	12.6361	16	50.5444	102.5	30.952	0.408248
48	8.3299	5	48.5911	108	29.0526	0.286718
49	12.6384	30.5	50.5537	123	30.8277	0.409969
50	11.5838	23.5	50.5473	118	30.7493	0.376718
51	12.6403	14	48.4546	105	30.6921	0.411842
52	10.5303	20	49.4923	109.5	31.1804	0.337722
53	10.5334	19	52.6669	111	31.6688	0.332611
54	9.4805	18	53.7226	101.5	31.5942	0.300071
55	9.4771	15.5	54.7565	114.5	31.4968	0.300891
56	9.4781	16.5	53.7092	114.5	31.4505	0.301366
57	8.4272	16.5	49.5099	87.5	30.8818	0.272886
58	7.3722	15	50.5524	88.5	30.8138	0.23925
59	9.4774	15.5	52.6523	87.5	31.3796	0.302024
60	12.6393	16	51.6104	95	31.3791	0.402794
61	12.6371	24	49.4953	96.5	31.2217	0.404754
62	11.5828	7	49.4902	81.5	32.0101	0.361848
63	11.5858	26	49.5031	79.5	31.4691	0.368164
64	10.5392	24.5	50.5883	93.5	31.5826	0.333703
65	13.7025	26.5	48.4857	106.5	31.6942	0.432335
66	12.651	28	49.5497	106.5	31.7108	0.398949
67	16.8476	11.5	52.6489	104.5	32.4174	0.519709

68	14.7431	13.5	49.4948	105	32.441	0.454459
69	15.7998	12.5	52.666	88.5	32.8209	0.481394
70	15.7986	15	52.6619	115	33.2668	0.474906
71	14.7458	26.5	54.7701	93.5	33.4359	0.441017
72	14.7418	34	55.8081	95	33.9379	0.434376
73	15.7952	23.5	56.8625	101	34.7844	0.454089
74	16.8527	19	53.7181	101	34.5908	0.487202
75	15.7973	25	55.8171	110.5	35.0973	0.4501
76	15.7949	26.5	57.9146	111.5	35.6119	0.443529
77	14.7476	23.5	57.9369	111	36.4876	0.404181
78	15.7962	29	63.1849	113.5	36.9996	0.426929
79	14.7422	30	64.2337	107.5	37.4454	0.393699
80	15.7939	32	64.2286	104.5	38.0412	0.415179
81	17.9097	18	63.2108	103.5	38.8835	0.460599
82	20.0084	1.5	61.0783	109	39.8737	0.501794
83	20.0189	0	61.1103	91.5	39.3816	0.508331
84	18.9717	0.5	62.1851	114.5	39.6465	0.478521
85	18.9504	0.5	62.1153	97.5	39.6356	0.478116
86	20.0133	0.5	61.0931	99.5	39.2654	0.509693
87	18.9715	0	60.0763	103.5	38.7499	0.489588
88	16.8565	14	61.105	97.5	38.3218	0.439867
89	16.8441	8	58.9545	109	37.9972	0.443298
90	14.742	13.5	61.074	97	37.7459	0.390559
91	13.6903	13.5	60.0266	100.5	37.3214	0.366822
92	12.6391	14.5	62.1422	95.5	37.1795	0.339948
93	12.6379	17	61.0831	98	37.4097	0.337824
94	10.5296	23	60.0185	85	36.6753	0.287103
95	11.5824	20.5	57.9121	79	36.4369	0.317876
96	13.6921	11	57.9279	91.5	36.2658	0.377549
97	12.6434	22	59.0025	107.5	36.349	0.347834
98	13.6912	5.5	60.0307	100.5	36.7602	0.372446
99	11.5852	6.5	60.0325	110	36.2704	0.319412
100	12.6354	16.5	60.0183	97.5	36.0983	0.350028

V) Fine-grained, pure shear, single-phase model.

Step	$N_L(\alpha)$ [px]	α [°]	$N_L(\gamma)$ [px]	γ [°]	$\bar{x}N_L(\theta)$ [px]	I_{min}
0	50.5282	8.5	68.4236	142.5	59.7292	0.845955
1	49.5393	8.5	72.245	68	59.5911	0.83132
2	48.5685	8	69.8172	87.5	59.6216	0.814612
3	47.6219	8	70.4407	66.5	59.8081	0.796245
4	46.694	7.5	72.9594	65.5	60.0756	0.777254
5	45.7798	7	73.4384	87	59.9603	0.763502
6	44.8836	7	75.7411	105.5	60.2235	0.745284
7	44.0068	6.5	78.8455	87	60.5398	0.726907
8	43.1445	6.5	77.3005	87	60.7772	0.70988
9	42.2992	6	79.311	107.5	60.9677	0.693797
10	41.4676	1.5	78.6157	108	61.4417	0.67491
11	40.6544	1	79.6149	86.5	61.7358	0.658522
12	39.8523	1	80.5349	109.5	62.1714	0.641007
13	39.8826	1	82.2071	79	62.5237	0.63788
14	39.0943	1	86.9649	78.5	63.0517	0.620036
15	38.3302	5	89.9586	78	63.5292	0.603348
16	37.5791	4.5	91.2636	86	63.9725	0.587426
17	37.5948	4.5	89.4756	113.5	64.6599	0.581424
18	34.8287	4.5	92.3717	85.5	65.3098	0.533284
19	35.5395	4	95.8022	85.5	65.7041	0.540902
20	33.1114	4	96.969	85	66.4523	0.498273
21	32.9828	4	97.3396	85	67.3526	0.489703
22	32.8347	3.5	98.5041	84.5	68.1138	0.482056
23	32.667	3.5	101.3514	84.5	68.7495	0.47516
24	30.7697	3.5	105.1297	84.5	69.7617	0.441069
25	32.2698	3	105.531	84	70.56	0.457338
26	31.1487	2.5	110.3555	84	71.5538	0.435319
27	29.968	3	111.6989	83.5	72.3978	0.413935
28	28.7263	1.5	113.0517	83.5	73.2146	0.392358
29	28.3669	2.5	114.4133	83	74.2799	0.381892
30	26.0514	2.5	116.749	83	75.2209	0.346332
31	26.5828	1.5	119.1304	82.5	76.3087	0.348359
32	26.1206	1.5	120.5567	82	77.4659	0.337188
33	25.6287	2	123.0175	82	78.5652	0.326209
34	25.6287	2	123.0175	82	78.5652	0.326209
35	22.4157	2	128.0897	81	80.777	0.277501
36	23.9624	2	127.4366	90.5	81.9167	0.292522

37	23.3401	1.5	132.2604	80.5	83.0198	0.281139
38	23.8164	1.5	134.9594	80	84.0989	0.283195
39	23.1452	1.5	135.3993	90	85.3836	0.271073
40	21.2557	1.5	136.9812	90.5	86.5558	0.245572
41	21.6895	1.5	139.777	80	87.7191	0.247261
42	22.1321	1.5	140.1703	78	88.8833	0.249002
43	20.0746	1.5	144.2862	78	90.0399	0.222952
44	20.4842	1.5	145.9502	91	91.2628	0.224453
45	20.9022	1.5	148.0284	76.5	92.2971	0.226466
46	22.6619	0.5	151.9677	76.5	93.2488	0.243026
47	21.7641	0.5	156.4294	76	94.4312	0.230476
48	20.8203	0.5	158.2341	75.5	95.8907	0.217125
49	21.2452	0.5	157.2147	90	96.8362	0.219393
50	20.2335	0.5	157.532	74	97.9682	0.206531
51	20.6464	0	160.7469	100	99.2148	0.208098
52	21.0677	0	162.5223	100.5	100.2793	0.21009
53	21.4977	1	164.3038	101	101.3569	0.212099
54	20.3696	1	164.5236	86	102.3673	0.198985
55	19.1864	0	167.8814	90	103.5474	0.185291
56	17.9464	1	171.3065	92	104.7186	0.171377
57	18.3128	0	173.1387	92	105.718	0.173223
58	18.6864	1	173.2738	90.5	106.5013	0.175457
59	19.0677	1	175.0765	90.5	107.415	0.177514
60	19.4569	0.5	175.1118	88.5	108.0567	0.180062
61	18.049	1	178.6856	88	108.9001	0.165739
62	18.4174	0.5	182.3323	88.5	109.9424	0.167519
63	18.7933	0.5	186.0541	90.5	110.6383	0.169863
64	17.2591	0.5	187.9326	88	111.4222	0.154898
65	17.6113	0.5	191.7679	90.5	111.8316	0.157481
66	17.9707	0.5	191.688	90	112.5657	0.159646
67	16.3	0.5	191.5249	90	112.8594	0.144427
68	14.5536	0.5	191.2755	89	112.6135	0.129235
69	14.8506	0.5	195.1793	90	113.27	0.131108
70	15.1537	0.5	199.1626	90	114.0864	0.132827
71	15.463	0.5	203.2275	90	115.4223	0.133969
72	15.7785	0.5	207.3743	90	116.4206	0.13553
73	16.1005	0.5	211.6062	90	116.9079	0.13772
74	16.4291	0.5	213.5778	90.5	117.2886	0.140074
75	16.7643	0.5	215.5416	90.5	117.6128	0.142538
80	15.8968	0	225.2047	91	120.0822	0.132383
90	12.9705	3.5	217.2565	88.5	119.1409	0.108867
100	11.9058	2	214.3042	90.5	120.1918	0.099057

VI) Fine-grained, simple shear, single-phase model.

Step	$N_L(\alpha)$ [px]	α [°]	$N_L(\gamma)$ [px]	γ [°]	$\bar{x}N_L(\theta)$ [px]	I_{min}
0	50.5282	19.5	71.5816	118.5	58.9116	0.857695
1	48.4287	33	71.5903	123.5	58.6472	0.825763
2	46.3189	62	70.5311	111	59.0244	0.784742
3	47.3714	41.5	70.5308	161.5	58.5058	0.809687
4	44.214	29.5	72.6373	166	59.0236	0.74909
5	43.1627	35.5	73.6925	145.5	58.8007	0.734051
6	41.0584	38.5	75.8	135.5	59.0914	0.694829
7	43.1624	39.5	74.7447	136.5	59.3784	0.726904
8	43.1618	48	77.9017	119.5	59.4608	0.725887
9	42.1141	25.5	78.9639	139.5	59.8096	0.704136
10	42.1104	34.5	83.168	122.5	60.6264	0.694588
11	42.1115	35.5	84.2231	129	60.6967	0.693802
12	42.1077	28	83.1627	121.5	61.189	0.688158
13	38.949	27	85.2667	97.5	61.8874	0.629353
14	38.9492	38	86.3199	113	62.1623	0.626573
15	37.9005	30	92.6457	139	63.3997	0.597803
16	37.8976	32.5	88.4276	116	64.0416	0.591765
17	37.8993	22	98.9593	123.5	64.8359	0.584542
18	35.7939	36	95.8012	119	64.5367	0.554629
19	37.8983	24.5	98.9567	124.5	65.4285	0.579232
20	35.795	42.5	98.9625	125.5	66.196	0.540743
21	34.742	35	95.8037	119	66.2059	0.524757
22	34.7409	32	97.9061	136.5	67.7515	0.512769
23	34.74	24	97.9037	112.5	68.3134	0.508539
24	33.6888	31	102.119	119	68.9355	0.4887
25	29.4772	34.5	105.2755	118	69.4614	0.424368
26	31.5811	31.5	105.2703	118	69.6901	0.453165
27	32.6348	26.5	103.168	102.5	71.0311	0.459444

28	31.5823	27.5	113.6964	121.5	73.2438	0.431194
29	30.528	32	110.5323	108	73.5232	0.415216
30	29.4757	27	113.6918	109	73.9841	0.398406
31	29.4751	20	110.5317	111	74.0353	0.398122
32	28.4235	30	115.7996	106.5	74.1711	0.383215
33	29.4755	23	120.0075	117	75.3285	0.391293
34	26.319	25.5	127.3837	123	77.4909	0.33964
35	27.3706	25.5	120.0094	124	77.4643	0.353332
36	27.37	29	124.2177	124.5	79.0001	0.346455
37	24.2117	23.5	126.3217	108.5	78.2459	0.309431
38	27.3695	20.5	122.1102	111.5	79.2119	0.345523
39	24.2112	26	125.2664	112	80.3277	0.301405
40	24.2122	30.5	131.5883	113	82.2352	0.294426
41	25.2658	16.5	132.6456	95	83.8617	0.301279
42	25.2658	19.5	134.7508	118.5	85.1128	0.296851
43	26.3198	22	140.0211	103.5	86.0222	0.305965
44	23.1586	29.5	133.6884	109	85.9039	0.269587
45	21.0551	22	140.0161	107	87.2923	0.241202
46	21.0531	24.5	145.2666	108	89.2013	0.236018
47	22.1064	19.5	149.4813	102.5	90.7485	0.243601
48	21.0536	22	149.4807	124	91.9482	0.228972
49	20.0006	19.5	154.7413	119.5	92.7204	0.215709
50	21.0544	20	157.908	119.5	93.7826	0.224502
51	22.1065	18	155.798	104	94.7639	0.23328
52	20.0028	21.5	167.3921	98	97.1303	0.205938
53	18.9478	20	160.0039	106	97.3496	0.194637
54	20.0003	21.5	155.7921	96	98.2906	0.203481
55	20.0008	23.5	165.27	102.5	99.7311	0.200547
56	21.0543	20	167.3813	104.5	100.7859	0.208901
57	20.0002	19	170.5276	107	102.401	0.195313
58	16.8423	19	168.4235	113.5	101.9257	0.165241
59	18.9477	20.5	168.4242	114	102.021	0.185724
60	18.9481	18	172.638	113.5	104.1793	0.18188
61	20.001	18	168.4292	100.5	103.3147	0.193593
62	20.0017	21.5	172.6466	115	103.7962	0.192702
63	18.9477	18.5	174.74	112	105.76	0.179158
64	20.0016	17	173.6981	104.5	106.3287	0.188111
65	18.9486	19.5	178.9592	119.5	107.3726	0.176475
66	20.0019	16	182.1224	107	108.7043	0.184003
67	18.9483	17.5	180.0088	101	110.1054	0.172092
68	18.9489	16.5	182.1198	110	110.1263	0.172065
69	18.9492	18.5	186.3334	108.5	110.8521	0.170941
70	17.8973	17.5	184.2374	107.5	112.337	0.159318
71	17.8951	20.5	188.425	96.5	113.9231	0.157081
72	17.8953	15.5	187.3743	119.5	114.7141	0.155999
73	17.8963	19	193.7011	113.5	116.5398	0.153564
74	15.7897	18	191.5812	104	117.7458	0.1341
75	12.6322	16	197.9052	111	118.5229	0.10658
80	16.8422	15	197.8962	114.5	121.8667	0.138202
90	13.6847	15	212.6391	113	128.1307	0.106803
100	14.738	15	223.1752	111	134.3239	0.10972

VII) Fine-grained, pure shear, two-phase model.

Step	$N_L(\alpha)$ [px]	α [°]	$N_L(\gamma)$ [px]	γ [°]	$\bar{x}N_L(\theta)$ [px]	I_{min}
0	50.5282	8.5	68.4236	142.5	59.7292	0.845955
1	49.5442	8.5	70.1876	52.5	59.6912	0.830008
2	49.5775	133	71.8368	52	59.7866	0.829241
3	48.6044	166.5	73.4025	51	60.0425	0.8095
4	45.708	167.5	72.9383	104.5	60.2687	0.758404
5	44.8112	168	72.4606	105	60.5077	0.740587
6	44.8772	5.5	74.7954	101.5	60.9346	0.736481
7	46.7412	4	75.1526	81.5	61.292	0.762599
8	44.9259	5	78.1711	81.5	61.589	0.729447
9	45.8034	3.5	79.2751	81	62.0408	0.738279
10	44.9259	5	78.1711	81.5	61.589	0.729447
11	43.1767	5	82.9669	78.5	63.164	0.683565
12	42.3305	3	84.661	79	63.7968	0.663521
13	39.8792	3	84.6416	100	64.4238	0.619013
14	41.4867	1.5	86.9624	100.5	65.0771	0.637501
15	40.762	1.5	87.6013	102.5	65.6587	0.620816
16	40.6421	1.5	88.9535	74.5	66.4134	0.611956
17	39.8438	177.5	90.9642	73	67.1672	0.593203
18	40.8874	1.5	91.6181	87	67.8411	0.602694

19	40.9508	1	98.1273	87	68.7225	0.595886
20	41.784	0	99.3355	87	69.6079	0.600277
21	38.614	6.5	101.3617	87	70.4598	0.548029
22	38.5808	6	105.0712	86.5	71.485	0.539705
23	37.6931	6	107.216	86.5	72.6271	0.518995
24	38.4621	5.5	106.8391	86.5	73.3275	0.524525
25	37.5033	5.5	109.0211	86.5	74.2541	0.505067
26	39.1598	5	109.4693	79.5	75.2545	0.520365
27	35.4171	5	112.6081	86.5	76.2426	0.464532
28	38.9197	5	115.8324	85.5	77.1981	0.504154
29	37.8227	4.5	116.3049	85.5	77.8579	0.485791
30	38.5954	175	115.7861	79.5	78.6949	0.490443
31	40.367	175	118.1474	85	79.7318	0.506285
32	40.1867	0	120.5602	85	80.2453	0.500798
33	38.9565	3	123.0205	85	80.9899	0.481004
34	38.7057	160	122.3936	80	81.8584	0.472837
35	40.5628	8	122.756	80	82.9571	0.488961
36	38.1226	161.5	125.2599	79.5	83.6717	0.455621
37	40.0122	1.5	127.8169	84	84.5381	0.473304
38	38.5611	7.5	132.6957	94	85.1746	0.45273
39	37.033	169.5	134.2447	94.5	86.0369	0.430432
40	36.6078	7	133.4414	77.5	86.5036	0.423194
41	38.5595	171	133.7533	77	87.0664	0.442875
42	39.3486	170	136.4903	77	88.055	0.446864
43	40.1523	7.5	139.2783	76	88.7556	0.452392
44	39.6888	5.5	140.8311	76.5	89.4263	0.443816
45	33.9666	7	146.3176	76.5	90.4157	0.375671
46	35.9925	6.5	145.3031	75.5	90.8919	0.395992
47	34.0073	6.5	140.1102	75	91.5736	0.371366
48	36.0888	7	141.579	79	92.1586	0.391594
49	33.9928	6.5	141.6366	79	92.5313	0.367365
50	36.1319	6	140.1919	97	92.9768	0.388612
51	33.9207	6	144.5315	97.5	93.6291	0.362288
52	34.6125	5.5	142.9646	97.5	93.9064	0.368585
53	33.7824	0.5	144.3432	98	94.055	0.359177
54	37.6074	5	144.1615	98.5	94.6682	0.397255
55	36.7749	5	148.6986	76	94.8346	0.387779
56	37.5252	0.5	148.4692	75.5	95.6629	0.392265
57	38.2913	0.5	151.5005	74.5	96.4591	0.396969
58	35.6765	0.5	152.8992	74.5	96.9186	0.368108
59	36.4023	0.5	154.2765	73.5	97.0103	0.375242
60	33.6083	0.5	150.353	101	97.5424	0.344551
61	34.294	3.5	148.0055	102	96.6835	0.354704
62	33.1517	0.5	149.1826	102.5	97.0871	0.341463
63	31.9501	4.5	154.1122	102.5	97.6019	0.327351
64	34.5191	1.5	157.2536	103.5	97.6525	0.353489
65	31.3095	4	154.5906	70	97.9046	0.319796
66	35.9422	0.5	153.7527	69	97.7097	0.367847
67	34.6378	3.5	156.8889	68.5	98.4367	0.351879
68	33.2663	172.5	155.936	68	98.6744	0.337132
69	31.8237	179.5	156.9967	67.5	98.6371	0.322634
70	34.6372	171	151.5378	90	98.6121	0.351247
71	35.3444	0	150.2139	90	98.0735	0.360387
72	31.5576	173.5	153.2798	90	97.9462	0.322193
73	32.2015	172	154.1072	89.5	98.206	0.327897
74	32.8583	172.5	152.5563	97.5	97.8359	0.335851
75	33.5297	173.5	153.2787	97	97.8886	0.342529
80	31.7944	2	166.9206	94	99.7525	0.318733
90	25.942	3	184837	84	106.9839	0.242485
100	23.8138	7	190.5105	87	109.832	0.21682

VIII) Fine-grained, simple shear, two-phase model.

Step	$N_L(\alpha)$ [px]	α [°]	$N_L(\gamma)$ [px]	γ [°]	$\bar{x}N_L(\theta)$ [px]	I_{min}
0	50.5282	19.5	71.5816	118.5	58.9116	0.857695
1	48.4308	40	69.4876	123.5	58.7547	0.824288
2	49.4808	59	69.4837	127.5	58.8259	0.84114
3	47.3736	27	70.5341	147	58.6618	0.807572
4	48.4253	18.5	71.5852	113	59.4168	0.81501
5	43.164	36	71.589	165.5	59.1703	0.729488
6	43.164	36	71.589	165.5	59.1703	0.729488
7	45.2674	42.5	77.902	128	60.3779	0.749735
8	47.3724	28	78.954	125.5	60.5672	0.782146
9	45.2657	41.5	77.8992	122	61.1671	0.740033

10	44.2128	23.5	78.9514	130.5	61.2748	0.721549
11	44.2123	34	84.2139	132	62.2392	0.710361
12	44.2171	36.5	83.1703	121.5	62.9542	0.702369
13	42.1081	25.5	84.2162	111.5	63.8645	0.659335
14	42.1081	40	88.427	119.5	64.5215	0.652621
15	42.1075	33.5	86.3204	101	64.7746	0.650062
16	41.0563	44.5	90.5344	122.5	66.0312	0.621771
17	42.1077	37.5	95.7949	105	66.9897	0.62857
18	40.007	45.5	96.8592	122.5	67.1963	0.595375
19	43.1612	30.5	97.9022	126.5	67.9299	0.635379
20	43.1648	42	97.9104	125	69.2453	0.623361
21	42.1117	46	101.068	124.5	69.8128	0.603209
22	45.2649	29.5	102.1092	102	71.57	0.632456
23	40.0051	33.5	101.0655	108	71.7341	0.557686
24	38.951	32	105.273	123	73.1698	0.532337
25	38.9498	36.5	106.3225	109	73.0581	0.533135
26	40.0023	33.5	107.3745	128	74.3761	0.537838
27	43.1607	26	113.6917	108.5	74.4322	0.579866
28	37.899	38.5	114.7498	110.5	75.8944	0.499365
29	42.1073	39.5	114.7424	121	77.551	0.542963
30	43.1606	29	112.6387	111	77.869	0.554272
31	43.1613	43.5	118.9566	122.5	78.6016	0.549115
32	38.9502	35.5	113.6926	100.5	77.9676	0.499569
33	40.0026	37.5	115.7969	129.5	78.6108	0.508869
34	35.7909	27	117.8994	124	78.7622	0.454417
35	38.9492	28	116.8477	122.5	79.7381	0.488464
36	41.0585	17.5	114.7531	111	80.5867	0.509495
37	43.1605	17.5	122.1127	107.5	81.3817	0.530347
38	41.0556	18.5	118.9559	102	82.5492	0.497347
39	38.9509	21.5	117.9053	100.5	82.3039	0.473257
40	38.949	16.5	123.1632	101	83.2301	0.467968
41	36.8438	21	121.0581	86	83.1223	0.443248
42	40.0013	15.5	126.32	117.5	83.3665	0.479825
43	41.0543	23.5	125.2682	118	85.4418	0.480494
44	36.8435	24	126.3206	133	85.6869	0.429978
45	42.1079	25	125.2711	102.5	86.6556	0.485922
46	41.0633	26.5	134.7719	119.5	86.7983	0.473089
47	38.9501	29.5	137.9043	113	87.6095	0.444588
48	38.9496	27	134.7444	129	88.0508	0.442354
49	36.8442	29	143.166	118.5	88.6523	0.415603
50	34.7382	24.5	143.1633	121	89.4829	0.38821
51	37.8959	12.5	143.1624	104	89.3757	0.424007
52	36.8465	16.5	144.2279	102.5	90.067	0.409101
53	32.6327	15	148.4261	127.5	91.6346	0.356118
54	32.6335	16	144.2192	124.5	91.9027	0.355088
55	35.7926	16.5	138.9597	106	92.834	0.385555
56	37.898	21.5	145.2757	115.5	93.3667	0.405905
57	33.6909	20	150.5564	118.5	94.4506	0.356704
58	40.002	19	147.3756	119	94.7809	0.422047
59	38.9497	19	149.4827	121	96.3924	0.404074
60	42.1102	9.5	156.8606	121.5	96.8871	0.434632
61	46.3187	9	149.4829	101.5	96.908	0.477966
62	43.1608	9	148.4309	121	97.5012	0.442669
63	45.2647	26.5	149.4789	123.5	96.6002	0.468578
64	44.2134	20.5	148.4309	107.5	96.8193	0.456659
65	47.3715	19.5	147.3781	96	97.3464	0.486628
66	41.0543	18.5	151.5851	110	97.633	0.420496
67	44.2127	25	151.5865	123	99.1654	0.445848
68	43.1597	23	152.6379	111.5	98.4769	0.438272
69	42.1078	22	154.7461	95.5	99.4103	0.423576
70	42.1072	13.5	158.9548	100	99.0849	0.424961
71	43.1589	27	150.5297	96	98.5452	0.43796
72	43.1598	25	157.9016	98.5	98.8787	0.436492
73	44.2145	17.5	153.6979	103.5	100.5827	0.439584
74	40.0039	15.5	156.8574	101.5	100.4493	0.39825
75	41.0569	13.5	160.0166	103	102.4488	0.400755
80	40.0012	13.5	161.0576	103.5	105.7234	0.378357
90	38.9497	24.5	166.3258	105.5	106.1893	0.366795
100	33.6854	17	170.5325	94.5	107.3388	0.313823

APPENDIX C

Supplementary material to chapter 4

C.1 Figures

Figure C.1: Twin sample cores of North Sea (Zechstein) anhydrite.

Figure C.2: Slabs of North Sea anhydrite before thin section preparation.

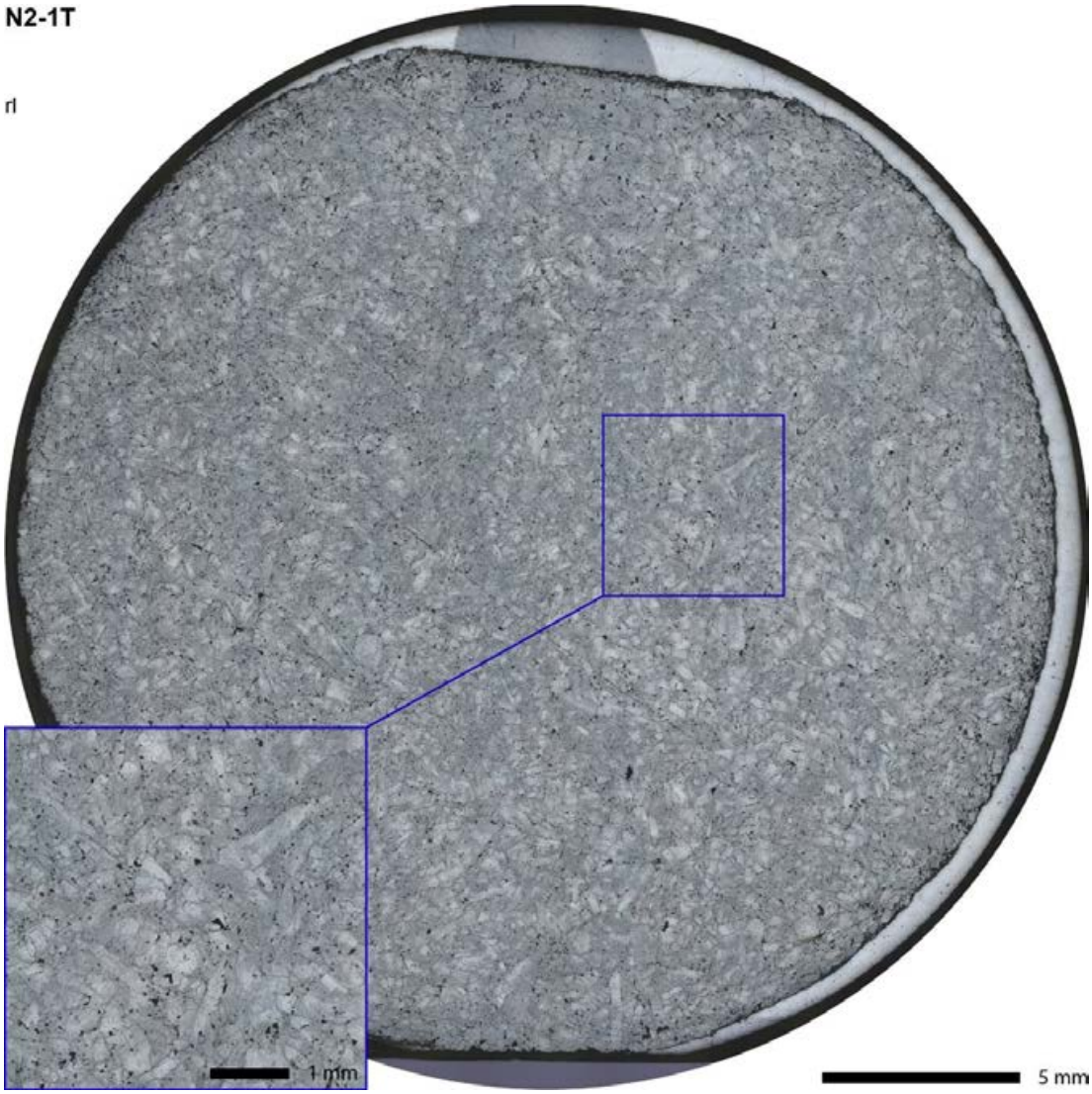

Figure C.3: Reflected light microscopy of thin section of Zechstein anhydrite sample N2-1T. Orientation: view on the Y,Z – Y,Z plane and perpendicular orientation to X direction (long core axis).

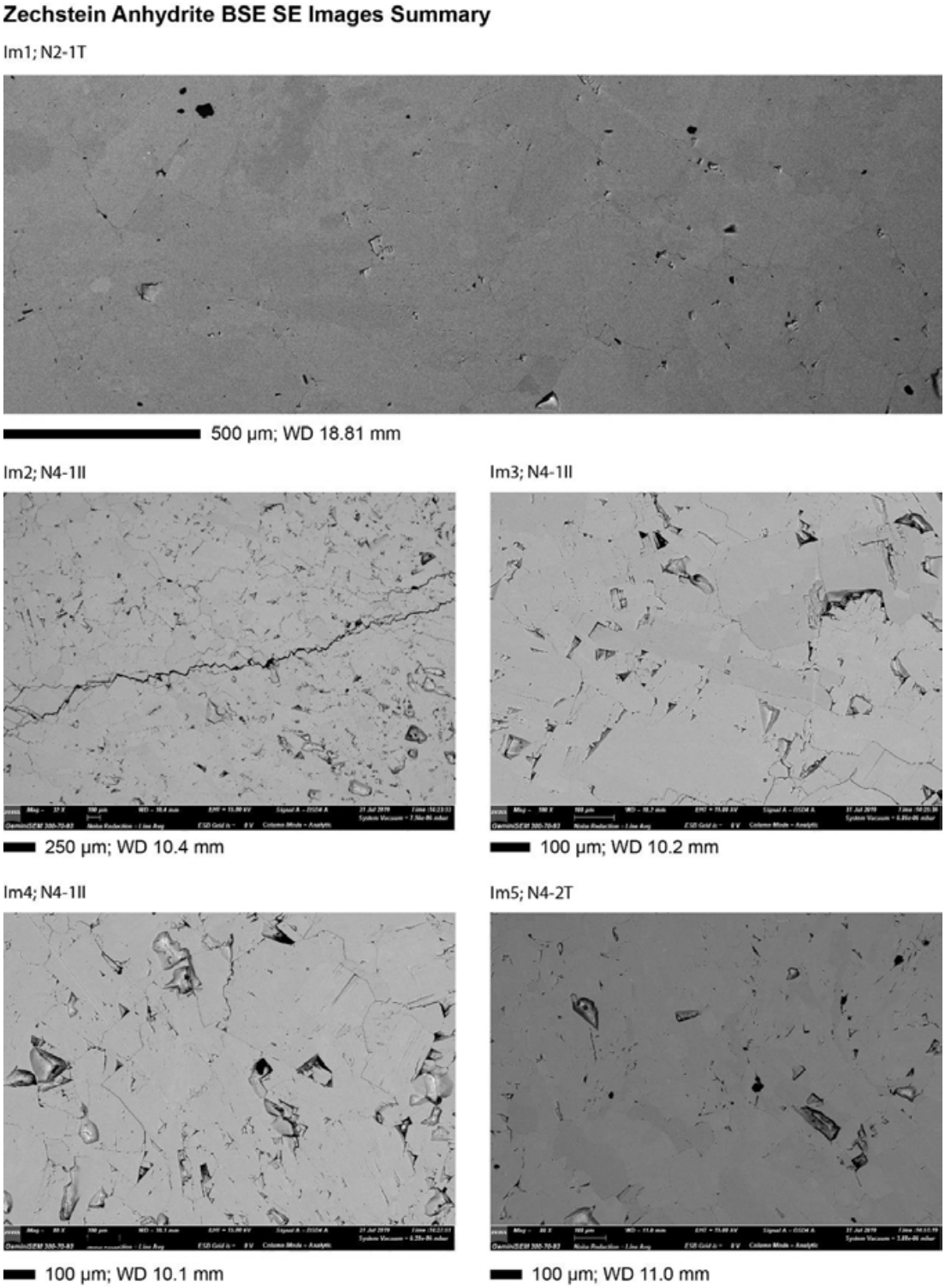

Figure C.4: Backscatter electron (BSE) images of pure anhydrite North Sea (Zechstein) anhydrite sample material. Orientation of Im1 and 5: view on the Y,Z – Y,Z plane and perpendicular orientation to X direction (long core axis). Orientation of Im2,3, and 4: X is horizontal.

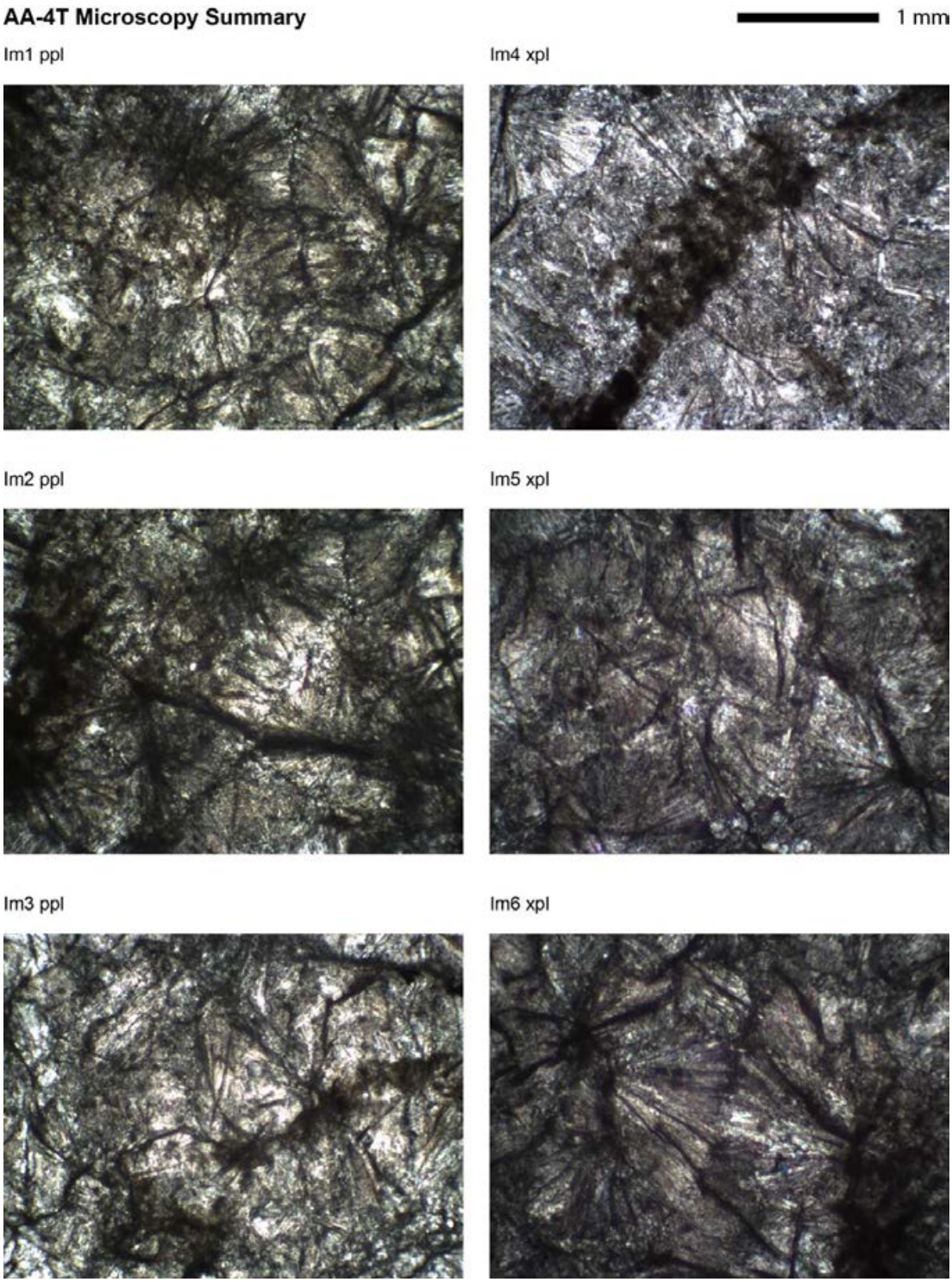

Figure C.5: Microscopic images of Òdena quarry sample material with spherulites and clay inclusions. Orientation: view on the Y,Z – Y,Z plane and perpendicular orientation to X direction (long core axis).

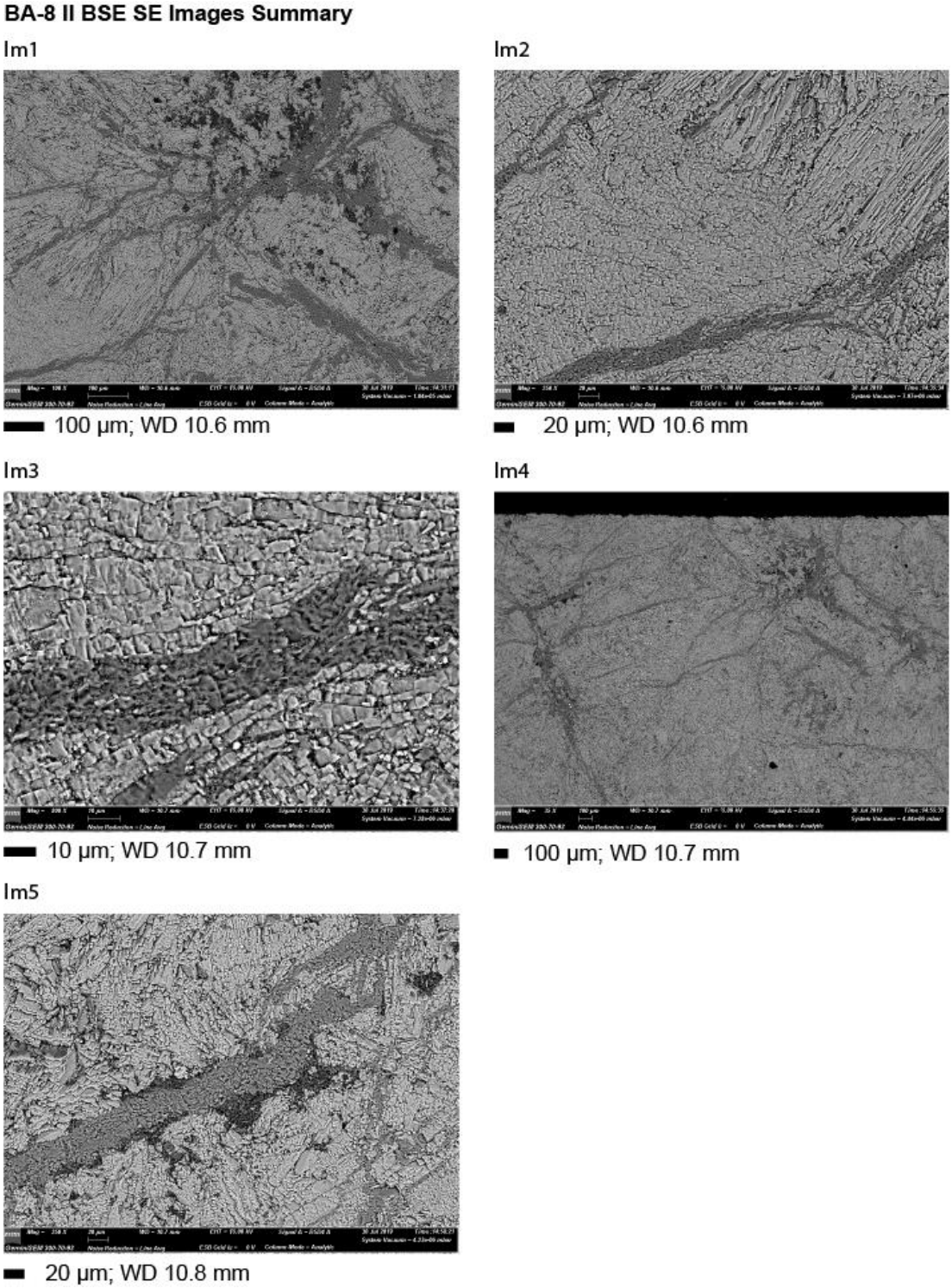

Figure C.6: Backscatter electron images of unpolished Òdena quarry sample material, Thin section BA-8II. Light grey: anhydrite, medium grey: gypsum, and dark grey: dolomite. Orientation: X direction is horizontal (long core axis).

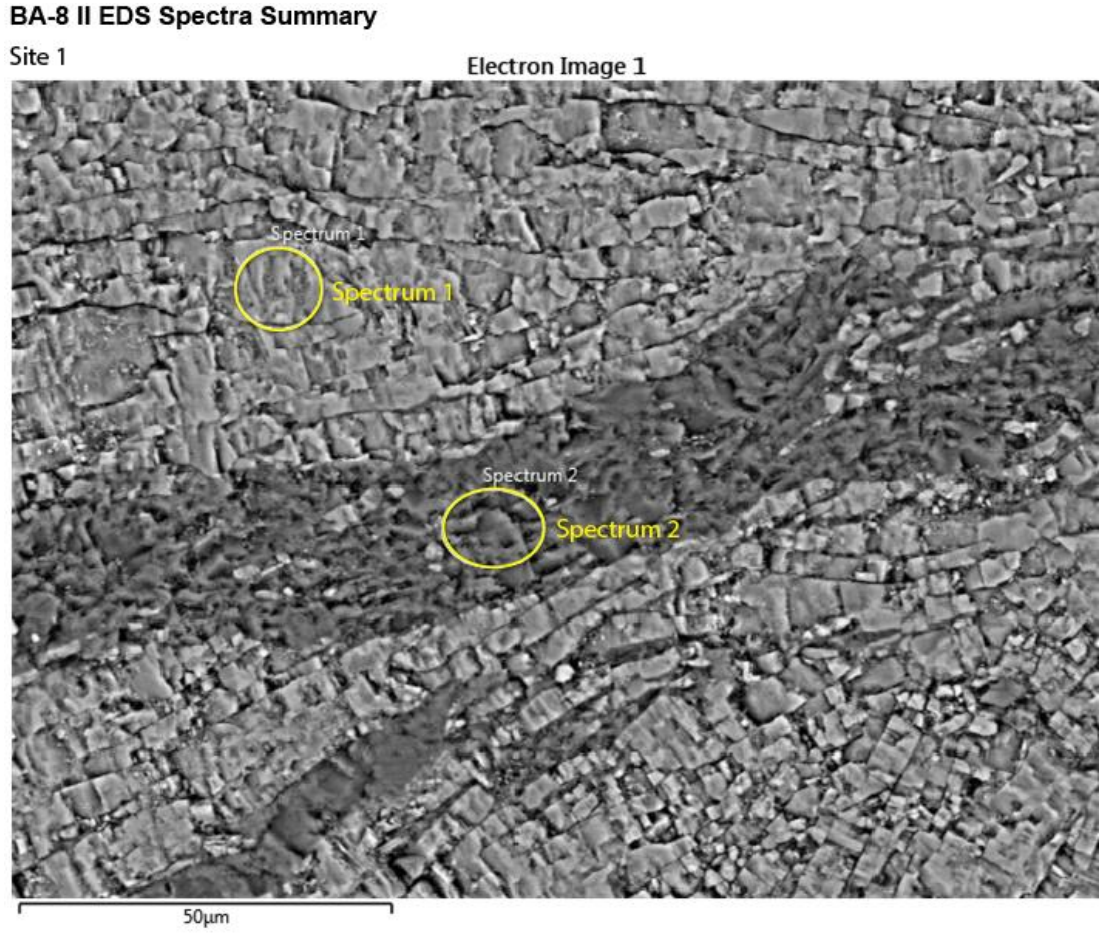

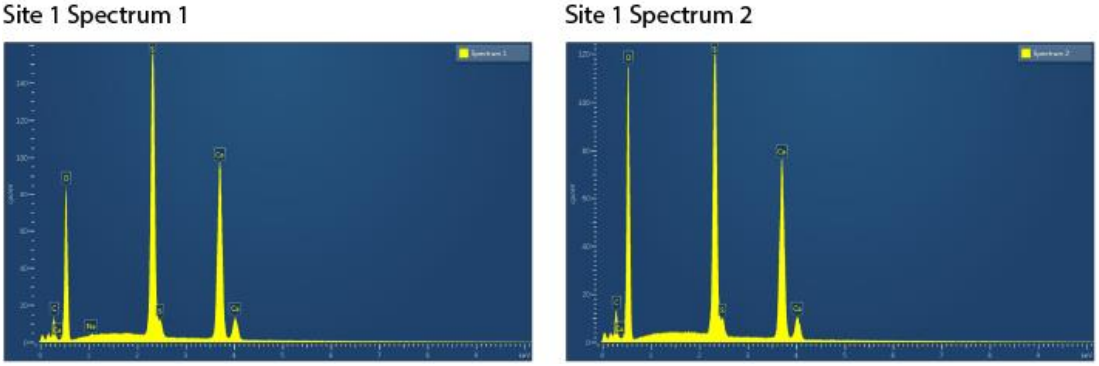

Figure C.7: EDS spectra of Òdena quarry sample material. Three main peaks in spectrum 1 (anhydrite): O with ~ 85 cps/eV, S with~ 162 cps/eV, and Ca with ~ 100 cps/eV. Spectrum 2 (gypsum): O with ~ 115 cps/eV, S with ~ 124 cps/eV, and Ca with ~ 78 cps/eV.

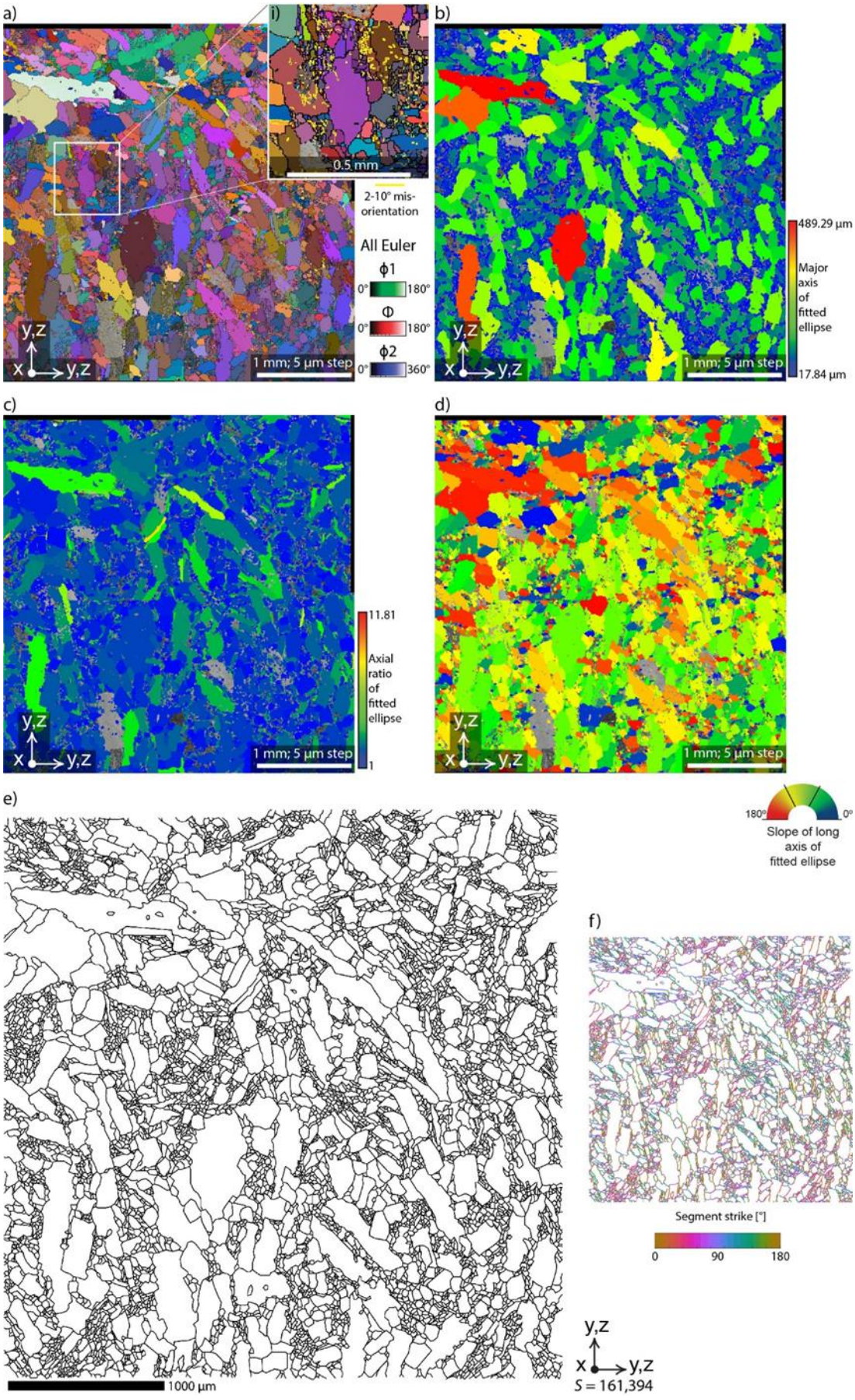
a)
i)
0.5 mm
2-10° mis-orientation
All Euler
ϕ1
0°
180°
Φ
0°
180°
ϕ2
0°
360°
y,z
x
y,z
1 mm; 5 µm step
b)
489.29 µm
Major axis of fitted ellipse
17.84 µm
c)
11.81
Axial ratio of fitted ellipse
1
d)
e)
180°
0°
Slope of long axis of fitted ellipse
f)
Segment strike [°]
0
90
180
1000 µm
S = 161,394

Figure C.8: Microstructural analysis of sample N2-1T, on a thin section with perpendicular orientation to X direction (long core axis). a) Crystallographic orientation map, with i) including low angle boundaries > 2° in yellow and grain boundaries (> 10°) in black (full map in Appendix C, Fig. C.6), b) grain size map, c) grain shape map, d) shape preferred orientation map. a) to d) are based on EBSD analysis. e) Grain boundary trace map, based on manual tracing of BSE and crystallographic orientation map. *S* is the number of trace segments of the map. f) Grain boundary segment orientation map, based on e) and analysed via GBPaQ.

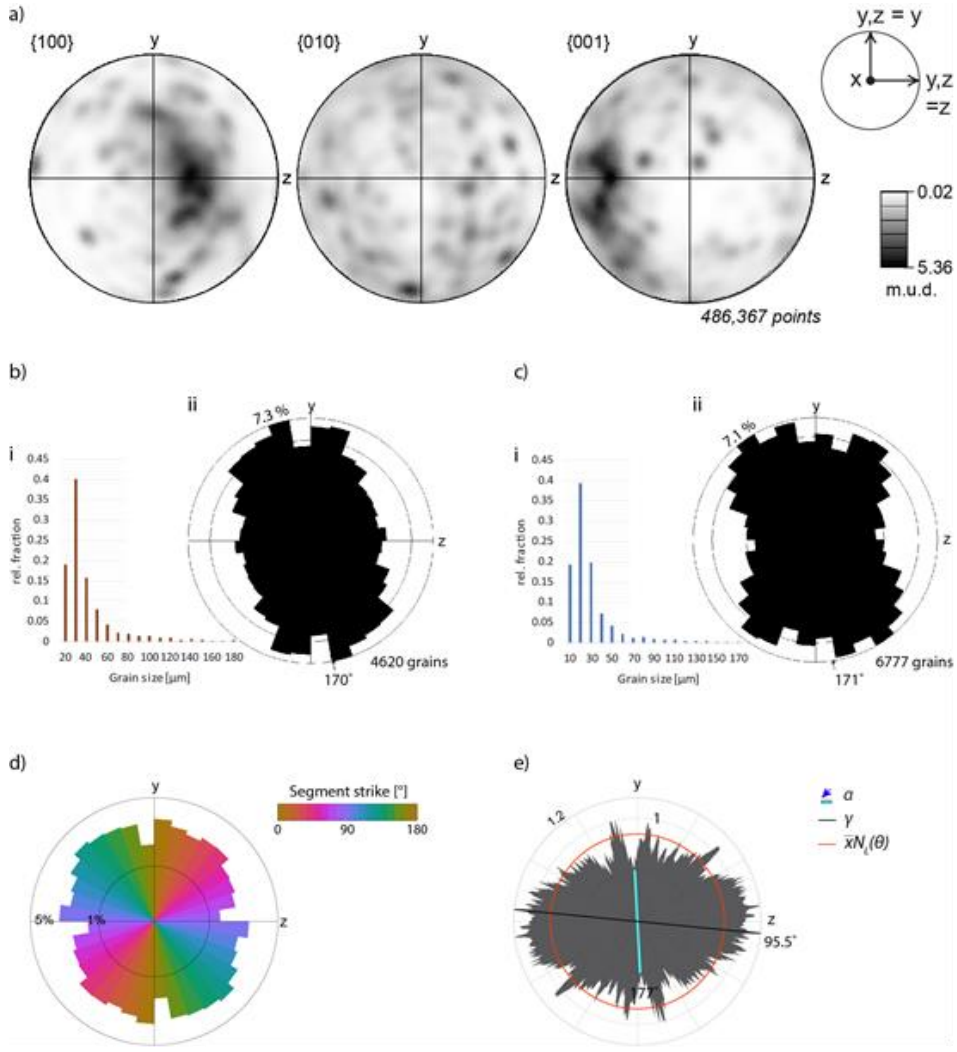

Figure C.9: Crystallographic and shape preferred orientation analysis of sample N2-1T, based on the maps shown in Fig. C.8. a) Crystallographic orientation pole figures for anhydrite based on EBSD data. b) Fitted ellipse analysis of EBSD data, i) grain size histogram and ii) rose diagram of the long axes angles of fitted ellipses. c) Fitted ellipse analysis of trace map data (161,394 segments), i) grain size histogram and ii) rose diagram of the long axes angles of fitted ellipses. d) Equal area, length-weighted grain boundary segment orientation rose of the trace map, resulting from GBPaQ analysis. e)

GBSI density rose plot from GBPaQ analysis. The angle between scan lines is 0.5°. α is the minimum GBSI density (scan line) angle. γ is the maximum GBSI density (scan line) angle. $\bar{x}N_L(\theta)$ is the average GBSI density, in GBSI per pixel.

The distinctive low magnitude peaks in 90° and 180° orientation are biased by artefacts from manual tracing. Segment traces with vertical and horizontal orientation were actively avoided during manual tracing for sample N2-1T (Fig. C.8,9 and N4-1II (Fig. C.13,14). As a consequence, the neighbouring bins contain segments that belong to these bins.

Based on the number of traced segments, the low probability to create segments with >10° deviation, and the nature of the fabric, minimum bins in 90° and 180° orientation are not unlikely. Additionally, only the vertical and horizontal bins, and their direct neighbours are impacted. The angle between scan lines of 0.5° used for GBSI density measurements does not allow of a huge impact of the biased tracing on the overall shape of the GBSI density rose. The orientation of minimum density is most likely effected, while several other minimum densities implicate that minimum intensity is only slightly lower due to the bias. In case of the N2-1T dataset (Fig. C.9e) another low GBSI density orientation is oriented ~ 150°, which would be more consistent with the results from Fig. C.9b,c,d.

The bias was does not apply to the trace mapping of the other samples (N3-1T and N4-2II) used in this study, as the tracing procedure was changed.

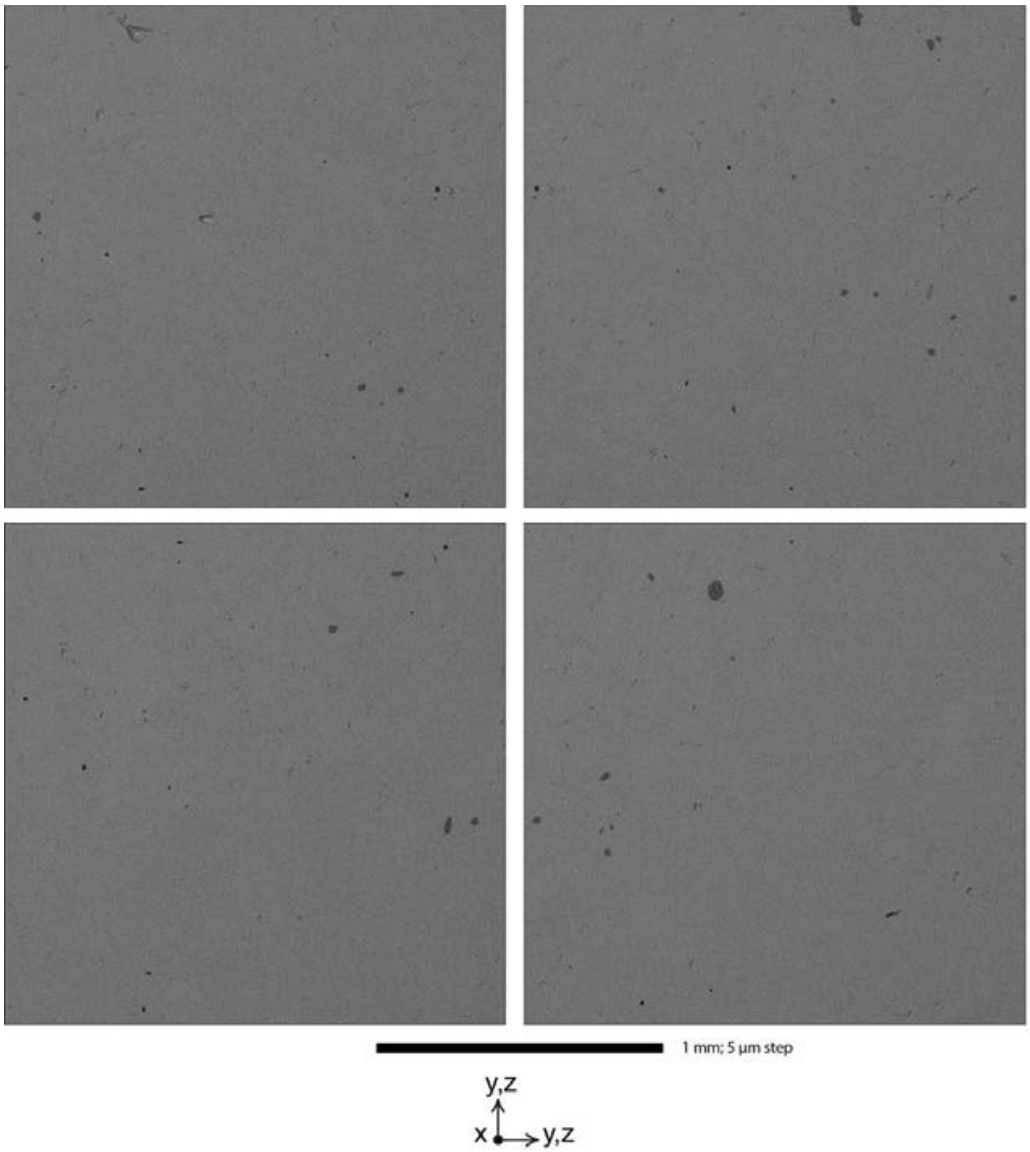

Figure C.8: Backscatter electron (BSE) images of the frames that build the crystallographic orientation map of N2-1 (Fig. C.9).

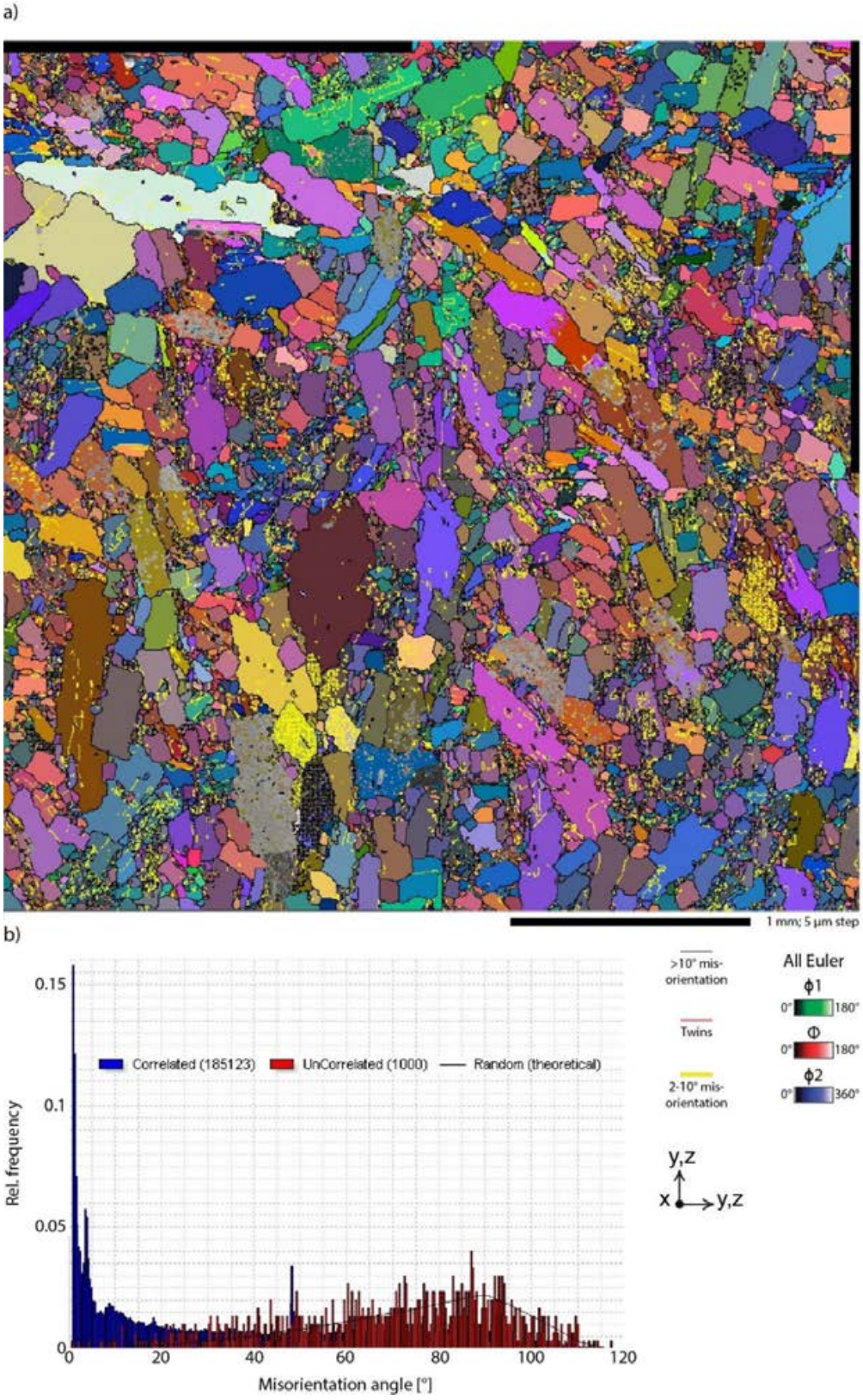

Figure C.10: Crystallographic orientation analysis of sample N2-1 (perpendicular to x axis of the core). a) Crystallographic orientation map with grain boundaries (>10° misorientation) in black, twin boundaries (83.5° / [100]) in red, and subgrain boundaries (2-10° misorientation) in yellow. b) Misorientation angle distribution.

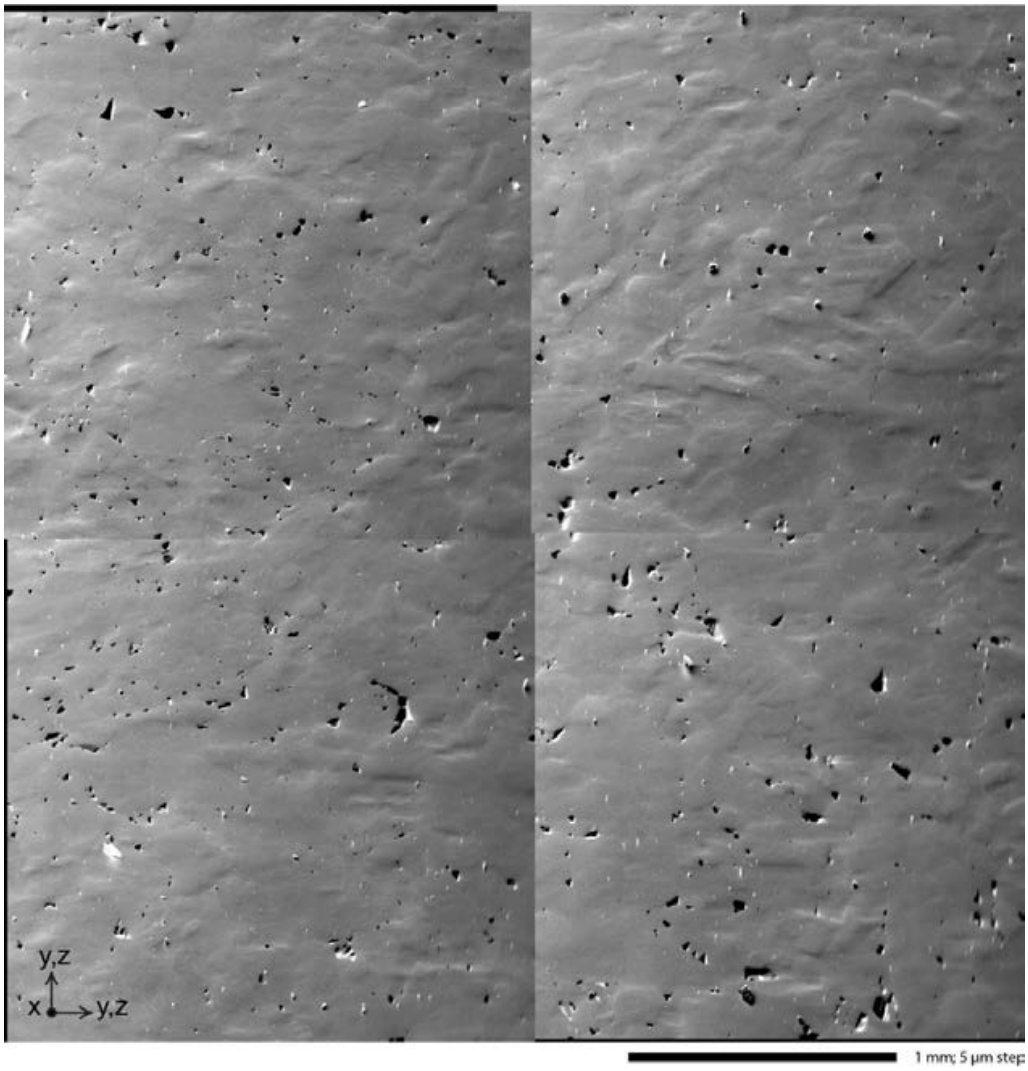

Figure C.11: Secondary electron (SE) image of the crystallographic orientation map of N3-1 (Fig. C.12).

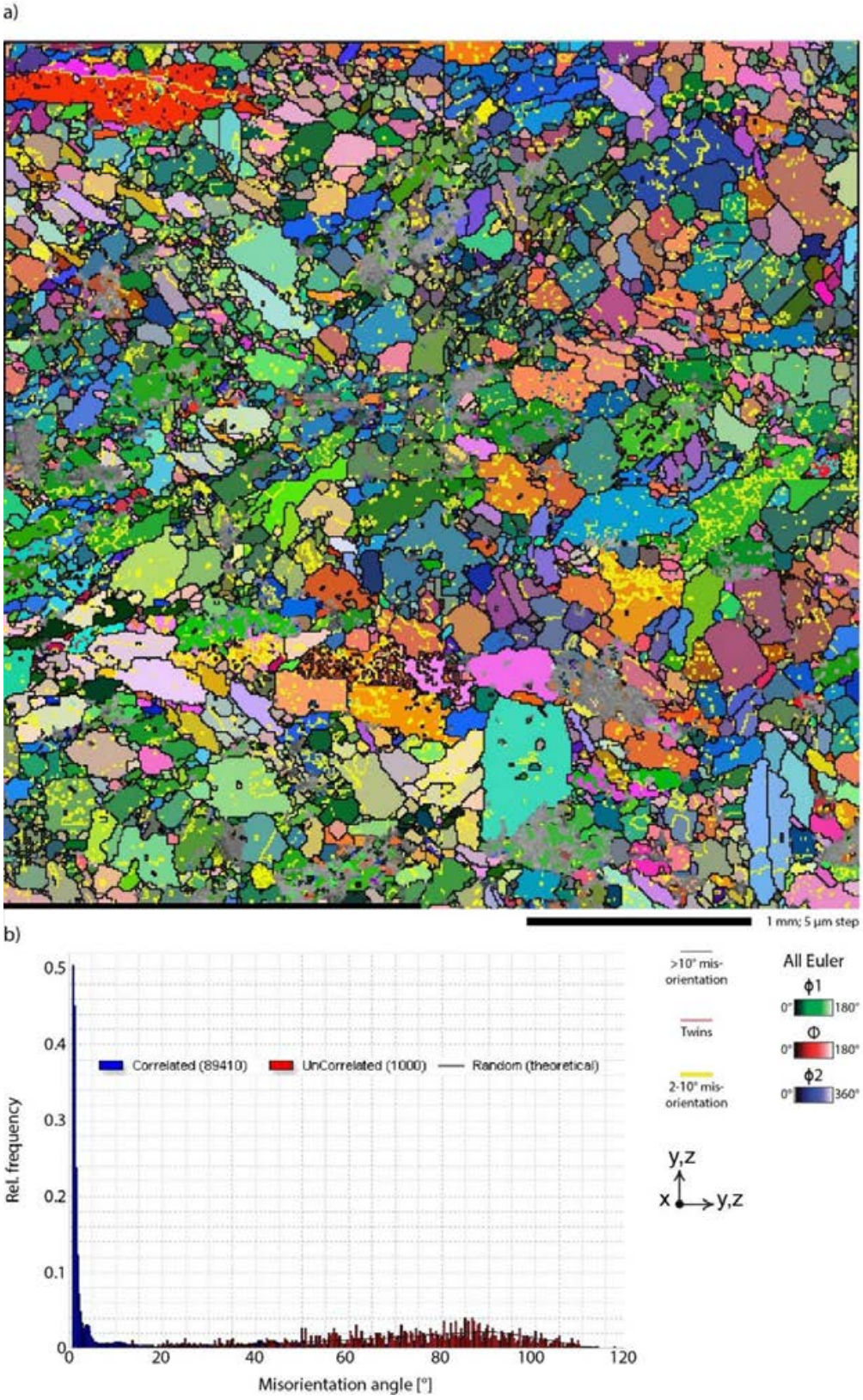

Figure C.12: Crystallographic orientation analysis of sample N3-1 (perpendicular to x axis of the core). a) Crystallographic orientation map with grain boundaries (>10° misorientation) in black, twin boundaries (83.5° / [100]) in red, and subgrain boundaries (2-10° misorientation) in yellow. b) Misorientation angle distribution.

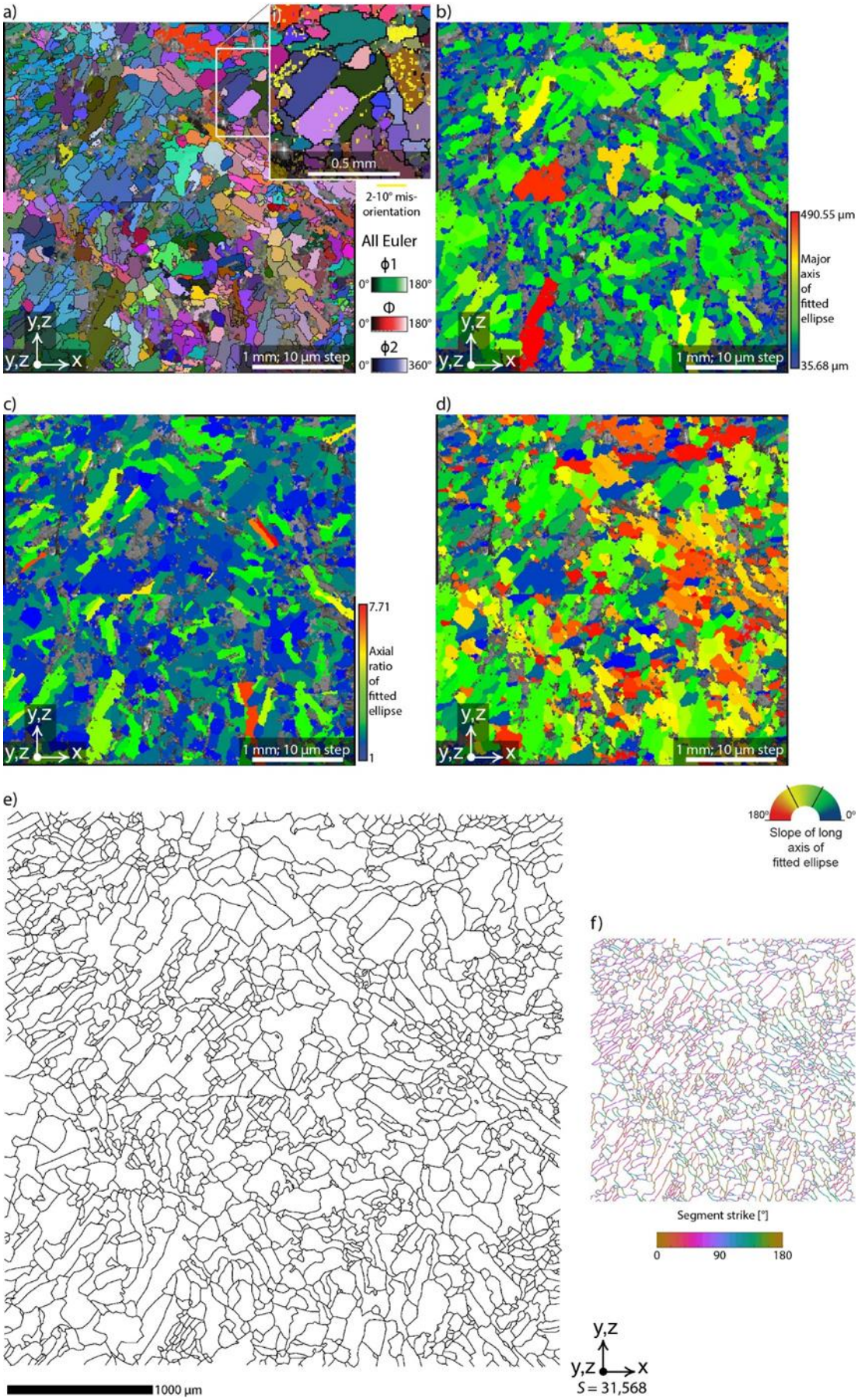
a)
0.5 mm
2-10° mis-orientation
All Euler
ϕ1
0° 180°
Φ
0° 180°
ϕ2
0° 360°
y,Z
y,Z x
1 mm; 10 µm step
b)
490.55 µm
Major axis of fitted ellipse
35.68 µm
c)
7.71
Axial ratio of fitted ellipse
1
d)
e)
180° 0°
Slope of long axis of fitted ellipse
f)
Segment strike [°]
0 90 180
1000 µm
S = 31,568

Figure C.13: Microstructural analysis of sample N4-1II, on a thin section with parallel orientation to X direction (long core axis). a) Crystallographic orientation map, with i) including low angle boundaries > 2° in yellow and grain boundaries (> 10°) in black (full map in Appendix C, Fig. C.15), b) grain size map, c) grain shape map, d) shape preferred orientation map. a) to d) are based on EBSD analysis. e) Grain boundary trace map, based on manual tracing of BSE and crystallographic orientation map. *S* is the number of trace segments of the map. f) Grain boundary segment orientation map, based on e) and analysed via GBPaQ.

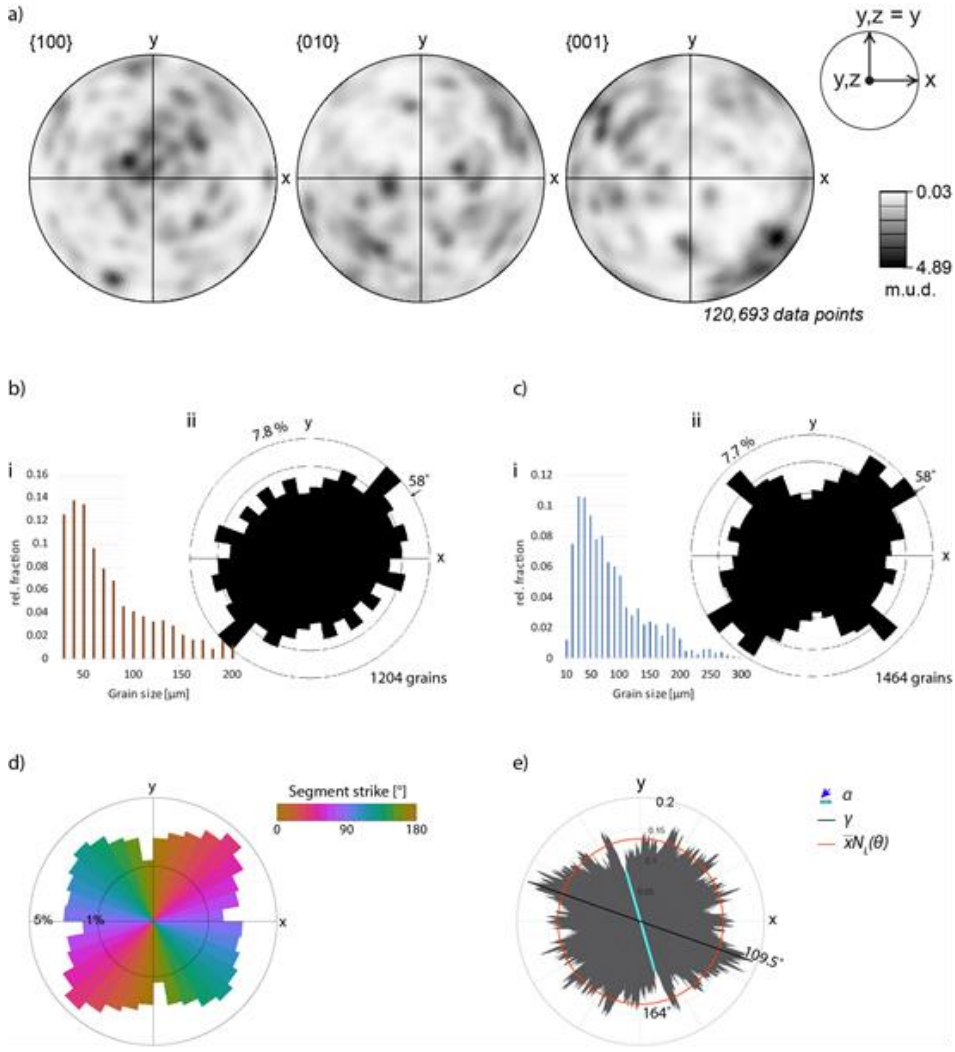

Figure C.14: Crystallographic and shape preferred orientation analysis of sample N4-1II, based on the map shown in Fig. C.13. a) Crystallographic orientation pole figures for anhydrite. b) Fitted ellipse analysis of EBSD data, i grain size histogram and ii rose diagram of the long axes angles of fitted ellipses. c) Fitted ellipse analysis of trace map data (31,568 segments), i grain size histogram and ii rose diagram of the long axes angles of fitted ellipses. d) Equal area, length-weighted grain boundary segment orientation rose of the trace map from GBPaQ analysis. e) GBSI density rose plot from GBPaQ analysis.

The angle between scan lines is 0.5°. α is the minimum GBSI density (scan line) angle. γ is the maximum GBSI density (scan line) angle. $\bar{x}N(\theta)$ is the average GBSI density, in GBSI per pixel.

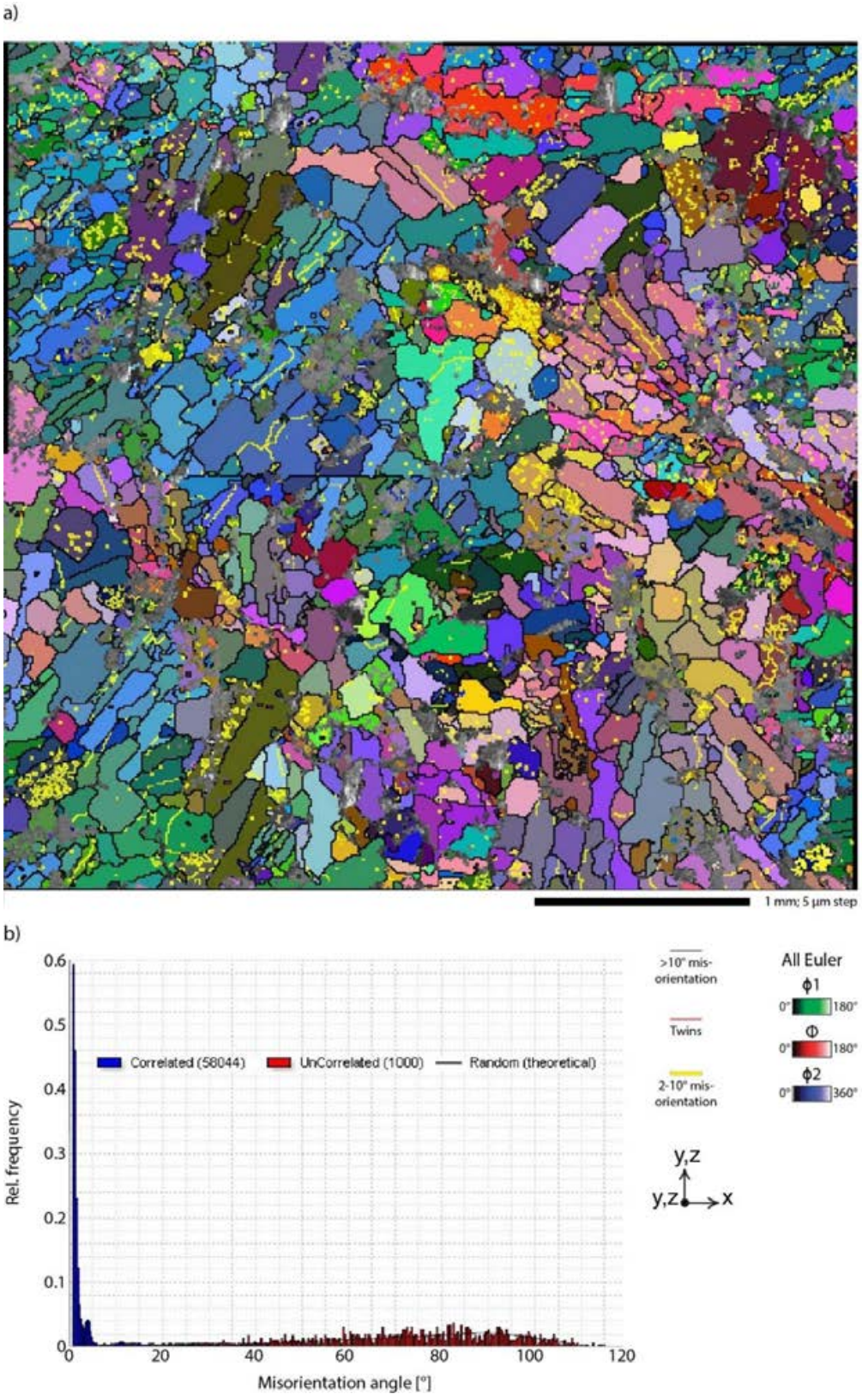

Figure C.15: Crystallographic orientation analysis of sample N4-1 (parallel to x axis of the core). a) Crystallographic orientation map with grain boundaries (>10° misorientation) in black, twin boundaries (83.5° / [100]) in red, and subgrain boundaries (2-10° misorientation) in yellow. b) Misorientation angle distribution.

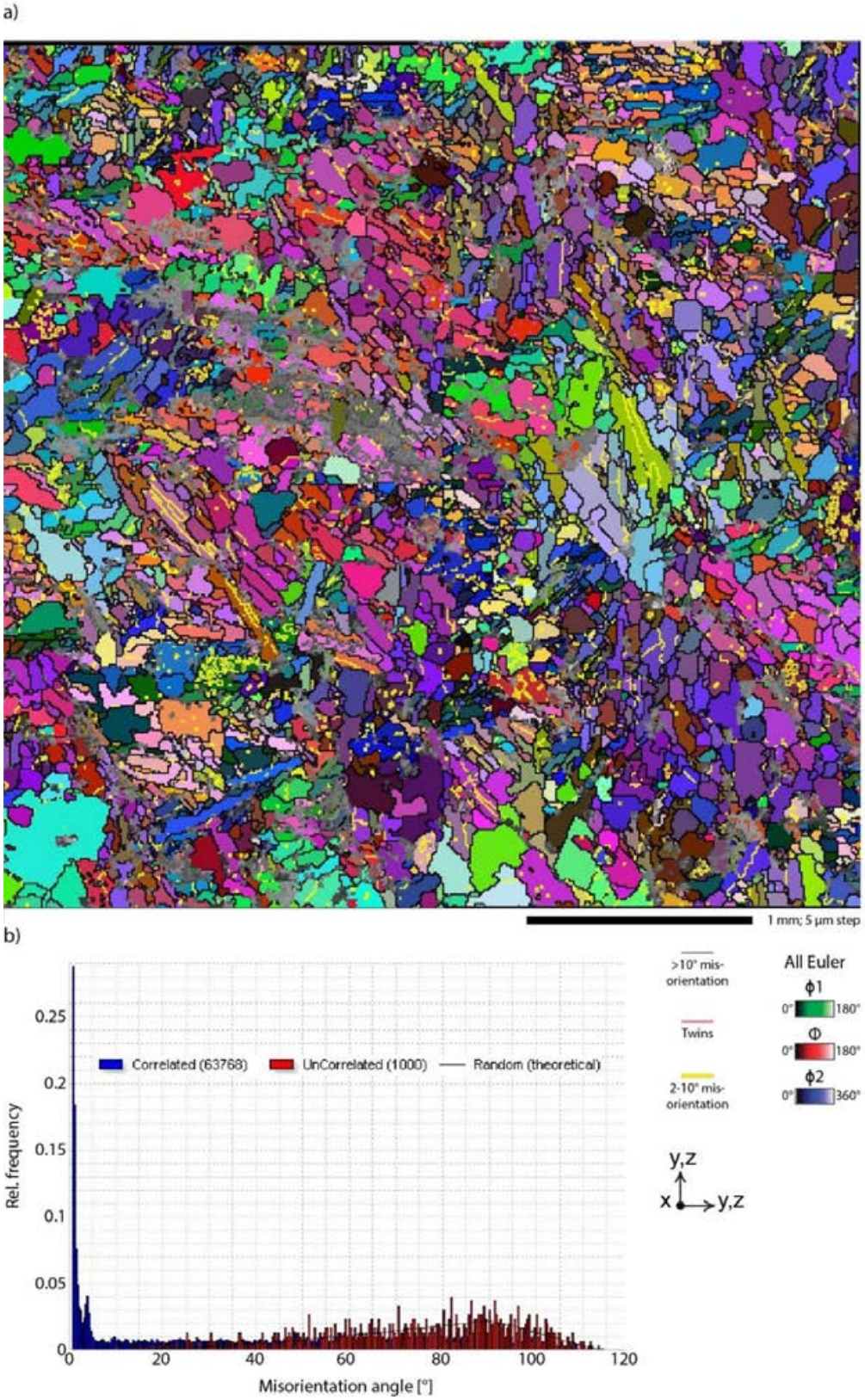

Figure C.16: Crystallographic orientation analysis of sample N4-2 (perpendicular to x axis of the core). a) Crystallographic orientation map with grain boundaries (>10° misorientation) in black, twin boundaries (83.5° / [100]) in red, and subgrain boundaries (2-10° misorientation) in yellow. b) Misorientation angle distribution.

A

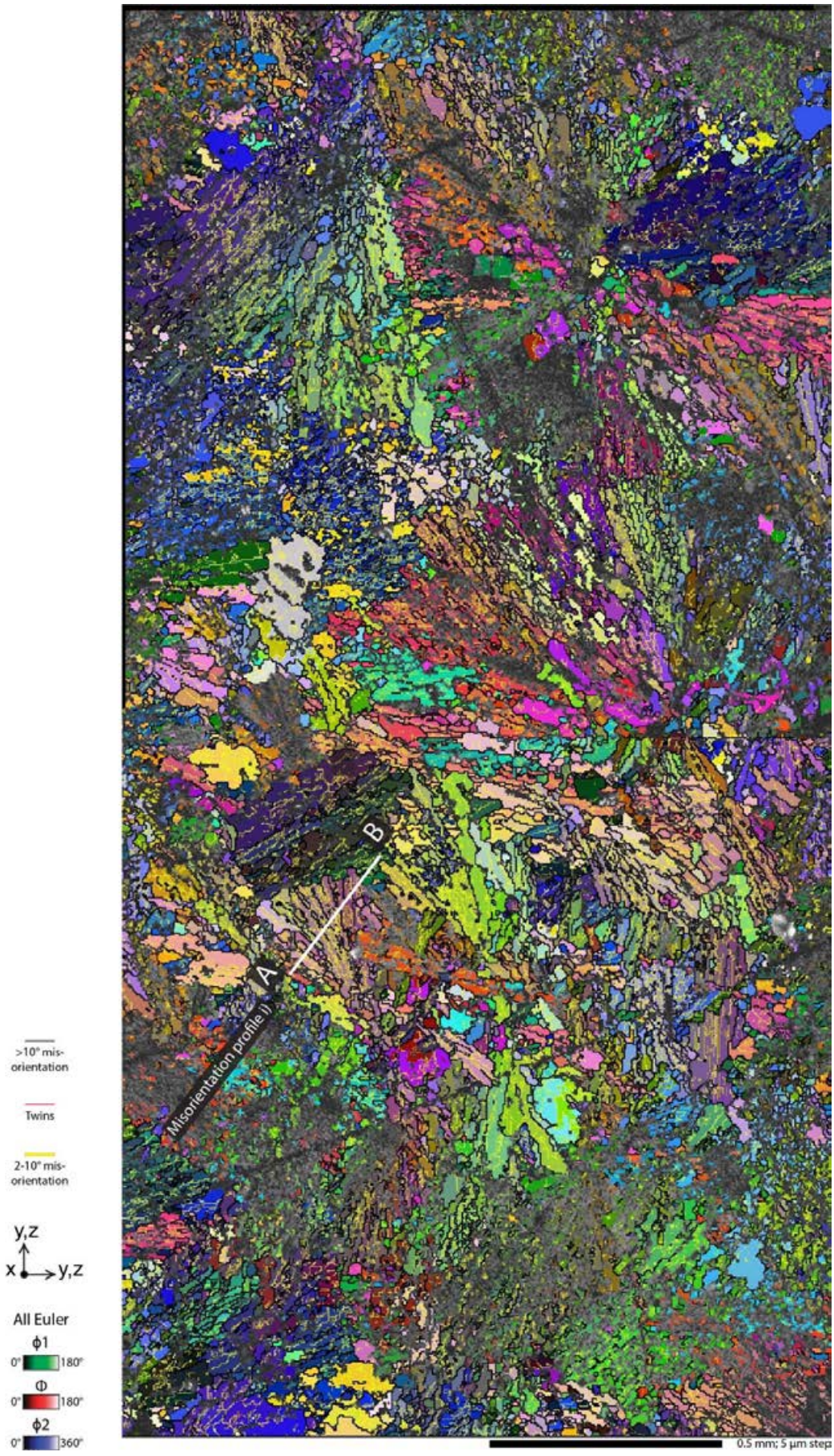
B
A
Misorientation profile I)
>10° mis-orientation
Twins
2-10° mis-orientation
y,z
x
y,z
All Euler
ϕ1
0°
180°
Φ
0°
180°
ϕ2
0°
360°
0.5 mm; 5 µm step


B
Misorientation profile ii)
A
B
>10° mis-orientation
Twins
2-10° mis-orientation
y,z
x
y,z
All Euler
ϕ1
0°
180°
Φ
0°
180°
ϕ2
0°
360°
0.5 mm; 5 µm step

C

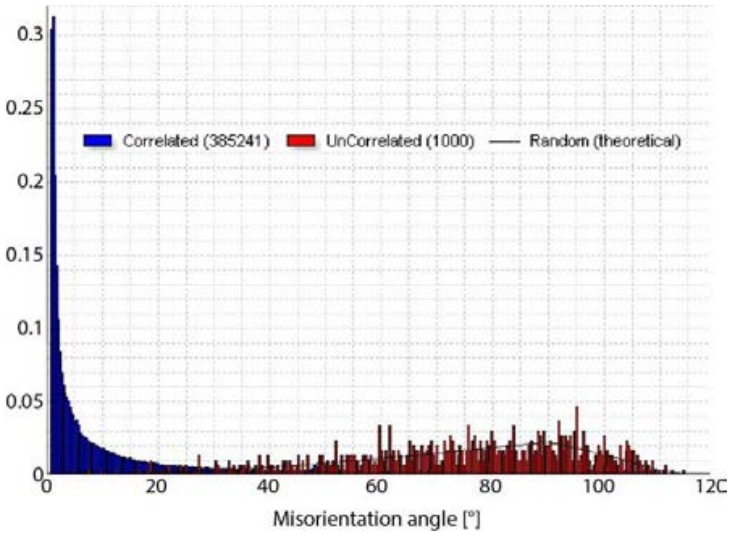

Figure C.17: Crystallographic orientation analysis of sample Òdena quarry sample material from thin section AA-4T (perpendicular to x axis of the core). A (left side) and B (right side): Crystallographic orientation map with grain boundaries (>10° misorientation) in black, twin boundaries (83.5° / [100]) in red, and subgrain boundaries (2-10° misorientation) in yellow. C: Misorientation angle distribution.

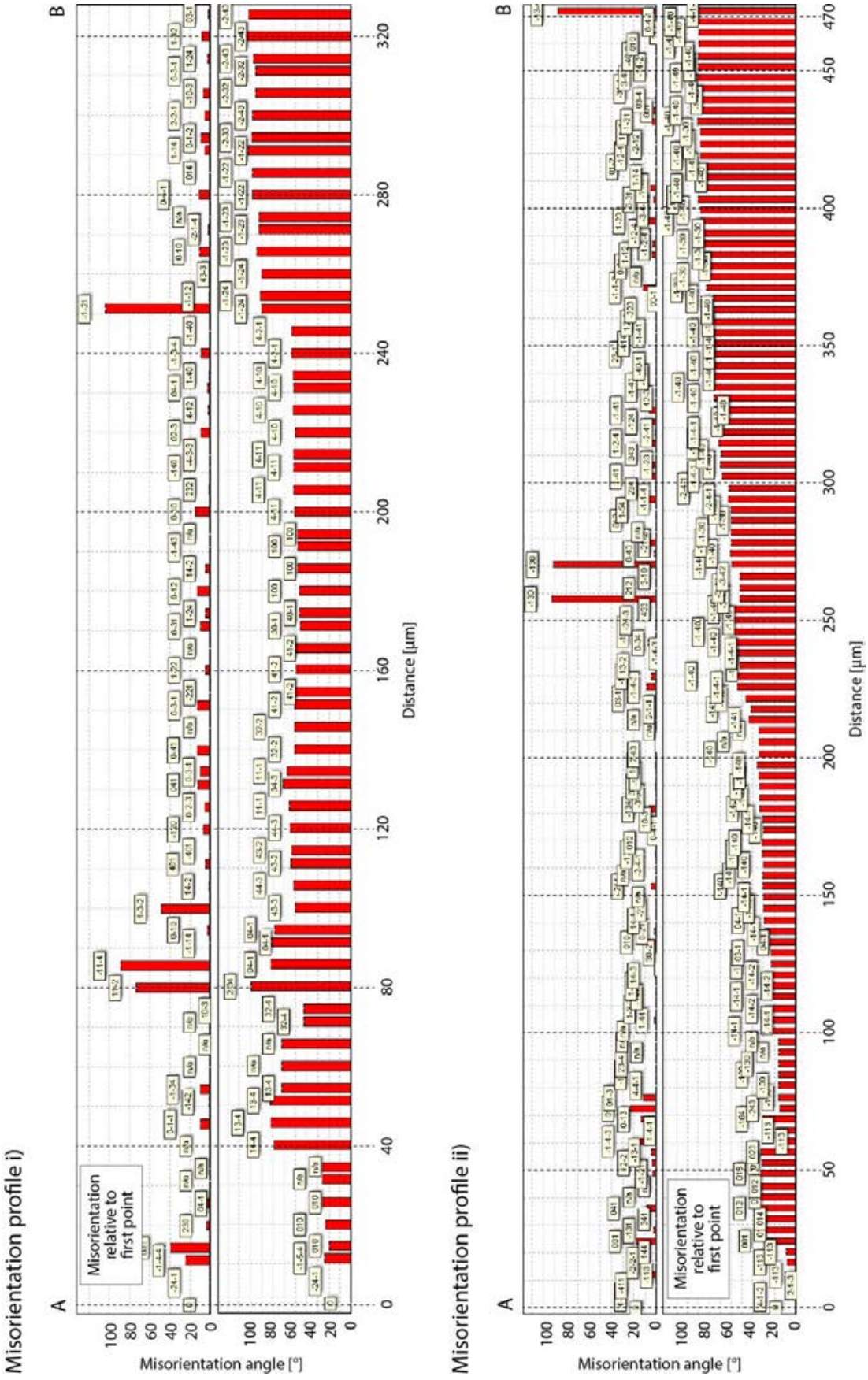

Figure C.18: Misorientation profiles i) and ii) based on the crystallographic orientation map from Figure C.17.

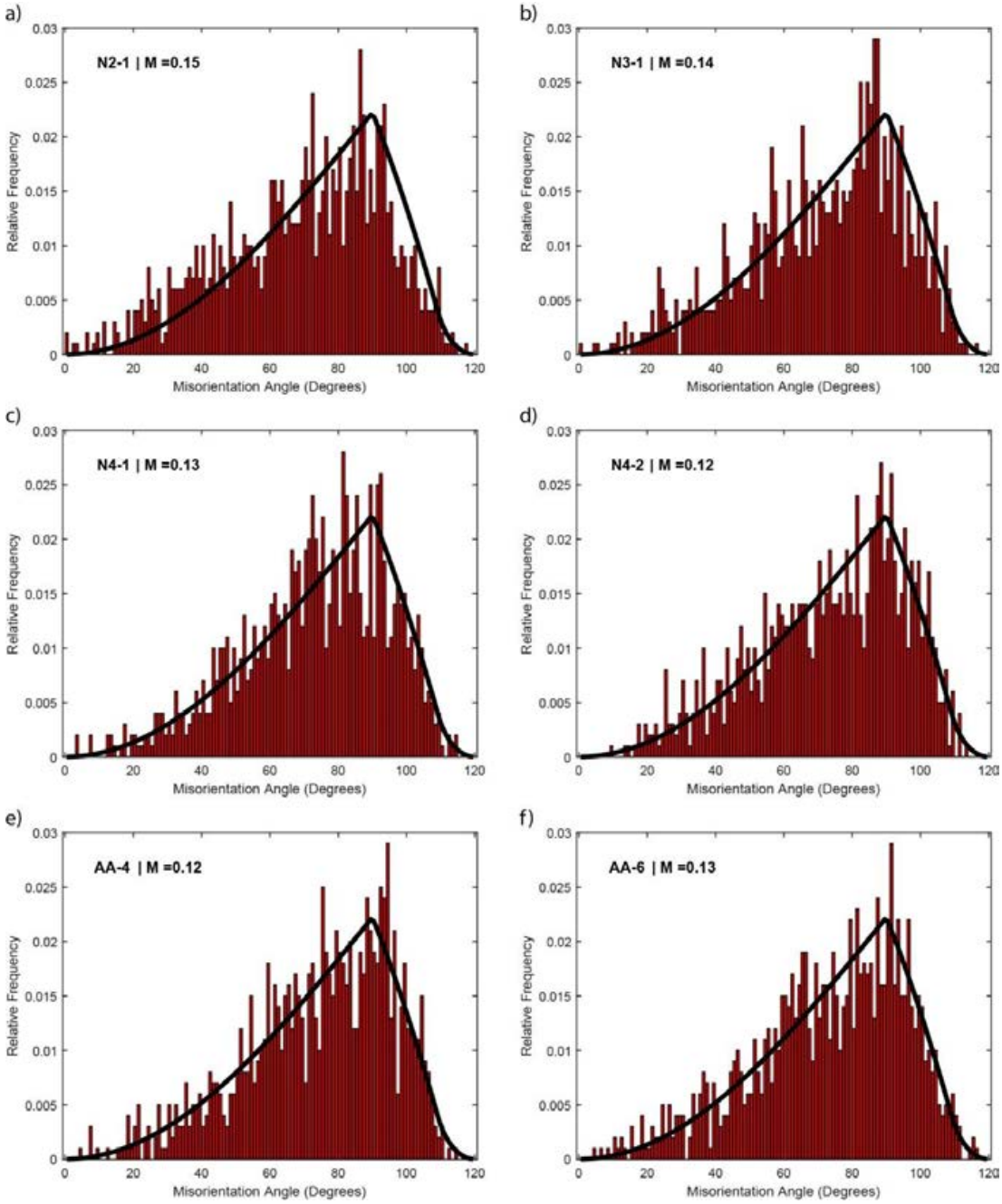

Figure C.19: Histograms of relative frequency versus uncorrelated misorientation angles and *M*-index based on calculations using the *M*-file script of Phil Skemer (2005) for an orthorhombic crystal system (i.e. anhydrite). The datasets are based on EBSD maps from Zechstein anhydrite samples and Òdena anhydrite. a) is based on the EBSD map shown in Appendix C, Fig. C.8. b) shows the analysis of the map from Fig. 12, c) of map from Fig. C.15, d) of map of Fig. C.16, e) of the map shown in Fig. 4.16 and Fig. C.17, and f) of the map shown in Appendix D Fig. D.5. Table C.5 lists the uncorrelated misorientation angles used to calculate the histograms and *M*-index.

C.2 Tables

Table C.1: List with misorientations that were disregarded for the crystallographic orientation analysis with Channel 5 software Tango.

Misorientations to be disregarded

No.	Disregard	Axis	Angle	Dev.	Laue group
1	☑	001	49.00	5.00	Orthorhombic | mmm
2	☑	00-1	49.00	5.00	Orthorhombic | mmm
3	☑	3-3-4	108.50	5.00	Orthorhombic | mmm
4	☑	-3-3-4	108.50	5.00	Orthorhombic | mmm
5	☑	-2-3-1	58.00	5.00	Orthorhombic | mmm
6	☑	231	58.00	5.00	Orthorhombic | mmm
7	☑	-12-1	89.00	5.00	Orthorhombic | mmm
8	☑	-1-2-1	89.00	5.00	Orthorhombic | mmm
9	☑	010	90.00	5.00	Orthorhombic | mmm
10	☑	014	80.00	5.00	Orthorhombic | mmm
11	☑	01-4	80.00	5.00	Orthorhombic | mmm
12	☑	4-33	80.00	5.00	Orthorhombic | mmm
13	☑	-4-33	80.00	5.00	Orthorhombic | mmm
14	☑	-1-22	69.00	5.00	Orthorhombic | mmm
15	☑	-1-2-2	69.00	5.00	Orthorhombic | mmm
16	☑	001	90.00	5.00	Orthorhombic | mmm
17	☑	00-1	90.00	5.00	Orthorhombic | mmm
18	☑	1-11	85.00	5.00	Orthorhombic | mmm
19	☑	-1-11	85.00	5.00	Orthorhombic | mmm
20	☑	-3-22	57.00	5.00	Orthorhombic | mmm
21	☑	-3-2-2	57.00	5.00	Orthorhombic | mmm
22	☑	-334	108.50	5.00	Orthorhombic | mmm
23	☑	100	41.00	5.00	Orthorhombic | mmm
24	☑	-100	41.00	5.00	Orthorhombic | mmm
25	☑	334	108.50	5.00	Orthorhombic | mmm
26	☑	3-34	108.50	5.00	Orthorhombic | mmm
27	☑	-33-4	108.50	5.00	Orthorhombic | mmm
28	☑	33-4	108.50	5.00	Orthorhombic | mmm
29	☑	100	42.00	5.00	Orthorhombic | mmm
30	☑	-100	42.00	5.00	Orthorhombic | mmm
31	☑	-410	41.00	5.00	Orthorhombic | mmm
32	☑	410	41.00	5.00	Orthorhombic | mmm
33	☑	-4-10	41.00	5.00	Orthorhombic | mmm
34	☑	001	47.00	5.00	Orthorhombic | mmm
35	☑	00-1	47.00	5.00	Orthorhombic | mmm
36	☑	0-10	47.00	5.00	Orthorhombic | mmm
37	☑	010	47.00	5.00	Orthorhombic | mmm
38	☑	-1-3-4	90.00	5.00	Orthorhombic | mmm
39	☑	-13-1	90.00	5.00	Orthorhombic | mmm
40	☑	00-1	47.50	5.00	Orthorhombic | mmm
41	☑	001	47.50	5.00	Orthorhombic | mmm
42	☑	0-10	52.50	5.00	Orthorhombic | mmm
43	☑	-12-1	100.00	5.00	Orthorhombic | mmm
44	☑	-1-3-1	100.00	5.00	Orthorhombic | mmm
45	☑	00-1	67.00	5.00	Orthorhombic | mmm
46	☑	12-1	100.00	5.00	Orthorhombic | mmm
47	☑	-1-31	100.00	5.00	Orthorhombic | mmm
48	☑	001	50.00	5.00	Orthorhombic | mmm
49	☑	00-1	50.00	5.00	Orthorhombic | mmm
50	☑	3-42	38.00	5.00	Orthorhombic | mmm
51	☑	3-3-4	109.00	5.00	Orthorhombic | mmm
52	☑	3-34	109.00	5.00	Orthorhombic | mmm
53	☑	131	109.00	5.00	Orthorhombic | mmm
54	☑	1-31	109.00	5.00	Orthorhombic | mmm
55	☑	110	68.00	5.00	Orthorhombic | mmm
56	☑	-110	68.00	5.00	Orthorhombic | mmm
57	☑	00-1	68.00	5.00	Orthorhombic | mmm
58	☑	-331	80.00	5.00	Orthorhombic | mmm
59	☑	-33-1	80.00	5.00	Orthorhombic | mmm
60	☑	-221	80.00	5.00	Orthorhombic | mmm
61	☑	-22-1	80.00	5.00	Orthorhombic | mmm
62	☑	142	83.00	5.00	Orthorhombic | mmm
63	☑	14-2	83.00	5.00	Orthorhombic | mmm
64	☑	-401	90.50	5.00	Orthorhombic | mmm
65	☑	410	90.50	5.00	Orthorhombic | mmm
66	☑	001	48.00	5.00	Orthorhombic | mmm
67	☑	00-1	80.00	5.00	Orthorhombic | mmm

Table C.2: Sample characteristics of cores of North Sea anhydrite and Òdena quarry samples, including core diameter, length, area, volume, and weight.

	TEST NUMBER	SAMPLE NAME	DIAMETER Decimal (mm)										AV. DIAMETER	
													mm	cm
5 In Mano, Out Menis	1	BA-9	25.34	25.44	25.31	25.22	25.44	25.43	25.44	25.37	25.33	25.46	25.38	2.54
	2	BA-7	25.43	25.46	25.43	25.44	25.40	25.41	25.40	25.46	25.44	25.43	25.43	2.54
	3	BA-6	25.44	25.43	25.45	25.44	25.43	25.44	25.44	25.44	25.43	25.44	25.44	2.54
	4	N5-1.1	25.46	25.46	25.36	25.39	25.43	25.39	25.42	25.35	25.41	25.42	25.41	2.54
	5	N5-1.2	25.45	25.44	25.43	25.45	25.47	25.46	25.44	25.44	25.46	25.45	25.45	2.54
	6	N5-4.2	25.38	25.36	25.45	25.45	25.39	25.38	25.43	25.46	25.45	25.40	25.42	2.54
	7	N5-5.1	25.46	25.47	25.38	25.47	25.37	25.46	25.47	25.42	25.43	25.39	25.43	2.54
	8	N4-1.2	25.39	25.39	25.40	25.35	25.41	25.41	25.39	25.43	25.40	25.44	25.40	2.54
	9	N4-3.1	25.27	25.25	25.25	25.30	25.44	25.30	25.26	25.23	25.46	25.50	25.33	2.53
	10	N2-1.1	25.46	25.44	25.41	25.47	25.33	25.44	25.42	25.41	25.45	25.30	25.41	2.54
	11	N2-1.2	25.35	25.38	25.30	25.33	25.36	25.35	25.36	25.34	25.40	25.36	25.35	2.54
	12	N2-2.2	25.45	25.40	25.33	25.40	25.45	25.42	25.42	25.37	25.42	25.45	25.41	2.54
	13	N5-5.1	25.46	25.47	25.38	25.47	25.37	25.46	25.47	25.42	25.43	25.39	25.43	2.54
	14	N2-1.1	25.46	25.44	25.41	25.47	25.33	25.44	25.42	25.41	25.45	25.30	25.41	2.54
	15	N2-1.2	25.35	25.38	25.30	25.33	25.36	25.35	25.36	25.34	25.40	25.36	25.35	2.54
	16	N3-1.2	25.58	25.45	25.43	25.40	25.40	25.38	25.35	25.59	25.38	25.37	25.43	2.54
	17	N4-2.2	25.41	25.40	25.37	25.40	25.41	25.45	25.44	25.41	25.38	25.38	25.41	2.54

	TEST NUMBER	SAMPLE NAME	LENGTH Decimal (mm)										AV. LENGTH	
													mm	cm
5 In Mano, Out Menis	1	BA-9	61.90	61.81	61.76	61.87	61.75	61.81	61.80	62.08	61.82	61.86	61.85	6.18
	2	BA-7	62.08	62.02	62.09	62.17	62.11	62.02	62.20	61.97	62.08	61.97	62.07	6.21
	3	BA-6	61.88	61.86	62.07	61.94	61.87	61.93	61.84	61.83	61.93	61.82	61.90	6.19
	4	N5-1.1	61.96	61.93	61.85	61.86	61.85	61.88	61.91	61.91	61.90	61.90	61.90	6.19
	5	N5-1.2	61.89	61.89	62.11	62.04	61.99	62.13	62.05	62.06	62.00	62.00	62.02	6.20
	6	N5-4.2	61.99	62.05	61.98	62.00	62.11	62.07	62.09	62.03	62.04	62.01	62.04	6.20
	7	N5-5.1	62.09	62.03	62.03	62.02	62.03	62.01	62.02	62.03	62.07	62.05	62.04	6.20
	8	N4-1.2	61.98	62.05	62.03	62.09	61.99	62.00	62.06	61.97	62.01	62.00	62.02	6.20
	9	N4-3.1	61.77	61.86	62.02	61.98	61.95	61.86	61.72	61.89	61.81	61.84	61.87	6.19
	10	N2-1.1	61.81	61.79	61.80	61.76	61.89	61.81	61.79	61.80	61.81	61.83	61.81	6.18
	11	N2-1.2	61.97	62.01	62.05	62.03	62.02	61.99	61.99	61.98	61.98	61.99	62.00	6.20
	12	N2-2.2	62.08	62.01	62.04	62.02	62.00	61.97	61.93	61.94	61.95	61.98	61.99	6.20
	13	N5-5.1	62.09	62.03	62.03	62.02	62.03	62.01	62.02	62.03	62.07	62.05	62.04	6.20
	14	N2-1.1	61.81	61.79	61.80	61.76	61.89	61.81	61.79	61.80	61.81	61.83	61.81	6.18
	15	N2-1.2	61.97	62.01	62.05	62.03	62.02	61.99	61.99	61.98	61.98	61.99	62.00	6.20
	16	N3-1.2	65.43	65.70	65.41	65.55	65.46	65.55	65.64	65.67	65.73	65.55	65.57	6.56
	17	N4-2.2	64.14	64.23	64.34	64.50	64.47	64.51	64.64	64.54	64.44	64.45	64.43	6.44

		L:D RATIO	AREA		VOLUME		WEIGHT
			mm^2	cm^2	mm^3	ml or cm^3	g
1	BA-9	2.44	505.83	5.06	31283.57	31.28	65.70
2	BA-7	2.44	507.91	5.08	31526.18	31.53	61.80
3	BA-6	2.43	508.22	5.08	31457.59	31.46	56.90
4	N5-1.1	2.44	507.07	5.07	31384.89	31.38	47.80
5	N5-1.2	2.44	508.66	5.09	31545.33	31.55	32.40
6	N5-4.2	2.44	507.31	5.07	31471.75	31.47	31.90
7	N5-5.1	2.44	507.99	5.08	31514.38	31.51	33.10
8	N4-1.2	2.44	506.75	5.07	31427.46	31.43	27.30
9	N4-3.1	2.44	503.76	5.04	31167.59	31.17	19.90
10	N2-1.1	2.43	507.23	5.07	31351.15	31.35	
11	N2-1.2	2.45	504.83	5.05	31300.21	31.30	65.70
12	N2-2.2	2.44	507.15	5.07	31439.02	31.44	61.80
13	N5-5.1	2.44	507.99	5.08	31514.38	31.51	56.90
14	N2-1.1	2.43	507.23	5.07	31351.15	31.35	47.80
15	N2-1.2	2.45	504.83	5.05	31300.21	31.30	32.40
16	N3-1.2	2.58	508.02	5.08	33310.69	33.31	31.90
17	N4-2.2	2.54	506.91	5.07	32657.99	32.66	33.10

Table C.3: Permeability measurements via steady-state flow method using N_2, Klinkenberg corrected)

In Gauge, Out Menis

Conversions				
Permeability:	1	m^2	=	1.01E+15 mD
Gas Pressure:	1	Psi	=	6894.76 Pa
Oil Pressure:	1	inch	=	248.65 Pa
Sample Size:	1	mm	=	0.001 m
Flow Rate:	1	ml	=	0.000001 m^3

Constants		
Viscosity:	0.0000177	Pa.s
Atmospheic Pressure:	101325	Pa

PERMEABILITY MEASUREMENTS MADE USING THE INLET PRESSURE GAUGE (RANGE 0-0 Psi) AND THE TRAVELLING MENISCUS FLOWMETER (min & sec)

Sample I.D.	Sleeve Pressure	Inlet Gauge Pressure	Time to travel 1 ml		Inlet Pressure, P_i		Outlet Pressure, P_o
					Gauge	Absolute	Absolute
	Psi	Psi	min	sec	Pa	Pa	Pa
1 BA-9	400.00	35.00	6.00	23.55	241316.60	342641.60	101325.00
		40.00	5.00	25.77	275790.40	377115.40	101325.00
		50.00	3.00	56.25	344738.00	446063.00	101325.00
		54.70	3.00	26.99	377143.37	478468.37	101325.00
		60.00	2.00	58.77	413685.60	515010.60	101325.00
					0.00		
2 BA-7	400.00	38.85	6.00	57.74	267861.43	369186.43	101325.00
		45.00	6.00	1.02	310264.20	411589.20	101325.00
		50.00	5.00	15.51	344738.00	446063.00	101325.00
		55.00	4.00	33.45	379211.80	480536.80	101325.00
		60.00	4.00	2.84	413685.60	515010.60	101325.00
					0.00		
3 BA-6	400.00	40.00	5.00	28.86	275790.40	377115.40	101325.00
		45.00	4.00	34.27	310264.20	411589.20	101325.00
		50.00	3.00	54.31	344738.00	446063.00	101325.00
		55.00	3.00	25.34	379211.80	480536.80	101325.00
		60.00	2.00	59.00	413685.60	515010.60	101325.00
					0.00		
4 N5-1.1	400.00	40.00	5.00	39.01	275790.40	377115.40	101325.00
		45.00	4.00	57.40	310264.20	411589.20	101325.00
		50.00	4.00	18.57	344738.00	446063.00	101325.00
		54.95	3.00	46.05	378867.06	480192.06	101325.00
		59.95	3.00	18.51	413340.86	514665.86	101325.00
					0.00		
5 N5-1.2	400.00	40.00	8.00	29.35	275790.40	377115.40	101325.00
		44.95	7.00	33.61	309919.46	411244.46	101325.00
		50.00	6.00	33.40	344738.00	446063.00	101325.00
		55.00	5.00	46.52	379211.80	480536.80	101325.00
		60.05	5.00	2.62	414030.34	515355.34	101325.00
					0.00		
6 N5-4.2	400.00	45.00	6.00	2.66	310264.20	411589.20	101325.00
		49.00	5.00	30.21	337843.24	439168.24	101325.00
		52.00	5.00	8.72	358527.52	459852.52	101325.00
		55.83	4.00	49.54	384934.45	486259.45	101325.00
		60.00	4.00	24.33	413685.60	515010.60	101325.00
					0.00		
7 N5-5.1	400.00	44.85	5.00	42.17	309229.99	410554.99	101325.00
		49.00	5.00	19.42	337843.24	439168.24	101325.00
		52.00	5.00	3.69	358527.52	459852.52	101325.00
		56.10	4.00	47.17	386796.04	488121.04	101325.00
		60.00	4.00	16.88	413685.60	515010.60	101325.00

In Gauge, Out Menis

Sample I.D.	Sleeve Pressure	Inlet Gauge Pressure	Time to travel 1 ml		Inlet Pressure, P_i		Outlet Pressure, P_o
					Gauge	Absolute	Absolute
	Psi	Psi	min	sec	Pa	Pa	Pa
1 N4-1.2	400.00	45.08	4.00	48.05	310781.31	412106.31	101325.00
		49.03	4.00	26.94	338015.61	439340.61	101325.00
		52.00	4.00	13.20	358527.52	459852.52	101325.00
		56.00	3.00	49.60	386106.56	487431.56	101325.00
		60.00	3.00	26.82	413685.60	515010.60	101325.00
					0.00		
2 N4-3.1	400.00	45.00	4.00	9.35	310264.20	411589.20	101325.00
		49.00	3.00	50.14	337843.24	439168.24	101325.00
		52.00	3.00	37.13	358527.52	459852.52	101325.00
		55.95	3.00	13.88	385761.82	487086.82	101325.00
		60.00	2.00	56.97	413685.60	515010.60	101325.00
					0.00		
3 N2-1.1	400.00	45.00	4.00	8.23	310264.20	411589.20	101325.00
		49.05	4.00	3.88	338187.98	439512.98	101325.00
		52.00	3.00	56.70	358527.52	459852.52	101325.00
		56.00	3.00	39.81	386106.56	487431.56	101325.00
		60.00	3.00	21.13	413685.60	515010.60	101325.00
4 N2-1.2	400.00	45.00	4.00	24.26	310264.20	411589.20	101325.00
		49.00	4.00	4.35	337843.24	439168.24	101325.00
		52.00	3.00	50.29	358527.52	459852.52	101325.00
		56.00	3.00	30.93	386106.56	487431.56	101325.00
		60.00	3.00	35.01	413685.60	515010.60	101325.00
					0.00		
5 N2-2.2	400.00	45.00	8.00	52.78	310264.20	411589.20	101325.00
		49.00	7.00	57.43	337843.24	439168.24	101325.00
		52.08	7.00	25.39	359044.63	460369.63	101325.00
		56.00	6.00	47.43	386106.56	487431.56	101325.00
		60.05	6.00	4.43	414030.34	515355.34	101325.00

	Flow	Length	Diameter	X Sect. Area	Permeability	Pav	1/Pav	Gradient	Permeability	r^2 Error
	$m^3.sec^{-1}$	m	m	m^2	Kapp, mD	Pa	Pa		mD	
	q	L	D	A					k_{KLINK}	
1 BA-9	2.61E-09	6.18E-02	2.54E-02	5.06E-04	0.01	221983	4.50E-06	828.069372	0.00699	0.9617
	3.07E-09				0.01	239220	4.18E-06			
	4.23E-09				0.01	273694	3.65E-06			
	4.83E-09				0.01	289897	3.45E-06			
	5.59E-09				0.01	308168	3.24E-06			
2 BA-7	2.39E-09	6.21E-02	2.54E-02	5.08E-04	0.01	235256	4.25E-06	1207.970991	0.00317	0.9347
	2.77E-09				0.01	256457	3.90E-06			
	3.17E-09				0.01	273694	3.65E-06			
	3.66E-09				0.01	290931	3.44E-06			
	4.12E-09				0.01	308168	3.24E-06			
3 BA-6	3.04E-09	6.19E-02	2.54E-02	5.08E-04	0.01	239220	4.18E-06	582.5421183	0.00782	0.9380
	3.65E-09				0.01	256457	3.90E-06			
	4.27E-09				0.01	273694	3.65E-06			
	4.87E-09				0.01	290931	3.44E-06			
	5.59E-09				0.01	308168	3.24E-06			

In Gauge, Out Menis

	Flow $m^3.sec^{-1}$ q	Length m L	Diameter m D	X Sect. Area m^2 A	Permeability Kapp, mD	Pav Pa	1/Pav Pa	Gradient	Permeability mD k_{equiv}	r^2 Error
4 N5-1.1	2.95E-09	6.19E-02	2.54E-02	5.07E-04	0.01	239220	4.18E-06	1199.267438	0.00480	0.9553
	3.36E-09				0.01	256457	3.90E-06			
	3.87E-09				0.01	273694	3.65E-06			
	4.42E-09				0.01	290759	3.44E-06			
	5.04E-09				0.01	307995	3.25E-06			
5 N5-1.2	1.96E-09	6.20E-02	2.54E-02	5.09E-04	0.01	239220	4.18E-06	900.8364815	0.00273	0.9384
	2.20E-09				0.01	256285	3.90E-06			
	2.54E-09				0.01	273694	3.65E-06			
	2.89E-09				0.01	290931	3.44E-06			
	3.30E-09				0.01	308340	3.24E-06			
6 N5-4.2	2.76E-09	6.20E-02	2.54E-02	5.07E-04	0.01	256457	3.90E-06	1741.413692	0.00092	0.9934
	3.03E-09				0.01	270247	3.70E-06			
	3.24E-09				0.01	280589	3.56E-06			
	3.45E-09				0.01	293792	3.40E-06			
	3.78E-09				0.01	308168	3.24E-06			
7 N5-5.1	2.92E-09	6.20E-02	2.54E-02	5.08E-04	0.01	255940	3.91E-06	2265.402174	-0.00074	0.9526
	3.13E-09				0.01	270247	3.70E-06			
	3.29E-09				0.01	280589	3.56E-06			
	3.48E-09				0.01	294723	3.39E-06			
	3.89E-09				0.01	308168	3.24E-06			
8 N4-1.2	3.47E-09	6.20E-02	2.54E-02	5.07E-04	0.01	256716	3.90E-06	1934.487124	0.00201	0.9278
	3.75E-09				0.01	270333	3.70E-06			
	3.95E-09				0.01	280589	3.56E-06			
	4.36E-09				0.01	294378	3.40E-06			
	4.84E-09				0.01	308168	3.24E-06			
9 N4-3.1	4.01E-09	6.19E-02	2.53E-02	5.04E-04	0.01	256457	3.90E-06	1998.247125	0.00331	0.9239
	4.35E-09				0.01	270247	3.70E-06			
	4.61E-09				0.01	280589	3.56E-06			
	5.16E-09				0.01	294206	3.40E-06			
	5.65E-09				0.01	308168	3.24E-06			
10 N2-1.1	4.03E-09	6.18E-02	2.54E-02	5.07E-04	0.01	256457	3.90E-06	3902.66674	-0.00431	0.9283
	4.10E-09				0.01	270419	3.70E-06			
	4.22E-09				0.01	280589	3.56E-06			
	4.55E-09				0.01	294378	3.40E-06			
	4.97E-09				0.01	308168	3.24E-06			
11 N2-1.2	3.78E-09	6.20E-02	2.54E-02	5.05E-04	0.011	256457	3.90E-06	3483.331337	-0.002864	0.9343
	4.09E-09				0.010	270247	3.70E-06			
	4.34E-09				0.010	280589	3.56E-06			
	4.74E-09				0.009	294378	3.40E-06			
	4.65E-09				0.008	308168	3.24E-06			
12 N2-2.2	1.88E-09	6.20E-02	2.54E-02	5.07E-04	0.0052	256457	3.90E-06	761.6425588	0.002259	0.9644
	2.09E-09				0.0051	270247	3.70E-06			
	2.25E-09				0.0049	280847	3.56E-06			
	2.45E-09				0.0048	294378	3.40E-06			
	2.74E-09				0.0048	308340	3.24E-06			

In Gauge, Out Menis GRAPHS

PERMEABILITY MEASUREMENTS MADE USING THE INLET PRESSURE GAUGE (RANGE 0-0 Psi) AND THE TRAVELLING MENISCUS FLOWMETER (min & sec)

1

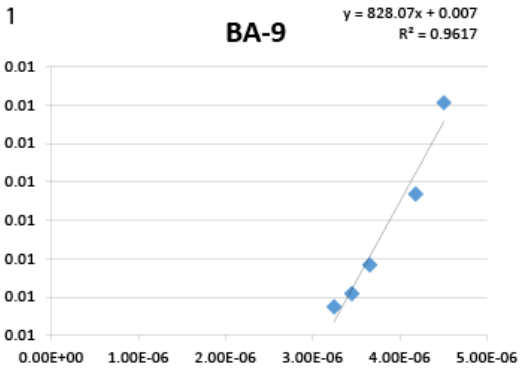

2

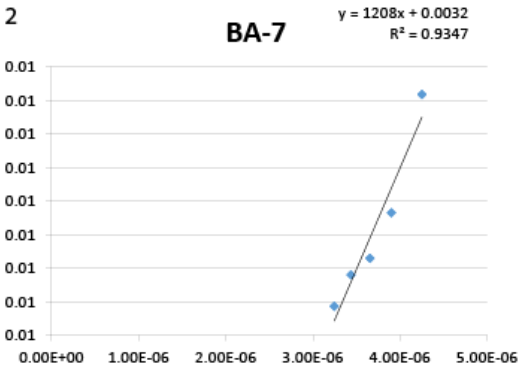

3

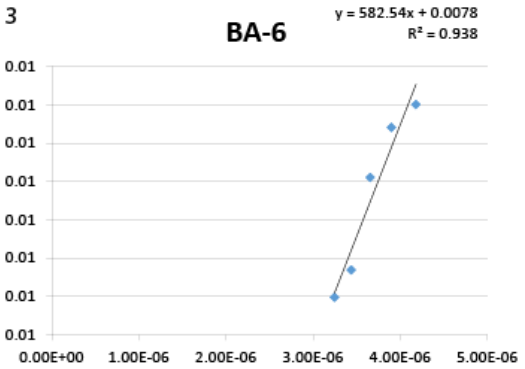

4

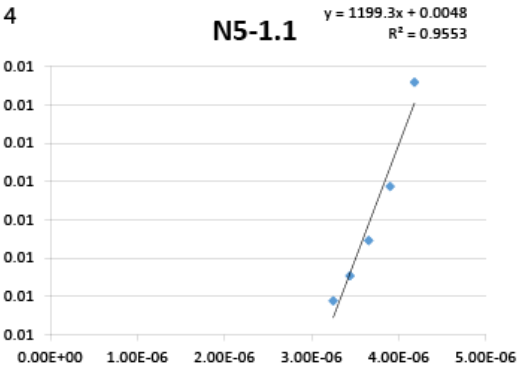

5

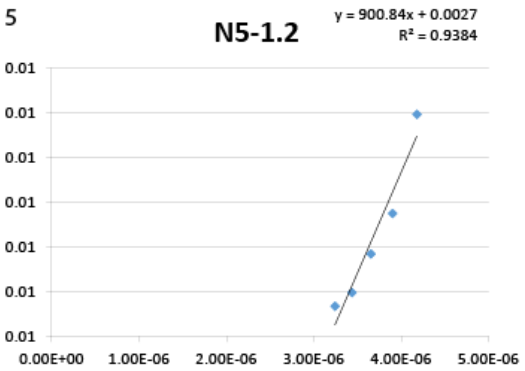

6

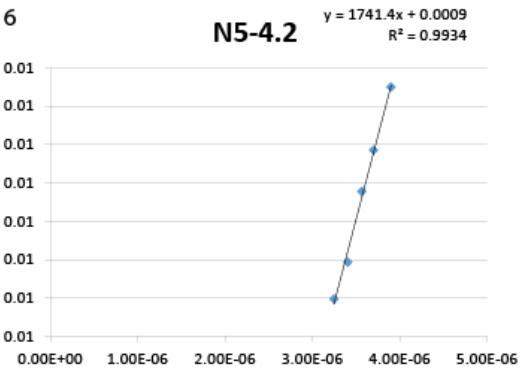

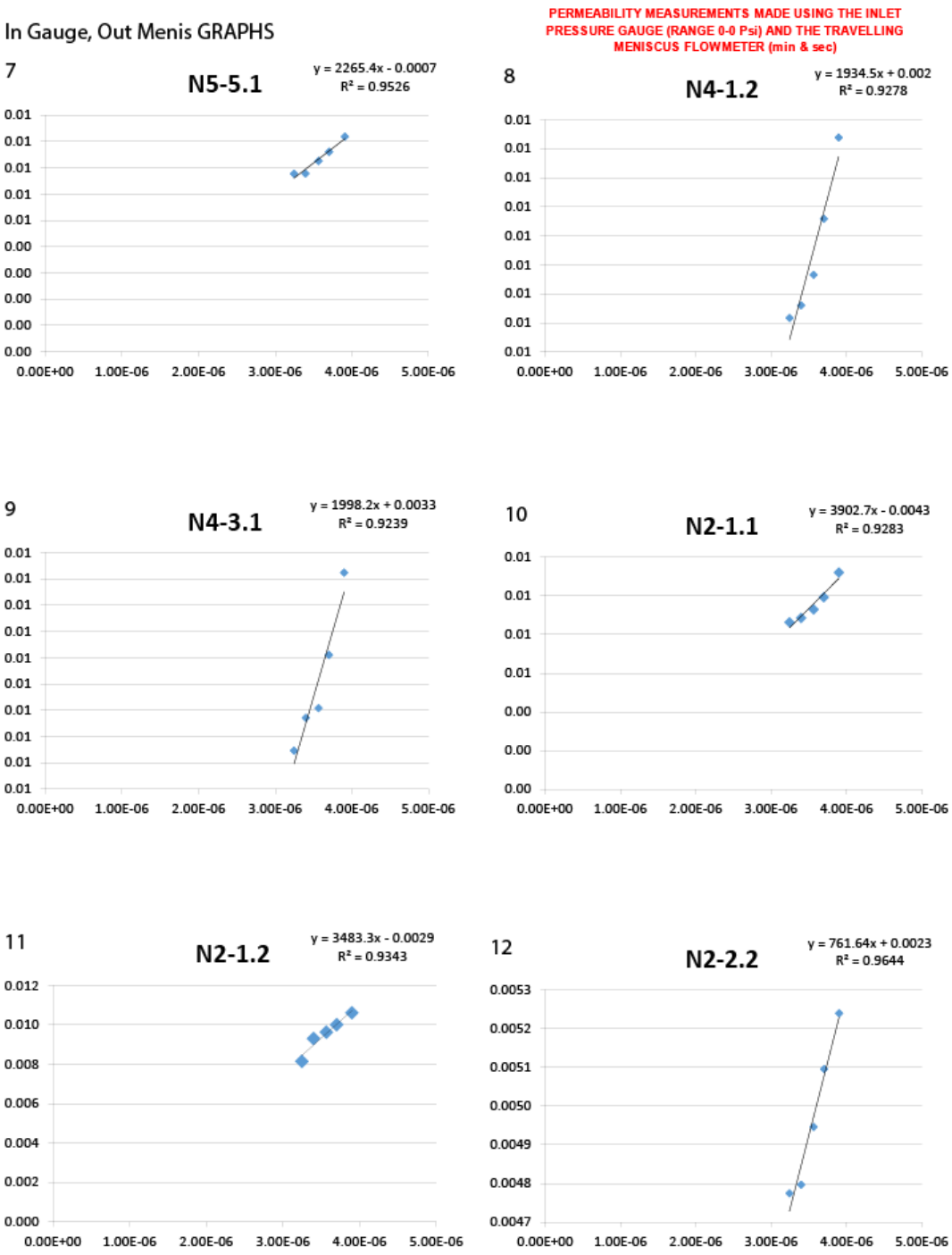

Permeability measurements of the core material after ultrasonic velocity measurements suggest that the permeability of the Òdena quarry samples is slightly higher (0.003 mD, 0.007 mD, and 0.008 mD; steady-state flow method using N_2, Klinkenberg corrected) than that of North Sea anhydrite (0 mD to 0.005 mD, with four samples between 0.001 mD and 0.003 mD) (Appendix C, Table C.2,3) for methods and results of permeability analysis). However, permeability measurements were performed on surfaces that had been coated by the lubricant gel for better contact of

the transducers and cleaning did not remove the gel completely, indicating that the permeability should be higher than measured. Despite this, it can be assumed that the Òdena quarry samples have higher permeability than the North Sea samples and that the overall permeability of both sample suites is relatively low.

In summary, the anhydrite samples with gypsum content have slower P- and S-wave velocities, and low AV_P and AV_S anisotropies (2 %) parallel to the long axis of the cores (X), and permeability.

Table C.4: Sample characteristics of cuboids from Boulby mine (Ba-7.2, potash; BP-1.2 polyhalite; BH-5.1, halite with clay; BH-2.2 pure halite) and North Sea anhydrite (N2-1, pure anhydrite), including cuboid dimensions (*lx, ly, lz*), mass (*M*), volume (*V*), and density (*ρ*).

$l_{x,y,z}$, M, V, ρ

Caliper Measurements cuboid dimensions					
name	M [g]	V [cm^3]	DEV V [cm^3]	ρ [g/cm^3]	DEV ρ [g/cm^3]
N2-1	353.68	121.124	1.427	2.920	0.034
Ba-7.2	111.24	54.041	0.376	2.058	0.014
BP-1.2	339.02	123.398	1.561	2.747	0.034
BH-5.1	353.08	168.005	1.909	2.102	0.024
BH-2.2	617.12	290.577	3.540	2.124	0.026

Density Literature	
Material	ρ [g/cm^3]
rock salt	2.170
potash	1.281
anhydrite	3.000
polyhalite	2.760
halite	2.170
Carnallite	1.602
gypsum	2.960

alternative names surfaces slabs cut for TS						
X1	X2	Y1	Y2	Z1	Z2	date of measurement
Na-2-1 X	c	-	d	a	b	25/09/2019
Ba-7.2 X	-	b	-	a	-	25/09/2019
BP-1.2 X	-	a	c	b	d	25/09/2019
BH-5.1 +	-	-	-	-	-	23/09/2019
BH-2.2 d,	x	-	a	b	c	23/09/2019

name	lx1	lx2	lx3	lx4	lx5	lx6	lx7	lx8	lx9	lx10	AVG lx	STDV lx
N2-1	38.32	38.3	37.95	38	37.76	37.43	37.46	37.86	37.92	37.93	37.893	0.2954112
Ba-7.2	59.05	59.16	59.4	59.34	59.24	59.13	59.11	59.02	58.9	59.16	59.151	0.1484326
BP-1.2	52.94	53.21	53.37	53.39	53.35	53.19	53.09	53.03	52.73	53.01	53.131	0.2123127
BH-5.1	44.66	44.57	44.25	44.22	44.43	44.57	44.72	44.99	44.96	44.7	44.607	0.259660
BH-2.2	81.84	81.8	81.75	81.69	81.37	81.22	81.31	81.38	81.45	81.75	81.556	0.2318141

name	ly1	ly2	ly3	ly4	ly5	ly6	ly7	ly8	ly9	ly10	AVG ly	STDEV ly
N2-1	64.2	64.35	64.15	64.18	64.11	64.19	64.12	64.15	64.18	64.18	64.181	0.066408
Ba-7.2	27.71	27.68	27.73	27.69	27.72	27.75	27.78	27.69	27.74	27.73	27.722	0.03084
BP-1.2	47.85	48.12	48.34	48.22	48.51	48.42	48.26	48.03	48.07	47.96	48.178	0.209645
BH-5.1	61.85	61.88	61.97	61.83	62.04	62.08	62.05	62.24	62.04	61.81	61.979	0.136663
BH-2.2	60.63	60.57	60.58	60.57	60.82	60.63	60.69	60.92	60.91	60.65	60.697	0.136386

name	lz1	lz2	lz3	lz4	lz5	lz6	lz7	lz8	lz9	lz10	AVG lz	STDEV lz
N2-1	49.63	49.95	49.84	49.62	49.85	50.03	49.95	49.78	49.74	49.65	49.804	0.145159
Ba-7.2	32.99	32.93	32.84	32.95	32.99	32.72	32.95	33.05	33.06	33.08	32.956	0.109158
BP-1.2	48.06	48.32	48.51	48.51	48.31	48.19	48.2	47.95	47.96	48.06	48.207	0.204833
BH-5.1	60.4	60.72	61.03	60.7	60.73	61.12	60.82	60.82	60.68	60.66	60.768	0.200322
BH-2.2	59.06	59.27	59.07	59.2	58.59	58.44	58.31	58.24	58.2	58.62	58.700	0.413817

Table C.5: Uncorrelated misorientation angles [°] used to calculate *M*-index.

N2-1T												
21.907	30.412	111.17	63.917	69.505	69.954	89.162	61.91	6.9276	43.438	63.677	45.108	80.214
59.628	61.556	84.812	73.643	21.618	98.103	36.036	80.942	67.718	69.1	76.954	62.315	49.388
95.916	86.153	75.604	67.663	79.087	37.645	78.583	66.371	69.334	43.719	57.861	98.331	84.386
60.179	88.156	88.491	70.649	93.14	91.823	49.605	105.24	105.37	29.39	69.008	70.208	60.973
93.105	69.585	96.505	92.804	59.345	91.326	87.536	68.698	94.181	69.241	80.408	93.421	65.86
86.903	83.962	68.475	45.978	18.466	77.369	50.263	86.337	64.857	72.928	102.44	74.999	59.911
56.801	86.612	102.08	90.341	52.971	70.48	60.898	67.018	55.589	38.884	47.282	37.526	57.006
50.955	33.925	34.089	68.094	79.421	38.642	62.373	73.176	85.667	80.058	89.08	84.8	101.54
55.648	76.009	48.089	62.454	78.677	89.865	31.55	96.283	94.111	21.761	83.628	76.954	46.787
77.329	113.5	82.933	85.214	68.256	101.54	55.243	69.058	20.452	44.523	9.7033	46.031	31.225
51.022	40.731	75.166	105.85	76.271	83.213	80.748	61.893	55.315	79.275	43.446	85.521	87.606
88.244	48.825	39.13	80.725	92.937	53.321	78.236	87.49	90.053	53.449	86.265	99.032	93.932
71.31	99.89	54.339	17.56	24.688	78.448	87.966	88.525	86.602	84.993	95.459	62.718	66.886
11.153	6.732	16.77	71.737	60.198	92.829	95.987	82.348	92.474	70.896	97.717	104.66	90.376
33.808	98.001	54.748	68.894	71.726	22.856	31.979	77.627	96.84	88.138	67.466	93.062	39.963
61.194	106.49	72.357	95.319	82.652	89.469	25.734	41.012	91.076	72.755	15.285	40.517	53.326
94.567	81.268	41.133	76.082	72.637	48.639	30.776	92.476	72.353	59.233	101.3	89.913	104.61
83.542	83.067	99.87	72.959	80.09	39.545	93.94	72.763	37.101	93.75	75.139	92.946	84.776
48.332	87.503	36.894	90.136	8.4377	54.98	25.75	95.63	87.059	108.64	94.197	92.055	69.745
56.801	72.209	45.683	93.441	77.26	76.739	34.253	74.327	81.273	81.078	48.245	91.821	75.597
75.85	98.848	84.013	54.146	95.777	61.098	113.25	82.003	42.312	60.139	87.802	101.52	98.08
75.064	89.164	60.064	92.266	36.175	76.283	51.629	64.984	70.933	76.625	60.926	71.927	93.91
91.079	89.459	85.809	43.873	72.669	53.528	92.866	40.729	103.75	107.24	88.908	33.681	31.926
72.824	104.22	19.905	59.127	48.73	67.081	84.066	32.375	56.306	80.801	27.402	109.41	29.698
43.288	67.897	87.086	96.942	76.968	103.69	70.777	65.557	38.621	14.303	75.422	81.259	108.14
86.238	90.924	86.856	32.015	55.284	90.585	61.211	24.402	72.691	82.829	69.597	101.94	80.617
72.54	83.198	41.018	27.039	50.026	99.412	48.47	64.376	36.539	77.077	101.85	43.27	48.961
75.611	102.27	89.479	18.774	0.88175	84.03	103.85	52.928	40.007	64.699	87.117	107.92	66.107
43.368	76.699	67.437	24.782	90.105	90.068	37.329	84.051	102.69	102.1	32.567	62.475	97.314
38.552	56.994	71.387	109.87	72.516	86.833	49.37	75.716	61.505	75.872	32.304	78.581	21.947
72.437	20.708	62.535	107.94	42.098	90.786	87.183	92.53	74.413	98.33	59.952	24.421	59.828
81.741	44.406	80.487	102.1	50.218	40.127	91.563	24.168	86.782	77.651	79.537	92.219	30.078
78.791	76.259	94.373	110.02	38.302	62.502	54.545	100.39	37.707	78.114	87.122	84.865	109.46
72.241	51.596	62.541	89.492	34.691	79.42	62.418	83.326	109.54	80.58	91.24	87.252	76.509
56.709	108.17	84.511	76.637	92.818	64.691	58.692	65.162	40.585	86.592	108.22	47.098	66.457
49.924	38.469	42.003	91.933	86.2	99.197	81.379	22.22	84.886	57.229	99.675	79.787	86.8
85.374	44.444	87.008	68.416	72.642	82.215	52.256	71.136	3.9404	91.571	48.582	85.508	85.612
84.94	93.791	54.722	66.419	93.212	94.837	86.447	87.236	40.352	114.08	84.11	98.644	59.26
89.212	28.681	108.72	93.505	79.824	93.063	38.839	62.132	22.532	94.759	72.297	92.361	83.759
53.477	69.535	90.475	72.787	95.137	52.292	46.704	52.724	89.143	74.679	11.237	82.889	97.807
103.01	91.971	72.587	109.12	65.057	58.832	93.314	63.954	91.982	72.306	49.364	27.374	83.447
77.283	80.623	91.6	78.392	93.539	59.575	71.954	80.22	86.197	95.057	71.467	71.196	2.0197
67.367	117.04	66.975	30.108	35.209	64.529	69.645	43.296	36.832	96.53	68.864	97.923	26.697
14.031	100.07	102.41	83.52	82.866	44.48	45.158	79.816	0.38773	45.859	101.42	102.75	70.873
83.944	101.32	101.67	61.965	82.982	109.08	65.47	86.527	67.38	96.431	93.251	74.486	92.886
60.412	91.021	87.247	36.185	84.656	86.873	24.219	43.556	39.054	36.101	70.719	94.564	57.05
85.254	75.256	51.469	49.997	65.637	63.349	94.939	86.426	52.775	89.553	78.796	52.986	63.641
106.34	45.543	43.112	87.907	86.819	91.502	52.271	58.143	88.005	30.562	87.562	102.76	23.62
83.041	61.948	33.783	70.23	49.125	61.077	55.799	98.954	83.037	98.858	45.03	82.298	50.847
84.778	46.878	74.515	73.223	24.326	91.666	102.87	72.587	90.505	91.988	70.91	27.285	84.404
34.175	26.056	15.637	72.059	60.176	53.057	47.807	35.985	63.816	73.599	38.805	77.236	51.781
46.311	86.713	61.348	100.42	46.957	97.255	49.481	74.142	68.472	81.004	35.127	65.695	63.075
39.36	71.574	37.305	42.162	63.569	97.232	79.829	55.422	83.614	62.388	71.173	64.491	46.827
79.839	77.289	66.049	95.566	105.35	100.37	58.028	35.137	26.109	54.088	52.718	85.651	64.185
14.225	62.806	61.049	70.073	87.066	42.899	93.556	18.175	79.226	58.542	92.051	88.637	37.906
83.422	23.745	46.322	62.019	30.395	76.501	70.758	84.018	48.963	85.058	70.291	66.912	47.26
82.18	70.641	84.399	63.575	93.604	62.515	99.548	73.713	47.951	97.307	86.697	63.332	25.379
99.969	91.868	53.205	73.201	41.909	65.409	87.838	80.784	93.449	69.634	85.954	75.384	78.405
74.964	9.22	89.508	94.333	50.283	74.205	81.635	64.942	48.917	76.984	24.847	25.053	112.37
63.699	90.11	66.103	45.978	84.244	87.526	35.594	77.172	94.426	30.446	70.297	78.445	64.631
82.216	56.938	80.78	78.115	65.948	60.592	76.864	31.838	76.223	105.29	76.759	99.881	61.113
106.08	95.233	76.513	78.802	60.877	40.681	51.288	68.701	74.972	91.015	80.431	83.971	53.759
81.312	86.051	73.558	31.607	60.232	76.1	85.702	57.892	67.058	85.215	78.881	70.68	95.568
57.484	97.273	59.142	88.228	48.948	78.86	63.029	109.3	52.043	95.513	70.152	61.523	91.774
86.996	32.206	74.833	96.549	20.76	61.618	86.068	69.862	86.829	86.888	50.22	78.537	54.891
103.67	53.736	58.361	49.176	67.691	69.981	68.09	41.019	92.169	35.072	74.652	93.465	40.281
109.28	89.674	81.434	85.766	70.987	73.818	47.866	56.548	45.918	51.624	52.105	40.959	60.02
11.326	36.473	50.029	72.298	80.068	67.953	66.696	89.713	85.212	80.652	96.112	75.686	93.53
100.94	103.51	41.171	58.011	82.712	39.614	80.736	93.805	44.972	86.323	91.446	66.379	77.84
78.736	93.909	66.637	44.016	56.371	90.384	88.54	65.622	105	27.857	38.819	45.224	83.633
106.24	34.645	82.891	18.392	98.306	72.379	54.559	92.108	61.803	60.629	84.784	51.738	95.828
20.921	75.084	60.049	83.181	51.081	79.762	100.24	63.038	56.701	33.505	87.524	87.977	107.9
42.478	89.624	48.961	94.266	74.767	92.333	96.457	95.531	22.399	71.579	63.117	68.863	92.621
33.215	71.263	79.677	27.077	65.749	82.149	110.04	79.357	43.682	70.787	75.128	30.204	73.606
105.27	64.533	58.283	23.587	68.313	63.453	65.771	88.825	39.71	60.676	86.862	69.917	71.754
54.562	89.348	25.973	71.164	59.216	91.191	92.764	65.281	38.125	34.819	63.901	92.82	94.131
22.308	26.478	88.035	55.317	53.99	79.016	42.523	58.763	35.366	71.189	48.686	32.651	

N3-1T

70.918	105.16	72.866	69.041	86.58	53.647	94.237	90.932	87.557	43.321	48.907	82.659	82.599
95.374	100.95	55.628	88.262	87.734	26.594	45.183	89.433	57.2	110.17	52.891	87.797	38.988
65.079	90.728	61.383	21.495	106.18	82.297	72.863	82.989	85.324	74.704	39.181	60.859	91.351
92.817	34.208	13.413	34.643	43.838	104.21	97.795	100.98	70.317	43.226	100.76	85.399	87.387
86.956	91.458	70.959	32.993	35.057	68.85	79.911	107.93	23.245	41.748	71.804	61.539	49.626
55.679	98.57	54.914	60.104	42.431	61.909	20.16	26.379	95.863	47.636	94.903	112.91	72.719
61.273	65.654	57.643	79.746	53.188	58.368	91.33	96.785	99.202	51.088	74.716	82.912	48.414
87.965	60.348	90.176	37.846	68.401	65.04	47.69	50.576	82.704	62.319	87.572	76.076	99.211
54.601	75.947	84.461	84.113	108.9	84.505	86.215	36.18	91.92	87.363	105.13	79.294	59.228
74.617	95.779	85.404	67.551	95.942	85.423	84.199	70.911	64.996	82.123	64.304	69.741	91.94
95.198	72.22	108.44	45.138	78.27	104.39	13.956	91.761	72.625	49.773	93.049	56.862	82.072
104.86	82.458	68.22	84.728	108.12	56.879	31.729	101.62	58.013	76.921	76.55	30.471	52.809
81.831	55.587	94.048	79.27	47.779	70.495	87.078	50.603	83.869	98.244	80.956	41.099	34.922
25.228	87.003	111.33	77.082	56.668	52.568	83.041	46.729	11.314	91.86	69.425	90.165	61.202
30.621	79.043	69.103	74.427	81.166	88.117	38.257	43.351	93.592	59.581	99.794	71.286	91.377
100.69	63.153	98.426	82.677	107.85	66.717	69.78	86.7	86.091	56.964	86.663	0.92946	80.759
91.322	88.996	94.487	83.999	94.443	58.426	76.888	56.531	69.797	101.04	82.755	72.094	33.71
94.51	51.407	23.158	66.352	86.338	97.489	77.85	56.066	104.74	48.147	105.41	88.356	107.48
86.559	53.479	61.985	70.518	63.719	77.148	88.14	101.55	98.91	88.8	28.221	88.682	42.424
88.558	106.63	40.698	81.697	52.925	82.873	73.735	88.166	19.808	33.154	85.102	57.518	61.667
102.87	42.078	45.824	95.287	103.97	56.388	44.641	15.603	101.99	35.084	83.935	18.149	97.448
72.715	60.666	23.166	58.754	56.571	75.055	51.342	86.773	43.006	84.999	98.276	85.118	27.226
79.496	79.182	86.221	50.836	75.867	65.683	88.108	64.941	83.797	67.048	68.857	91.104	90.834
96.514	73.794	61.606	91.392	87.929	51.62	74.158	82.296	84.747	84.431	56.911	104.77	89.979
48.814	80.471	75.667	47.734	23.76	40.323	85.266	87.763	60.523	92.214	45.823	73.821	85.442
101.2	97.024	66.254	80.194	66.435	37.235	66.062	91.687	81.95	44.082	86.362	89.426	24.891
50.695	59.599	83.025	86.7	83.974	74.39	103.07	55.93	78.537	78.153	104.6	76.561	21.403
87.437	100.16	65.706	50.081	35.978	100.05	57.538	5.2935	28.398	91.527	92.628	61.311	79.078
65.943	84.708	41.949	28.496	36.034	74.569	96.221	82.773	90.337	99.619	86.69	71.298	24.796
75.145	94.023	101.41	80.491	85.972	76.655	80.313	48.173	99.159	99.867	82.176	92.429	55.52
72.255	109.04	81.871	58.16	99.691	99.094	77.628	63.591	86.583	70.343	69.298	78.213	95.449
71.441	99.427	86.566	78.877	90.257	23.197	13.475	67.974	44.474	47.753	52.903	70.731	89.058
71.401	63.245	73.279	39.202	44.853	89.819	100.45	83.796	89.43	62.253	71.635	28.055	70.929
75.339	53.638	68.357	77.278	51.478	84.86	62.446	60.426	24.559	82.408	80.231	80.334	90.714
30.955	107.07	100.05	93.596	65.888	83.755	64.39	57.125	39.571	84.388	93.071	76.397	108.49
34.572	85.844	93.007	99.389	89.471	86.791	61.265	55.143	23.18	88.059	27.94	89.127	94.707
89.511	89.019	93.077	62.977	60.877	91.309	93.307	87.708	45.232	87.53	34.105	60.082	42.04
98.52	94.901	90.598	51.213	79.128	51.092	73.43	72.084	54.945	55.194	83.541	58.355	91.106
56.585	89.449	87.625	109.79	74.658	103.49	50.651	61.364	93.245	94.994	90.905	65.782	96.799
94.804	80.557	57.398	97.988	34.582	71.336	92.914	68.64	88.283	81.065	73.661	108.39	78.537
32.19	58.509	68.512	87.09	31.387	92.62	32.388	89.834	73.035	97.361	80.236	62.482	82.756
94.944	87.982	94.748	40.773	54.581	70.902	66.209	19.714	81.863	66.619	81.993	104.11	79.78
101.11	40.356	84.756	60.921	42.789	81.098	74.326	78.115	77.464	101.09	100.26	90.568	46.73
68.159	98.701	95.239	38.65	25.705	46.506	71.212	73.895	77.75	66.902	71.806	61.212	104.98
90.714	84.838	55.327	85.79	61.356	78.686	98.581	50.545	57.808	90.138	96.62	31.101	69.594
51.598	94.993	89.584	90.605	46.859	75.862	54.459	86.286	48.496	105.66	63.331	54.376	87.289
104.82	78.338	54.454	61.37	96.998	79.979	86.408	89.838	57.082	70.405	71.625	65.013	26.569
34.245	101.93	84.824	66.156	46.384	81.98	46.586	45.915	47.367	77.688	23.865	72.167	86.228
63.978	79.083	62.547	80.274	74.134	99.398	70.885	42.834	90.093	62.757	91.925	72.954	20.924
68.957	84.676	56.415	34.948	67.161	56.324	37.868	72.111	42.06	86.429	99.869	50.738	32.643
51.859	91.41	96.649	104.44	50.655	99.602	49.642	53.234	42.783	80.723	101.19	62.329	92.366
77.829	89.79	82.998	74.133	85.915	87.792	68.201	66.786	33.537	85.722	36.628	38.723	83.524
97.231	65.072	81.2	71.155	94.365	73.577	44.993	66.596	17.448	57.591	57.273	74.732	86.556
65.612	75.959	109.83	10.713	97.899	96.361	94.632	45.971	75.154	68.357	84.455	99.247	56.221
86.136	56.822	91.463	81.994	67.772	82.548	70.786	56.05	82.774	49.708	107.14	24.666	33.066
65.635	101.72	103.29	25.765	63.645	93.15	81.668	93.788	22.069	86.961	56.651	24.447	101.97
96.118	107.27	89.164	103.84	92.265	65.921	91.531	87.333	94.753	103.96	96.139	80.441	103.37
73.369	42.17	84.911	75.263	86.389	54.253	82.3	61.483	43.805	59.933	87.402	65.585	71.196
87.652	80.452	70.335	102.57	49.773	66.745	51.062	58.8	56.335	76.568	52.79	42.304	77.683
88.137	110.9	80.881	54.412	107.01	107.3	87.419	72.543	85.016	96.296	78.18	81.403	83.946
41.016	62.129	85.059	102.24	84.754	105.65	65.197	70.463	43.101	89.366	18.929	42.124	56.171
107.1	59.744	74.332	52.782	92.062	40.179	104.62	60.266	67.11	69.457	84.771	65.585	24.603
97.436	63.706	23.248	94.741	86.123	15.731	65.261	75.878	54.886	67.843	89.424	73.016	84.432
105.56	71.559	94.508	77.022	97.516	86.884	113.34	76.16	21.123	79.024	57.323	16.806	57.672
59.949	93.635	89.307	75.53	37.819	52.32	93.643	107.44	87.353	66.279	64.98	78.557	66.483
52.257	65.495	77.789	84.253	103.42	104.26	65.809	47.521	85.896	59.982	96.102	9.7054	36.609
55.683	62.698	91.785	63.433	102.12	81.375	60.049	55.176	25.381	96.712	49.62	64.142	78.761
61.625	103.11	104.44	85.451	76.35	82.588	77.217	110.63	68.503	82.688	98.589	102.13	81.207
74.739	57.05	85.169	82.92	77.173	75.578	86.179	76.479	86.184	85.472	50.879	92.127	84.65
87.03	85.061	92.662	57.745	62.662	67.373	73.137	97.898	35.208	39.24	65.509	84.819	87.958
68.437	90.159	32.599	51.426	4.5432	57.675	77.249	83.895	56.364	80.116	68.971	85.395	93.19
82.088	102.32	80.921	54.806	96.579	94.503	54.827	81.774	51.503	71.374	11.771	116.99	87.119
59.528	89.555	93.002	93.062	66.237	31.933	22.879	91.933	93.747	81.401	85.041	65.725	64.702
108.07	83.753	43.236	52.618	74.376	93.079	41.3	62.026	52.678	84.026	83.617	96.532	79.775
87.091	28.866	68.91	79.451	46.467	21.885	85.498	66.532	93.611	73.023	94.299	87.809	104.63
101.65	52.706	75.941	78.58	59.849	69.009	63.484	64.438	83.833	43.563	86.231	64.495	76.189
67.219	51.708	75.137	42.788	55.491	83.408	30.307	70.979	75.02	93.114	84.043	78.095	

N4-1II

91.343	72.758	49.852	56.299	90.42	78.416	85.018	68.871	98.515	71.962	74.761	107.73	52.088
53.781	61.452	79.459	84.711	97.935	91.099	84.498	56.272	43.166	52.781	58.817	99.923	79.71
51.514	17.132	72.097	103.89	34.39	103.96	74.205	92.592	74.308	88.215	19.786	46.179	23.927
76.178	68.618	57.621	78.866	76.97	78.721	88.176	100.74	74.166	67.003	66.083	93.714	34.009
66.934	14.009	56.327	29.166	62.887	44.212	65.514	82.445	96.013	87.261	64.653	38.331	85.331
48.133	65.67	46.707	70.404	88.001	52.486	91.731	51.566	48.07	55.453	98.504	32.95	54.866
74.518	85.384	91.89	45.136	62.422	47.804	77.782	89.693	20.144	91.614	97.601	82.544	71.949
86.046	72.63	102.85	53.221	98.986	62.073	46.547	101.81	68.579	74.113	78.67	75.944	43.55
42.948	78.283	76.273	60.611	83.987	89.18	17.842	78.662	92.09	65.844	63.511	82.455	56.728
70.825	79.346	93.538	63.196	103.46	81.572	93.947	62.967	67.746	95.852	76.094	82.588	50.266
47.682	59.518	100.39	73.497	101.94	33.006	79.908	84.935	52.008	85.858	88.794	89.732	60.147
89.356	82.08	51.102	75.447	73.231	30.64	91.2	49.558	62.512	85.786	102.04	92.95	91.167
37.112	74.059	77.153	71.171	93.742	79.473	69.055	59.273	83.188	99.404	78.456	98.451	107.27
106.36	101.26	78.94	46.452	42.764	97.357	84.708	79.134	92.312	98.386	82.261	90.369	55.112
68.322	40.331	67.888	47.073	84.287	37.1	107.9	37.033	92.532	108.6	82.344	49.391	74.041
109.59	67.644	67.156	54.778	60.655	45.933	84.974	89.51	97.24	68.768	25.161	57.833	49.899
31.867	62.301	101.37	76.998	65.439	98.414	69.183	81.19	72.855	59.016	98.534	63.668	48.79
92.41	96.663	52.769	99.17	32.11	61.925	13.097	98.685	51.734	52.536	55.582	82.386	87.084
84.262	104.48	105.3	82.156	92.789	94.741	99.377	86.083	61.529	67.718	82.346	49.968	89.288
78.827	75.089	35.207	68.595	98.768	94.548	77.308	86.459	52.573	97.266	94.317	81.087	84.51
75.665	104.88	72.538	96.469	76.934	54.209	72.45	95.398	64.645	103.08	85.589	43.285	75.353
72.092	83.115	45.779	82.253	61.407	60.217	57.07	89.595	113.56	12.605	109.2	72.424	73.212
49.183	97.167	64.759	108.12	73.546	72.786	26.44	70.265	78.497	75.666	80.224	77.735	74.41
89.833	94.367	43.905	58.747	78.713	71.502	65.644	84.111	80.576	67.184	55.718	75.615	99.881
87.196	101.32	87.272	83.422	86.74	70.877	79.515	79.657	86.976	60.275	91.671	74.589	86.321
63.332	88.955	64.181	103.97	93.915	27.961	73.819	66.188	68.723	81.825	66.991	84.144	86.02
63.596	84.985	68.922	60.107	72.579	92.292	44.649	81.728	57.499	106.97	74.192	58.64	29.228
36.231	92.121	93.718	90.509	40.153	65.354	101.4	66.084	99.702	28.977	50.294	64.094	75.676
75.096	66.827	66.481	86.518	62.85	82.568	41.564	93.776	67.429	22.141	60.276	70.168	52.902
98.86	38.188	96.38	96.322	92.496	47.309	68.085	83.987	81.16	88.11	98.017	84.205	81.889
104.06	44.529	73.309	96.84	85.199	100.94	58.789	100.02	49.835	94.185	87.743	71.254	60.88
73.152	79.903	99.922	51.057	53.956	81.14	16.702	95.945	70.059	98.948	99.369	100.84	85.972
82.769	99.607	62.286	69.092	77.171	35.784	80.234	83.132	112.29	60.766	64.414	87.3	85.493
77.534	93.161	107.77	73.64	70.874	103.61	62.117	38.141	38.505	95.476	77.148	72.308	34.186
99.049	59.614	106.68	62.801	69.379	77.424	71.587	61.253	88.068	91.899	69.639	70.805	86.046
57.144	114.05	85.366	44.843	26.403	75.455	67.116	69.992	97.396	68.632	62.19	84.081	57.393
89.888	61.892	37.064	82.767	81.079	50.506	64.083	33.081	64.021	27.518	47.218	89.798	82.277
63.625	51.259	39.469	81.708	84.16	64.93	77.57	104.67	54.695	47.893	57.602	75.698	56.964
72.045	27.228	89.709	81.139	91.097	58.993	45.479	84.034	84.148	80.489	92.448	68.034	79.076
89.815	71.408	52.135	97.9	61.299	94.837	100.84	90.06	83.882	99.348	58.662	64.023	96.448
46.165	81.778	81.705	81.117	57.469	91.804	78.069	66.796	55.265	68.393	72.991	74.496	60.642
78.846	114.62	85.223	73.734	102.59	67.306	85.529	51.001	70.811	89.412	43.048	103.71	91.121
71.235	24.22	48.39	63.701	75.662	72.407	91.666	46.96	47.427	69.46	36.388	90.638	30.706
42.911	68.519	67.177	85.322	95.426	75.898	40.805	97.999	73.128	106.44	72.347	79.013	58.66
73.951	55.143	91.502	46.098	80.624	104.52	74.928	103.42	93.653	75.078	82.167	92.943	89.001
34.523	81.018	82.884	102.88	96.452	92.173	99.274	73.128	68.749	106.24	104.27	73.37	50.751
67.652	97.895	92.364	86.729	75.903	90.366	81.665	89.304	47.341	85.307	93.874	104.14	78.586
83.721	92.649	98.586	104.19	75.904	69.348	93.558	44.586	100.91	63.32	50.784	72.57	89.475
63.955	79.352	91.819	93.894	70.21	75.476	61.562	40.634	67.504	85.29	52.364	83.912	84.989
90.446	58.708	32.863	108.15	72.215	39.511	68.363	76.854	85.048	84.437	67.345	92.98	99.763
79.406	58.817	75.396	66.192	92.134	45.301	3.7807	82.599	26.86	69.417	27.273	66.388	85.676
43.342	31.879	101.76	88.732	82.376	82.29	109.11	93.495	67.266	46.395	82.942	67.094	105.26
61.08	101.42	80.171	98.739	78.125	89.842	89.123	91.112	99.782	49.364	87.994	87.753	73.495
81.469	68.204	70.177	100.12	81.796	47.773	86.262	91.559	62.417	86.722	92.166	71.401	96.728
93.394	85.758	56.594	43.927	104.52	65.227	101.89	40.889	19.325	71.588	75.53	96.177	81.498
55.162	53.526	7.2335	100.99	45.976	74.072	102.24	94.148	81.583	61.72	48.143	45.2	97.254
60.26	76.675	72.767	71.402	43.586	59.921	70.601	89.983	94.82	40.934	92.428	85.027	90.895
13.659	76.922	80.891	69.678	97.118	95.877	102.98	78.522	85.943	88.724	55.588	102.48	77.605
86.563	17.865	87.897	55.318	71.561	77.121	91.548	71.993	84.279	74.917	71.779	43.322	59.043
105.9	110.87	45.39	70.475	61.988	86.428	72.186	88.25	53.524	97.073	102.61	72.15	82.409
70.523	96.223	21.518	61.779	64.294	56.882	74.311	70.078	97.186	78.623	88.42	92.02	67.477
66.366	32.449	56.293	101.07	73.256	93.285	79.942	42.823	83.177	90.359	81.062	73.417	50.264
52.854	46.143	28.77	66.627	81.315	72.717	73.21	61.604	77.282	83.338	94.5	78.267	46.226
78.797	72.228	87.316	95.893	106.98	101.66	81.84	112.36	3.8876	63.497	75.68	69.6	47.999
39.705	44.399	70.251	51.961	71.585	40.475	30.513	85.913	79.936	41.046	68.988	69.039	80.295
80.044	71.956	109.83	53.895	54.564	81.642	51.365	41.626	45.704	23.303	104.89	91.964	105.74
38.209	81.345	77.809	81.566	7.6729	89.034	62.022	71.748	82.985	91.222	66.649	61.436	86.114
71.979	38.247	43.585	57.286	89.086	61.636	88.83	93.521	95.32	93.858	56.904	70.689	103.06
95.353	91.426	64.348	49.121	64.242	26.91	47.871	92.785	20.453	33.626	92.881	49.138	103.8
70.214	73.033	55.11	80.14	60.908	96.805	58.715	95.042	65.967	58.61	76.758	52.629	33.78
36.184	92.369	45.505	73.125	24.379	57.62	85.387	100.61	103.51	105.94	54.669	92.874	107.94
53.892	59.399	95.465	41.716	103.9	72.134	87.725	85.528	89.009	66.177	52.835	71.146	92.658
71.926	91.651	70.882	63.304	66.449	72.521	75.467	97.61	79.829	81.956	97.168	99.108	83.224
80.195	89.454	58.688	89.352	91.424	32.722	96.64	91.329	28.607	60.069	44.202	94.007	83.621
83.173	74.549	54.866	66.37	103.75	32.195	75.406	85.153	96.9	80.155	39.236	64.489	55.296
77.247	63.2	28.075	59.045	92.389	81.272	55.537	82.84	54.346	90.644	89.358	12.969	90.865
93.985	66.911	66.592	60.795	79.189	66.037	68.073	59.619	79.241	73.106	83.637	91.735	

N4-2T

91.15	86.678	104.02	81.236	77.39	106.71	95.198	77.745	75.794	64.586	96.333	86.4	64.517
61.063	48.775	73.3	59.927	100.65	83.866	73.76	69.293	70.288	91.71	102.19	77.256	71.998
57.556	43.658	72.984	23.993	59.072	97.937	94.194	62.957	17.783	97.566	65.674	65.276	42.731
51.259	93.882	104.88	86.061	69.817	38.354	99.904	101.77	97.178	25.089	54.91	58.783	96.07
66.899	75.186	52.161	107.15	70.127	94.35	107.72	61.697	19.325	31.241	60.736	69.302	65.358
75.939	36.74	39.382	93.575	30.67	75.102	32.377	98.26	49.388	27.494	58.637	71.045	55.246
83.221	101.22	26.378	65.927	81.496	96.83	89.913	89.328	68.494	61.739	95.992	79.084	57.168
66.414	66.018	73.52	88.679	62.874	72.916	62.156	97.143	59.741	103.38	105.44	88.18	84.421
17.539	45.521	30.249	43.807	68.323	22.378	73.279	36.683	24.969	98.053	58.936	59.016	95.349
85.872	20	53.538	102.81	101.97	95.842	64.774	89.459	85.564	57.418	100.46	30.295	73.055
93.199	72.12	98.122	38.509	74.443	65.996	104.49	86.714	85.723	25.217	24.877	80.79	99.481
63.614	71.878	49.619	99.081	81.048	43.842	86.732	87.691	88.632	95.468	36.127	31.152	84.427
87.71	111.04	87.276	103.52	95.746	90.829	72.48	91.559	85.803	46.212	67.948	80.057	79.66
49.96	92.662	52.201	54.742	58.101	68.217	107.01	98.361	73.483	54.368	99.635	84.035	110
88.537	41.643	102.59	70.896	82.636	100.41	56.559	88.187	85.938	65.658	64.276	81.358	83.747
71.639	67.574	85.977	101.85	85.314	80.036	91.172	86.035	90.434	87.974	34.669	102.9	80.566
92.405	86.662	18.693	104.83	64.634	70.988	54.292	94.44	103.37	55.824	65.974	106.84	71.519
13.56	86.546	107.65	42.473	56.723	74.06	76.248	59.709	49.165	46.724	94.629	35.675	60.832
97.328	56.776	88.505	84.473	99.328	41.729	54.752	43.8	86.462	44.339	63.906	52.219	81.71
46.198	72.262	70.265	79.19	81.267	35.728	97.779	74.945	94.742	69.337	74.71	53.575	101.34
104.71	86.777	81.997	102.19	87.773	51.834	61.484	49.815	91.34	66.075	102.04	81.844	88.451
38.81	25.16	75.383	102.21	63.915	109.86	56.715	80.317	51.138	14.812	69.017	97.353	63.303
67.279	93.662	93.714	34.835	85.997	54.89	99.631	19.931	90.267	82.541	51.223	75.921	91.534
90.676	58.758	83.167	61.998	69.057	77.39	106.66	51.121	85.424	91.209	75.105	95.957	51.111
95.169	105.05	80.242	73.982	78.826	63.74	83.258	64.995	62.647	103.51	70.457	48.886	87.669
56.41	25.162	71.53	96.805	76.273	96.415	97.279	55.965	86.664	96.235	73.091	82.754	66.461
76.173	88.019	81.766	73.435	69.728	47.037	44.618	45.942	40.951	100.11	63.913	100.64	103.11
86.8	90.1	89.379	92.104	46.092	54.501	55.704	102.49	66.229	47.38	90.584	101.85	75.829
41.372	99.896	62.66	89.224	22.877	78.916	46.074	57.573	78.854	101.06	78.468	57.025	84.886
92.507	67.208	105.48	63.468	72.193	48.708	98.163	81.666	91.551	62.052	79.854	67.928	45.884
88.427	91.01	72.562	33.361	62.629	85.893	89.847	93.679	78.071	68.318	102.39	104.58	66.3
42.105	81.415	69.144	58.807	80.283	106.4	56.331	92.207	91.357	86.503	57.847	106.57	93.791
64.892	78.251	58.999	107.98	84.937	43.56	74.301	70.453	78.863	93.966	89.894	67.493	70.461
102.58	71.913	61.132	70.915	103.84	49.373	72.377	59.025	45.196	97.031	64.711	78.919	97.054
104.52	75.403	73.696	101.56	31.962	109.75	88.489	40.017	80.489	34.015	85.804	54.898	98.339
47.029	81.845	86.171	95.291	50.912	61.521	78.693	41.264	81.749	48.473	92.284	87.508	75.034
60.519	88.876	70.004	67.399	95.952	87.732	80.874	36.509	87.134	101.94	74.727	62.193	98.578
68.641	40.248	60.026	99.567	61.826	78.937	63.399	71.987	65.979	98.743	88.96	91.836	93.414
91.735	53.451	43.726	102.94	88.341	76.495	83.115	47.256	88.632	61.175	91.269	49.28	62.535
96.35	82.725	88.753	41.195	84.148	100.77	70.401	25.637	95.718	85.235	74.304	85.681	98.363
20.361	37.024	96.487	94.256	76.387	78.661	65.187	78.387	80.062	41.977	43.67	46.584	54.942
91.753	96.921	72.297	87.211	66.141	82.953	36.458	74.612	85.348	73.415	69.758	99.981	99.549
51.283	58.94	87.386	90.735	47.051	111.87	56.601	65.19	102.11	72.595	82.76	76.855	60.188
105.9	37.527	85.475	70.233	97.873	50.157	87.348	73.505	87.103	35.029	69.135	88.834	89.848
71.984	97.563	44.528	56.081	105.82	94.353	62.169	81.755	86.733	97.993	101.06	81.182	70.328
61.258	50.095	109.67	87.634	68.409	89.79	79.295	84.755	45.498	77.334	79.808	64.766	75.762
36.023	20.903	59.779	81.163	88.34	62.739	93.591	79.433	61.168	57.859	46.194	103.4	36.117
85.339	89.682	92.172	83.055	90.436	86.393	65.345	104.62	109.38	82.679	55.863	36.306	77.422
86.216	74.046	88.91	90.064	55.156	59.582	102.95	73.66	48.121	22.882	91.035	33.348	91.415
66.288	77.496	78.798	88.502	30.855	35.798	104.82	76.479	72.817	94.996	95.462	29.458	50.814
113.17	108.38	48.505	99.654	58.306	56.794	73.238	107.58	82.357	107.5	41.385	101.74	79.346
98.903	99.206	91.187	92.811	91.921	100.07	72.668	70.438	111.37	89.047	91.987	97.529	92.925
33.227	64.067	46.558	40.979	43.436	94.787	72.662	73.847	99.941	92.709	81.838	88.531	99.698
74.116	90.852	95.881	25.435	51.503	85.128	93.12	101.69	74.464	95.962	58.478	25.786	97.318
103.13	58.677	66.143	87.62	73.2	50.634	63.88	56.737	90.611	63.017	68.563	56.38	86.474
98.155	92.293	39.988	60.294	54.295	57.573	54.449	69.923	38.248	66.465	82.112	90.916	98.669
101.84	62.375	61.984	91.41	81.29	29.319	94.487	94.373	89.976	38.594	71.452	49.121	47.555
43.383	86.986	58.093	31.28	55.156	89.541	96.334	29.735	90.126	76.88	88.949	95.147	72.029
60.421	49.57	81.804	47.183	88.347	76.599	89.744	53.612	78.528	89.947	91.309	64.226	54.447
63.431	84.406	90.642	79.447	91.048	99.901	34.798	84.704	36.59	74.568	102.79	90.124	70.549
87.415	87.009	87.574	51.069	57.725	93.981	77.919	91.163	28.138	109.24	59.481	74.468	70.645
77.758	84.173	65.608	95.156	16.272	78.079	85.322	46.901	62.115	77.765	82.65	57.809	85.46
87.323	53.777	79.501	21.065	48.62	57.931	75.236	56.84	78.185	67.234	89.449	51.218	85.924
81.412	49.845	90.342	44.518	40.485	59.612	88.241	100.22	81.831	98.024	9.9233	29.683	78.422
30.059	64.696	102.83	71.494	94.406	59.766	76.276	107.49	104.33	94.006	34.458	80.097	65.726
85.716	82.671	75.588	103.6	76.976	90.357	86.965	92.783	62.249	72.913	26.66	83.27	30.399
59.935	95.869	90.962	95.426	55.831	54.606	102.85	79.94	60.537	84.561	73.585	95.717	66.776
60.058	82.905	26.174	92.815	25.95	99.248	88.443	44.598	93.989	58.264	100.72	67.024	52.973
54.903	92.484	47.589	27.644	94.133	80.814	89.375	39.802	84.871	64.12	73.583	68.48	69.558
103.33	82.467	99.53	67.771	98.169	30.28	92.576	71.253	27.506	52.421	76.75	83.509	87.893
40.515	81.256	79.126	81.868	40.641	28.084	81.634	79.632	99.932	69.092	47.4	52.306	95.214
76.187	80.083	47.624	111.36	98.03	91.849	74.636	59.889	97.716	91.396	97.72	100.04	70.731
34.408	47.693	50.89	66.891	92.376	60.017	88.676	87.143	87.215	95.424	52.216	21.717	48.307
92.307	88.998	77.864	78.568	103.77	60.979	69.534	98.575	83.084	97.874	44.087	92.993	94.473
84.679	71.718	47.937	89.954	63.946	77.027	79.969	73.495	76.353	102.09	17.387	86.004	79.397
90.154	78.579	64.278	70.204	68.586	77.196	54.143	100.57	75.452	33.204	66.078	90.913	39.292
34.023	65.031	87.343	36.233	88.8	76.733	58.127	43.438	84.399	87.34	91.162	60.705	

AA-4T

69.136	82.246	91.791	103.28	75.909	72.785	106.17	51.413	95.072	93.415	61.757	79.084	59.458
87.03	27.245	77.569	52.896	78.351	72.143	57.324	63.479	93.106	104.04	61.299	35.748	77.914
99.688	42.398	76.696	93.148	68.615	101.19	68.114	42.811	70.312	83.4	92.983	49.327	60.603
102.74	86.347	80.122	61.246	90.138	80.074	58.247	24.584	18.519	51.054	73.815	59.428	56.88
90.775	101.39	79.436	64.4	72.676	92.192	97.421	81.321	44.592	24.846	99.964	39.583	51.849
64.962	96.594	104.57	66.352	105.26	60.118	72.215	46.65	48.689	57.609	51.077	59.468	45.667
52.82	59.988	89.421	79.914	92.343	44.928	33.364	83.603	85.849	55.842	89.249	7.0736	103.82
96.099	62.936	95.565	78.291	62.067	77.55	77.237	96.608	69.421	53.951	72.995	60.731	102.9
48.719	64.779	85.659	82.187	49.38	109.05	75.725	61.606	50.509	79.77	83.638	84.484	96.828
82.613	82.868	95.099	87.819	75.16	66.345	60.816	59.251	89.333	81.491	62.328	94.842	88.168
71.512	70.535	110.91	78.705	61.425	54.402	59.188	15.461	45.734	45.5	71.985	90.204	66.952
72.894	68.94	85.138	84.673	27.028	61.486	95.035	39.526	37.807	77.42	28.178	93.385	74.176
48.154	92.883	68.976	71.401	100.37	91.637	51.738	87.956	96.042	104.1	104.5	94.987	92.727
75.431	99.49	93.619	88.849	81.125	59.606	94.891	92.593	37.894	98.755	90.168	78.047	90.584
39.53	81.054	31.564	40.575	62.222	80.822	81.352	70.85	69.202	86.758	65.411	104.3	100.62
59.106	74.085	16.447	90.519	93.151	93.498	94.877	68.313	105.65	80.661	83.871	77.075	92.029
63.624	103.83	88.641	76.314	42.634	81.2	50.324	89.957	69.814	97.095	64.756	99.651	96.242
62.772	65.41	93.915	89.48	72.747	93.658	75.965	84.043	73.94	87.937	94.601	91.249	83.085
90.019	100.24	71.331	67.658	86.211	60.217	23.793	71.352	55.54	43.19	80.618	101.28	55.458
46.57	89.508	43.463	51.127	41.143	109.64	100.22	88.808	77.541	106.41	73.519	35.022	73.785
107.98	102.68	81.912	76.519	86.757	104.5	78.888	64.986	89.143	59.759	95.18	99.815	64.046
54.675	94.566	30.298	53.684	108.38	92.862	80.31	38.667	98.53	94.244	94.872	36.172	26.326
97.645	75.284	105.7	107.53	92.658	74.888	48.058	107.26	79.434	93.934	89.973	62.755	80.167
75.947	73.136	101.05	92.238	88.145	93.267	93.8	81.917	63.792	66.41	90.656	97.811	64.373
83.566	67.125	75.739	77.794	32.817	88.802	73.646	61.965	100.89	20.359	96.322	62.668	65.873
106.86	21.486	103.68	62.405	91.923	79.794	74.269	62.052	63.128	42.466	90.828	17.983	52.754
95.19	80.403	59.585	58.902	79.796	91.583	76.903	102.66	88.596	94.906	80.186	105.16	104.82
67.879	47.869	65.796	44.773	57.251	100.24	80.384	61.229	92.198	47.166	90.458	78.527	94.662
79.588	87.058	80.987	97.098	54.866	104.58	101.58	84.472	65.503	54.568	83.582	71.276	86.84
56.843	86.66	73.252	86.02	85.584	88.429	92.176	71.73	61.865	71.631	87.517	99.436	66.272
67.395	89.109	38.074	56.48	95.28	91.506	32.643	103.14	98.016	86.134	75.56	92.621	69.743
90.042	73.886	68.731	78.727	59.439	91.178	78.635	59.648	92.738	102.89	58.091	92.432	27.01
45.8	84.487	51.608	37.395	101.86	101.97	91.227	60.899	58.708	66.046	61.525	91.702	67.688
80.821	82.273	83.388	54.727	62.009	41.337	75.191	66.204	86.544	106.1	21.691	50.704	78.494
79.508	94.517	38.443	72.161	98.905	49.58	63.254	102.38	71.449	72.885	83.74	72.996	90.908
78.757	74.5	88.221	64.873	99.411	26.521	106.67	76.308	64.559	96.347	93.863	68.276	69.115
64.667	105.23	75.56	54.997	94.421	74.968	20.734	86.383	67.954	94.645	53.377	90.781	65.784
77.816	101.62	60.574	41.491	38.835	47.62	64.928	62.997	81.96	31.125	75.429	42.128	88.338
98.51	49.601	43.894	75.586	59.569	68.79	21.858	50.98	83.564	24.641	69.646	77.042	66.137
91.646	61.767	56.316	100.45	67.281	87.492	64.879	95.094	42.725	65.669	70.68	89.432	101.66
68.796	72.174	82.508	61.224	105.24	56.494	91.438	106.33	70.397	86.982	96.785	32.309	65.388
92.366	84.215	99.763	65.445	83.992	93.573	74.149	42.156	102.94	84.082	89.292	81.81	69.812
69.527	76.691	82.852	94.811	12.312	83.272	97.018	75.551	44.962	94.797	90.902	35.73	57.834
93.136	71.822	44.448	99.794	98.4	94.999	108.34	51.733	59.642	60.495	27.811	67.2	75.856
92.04	93.66	96.183	76.257	79.122	65.091	79.327	98.792	77.471	96.259	104.01	98.28	74.463
57.726	92.149	79.436	60.665	50.301	96.694	79.18	76.745	86.515	91.859	35.348	85.084	90.011
99.896	68.372	84.622	32.422	79.674	77.362	105.03	54.255	51.437	68.344	64.482	44.8	86.371
96.284	71.729	94.793	65.468	98.294	89.835	90.427	86.614	67.168	94.426	76.317	99.052	37.491
81.819	94.867	78.582	86.845	103.93	83.062	91.788	90.319	33.453	27.2	61.237	75.585	80.438
90.125	95.784	76.017	95.529	58.13	102.38	73.86	106.25	102.26	83.691	85.915	72.297	30.526
96.416	88.932	77.823	48.612	80.993	93.889	86.49	87.53	39.849	58.909	56.436	94.23	40.425
88.088	94.421	83.566	45.227	112.08	88.369	62.824	75.808	71.331	92.882	89.398	85.418	94.238
100.78	104.01	108.52	37.618	84.65	93.629	83.631	104.53	20.435	73.476	78.408	66.621	87.681
96.286	99.161	67.811	49.287	53.816	29.932	96.514	50.551	79.802	80.085	95.761	49.239	92.086
83.415	79.263	76.942	81.569	56.565	23.928	87.994	82.385	54.726	59.984	88.061	65.188	60.039
106.51	101.1	82.289	67.037	83.274	67.295	83.663	57.255	96.261	75.81	98.362	88.311	79.934
107.72	61.438	100.6	99.082	110.58	66.515	88.965	87.721	58.167	39.534	52.721	84.296	95.565
76.648	67.929	54.52	69.849	99.063	57.567	32.573	93.332	92.108	88.666	87.642	57.404	72.291
79.408	93.769	104.34	84.928	58.219	101.11	82.62	40.353	88.769	74.309	43.976	81.569	81.681
87.439	98.764	70.742	86.291	36.236	22	35.016	67.039	43.68	83.326	88.423	91.548	105.64
54.917	92.738	55.628	85.172	73.736	107.14	44.3	30.012	86.771	52.162	75.966	72.019	72.725
62.168	63.473	76.476	54.236	103.72	59.93	50.394	98.97	68.013	87.681	53.461	65.928	101.96
54.986	65.833	80.375	93.24	41.817	76.684	66.087	68.224	82.997	105.79	39.713	55.134	82.451
87.482	78.723	81.099	94.894	19.463	18.54	71.392	63.258	34.787	89.638	88.883	43.422	35.381
85.619	75.074	88.06	74.24	63.191	46.738	89.089	92.973	89.859	53.542	76.136	82.863	54.327
100.7	94.471	81.213	96.034	54.271	114.28	82.344	58.543	57.123	89.061	76.715	36.918	56.376
75.417	107.3	89.573	93.531	59.88	76.871	96.44	67.576	51.703	34.215	91.539	69.984	87.279
30.387	103.6	93.402	61.212	92.469	48.748	75.915	110.71	94.131	4.6713	70.048	68.879	46.582
33.894	81.817	68.717	71.564	99.85	99.323	52.542	99.669	66.429	103.96	89.957	76.654	65.256
91.52	79.564	71.174	34.427	88.165	18.337	78.042	71.17	104.32	7.3883	96.657	90.626	55.541
57.25	72.103	91.03	54.183	73.06	62.57	98.297	64.314	80.9	81.657	80.083	86.875	75.462
102.7	100.01	58.698	50.085	77.836	21.135	42.005	88.216	102.77	52.112	75.45	72.932	51.858
87.045	104.36	69.843	96.721	84.064	82.808	61.226	77.284	80.355	94.696	45.29	89.048	18.144
93.14	78.749	91.696	69.227	60.469	73.827	52.608	92.08	53.758	99.035	56.811	38.028	72.82
63.495	67.205	94.594	103.5	94.419	30.013	9.5091	51.651	76.48	63.4	64.14	95.451	85.708
65.019	88.406	85.572	7.6338	35.958	55.445	94.45	79.795	89.746	100.95	58.069	71.841	104.16
98.762	75.148	103.53	67.546	53.458	85.085	77.541	82.564	77.426	79.654	59.578	43.389	

AA-6II

62.774	27.338	73.717	22.925	46.11	92.868	58.137	80.078	61.602	104.9	84.355	99.446	84.815
79.946	90.004	94.916	71.875	49.177	91.62	52.175	100.99	56.954	86.637	98.385	109.77	89.115
61.094	111.32	74.975	24.249	15.811	26.369	78.087	66.822	101.11	115.89	103.08	66.756	81.951
87.243	76.116	105.95	89.685	55.214	91.715	65.557	93.418	97.951	98.013	54.726	78.174	90.107
93.167	61.262	81.753	89.93	73.391	87.242	65.514	95.741	92.204	86.896	68.99	29.754	65.591
32.112	26.484	91.682	61.538	28.236	92.421	93.04	66.652	44.854	43.374	66.433	95.762	94.409
104.21	90.691	85.302	77.099	100.57	75.423	77.333	103.24	60.708	78.168	106.44	47.383	66.842
69.21	61.839	71.122	82.451	57.436	21.275	62.098	80.458	79.002	57.048	68.277	97.333	72.687
110.48	74.001	87.899	107.62	90.202	65.826	87.363	36.734	91.078	35.728	46.346	83.427	35.618
60.444	96.893	78.016	72.79	65.141	109.6	84.411	73.211	95.938	87.417	95.34	85.514	81.722
69.201	23.269	91.073	60.734	79.923	84.15	92.516	53.565	56.148	63.486	90.573	93.426	76.527
74.914	54.694	87.542	79.882	32.071	101.11	70.107	56.077	96.501	52.805	46.674	75.19	87.963
28.286	62.923	102.59	100.65	90.07	70.755	77.882	59.785	64.545	62.885	76.145	85.48	34.702
54.131	81.284	69.421	59.069	72.063	62.968	90.502	39.498	68.378	49.769	52.449	68.439	89.372
26.02	81.282	108.11	64.536	80.775	11.043	71.008	98.86	92.223	102.95	72.561	55.069	75.634
81.261	54.346	36.689	96.351	87.409	81.189	51.326	40.634	85.804	81.521	59.187	15.357	102.87
70.021	49.772	59.17	40.734	100.54	12.308	78.842	62.475	104.62	104.83	24.842	29.172	44.564
94.43	66.799	102.69	55.911	98.766	98.66	74.388	85.128	62.989	65.546	98.357	55.132	57.421
92.526	45.663	39.957	63.212	70.349	4.6634	90.895	89.475	62.978	70.836	99.512	18.624	71.242
67.788	82.582	62.558	99.39	44.931	70.541	51.906	95.269	63.235	64.53	64.963	64.019	102.26
77.981	67.049	75.692	39.075	18.568	83.936	64.481	62.834	60.108	87.222	86.14	63.89	74.684
77.732	97.351	97.721	75.901	60.64	66.216	88.878	76.91	54.909	99.201	101.64	100.62	48.041
86.169	98.044	80.679	85.995	98.707	103.88	47.355	96.31	37.837	99.373	82.834	24.877	52.029
70.703	46.919	55.32	81.27	94.07	82.129	47.857	58.248	90.741	98.437	60.848	76.673	110.24
51.743	89.277	53.257	108.3	77.084	82.375	83.821	39.865	104.16	75.108	82.867	90.859	43.791
91.876	87.035	101.25	81.775	85.414	83.39	88.209	102.68	73.228	62.672	88.804	90.523	98.771
94.528	96.49	36.565	79.376	108.79	62.533	47.465	101.5	79.097	65.829	84.019	89.358	96.274
51.305	72.746	49.602	81.543	89.614	91.09	81.954	58.574	64.178	65.218	81.023	103.06	88.105
90.639	44.513	91.753	111.96	87.447	63.62	78.982	97.278	85.65	78.354	68.64	28.317	59.533
71.047	29.692	87.355	98.6	94.551	72.663	85.9	74.942	114.42	79.604	99.123	85.06	85.154
72.337	57.581	91.494	80.43	50.134	103.99	30.702	58.045	95.259	25.967	110.13	71.071	50.535
19.766	38.777	89.104	84.038	81.491	71.676	74.272	27.364	86.508	76.121	97.962	96.206	75.903
57.984	51.535	73.51	67.23	83.43	64.618	109.56	87.012	61.634	79.969	30.34	42.946	106.6
86.282	100.26	95.117	83.504	62.367	55.962	95.056	104.42	56.452	33.405	23.194	70.802	41.217
93.617	89.56	64.396	96.301	40.684	78.058	74.152	58.779	40.558	86.46	106.25	37.74	79.615
58.019	93.367	59.203	68.252	25.933	81.029	102.29	65.155	47.14	34.338	111.98	116.34	66.429
47.476	94.419	91.638	63.205	93.704	84.272	52.403	76.483	46.352	61.866	82.98	100.16	45.066
96.232	95.477	85.93	85.947	78.449	33.349	73.313	88.207	75.994	45.085	72.851	92.154	60.384
93.348	81.558	57.295	33.65	86.115	41.511	73.508	107.03	74.491	100.61	43.247	84.142	60.382
53.652	79.806	45.313	109.14	100.91	55.354	96.426	78.119	99.512	46.334	67.337	87.662	54.881
36.991	92.159	81.578	71.88	6.0956	75.767	75.622	87.399	82.131	91.133	87.792	85.441	106.78
79.003	50.629	92.458	51.533	64.245	89.838	86.754	45.001	63.765	83.764	88.187	99.449	63.744
26.865	83.762	78.107	99.506	81.383	75.396	15.292	97.617	61.2	85.922	33.444	79.03	101.26
95.572	74.709	83.169	55.728	30.695	82.726	76.756	96.427	43.505	70.136	100.43	65.778	96.714
86.14	53.902	58.259	91.333	84.041	88.527	67.755	69.382	18.594	36.048	46.057	91.58	74.267
67.098	103.04	42.166	37.676	107.86	66.176	72.104	60.008	81.523	84.288	42.858	79.261	72.231
40.614	74.132	59.966	94.542	29.047	65.223	72.433	84.561	79.58	56.804	83.47	90.071	45.405
87.041	74.716	88.692	87.134	57.311	95.384	96.045	90.944	74.517	94.223	96.292	79.013	67.053
91.379	66.249	91.729	105.32	12.867	97.704	84.964	53.987	48.919	104.3	74.883	44.318	97.169
92.652	52.431	82.068	77.203	10.575	85.094	77.284	90.837	51.871	65.834	96.159	59.392	66.195
70.853	93.239	39.881	90.48	87.999	94.233	84.108	69.713	57.589	99.382	79.811	102.3	63.255
24.017	57.214	44.856	68.875	56.457	82.891	69.626	69.903	99.747	104.85	99.129	62.715	46.884
101.63	42.481	115.05	74.373	69.488	61.151	49.344	93.679	93.83	58.362	22.695	65.519	50.14
33.858	78.854	66.417	36.337	75.878	107.14	80.952	36.839	91.936	91.695	44.72	66.31	91.24
90.017	69.673	107.52	86.179	95.344	39.513	68.637	54.064	28.941	87.313	34.412	69.34	95.876
88.723	65.336	71.471	73.475	54.543	88.631	56.229	26.964	59.472	63.679	93.035	72.119	96.332
92.878	77.767	72.309	84.111	66.846	79.138	48.495	89.219	52.218	108.08	69.832	61.343	73.441
69.234	58.481	85.587	84.515	104.06	61.23	59.102	102.84	79.52	46.52	105.47	45.263	83.244
93.37	82.264	44.708	91.016	81.841	46.369	64.901	96.729	91.27	91.293	94.434	47.86	80.159
55.289	83.293	90.031	51.979	83.175	61.65	18.223	66.129	60.189	97.272	82.606	94.895	97.583
100.86	60.67	96.194	21.713	99.256	82.693	74.799	69.598	61.268	94.596	86.249	105.91	41.289
67.886	37.298	100.05	93.548	59.806	96.863	80.918	89.708	69.319	74.513	90.899	65.498	64.556
47.554	68.482	91.617	89.41	91.706	67.979	54.241	69.752	34.114	39.774	78.486	81.194	88.288
88.541	88.437	91.075	87.727	37.797	50.193	92.349	54.741	51.847	61.523	83.107	79.484	90.533
90.941	71.652	65.132	59.897	77.561	64.908	59.033	87.21	57.065	49.003	88.155	104.06	108.49
93.89	53.105	71.038	35.417	52.779	64.005	55.434	76.298	84.694	67.044	102.7	73.065	37.771
77.609	77.405	94.677	66.49	105.65	64.814	99.99	70.937	8.662	87.903	63.452	37.614	93.06
93.689	91.568	93.971	92.473	101.55	89.004	62.847	30.339	48.738	69.295	109.54	87.761	74.336
75.84	72.7	82.239	79.998	109.17	21.108	83.651	80.294	63.989	80.777	62.819	77.88	59.316
13.096	103.28	59.163	75.585	57.583	93.192	45.114	80.475	91.54	83.19	98.743	95.737	55.388
72.872	71.209	72.341	82.504	101.73	71.927	51.077	96.441	88.02	100.65	92.103	96.947	71.852
90.915	45.114	97.332	83.865	94.913	35.697	81.389	82.462	78.124	33.638	63.859	10.298	58.179
92.422	76.534	54.497	35.315	79.019	95.697	67.625	16.394	66.76	103.72	65.994	35.801	80.658
65.964	97.508	60.656	67.862	69.823	78.241	24.131	60.999	60.827	48.407	93.293	65.344	81.331
66.505	64.146	100.5	97.073	51.62	91.817	36.275	88.543	57.322	71.413	110.03	50.038	91.951
66.442	77.256	86.724	85.461	69.057	55.98	71.85	70.201	93.486	62.594	17.395	92.807	79.432
96.669	75.007	99.555	20.767	60.147	73.146	93.096	84.616	91.591	83.484	89.16	70.473	

APPENDIX D

Supplementary material to chapter 5

D.1 Figures

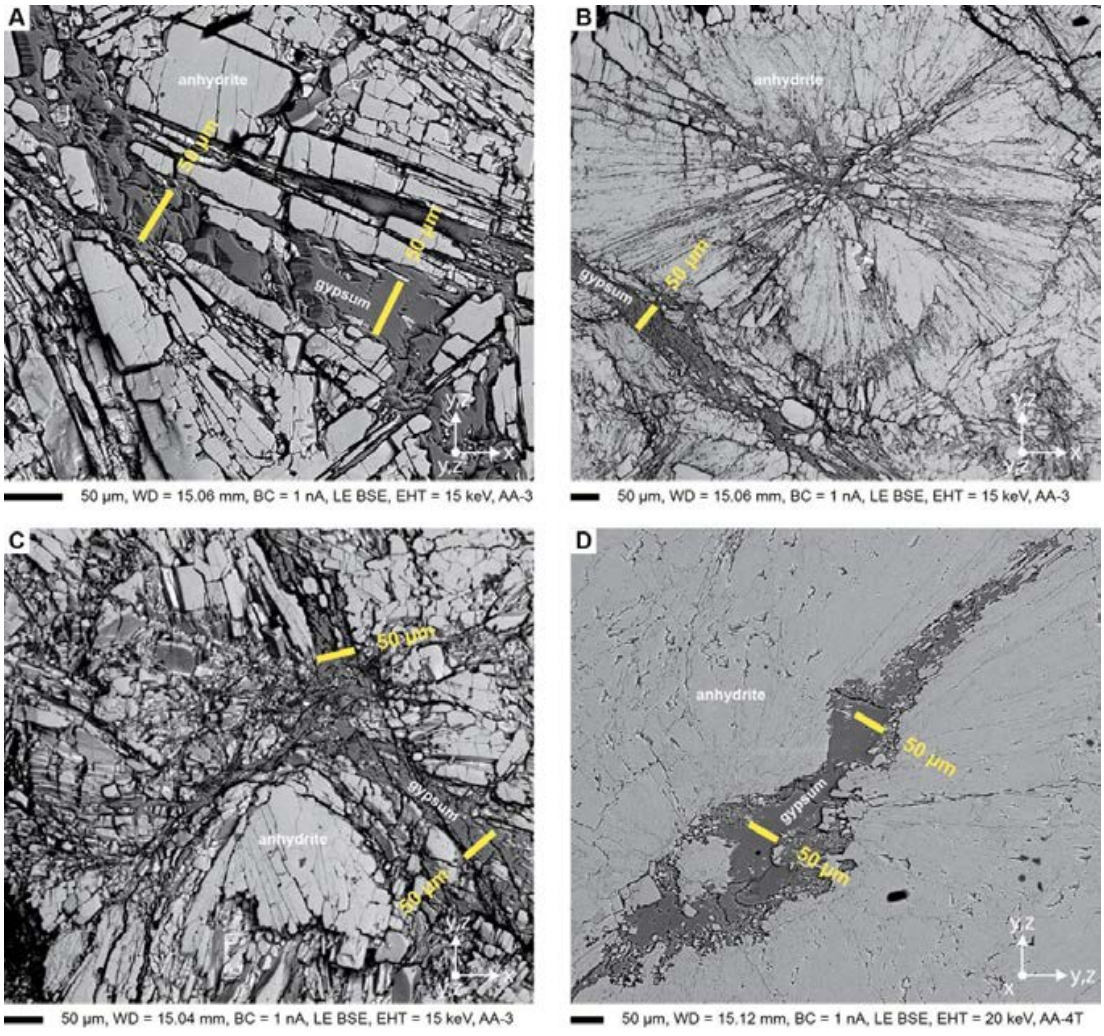

Figure D.1: Electron backscatter images of Òdena anhydrite. A: gypsum vein in anhydrite, sample Ò8. B: Gypsum vein next to a spherulite with gypsum in the centre and between grains, sample Ò8. C: Gypsum vein in anhydrite, sample Ò8. D: Gypsum vein cutting through spherulites, sample not used for experiments.

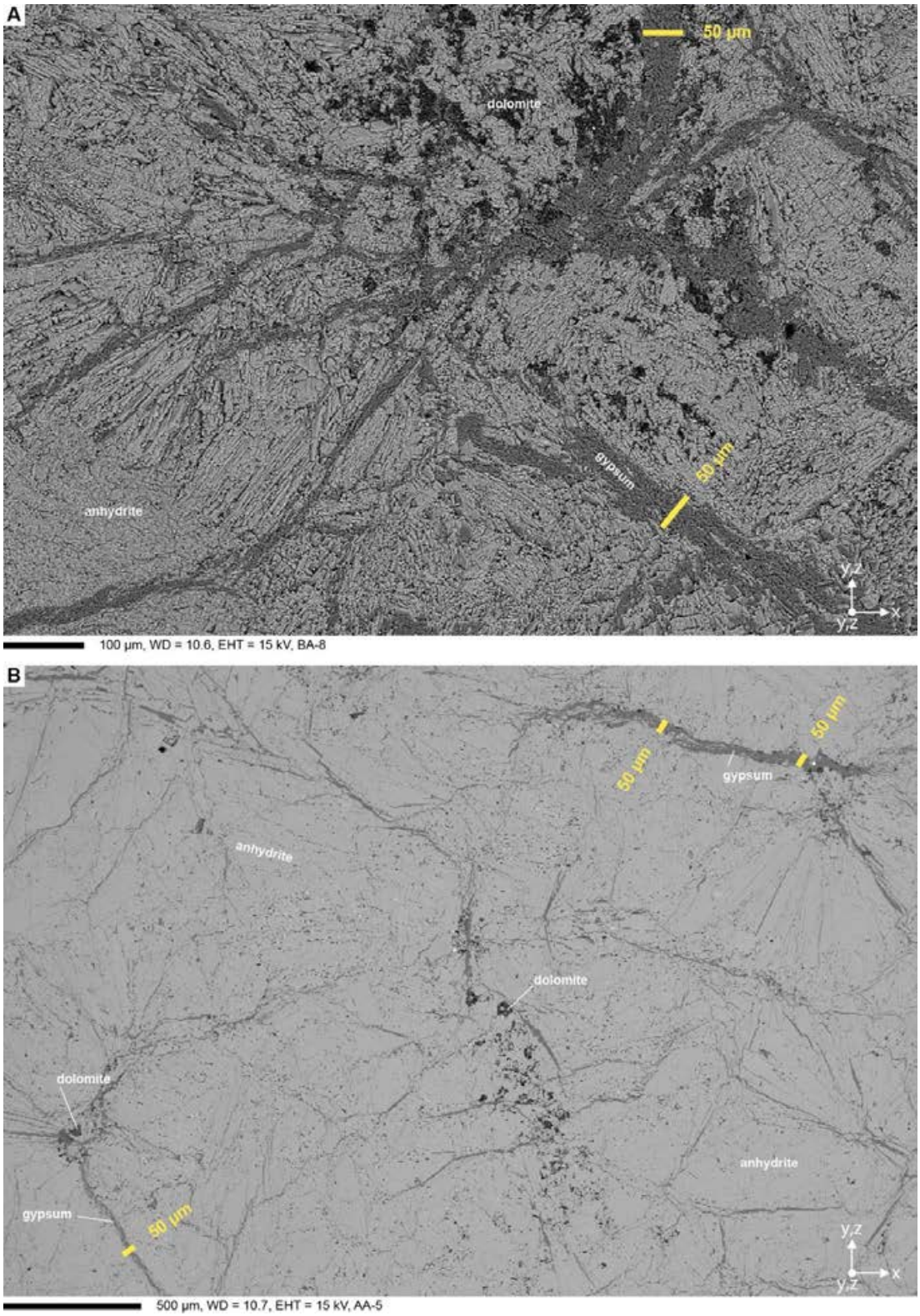

Figure D.2: Electron backscatter maps of Òdena anhydrite. A: Gypsum vein systems, sample not used for experiments. B: Map of sample Ò3.

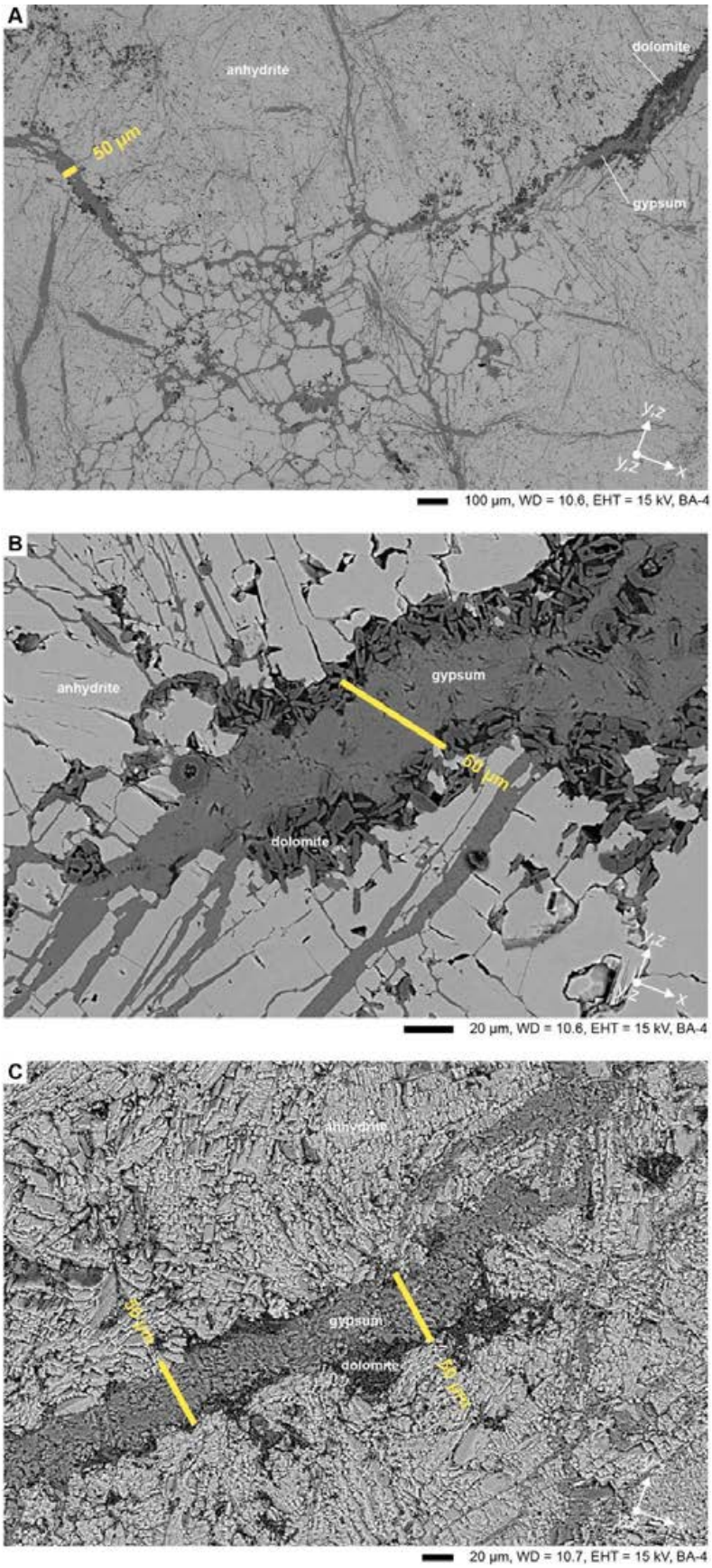

Figure D.3: Electron backscatter images of Òdena anhydrite sample Ò2.

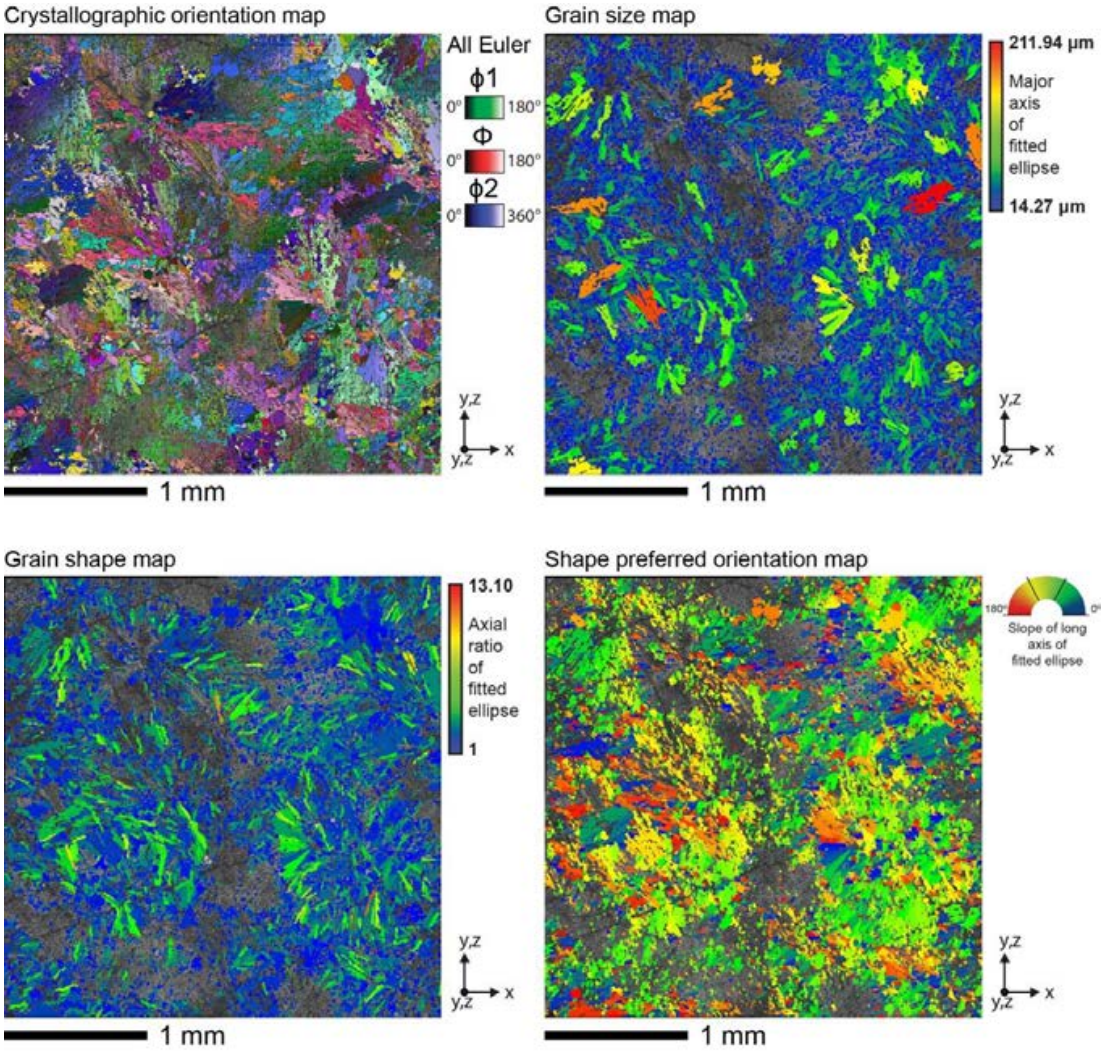

Figure D.4: Electron backscatter diffraction analysis of initial Òdena anhydrite sample material. See Fig. 5.2c) and d) for IPFx EBSD map and equal area, lower hemisphere pole figures of anhydrite. Step size was 4 µm.

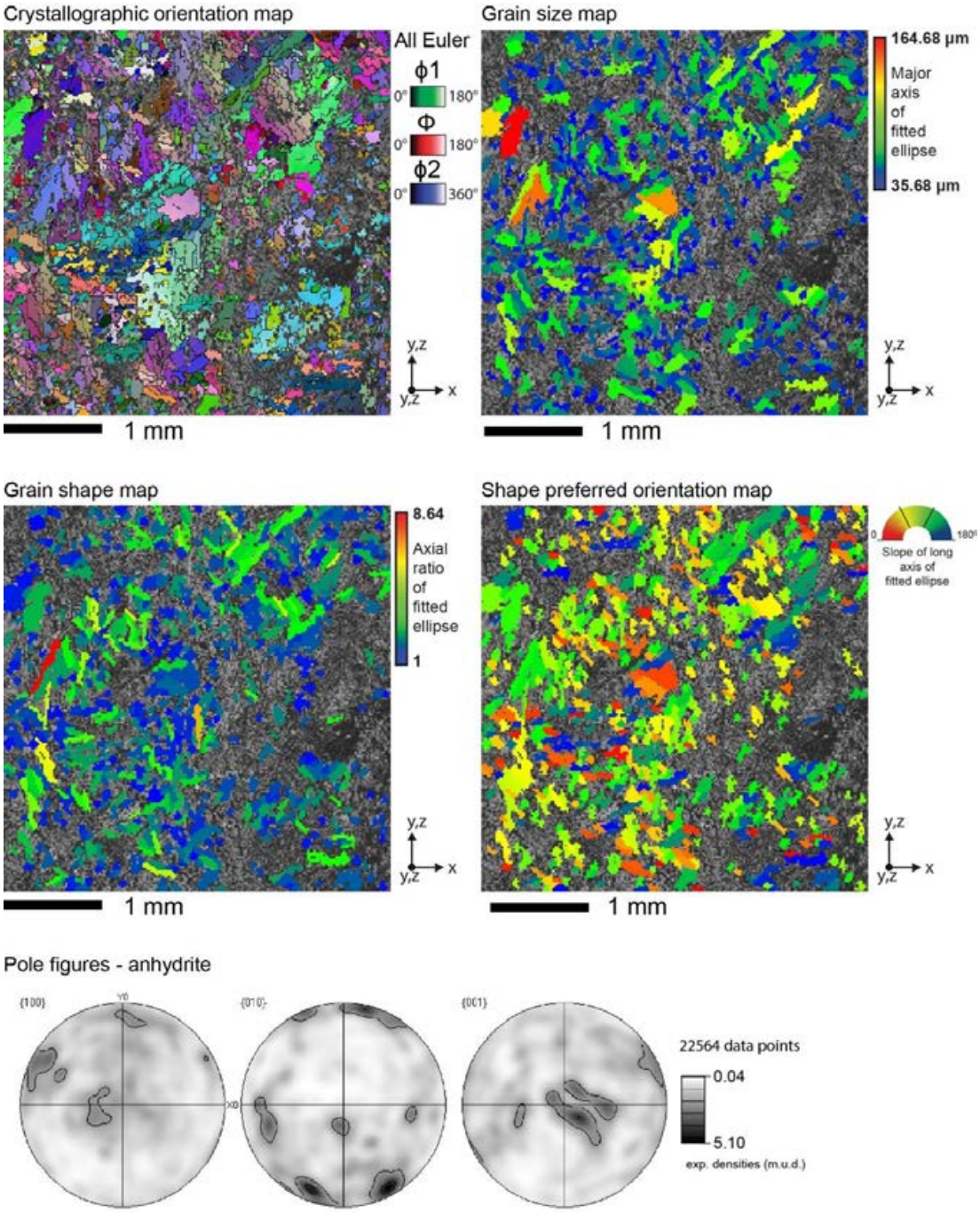

Figure D.5: Electron backscatter diffraction analysis of initial Òdena anhydrite sample material, including equal area, lower hemisphere pole figures of anhydrite. Step size was 10 µm.

Figure D.6: Photographs of additional samples Fig. 5.2a and Fig. D.7a of post-experiment cores after undergoing all three test modes.

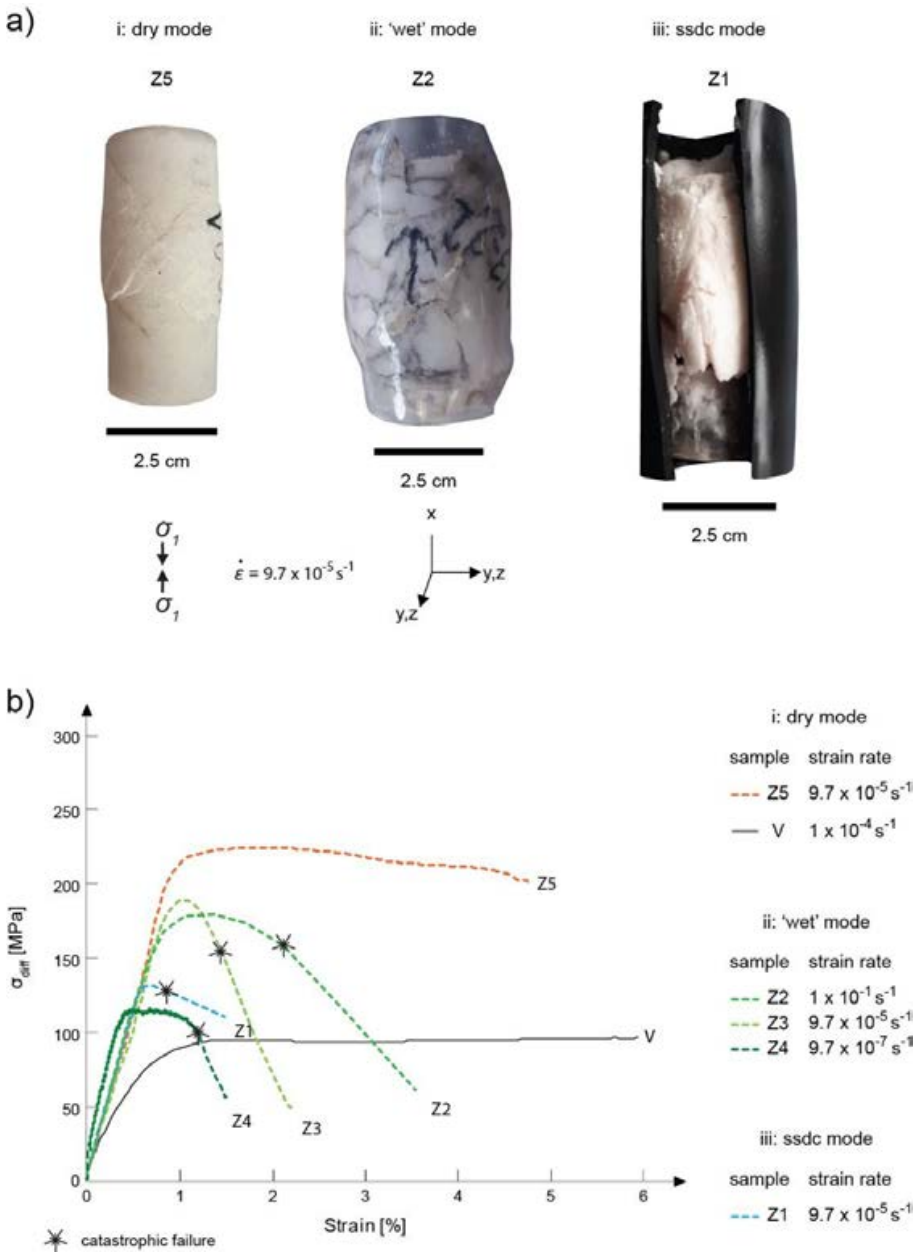

Figure D.7: Post-experimental mechanical results of Zechstein anhydrite samples. a) Photographs of post-experiment cores after undergoing all three test modes. b) Stress versus strain curves, strain (%) in the shortening direction x (σ_1) on the x-axis is plotted against differential stress (σ_{diff}, axial stress/radial pressure) on the y-axis. Stress and strain values are in digital Appendix D.

A

		Sample		$\dot{\varepsilon}$	σ_{diff} [MPa]	Axial stress σ_1 [MPa]	Confining Pressure σ_3 [MPa]	Pore fluid pressure P_{fluid} [MPa]	$\sigma_{1\,eff} = \sigma_1 - P_{fluid}$ $\sigma_{1\,eff}$ [MPa]	$\sigma_{2\,eff}$ [MPa]
Òdena anhydrite (Ò)	h.c.	Ò1	BA-3	$9.7 \times 10^{-5} s^{-1}$	99.09	149	50	40	109	10
		Ò2	BA-4	$9.7 \times 10^{-5} s^{-1}$	55.006	108	50	40	68	10
	'wet'	Ò3	AA-5	$4.4 \times 10^{-5} s^{-1}$	41.456	91	50	40	51	10
		Ò4	BA-1 *	$9.7 \times 10^{-7} s^{-1}$	86.379	187	100	90	97	10
		Ò5	BA-2	$9.7 \times 10^{-5} s^{-1}$	60.96	111	50	40	71	10
Zechstein anhydrite (Z)	h.c.	Z1	N4-1.1	$9.7 \times 10^{-5} s^{-1}$	84.5	135	50	40	95	10
		Zx	N3-2.1 *	$1.6 \times 10^{-7} s^{-1}$	21.0/0.6	121/101	50	40	31/11	10
	'wet'	Z2	N3-2.2	$1.0 \times 10^{-3} s^{-1}$	61.7	92	50	40	72	10
		Z3	N4-2.1	$9.7 \times 10^{-5} s^{-1}$	52.7	103	50	40	63	10
		Z4	N5-4.1	$9.7 \times 10^{-7} s^{-1}$	56.1	157	100	90	67	10

Data collected at point of failure (see stress versus strain curves all sanchez experiments)

B

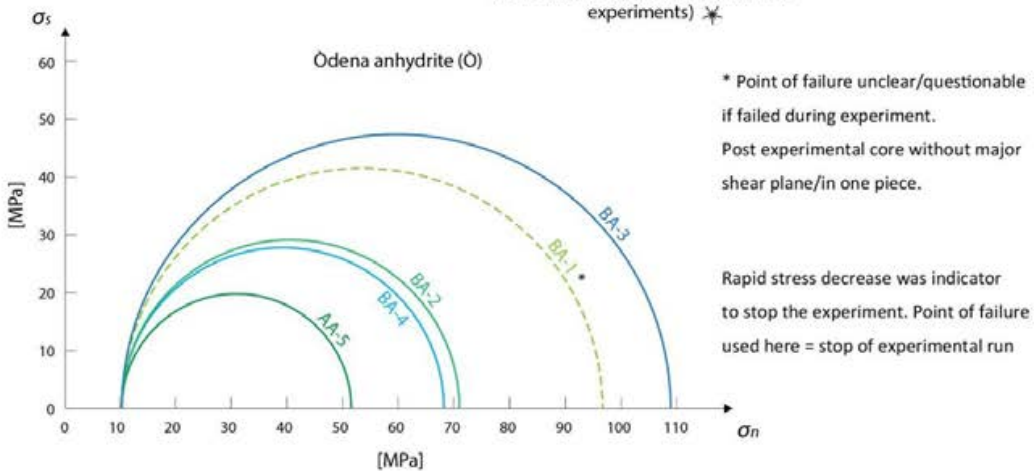

C

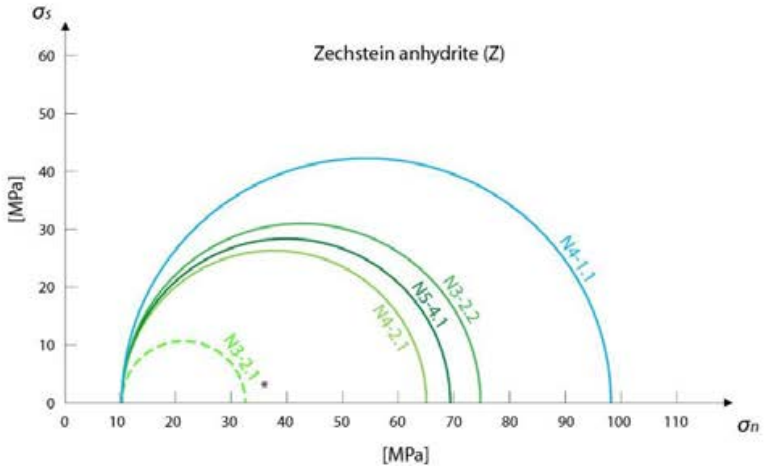

Figure D.8: Failure behaviour of Zechstein anhydrite and Òdena quarry samples during triaxial experiments. A: lists the point of failure, determined via analysis of the differential stress vs. strain curve analysis (Figure 5.3 and Figure D.7). h.c. = steady state differential compaction mode tests. $\dot{\varepsilon}$ = strain rate, σ_{diff} = differential stress, σ_{eff} = effective stress, σ_n = normal stress, σ_s = shear stress. B and C: resulting failure envelopes.

A

sample		ultimate strengt		yield point		R^2
		σ_{diff} [MPa]	Strain [%]	σ_{diff} [MPa]	Strain [%]	
Ò1	BA-3					
Ò2	BA-4	147.629	1.371	127.342	0.979	0.998
Z1	N4-1.1					
Ò3	AA-5	122.687	1.161	89.861	0.594	0.996
Ò4	BA-1	118.645	0.625	85.926	0.334	0.995
Ò5	BA-2	170.918	1.576	111.402	0.634	0.997
Ò6	BA-5	169.064	1.556	110.802	0.662	0.996
Z2	N3-2.2	197.695	1.351	147.923	0.656	0.998
Z3	N4-2.1	189.204	1.079	179.311	0.849	0.998
Z4	N5-4.1	115.657	0.678	97.45	0.302	0.995
Ò7	AA-2			158.138	0.506	0.997
Ò8	AA-3	214.802	3.173	133.904	0.763	0.998
Z5	N2-2.1	224.739	1.898	200.356	0.855	0.999
V	V3-5	98.822	8.037			

B

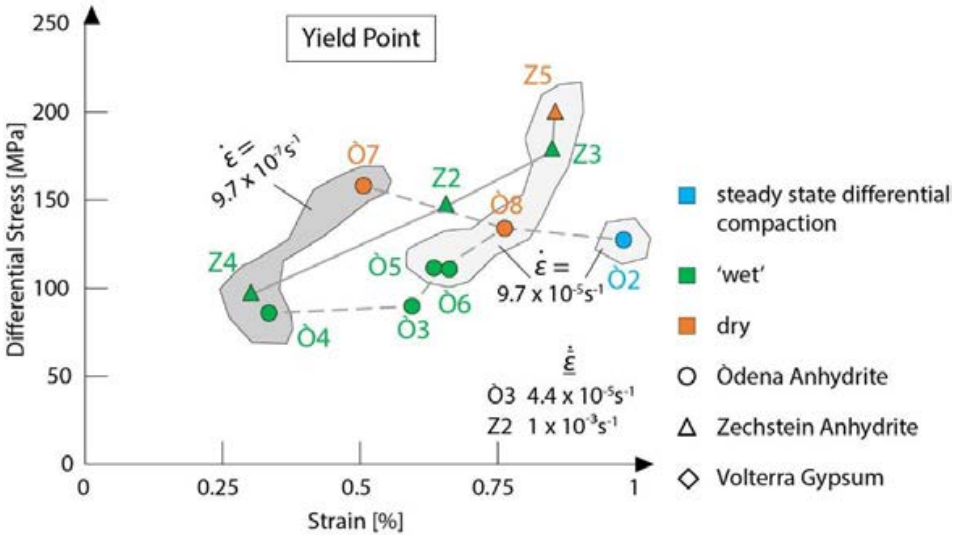

Figure D.9: Analysis of ultimate strength and yield point, based on mechanical data and stress vs. strain curves (Figure 5.3 and Figure D.7).

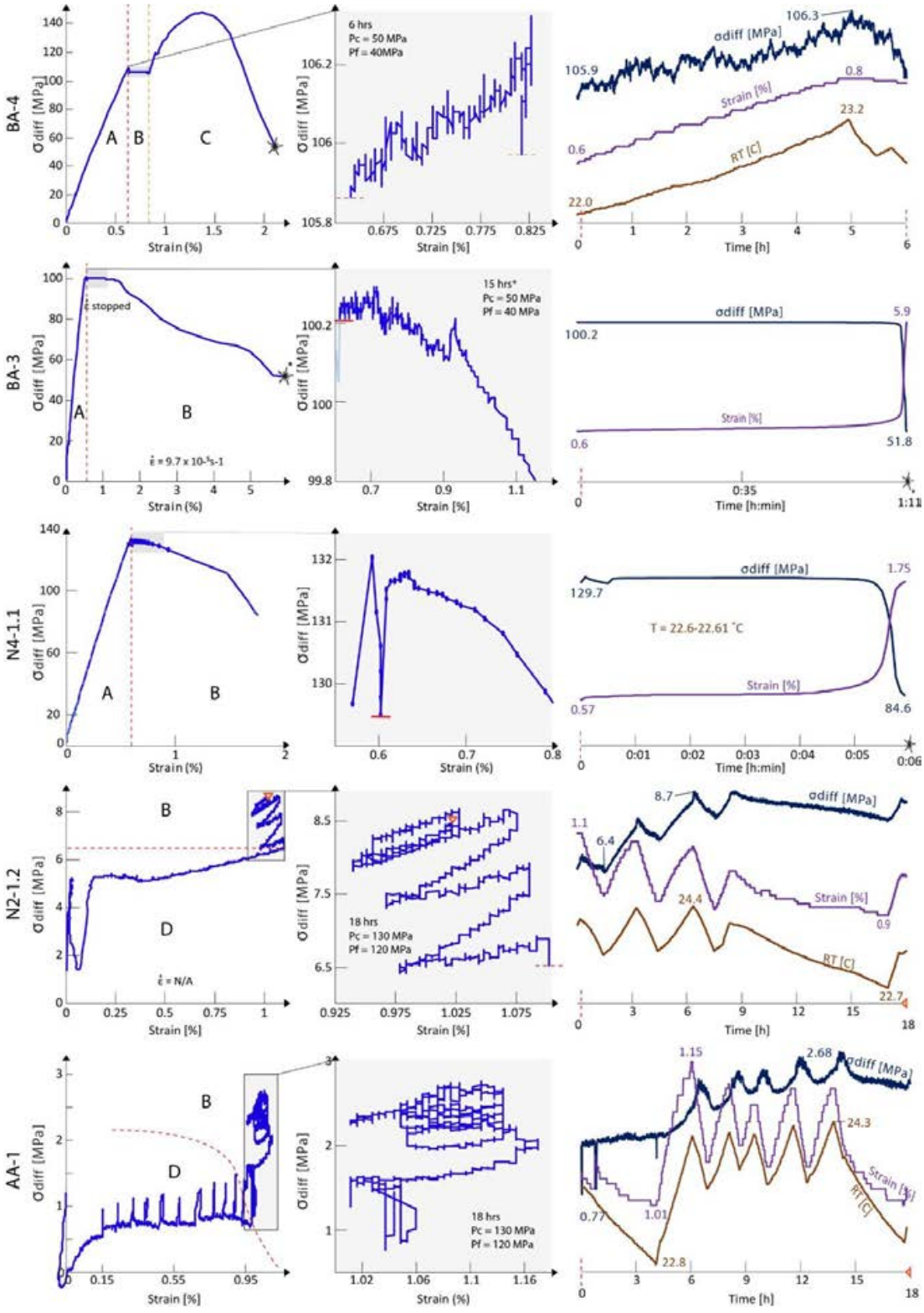

Figure D.10: Stress (σ_{diff}) vs. strain behaviour of all steady state differential compaction tests. Left: stress vs. strain curves. B = Steady state differential compaction, D = $\dot{\varepsilon}$ applied; and C = reapplication of $\dot{\varepsilon}$. Middle: stress vs. strain behaviour during B. Red lines mark beginning/ end. Right: differential stress, strain, and room temperature (*RT*) evolution.

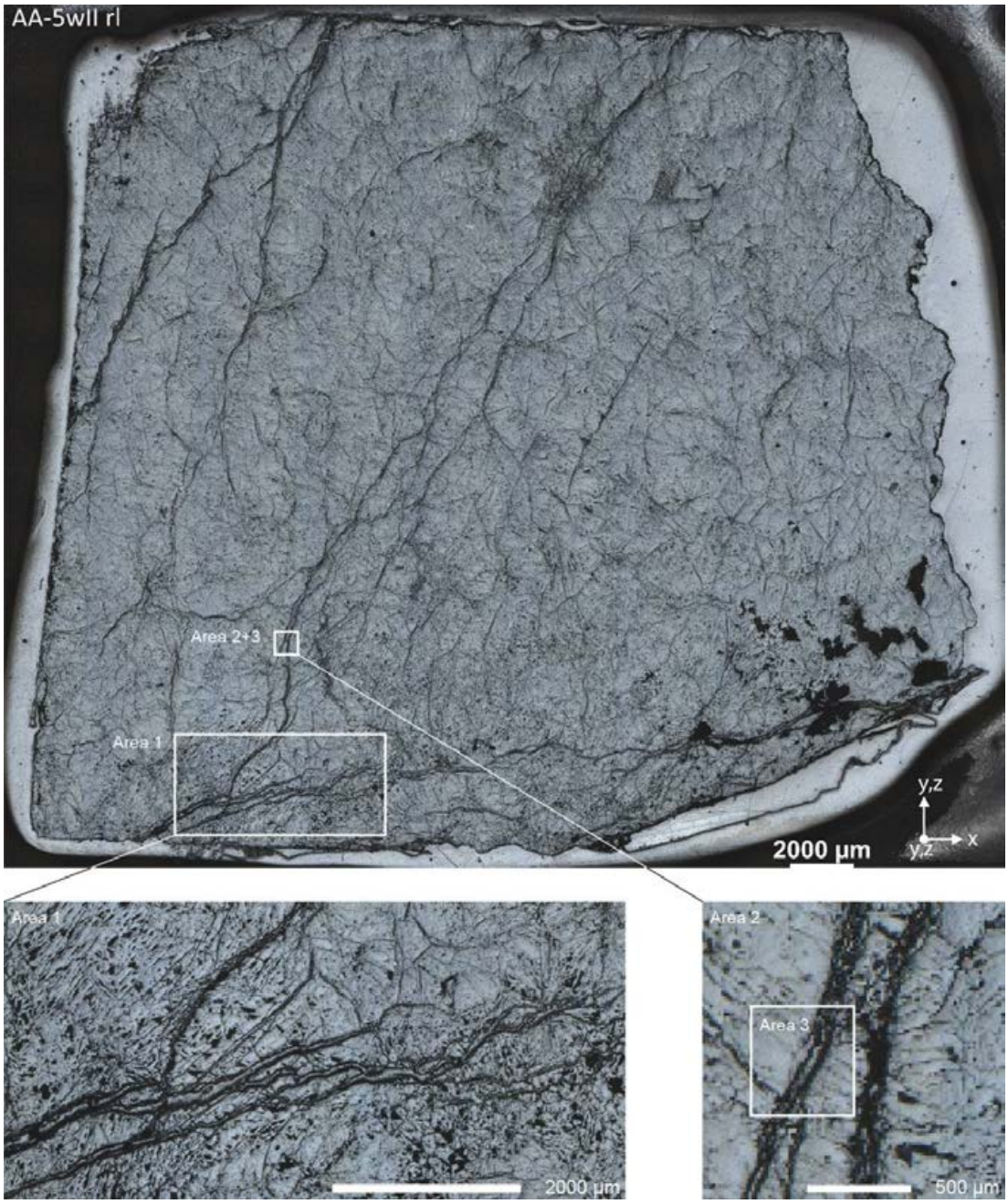

Figure D.11: Reflected light microscopy images of a thin section of sample Ò3 (post 'wet' mode experiment) with areas marked for further analysis. Area 1 covers the same location seen in Fig. 5.4 and 5.5. and is part of a ~ 2.7 cm long vein system. The following figures show results from electron backscatter diffraction analysis of the marked areas.

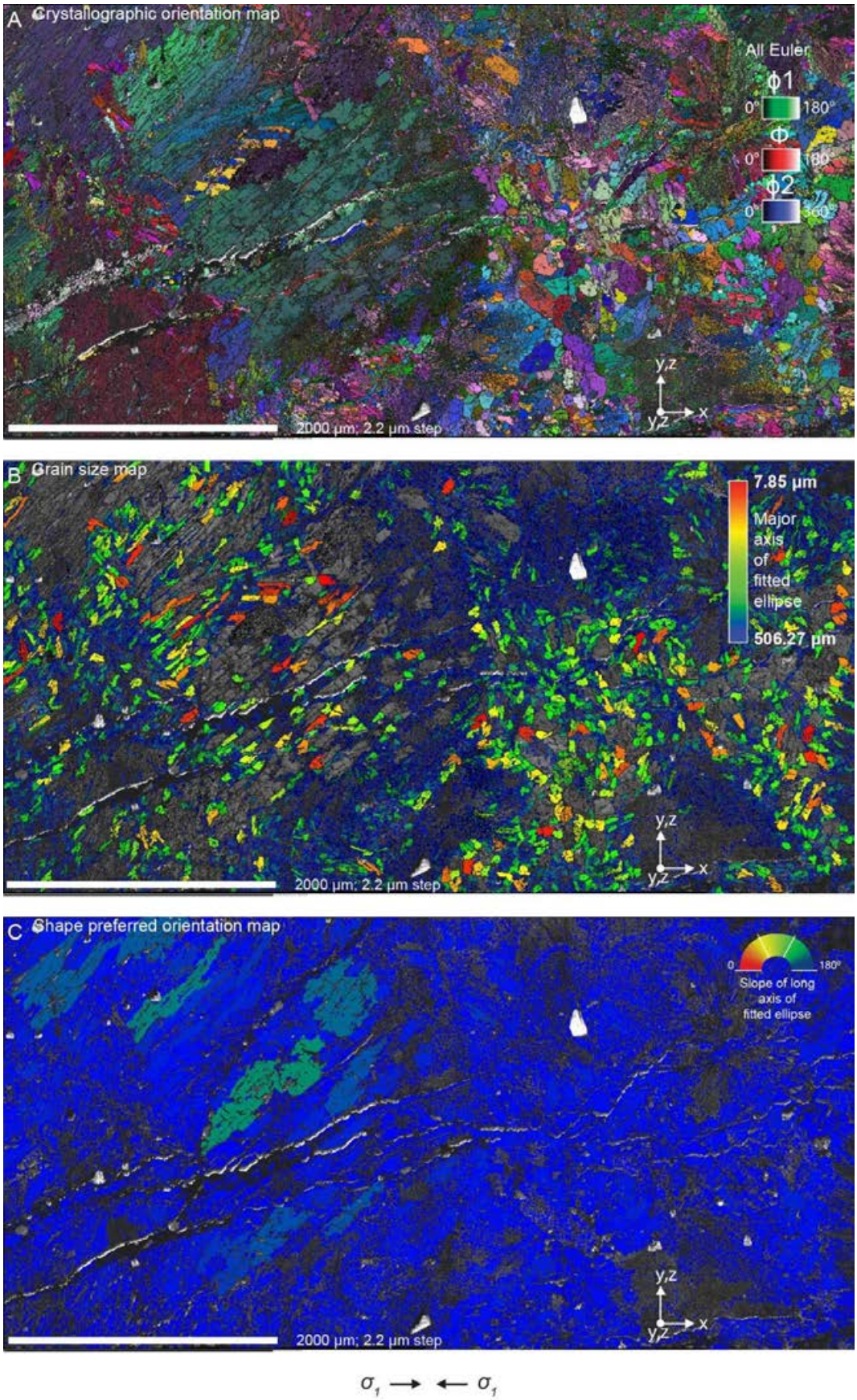

Figure D.12: Additional electron backscatter diffraction analysis from the area of sample Ò3 (‘wet’ mode experiment) shown in Fig. 5.4 and 5.5 and marked as Area 1 in Fig. D.11.

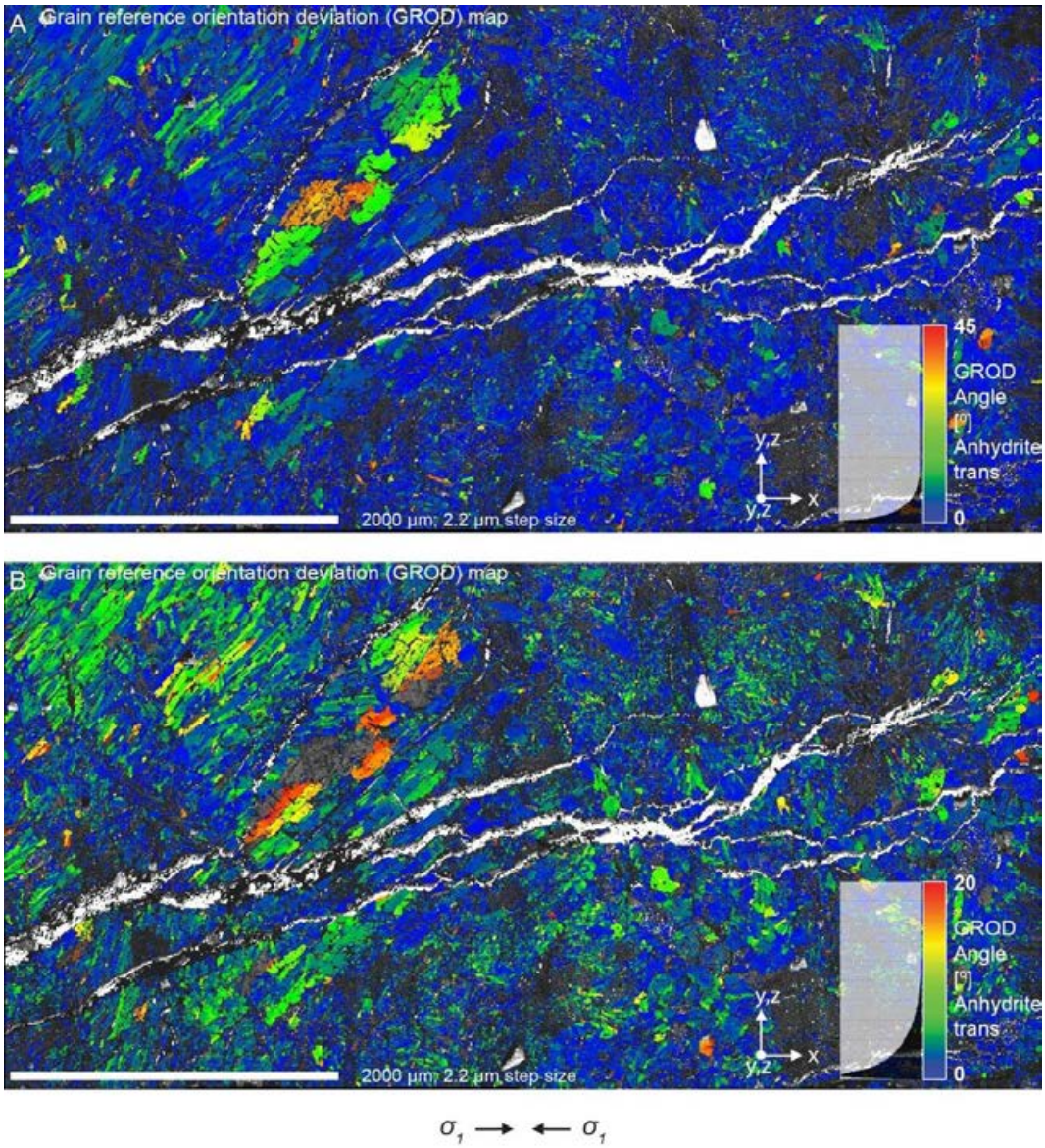

Figure D.13: Grain reference orientation deviation (GROD) maps of anhydrite from the Area 1 electron backscatter diffraction dataset of Ò3 ('wet' mode experiment) (Fig. 5.4 and 5.5; Area 1 in Fig. D.11). GROD analysis shows orientation heterogeneities that form during deformation, and hence displays internal deformation of grains. Each pixel is coloured based on the misorientation of the point relative to a reference orientation for the grain to which the point belongs to. Component limits (GROD angle) were at a range of 0 to 45° for A and to 0 to 20° for B. Exclusion of higher angles results in loss of data and is more sensitive to low angle heterogeneities.

GROD analysis shows that the blocky area has slightly higher internal deformation, with angles ~40° in one large grain and ~20° in surrounding grains. The rest of the anhydrite appears heterogeneous, with GROD angles commonly between 0 and 15°.

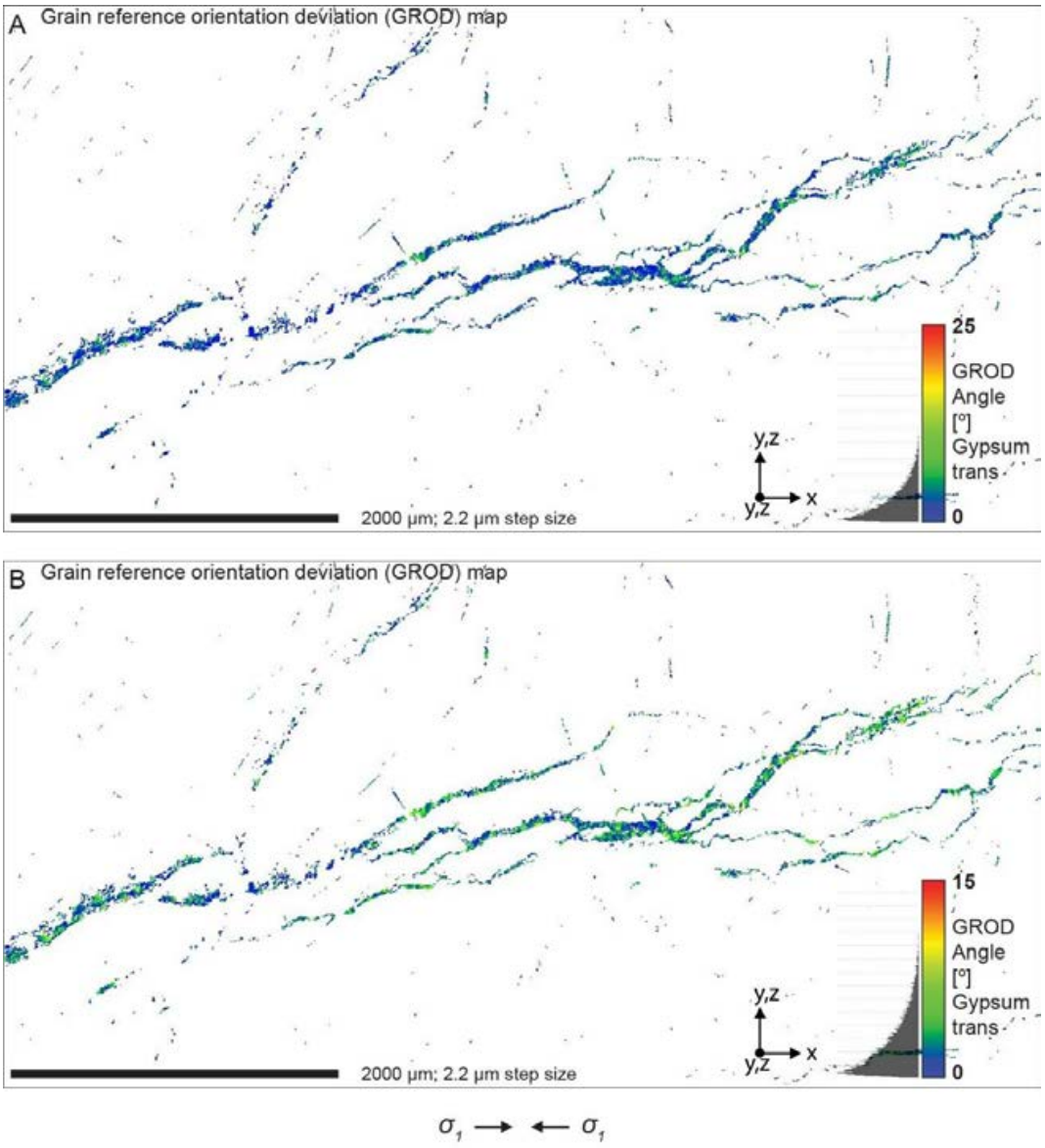

Figure D.14: Grain reference orientation deviation (GROD) maps of vein-hosted gypsum from the Area 1 electron backscatter diffraction dataset of Ò3 (post 'wet' mode experiment) (Fig. 5.4 and 5.5, Area 1 in Fig. D.11.). Component limits (GROD angle) were at a range of 0 to 25° for A and to 0 to 15° for B. Exclusion of higher angles results in loss of data and is more sensitive to low angle heterogeneities.

Summary grain statistics

			no grains	Grains%	Area	%	AVG d	STDV d	AVG slope	STDV slop	AVG AR	STDV AR
anh	2	23453	23452	90.76905	1.03E+07	9.508E+01	16.86657	16.54946	84.1283	51.02407	2.082103	0.896492
gyp	23454	25838	2385	9.230948	5.33E+05	4.923E+00	14.70951	8.242795	74.57741	49.84299	2.15751	1.020427
total			25837		1.08E+07							

EX	16.62	Average, expectation
D^2X	249.65	Variance, dispersion
s	15.8	Standard deviation
s/EX	0.95066	Coefficient of variation
Xmin	7.8501	Minimum value
Xmax	506.27	Maximum value
N	25760	Size of the data set

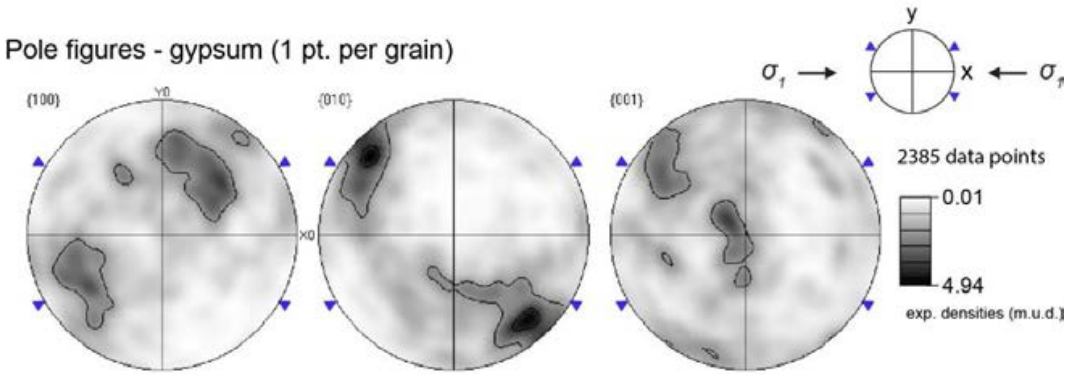

Figure D.15: Grain statistical data and one point per grain, equal area, lower hemisphere pole figures of gypsum from analysis of the electron backscatter diffraction data set of Area 1 in sample Ò3 (post 'wet' mode experiment).

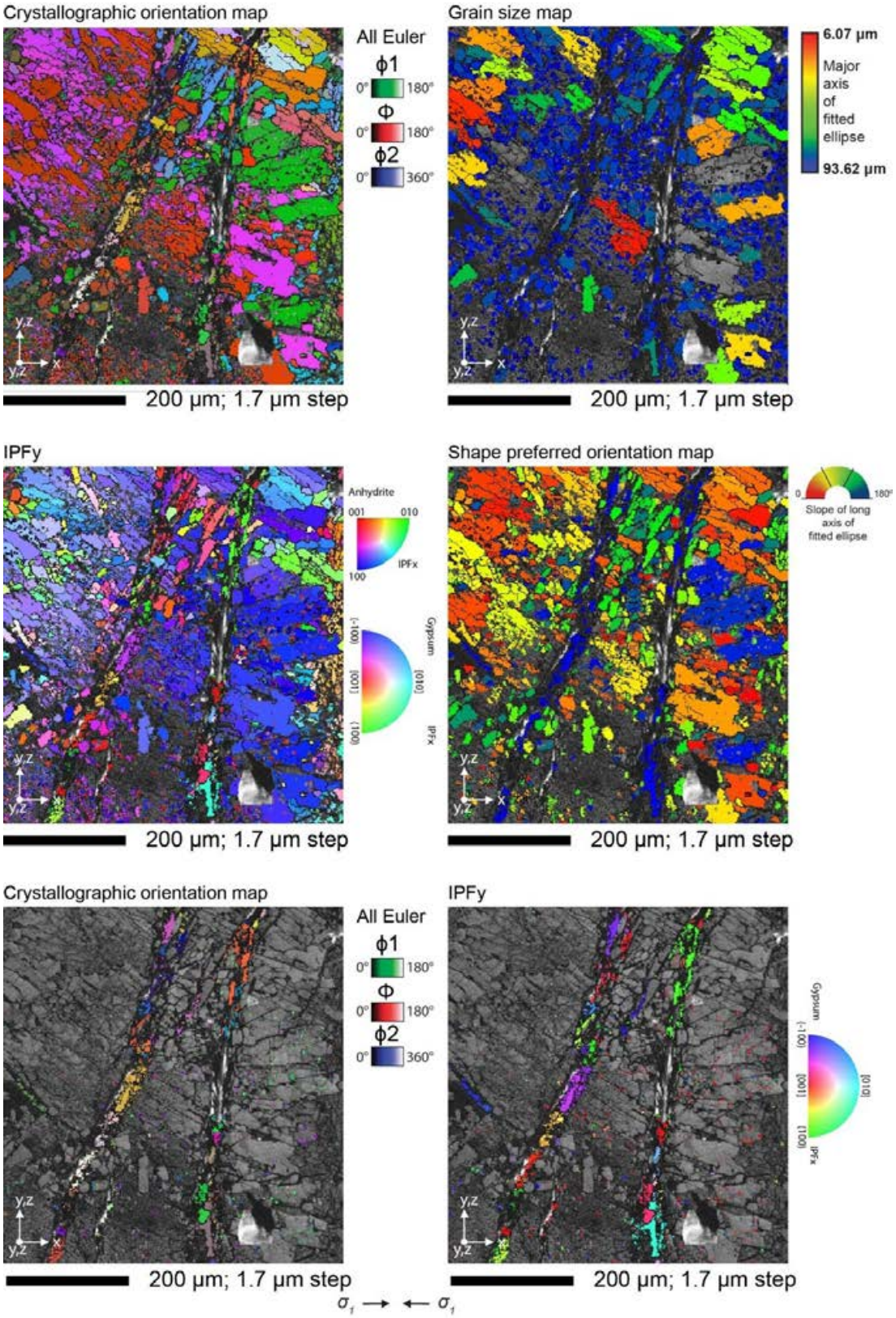

Figure D.16: Electron backscatter diffraction analysis of gypsum veins (Area 2) in anhydrite from sample Ò3 (post 'wet' mode experiment) (marked as Area 2 in Fig. D.11).

Summary grain statistics

			no grains	Grains%	Area	%	AVG d	STDV d	AVG slope	STDV slop	AVG AR	STDV AR
anh	2	674	673	88.90357	139893.2	94.43414	12.74307	10.12065	100.2109	52.37487	1.972796	0.762692
gyp	675	758	84	11.09643	8245.17	5.565856	10.19866	4.606101	81.53096	33.77616	2.245886	1.017849
total			757		148138.4							
EX	11.983	Average, expectation										
D^2X	78.603	Variance, dispersion										
s	8.8658	Standard deviation										
s/EX	0.73988	Coefficient of variation										
Xmin	6.066	Minimum value										
Xmax	93.621	Maximum value										
N	700	Size of the data set										

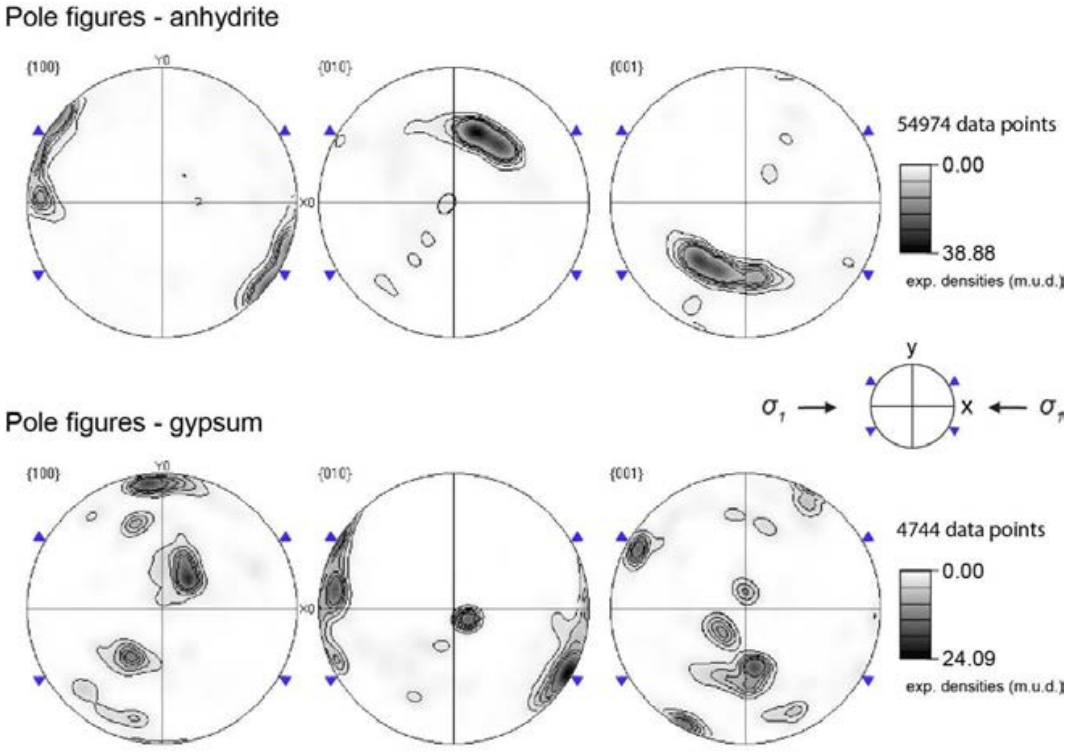

Figure D.17: Grain statistical data and equal area, lower hemisphere pole figures of anhydrite and gypsum from analysis of the electron backscatter diffraction data set of Area 2 (Fig. D.11, and D.16) in sample Ò3 (post 'wet' mode experiment). (y = z = y,z).

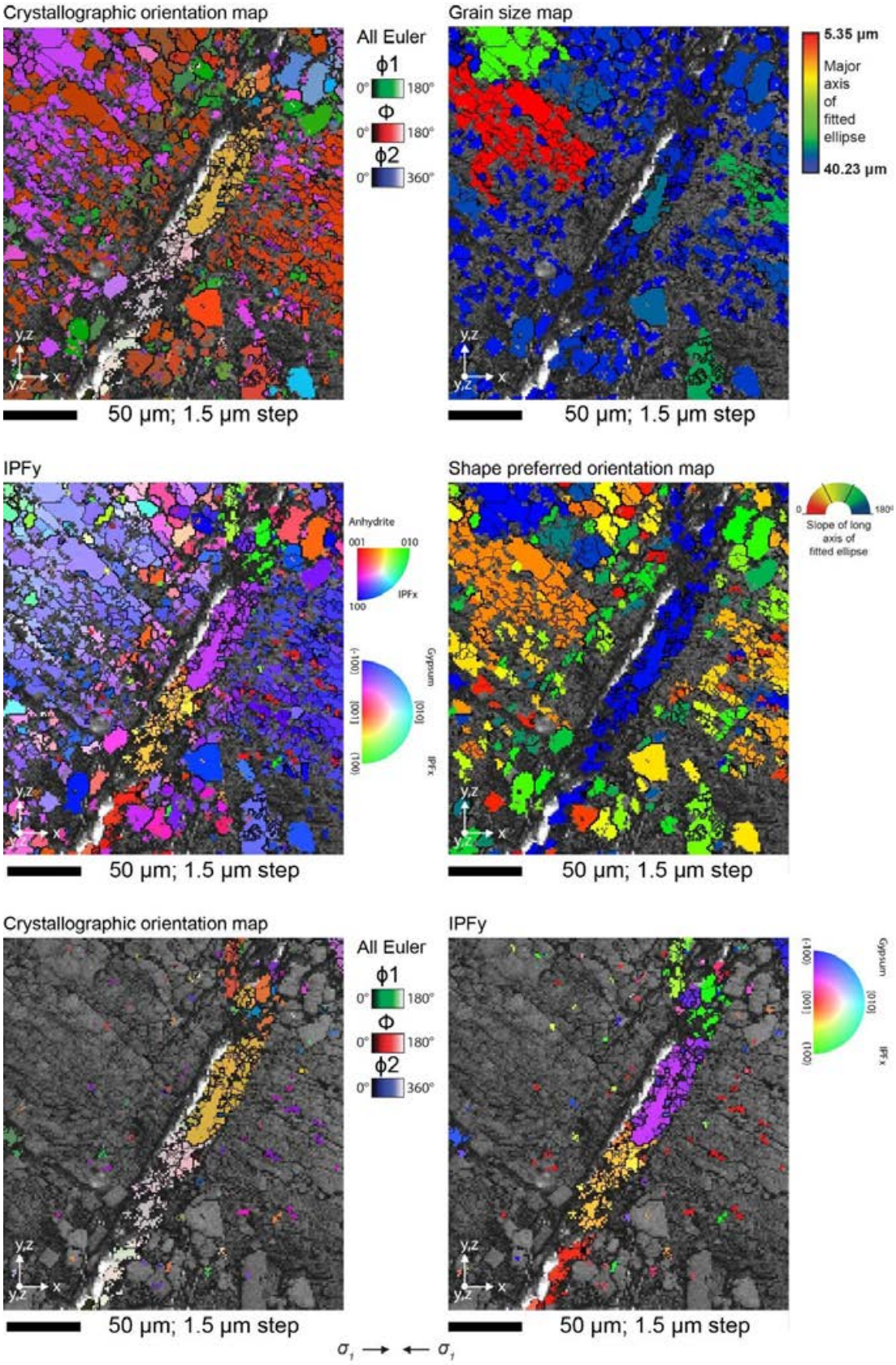

Figure D.18: Electron backscatter diffraction analysis of a gypsum vein in anhydrite from Area 3 (Fig. D.11) in sample Ò3 (post 'wet' mode experiment).

Summary grain statistics

			no grains	Grains%	Area	%	AVG d	STDV d	AVG slope	STDV slop	AVG AR	STDV AR
anh	2	185	184	82.51121	21208.6	86.60424	10.02499	6.819823	95.9797	51.40072	1.808179	0.543171
gyp	186	224	39	17.48879	3280.5	13.39576	9.352636	4.488153	74.08688	42.97372	1.906915	0.533209
total			223		24489.1							

EX	9.1087	Average, expectation
D^2X	23.661	Variance, dispersion
s	4.8643	Standard deviation
s/EX	0.53403	Coefficient of variation
Xmin	5.3524	Minimum value
Xmax	40.232	Maximum value
N	187	Size of the data set

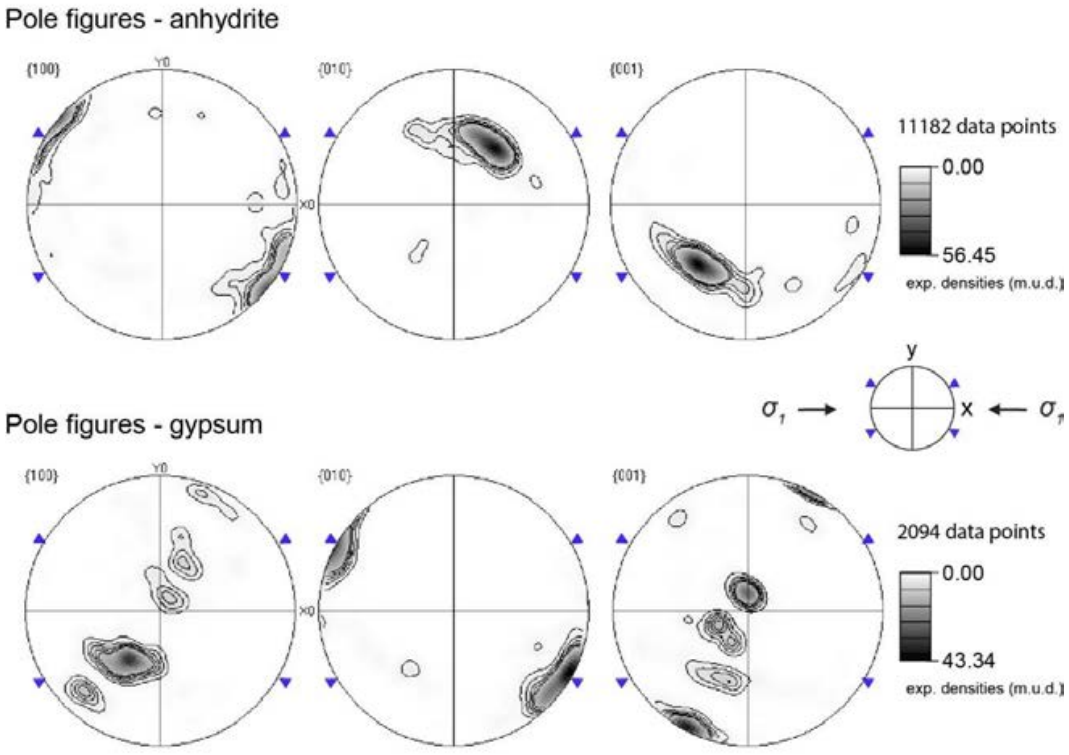

Figure D.19: Grain statistical data and equal area, lower hemisphere pole figures of anhydrite and gypsum from analysis of the electron backscatter diffraction dataset of Area 3 (Fig. D.11 and D.18) in sample Ò3 (post 'wet' mode experiment). (y = z = y,z).

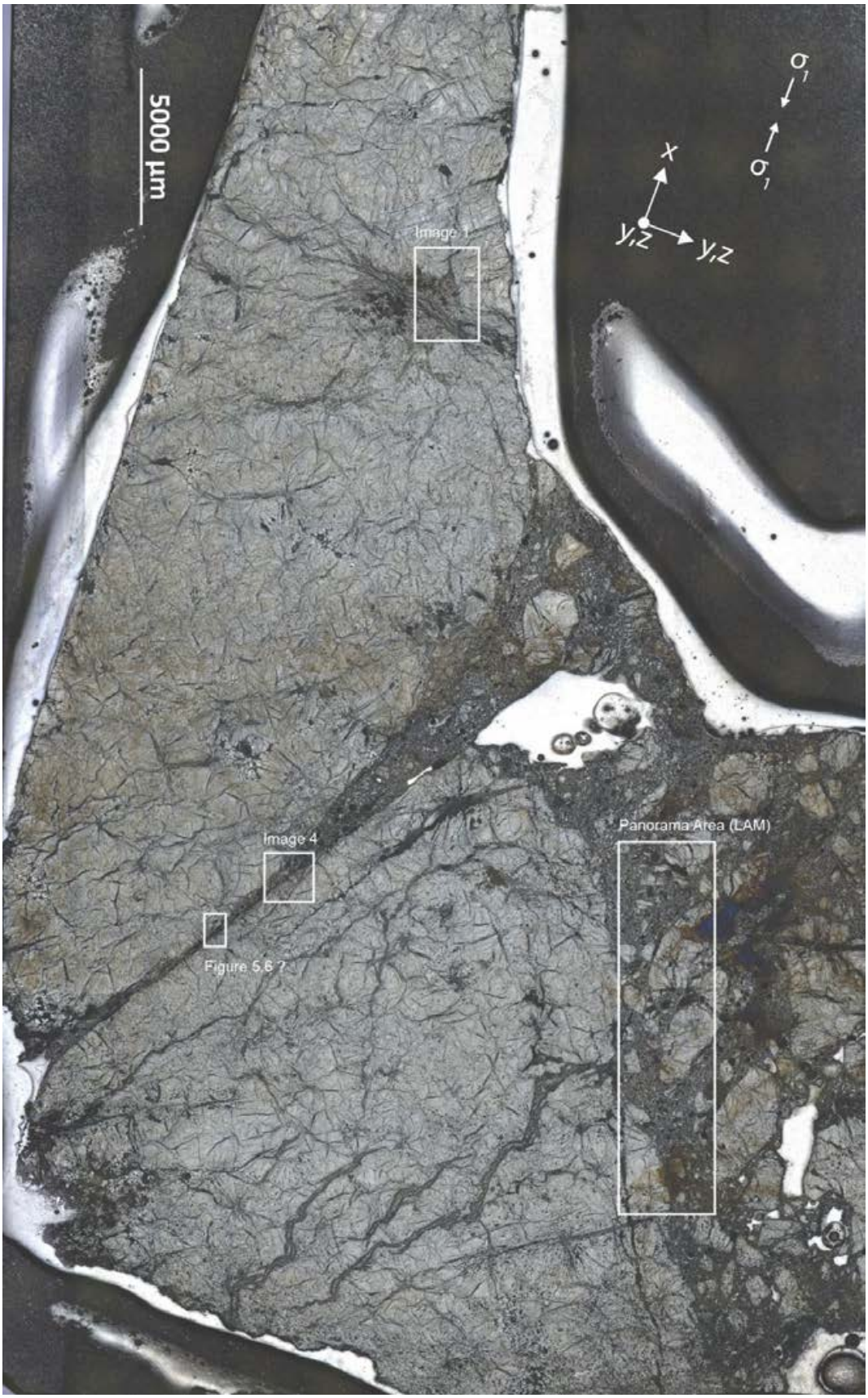

Figure D.20: Reflected light microscopy images of a thin section of sample Ò2 (post ssdc mode experiment) with areas marked where further analysis was done. The area marked as Figure 5.6 ? is an estimate, as the thin section was polished for EBSD between imaging.

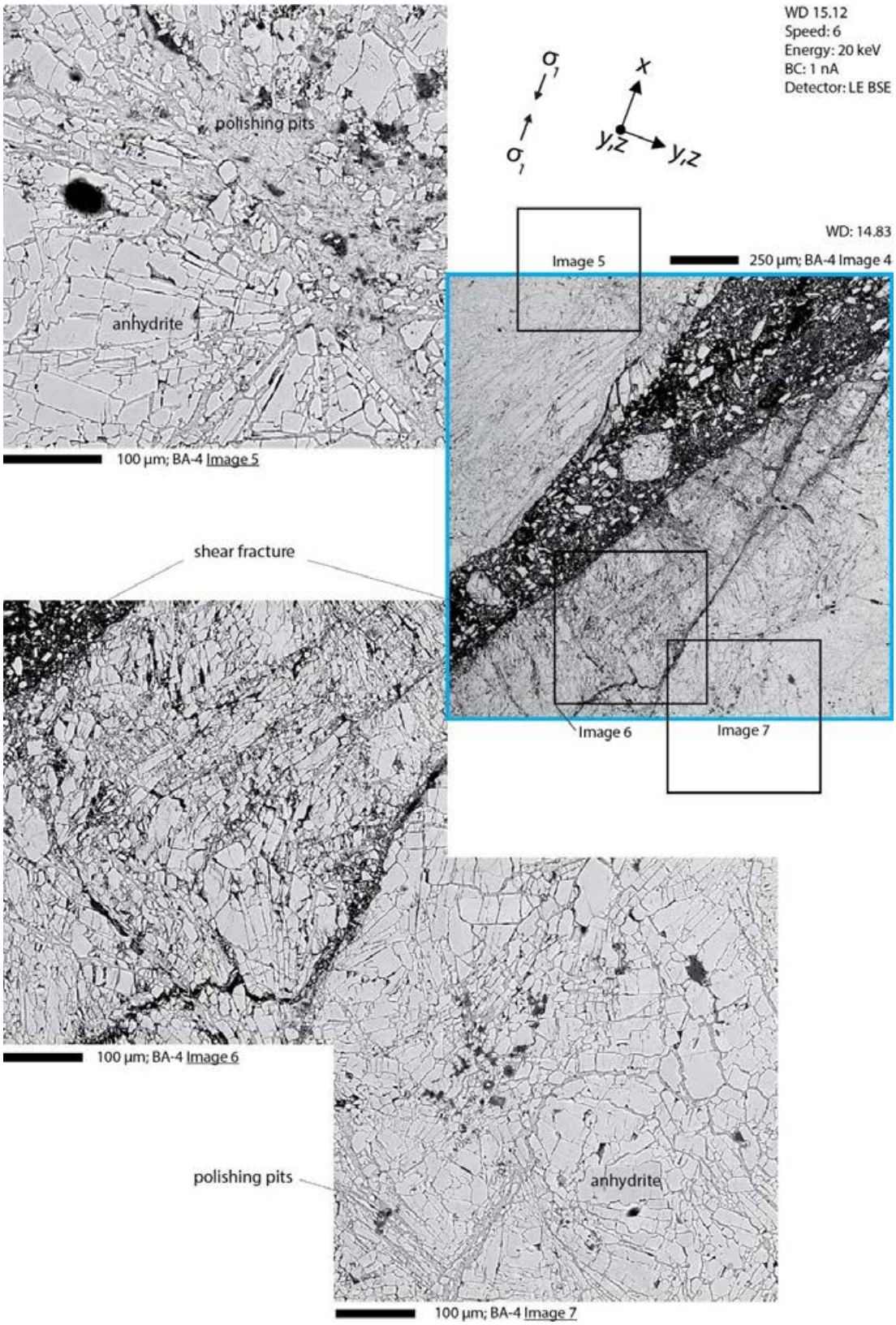

Figure D.21: Backscatter electron images of Ò2 after ssdc. Image 4: shear fracture map, location marked in Figure D.20. Image 5: ~ 100 µm wide polishing pit (gypsum vein that lost gypsum due to polishing), and spherulitic radial anhydrite laths. Image 6: cataclastic

zone with shear bands between the open shear fracture (no matrix, filled with clasts). A long fracture divides the cataclastic zone (Image 6) from the intact fabric of Image 7.

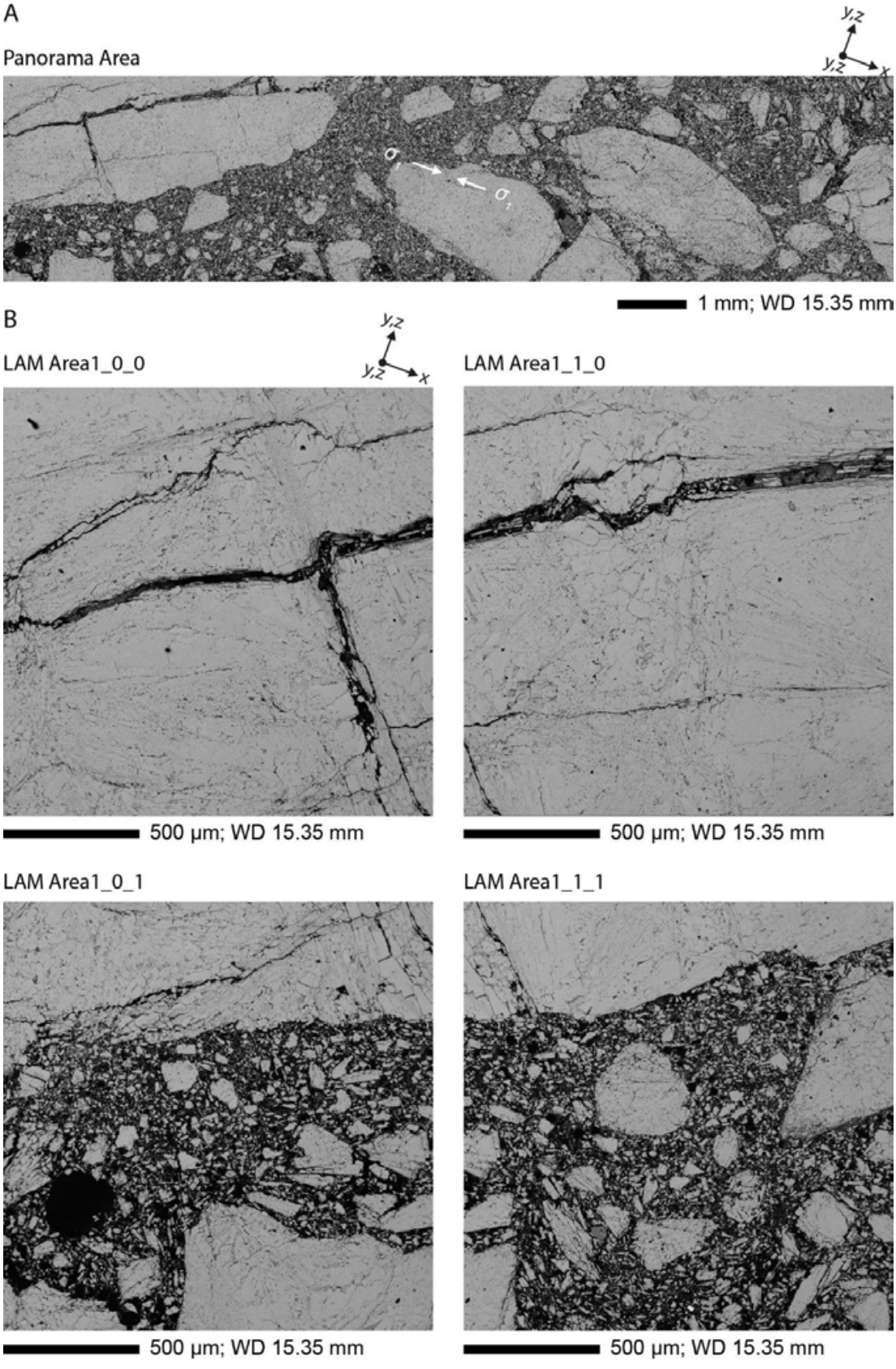

C

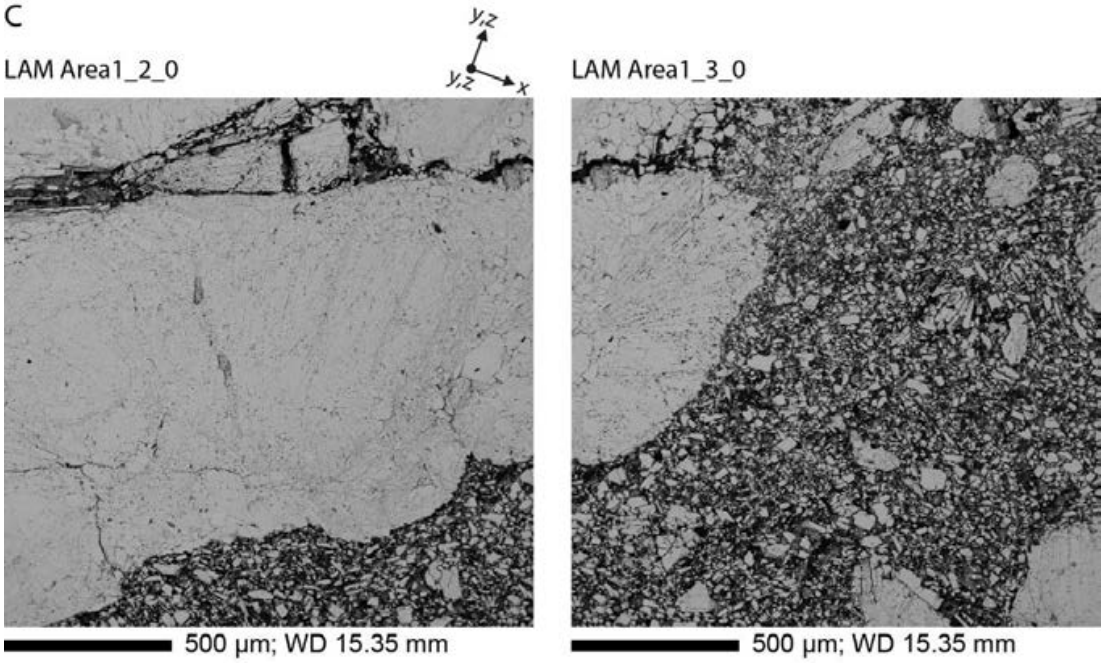
LAM Area1_2_0
y,z
y,z
x
LAM Area1_3_0
500 µm; WD 15.35 mm
500 µm; WD 15.35 mm
LAM Area1_2_1
LAM Area1_3_1
500 µm; WD 15.35 mm
500 µm; WD 15.35 mm

D

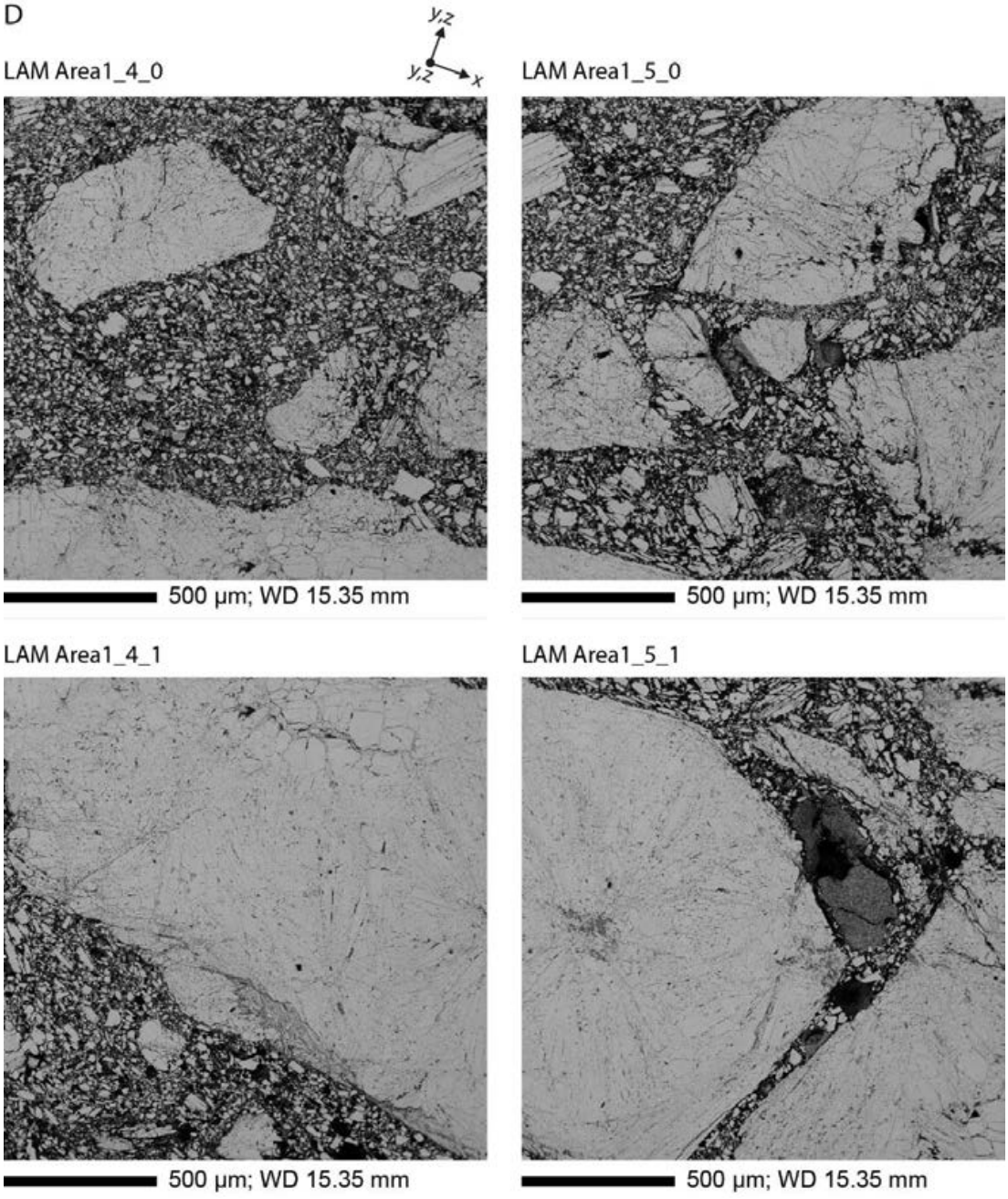
y,z
y,z
x
LAM Area1_4_0
LAM Area1_5_0
500 µm; WD 15.35 mm
500 µm; WD 15.35 mm
LAM Area1_4_1
LAM Area1_5_1
500 µm; WD 15.35 mm
500 µm; WD 15.35 mm

E

LAM Area1_6_0

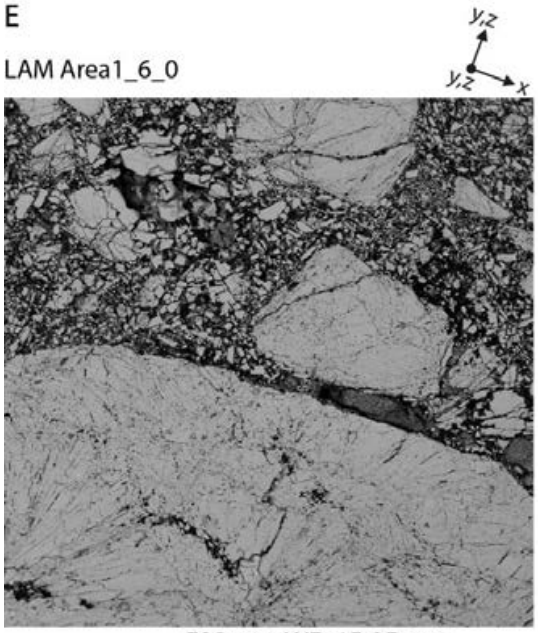

500 µm; WD 15.35 mm

LAM Area1_7_0

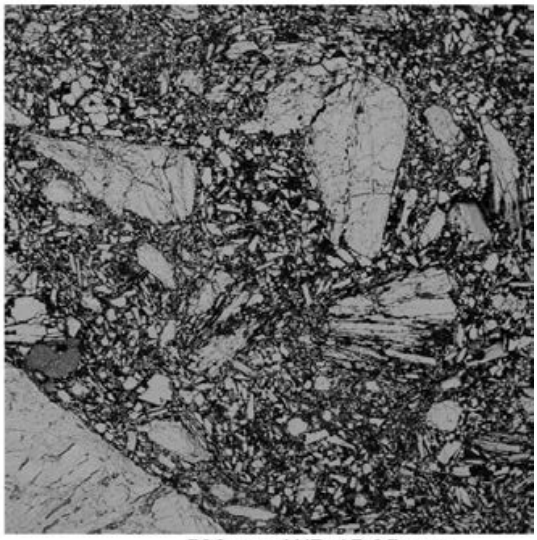

500 µm; WD 15.35 mm

LAM Area1_6_1

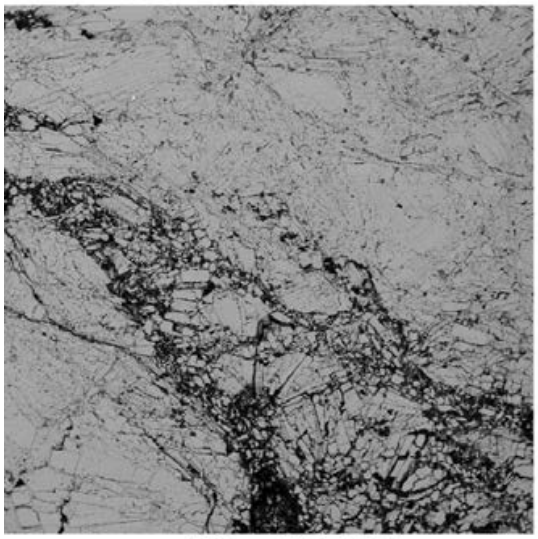

500 µm; WD 15.35 mm

LAM Area1_7_1

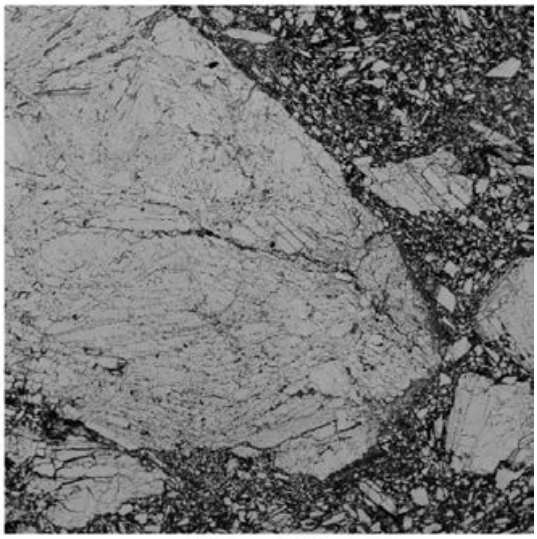

500 µm; WD 15.35 mm

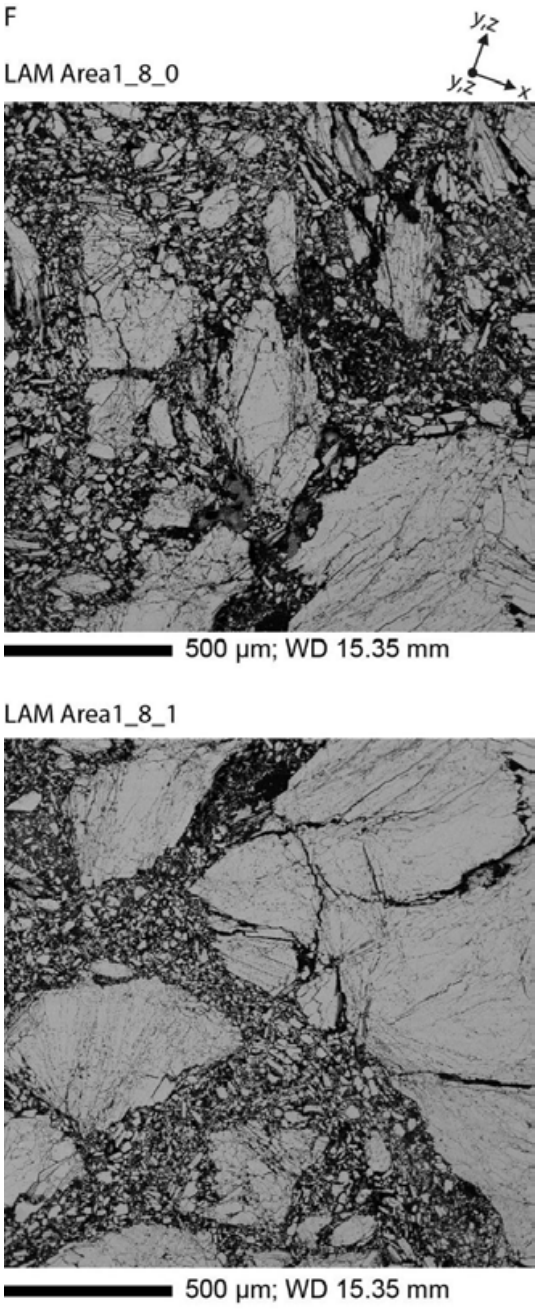

Figure D.22: Backscatter electron panorama of a cataclastic shear zone in Ò2 after steady state differential compaction. A: Panorama, B to F single panorama frames. Light grey: anhydrite, medium grey: gypsum, black: open fractures. A mixed matrix of < 100 µm sized gypsum and anhydrite particles contains up to millimetre-scale anhydrite clasts with intense internal fracturing and low gypsum content. The amount of gypsum is difficult to identify from the images, as the sample lost gypsum due to polishing. The location of the panorama is marked as Panorama Area (LAM) in Figure D.20.

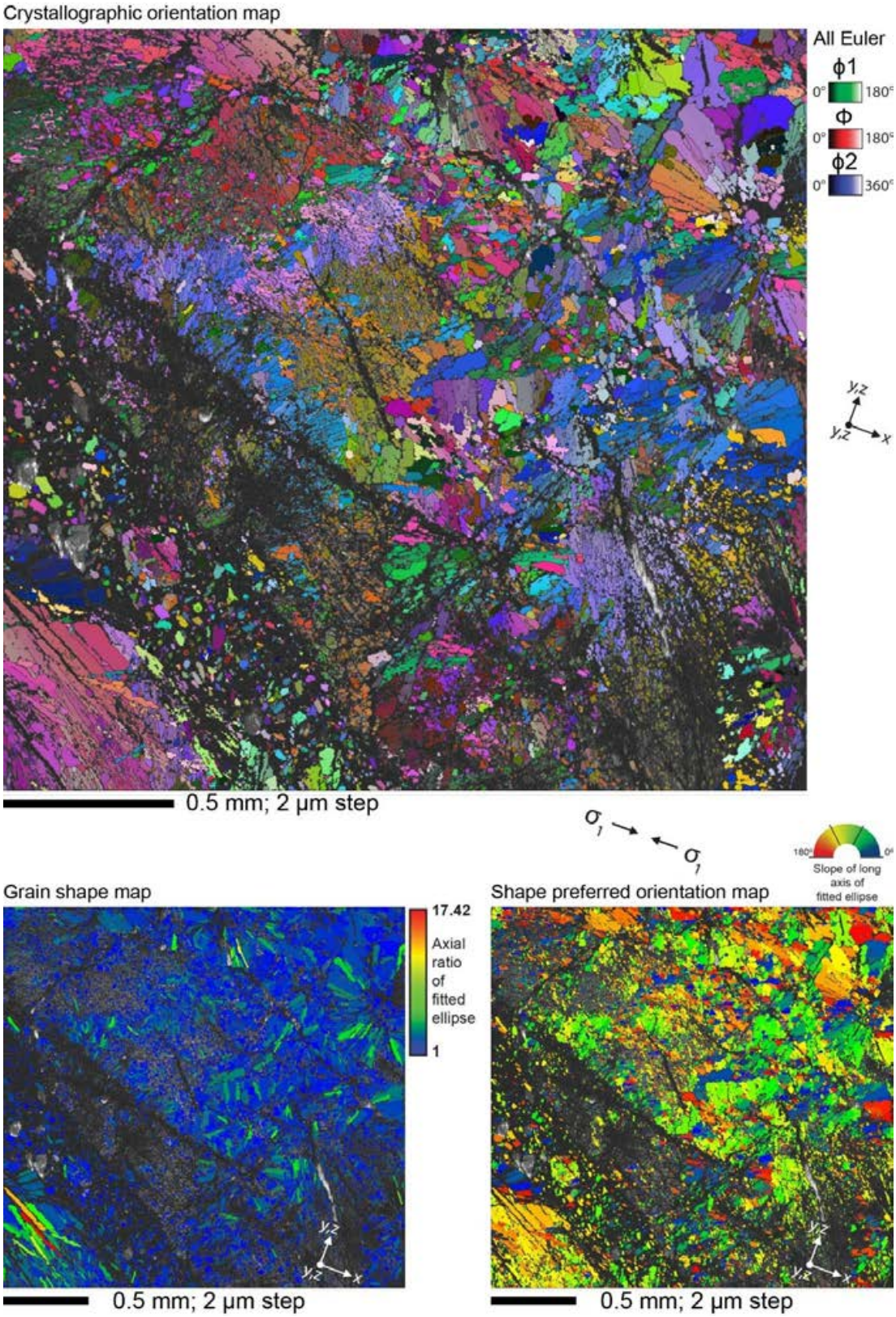

Figure D.23: Electron backscatter diffraction analysis of a cataclastic shear zone and surrounding fabric with spherulites in sample Ò2 after steady state differential compaction. Gypsum was not detected, due to polishing pits.

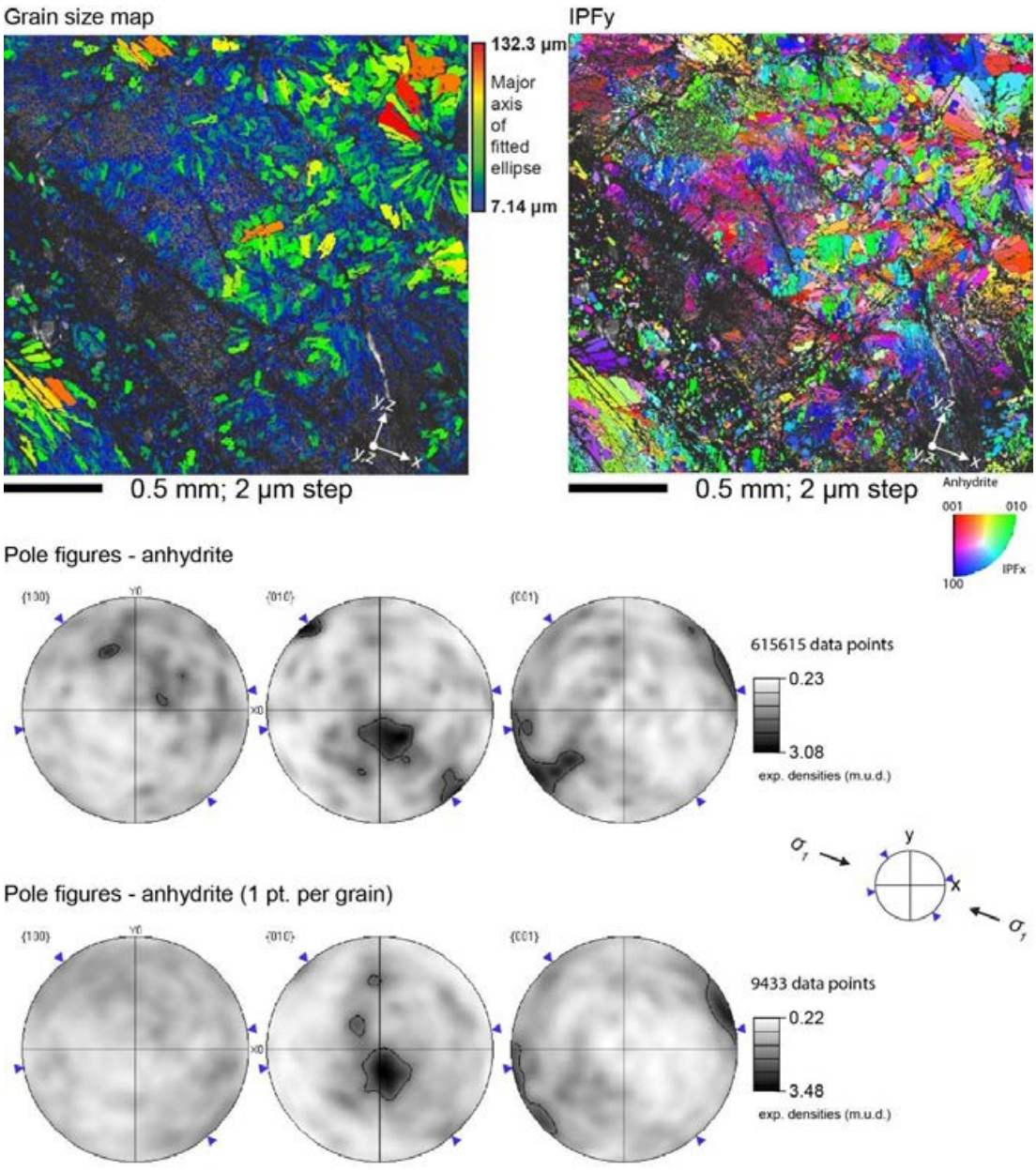

Figure D.24: Second part of backscatter diffraction analysis of a cataclastic shear zone in sample Ò2 (see Fig. D.23). Equal area, lower hemisphere pole figures of anhydrite based on the complete dataset and based on 1 point per grain subset.

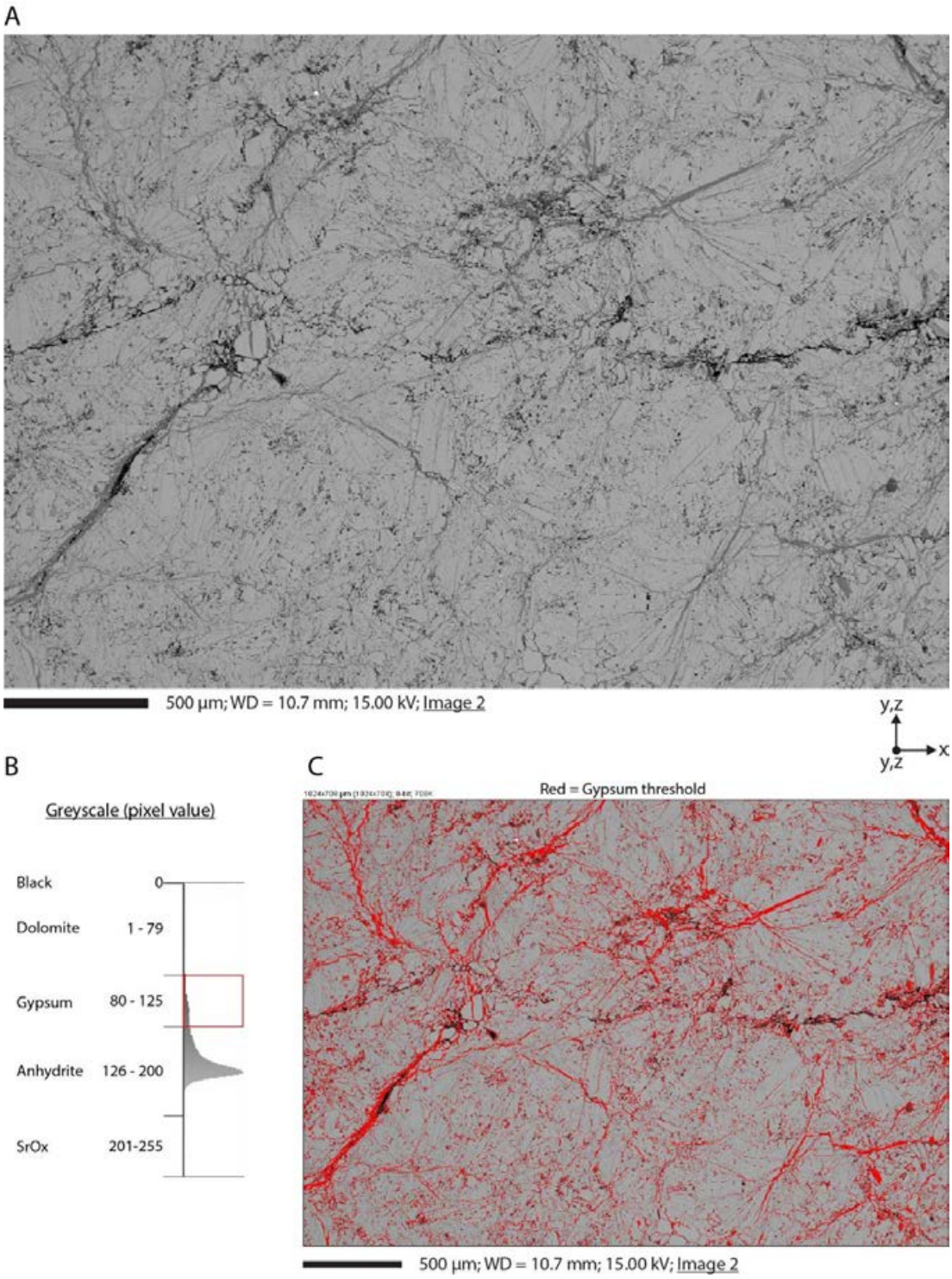

Figure D.25: Phase content analysis via greyscale threshold (ImageJ) from A: backscatter electron Image 2 of Òdena quarry sample Ò8 (AA-3). This sample went through a dry mode test and no signs of new formed gypsum was found. B: Greyscale threshold settings defined to quantify %. SrO_x = strontium oxides. C: Image 2 with all pixels that fall into the gypsum threshold in red. See table D.1 for further results.

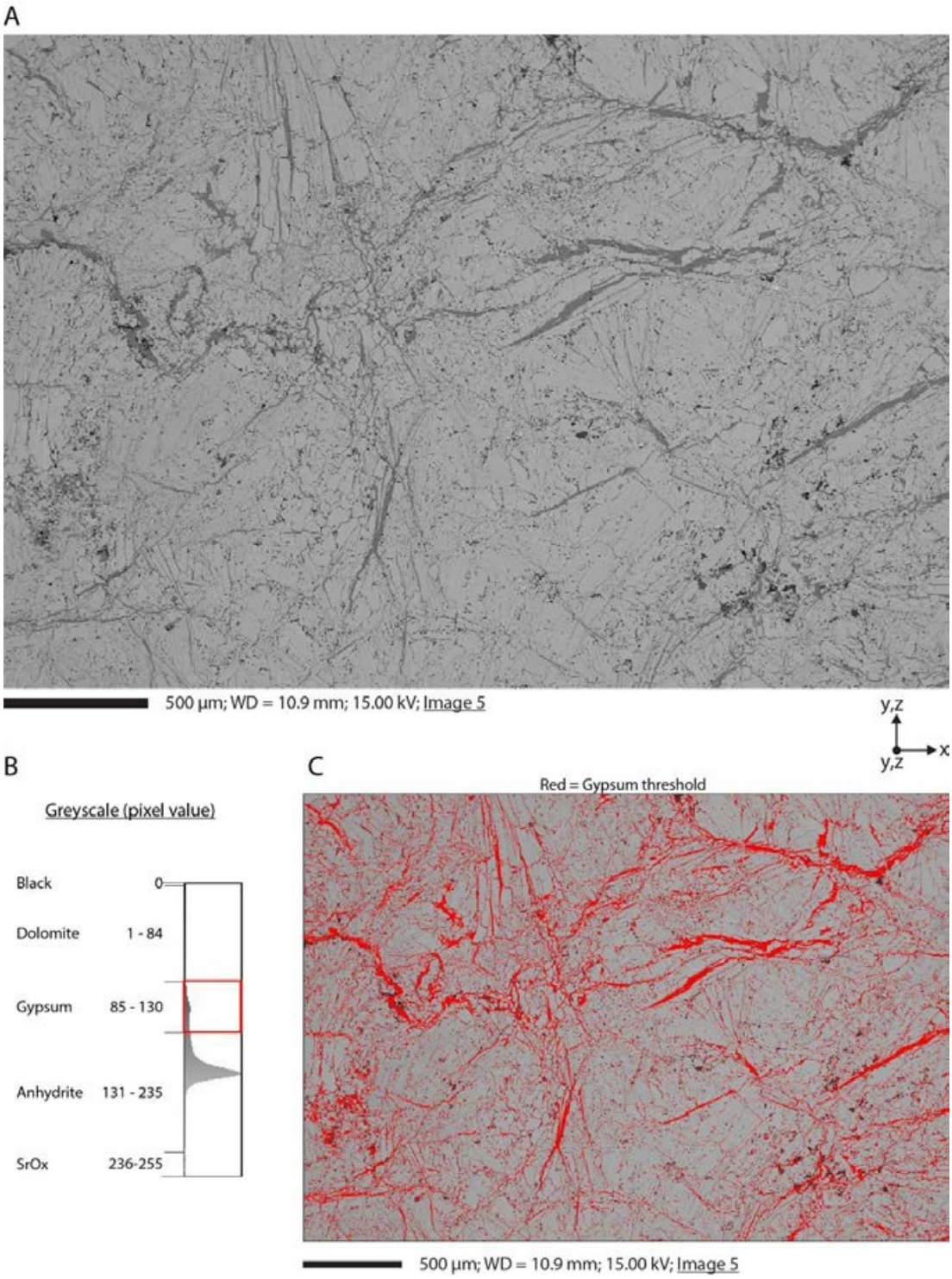

Figure D.26: Phase content analysis via greyscale threshold (ImageJ) from A: backscatter electron Image 5 of Òdena quarry sample Ò8 (AA-3). B: Greyscale threshold settings defined to quantify %. SrO_x = strontium oxides. C: Image 5 with all pixels that fall into the gypsum threshold in red. See table D.1 for further results.

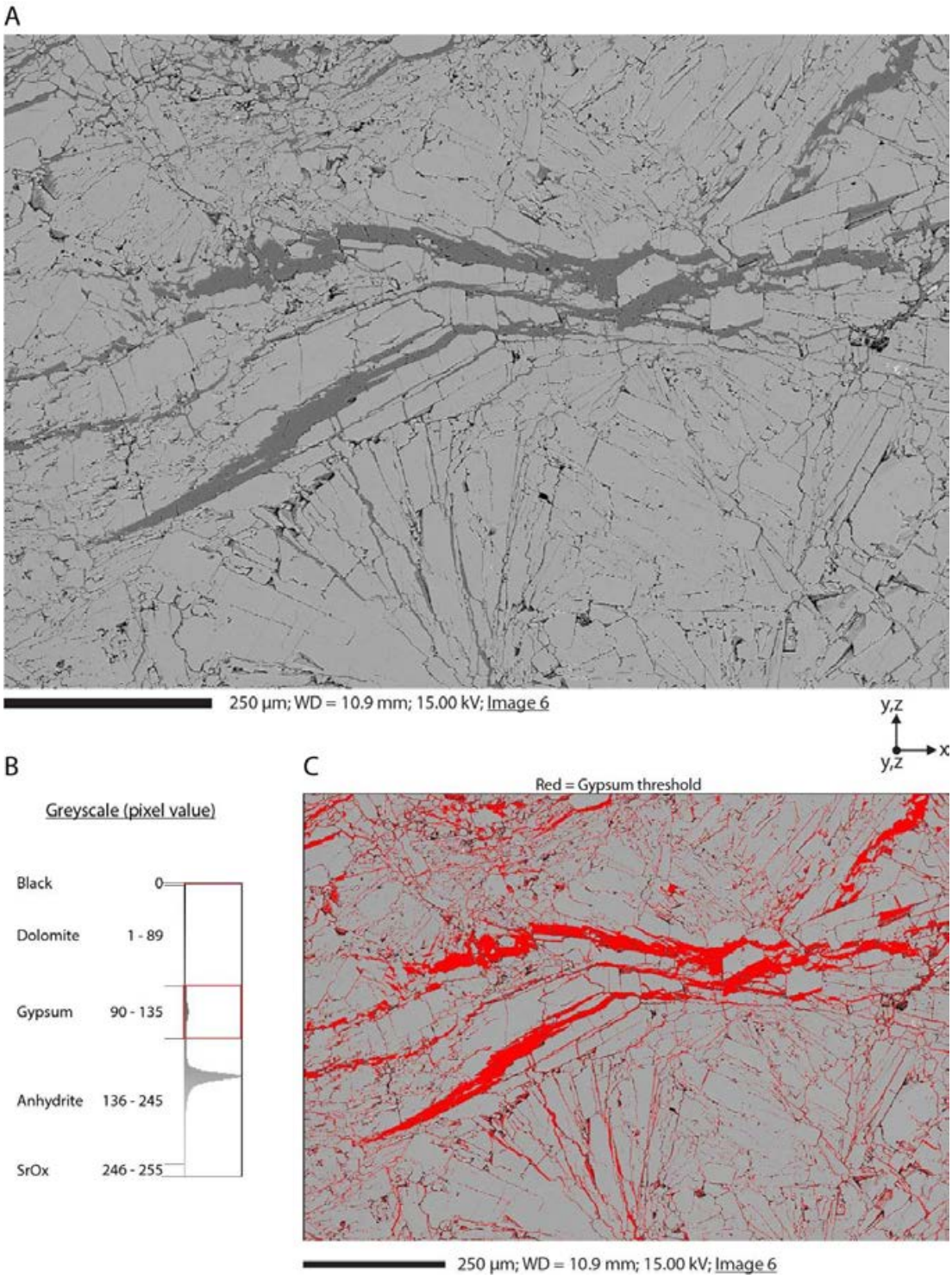

Figure D.27: Phase content analysis via greyscale threshold (ImageJ) from A: backscatter electron Image 6 of Òdena quarry sample Ò8 (AA-3). B: Greyscale threshold settings defined to quantify %. SrO_x = strontium oxides. C: Image 6 with all pixels that fall into the gypsum threshold in red. See table D.1 for further results.

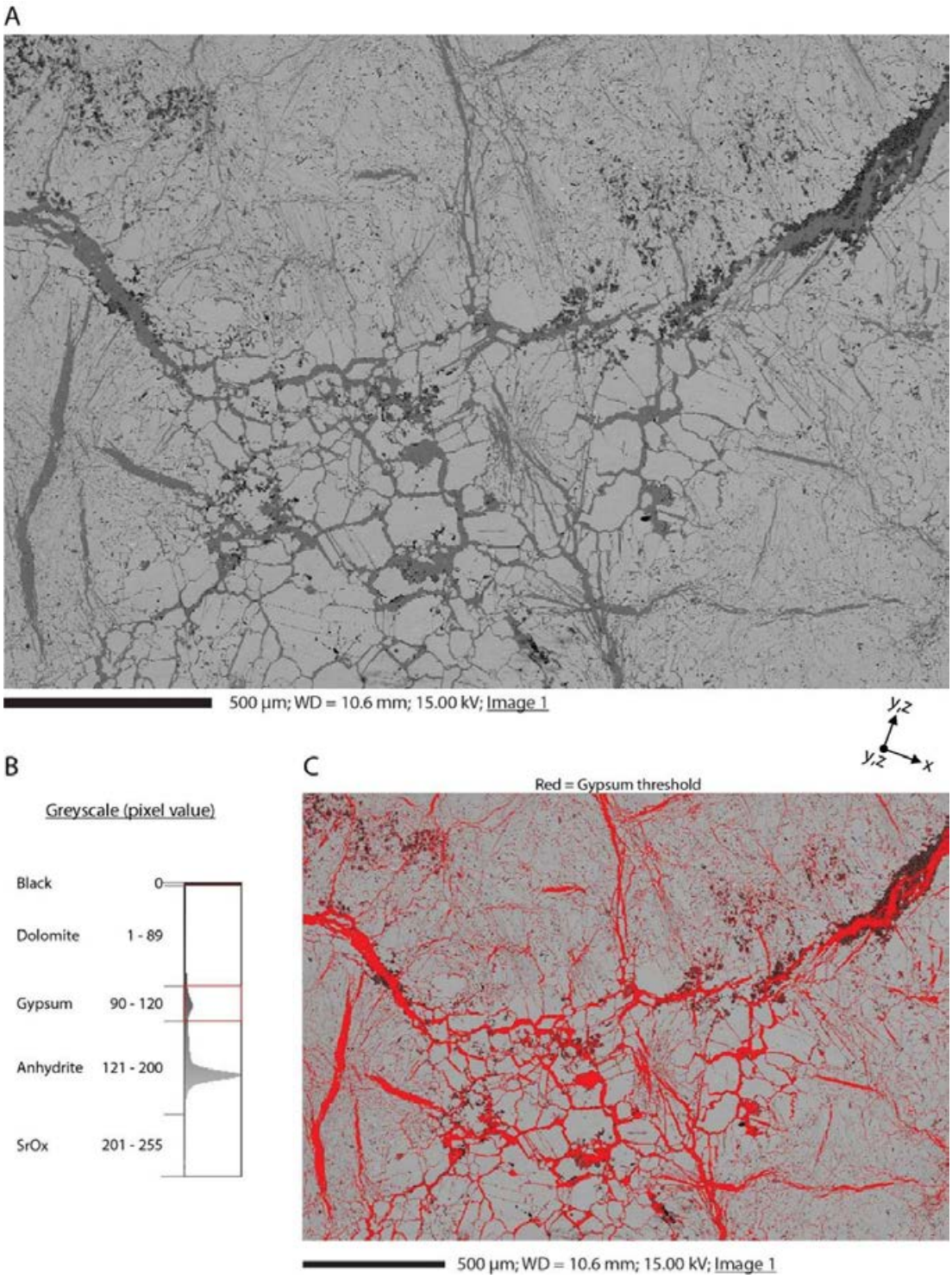

Figure D.28: Phase content analysis via greyscale threshold (ImageJ) from A: backscatter electron Image 1 of Òdena quarry sample Ò2 (BA-4) after steady state differential compaction (ssdc). The section where Image 1 was taken is from a part of the sample that shows no sign of shear fractures. B: Greyscale threshold settings defined to quantify %. SrO_x = strontium oxides. C: Image 1 with all pixels that fall into the gypsum threshold in red. See table D.1 for further results. The location of the image is marked as 'Image 1' in Figure D.20.

D.2 Tables

Table D.1: Phase content greyscale threshold analysis on four backscatter electron images from two Òdena quarry samples from sections with no visible impact from deformation or hydration. Image 1 is from BA-4h (Ò2) after steady state differential compaction, but from a section that shows no sign of hydration through the experiment. Figures D.25, D.26, D.27, and D.28 present the Images and thresholds used for the analysis. Hal = halite, gyp = gypsum, dol = dolomite, SrO_x = strontium oxide phase, black = open fractures. Deviation = difference between the image area and the sum of the pixels that were sorted by the greyscale threshold. SUM is the content calculated by adding phase area up, meaning that the different images were treated as one. Mean is the statistic mean of all four grey scale threshold case studies, and STDEV is the corresponding standard deviation. The marked values (bold) are the data presented as initial material phase content for Òdena quarry anhydrite in chapter 5 (Figure 5.6c).

	Ò8 (AA-3)			Ò2 (BA-4)			
	Image 2	Image 5	Image 6	Image 1	***SUM***	***Mean***	***STDEV***
Image Area [px²]	724992	724992	724992	724992	2899968		
Image Area [µm²]	724992.00	7080000.00	875482.57	2837203.17	11517677.74		
Anh Area [µm²]	616855.00	5943632.86	720518.20	2283682.42	9564688.49		
Gyp Area [µm²]	87018.00	962200.66	111973.72	403149.46	1564341.84	391085.46	406890.03
Dol Area [µm²]	20165.00	168674.00	39121.10	139005.57	366965.67	91741.42	73131.40
SrO_x Area [µm²]	96.00	175.78	227.08	5008.77	5507.63	1376.91	2421.84
Black [µm²]	858.00	5215.01	3654.93	6351.00	16078.93	4019.73	2379.99
Sum [µm²]	724992.00	7079898.32	875495.03	2837197.22	11517582.57	2879395.64	2961028.89
Deviation [µm²]	0.00	101.68	-12.46	5.96	95.17		
Deviation [%]	0.00	0.00	0.00	0.00	0.00083	0.00	0.00
Anh [%]	85.08	83.95	82.30	80.49	83.04	**82.96**	2.00
Gyp [%]	12.00	13.59	12.79	14.21	13.58	**13.15**	0.96
Dol [%]	2.78	2.38	4.47	4.90	3.19	**3.63**	1.24
SrO_x [%]	0.01	0.00	0.03	0.18	0.05	**0.05**	0.08
Black [%]	0.12	0.07	0.42	0.22	0.14	**0.21**	0.15